University of Technology Sydney

Faculty of Engineering and Information Technology

# An Investigation of Free Surface Hydraulic Structures Using Large Eddy Simulation and Computational Fluid Dynamics

**Peter David McKellar Brady**

A dissertation submitted in fulfilment of the
requirements for the degree of Doctor of Philosophy.

13 April 2011

*Supervisors:*

Adjunct Professor John Reizes

Dr Matthew Gaston

# CERTIFICATE OF ORIGINALITY

I certify that the work in this dissertation has not previously been submitted for a degree nor has it been submitted as part of requirements for a degree except as fully acknowledged within the text.

I also certify that the dissertation has been written by me. Any help that I have received in my research work and the preparation of the dissertation itself has been acknowledged. In addition, I certify that all information sources and literature used are indicated in the dissertation.

Production Note:
Signature removed prior to publication.

Signature of Candidate

# Acknowledgements

The author wishes to specifically thank his supervisors who have contributed the most to the successful completion of this project: Adjunct Professor John Reizes and Dr Matthew Gaston. Without their understanding, support and input this work would not have reached such a satisfactory conclusion. The author also wishes to thank his previous supervisors, Professors Archie Johnston and Simon Beecham, for their past contributions.

This highly computationally intensive research would not have been possible without the support of the Faculty of Engineering and IT computer support program and personnel, including: Robert Corran, Anthony Dumbrell, James Lucas, Frank Ng, Phi Nguyen, Andrew de Thame, Michel de la Villefromoy and Peter Yardley. In particular, having access to the Faculty student laboratories over the semester breaks to run grid computation projects was much appreciated.

I must also thank my family and friends for their support during this work – especially my parents for their love and extensive support, in particular financial at the later stages of this research. Finally, I would like to extend a thank you to my friend and figure skating coach, Jean McGregor, for her support and understanding of my numerous last minute absences and skipped training sessions.

# Contents

## *Table of Contents*

## List of Figures

## List of Tables

## List of Appendices

## *Nomenclature*

### English Symbols

| Symbol | Definition |
|---|---|
| $A$ | area |
| $a$ | finite volume equation general coefficient variable |
| $b$, $B$ | bottom face/cell |
| $C_s$ | Smagorinsky constant |
| $C_{\varepsilon 1}$, $C_{\varepsilon 2}$, $C_\mu$ | closure constants for the $k-\varepsilon$ RANS model |
| $c_{surf}$ | surface coefficient for VOF surface reconstruction |
| $c_i$ and $c_\mu$ | constants of proportionality for the viscous and inertial "effects" |
| $d$ | circular cylinder diameter, square cylinder side length |
| $e$, $E$ | east cell face/cell |
| $E_k$ | kinetic energy |
| $E(\kappa)$ | energy as a function of wave number |
| $F_E$ | ensemble average of a general function |
| $f_i$ | inertial effects |
| $f$ | general function |
| $F_p$ | force due to pressure |
| $F_{st}$ | surface tension forces |
| $F_T$ | time average of a general function |
| $F$ | volume fraction with VOF |
| $F_\vartheta$ | volumetric, spatial, average of a general function |
| $f_\mu$ | viscous effects |
| $F_s$ | wall shear stress |

| | |
|---|---|
| $G$ | filter function |
| $\mathbf{g}$ | gravitation vector |
| $H$ | channel height |
| $h$ | depth from a reference point, for example when computing hydrostatic pressures |
| $I_{\phi}$ | general time integral for a variable $\phi$ |
| $k$ | turbulent kinetic energy |
| $l$ | integral length |
| $l_c$ | characteristic length |
| $m$ | mass |
| $n/N$ | north cell face/cell |
| $N$ | cell count, number of experimental repetitions |
| $\mathbf{n}$ | surface normal vector |
| $P$ | a general point when discussing the finite volume method |
| $p$ | thermodynamic pressure |
| $p_h$ | hydrostatic pressure |
| $S_{\phi}$ | source term for variable $\phi$ |
| $s/S$ | south cell face/cell |
| $S_{ij}$ | resolved strain rate tensor with LES |
| $s_{ij}$ | strain rate tensor with RANS |
| $\overline{S}$ | volume averaged source term |
| $t$ | time (s); top cell face |
| $T$ | time, when used in the temporal RANS average, or the top cell in the finite volume method |
| $t_{ij}$ | viscous stress tensor with RANS models |

| | |
|---|---|
| $U_i$ | average velocity in the *i*th direction |
| $u_c$ | characteristic velocity |
| $\hat{u}_i$ | filtered velocity with each hat representing one filtering iteration |
| $u_i'$ | fluctuating velocity in the *i*th direction |
| $u_i$ | instantaneous total velocity in the *i*th direction |
| $u^+$ | non-dimensional wall velocity, $u^+ \triangleq \frac{U}{u_\tau}$ |
| u, v, w | principle velocity components in a Cartesian reference frame |
| $u_\tau$ | wall velocity, $u_\tau \triangleq \sqrt{\frac{\tau_w}{\rho}}$ |
| **u** | velocity vector (m/s) |
| $U_\infty$ | free stream velocity |
| *w/W* | west cell face/cell |
| $x_i$ | *i*th coordinate direction |
| **x** | spatial coordinate vector |
| x, y, z | principle Cartesian coordinate axes |
| $y^+$ | non-dimensional wall distance, $y^+ \triangleq \frac{u_\tau y}{\nu}$ |

## Greek Symbols

| Symbol | Definition |
|---|---|
| $\sigma_k$, $\sigma_\varepsilon$ | closure constants for the $k-\varepsilon$ RANS model |
| $\theta$ | wall contact angel with VOF |
| $\rho$ | density |
| $\Gamma$ | diffusion coefficient when discussing the finite volume method |
| $\varepsilon$ | dissipation rate |
| $\mu$ | dynamic viscosity |

| | |
|---|---|
| $\tau_{ij}$ | fluid stress tensor for a general fluid; specific Reynolds stress tensor with RANS |
| $\alpha$ | $\frac{1}{\mathrm{Re}}$ |
| $\nu = \frac{\mu}{\rho}$ | kinematic viscosity |
| $\eta$ | Kolmogorov length |
| $\tau$ | Kolmogorov time scale |
| $\upsilon$ | Kolmogorov velocity scale |
| $\Delta$ | LES filter width |
| $\xi$ | point distance vector when filtering for LES |
| $\sigma$ | surface tension coefficient |
| $\nu_T$ | turbulent viscosity |
| $\lambda$ | wave length |
| $\kappa$ | wave number |
| $\tau_w$ | wall shear stress |
| $\vartheta$ | volume |
| $\delta$ | a small increment of a variable, for example $\delta x$ |
| $\phi$, $\psi$, $\xi$ | general variables used for the explanation of RANS correlations |

## Mathematical Operators

| | |
|---|---|
| $\nabla\times$ | curl operator |
| $\nabla\cdot$ | divergence operator |
| $\nabla$ | gradient operator |
| $\frac{D}{Dt}$ | substantive derivative |
| $\mathbb{N}(u_i)$ | Navier-Stokes operator with RANS |

| | |
|---|---|
| $\Delta t$ | a small time increment |
| $\Delta x$ | a small spatial increment |
| $O$ | order operator |

## Subscripts

| Symbol | Definition |
|---|---|
| $i, j, k$ | directional indices |
| $w$ | wall |

## Superscripts

| Symbol | Definition |
|---|---|
| $^{o}$ | indicates a variable at the current time step |
| $^{+}$ | non-dimensional quantity |
| $UP$ | variable computed from a first order upwind scheme |
| $2UP$ | variable computed from a second order upwind scheme |

## Other Operators and Variables

| Symbol | Definition |
|---|---|
| $\eth$ | general scalar when discussing the finite volume method |
| $\mathfrak{X}$ | blending factor for finite volume time integration |
| $\mathfrak{S}$ | blending factor for the finite difference schemes between a first order upwind method and a higher degree scheme |
| $\mathfrak{K}$ | geometric blending factor for central difference schemes |
| $\mathfrak{L}$ | length from the centre of the cylinder to the outlet boundary |
| $\mathfrak{F}$ | wall normal cell length. |
| $\mathfrak{D}$ | two-dimensional distance of a point from a line |

## Non-dimensional Groups

| Symbol | Definition |
|---|---|
| $\mathrm{Re} \triangleq \frac{u_c l_c}{\nu}$ | Reynolds number based on a characteristic velocity and length |
| $\mathrm{Re}_\tau$ | turbulent Reynolds number |
| $\mathrm{Re}_H$ | Reynolds number based on the channel height |
| $\mathrm{We} \triangleq \frac{\rho u_c^2 l_c}{\sigma}$ | Weber number for describing surface tension |

## Acronyms

| Acronym | Definition |
|---|---|
| 2D | Two Dimensions |
| 2OU | 2nd Order Upwind |
| 3D | Three Dimensions |
| CFD | Computational Fluid Dynamics |
| CFL | Courant-Freidrichs-Lewy |
| CPU | Central Processing Unit |
| DCP | Development Control Plans |
| DES | Detached Eddy Simulation |
| DFT | Digital Fourier Transform |
| DLES2 | 2nd Conference on Dynamic and Large Eddy Simulation |
| DNS | Direct Numerical Simulation |
| FS | Free Surface |
| GPT | Gross Pollutant Traps |
| HEC-RAS | Hydraulic Engineering Corp – River Analysis System |
| HR | High Resolution |
| HS | High Speed |

| | |
|---|---|
| ILES | Implicit Large Eddy Simulation |
| L&R | Abbreviation of papers by D Lynn and W Rodi (Lyn and Rodi, 1994, Lyn et al., 1995) |
| LDA | Laser Doppler Anemometry |
| LEP | Local Environment Plans |
| LES | Large Eddy Simulation |
| LES Dyn | Dynamic Large Eddy Simulation model |
| LES LD | Locally Dynamics Large Eddy Simulation model |
| LR | Low Resolution |
| LS | Low Speed |
| MAC | Marker And Cell |
| MILES | Monotonically Integrated Large Eddy Simulation |
| MR | Medium Resolution |
| PIV | Particle Image Velocimetry |
| PLIC | Piecewise Linear interface Construction |
| POTEO | Protection of the Environment Operations |
| PSD | Power Spectral Density |
| RAM | Random Access Memory |
| RANS | Reynolds Averaged Navier-Stokes |
| RMS | Root Mean Squared |
| SF | Single Fluid |
| SGS | Sub-Grid Scale |
| SIMPLEC | Semi-Implicit Method for Pressure Linked Equations - Corrected |
| SLIC | Single Linear Interface Construction |
| SMAG | Smagorinsky |

| | |
|---|---|
| SPH | Smoothed Particle Hydrodynamics |
| UNSW | University of New South Wales |
| UTS | University of Technology Sydney |
| VOF | Volume of Fluid |
| WT | Water Tunnel geometric configuration |

# Abstract

The work presented in this dissertation is essentially a thesis in three distinct parts (single fluid validation, two fluid validation and data analysis) rather than the established approach for the development of a novel computational fluid dynamics solver. First, the progression is a traditional one, in which an existing technique was applied to a new area and subsequently extended. Second, from detailed analysis of the large volume of data generated in the validation process, a number of insights were gained into the flow features of the prototypes investigated that extended beyond a traditional validation study and discovered a number of new physical phenomena.

Previous researchers have used monotonically integrated large eddy simulation (MILES) methods to investigate a range of flows including turbulent decay in rotary valve engines and rocket body dynamics. MLES methods have the distinct advantage over standard LES simulation techniques in that they promise to provide similar levels of detail and accuracy but at a fraction of the computational cost. However, to the author's knowledge these techniques have not been applied to the prototype problem of this thesis: cylinders in cross flow without and with free surfaces. Hence the *raison d'étre* of this thesis: to apply a faster yet equally accurate CFD method to a free surface problem via a validated single fluid investigation. Specifically, the progression was to first validate the method against a single right square cylinder in cross flow without a free surface and then to extend the method to a right circular cylinder in cross flow with a free surface.

With the right square cylinder without free surface the research focussed on the extensively studied configuration of a two dimensional square cylinder at a Reynolds number of $22 \times 10^3$. Despite the agreement of the validation parameters with published data, detailed examination of the flow field revealed inconsistencies in the modelled results. In particular the power spectrum decay of the data appear too "easy" to obtain, indicating possible flaws in the theoretical basis, while correlation data apparently supports a conclusion that the previous assumption of four diameters domain width is too narrow to provide an uncorrelated flow region.

The free surface physics of the circular cylinder model was captured with the volume of fluid method and was applied to Reynolds number flows based on cylinder diameter of between $27 \times 10^3$ and $54 \times 10^3$. These flows, at the provided grid resolution, push the

lower boundary of what can be called MILES, yet interpretations of the results indicates that the model is accurately capturing the physics of the flows.

# 1. Introduction

## *1.1. Scales of Fluid Dynamics*

Fluid dynamics is a diverse discipline that encompasses a vast range of length and time scales. The characteristic length scale, $l_c$, is often used as a measure is, therefore, generally dominant. For example, the smallest scales, where $l_c = O(100\text{pm})$, are connected with the study of phenomena such as rarefied gases and atmospheric proton showers (Surendran, 2006, Bergmann et al., 2007) so that Monte Carlo simulations dominate. Conversely, at galactic scales, where $l_c = O(10\text{Em})$, smoothed particle hydrodynamic techniques (Bekki, 2004, Bate, 2008) are generally utilised. This spread of length scale equates to a change in $l_c$ of over 30 orders of magnitude, as illustrated in Figure 1-1. However, it must be noted that there is no hard division between the scales of $l_c$ at which the different approaches for studying the various phenomena associated with particular scales are applicable. For example, the lower boundary of the computational fluid dynamics region overlaps with the upper boundary of Monte Carlo simulations. Similarly, smoothed particle hydrodynamics simulations have been employed on problems with $l_c \le O(10\text{m})$ in contrast to the galactic scales for which the method was originally designed (Monaghan, 1988, Monaghan et al., 1994).

Within this broad expanse of length scales, civil engineers predominately operate in the range of

$$10^{-2}\,\text{m} \le l_c \le 10^{4}\,\text{m}. \tag{1.1}$$

Over this subset of length scales, the lower bound of Equation (1.1) is roughly equivalent to the diameter of the pipes that would be used in a domestic water supply system. Alternatively, at the upper bound of Equation (1.1), $l_c$ would be related to the length of an entire river basin.

Despite the possibility, and the appeal due to its apparent simplicity, of reducing a fluid dynamics problem to merely defining a length scale and then choosing the most appropriate simulation technique, there are external constraints that must be satisfied.

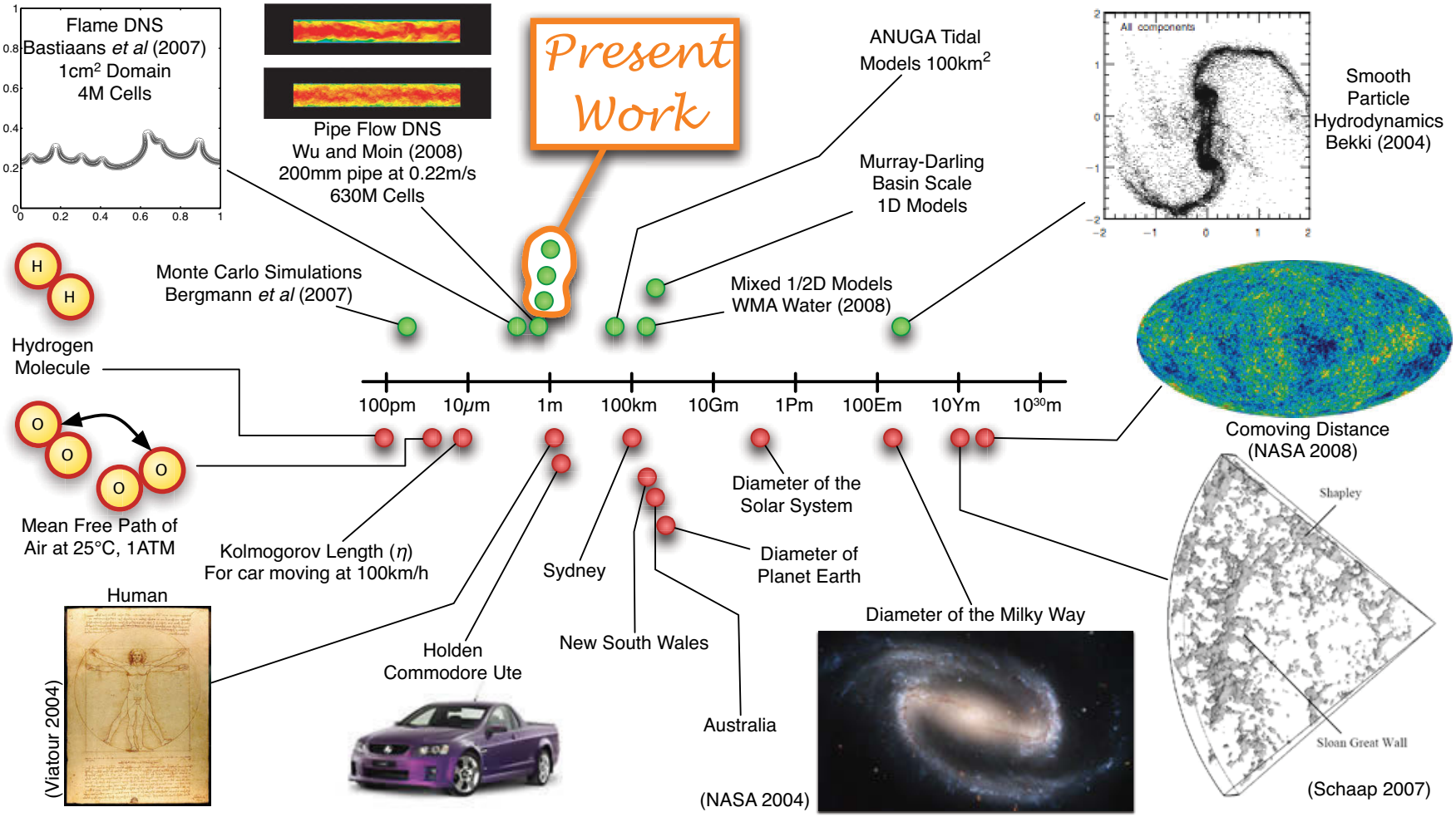


**Figure 1-1 – Relative scales of fluid mechanics and dynamics research. Points above the number line represent published model scales with points below the number line representative of identifiable physical objects for comparison of sizes.**

In a manner reminiscent of an arms race, or, perhaps in a civil engineering context at least, a feedback loop, there is always a tandem development of the legislative frameworks and simulation techniques.

## *1.2. Policy Framework*

In recent years, spurred by a voting population with both an increased environmental awareness and a consequent willingness to demand a clean environment, a need has developed for asset owners to reduce water based pollutant loads that are discharged into receiving waters. In a response to these concerns a number of landmark planning instruments have been enacted at all levels of government from international treaties to local planning guidelines. In the Australian context these instruments include the local government development control plans (DCP) and local environment plans (LEP), for example Hornsby Shire Council (1997) and state government legislation, such as the *Protection of the Environment Operations Act 1997* (NSW).

These DCP and LEP planning instruments are limited in their effectiveness in that they apply only to future developments whereas asset managers also have a number of responsibilities under the *POTEO Act 1997* to increase the effectiveness of their current systems. Specifically for the greater Sydney metropolitan area, the asset managers are predominantly statutory authorities such as the Sydney Water Corporation or local government authorities and the discharges are made through wet weather sewer overflows or uncontrolled stormwater runoff. Traditionally the level of funding that was available for retrofits has been less than that for developments. However, to address this imbalance some local government authorities, for example Hornsby Shire Council, have implemented catchment remediation levies (Hornsby Shire Council, 2009), which tax residents to provide funds for retrofits and developments that are not associated with activities that would nominally be covered under LEPs or DCPs.

Both of these scenarios – green/brownfield development or retrofitting – suffer from the same problems. Firstly, while the planning and legislative instruments provide detailed mechanisms to assess and specify the level of discharges that are allowed from specific sites, they do not specify the methods that designers must use to meet those requirements. Secondly, there is only so far that source controls of pollutants can be used successfully and then the only remaining choice is to treat the effluent prior to discharge with the use of overflow type devices. Thirdly, if stormwater and overflow

devices must be used, the individual devices must be designed or evaluated to test their efficacy.

While physical laboratory testing of scaled devices is, and will no doubt for some time remain an effective method of evaluating alternate designs, there are a number of inherent difficulties associated with laboratory scale testing. Firstly, performing a parametric study with a large number of models to investigate a distribution of variables can be very costly due to the time and labour that is intrinsic to the experimental process. Secondly, as with all similitude problems, not all parameters can be scaled in the same way. Specifically in the case of free surface flows, the experimenter can generally scale either the free surface (Froude scaling) effects or the turbulent (Reynolds scaling) phenomena but not both simultaneously. For example, changing the length scale while keeping a constant Re changes Fr, and similarly for a constant Fr alters Re, as shown in Table 1-1.

**Table 1-1 – Example of the limitations of simultaneously scaling both Re and Fr.**

| Parameter | Bridge Pier | 50mm Scale Constant $Re_d$ | 50mm Scale Constant $Fr_d$ | Units |
|---|---|---|---|---|
| $d$ | 1 | 0.05 | 0.05 | m |
| $U$ | 2 | 40.00 | 0.45 | m/s |
| $\nu$ | $1.00\times10^{6}$ | $1.00\times10^{6}$ | $1.00\times10^{6}$ | $m^2/s$ |
| $Re_d$ | $2.00\times10^{6}$ | $2.00\times10^{6}$ | $2.24\times10^{4}$ | |
| $Fr_d$ | 0.41 | 3261.98 | 0.41 | |

Finally, there are some fluids which, due to their hazardous nature, cannot be easily employed in a laboratory. Therefore, selected laboratory physical investigations must be exploited in conjunction with computational methods. Further, it must then be asked if the software available to civil designers is capable of working in the range $10^{-2}\,\mathrm{m} \le l_c \le 10^{1}\,\mathrm{m}$.

## 1.3. The Scales and Types of Civil Engineering Simulations

In civil design work in Australia there are three classes of simulation software used with the classification based on the mathematical approximations they employ. Unfortunately, as the level of the "approximations" is increased there is, generally, a corresponding decrease in the detail of the simulation results. These approximations were introduced to overcome a, perhaps perceived, lack of computational resources and the axiom "any answer is better than no answer".

Primarily these approximations are based on a reduction of the spatial dimensions of the simulation and a corresponding simplification of the mathematical model used within the simulations. At the largest scales, such as a river basin, one-dimensional models will generally be used, whereas for street scale flood routing two- and three-dimensional models are now commonly used[*]. There are a number of commercial and open source codes that are in common use in Australia (listed by their spatial approximations) including:

1. One dimensional: HEC-RAS (U.S. Army Corps of Engineers, 2008), MIKE11 (DHI Group, 2008b) and SOBEK River (Delft Hydraulics Software, 2008b);
2. Two dimensional: TUFLOW (*TUFLOW*, 2008), MIKE21 (DHI Group, 2008c), SOBEK Urban (Delft Hydraulics Software, 2008c), RMA-2 (Coastal and Hydraulics Laboratory, 2008a) and ANUGA (*ANUGA*, 2008);
3. Three dimensional: MIKE3 (DHI Group, 2008a), RMA-10 (Coastal and Hydraulics Laboratory, 2008b) and DELFT3D (Delft Hydraulics Software, 2008a).

[*] With all these methods, time is not included as a dimension but is implicitly assumed to be present. Therefore, a one-dimensional simulation is linear in space even though it will generally be run in an unsteady temporal configuration.

These codes all have a specific focus in that they are designed for the simulation of flows at scales of $l_c \gg 1\text{m}$ and are of no use for detailed design and analysis at scales in the order of $10^{-2}\text{m} \le l_c \le 10^{1}\text{m}$. Therefore, as specific software techniques must be developed to fill this void the characteristics of the flows and devices should be thoroughly understood prior to examining any numerical approaches.

## *1.4. Sewer Overflows and Stormwater Discharge Devices*

### 1.4.1. Characteristics of Flows to Be Simulated

For sewer overflow structures and stormwater gross pollutant traps* (GPT) there are three broad classes of pollutants that must be managed, namely physical, chemical and biological (Shon et al., 2006). Each of these pollutants possesses different properties that, in turn, require different treatment or capture procedures to manage.

The first class of pollutants, physical pollutants, include items such as suspended sediments and particulate matter as well as anthropogenic litter such as discarded drink bottles, plastic bags and syringes (Wong, 2005). However, because the size distribution of the suspended sediments, while varying significantly between individual catchments, ranges from $O(1\mu\text{m})$ to $O(10\text{mm})$ (Walker et al., 1999), as illustrated in Figure 1-2, the simultaneous separation of all the components within one device is non-trivial.

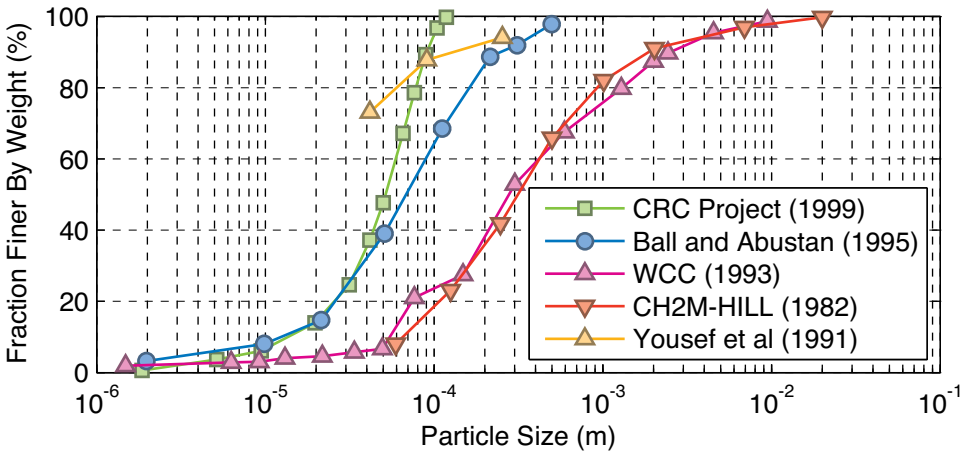


**Figure 1-2 – Particle size distribution of solids recovered from stormwater runoff from road catchments, extracted from a meta-study by Walker et al (1999).**

* For the remainder of this chapter generic overflow structures and stormwater gross pollutant traps will be referred to as "devices".

In addition to the suspended solids, many devices are also required to trap gross pollutants, which are generally human litter and, in the case of stormwater devices, include waste such as drink cans and wrapping paper that has been discarded. In contrast, sewer overflow devices may have to deal with smaller objects such as condoms, tampons and "grit" from faecal waste (United States Environmental Protection Agency, 2004). Figure 1-3 shows an image of the sump of a continuous deflection type stormwater device that is full of gross pollutants. A typical location for a device of this type would be downstream of a shopping precinct or dense urban precinct.

**Figure 1-3 – Photograph of the full sump of a continuous deflection device prior to cleaning (Rocla, 2009).**

Sewer overflow devices, in particular, can be expected to deal with high concentrations of both of the remaining two classes of pollutants, i.e. chemical and biological. Some of these pollutants are dissolved within the effluent and, hence, cannot be removed during the, nominally, short residence time in an overflow device. However, the remaining pollutants are either physically or chemically bonded to the suspended solids (Wong, 2005) and, therefore, can potentially be removed through filtration.

While the sources of chemical and biological pollutants are remarkably common across different catchments, as listed in Table 1-2, the corresponding concentrations may vary significantly. For example, the coliform load for raw sewage would be several orders of magnitude higher than for urban stormwater runoff. With these typical pollutants in mind, there are a number of devices and systems currently in place to manage these flows.

**Table 1-2 – Major types of chemical and biological pollutants in sewage and stormwater and their principle sources, from Wong (2005) and Shon et al (2006).**

| Type of Pollutant | Major Source/s |
|---|---|
| Biochemical Oxygen Demand | Oxidation of sulphides and ferrous irons |
| Carbohydrate | Domestic, commercial and agricultural wastes |
| Chemical Oxygen Demand | Empirically related to organic carbon or organic matter |
| Coliforms | Faecal contamination; domestic wastes |
| Endocrine Disrupters | Domestic, commercial and agricultural wastes |
| Fat, Oil and Grease | Domestic, commercial and industrial wastes |
| Heavy Metals, e.g. lead and cadmium | Industrial wastes |
| Nitrogen | Domestic and agricultural wastes |
| Pesticides | Agricultural runoff |
| pH | Industrial wastes; natural runoff |
| Phenols | Industrial wastes |
| Phosphorous | Domestic, commercial and agricultural wastes; natural runoff |
| Surfactants | Industrial wastes |
| Total Organic Carbon | Natural organic substances |
| Viruses | Domestic wastes |

### 1.4.2. Common Overflow Management Devices Installed

For the management of overflows there are several devices in common use which can be classified in two general types namely physical filtration devices or chemical and/or biological treatment devices. Despite the clear distinction between these devices the best practise for stormwater management is to include both types in a two-stage treatment system (Wong, 2005). These best management recommendations were recently implemented by Hornsby Shire Council at the Clarinda Street stormwater

discharge where a three stage, primary gross pollutant trap (GPT) and two-stage macrophyte pond for nutrient removal and aeration, was installed with associated stream way rehabilitation. A schematic representation of this system is shown in Figure 1-4.

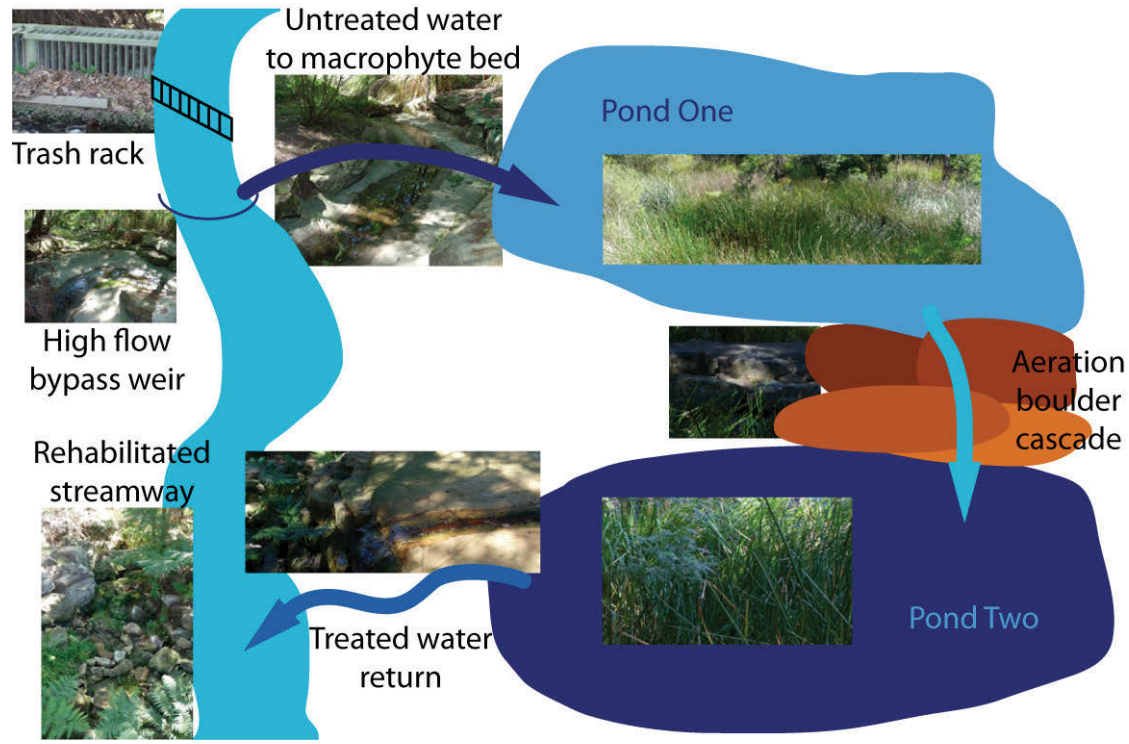


**Figure 1-4 – Schematic representation, with indicative photographs, of a three stage offline stormwater treatment system and associated creek rehabilitation.**

As suitable sites, and sufficient funds, are generally not available to install such extensive treatment systems, smaller scale filtration only devices are often installed in a stand-alone configuration where the chemical and biological contaminant loads are low relative to the physical pollutant load, as shown in Figure 1-5 for a typical system.


**Figure 1-5 – Trash rack GPT, with trapped leaf litter and low flow outlet.**

In contrast, sewer overflows are often unfiltered and discharge into natural and engineering waterways, as shown in Figure 1-6, where the sewage is discharged into a concrete lined creek near Punchbowl in the west of Sydney, NSW.

**Figure 1-6 – A photograph of sewer overflow structure in Sydney that is designed to discharge effluent directly into a concrete lined stormwater channel near Punchbowl (Avis, 2001).**

For all mechanical filtration systems, the flows are essentially chemically frozen in that the devices perform no direct treatment on the dissolved contaminants. Some researchers have proposed that chemical dosing could be installed (Wojtenko et al., 2002) to treat the discharges but installations such as these would be relatively expensive to implement and maintain for low-frequency events. By definition overflow devices only operate infrequently at high flows when the biological and dissolved chemical loads are at their lowest, having been diluted, but when the physical pollutants are highest after they have been mobilised in the high flows (Beecham, 1991, Wong, 2005). Therefore, to reduce operating costs and improve functionality the design of discharge devices could be improved.

### 1.4.3. Sewer and Combined Sewer Overflow Design and Research

Research into sewer overflow management, or at least the presentation of case studies of field sites, was presented in an annual literature review by Moffa et al (1983) who examined over 50 papers published, predominantly in the USA, in the previous year. They identified six key areas of research, namely:

1. "Characteristics" or descriptions of the runoff constitution.
2. "Hydrology" which is, apparently a misclassification, in that most of the research listed applied hydraulic routing models to sewer systems instead of hydrologic computations of system load.
3. "Receiving water" that investigated the effect of sewer overflows on environment that the overflows discharged into.
4. "Control" that detailed case studies and research target at developing control systems for the management of sewer systems that contained sewer overflow structures.
5. "Treatment", which as the name suggests lists papers that detail research into devices designed to treat rather than just filter sewage.
6. "Management" that listed papers detailing case studies of regional, predominantly local government, administration authorities dealing with the operation of sewer overflow devices.

None of the 54 papers listed appeared to discuss or investigate design methods or operating flow patterns of sewer overflow devices.

Alternatively, in the United Kingdom at the University of Sheffield with researchers such as Adrian Saul the focus was more on the design of individual devices. In 1996 this research group formed the core of the loose coalition titled the "*Combined Sewer Overflow Research Club"* (Thompson, 2006). The "club" swiftly increased its membership base to include the major research institutions engaged in sewer overflow research and "every UK water company" (Thompson, 2006) and was incorporated in March 1997 under the auspices of the UK Water Research organisation (Thompson, 2006).

Initial research into the use of sewer overflows, primarily as flood control mechanisms, was performed by Saul and Delo (1983) however focus soon shifted to pollution control rather than flood management. As sewer overflow devices do not moderate chemical or biological pollutants, research focussed on the efficiency of the removal of "aesthetic" pollutants where aesthetic pollutants are the gross pollutants visible to the general population, that is the grits, rags and suspended solids. Beecham (1991) therefore, investigated the split between retained and discharged solids using laboratory-based experiments that counted the distribution of seed particles between the two outlets of model flumes and devices, as shown in Figure 1-7. Research such as this, while producing useful data for the design and operation of sewer overflow devices, is necessarily limited to the usual laboratory approximations, in particular: scale reductions, idealised fluids and model pollutants. Consequently, to avoid scale similarity problems, CFD can be used to model full-scale devices with real fluids.

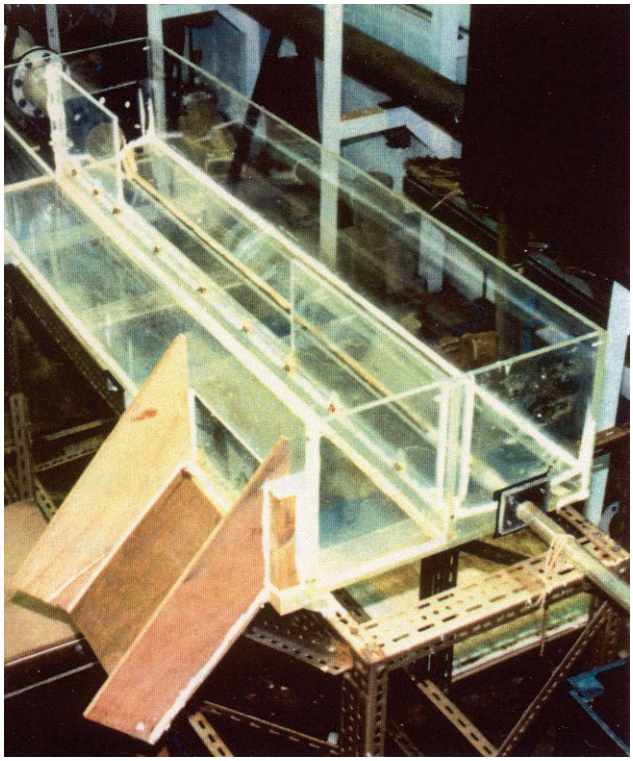

**Figure 1-7 – Photograph of a scale model of a single side weir sewer overflow chamber (Beecham, 1991). The overflow outlet is the wooden chute shown in the foreground while the low flow outlet pipe is located on the bottom right of the image.**

The increase in the availability of both computational resources and CFD packages in the 1990's lead to an increase in the use of, and publication of results from, CFD based research into sewer overflow structures. From the University of Sheffield, Stovin and her colleagues focussed on investigating particulate settlement within sewer storage chambers using a mixture of CFD and laboratory experimentation (Stovin and Saul, 1996, 1998, 2000, Stovin et al., 2002a, Stovin et al., 2002b).

A $2 \times 0.972 \times 0.196$ m (long by wide by high) chamber was used in their numerical simulations, as shown in Figure 1-8. With the entry flow rate fixed at 15.9 L/s, and the statement that this was a steady condition, the mean inlet velocity was 0.561 m/s and a Reynolds number of

$$\mathrm{Re}_{d_{inlet}} = \frac{\overline{U_{inlet}} d}{\nu_{water}} \cong 100 \times 10^3 \tag{1.2}$$

in which $d$ is the pipe diameter. Similarly, the mean velocity at the outlet pipe was 0.90m/s with a corresponding Reynolds number of $135 \times 10^3$. Hence, at a minimum the inlet and outlet pipe flow would be turbulent but as no velocity distributions were described it is not known if the chamber flows would be fully turbulent.

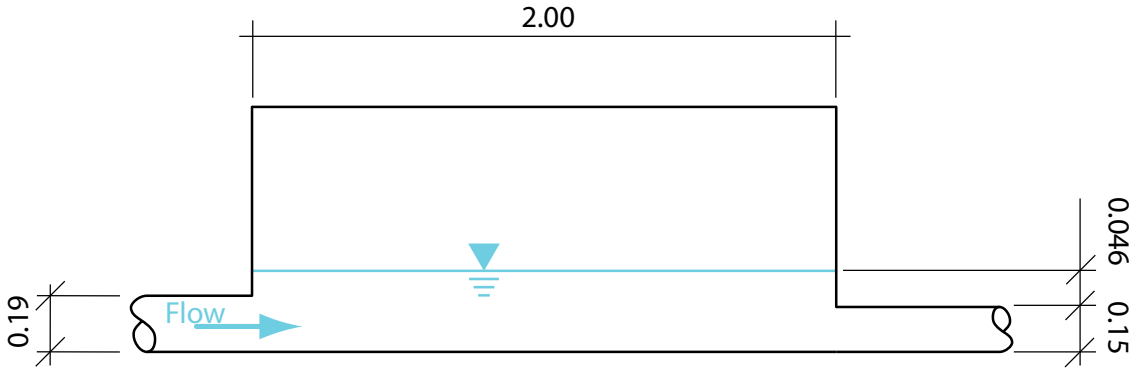


**Figure 1-8 – Sketch of the centre plane of the sewer storage chamber used by Stovin and Saul (1996), dimensions in metres.**

Conceptually, it is hard to envisage that the flows throughout the chamber would be fully turbulent as Stovin and Saul (1996) themselves describe an offset jet with two low speed recirculation regions, as sketched in Figure 1-9. Therefore, it is highly likely that the central jet would remain turbulent while the majority of the chamber would be laminar with transition regions in between.

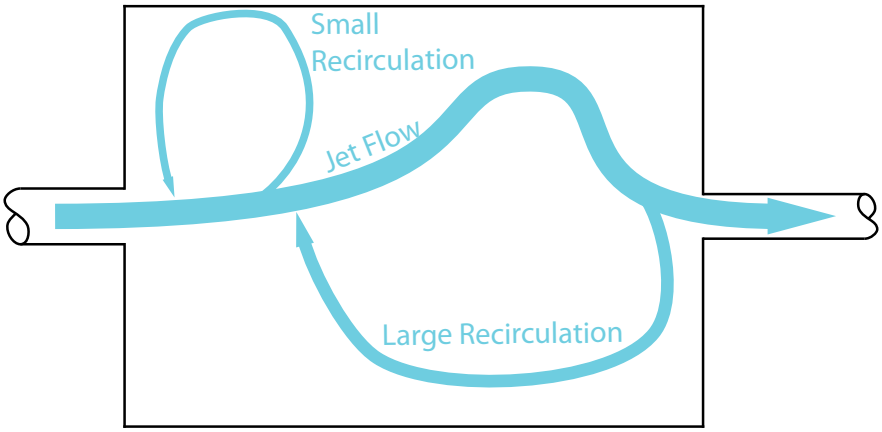


**Figure 1-9 – Dominant flow regime identified by Stovin and Saul (1996).**

As the CFD mesh that was developed by the researchers was 82 x 32 x 12 (long x wide x high) it is highly likely that the solution was severely under resolved. That is, with 32 cells that were uniformly distributed across the width* the average cell length would be in the order of 30mm or, assuming the diameter of the jet is in the order of the inlet pipe diameter, 6 cells across the jet. While Roache (1998a) and Chung (2002) argue that 5 cells is the absolute minimum requirement to resolve a wave it is likely that to adequately resolve the jet many more cells are required.

Despite the promise of improved data from these CFD simulations over physical models, the results have been severely limited by a number of factors including low mesh resolution, the turbulence modelling assumptions and the treatment of the free surface as a zero-friction fixed wall. Unfortunately, the under-resolved mesh detailed in the primary paper (Stovin and Saul, 1996), discussed above, was subsequently in the subsequent work by Stovin and her co-workers. In addition to the mesh being under-resolved no data was presented on the independence of the solution to the mesh used.

A $k$-$\varepsilon$ turbulence model was used for all the simulations performed by this group, which was probably employed more because it was available in the package rather than being applicable to the problem. Firstly, the $k$-$\varepsilon$ model is known to incorrectly calculate the reattachment of separated flows and such flows are present within this device. As previously discussed, it is highly likely that the majority of the flows in the computational domain would be laminar. Since the $k$-$\varepsilon$ turbulence model does not allow

* Based on a visual inspection of Figure 4 from Stovin and Saul (1996).

"re-laminarisation" it would produce an artificially high dissipation in the low velocity regions further damping the already laminar flows.

In conjunction with Stovin, Harwood (Harwood and Saul, 1999, Harwood, 2002), who was also based at the University of Sheffield, investigated weir type sewer overflow structures using CFD. As with the studies of Stovin, Harwood treated the free surface as a rigid, zero-friction fixed plane and the use of a specific turbulence model was not discussed. As well, a review paper by Harwood and Saul (2001) does not discuss either the free surface or a turbulence model.

Further to the research into settlement chambers and end weir separators Harwood and Saul (1996) and Faram and Harwood (2002) developed models to investigate the flow and particle traces within hydrodynamic vortex type separators. These studies also treated the free surface as rigid, zero-friction boundaries but these boundaries had been derived from experimental data while the shape of the plunging inlet was "…approximated based on projectile theory" (Faram and Harwood, 2002). While both of these approximations are better than a fixed rigid plane, it is unlikely that they correctly capture the dynamics of the free surface. For example, the interface in the region of the intersection of the main fluid body and the plunging jet would be highly deformed and most likely include splashing and entrainment neither of which is captured with rigid, zero friction boundaries.

Hence, there are two areas of research, both of which were specifically excluded by the assumptions, that have not been adequately addressed in these studies, namely the treatment of the free surface and the development of a turbulence model that is capable of dealing with laminar and turbulent regions. This formed the fundamental task for this research: that was to develop a method of modelling both the free surface numerically and to properly account for the turbulent and non-turbulent regions of the flow. Naturally, any simulation technique would also have to account for factors such as the modification of turbulence close to the free surface. In order to develop such techniques a more fundamental approach was instigated so that through the use of simpler, but extensively studied, geometric configurations the turbulence and free-surface mathematical models could be isolated and reviewed in detail.

## 1.5. Flow Features to be Simulated

In order for the simulations of the simplified geometric configurations to be effective, they must be representative of a particular aspect of the flows encountered in overflow devices. What then, are the key flow features related to overflow type structures?

From an inspection of the research into sewer overflows, described above, combined with the present author's personal experience as a practicing hydraulic engineer, three key flow features were identified that would need particular attention:

1. Simultaneous simulation of at least two immiscible fluids, for example air and water.
2. Simultaneous simulation of separated and attached flow regions, such as would occur with flow around obstructions and for jets from inlet pipes into chambers.
3. Simultaneous simulation of mixed turbulent and laminar regimes.

In addition to these three flow criteria the availability of computational resources enforced a further criterion, namely to limit the Reynolds number. That is, as the Reynolds number is increased, so the cell size must be concurrently decreased in order to simulate the smaller turbulent structures and, hence, the cell count must necessarily be increased to simulate the same volume (Versteeg and Malalasekera, 1996, Chung, 2002). For example, Wilcox (1998) estimated that the minimum cell count required to simulate open channel flow at $\mathrm{Re}_H \cong 30 \times 10^3$, in which $H$ is the channel height, would be

$$n_{cells} = O\left(4 \times 10^7\right) \tag{1.3}$$

for direct numerical simulations and

$$n_{cells} = O\left(3 \times 10^6\right), \tag{1.4}$$

for large eddy simulations, which was beyond and close to, respectively, the limits of the computational resources available at the start of this research. Therefore, the Reynolds number was initially limited to less than $30 \times 10^3$ but with the caveat that this upper limit would increase as additional computational resources became available.

With these three flow requirements for any simulation software and the computational resources specified the program of investigation that was followed can be presented.

## 1.6. Outline of the Research Program

Despite the intrinsic appeal of attempting to simultaneously simulate all three of these flow components, the research program presented within this dissertation took a slower path and followed the axiom of building up to complexity via studies designed to investigate particular fundamental aspects of the larger problem. Hence, the first step to reduce the complexity of the flow field was to eliminate the second fluid. This allowed for the research to first focus on the correct simulation of flows with features of type 2 and 3 from the list presented in §1.5, that is combined separated/un-separated and laminar/turbulent flows.

The reader would have noted that the present author could have further simplified the configuration and eliminated the separated/un-separated region. This would have then focused the work purely on the mixture of laminar and turbulent regimes and, hence, possibly lead to the development of a novel turbulence model. A new turbulence model, such as the $k$-$\varepsilon$, was not specifically developed in this dissertation because of the extensive body of work already conducted within both the CFD research community and the research group based at both UTS and UNSW of which the present author was a member. It just remained for the present author to decide which turbulence model or simulation technique would meet these requirements.

Therefore, the research program discussed for the remainder of this dissertation followed the trajectory of:

1. Identification of fundamental physical and numerical studies that could be used to validate the flow regimes that were identified above.
2. Identify the appropriate CFD techniques that could be combined to simulate the configurations described in the validation studies.
3. Validation of the software technique to combined separated/un-separated and laminar/turbulent flows.
4. Validation of final configuration with the software extended to include the simulation of flows with a free surface.

Despite the elegance of a four-step research project questions remained such as what criteria would be used to determine if the software had indeed been validated? How

would it be determined if the software performed better than the alternative programmes? Therefore, the following two criteria were proposed:

1. Does the method simulate the validation parameters against which the code was to be tested to the same standard or better than the alternative techniques?
2. Is the method faster than, or at least as quick as, the alternative approaches?

With these four steps conducted, the validated software could then be used with confidence to investigate similar flow phenomena and configurations. Naturally, the fundamental studies that will underpin the validation studies must be identified.

## *1.7. Selection Criteria for the Validation Studies*

Before discussing the search for a set of studies from which the validation configuration would be drawn, it is necessary to identify the requirements that must be considered for validation, namely:

- Fully described configuration: any studies must fully describe the conditions measured or simulated so that the simulations can be a very close match.
- Extensive and detailed measurements: the configuration must be extensively measured and documented so that as many varied parameters can be used for comparison.

Unfortunately, from the present author's experience, the first condition is rarely met in modern papers with some key detail usually missing. In contrast, the second requirement can generally be met with reference to different publications as one journal publication rarely contains sufficient detail. With these requirements for validation studies and the flow requirements documented in §1.5, the specific configurations to be used can be identified.

From the observation of civil flow structures, a list of structures that could potentially be used as validation configurations is:

1. Flow through sewer overflow structures;
2. Flow around piers;
3. Open channel flows, in particular at channel junctions;
4. Hydraulic jumps.

Of these possibilities, only the second and third cases can be simulated without a free surface. That is, the flow around a pier could be reduce to single-phase flow around an obstruction while the flow through open channel junctions can be reduced to wall bounded flows such as those at pipe junctions. Since pier flows have massively separated regions and, depending on the Reynolds number, a mixture of turbulent and laminar regimes as well as a deformed free surface it follows that this thesis is focussed on flows in the vicinity of piers.

## *1.8. Selection of the Single Phase Validation Configuration*

Therefore, with the decision to use flows around piers as the free surface case, the single fluid validation study would have to be the flow around an obstacle. Further, to reduce the complexity of the computational geometry – a perennial problem with CFD – the obstruction ideally should be a simple geometric shape that extends across the entire width of the domain. The simplest geometric shapes is either a right triangular or rectangular or circular cylinders in which the "right" indicates the orientation of the prismatic face relative to the long axis of the cylinder.

The literature overflows about triangular cylinders but this shape was discarded because the majority of publications were concerned with either cavitation or supersonic flows, so that the previous research had not been focussed on the issues with which validation was required. In addition, triangular cylinders would be an unusual shape for a pier.

While rectangular cylinders are simpler to grid than circular cylinders, circular cylinders are more appropriate with respect to the pier analogy. Hence, it would be preferable to work with single-phase flows in the neighbourhood of circular cylinders. Despite the extensive monograph of Zdravkovich (1997) the highlighted the breadth of research into right circular cylinders, the volume of literature dedicated to flows near right circular cylinders that would be suitable for the present validation is dwarfed by that focussed on flows in the environs of right square cylinders. Therefore, the validation of the single-phase techniques was focussed on flows around right square cylinders.

Historically, for flows in the vicinity of right square cylinders there has been great interest in the pressure forces and their fluctuations with a focus on physical studies (Lee, 1975, Bearman and Obasaju, 1982, Okajima, 1982) but also some numerical investigations (Clements, 1973, Nagano et al., 1982). Publications and research based

on right square cylinders accelerated markedly following the publications of Lyn and Rodi (1994) and Lyn et al (1995)* whose extensively described experimental study of a right square cylinder, mounted in cross flow at a Reynolds number of

$$\mathrm{Re}_d = \frac{U_{ref} d}{\nu} = 22 \times 10^3 \tag{1.5}$$

in which $d$ is the side length of the cylinder was meets the first requirement for use as a validation study. They also presented some data based on LDA measurements within their water tunnel but these were either time and/or phase averaged.

Following the specification of the L&R configuration as the basis for two workshops – described by Voke (1996) and Rodi (1997), respectively – numerous results have been published on this configuration. A recent, brief, survey by the present author revealed over 50 publications, for example Bouris and Bergeles (1999), Fureby et al (2000), Srinivas et al (2006) and Song and Park (2009), with different turbulence models of the same configuration yet, somewhat surprisingly given the specifications by L&R and the two workshops, there was also notable variation of the geometric configurations.

## *1.9. Selection of the Two-Phase Validation Studies*

For the validation of the two-phase flows, the choice was not as simple as using the L&R geometry and being able to use all the studies that were subsequently based on it. Instead, the two-phase validation was based on a combination of studies that when grouped together provided the necessary data across a number of individual papers.

The laboratory experiments of Inoue et al (Inoue et al., 1993) were originally selected because they published detailed measurements of both the free surface and velocity profiles and were at a Reynolds number based on the cylinder diameter of $27 \times 10^3$. Three numerical investigations were also based on this configuration, namely

1. Chen et al (2000);
2. Kawamura et al (2002);
3. Yu et al (2008)

* To avoid extensive repetition during the remainder of this chapter these two studies will be referred to only as L&R.

However, if the validation study was to be completely focussed on these studies it would ignore the most extensive experimental data set recorded of free surface flows, namely that of Hay (1947). Within this excellent study Hay measured over thirty combinations of cylinder diameter and depth of submergence were tested with diameters that ranged from 3.175mm (1/8") up to 203.2mm (8") and depths of submergence from 25.4mm (1") up to 812.8mm (32"), as listed in Table 1-3.

**Table 1-3 – Cylinder depth and diameters investigated by Hay.**

| | **Cylinder Diameter (mm)** | | | | | | |
|---|---|---|---|---|---|---|---|
| | **3.175** | **6.35** | **12.7** | **25.4** | **50.8** | **101.6** | **203.2** |
| **Depth of Immersion in millimetres** | 25.4 | 25.4 | 25.4 | 25.4 | 50.8 | 101.6 | 203.2 |
| | 50.8 | 50.8 | 50.8 | 50.8 | 101.6 | 203.2 | 406.4 |
| | 101.6 | 101.6 | 101.6 | 101.6 | 203.2 | 406.4 | 812.8 |
| | | 203.2 | 203.2 | 203.2 | 406.4 | 812.8 | |
| | | | 406.4 | 406.4 | 812.8 | | |
| | | | | 812.8 | | | |

In addition to the drag data collected, the tow tests were photographed from three different locations to measure and describe the changes in the free surface over different Reynolds and Froude numbers. To provide a perspective view of the width of the wake region, the first camera was located behind the cylinder and looking upstream. The second two cameras were placed perpendicular to the direction of cylinder movement with one slightly above the free surface shooting generally downwards and the second camera side on. Of these two cameras, the upper camera was used to provide indicative images of the free surface deformation – much as with the first, downstream, camera. In contrast to the purely visual data collected by the first two cameras the third camera also collected images that could be used to estimate free surface positions via photogrammetric techniques. Sample images from the three cameras are shown in Figure 1-10.

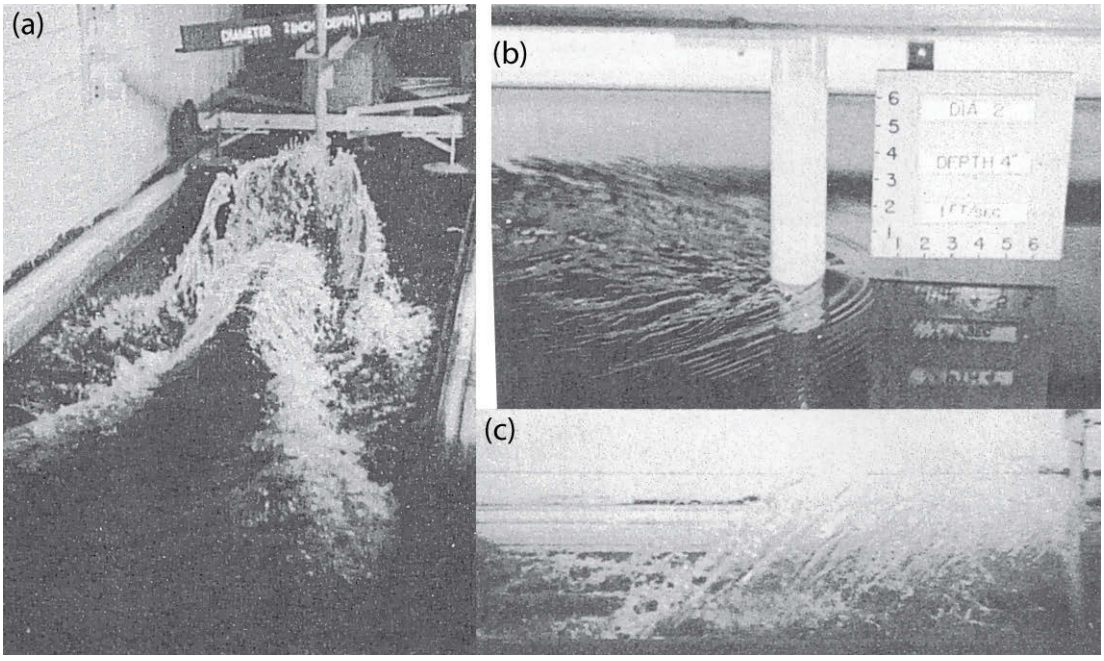


**Figure 1-10 – Example images from the three camera locations: (a) the camera behind the cylinder showing a perspective of the wake; (b) the camera side-on and above the free surface, and; (c) the camera side-on and parallel with the free surface, an image suitable for photogrammetry.**

While the Reynolds number to be used in the present simulations with a free surface set to match that of Inoue et al (1993), the data of Hay must also be included. Therefore, with the free surface validation configuration decided the particular turbulence model and the technique that will be used to simulate the free surface must be decided, discussed in §2 and §1, respectively.

## *1.10. Mapping of the Research Program to this Document*

It has been identified that previous numerical studies of turbulent flows with a free surface have been inadequate in the treatment of both the turbulence and the free surface. Therefore, the work described within the reminder of this thesis describes a, successful, attempt to remedy this gap. Of the four tasks identified for this research program, as discussed in §1.6, the first has already been presented in §1.7, namely the selection of the validation studies. The remaining three tasks will be distributed though out the body of this dissertation.

The second task that is to identify the appropriate CFD techniques can be developed along similar lines as that used in the selection of the studies to be used for validating

the code. Firstly, the selection of the method that will be used to simulate the mixed laminar and turbulent flows must be presented, as discussed in §2. Secondly, the numerical techniques that will be used to implement this flow simulator need to be critically examined in §1 because the results depend on the accuracy of the numerical approximations used to implement the theoretical models. Lastly, both the mathematical model and numerical methods that will be used to simulate the free surface must be critically examined, as presented in §1.

With the theoretical foundations presented, the validation studies can then be examined first for the single-phase simulations in §5 and §6 and then for the two-phase systems. As the extension from single to two-phase simulation introduced a number of new physical effects some preliminary studies were undertaken in order to examine some specific features, as discussed in §8. These preliminary studies were then used as guides in the development and analysis of the two-phase validation studies and explorations, which are documented in §9 to §11.

# 2. Mathematical Models of Single Phase Fluids

## *2.1. Introduction*

The single-phase flow computations described within this dissertation were based on two fundamental equations based on the assumption of there being a continuum, namely:

1. The continuity equation that describes the conservation of mass, and
2. The Navier-Stokes Equations that describe the conservation of momentum equations (Constantin and Foias, 1988, Drazin and Riley, 2006).

As both of these equations are continuum equations they must, therefore, be discretised prior to performing any computations. Before an informed decision can be made as to which, if any, simplifications and implementations should be used in the work described in this dissertation the fundamental equations and the alternatives must be presented and discussed[*].

## *2.2. Conservation Equations*

### 2.2.1. Conservation of Mass

The conservation of mass for an incompressible fluid requires that the volumetric strain be zero

$$\nabla \cdot \mathbf{u} = 0 , \tag{2.1}$$

in which $\mathbf{u}$ is the fluid velocity vector and $\nabla \cdot$ is the divergence operator. As noted with a certain dry humour by White (1991), and repeated here, there is a fashion to add the clarification that as the research described in this dissertation does not deal with nuclear reacting flows, mass is *always* conserved. To complete the description of the

[*] Because the derivation of the Navier-Stokes equations and turbulence models is extensively described in the literature, the derivations presented below are brief. Instead, the discussion will focus on the merits of each method and their application to the present work. The interested reader is referred to monographs such as those by Tennekes and Lumley (1972), White (1991), Wilcox (1998) or Pope (2001) if they require a more thorough review.

non-nuclear flows in the current work, Equation (2.1), must be supplemented with a description of the forces and momentum involved.

### 2.2.2. Conservation of Momentum

The conservation of momentum for a fluid observed from within an inertial frame of reference (White, 1991) can be written as

$$\rho\frac{\partial u_i}{\partial t}+\rho u_j\frac{\partial u_i}{\partial x_j}=\rho g_i+\nabla\cdot\tau_{ij}\,, \tag{2.2}$$

in which $\rho$ is the fluid density, $\mathbf{g}$ is the gravitation vector and $\tau_{ij}$ is the fluid stress tensor. With the assumptions in this research of constant properties, incompressibility and Newtonian fluids an expression of the stress tensor in Equation (2.2) can be developed such that Equation (2.2) becomes

$$\rho\left(\frac{\partial u_i}{\partial t}+u_j\frac{\partial u_i}{\partial x_j}\right)=\rho g_i-\frac{\partial p}{\partial x_i}+\mu\frac{\partial^2 u_i}{\partial x_j\partial x_i} \tag{2.3}$$

in which $p$ is the thermodynamic pressure and $\mu$ is the coefficient of dynamic viscosity.

While Equations (2.1) and (2.3) can provide a complete description of the motion of an incompressible, constant property Newtonian fluid, the non-linear inertial term means that as the velocity changes there can be huge changes in the flow regime. Following the dimensional reasoning of Bird, Stewart and Lightfoot (2002), namely that "typical" values of the terms in Equation (2.3) can be estimated by replacing the variables with characteristic "yardstick" estimates, the effects of the non-linear inertial term in Equation (2.3) can be estimated as

$$f_i\propto\frac{\rho u_c^2}{l_c} \tag{2.4}$$

in which $u_c$ is a characteristic velocity and $l_c$ is a characteristic length. Similarly the effects of the viscous term in Equation (2.3), $\mu\frac{\partial^2 x_i}{\partial x_j\partial x_i}$, can be determined from

$$f_\mu \propto \frac{\mu u_c}{l_c^2}. \tag{2.5}$$

Further, for a given case the fluid thermodynamic properties, that is the density and viscosity, and the length scale can be assumed constant. Therefore, the estimates in Equations (2.4) and (2.5) reduce to functions of the characteristic velocity only:

$$f_i\left(u_c\right) = c_i \frac{\rho u_c^2}{l_c} \tag{2.6}$$

and

$$f_\mu\left(c_c\right) = c_\mu \frac{\mu u_c}{l_c^2} \tag{2.7}$$

in which $c_i$ and $c_\mu$ are constants of proportionality. It can be deduced from an inspection of Equations (2.6) and (2.7), that when the characteristic velocity is very large the inertial effects will be proportionally larger than the viscous effects and vice versa.

By inspection, both Equations (2.4) and (2.5) have the same dimensions. Therefore, they can be divided to produce a non-dimensional number,

$$\mathrm{Re} = \frac{\rho l_c u_c}{\mu}, \tag{2.8}$$

that is indicative of which forces, inertial or viscous, are dominant for a given flow configuration. This parameter is referred to as the Reynolds number (Rott, 1990) and was named in honour of Osborne Reynolds who originally proposed the grouping in 1883 (Reynolds, 1883). At small Reynolds numbers viscous damping is dominant and the flows are called laminar since one layer, or "lamila", slides on the next lamila without mixing. Conversely for flows at high Reynolds numbers the inertial stresses dominate so that the viscous stresses cannot damp out the inherent instabilities resulting from the non-linearity of the Navier-Stokes equation, leading to turbulence that is characterised by unsteady, perhaps, chaotic motions with significant mixing. These limits are shown in Figure 2-1 where the $c_i \equiv c_\mu = 1$, $l_c = 0.05\mathrm{m}$ for water at room temperature and pressure.

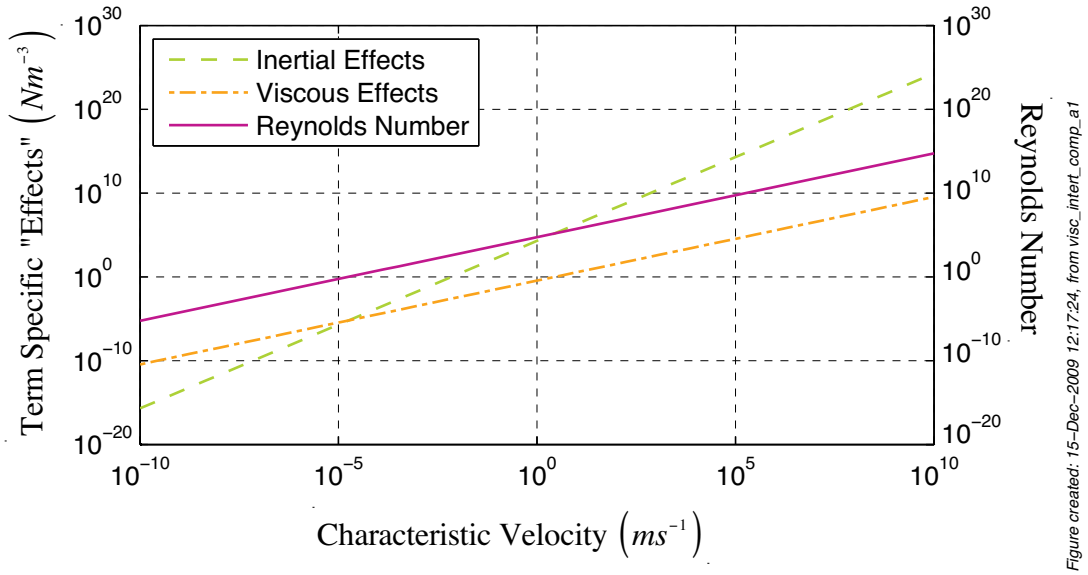


**Figure 2-1 – Plot of Equations (2.6), (2.7) and (2.8) with constants of proportionality of unity and a characteristic length of 0.05m for water at 20°C.**

Nearly all flows of practical interest to engineers are turbulent but, unfortunately, as the physical understanding of turbulence is still limited, turbulence has been described as one of the great remaining challenges of physics and engineering (Yaglom, 2001).

## 2.3. Introduction to Turbulence

A general definition of turbulence quoted by Wilcox (1998) and attributed to an amalgamation of the work of pioneers such as G. I. Taylor, von Kármán and, more recently, Bradshaw is that:

> *"Turbulent fluid motion is an irregular condition of flow in which the various quantities show a random variation with time and space coordinates, so that statistically distinct average values can be discerned. Turbulence has a wide range of scales."*

However, conclusions from recent studies indicate that the above definition may not be a complete description of turbulence, where in fact turbulent flows may actually be chaotic (Sreenivasan, 1999), that is, turbulent flows show an order of scale similarity, a pointer to chaos, which can be interpreted as an indicator of an underlying order to the apparently random macro-scale fluid motions.

An alternative, descriptive, conceptualisation of turbulence captured by a rhyme attributed to L. F. Richardson (Batchelor and Towsend, 1949) is that

*"Big whirls have little whirls,*

*That feed on their velocity;*

*And little whirls have lesser whirls,*

*And so on to viscosity."*

That is, a turbulent flow is composed of a multitude of randomly rotating eddies, or vortices, of different sizes superimposed on each other as illustrated in Figure 2-2.

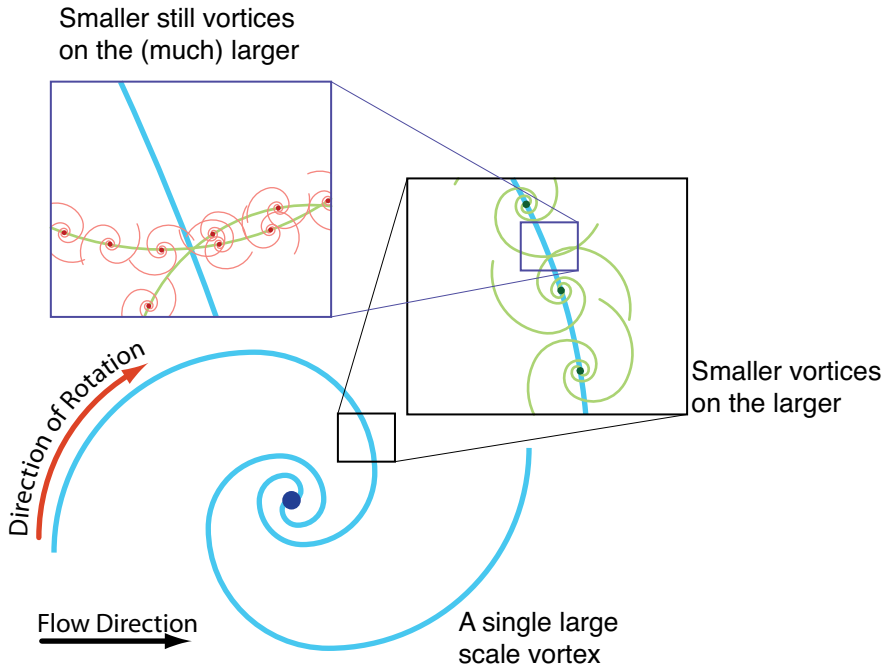


**Figure 2-2 – Schematic illustration of the vortex-on-vortex conceptualisation of turbulence.**

While the Reynolds number can be used to classify flows into either the laminar or turbulent regimes, it provides no insight as to the range of length scales, or eddy sizes, within a particular flow. Fortunately, the conceptualisation of turbulence described in the rhyme above can be formalised with the introduction of a wave number,

$$\kappa = \frac{2\pi}{\lambda}, \tag{2.9}$$

in which $\lambda$ is the wave length of a given eddy, that is the characteristic "size" of the eddy, to provide a general purpose spatial length scale. The wave numbers, or indeed wave lengths, are generally not directly measured, instead they are calculated using a Fourier transform (Tennekes and Lumley, 1972). For example, a Fourier transform of time domain data will result in a frequency spectrum, which must be converted to a

wave number spectrum using Taylor's frozen turbulence hypothesis. A similar transform of data extracted from the spatial domain gives a wave number spectrum (Pope, 2001).

If the eddy size analogy were to be further extended to include the energy contained as a function of eddy size, it would be logical to suppose that the larger eddies, which are described by small wave numbers, would contain more energy. That is, since rotating kinetic energy is defined as

$$E_{k,\,\text{rotating}} = \int \frac{u_c^2 dm}{2}, \tag{2.10}$$

in which $m$ is mass, then a larger eddy which can be imagined to, simultaneously, be comprised of more mass that is in turn spread over a larger area will contain more energy. By extension then the smaller eddies – at larger wave numbers – will contain less energy per vortex than the larger vortices.

In the first definition of turbulence given above, it was noted that turbulence possessed "statistically distinct averages" and as such, with all averages the general variable can be split into averages and fluctuations. In turbulence research this generally refers to velocity averages and fluctuations that can be written as

$$u_i = U_i + u_i' \tag{2.11}$$

in which the three terms represent the instantaneous, averaged and fluctuating velocity components, respectively. Further, it should be noted that in turbulence studies, the kinetic energy described here is referred to as turbulence (or turbulent) kinetic energy (Wilcox, 1998) which can be written as

$$k = \frac{1}{2}\overline{u_i' u_i'} \tag{2.12}$$

rather than the general form of kinetic energy in Equation (2.10).

Finally, as the rhyme suggested, if the smaller eddies are superimposed on top of the larger eddies it therefore follows that there must be a larger number of smaller eddies than larger eddies. Perhaps the count of smaller vortices is exponentially greater than larger vortices. Unfortunately, the total turbulent kinetic energy of the system cannot be estimated simply from a summation of all the energy containing eddies.

Therefore, with the use of spectral methods it is possible to examine the distribution of energy as a spectrum of turbulence kinetic energy in wave number space (Wilcox, 1998). This is generally referred to as the energy spectral density or power spectral density and is conveniently computed from velocity distributions, in either temporal or spatial domains, via Fourier methods (Tennekes and Lumley, 1972, Pope, 2001). The shape of the turbulence kinetic energy spectrum was first posited in the ground-breaking theoretical investigations of both Taylor (1935) and Kolmogorov (1941) who investigated flows of homogenous turbulence at very large Reynolds numbers, as sketched in Figure 2-3.

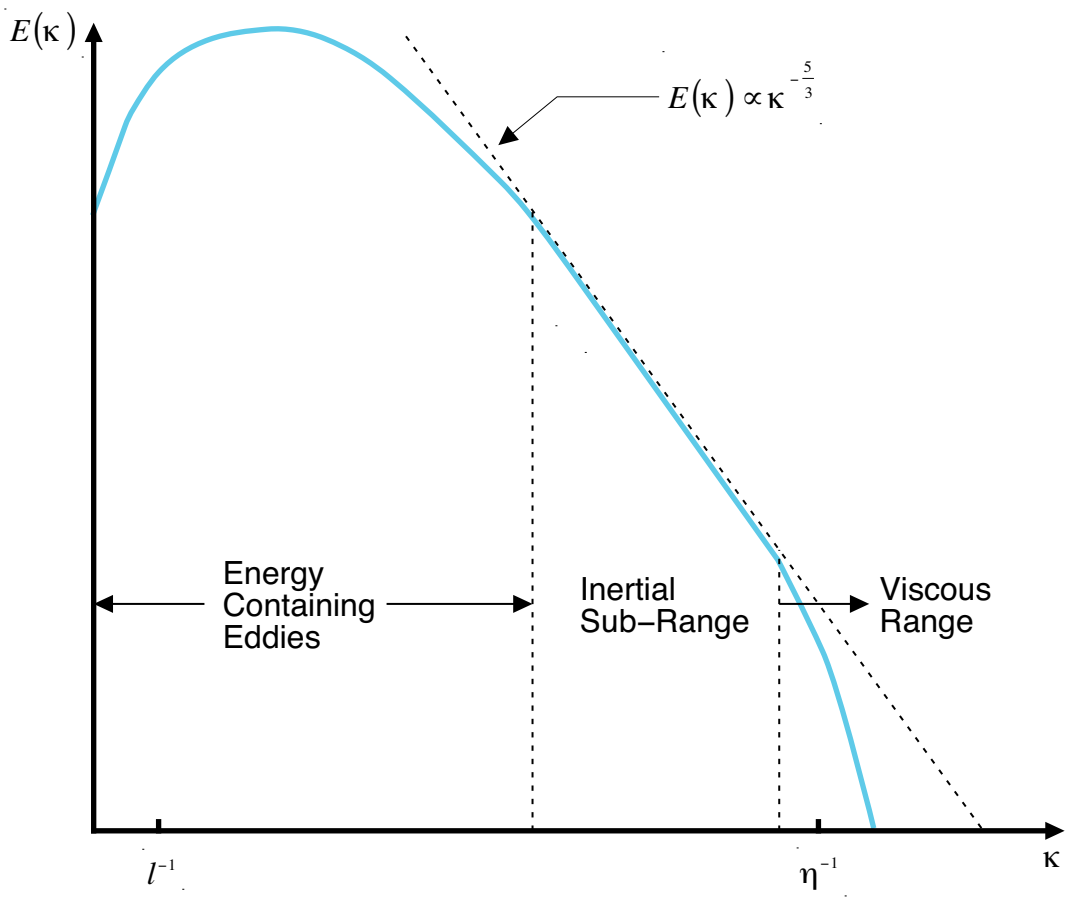


**Figure 2-3 – Idealised turbulent energy spectrum as a function of wave number on log-log scales, adapted from Wilcox (1998) and Nezu and Nakagawa (1993).**

Numerous experimental results have confirmed these predictions such that the shape of the spectrum, as sketched in, has assumed the significance of a physical law (Rogallo and Moin, 1984).

As can be seen in Figure 2-3 the majority of the turbulence kinetic energy is contained in the largest eddies, that is the smallest wave numbers, therefore this region of the spectrum is referred to as the energy-containing region (Wilcox, 1998, Pope, 2001). Conversely, at the largest wave numbers, or the smallest vortices, viscous forces dominate and the turbulence kinetic energy is transformed into heat via molecular dissipation. This high wave number region is termed the viscous range. The region between the viscous range and the energy containing range is referred to as the inertial sub-range and is defined as the region in which the turbulent kinetic energy spectrum decays as a power law function of wave number. Kolmogorov (1941) showed by a dimensional argument that in this region the energy density and the wave number were related by

$$E(\kappa) \propto \kappa^{-\frac{5}{3}}. \tag{2.13}$$

This power law has become so entrenched in the study of fluid dynamics that "compatibility with [Kolmogorov's power law decay theory] is required of any theory or simulation" (Rogallo and Moin, 1984).

As already noted, the majority of the energy is contained at small wave numbers yet is dissipated at the high wave numbers. Therefore, given that energy is *always* conserved, energy must in turn be transferred from the small wave numbers to the large. In turbulence research, this supply of energy from small wave numbers to the large wave numbers and its subsequent dissipation into heat is known as the turbulent energy cascade and is referred to as Kolmogorov's universal equilibrium theory (Pope, 2001).

Thus far, only qualitative descriptions of small and large have been used to describe eddy sizes but, as with the dimensional arguments in the derivation of the Reynolds number, dimensional reasoning can be used to quantify the length scales of turbulent flows. From an inspection of the turbulent energy cascade it would appear that there are two quantities that are important in the transfer and dissipation of energy:

1. The kinematic viscosity that describes the rate at which kinetic energy can be transferred into thermal energy.
2. The rate at which energy can be transferred through the inertial sub-range.

These two quantities do not operate completely independently. For example, if the rate of transfer can be thought of as a number of railroad trains that transport energy, then the viscosity can be considered to be handling facility at the end of the line. Therefore, the

viscosity can limit the cascade in that only the amount of energy handled by the end facility can be shipped through the network. In contrast, if the rate of transfer is less than the dissipation – if the handling facility is more efficient than the transportation network – then all the available energy can be dissipated.

Kinematic viscosity $(\nu)$ has the units of $m^2 s^{-1}$ but in contrast to viscosity, the dissipation rate has not been formally defined yet in this dissertation. The dissipation rate must be the rate at which turbulence kinetic energy is transferred therefore it is defined as

$$\varepsilon = -\frac{dk}{dt}, \tag{2.14}$$

which is in units of $m^2 s^{-3}$. These two quantities, ν and ε, can be combined into three, dimensional groups:

$$\eta = \left(\frac{\nu^3}{\varepsilon}\right)^{\frac{1}{4}}, \tag{2.15}$$

$$\tau = \left(\frac{\nu}{\varepsilon}\right)^{\frac{1}{2}} \tag{2.16}$$

and

$$\upsilon = (\nu\varepsilon)^{\frac{1}{4}} \tag{2.17}$$

that are the Kolmogorov scales of length, time and velocity, respectively (Kolmogorov, 1941, Wilcox, 1998). These three parameters are used to quantify the smallest scales of turbulent flows at the largest wave numbers.

As an example of how small these parameters are Wilcox (1998) quotes a value of $\eta \approx 5$ μm at the windscreen for a car travelling at approximately 100km/h that, for standard temperature and pressure. This length is only 72 times the mean free path of the air molecules.

Conversely for the largest eddies, at small wave numbers, Taylor (1935) proposed that the integral length scale,

$$l \propto \frac{k^{\frac{3}{2}}}{\varepsilon}, \tag{2.18}$$

would be the appropriate descriptor. Both of these length scales, $\eta$ and $l$, are shown diagrammatically on Figure 2-3 for comparison.

With this very brief description of turbulence, and assuming that suitable discretisation and solution schemes have been developed, the first step in computing general flows would be to directly model the continuity and momentum equations, Equations (2.1) and (2.3) respectively.

## 2.4. Direct Numerical Simulation

Direct Numerical Simulation (DNS) is, as the name suggests, the process of directly modelling the continuity and Navier-Stokes equations – Equations (2.1) and (2.3) – within a computational solver. Therefore, DNS is based on the assumption that both the computational mesh and numerical schemes are of sufficient accuracy to correctly capture all of the physics of the flow problem being studied. This leads immediately to the primary problem with DNS: that in order to capture all the physics (that is the entire turbulence cascade), the mesh must be fine enough to resolve structures with wave numbers at, if not larger than, the Kolmogorov length scale, and diagrammatically in Figure 2-3. In practice, the computational requirements for not only the numerical operations as well as the storage of the resultant data are too expensive for most flows of engineering interest. For example, Wilcox (1998) estimated that for a DNS of channel flows at $\mathrm{Re}_H \cong 30\times10^3$ the cell count would be $O\left(n_{cells}\right)=40\times10^6$, while Wu and Moin (2008) utilised $O\left(n_{cells}\right)=630\times10^6$ cells to simulate a single phase pipe flow at a $\mathrm{Re}_\phi = 44\times10^3$, in which $\phi$ is the pipe diameter. Suppose that $\phi = 200$ mm and that the fluid was water at room temperature and pressure, then the mean velocity would be in the order of 0.2 m/s, which is equivalent to a volumetric flow rate of only 7 L/s. Further, the authors stated that each snapshot data file was approximately 25GB in size while the simulation required 1024 processing cores distributed across 128 computers. No wall times were discussed, only simulation times* but the wall time was likely to have been in the order of 6-12 months.

* Simulation time is the time that is simulated within the model whereas wall time is the total computational time required that includes input/output wait, processing times and other operating system overheads.

With these computational limitations DNS remains, essentially, a research only approach with computational requirements in excess of practical, industrial use. Even with the extensive computational infrastructure associated with large research institutions, DNS is still limited to simplistic geometries of low speed flows. However, it can be noted from an inspection of Figure 2-3, with its logarithmic scales, that the majority of the turbulence kinetic energy is carried at wave numbers at or below the inertial sub-range – that is for wave number scales several orders of magnitude smaller than the Kolmogorov microscale (measured as a wave number) shown in Figure 2-3. Therefore, the next approach, in an attempt to reduce the cell count, would be to assume that a grid could capture the flow features up to the inertial-sub range, on which the majority of the flow physics could be calculated. A sub-grid model would be employed to generate the necessary diffusive effect.

## *2.5. Large Eddy Simulation*

### 2.5.1. Filtering the Navier-Stokes Equations

Large Eddy Simulation (LES) is based on the assumption that the majority of the turbulence kinetic energy is contained within the larger eddies and therefore it is only these eddies that must be captured by the computational grid. The remainder of the turbulence kinetic energy can then be accounted for with a suitable sub-grid scale model. With these assumptions, Wilcox (1998) estimated that the required number of cells for the same DNS configuration discussed above would be $n_{cells} = O\left(3 \times 10^6\right)$, which is an order of magnitude reduction to the DNS requirements.

Logically, using Figure 2-3 as a reference, all the energy containing eddies must be simulated by an appropriate numerical method at a grid scale. Further, to obtain any reduction in the cell count the physics of the viscous range must be captured by a suitable model. Therefore, the break between the grid resolved and the sub-grid scale is traditionally assumed to fall into the inertial sub-range and towards the larger wave numbers therein (Sagaut et al., 2006).

While it is conceptually simple to say which components of the flows are simulated by which method, in order to obtain the grid resolved/sub-grid scale split the Navier-Stokes

equations must be filtered. Filtering is usually performed with a generalised filter function defined as a convolution integral (Leonard, 1974) such as

$$\hat{u}_i(\mathbf{x},t) = \int\int\int G(\mathbf{x}-\boldsymbol{\xi};\Delta)u_i(\boldsymbol{\xi},t)d^3\boldsymbol{\xi}, \tag{2.19}$$

in which $\Delta$ is the filter width and $\boldsymbol{\xi}$ is a distance vector from the general point $\mathbf{x}$. The filter function, *G*, is normalised by requiring that

$$\int\int\int G(\mathbf{x}-\boldsymbol{\xi};\Delta)d^3\boldsymbol{\xi} = 1. \tag{2.20}$$

Therefore, with the filtered velocity defined in Equation (2.19), the sub-grid scale (SGS) velocity can be calculated as

$$u_i'(\mathbf{x},t) = u_i(\mathbf{x},t) - \hat{u}_i(\mathbf{x},t). \tag{2.21}$$

in which $u_i(\mathbf{x},t)$ is the instantaneous velocity at point **x** and time *t*. Numerous filters have been proposed but one of the earliest, and simplest, is the volume averaged box filter proposed by Deardoff (1970)

$$G(\mathbf{x}-\boldsymbol{\xi};\Delta) = \begin{cases} \dfrac{1}{\Delta^3}, & \left|x_i-\xi_i\right| < \dfrac{\Delta x_i}{2} \\ 0, & \text{otherwise} \end{cases}. \tag{2.22}$$

With a suitable filter function defined, the resolvable-scale continuity and momentum equations, with body forces ignored, become (Wilcox, 1998)

$$\frac{\partial \hat{u}_i}{\partial x_i} = 0 \tag{2.23}$$

and

$$\frac{\partial \hat{u}_i}{\partial t} + \frac{\partial}{\partial x_j}\left(\hat{u}_i\hat{u}_j\right) = -\frac{1}{\rho}\frac{\partial P}{\partial x_i} + \frac{\partial}{\partial x_j}\left[\nu\frac{\partial \hat{u}_i}{\partial x_j} + \tau_{ij}\right] \tag{2.24}$$

respectively, where

$$\left.\begin{aligned} \tau_{ij} &= -\left(Q_{ij} - \frac{1}{3}Q_{kk}\delta_{ij}\right) \\ P &= \bar{p} + \frac{1}{3}\rho Q_{kk}\delta_{ij} \\ Q_{ij} &= R_{ij} + C_{ij} \end{aligned}\right\}. \tag{2.25}$$

Equations (2.24) and (2.25) have been simplified from that which is obtained directly from filtering by noting that the convective flux term $\left(\widehat{u_i u_j}\right)$ is a summation of four components

$$\widehat{u_i u_j} = \hat{u}_i \hat{u}_j + L_{ij} + C_{ij} + R_{ij} \tag{2.26}$$

in which (Wilcox, 1998)

$$\left.\begin{aligned} L_{ij} &= \widehat{\hat{u}_i \hat{u}_j} - \hat{u}_i \hat{u}_j \\ C_{ij} &= \widehat{\hat{u}_i u'_j} + \widehat{\hat{u}_j u'_i} \\ R_{ij} &= \widehat{u'_i u'_j} \end{aligned}\right\} \tag{2.27}$$

and that the contribution of the Leonard stress tensor $\left(L_{ij}\right)$ is negligible (Shaanan et al., 1975). The remaining tensors listed in Equation (2.27) are the cross-term stress $\left(C_{ij}\right)$ and the SGS Reynolds stress tensor $\left(R_{ij}\right)$. It must also be noted that filtering differs from standard averaging in that (Wilcox, 1998)

$$\hat{\hat{u}}_i \neq \hat{u}_i \,. \tag{2.28}$$

Therefore, the fundamental problem of Large Eddy Simulation is that the tensor $Q_{ij}$ must be modelled (Wilcox, 1998).

### 2.5.2. LES Models

There are numerous sub-grid scale (SGS) LES models available for the CFD user but only the Smagorinsky model (1963), probably the most popular model, will be explicitly described. The Smagorinsky model was developed from the assumption that the dissipation at sub-grid scales, are similar to the gradient diffusion mechanism of molecular motion (Wilcox, 1998) and that they can, therefore, be computed from the local strain rate (ESI CFD Inc., 2007a). It therefore follows that the sub-grid scale stress can be defined in terms of a turbulent viscosity, $\nu_T$, so that the stresses can be written as

$$\tau_{ij} = 2\nu_T S_{ij} \tag{2.29}$$

in which

$$S_{ij} = \frac{1}{2}\left( \frac{\partial \hat{u}_i}{\partial x_j} + \frac{\partial \hat{u}_j}{\partial x_i} \right). \tag{2.30}$$

$S_{ij}$ is known as the "resolved strain rate" tensor and

$$\nu_T = \left(C_S \Delta\right)^2 \sqrt{S_{ij} S_{ij}} \tag{2.31}$$

is the "Smagorinsky eddy viscosity", conceptually akin to a turbulent viscosity, and $C_S$ is the Smagorinsky constant that commonly ranges from 0.05 to 0.2 (ESI CFD Inc., 2007a).

Despite cell counts in the order of 10% of that required for DNS, the computational requirements for LES are still large. Therefore, for larger Reynolds number flows, which are generally of more interest in practical situations, a method to further reduce the cell count is, at present, required. Having already moved down the wave number spectrum to the inertial sub-range the next step is to further expand the mesh to such a size that the computational cells are comparable to the energy producing length scales. At this scale only the largest flow features would be simulated and the remainder would be averaged due to the large mesh size. Averaging methods at this scale promise much lower cell counts than either LES or DNS and despite being discussed second are more often used in industry than either LES or DNS.

## *2.6. Is Averaging A Solution to the Resolution Requirements of DNS and LES?*

### 2.6.1. Averaging the Navier-Stokes Equations

As noted in the description of turbulence in §2.3, turbulence is characterised by variations with "…statistically distinct average values…" therefore an alternative to either LES or DNS would resolve *only* the average values at the grid scale and statistically, or otherwise, model the fluctuations. Hence as the average structures are relatively large, being comparable to the largest of the energy containing eddies that are at or near to the integral length scale, shown in Figure 2-3, the corresponding cell size can be very large compared with both LES and DNS scales. Computational solvers based on this technique are referred to as Reynolds Averages Navier-Stokes (RANS)

solvers and since closure models are needed to "close" the equations. These include such well-known models as the $k$-$\varepsilon$ and $k$-$\omega$ models (Wilcox, 1998) and many others.

Three forms of averaging were originally introduced by Reynolds (1895) namely: (1) temporal averaging; (2) spatial averaging and (3) ensemble averaging.

1. Temporal averaging

Temporal averaging is appropriate for stationary turbulence, which is a flow where the mean values do not change over time. The temporal mean for a quantity is defined as

$$F_T(\mathbf{x}) = \lim_{T\to\infty} \frac{1}{T} \int_t^{t+T} f(\mathbf{x},t)\,dt \tag{2.32}$$

2. Spatial averaging

Spatial averaging is used with homogenous turbulence; turbulence that is, on average, uniform in all directions and is defined as

$$F_\vartheta(t) = \lim_{\vartheta\to\infty} \frac{1}{\vartheta} \iiint_\vartheta f(\mathbf{x},t)\,d\vartheta \tag{2.33}$$

3. Ensemble averaging

Ensemble averaging is the most general form of averaging and is suitable for all flow types including flows that decay in time or have non-uniform periodic fluctuations. An ensemble average is an average of a quantity measured as a result of $N$ identical experiments that differ by random infinitesimal perturbations of the initial and boundary conditions (Wilcox, 1998),

$$F_E(\mathbf{x},t) = \lim_{N\to\infty} \frac{1}{N} \sum_{n=1}^{N} f_n(\mathbf{x},t)\,. \tag{2.34}$$

It should be noted that the averages defined by Equations (2.32), (2.33) and (2.34) represent the "perfect" averages in that $T$, $V$, and $N$, respectively, all tend to infinity. However, in real numerical or physical experiments the average will, perforce, be always taken over a finite time, computational volume or number of experiments. Therefore, it is the responsibility of the experimenter to both test for and to justify the choice in length of time used in the averaging process, the size of the volume averaged employed or the number of repetitions undertaken, respectively.

Once a suitable method of averaging has been chosen the instantaneous value of each variable can then be decomposed from instantaneous values into a mean and a fluctuating component, for example with the velocity vector,

$$u_i(\mathbf{x},t) = U_i(\mathbf{x}) + u_i'(\mathbf{x},t) \tag{2.35}$$

respectively.

Prior to deriving the averaged Navier-Stokes equations, it is necessary to note the effect of averaging combinations of quantities, that is correlations. Since the average of any fluctuating component has to be zero, the product of two quantities is

$$\overline{\phi\psi} = \overline{(\Phi+\phi')(\Psi+\psi')} = \overline{\Phi\Psi + \Phi\psi' + \Psi\phi' + \phi'\psi'} = \Phi\Psi + \overline{\phi'\psi'}, \tag{2.36}$$

while the average of the product of three quantities becomes

$$\overline{\phi\psi\xi} = \Phi\Psi\Xi + \overline{\phi'\psi'}\Xi + \overline{\psi'\xi'}\Phi + \overline{\phi'\xi'}\Psi + \phi'\psi'\xi'. \tag{2.37}$$

The simplifications that are not immediately obvious in Equations (2.36) and (2.37) were made by utilising the mathematical identity that an average of an average is itself (Wilcox, 1998).

To average the Navier-Stokes equations, Equation (2.3), will be recast in conservative form using tensor notation and with the viscous stress tensor defined as

$$t_{ij} = 2\mu s_{ij}, \tag{2.38}$$

in which

$$s_{ij} = \frac{1}{2}\left(\frac{\partial u_i}{\partial x_j} + \frac{\partial u_j}{\partial x_i}\right) \tag{2.39}$$

is the strain-rate tensor. Therefore, for an incompressible fluid, the continuity and the momentum equations, ignoring body forces, become

$$\frac{\partial u_i}{\partial x_i} = 0 \tag{2.40}$$

and

$$\rho\frac{\partial u_i}{\partial t} + \rho\frac{\partial}{\partial x_j}\left(u_j u_i\right) = -\frac{\partial p}{\partial x_i} + \frac{\partial}{\partial x_j}\left(2\mu s_{ji}\right), \tag{2.41}$$

respectively. Performing a time average of Equations (2.40) and (2.41) yields the time averaged continuity and momentum equations, namely

$$\frac{\partial U_i}{\partial x_i} = 0 \tag{2.42}$$

and

$$\rho \frac{\partial U_i}{\partial t} + \rho \frac{\partial}{\partial x_j}\left(U_j U_i + \overline{u_j' u'}_i\right) = -\frac{\partial P}{\partial x_i} + \frac{\partial}{\partial x_j}\left(2\mu S_{ji}\right), \tag{2.43}$$

respectively*. Equation (2.43) can be rewritten

$$\rho \frac{\partial U_i}{\partial t} + \rho U_j \frac{\partial U_i}{\partial x_j} = -\frac{\partial P}{\partial x_i} + \frac{\partial}{\partial x_j}\left(2\mu S_{ji} - \rho \overline{u_j' u_i'}\right). \tag{2.44}$$

Equation (2.44) is generally referred to as the Reynolds-Averaged Navier-Stokes (RANS) equation and the quantity $-\rho \overline{u_j' u'}_i$ as the Reynolds stress tensor, from which the "specific Reynolds stress tensor" is defined as

$$\tau_{ij} = -\overline{u_i' u_j'}. \tag{2.45}$$

By inspection, the specific Reynolds stress tensor is symmetric and it therefore has only six unknowns rather than nine, which, when combined with the primitive variables (*u, v, w* and *p*) results in ten unknowns but only four fundamental equations to solve. Hence, the system of equations is not closed, which forms the definition of the problem with Reynolds-averaging: that a method or model is required to solve for the specific Reynolds stress tensor, Equation (2.45). There are two methods available to attempt to close the equation/variable imbalance, either:

1. Develop additional equations to solve so that the equation/unknown system can be closed, or;
2. Directly model the specific Reynolds stress tensor.

* The process for averaging with either the spatial or ensemble methods is essentially the same and, therefore, will not be repeated.

### 2.6.2. The Closure Problem

If the first option is attempted then, in an effort to develop additional equations, moments of the Navier-Stokes equations can be taken: that is the Navier-Stokes equations can be multiplied by a fluctuating quantity with the resultant expression time averaged to develop a differential equation for the Reynolds-stress tensor[*]. To demonstrate this procedure a "Navier-Stokes operator" (Wilcox, 1998) is defined for the constant properties Navier-Stokes equation, such that

$$\mathbb{N}\left(u_i\right) = \rho\frac{\partial u_i}{\partial t} + \rho u_k\frac{\partial u_i}{\partial x_k} + \frac{\partial p}{\partial x_i} - \mu\frac{\partial^2 u_i}{\partial x_k \partial x_k} \tag{2.46}$$

and noting that from mass conservation and for incompressible flow $s_{ij} = u_{i,kk}$ the viscous term can be simplified. Using the new notation the Navier-Stokes equation becomes

$$\mathbb{N}\left(u_i\right) = 0\,. \tag{2.47}$$

To derive an equation for the Reynolds stress tensor a time average can be performed such that

$$\overline{u_i'\mathbb{N}\left(u_j\right) + u_j'\mathbb{N}\left(u_i\right)} = 0\,. \tag{2.48}$$

In the following section, subscript comma notation will be used to represent derivatives, for example

$$\left(u_i\right)_{,t} \equiv \frac{\partial u_i}{\partial t}\,. \tag{2.49}$$

Therefore, proceeding term by term:

1. The unsteady term

[*] The derivations presented in this section follow closely from that given by Wilcox (1998).

$$\begin{aligned}\overline{u_i'\left(\rho u_j\right)_{,t}+u_j'\left(\rho u_i\right)_{,t}} &= \overline{\rho u_i'\left(U_j+u_j'\right)_{,t}}+\overline{\rho u_j'\left(U_i+u_i'\right)_{,t}}\\ &= \overline{\rho u_i'U_{j,t}}+\overline{\rho u_i'u_{j,y}'}+\overline{\rho u_j'U_{i,t}}+\overline{\rho u_j'u_{i,t}'}\\ &= \overline{\rho u_i'u_{j,y}'}+\overline{\rho u_j'u_{i,t}'}\\ &= \overline{\rho\left(u_i'u_j'\right)_t}\\ &= -\rho\frac{\partial\tau_{ij}}{\partial t}\end{aligned} \tag{2.50}$$

2. The convective term

$$\begin{aligned}\overline{\rho u_i'u_ku_{j,k}+\rho u_j'u_ku_{i,k}} &= \overline{\rho u_i'\left(U_k+u_k'\right)\left(U_j+u_j'\right)_{,k}}+\overline{\rho u_j'\left(U_k+u_k'\right)\left(U_i+u_i'\right)_{,k}}\\ &= \overline{\rho u_i'U_ku_{j,k}'}+\overline{\rho u_i'u_k'\left(U_j+u_j'\right)_{,k}}+\overline{\rho u_j'U_ku_{i,k}'}+\overline{\rho u_j'u_k'\left(U_i+u_i'\right)_{,k}}\\ &= \rho U_k\overline{\left(u_i'u_j'\right)_{,k}}+\rho\overline{u_j'u_k'}U_{j,k}+\rho\overline{u_j'u_k'}U_{i,k}+\rho\overline{u_k'\left(u_i'u_j'\right)_{,k}}\\ &= -\rho U_k\frac{\partial\tau_{ij}}{\partial x_k}-\rho\tau_{ik}\frac{\partial U_j}{\partial x_k}-\rho\tau_{jk}\frac{\partial U_i}{\partial x_k}+\rho\frac{\partial}{\partial x_k}\overline{\left(u_i'u_j'u_k'\right)}\end{aligned} \tag{2.51}$$

3. The pressure gradient term

$$\begin{aligned}\overline{u_i'p_{,j}+u_j'p_{,i}} &= \overline{u_i'\left(P+p'\right)_{,j}}+\overline{u_i'\left(P+p'\right)_{,i}}\\ &= \overline{u_i'p_{,j}'+u_j'p_{,i}'}\\ &= \overline{u_i'\frac{\partial p'}{\partial x_j}}+\overline{u_j'\frac{\partial p'}{\partial x_i}}\end{aligned} \tag{2.52}$$

4. The viscous term

$$\begin{aligned}\overline{\mu\left(u_i'u_{j,kk}+u_j'u_{i,kk}\right)} &= \mu\overline{u_i'\left(U_j+u_j'\right)_{,kk}}+\mu\overline{u_j'\left(U_i+u_i'\right)_{,kk}}\\ &= \mu\overline{u_i'u_{j,kk}'}+\mu\overline{u_j'u_{i,kk}'}\\ &= \mu\overline{\left(u_i'u_{j,k}'\right)_{,k}}+\mu\overline{\left(u_j'u_{i,k}'\right)_{,k}}-2\mu\overline{u_{i,k}'u_{j,k}'}\\ &= \mu\overline{\left(u_i'u_{j,k}'\right)_{,kk}}-2\mu\overline{u_{i,k}'u_{j,k}'}\\ &= -\mu\frac{\partial^2\tau_{ij}}{\partial x_k\partial x_k}-2\mu\overline{\frac{\partial u_i'}{\partial x_k}\frac{\partial u_j'}{\partial x_k}}\end{aligned} \tag{2.53}$$

Collecting the four terms detailed above, the equation for the Reynolds stress tensor becomes

$$\frac{\partial \tau_{ij}}{\partial t} + U_k \frac{\tau_{ij}}{\partial x_k} = -\tau_{ik}\frac{\partial U_j}{\partial x_k} - \tau_{jk}\frac{\partial U_i}{\partial x_k} + 2\nu\overline{\frac{\partial u_i'}{\partial x_k}\frac{\partial u_j'}{\partial x_k}} + \overline{\frac{u_i'}{\rho}\frac{\partial p'}{\partial x_j}} + \overline{\frac{u_j'}{\rho}\frac{\partial p'}{\partial x_i}} + \frac{\partial}{\partial x_k}\left[\nu\frac{\partial \tau_{ij}}{\partial x_k} + \overline{u_i' u_j' u_k'}\right] \quad (2.54)$$

Hence, an additional six equations have been generated: being one for each unknown quantity in the Reynolds stress tensor. However, an additional 22 unknown correlations have simultaneously been generated. This illustrates the closure problem for turbulence modelling, which is that, due to the non-linearity in the Navier-Stokes equations, as higher moments of the Navier-Stokes equations are taken, additional correlations are generated at an increasing rate. Therefore, as it is apparent that the equation/unknown system cannot be closed, that models must be developed instead to account for the unknown correlations.

## 2.7. Turbulence Models for the Reynolds Averaged Formulation

There are numerous models that have been designed to close the Reynolds stress equation that vary from simple algebraic models such as the Prandtl mixing length model (Prandtl, 1925) to complex multi-equation models such as the $k$-$\varepsilon$-$v^2$ model proposed by Durbin (1995). However, perhaps the most popular model of the RANS class is the $k$-$\varepsilon$ model (Wilcox, 1998), which was originally proposed by Jones and Launder (1972) and subsequently revised by Launder and Sharma (1974), or it's derivatives such as the RNG $k$-$\varepsilon$ model (Yakhot et al., 1992). As it is probably the most popular RANS model $k$-$\varepsilon$ model will be briefly described.

The $k$-$\varepsilon$ model is a two-equation model in which additional transport equations are solved for two turbulence quantities (Pope, 2001), namely the turbulence kinetic energy, $k$, and the turbulent dissipation rate, $\varepsilon$. However, despite the potential elegance of a solution derived from, apparently, rigorous transport equations Wilcox (1998) cautions that the CFD user must "…avoid modelling the differential equations rather than the physics of turbulence…". That is, with the $k$-$\varepsilon$ model as there are five empirical coefficients that must be adjusted for the particular simulation, it is entirely possible for any desired solution to be found with appropriate "tuning".

Nevertheless, the standard the $k$-$\varepsilon$ model consists of the turbulence kinetic energy equation

$$\frac{\partial k}{\partial t} + U_j \frac{\partial k}{\partial x_j} = \tau_{ij} \frac{\partial U_i}{\partial x_j} - \varepsilon + \frac{\partial}{\partial x_j}\left[\left(\nu + \frac{\nu_T}{\sigma_k}\right)\frac{\partial k}{\partial x_j}\right]; \tag{2.55}$$

the dissipation rate equation

$$\frac{\partial \varepsilon}{\partial t} + U_j \frac{\partial \varepsilon}{\partial x_j} = C_{\varepsilon 1} \frac{\varepsilon}{k} \tau_{ij} \frac{\partial U_i}{\partial x_j} - C_{\varepsilon 2} \frac{\varepsilon^2}{k} + \frac{\partial}{\partial x_j}\left[\left(\nu + \frac{\nu_T}{\sigma_\varepsilon}\right)\frac{\partial \varepsilon}{\partial x_j}\right]; \tag{2.56}$$

and the kinematic eddy viscosity equation

$$\nu_T = \frac{C_\mu k^2}{\varepsilon}. \tag{2.57}$$

The five closure coefficients for the standard model are (Launder and Spalding, 1974):

$$C_{\varepsilon 1} = 1.44; \tag{2.58}$$

$$C_{\varepsilon 2} = 1.92; \tag{2.59}$$

$$C_\mu = 0.09; \tag{2.60}$$

$$\sigma_k = 1.0 \tag{2.61}$$

and

$$\sigma_\varepsilon = 1.3. \tag{2.62}$$

The compromise for the significant reduction in computational expense with RANS models is a corresponding reduction in the flow physics that can be captured; or an average based solver can only produce average results. For example, a flow that is known to contain separated flow regions and a fluctuating, separated wake zone will become steady, and thus provide no, or limited at best, data on the periodic shedding phenomena, but may still accurately compute the average drag on the body. Therefore, in an attempt to increase the accuracy of RANS models but without the full computational cost of LES or DNS a number of hybrid techniques have been developed, which strive to combine the increased accuracy of LES methods with the speed of RANS models.

## 2.8. Hybrid Turbulence Models: Detached Eddy Simulation

Methods of computing turbulent flows that allow for the application of alternate modelling techniques at differing wave numbers is commonly referred to as hybrid, or multi-resolution, turbulence modelling (Sagaut et al., 2006). Popular multi-resolution methods include both multi-level large eddy simulation and detached eddy simulation (DES). Detached eddy simulation is a method that applies both RANS and LES models in different flow regions. A recent review of, and introduction to, scale separation methodologies has been published by Sagaut et al (2006) and the reader is referred to that work for more detail.

DES is a hybrid turbulence model that uses RANS in the near wall region and LES in the bulk of the flow domain. Because the near wall resolution requirements for RANS models are significantly smaller than LES, that is RANS models demand larger cells, using RANS models in the near wall region can significantly reduce the required cell count. Simultaneously, the cells in the body of the domain where the majority of the flow energy is contained are computed by the LES solver, which allows for the majority of the flow physics to be captured and computed rather than averaged.

One of the earliest DES models was proposed by Spalart *et al* (1997) and was based on the Spalart-Allmaras one equation RANS model (Spalart and Allmaras, 1992). The original RANS model was modified with an alternate distance function to facilitate the transition between the RANS and LES regions.

It has been noted that despite the promise of increased speed of DES, actual computations may not achieve these increases (*'Detached Eddy Simulation,'* 2009). That is, the increased computational cost associated with splitting the regions into either RANS or LES zones may outweigh the savings from the reductions from the RANS solver.

## 2.9. ILES: The Alternative Used in this Research

Of these methods discussed above all have their strengths and weaknesses but it is the present author's opinion that LES provides the most promise because:

1. LES does not suffer from the averages introduced with RANS.

2. It approaches the grid resolved "accuracy" of DNS.

3. It does not suffer from the computational cost of DNS.

The limitation of LES is, therefore, the quality of the sub-grid scale model that is chosen for the simulation. Unfortunately, or perhaps fortunately depending on the position of the observer, it appears that a primary goal of the turbulence modelling community to develop "…more complex subgrid-scale models [and is therefore the] *raison d'etre*" of the turbulence modelling community (Grinstein et al., 2007). The present author would argue that it is not always better to have a more complex model, which will almost certainly increase the computational requirements, for a potentially marginal, if any, increase in the accuracy of the solution. Hence the appeal for simpler methods that utilise the properties of the spatial difference scheme that would be required for the grid resolved components to approximate the SGS contribution. These are the so-called Monotone Integrated Large Eddy Simulations (MILES) or Implicit Large Eddy Simulations (ILES).

Interest has been growing in disparate research groups, including our own based loosely at the University of Technology Sydney, Australia; the University of NSW, Australia and the University of Rome 1 la Sapienza, Italy, despite the entrenched resistance of the turbulence community. Grinstein et al (2007) argue that this resistance is natural given the focus on developing new, more complex models rather than, relatively simple, numerical difference schemes. The specific method used in the research described in this dissertation has been used with great success within our group (Horrocks, 2001) and is based on an implementation of a $2^{nd}$ Order Upwind with limiter numerical scheme for the convective term in the momentum equation. As this scheme includes a limiter which is designed to preserve the monotonicity of the solution (Barth and Jespersen, 1989) the present author would argue that it meets the definition of a MILES scheme (Boris, 2007). It is, however, a lower order than most schemes (Boris, 2007) and it remains to be seen as to the applicability of the $2^{nd}$ order scheme to the flow configurations proposed for this research. A presentation of a numerical scheme would not be complete without a simultaneous introduction to the finite volume method used.

# 3. The Finite Volume Method

## *3.1. Introduction and Conventions*

Because the mathematical models used to describe fluid flow that were presented and discussed in the previous chapter are non-linear, partial differential equations, there are generally no analytic solutions to realistic flows (Constantin and Foias, 1988, Drazin and Riley, 2006). Therefore, solutions for flows that are of practical interest to engineers and scientists require the introduction numerical methods. The first step in developing a numerical method is to transform the continuum equations developed above from partial differential equations to algebraic equations by an appropriate means of discretisation. Then, the discretised equations must be solved with an appropriate solution algorithm. Again, as both of these procedures are thoroughly documented in the available literature, for example Verseteeg and Malalasekera (1996) or Roache (1998a), the discussion in this chapter will be brief and limited to introducing the major methods used in this research.

The general procedure for any finite volume based solver is to:

1. Integrate the conservation equations over the finite volumes;
2. Apply finite difference approximations to the integrated conservation equations, including the boundary conditions and;
3. Solve the finite difference equations iteratively until the desired level of convergence is obtained;
4. For unsteady problems repeat step three as required until the desired simulation time is reached.

The integration step is usually only performed once at the development stage of a CFD code. Once the integration has been performed, the finite difference approximations are applied at run time to the computational mesh that has been developed for the simulation.

For each specific geometric configuration, a computational mesh must be developed to map the discretised equations to. There is a number of requirements that must be met to

ensure a high "mesh quality" such as the resolution requirements in regions of high curvature (for both geometric curvature and flow gradients) and suitable expansion ratios from small cells to larger cells. Therefore, the process of mesh generation is an optimisation process to balance the need for a highly accurate mesh, that is a high-resolution grid with many cells, with the need to restrict computational resources.

For this discussion of numerical methods, the standard CFD convention of using cardinal directions to identify faces will be used (Versteeg and Malalasekera, 1996), as illustrated in Figure 3-1. That is, the sides facing the positive *x*-direction and the

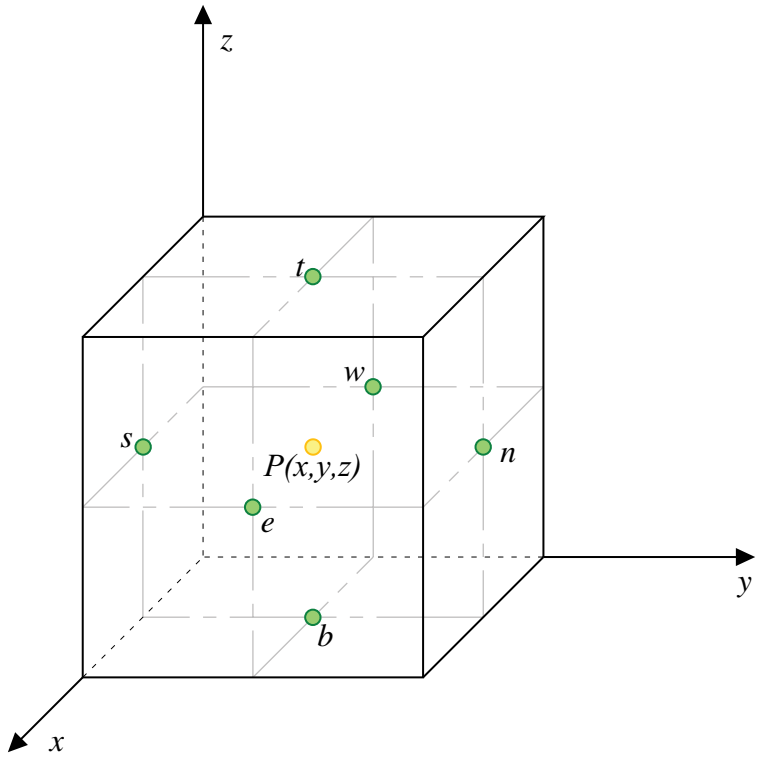


**Figure 3-1 – Definition sketch for a finite volume cell using standard cardinal directions to identify cell faces.**

negative *x*-direction are categorised as the east, *e*, and the west, *w*, faces respectively. Similarly, in the *y*-direction the sides are referred to as north (*n*) and south (*s*), while the *z*-direction faces are called top (*t*) and bottom (*b*). The cardinal direction convention is further defined to differentiate between adjacent cells and faces with the use of uppercase and lowercase letters respectively. The general cell-centre point under consideration is denoted as *P*.

In order to preform the finite volume integration the Navier Stokes equation, Equation (2.3) developed previously, is first recast into the form of a conservation law for the transport of a generic scalar $(\eth)$ in unsteady flow

$$\underbrace{\frac{\partial}{\partial t}(\rho\eth)}_{1} + \underbrace{\nabla\cdot(\rho\mathbf{u}\eth)}_{2} = \underbrace{\nabla\cdot(\Gamma\nabla\eth)}_{3} + \underbrace{S_{\eth}}_{4}, \tag{3.1}$$

in which the numbered terms represent: (1) the unsteady term; (2) the convective term; (3) the diffusion term and (4) the source term. Recasting the Navier-Stokes equation in this format allows for, with careful selection of the primary variable $(\eth)$, the diffusion coefficient $(\Gamma)$ and the application of sources, a single finite difference equation to represent any transported property such as an individual component of momentum, mass or passive scalars. For example, if $\eth = u$, $\Gamma = \mu$ and with zero sources then Equation (3.1) becomes

$$\frac{\partial}{\partial t}(\rho u) + \nabla\cdot(\rho\mathbf{u}u) = \nabla\cdot(\mu\nabla u), \tag{3.2}$$

which is the *x*-direction momentum equation with no sources. Further, if $\eth = 1$, $\Gamma = 0$ and with no sources Equation (3.1) becomes

$$\frac{\partial}{\partial t}(\rho) + \nabla\cdot(\rho\mathbf{u}) = 0 \tag{3.3}$$

which is the continuity equation for unsteady, compressible flow.

Therefore, to develop a general method that is applicable to all flow types and variables a general method to discretise the four terms of Equation (3.1) must be developed. This general method would proceed through the four steps listed above with the first task to integrate the continuum equations – Equation (3.1) – over both a suitably small control volume and, for an unsteady simulation, a short time increment.

## *3.2. Integration of the General Conservation Equation*

The fundamental step of the finite volume method is the integration of the general transport equation over a control volume (Versteeg and Malalasekera, 1996), that is

$$\int_{\vartheta}\frac{\partial}{\partial t}(\rho\eth)d\vartheta + \int_{\vartheta}\nabla\cdot(\rho\mathbf{u}\eth)d\vartheta = \int_{\vartheta}\nabla\cdot(\Gamma\nabla\eth)d\vartheta + \int_{\vartheta}S_{\eth}d\vartheta\,. \tag{3.4}$$

The volume integrals that contain divergence terms in Equation (3.4) are difficult to evaluate numerically compared to surface flux integrals. Therefore, as the Gauss divergence theorem provides a link between divergence volume integrals and surface flux integrals, an application of Gauss' theorem to the divergence terms in Equation (3.4) results in

$$\int_{\vartheta} \frac{\partial}{\partial t}(\rho\tilde{\phi})d\vartheta + \int_{A} \hat{\mathbf{n}} \cdot (\rho\mathbf{u}\tilde{\phi})dA = \int_{A} \hat{\mathbf{n}} \cdot (\Gamma\nabla\tilde{\phi})dA + \int_{\vartheta} S_{\tilde{\phi}}d\vartheta \tag{3.5}$$

in which $\hat{\mathbf{n}}$ is the outward pointing surface normal vector. Then, for unsteady problems, Equation (3.5) must be also integrated over a small time step, $\Delta t$,

$$\begin{aligned} \int_{t}^{t+\Delta t} \left( \int_{\vartheta} \frac{\partial}{\partial t}(\rho\tilde{\phi})d\vartheta \right) dt + \int_{t}^{t+\Delta t} \left( \int_{A} \hat{\mathbf{n}} \cdot (\rho\mathbf{u}\tilde{\phi})dA \right) dt \\ = \int_{t}^{t+\Delta t} \left( \int_{A} \hat{\mathbf{n}} \cdot (\Gamma\nabla\tilde{\phi})dA \right) dt + \int_{t}^{t+\Delta t} \int_{\vartheta} S_{\tilde{\phi}}\, d\vartheta\, dt. \end{aligned} \tag{3.6}$$

Equation (3.6) is the result of the integration of the general transport equation over both a control volume and a suitably small time step but is still a continuum equation. It must therefore be transformed into a discrete equation by converting the integrals into summations.

## *3.3. Discretisation of the General Conservation Equation*

### 3.3.1. The Surface Flux Integral Terms

Numerically*, surface flux integrals are computed with the assumption that the variable value at the face acts uniformly over the same face. For example, using the one-dimensional control volume, shown in Figure 3-2, and the naming convention outlined in §3.1 the mass transferred through the east face of the element over a given time increment, $\Delta t$,

$$m_e = \rho u_e A_e \Delta t \tag{3.7}$$

in which $u_e$ is the velocity at the east face and $A_e$ is the area of the east face.

* For this and the next subsection the integration over time will be ignored to focus on a discussion of the spatial terms.

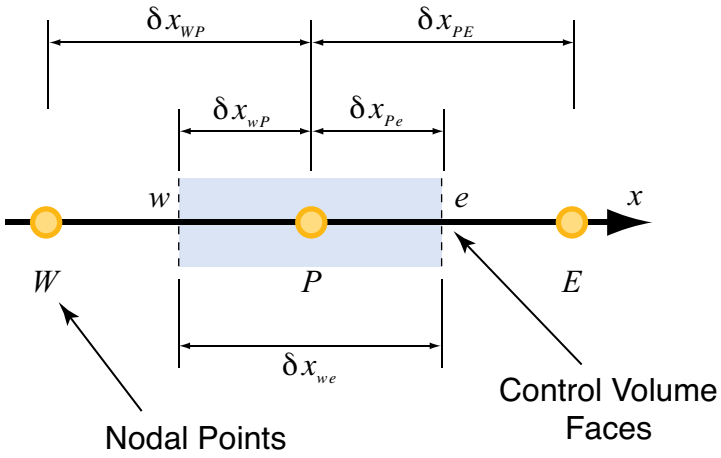


**Figure 3-2 – Sketch of the nodes and faces used in a one-dimensional control volume, adapted from Versteeg and Malalasekera (1996).**

While it is a computationally trivial task to compute the face areas, the velocities – and all the other flow variables such as the pressure are stored in a "co-located cell-centred variable arrangement" (ESI CFD Inc., 2007b). Therefore, the next step in the discretisation process is to develop suitable expressions to transfer the cell centred values to cell faces, where the surface flux integrals are computed. From an inspection of the surface integrals in Equation (3.5) there are two quantities that must be moved from the cell centre: (1) a variable and (2) a gradient of a variable.

With the variables, perhaps the simplest method to transfer a value from the cell centres to the intermediate cell face is to assume a linear distribution between the nodes,

$$\Gamma_e = \frac{\Gamma_P + \Gamma_E}{2}, \tag{3.8}$$

that is an average of the nodal values.

The gradient term can be computed directly from first principles: that the slope is equal to the change in the variable divided by the distance over which the change takes place. Hence, the gradient at face *e* in Figure 3-2 would be evaluated as

$$\nabla\tilde{\partial} = \frac{\tilde{\partial}_E - \tilde{\partial}_P}{\delta x_{EP}}. \tag{3.9}$$

This gradient is then assumed to act uniformly across the interval between the nodes and is therefore directly applicable at the east face.

Next, the surface integral itself is discretised into a summation over the faces of the cell. Continuing with the one-dimensional example, the summation is

$$\int_A \mathbf{n} \cdot (\Gamma \nabla \phi) dA = (\Gamma \nabla \phi A)_e - (\Gamma \nabla \phi A)_w \tag{3.10}$$

in which the terms on the right hand side of the equation are to be further expanded using the rules discussed above. This procedure is then repeated as required for further surface integral terms in Equation (3.5). Of the spatial terms, a technique to evaluate the volume integrals needs to be developed.

### 3.3.2. The Source and Volume Integral Terms

The volume terms are evaluated by assuming that the cell-centred variables act over the entire cell volume. Hence, the required integrations are reduced to a multiplication of the variable and the cell volume. Continuing with the one-dimensional example from the volume integral term of Equation (3.5), term (1) becomes

$$\int_\vartheta \rho \phi d\vartheta = \rho_P \phi_P \vartheta_{cell} . \tag{3.11}$$

As the source term in Equation (3.5) is also a volume integral it can be evaluated in a similar manner such that

$$\int_\vartheta S_\phi d\vartheta = \overline{S} \vartheta_{cell} \tag{3.12}$$

in which $\overline{S}$ is the volume averaged source term. However, as there are numerous cases where the source term is a function of the dependent variable (Versteeg and Malalasekera, 1996) it is convenient to approximate the source term in Equation (3.5) using a linear form

$$\overline{S} \vartheta_{cell} = S_u + S_P \phi_P \tag{3.13}$$

in which both the $S_u$ and $S_P$ terms are assumed to be volume averaged values (Patankar, 1980, ESI CFD Inc., 2007b). The $S_u$ and $S_P$ coefficients must be evaluated for each particular case and their specific implementation will not be discussed further, rather the interested reader is referred to the treatise by Patankar (1980) for a fuller discussion of source term linearisation. At this point in the discussion of the finite volume method, all the terms have been discretised in space but the effect of the

integration over time has been ignored. Therefore, suitable methods for computing the unsteady effects must be developed.

### 3.3.3. The Unsteady Term and Time Integrals

To discretise the unsteady term, term (1) in Equation (3.6), the order of the integration is reversed so that the time integral becomes the inner integral. Then, it is necessary to assume that the value of the general variable at the next forward time step can be linearly projected in time as

$$\bar{\delta}_P = \bar{\delta}_P^o + \left(\frac{\partial \bar{\delta}}{\partial t}\right)^o \Delta t \tag{3.14}$$

in which the superscript, $^o$, indicates the current time step with values of the variable at the forward time step not superscripted. Equation (3.14) can then be re-arranged such that

$$\left(\frac{\partial \bar{\delta}}{\partial t}\right)^o = \frac{\bar{\delta}_P - \bar{\delta}_P^o}{\Delta t}, \tag{3.15}$$

which, when substituted into the unsteady term of Equation (3.6), combined with the change of order of the integrals and an assumption that the cell centred variables act over the entire cell gives

$$\begin{aligned}
\int_t^{t+\Delta t}\left(\int_\vartheta \frac{\partial}{\partial t}(\rho\bar{\delta})d\vartheta\right)dt &= \int_\vartheta \int_t^{t+\Delta t} \rho\left(\frac{\partial \bar{\delta}}{\partial t}\right)dt\,d\vartheta \\
&= \int_\vartheta \rho\left[\frac{\partial \bar{\delta}}{\partial t}t\right]_t^{t+\Delta t} d\vartheta \\
&= \int_\vartheta \rho\frac{\partial \bar{\delta}}{\partial t}\Delta t\,d\vartheta \\
&= \rho\left(\frac{\bar{\delta}_P - \bar{\delta}_P^o}{\Delta t}\right)\Delta t\Delta\vartheta \\
&= \rho\left(\bar{\delta}_P - \bar{\delta}_P^o\right)\Delta\vartheta \quad .
\end{aligned} \tag{3.16}$$

A similar argument to that expressed in Equation (3.15) for the unsteady term can be used to develop expressions that describe the change over time for the nodal variables already discretised in the spatial terms, as discussed in §3.3.1 and §3.3.2. However, to generalise these terms a blending factor, $\mathfrak{X}$, that is defined for

$$0 \le \chi \le 1 \tag{3.17}$$

will be introduced so that the general integral over time of a spatial variable becomes

$$\begin{aligned} I_{\phi} &= \int_{t}^{t+\Delta t} \phi_P \, dt \\ &= \left[ \chi \phi_P - (1-\chi) \phi_P^o \right] \Delta t. \end{aligned} \tag{3.18}$$

At this point suitable discretisation schemes have been developed for all the spatial terms and the effects of the unsteady term and integration over time have been accounted for. The discretisations discussed that were designed to transfer the variables from cell centred to face centred values have assumed linear distributions of the adjacent cells. Clearly there are other schemes not based on the assumption of linearity that could instead be used.

## *3.4. Finite Difference Schemes*

### 3.4.1. Spatial and Temporal Schemes in CFD-ACE+

In the discussion of discretisation of the Navier-Stokes equations in §3.3, finite spatial differences have been implicitly used, for example the central difference in Equation (3.9), but their strengths, weaknesses or alternatives have not been discussed. There are a number of discretisation schemes available but the discussion in this section will be limited to the specific schemes used in the research presented in this dissertation*.

The specific discretisation of the diffusion term and the source term that was used in the work described herein is no different from that given in the general description given above in §3.3. In contrast, there are some additions to the unsteady term over the method previously described. The crux of this research lies with the MILES scheme implemented to discretise the convection term, which will be presented after the discretisation of the unsteady term.

* For full details on additional numerical schemes the reader is referred to the treatises by Roache (1998a) or Chung (2002).

### 3.4.2. The Unsteady Term

The unsteady term has already been discretised in §3.3.3 and this is the dominant scheme used in CFD-ACE+. However, there are a number of temporal differencing schemes implemented within CFD-ACE+, which are based on varying the blending factor, $\mathfrak{X}$, in Equation (3.18). Three separate cases of $\mathfrak{X}$ can be considered.

Firstly, suppose that

$$\mathfrak{X} = 0 \tag{3.19}$$

then the time integration scheme is described as explicit because the forward in time values depend only on the known, explicit, values from the current time. Conversely, when

$$\mathfrak{X} = 1 \tag{3.20}$$

the scheme is known as a "fully implicit", or backward in time, scheme because the forward in time values can not be explicitly computed and iterative numerical methods must be used.

For the final case where

$$0 < \mathfrak{X} < 1 \tag{3.21}$$

the time integration method is known as a semi-implicit scheme because it is neither fully implicit nor fully explicit. However, there is a special case when

$$\mathfrak{X} = 0.5 \tag{3.22}$$

which is known as the Crank-Nicolson scheme (Crank and Nicolson, 1947).

Although the value of $\mathfrak{X}$ can be specified across the entire range of values defined by Equation (3.17) within CFD-ACE+ the developers have set the defaults to either a Crank-Nicolson scheme or fully implicit backward Euler scheme (ESI CFD Inc., 2007a). This decision appears to have been made because for both these schemes, and indeed for any time integration scheme with

$$\frac{1}{2} \le \mathfrak{X} \le 1, \tag{3.23}$$

the solution is unconditionally stable (Fletcher, 1991, Roache, 1998a) for all values of the time step size. However, as noted by Roache (1998a) the accuracy of the backward Euler scheme is low with errors in the

$$O\left(\Delta t, \Delta x^2\right) \tag{3.24}$$

while the errors from the Crank-Nicolson scheme are in the

$$O\left(\Delta t^2, \Delta x^2\right). \tag{3.25}$$

Therefore, the Crank-Nicolson scheme, while still being unconditionally stable (for simple equations), has higher time accuracy than the fully implicit backward Euler scheme. Roache (1998a) further notes a caveat to the unconditional stability of the Crank-Nicolson scheme: specifically that for large $\Delta t$, while remaining stable, the accuracy of the solution will be reduced to $O\left(\Delta t, \Delta x^2\right)$ or worse.

Finally, the forward Euler scheme is not available because although it has the same order of magnitude error as the backward Euler scheme – Equation (3.24) – it is conditionally stable dependent on the time step size. That is, the forward Euler scheme is stable, according to Roache (1998a), if the Courant-Freidrichs-Lewy number (Courant et al., 1967),

$$CFL \triangleq \frac{u_c \Delta t}{\Delta x} \tag{3.26}$$

in which $u_c$ is the velocity in the cell in question and is restricted to the range

$$CFL \leq 1 \tag{3.27}$$

and

$$\Delta t \leq \frac{2\alpha}{u_c^2} \tag{3.28}$$

in which

$$\alpha = \frac{1}{\mathrm{Re}}. \tag{3.29}$$

Therefore, if the CFL inequality is not met the solution is unstable and may result in unpredictable solutions.

### 3.4.3. Convection Term

Following the general procedure outlined above, the convection term is discretised as

$$\begin{aligned}\nabla\cdot\left(\rho\mathbf{u}\tilde{\phi}\right) &= \int_{\vartheta}\nabla\cdot\left(\rho\mathbf{u}\tilde{\phi}_i\right)d\vartheta \\ &= \oint_{A}\hat{\mathbf{n}}\cdot\mathbf{u}\rho\tilde{\phi}_i\,dA \\ &= \sum_{i=1}^{n_{faces}}\hat{\mathbf{n}}_i\cdot\mathbf{u}_i\rho\tilde{\phi}_i A_i \\ &= \sum_{i=1}^{n_{faces}}C_i\tilde{\phi}_i \qquad .\end{aligned} \tag{3.30}$$

in which $C_i$ is the mass flux across the face $i$. Therefore, the variable $\tilde{\phi}$ must be transferred from the cell centre to the face prior to being evaluated. In the example above, the variable at the face was evaluated via an average of the two adjacent cell centred values. An alternative to this method is to estimate the gradient of variable across the cell then, with the assumption that the gradient was constant across the entire cell, project from the known cell centred value to the face in question. Barth and Jespersen (1989) developed such a method with an additional limiter to constrain the projected value such that it would remain within the certain bounds. It is the Barth and Jespersen scheme that was used in this research and the discussion of the method necessarily follows closely with their original paper (Barth and Jespersen, 1989). It should be noted that to reduce extensive repetition, Barth and Jaspersen (1989) may be referred to as B&J.

Suppose that it is required to calculate the gradient across a general cell $P$ that was located in a two-dimensional grid, as shown in Figure 3-3.

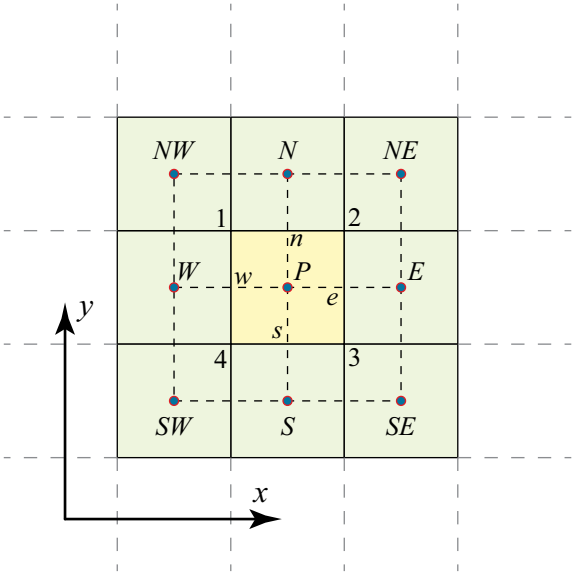


**Figure 3-3 – Regular two-dimensional grid for the explanation of the Barth and Jespersen gradient estimation technique (Barth and Jespersen, 1989).**

To compute the gradient across the cell *P,* B&J noted that the Green theorem is

$$\int_{\Omega} \nabla \eth \, dA_{\Omega} = \oint_{\partial\Omega} \eth \hat{\mathbf{n}} \, d\hat{\mathbf{s}} \tag{3.31}$$

in which $\Omega$ is an arbitrary area and $\partial\Omega$ is the path around that area. Therefore, the cell averaged gradient can be computed from

$$\nabla \eth_P = \frac{1}{A_{\Omega}} \oint_{\partial\Omega} \eth \hat{\mathbf{n}} \, d\hat{\mathbf{s}} \, . \tag{3.32}$$

As $\Omega$ is an arbitrary area both the "path and numerical quadrature" (Barth and Jespersen, 1989) must be chosen with care. B&J therefore defined two requirements which must be met for any path:

1. The gradient must be calculated exactly when there is a liner variation of the variable.
2. The gradient must be defined for arbitrary meshes.

Barth and Jespersen (1989) recommended the

> *...centroid-centroid path tracing the convex hull of the neighbor* [sic] *set of all centroids that share a common vertex with face* [P] *and compute the gradient via the trapezoidal rule..."*

that for the present two-dimensional example is the path

$$NW \rightarrow N \rightarrow NE \rightarrow E \rightarrow SE \rightarrow S \rightarrow SW \rightarrow W \rightarrow NW \,. \tag{3.33}$$

With the gradient computed the cell centred value could simply be projected to any point, $\eth(x,y)$, including the face centred that is required, using

$$\eth(x,y) = \eth(x_P, y_P) + \nabla\eth_P \cdot \Delta r \,. \tag{3.34}$$

However, they further suggested that the gradient should be "limited"

$$\eth(x,y) = \eth(x_P, y_P) + \Phi_P \nabla\eth_P \cdot \Delta r \tag{3.35}$$

in which

$$0 \le \Phi \le 1 \,. \tag{3.36}$$

Then $\Phi$ must be maximised but still conserve the monotonic principle that the "…values of a linearly reconstructed function must not exceed the maximum and minimum of neighboring [*sic*] centroid values (including the centroid value at *P*)…" (Barth and Jespersen, 1989). With these constraints on $\Phi$ the calculation is relatively straight forward. First it is necessary to define

$$\eth_P^{\min} = \min\left(\eth_P, \eth_{neighbours}\right) \tag{3.37}$$

and

$$\eth_P^{\max} = \max\left(\eth_P, \eth_{neighbours}\right), \tag{3.38}$$

so that

$$\eth_P^{\min} \le \eth(x,y) \le \eth_P^{\max} \,. \tag{3.39}$$

Next, after it was noted that for all linear reconstructions the extrema would occur at the vertices, the value of the variable can be computed at each face,

$$\eth_i = \eth(x_i, y_i) \tag{3.40}$$

in which

$$i = 1,2\ldots,n_{vertices}\,, \tag{3.41}$$

and then minima of $\Phi_P$ in Equation (3.35) are computed from the vertices as

$$\Phi_P = \begin{cases} \min\left(1, \dfrac{\tilde{\sigma}_P^{\max} - \tilde{\sigma}_P}{\tilde{\sigma}_i - \tilde{\sigma}_P}\right) & \text{if } \tilde{\sigma}_i - \tilde{\sigma}_P > 0 \\ \max\left(1, \dfrac{\tilde{\sigma}_P^{\min} - \tilde{\sigma}_P}{\tilde{\sigma}_i - \tilde{\sigma}_P}\right) & \text{if } \tilde{\sigma}_i - \tilde{\sigma}_P < 0 \\ 1 & \text{if } \tilde{\sigma}_i - \tilde{\sigma}_P = 0 \end{cases} . \tag{3.42}$$

Thus far the evaluation of the mass flux at the cell face, $C_i$, has been ignored but this will be remedied later in the discussion of the coupling of the velocity and the pressure fields.

## 3.5. The General Finite Volume Equation

As the continuum equations have been discretised in both the spatial and temporal domains in the preceding sections the individual terms must be brought together and combined in a form suitable for the numerical solver. This condensed form, where like terms are collected with faces on the right hand side and cell centred on the left hand side, is referred to as the general finite volume equation (Patankar, 1980). Further, the general equation can be arranged in a form that is considerably simpler to read than that obtained by expanding the rules described above. That is, a coefficient summation convention can be implemented such that the notation reduces to (Patankar, 1980)

$$\left(a_P - S_P\right)\tilde{\sigma}_P = \sum_{faces} a_{face}\tilde{\sigma}_{face} + S_U \tag{3.43}$$

in which $a$ is a general coefficient. The coefficients identified with the subscript *face* depend on the neighbouring cells and are also known as link coefficients. Although it is arguably not part of a discretisation process, the final step that will be discussed here is the application of boundary conditions.

## 3.6. Boundary Conditions

### 3.6.1. Application of Boundary Conditions

Boundary conditions within CFD-ACE are all implemented as modifications to the source terms of the momentum equation, Equation (3.1), and these are internally classified as "Fixed Value Boundaries" (ESI CFD Inc., 2007b). Wall boundaries present a particular problem in computing the source term coefficients in that the cell centre

velocity is usually computed from wall function approximations, either laminar or turbulent, rather than directly specified. Laminar wall functions fit the cell centre velocity based on an assumption of a linear increase in velocity from the wall.

### 3.6.2. Fixed Value Boundaries

Fixed value boundaries are those where the boundary condition, for example pressure or velocity, is fixed at a defined value. However, to add confusion the "fixed" value may change over time as a prescribed rate – it is merely fixed, as far as the solver is concerned, for the immediate time step. A two-dimensional control volume adjacent to a boundary, shown in Figure 3-4, will be considered for the discussion of fixed value boundaries.

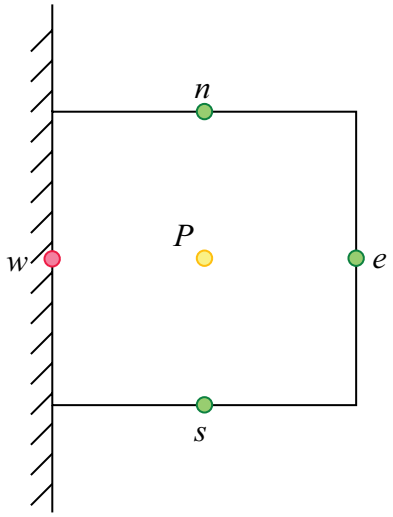


**Figure 3-4 – Wall Adjacent Computational Cell Example Sketch**

The finite volume equation for the cell is defined as

$$a_P \tilde{\theta}_P = a_e \tilde{\theta}_e + a_n \tilde{\theta}_n + a_s \tilde{\theta}_s + \bar{S} \tag{3.44}$$

in which $S$ is a general source term and $a_i$ are general source terms. The west coefficient, $a_w$, was set to zero and the effect of the boundary is transferred to a linearised source term, previously described in Equation (3.13),

$$\bar{S} = S_U + S_P \tilde{\theta}_P . \tag{3.45}$$

For fixed boundaries, the source terms in Equation (3.45) are redefined to include the wall term as

$$\begin{aligned} S_U &= S_U + a_w \delta_b \\ S_P &= S_P - a_w \end{aligned}, \tag{3.46}$$

in which $\delta_b$ becomes the value of the variable to be set at the west face of the cell due to the boundary. The terms $S_U$ and $S_P$ are repeated in Equation (3.46) to allow for the application of sources in addition to the boundaries. Special treatment is required for wall-bounded cells to compute the velocity sources via wall functions.

### 3.6.3. Wall Functions

Wall functions are used to provide an estimate of the velocity at a cell centre $\Delta y_P$ from the wall, as shown in Figure 3-5. To aid in the discussion of wall functions two non-dimensional groups will be defined: (1) the non-dimensional wall velocity

$$u^+ \triangleq \frac{U}{u_\tau}, \tag{3.47}$$

in which

$$u_\tau \triangleq \sqrt{\frac{\tau_w}{\rho}} \tag{3.48}$$

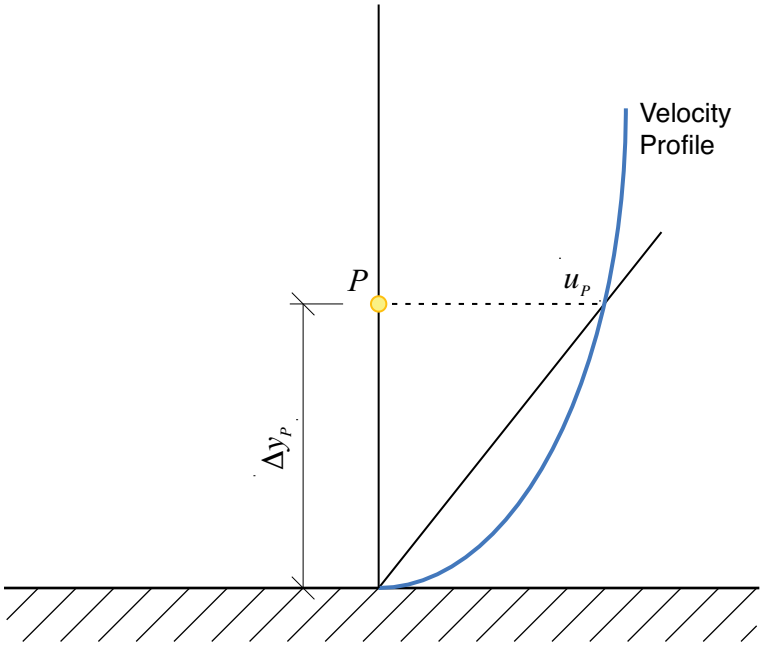


**Figure 3-5 – Assumed Laminar Velocity Distribution at a Wall, Reproduced from Versteeg and Malalasekera (1996)**

and $\tau_w$ is the wall shear and (2) the non-dimensional wall distance

$$y^+ \triangleq \frac{u_\tau y}{\nu}. \tag{3.49}$$

In laminar flows, the velocity in the vicinity of non-slip walls is assumed to be a linear function of the distance from the wall and the wall shear stress

$$\tau_w = \mu \frac{u_P}{\Delta y_P}, \tag{3.50}$$

with the distances and velocities shown in Figure 3-5.

The wall shear force is computed as

$$\begin{aligned} F_s &= -\tau_w A_{Cell} \\ &= -\mu \frac{u_P}{\Delta y_P} A_{Cell} \end{aligned} \tag{3.51}$$

in which $A_{Cell}$ is the wall area of the wall bounded cell. The volume averaged source term for the *u*-momentum equation is then computed as

$$S_P = -\frac{\mu}{\Delta y_P} A_{Cell}. \tag{3.52}$$

With this description of the implementation of boundary conditions for the finite volume method, the discussion of the discretisation of the continuum equations is now complete. However, it remains to discuss the implementation of an iterative solver that is at once robust, fast and has the numerical capability to solve the non-linear equations developed in the preceding sections.

## *3.7. Coupling of the Velocity and Pressure Fields*

### 3.7.1. Continuity and Mass Conservation

As noted by the developer of the CFD-ACE+ code (ESI CFD Inc., 2007b) the continuity equation requires special attention because it is a 1st order partial differential equation so that it cannot be written in the form of a general convection diffusion equation, as in Equation (3.43) for the momentum equations. Suppose that the continuity equation, Equation (2.1), is rewritten in its most general form,

$$\frac{\partial \rho}{\partial t} + \nabla \cdot (\rho \mathbf{u}) = \dot{m}. \tag{3.53}$$

Then, if the general finite volume method is followed, as discussed previously in this section, Equation (3.53) would be integrated and transformed to face centred values, where appropriate, to give

$$\frac{\rho\vartheta - \rho^{o}\vartheta^{o}}{\Delta t} + \sum_{i=1}^{n_{faces}} \rho_i \hat{\mathbf{n}}_i \cdot \mathbf{u}_i A_{face} = \dot{m}\vartheta \,. \tag{3.54}$$

As with the previous discussions, the cell centred variables need to be transformed to the face centred Equation (3.54) can be solved. Unfortunately, linear interpolation would result in the velocity and pressure fields becoming decoupled, which can give rise to the checkerboard instability (Roache, 1998a, Chung, 2002). Fortunately, numerical methods are available that can avoid the checkerboard effect with the method used herein originally proposed by Rhie and Chow (1983) and improved by Perić et al (1988). Detailed derivations of this method will not be given, instead the interested reader is encouraged to review the original papers.

Now through the use of Perić's scheme (Perić et al., 1988) the mass flux evaluation at the faces is complete. It just remains to present the iterative solver that was used to solve the discretised momentum and continuity equations.

### 3.7.2. SIMPLEC for Transient Problems

The CFD-ACE+ solver used in the numerical investigations outlined in this dissertation is a SIMPLEC based code. SIMPLEC, or Semi-Implicit Method for Pressure Linked Equations – Consistent, is a pressure corrector type algorithm and was proposed by Van Doormal and Raithby (1984) as an improvement of the SIMPLE algorithm of Patankar and Spalding (1972). Although the algorithm will not be discussed in detail, the interested reader is referred to the original papers or an introductory text for more details.

SIMPLEC employs a guess and correct approach shown as a block diagram in Figure 3-6. That is, the initial pressure field is guessed and the momentum equations solved using the initial pressure field. A pressure correction equation is then solved and the

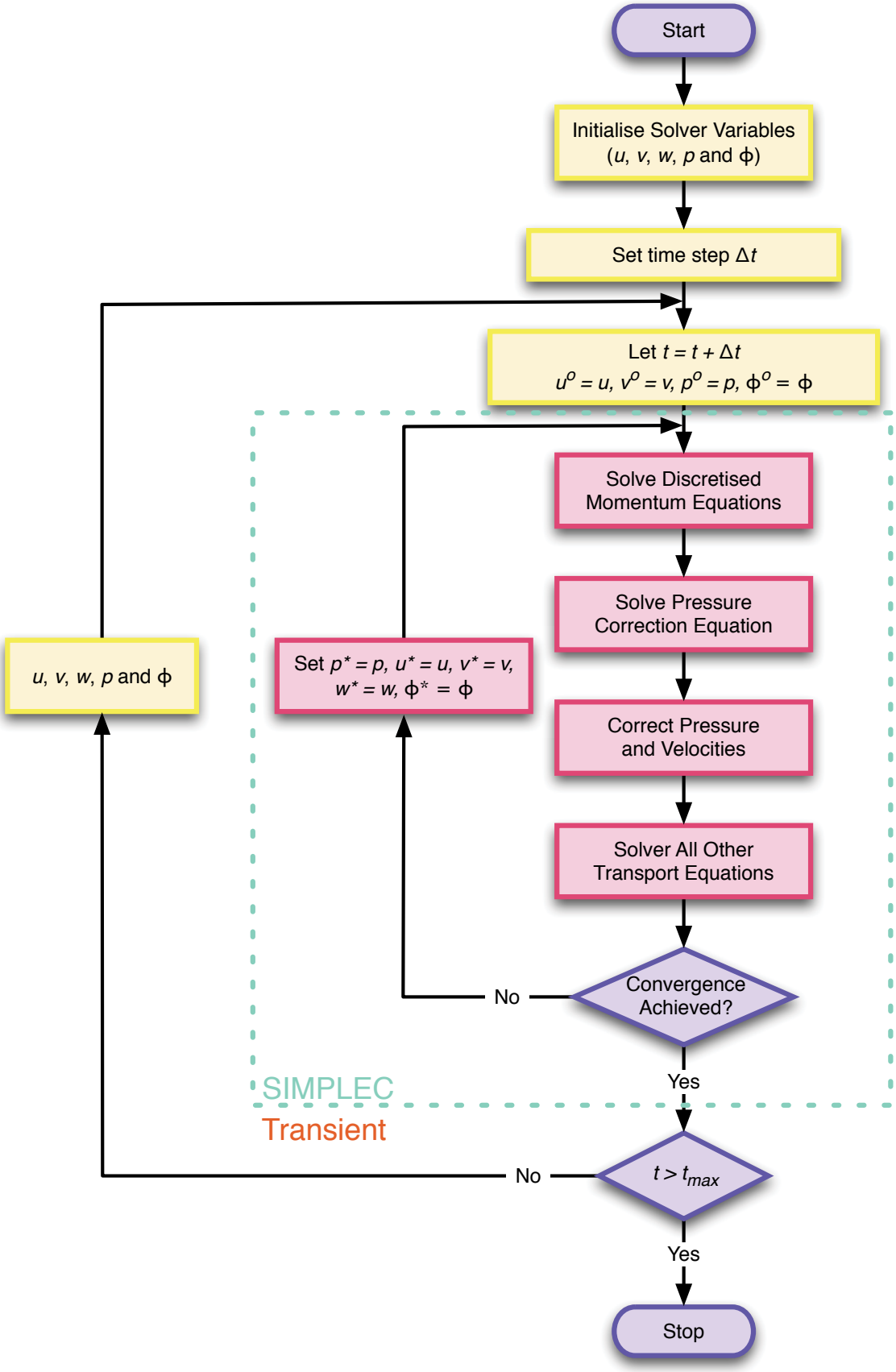


**Figure 3-6 – Flow Diagram of the Transient SIMPLEC Algorithm**

pressure and velocity fields adjusted using the correction factors. Finally, any additional transport equations are solved and the variables are checked for iterative convergence. This process is repeated for each time step until the maximum time is reached with the general algorithm.

## 3.8. Fluid Properties

For the entirety of this dissertation the fluids used will be, unless specifically noted otherwise, either air or water with both phases assumed to be isotropic and incompressible. The physical properties of the water phase, specifically the density $(\rho)$ and the kinematic viscosity $(\nu)$, were assumed to be $1000\ \text{kg/m}^3$ and $1\times10^{-6}\ \text{m}^2/\text{s}$, respectively. Similarly, the properties of the air phase were fixed at $\rho = 1.16\ \text{kg/m}^3$ and $\nu = 1.59\times10^{-5}\ \text{m}^2/\text{s}$. For all the simulations with two phases, the coefficient of surface tension, $\sigma$, was set to $0.0725\ \text{N/m}$ with a fixed contact angle, for the meniscus, of $76°$.

This chapter presented the numerical methods that will be used to solve the continuum equations introduced in §2. However, the mathematical models and methods that can be used to deal with an interface between the two fluids, in this case the free surface, need to be discussed as it is a vital component of this research they must be presented.

# 4. Numerical Simulation of Free Surfaces

## *4.1. Model Requirements*

The physics in and around the free surface are complex yet, as with a turbulence model, any free surface model must be as simple as possible while still having the capability to capture the requisite details. Of the required physics, the primary requisite is to track the location of the free surface to a resolution of, at least, the size of a computational cell. In addition to tracking the location of the free surface, and depending on the "size" of the problem surface tension effects may need to be included that are categorised by the Weber number, which is defined as

$$We = \frac{\rho u_c^2 l_c}{\sigma}, \tag{4.1}$$

in which $\sigma$ is the surface tension coefficient and $l_c$ is a characteristic length. If the Weber number is sufficiently small the curvature and surface tension effects must also be considered. Further, when considering surface tension the contact angle of the meniscus must be modelled as a boundary condition. Naturally, with a specification of the requirements of a numerical model capable of handling free surfaces there will be numerous methods to achieve these requirements.

## *4.2. Numerical Models of Free Surfaces*

There are numerous types of mathematical models that attempt to compute the physics of free surface flows, which vary from the simplest grid based rigid lid approach to complex Volume of Fluid (VOF) models with advanced advection schemes including meshless smoothed particle hydrodynamic simulations. Prior to a detailed discussion of the specific free surface models the reader should be reminded of the concept, most recently enunciated by Shepel and Smith (2009), that no model is perfect and compromises must be made with each model having its own strengths and weaknesses.

The primary classification of numerical models that are designed to simulate free surface flows is the same as that within single fluid CFD simulations, namely whether a mesh is used or not: that is Eularian or Lagrangian approaches.

Fully meshless Lagrangian methods, such as smoothed particle hydrodynamics (SPH) and lattice-boltzman models*, have not been considered in this research because it is only recently that turbulence models have been investigated, let alone incorporated into, these models (Violeau and Issa, 2007). For example the very recent studies of blunt objects falling into fluids using SPH described by Shao (2009) who implemented a Smagorinsky type LES model (Smagorinsky, 1963).

In terms of the Eularian methods, Scardovelli and Zaleski (1999) proposed that grid based free surface models could be classified by the method used to grid the free surface boundary. Broadly, this distinction split free surface numerical models into two distinct groups namely interface capturing and interface tracking models. Despite the apparent simplicity of this arbitrary division, the boundary is somewhat blurred, especially in the light of recently described hybrid models, such as the Front Tracking/Level Set model proposed by Shin and Duric (2009).

Interface capturing methods are based on the premise that the interface can be computed implicitly from the distribution of a scalar that is computed over a fixed grid system. In this case a passive scalar, commonly identified by $F$, is introduced into the model and is subsequently advected as part of the iterative procedures. The location of the interface can then be computed as part of the iterative cycle based on the distribution and gradients of $F$. Common models of the interface capture type include the Volume of Fluid (VOF) model (Hirt and Nichols, 1981, Rider et al., 1995, Kothe et al., 1996), the Marker and Cell (MAC) model (Amsden and Harlow, 1970, Harlow and Welch, 1965, Harlow and Amsden, 1970) and the Level Set models (Sussman et al., 1994, Sethian, 1999, Sussman and Fatemi, 1999, Losasso et al., 2006, Sussman et al., 2007).

In contrast to the fixed meshes of the interface capture methods, interface tracking models explicitly track the position of the free surface, either by re-meshing the grid at each time step or by introducing tracer particles distributed across the interface. Therefore, as the interface is tracked no reconstruction step is needed. However, re-griding the computational domain at each time step can be very computationally

* Technically with lattice-boltzmann models the fluid particles are constrained to a "lattice" that can be considered as a mesh. However, as the fundamental consideration is a fluid particle rather than a control volume (Buick, 1997) LB models have been considered as particle based Lagrangian methods for this thesis.

expensive. An example of the re-meshing procedure is shown diagrammatically in Figure 4-1 where a number of structured cells have been cut by the interface and will be re-grided into unstructured cells along the interface boundary. Some interface tracking models contain elements of both interface tracking and capturing methods and, as such, could be classified as hybrid models, for example single, value height functions (Hirt et al., 1975) and particle finite element methods (Tang et al., 2008).

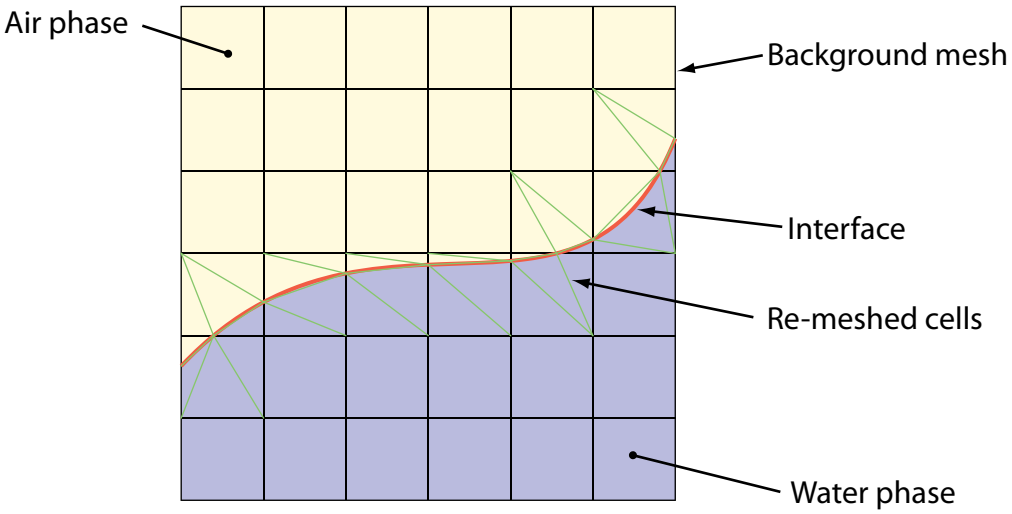


**Figure 4-1 – Schematic of a selection of cells that are cut by an interface that would in turn need to be re-meshed with an interface tracking scheme (Bai et al., 2009).**

Interface tracking methods have a major advantage over interface capturing methods in that the location of the interface is accurately prescribed by the grid (Scardovelli and Zaleski, 1999), which allows the boundary conditions to be specified exactly rather than being smeared or redistributed (Bai et al., 2009). However, this formulation leads directly to the major limitation of interface tracking methods: that the computational grid must be re-meshed at each time step to the new interface location, which for large or complex topologies is a difficult, computationally intensive step. As an extension of the computational cost problem the topological complexity of the interface can be limited with interface tracking methods as the re-meshing algorithm cannot cope with highly deformed and complex surfaces. Recent research into interface tracking methods, for example the Level Contour Reconstruction Model (Shin and Juric, 2002, Shin and Juric, 2009), sought to reduce the computational complexity with limited results: re-meshing the interface grid at each time step remains computationally prohibitive.

Interface capturing methods are generally superior to interface tracking methods due to their conceptual and programmatic simplicity (Scardovelli and Zaleski, 1999). That is, interface capturing algorithms can generally handle complex interface topologies, are programmatically simpler and computationally cheaper than alternate interface tracking methods (Hirt and Nichols, 1981, Rider et al., 1995, Scardovelli and Zaleski, 1999, Bai et al., 2009). However, despite the attraction of interface capturing methods the computational cost of the grid re-meshing has been replaced with an alternate, albeit reduced, CPU cost to compute the shape of the interface across the fixed grid (Bai et al., 2009). Further, as noted by the original proponents, the interface, and hence the fluid properties in the region of the boundary, can become smeared across a number of adjacent cells (Hirt and Nichols, 1981), as shown in Figure 4-2. Attempts to reduce this

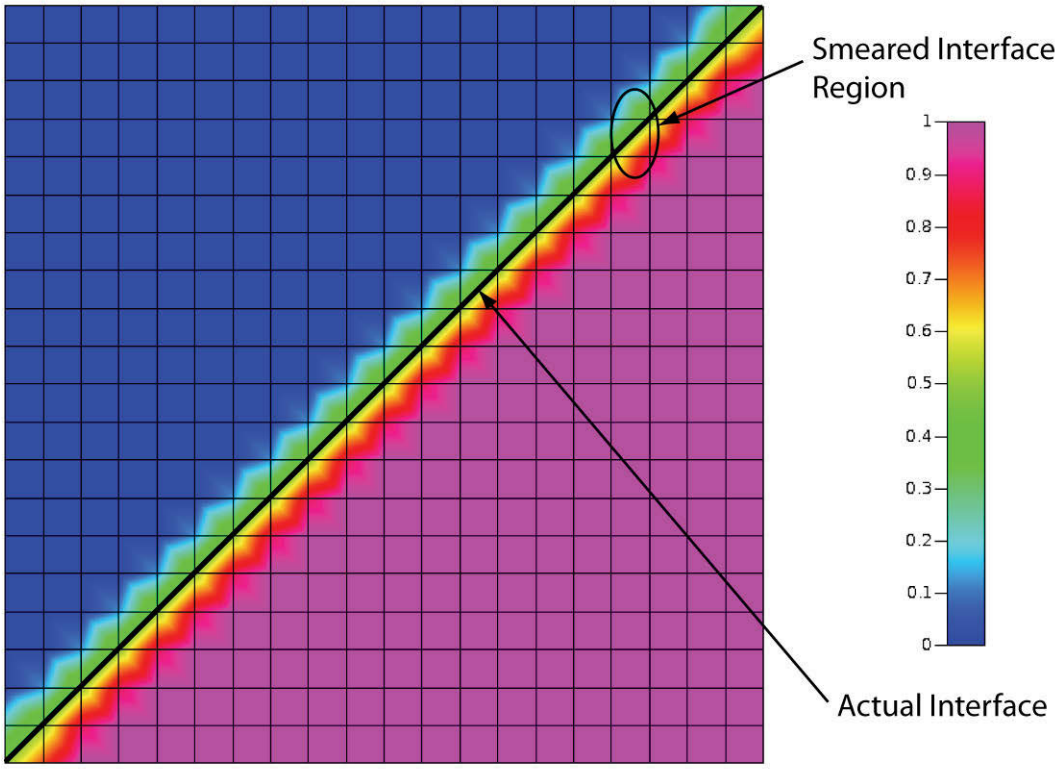


**Figure 4-2 – Inclined free surface showing smearing of the interface due to the interface capturing method used in VOF.**

smearing by reducing the cell size and the time step can, in some cases significantly, increase the computational requirements (Bai et al., 2009). For example if the grid is too large in the region of the free surface the discretisation errors can become large enough that "spurious currents", or unphysical flow features, develop (Scardovelli and

Zaleski, 1999). Further, the time discretisation scheme used to advect the interface is of critical importance (Hirt and Nichols, 1981) with higher order schemes a requirement (Rider et al., 1995, Rider and Kothe, 1998 ).

Due to the reduced computational complexity and the ability to handle complex topologies, interface capturing is an appropriate compromise. In addition to the usual CFD constraint of grid care, and as noted above, extra care must be taken with the selection and implementation of the advection scheme

Therefore, the Volume of Fluid (VOF) model was chosen for the work described in this dissertation because it is one of the most studied and simplest of the interface capturing models. In addition to the theoretical advantages of the VOF formulation, our research group has extensive experience with this model, for example Chen et al (1999) and Gaston et al (2002). The VOF model must then be presented for critical examination by the reader.

## *4.3. The Volume of Fluid Model*

There are two major components in the application of the volume of fluid model* (Hirt and Nichols, 1981):

1. The distribution of the two fluids.
2. The reconstruction of the shape of the interface to evaluate the effects of surface tension.

The distribution of the two fluid phases is tracked via the spread of a passive scalar ($F$) that is a real number defined over the range

$$0 \le F \le 1 \tag{4.2}$$

in which $F = 0$ and $F = 1$ represents either 100% of fluid one or two, respectively. It follows then that computational cells that have a non-integer value of $F$ must contain an interface.

The transport of $F$ is computed by introducing an additional passive transport equation

* Please note that the term "Volume of Fluid" may be abbreviated to the VOF acronym.

$$\frac{\partial F}{\partial t} + \nabla \cdot \mathbf{u}F = 0 \,. \tag{4.3}$$

Equation (4.3) must be solved in conjunction with the Navier-Stokes equations because the local value of $F$ is used to determine the cell fluid properties. For example, if $\eth$ is defined as a general fluid property of both fluids, such as the density, then the volume-averaged value is evaluated from

$$\eth_{cell} = F\eth_2 + (1-F)\eth_1 \,. \tag{4.4}$$

Hence, the mixture dependant parameters must be fed back into the Navier-Stokes equation for the next iterative cycle. While the transport of the two fluids is accomplished through the action of Equation (4.3) this equation contains no information about either the location of the free surface within the cell or the orientation of the free surface. The surface orientation must be reconstructed from the distribution of $F$ within the computational domain.

## *4.4. The PLIC Method for Surface Reconstruction*

### 4.4.1. Overview of the PLIC Method

The Piecewise Linear Interface Construction (PLIC) method is a surface-tracking algorithm that computes the volume flux components geometrically (Kothe et al., 1996). With PLIC methods the interface is locally described in each cell as either a plane (in 3D) or a straight line (in 2D), as sketched in Figure 4-3 for two-dimensions. The general expression of the plane, or line, is expressed in vector notation as

$$\mathbf{x} \cdot \hat{\mathbf{n}} - c_{surf} = 0 \,, \tag{4.5}$$

in which $c_{surf}$ is the interface coefficient that must be computed, $\hat{\mathbf{n}}$ is the surface normal vector and $\mathbf{x}$ is an arbitrary point on the surface. The interface constant is a real number defined over the range

$$-\infty < c_{surf} < \infty \,, \tag{4.6}$$

while the surface normal vector is defined according to the gradient of the volume fraction scalar

$$\hat{\mathbf{n}} = \frac{\nabla F}{|\nabla F|}. \tag{4.7}$$

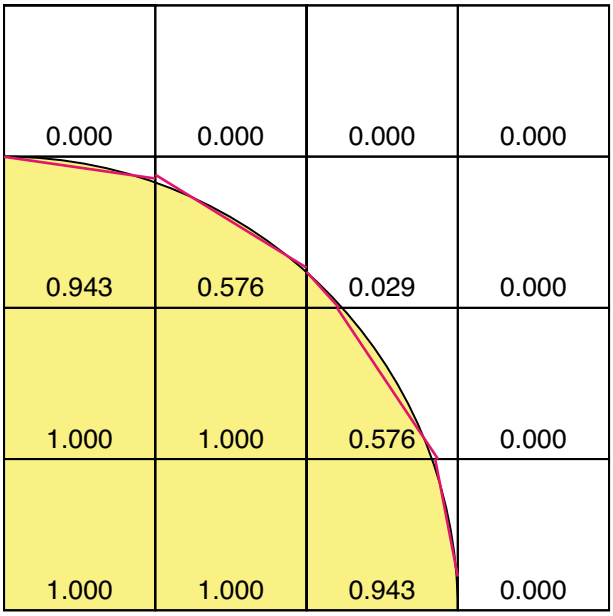


**Figure 4-3 – Reconstruction of a circular arc using the PLIC approximation, numbers are cell volume fractions (Kothe et al., 1996)**

By convention the directions of "in front of" and "behind" the interface are based on the interface normal with the positive direction being in front and *vice versa* (Kothe et al., 1996). This then allows the cell to be divided into three regions, for a general point, $\mathbf{x}_0$,

$$\mathbf{x}_o \cdot \hat{\mathbf{n}} - c_{surf} \begin{cases} < 0, & \text{if } \mathbf{x}_o \text{ is behind the interface} \\ = 0, & \text{if } \mathbf{x}_o \text{ is on the interface} \\ > 0, & \text{if } \mathbf{x}_o \text{ is in front of the interface.} \end{cases} \tag{4.8}$$

With these conventions the solution process for VOF calculations follows from the basic template provided by Kothe *et al* (1996), namely to:

1. Compute the interface normal, $\mathbf{n}$, from the volume fraction distribution;
2. Detect interface cells;
3. Reconstruct the interface;
4. Compute the volume fluxes in interface cells by truncating the total volume flux with the interface;
5. Advance the volumes in time;

6. Apply a bounds check to restrict volume fractions to the limit specified by Equation (4.2).

### 4.4.2. Computation of Truncation Volumes

The key step in using the VOF model is the reconstruction of the interface, which requires an efficient method to calculate the truncation volume (Kothe et al., 1996) that are, in turn, a function of $c_{surf}$. Because there are no explicit solutions to the truncation volume calculation, efficient iterative methods must be employed*.

As the gradient of the free surface and the fractional volume of the phases $\left(\delta\vartheta^k\right)$ are directly supplied by the solver an iterative approach must used to compute the location of the free surface such that

$$\delta\vartheta^k = \vartheta_{cut} = F\vartheta_{cell}. \tag{4.9}$$

On most two- and three-dimensional meshes the truncation volume is a non-linear function of $c_{surf}$ and must be solved iteratively. Therefore, in a manner reminiscent of the limiter computations of the gradient discussed in §3.4.3, the range of $c_{surf}$ can be limited by looping over the cell vertices and computing a set of bounds for $c_{surf}$. With these bounds established iterative methods must be used to solve for $c_{surf}$ and Kothe *et al* (1996) recommend the Brent solver over the Newton method because the Brent method does not directly evaluate the gradient, and is therefore generally quicker than Newton's method.

For example, the truncation volume shown in Figure 4-4, behind the interface can be computed using the line integral,

$$A_{xy} = \frac{1}{2}\sum_{i=1}^{n}\left(x_i y_{i+1} - x_{i+1} y_i\right), \tag{4.10}$$

over the path

$$1 \to 5 \to 6 \to 4 \to 1. \tag{4.11}$$

* The derivations presented for the remainder of this section rely heavily on the publications by Rider et al (1995), Kothe et al (1996) and Rider and Kothe (1998).

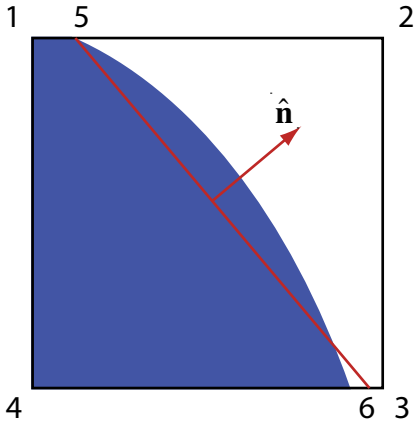


**Figure 4-4 – Two-dimensional cell for a sample truncation volume computation.**

Clearly, the position of the line 56 is unknown in advance, whereas the area it must enclose is. Therefore, $c_{surf}$ is iteratively adjusted to evaluate the two-dimensional equivalent of Equation (4.9).

The extension to 3D is more complicated but can be simplified by noting that

$$\vartheta = \int d\vartheta = \frac{1}{3}\int \nabla \cdot \mathbf{x}\, d\vartheta = \frac{1}{3}\int \nabla \cdot \left(\mathbf{x} - \mathbf{n}c_{surf}\right) d\vartheta \tag{4.12}$$

(Zemach, Unpublished Manuscript). Converting the volume integral in Equation (4.12) to a surface integral and confining the surface integral to only the portions behind the plane gives

$$\vartheta_{TR} = \frac{1}{3}\left[\sum \int \left(\mathbf{x} - \mathbf{n}c_{surf}\right) \cdot dA_f - \int \left(\mathbf{x} - \mathbf{n}c_{surf}\right) \cdot dA_p \right], \tag{4.13}$$

where $dA_f$ and $dA_p$ are elemental areas on the faces and plane respectively. As the dot product in the plane integral is zero Equation (4.13) reduces to

$$\vartheta_{TR} = \frac{1}{3}\sum_f \vartheta_{f,TR}\,, \tag{4.14}$$

where

$$\vartheta_{f,TR} = \int \left(\mathbf{x} - \mathbf{n}c_{surf}\right) \cdot dA\,. \tag{4.15}$$

## *4.5. Surface Tension and Contact Angles*

### 4.5.1. Surface Tension

The method used to compute the surface tension forces is a three-step process specifically (ESI CFD Inc., 2007a):

1. Find the fluid-fluid interface in each cell.
2. Compute the surface normal vector to the interface in each cell
3. Integrate over the surface to find a volume averaged force

As steps (1) and (2) must already be performed as part of the surface reconstruction of the PLIC method, step (3) is the only additional step required. The volume averaged total force is equal to the integral of the tangential forces along the faces of the cell

$$\int \Delta p \, ds = \int f_{st} \, |dx| \,, \tag{4.16}$$

in which the tangential forces due to surface tension are defined as

$$F_{st} = \sigma \mathbf{n} \times \frac{d\mathbf{x}}{|d\mathbf{x}|} \,. \tag{4.17}$$

As above in §4.4, $\mathbf{n}$ is the surface normal vector computed as

$$\mathbf{n} = \nabla F \tag{4.18}$$

however, $\mathbf{x}$ is the cell edge vector. Substituting Equation (4.17) into Equation (4.16) gives

$$\int \Delta p \, ds = \int \sigma \mathbf{n} \times d\mathbf{x} \,, \tag{4.19}$$

which results in a volume averaged force expressed in terms of the fluid boundaries. These fluid boundaries have been computed via the surface reconstruction algorithm discussed above. This volume-averaged force can then be included as a source term directly in the momentum equations.

### 4.5.2. Wall Contact Angle

The wall contact angle is calculated explicitly as either a fixed value or a real valued function of the wall parallel velocity (ESI CFD Inc., 2007a). Once the contact angle has

been evaluated, its effect is imposed on the surface tension computations via the wall boundary source terms. As the evaluation of the contact angle is computed after the curvature and associated momentum source terms have been computed these source terms do not explicitly account for the presence of the wall. Therefore, the boundary condition is imposed by rotating the surface momentum source terms in the contact cell so that the computed force vector, Equation (4.19), is aligned to the interface normal (ESI CFD Inc., 2007a). For contact cells the surface normal is computed as

$$\mathbf{n} = \mathbf{n}_w \cos\theta + \mathbf{t}_w \sin\theta\,, \tag{4.20}$$

in which $\mathbf{n}_w$ and $\mathbf{t}_w$ are the unit wall and tangent vectors, respectively, and $\theta$ is the computed contact angle, as sketched in Figure 4-5.

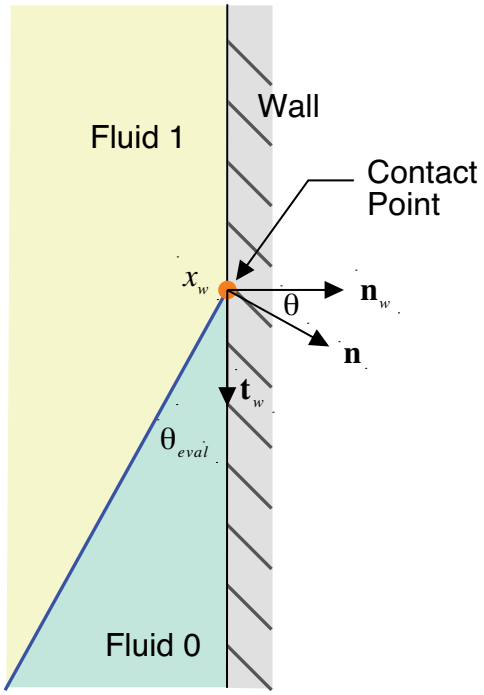


**Figure 4-5 – Sketch of Contact Angle and Wall Vectors (ESI CFD Inc., 2007a).**

The presentation of the numerical methods that will be employed in this research is now complete and, therefore, the discussion can turn to the numerical tests. As previously mentioned in §1 the validation process for this novel MILES solver will begin from the simplest, but still realistic configuration, of a right square cylinder in cross flow. After which attention can be turned to the two-phase simulations of right circular cylinder.

# 5. Single Phase Validation: Configuration and Flow Field

## 5.1. Introduction

The geometric configuration used in the single-phase validation component of this research was based on the extensively studied test case of a right square cylinder mounted through the cross flow in a water tunnel, shown in Figure 5-1. The Reynolds number for this configuration is defined as

$$\mathrm{Re}_d = \frac{U_\infty d}{\nu} \tag{5.1}$$

in which $U_\infty$ and $d$ represented the average cross sectional velocity in the working section upstream of the cylinder and side length of the cylinder, respectively, was set to $22 \times 10^3$.

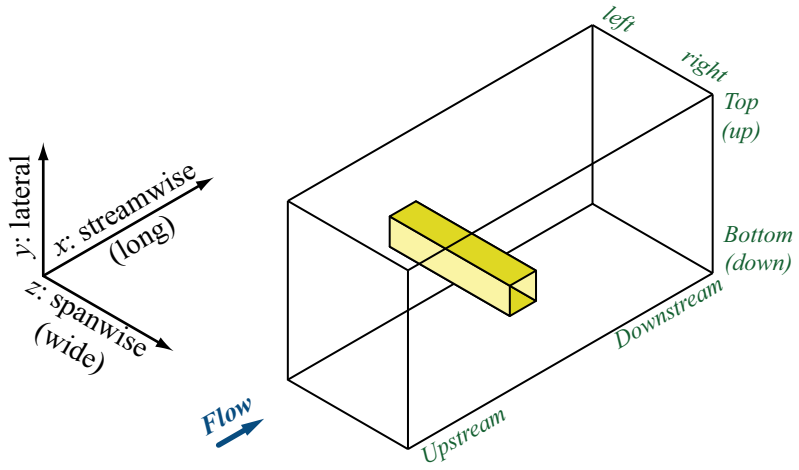


**Figure 5-1 – Sketch of the square cylinder in a duct configuration with the principle coordinate axes and naming scheme identified.**

Despite most of the details of the experimental conditions having been published by Lyn and Rodi (1994) and Lyn et al (1995), the majority of the previous numerical simulations utilised a number of simplifications designed to reduce the spatial extent of the computational domains that therefore also reduced the computational requirements. Therefore, two distinct geometric configurations were investigated in the research that formed the basis of this dissertation. The first configuration was envisioned to reproduce the simplified configuration generally used in the published literature, while

the second geometry was intended to represent the conditions of the actual, physical water tunnel. For the remainder of this dissertation these two configurations will be referred to as the spanwise periodic and water tunnel simulations, respectively.

The differences between the spanwise periodic simulations and the physical water tunnel appear to have occurred following their use as a test case in a workshop held in 1995 as described by Rodi et al (1997). Specifically the approximations introduced were:

1. that the length of the cylinder in the spanwise direction was reduced from 9.75d to 4d;
2. that the spanwise tunnel non-slip walls were replaced by periodic boundary conditions;
3. that the lateral (top and bottom) boundaries were extended to $|y| = 314$ mm from $|y| = 280$ mm in the physical water tunnel and were set as zero friction walls;
4. that the outlet boundary was to be located at least 14*d* downstream of the downstream face of the cylinder;
5. the inlet boundary was to be located at least 4.5*d* upstream of the upstream face of the cylinder.

Whilst the geometric configuration of the periodic models was specified, as discussed above, the layout of the mesh within the computational domain was left to the participants. Therefore, to evaluate the effect of mesh size and layout the present author investigated a number of two-dimensional tests cases prior to developing the three-dimensional meshes.

## *5.2. Preliminary Two-Dimensional Investigations*

Two, two-dimensional parameter studies, were undertaken as part of this preliminary study* that were designed to investigate: (1) the effect of varying the length to the outlet

* The preliminary investigations are fully described in Appendix C, therefore only a brief discussion of the tests conducted, results obtained and conclusions drawn will be presented within this section.

boundary, $\mathfrak{L}$, and (2) the effect of changing the size of the cell adjacent to the cylinder, $\mathfrak{F}$, shown in Figure 5-2 and Figure 5-3, respectively.

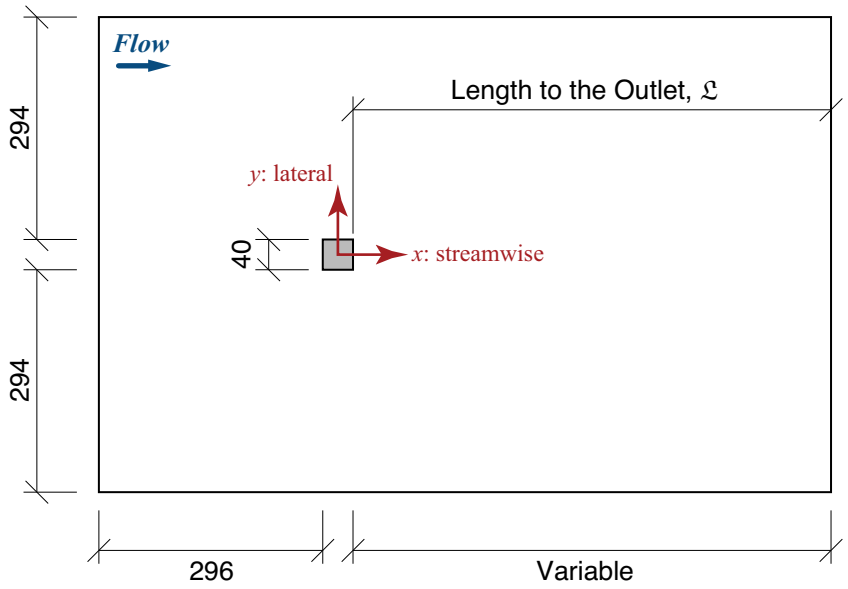


**Figure 5-2 – Diagram of the two-dimensional geometry used as the basis for the preliminary tests.**

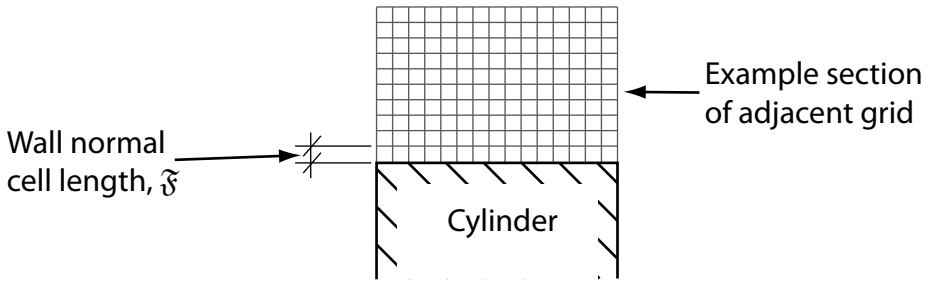


**Figure 5-3 – Sketch of the definition of the wall normal cell length.**

For the $\mathfrak{L}$ parameter study, $\mathfrak{L}$ was varied over

$$160 \text{ mm} \leq \mathfrak{L} \leq 1600 \text{ mm} \tag{5.2}$$

in uniform 160 mm increments while $\mathfrak{F}$ was tested through

$$50\ \mu\text{m} \leq \mathfrak{F} \leq 5 \text{ mm} \tag{5.3}$$

in non-uniform increments.

The results from both parametric studies were similar in that there was a region in the respective parameter spaces, namely $\mathfrak{F} \leq 1$ mm and $\mathfrak{L} \geq 400$ mm, where the simulated

flow field was independent of changes to the parameter. Further, the simulated flow fields over this range were "acceptable", subject to the caveats that will be discussed below. Conversely, the flow fields and results from the simulations outside these parameter spaces, that is $\mathfrak{F} > 1\,\text{mm}$ and $\mathfrak{L} < 400\,\text{mm}$, resulted in unphysical and, hence, unacceptable flow fields and results. These bounds were identified through the appraisal of three criteria specifically defined to compare the results namely, a visual inspection of the flow field, a visual examination of $C_D(t)$ and $C_L(t)$ and an evaluation of the statistical properties of the force coefficients, which will be presented in order.

The simulated flow field from the majority of the simulations was characterised by a von Kármán vortex street. However, the resultant vortex street from the present simulations was observed to be irregular and contain large, high-speed blobs of fluid that were ejected laterally from the wake, as shown in Figure 5-4. Because these lateral fluid ejections have not been reported elsewhere, for example see the uniform yet periodic results of Johansen, Wu and Shyy (2004) as shown in Figure 5-5, and that they were observed in 15 of the 16 present simulations they were deemed to be an unphysical manifestation of the underlying assumptions of two-dimensional flow.

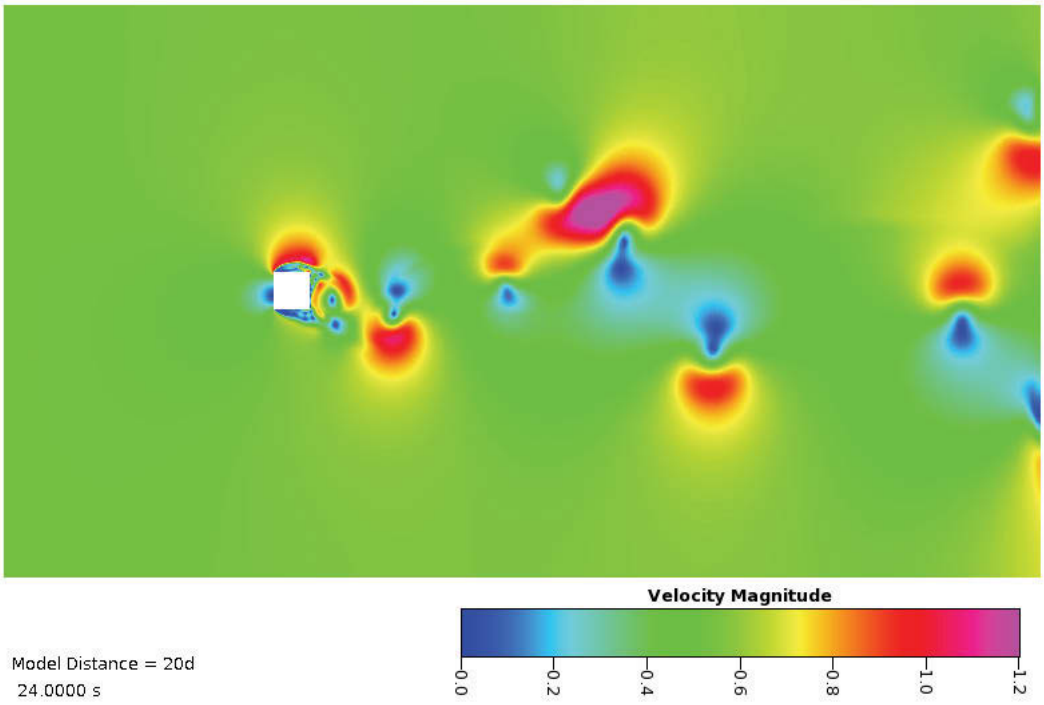


**Figure 5-4 – Image of the velocity magnitude showing a high-speed event that was subsequently ejected out of the wake towards the top wall.**

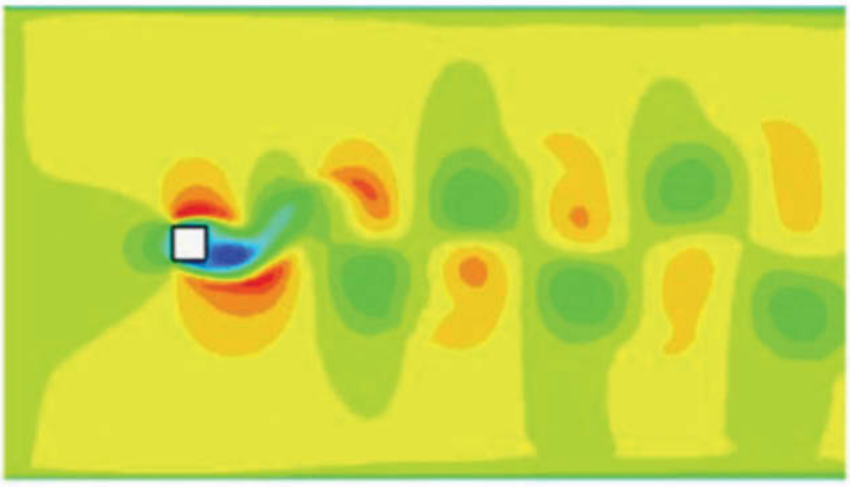

**Figure 5-5 – Velocity magnitude visualisation of a von Kármán vortex street behind a square cylinder, reproduced from Johansen, Wu and Shyy (2004).**

The remaining simulation where a von Kármán vortex street was not observed was the $\mathfrak{F} = 5$ mm simulation. In this simulation, the resolution of the boundary layer was so poor, that is $\mathfrak{F}$ was so large, that shedding could not develop, let alone compute the detail required to resolve recirculation zones, as shown in Figure 5-6.

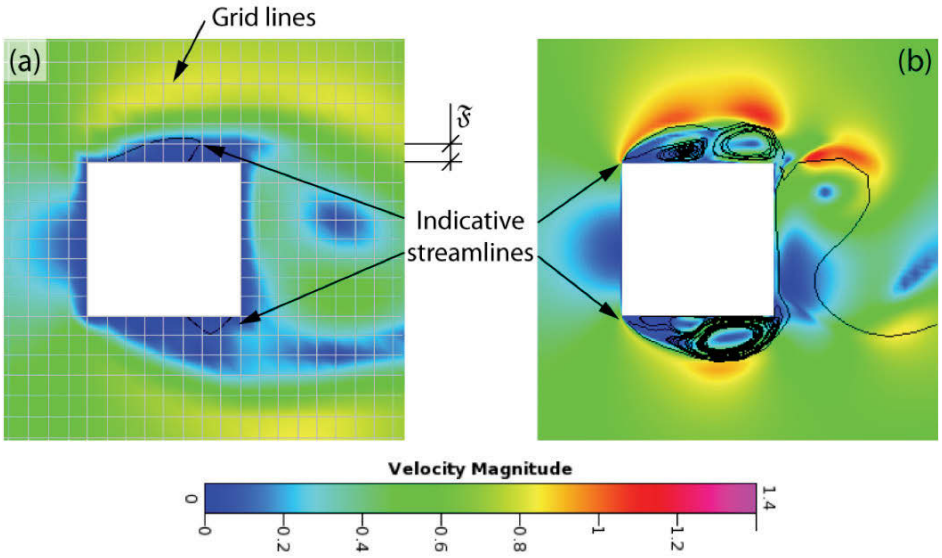


**Figure 5-6 – Comparison of the resolved flow features in the $\mathfrak{F}$=5mm (a) and the $\mathfrak{F}$=50µm (b) simulations with the flow visualised by the velocity magnitude and instantaneous streamlines to indicate the recirculation zones.**

The effective elimination of the vortex street as $\mathfrak{F}$ was increased was also observed in the plot of $C_D(t)$ in which the values of $C_D(t)$ from the $\mathfrak{F} = 5$ mm simulation are

simultaneously smoother with the amplitudes of the fluctuations reduced compared to the results from the shorter $\mathfrak{F}$ simulations, as shown in Figure 5-6. For example, the "smoothness" is particularly visible in the development time, roughly for a simulation time of $t \leq 9$ s with the virtual elimination of small scale shedding in the $\mathfrak{F} = 5$ mm simulation.

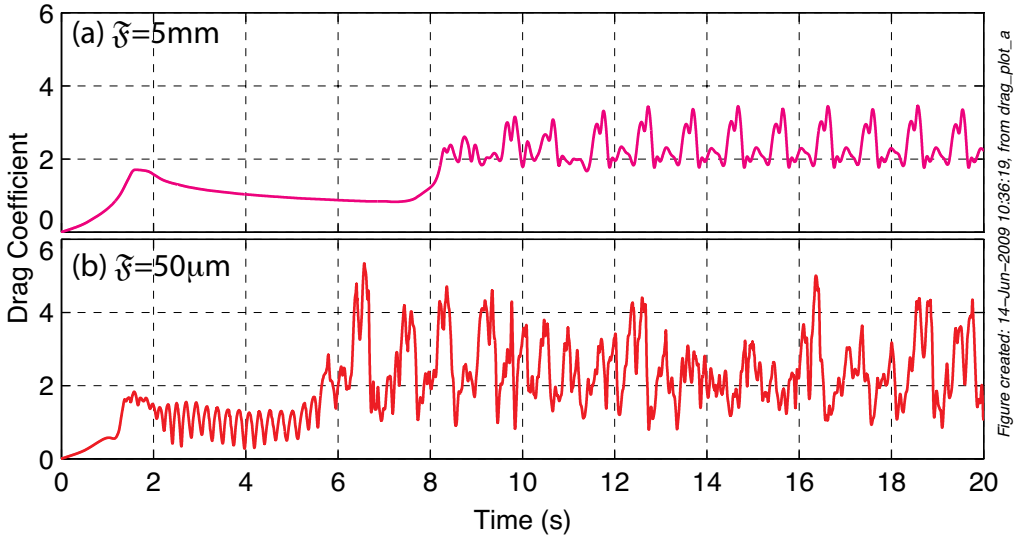


**Figure 5-7 – Drag coefficients as a function of time for $\mathfrak{F}$=5mm and $\mathfrak{F}$=50μm.**

Given that the flow field from the two-dimensional simulations is unphysical, the present author questioned what the real value of these two-dimensional simulations was? In an attempt to answer this question it was noted that the majority of papers surveyed by the author that reported results on the two-dimensional flow around a square cylinder at $\mathrm{Re}_d = 22 \times 10^3$, only average flow fields and statistical representations of the force coefficients were presented. Therefore, as no average flow fields were computed in these parametric studies the distributions of the force coefficients were examined.

The distributions were computed and examined with the result that the distribution of $C_L$ provided the clearest indicator of the effect of changing $\mathfrak{L}$ and $\mathfrak{F}$, as shown in Figure 5-8 and Figure 5-9, respectively. As alluded to above with the comparably little

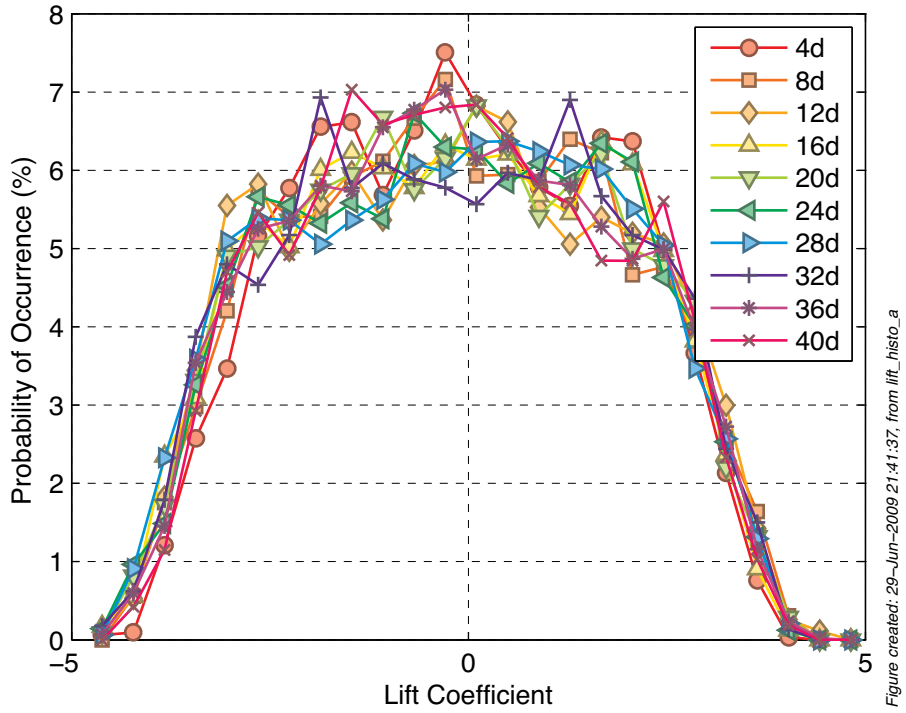


**Figure 5-8 – Probability distribution function of the lift coefficients computed across the simulation time interval of $10 \leq t \leq 100$ s from the ten $\mathfrak{L}$ simulations.**

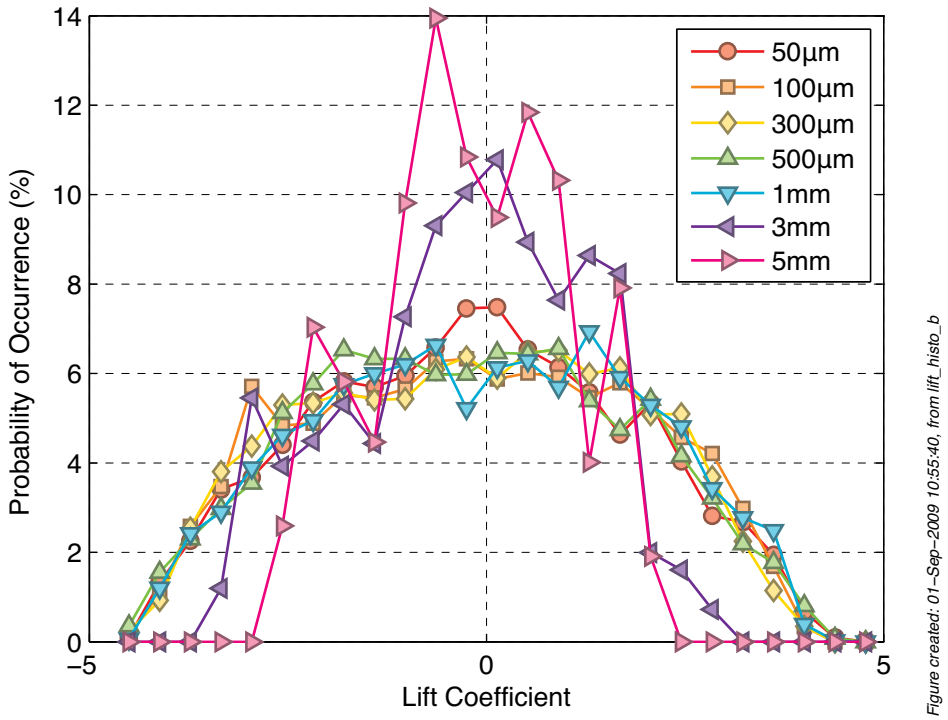


**Figure 5-9 – Probability distribution functions of the lift coefficients computed across the simulation time interval $10 \leq t \leq 100$ s from the seven $\mathfrak{F}$ simulations.**

discussion there was no strong effect of $\mathfrak{L}$ on $C_L$, as shown in Figure 5-8. It could be argued that the distribution of $C_L$ for $\mathfrak{L} \leq 400$ mm, or when non-dimensionalised 10*d*, is slightly more peaky than the remaining simulations of $\mathfrak{L}$.

In contrast to the results from the simulations of $\mathfrak{L}$, the distributions of $C_L$ from the simulations of $\mathfrak{F}$ are markedly peaky for $\mathfrak{F} > 1$ mm. Both sets of results support the observations of the flow field discussed first in that there are marked changes in the flow either side of the respective critical points.

There are several conclusions from these preliminary investigations concerning the applicability of two-dimensional studies and the size and layout of the computational domain. With respect to the applicability of the assumptions of two-dimensionality to the modelling of a square cylinder, the present author has concluded that two-dimensional methods are not generally applicable to this configuration for accurate simulation. However, despite the unphysical flow field, distinct trends were observed in the coefficients that should transfer to the three-dimensional models. Specifically the length from the downstream cylinder face to the outlet boundary should be longer than 400mm and that the wall normal cell length adjacent to the cylinder face should be shorter than 500μm.

With these conclusions, which are more fully outlined together with detailed results in Appendix C, the next section will present the three-dimensional models that were developed for the investigations set out in this dissertation.

## *5.3. Configuration of the Three-Dimensional Simulations*

### 5.3.1. Geometry and Computational Mesh

The three-dimensional computational domains that were used in the present work were designed to firstly include the recommendations from the preliminary studies. Secondly, the domains were intended to represent either the physical water tunnel used by Lyn and Rodi or to, at least, meet the specifications of the two LES workshops described above. Therefore, the inlet boundary was located at $x = -316$ mm while the outlet boundary was located at $x = 652$ mm with $d = 40$ mm, as shown in Figure 5-10. The lateral and spanwise boundaries were set to match the specific configuration, that is either the spanwise periodic or water tunnel configuration and are shown in Figure 5-10.

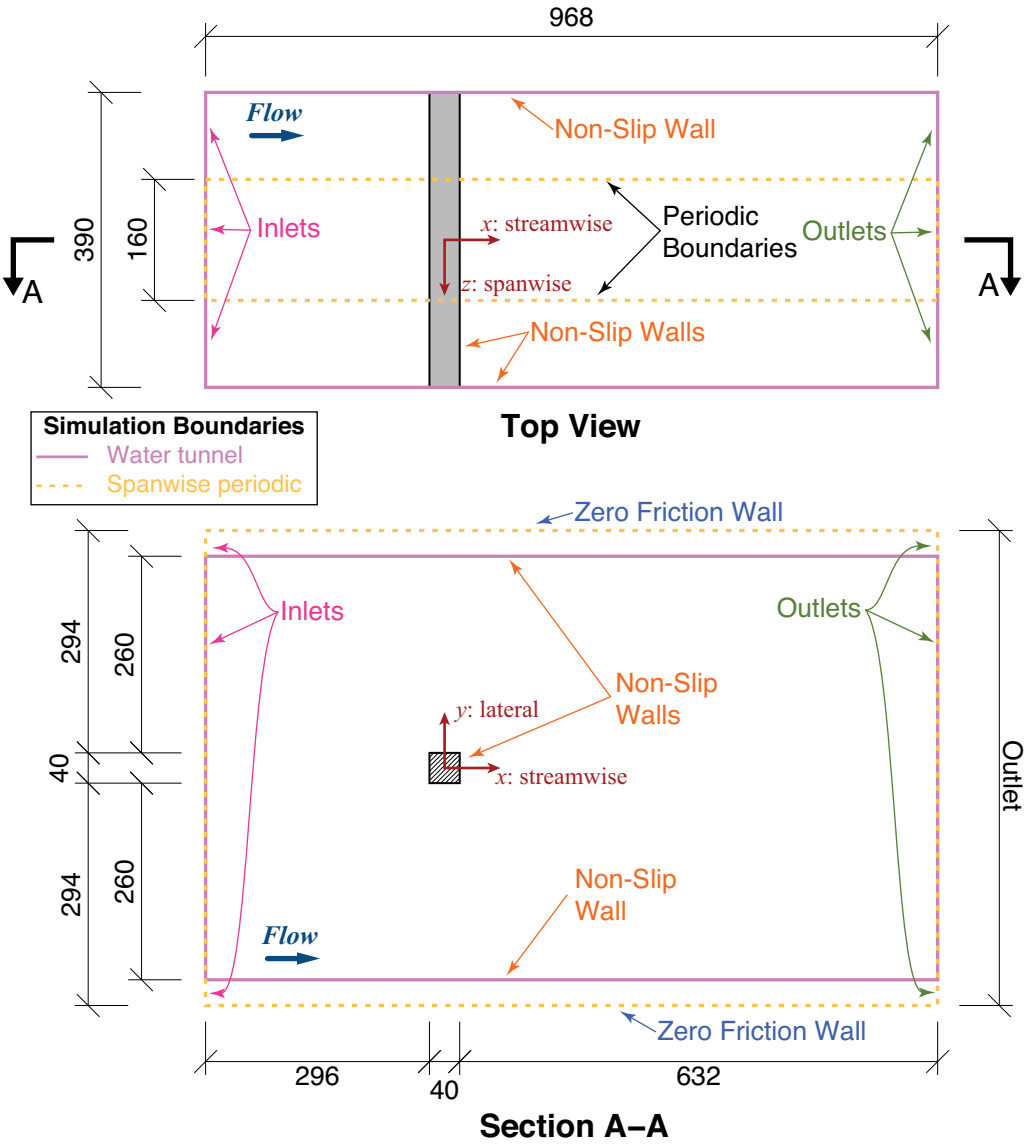


**Figure 5-10 – Comparative diagram of the geometry of the spanwise periodic and water tunnel configurations showing the cylinder centred coordinate origin.**

In addition to the meshes based on the spanwise periodic assumptions being close to those of published simulations, they were also designed for a mesh refinement study to be undertaken. Therefore, the computational volume was constructed with a common domain and edge layout as sketched in Figure 5-11[*]. Each of the four computational domains was composed of structured, hexahedral cells.

[*] The edges that are not specifically labelled in Figure 5-11 are identical to their corresponding labelled edge via block mirroring, that is the opposite edges of a given block are the same.

From this common framework for the periodic simulations, three different resolution grids were developed, herein referred to as the Low, Medium and High Resolution or LR, MR and HR cases, respectively. One further mesh, based on a modification of the medium resolution spanwise periodic configuration, was designed to represent the water tunnel geometry and is abbreviated as the WT simulation.

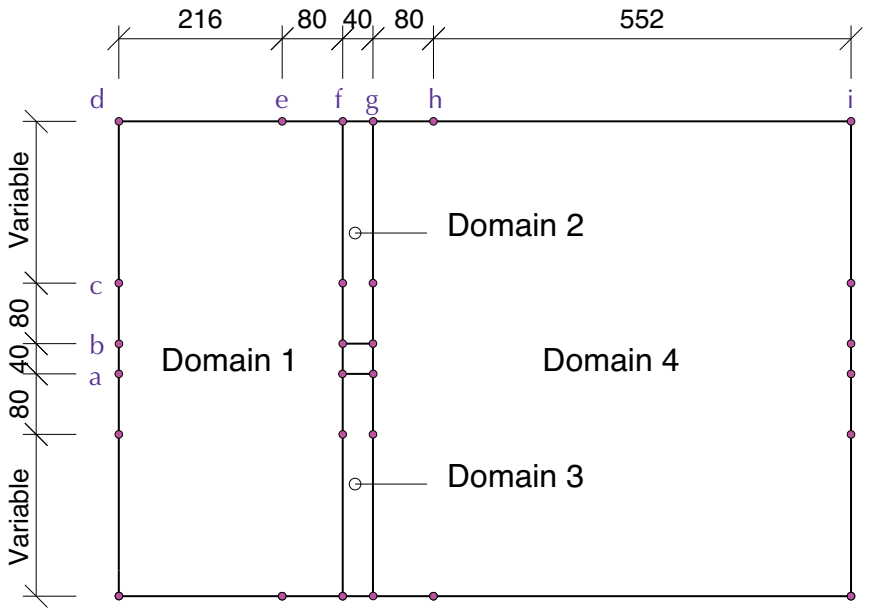


**Figure 5-11 – Grid and domain layout for the right square cylinder models.**

To minimise the cell count across all the computational meshes while still maintaining the accuracy of the solution, a non-uniform mesh with two zones of refinement was constructed. The first zone of refinement was close to the cylinder and was designed to capture the small-scale wall effects while the second zone of refinement was constructed within the predicted wake zone to ensure a sufficiently high resolution to capture the Kármán vortex street present behind bluff body (Nakamura, 1993). Outside these refined regions, the cells were kept at a constant but larger size. The nodal spacing along edges with non-uniform nodal spaces was adjusted using a hyperbolic tangent function defined by Vinokur (1980, 1983). Briefly, as the spacing function is fully detailed in Appendix B, the location of the nodes along a given edge were computed from a non-dimensional spacing function

$$\mathbf{s}(\xi) = \frac{\mathcal{Q}(\xi)}{A + (1 - A)\mathcal{Q}(\xi)} \tag{5.4}$$

in which

$$\mathcal{Q}(\xi) = \frac{1}{2}\left[1 + \frac{\tanh\left[\delta\left(\frac{\xi}{n-1} - \frac{1}{2}\right)\right]}{\tanh\left(\frac{\delta}{2}\right)}\right]. \tag{5.5}$$

where $\xi$ is an integer index vector defined for

$$\xi = 0,1,2,\ldots,n-3,n-2,n-1\,. \tag{5.6}$$

The stretching factor, $\delta$, in Equation (5.5) is defined from the implicit relation

$$\frac{\sinh(\delta)}{\delta} = B\,. \tag{5.7}$$

which must be solved iteratively. The constants $A$ and $B$ depend solely on the size of the spacing between the end nodes that is

$$A = \frac{\sqrt{\Delta s_{end}}}{\sqrt{\Delta s_{start}}} \tag{5.8}$$

and

$$B = \frac{1}{n\sqrt{\Delta s_{start}\Delta s_{end}}}\,. \tag{5.9}$$

Therefore, from these equations it is clear that there are three parameters that the user must specify, namely $n$, $\Delta s_{start}$ and $\Delta_{end}$, which for the spanwise periodic meshes is listed in Table 5-1 while the specifications for the water tunnel mesh is listed in Table 5-2. The application of these node parameters resulted in four meshes with 468 550, 993 792, 1 492 128 and 2 496 880 cells for the low, medium, high and water tunnel meshes, respectively, as shown in Figure 5-12. Within Table 5-1 and Table 5-2 the edge ends are labelled according to the node schema in Figure 5-11.

**Table 5-1 – Edge details for the spanwise periodic meshes with Dist = Distribution type; HT = Hyperbolic tangent distribution; U = Uniform node distribution.**

| Edge | End | Low Resolution | | Medium Resolution | | High Resolution | | Dist |
|---|---|---|---|---|---|---|---|---|
| | | Spacing (mm) | Nodes | Spacing (mm) | Nodes | Spacing (mm) | Nodes | |
| ab, fg | Symmetrical | 0.32 | 26 | 0.32 | 33 | 0.21 | 37 | HT |
| bc, ef | b, f | 0.32 | 21 | 0.32 | 29 | 0.21 | 30 | HT |
| | c, e | 10.00 | | 6.29 | | 6.90 | | |
| de | - | 10.30 | 22 | 6.35 | 35 | 6.75 | 32 | U |
| | - | | | | | | | |
| cd | - | 10.20 | 22 | 6.29 | 35 | 6.90 | 32 | U |
| | - | | | | | | | |
| gh | g | 0.32 | 30 | 0.32 | 41 | 0.21 | 50 | HT |
| | h | 6.40 | | 4.00 | | 4.20 | | |
| hi | - | 6.40 | 87 | 4.00 | 139 | 4.28 | 130 | U |
| | - | | | | | | | |
| z-dir | - | 6.40 | 26 | 6.67 | 25 | 4.40 | 37 | U |
| | - | | | | | | | |

**Table 5-2 – Edge details for the water tunnel mesh.**

| Edge | End | Spacing (mm) | Nodes | Distribution |
|---|---|---|---|---|
| ab, fg | Symmetrical | 0.32 | 33 | HT |
| bc, ef | b, f | 0.32 | 29 | HT |
| | c, e | 6.40 | | |
| de | - | 6.35 | 35 | U |
| | - | | | |
| cd | - | 6.43 | 35 | U |
| | - | | | |
| gh | g | 0.32 | 100 | HT |
| | h | 4.00 | | |
| hi | - | 4.00 | 109 | U |
| | - | | | |
| z-dir | - | 6.61 | 60 | U |
| | - | | | |

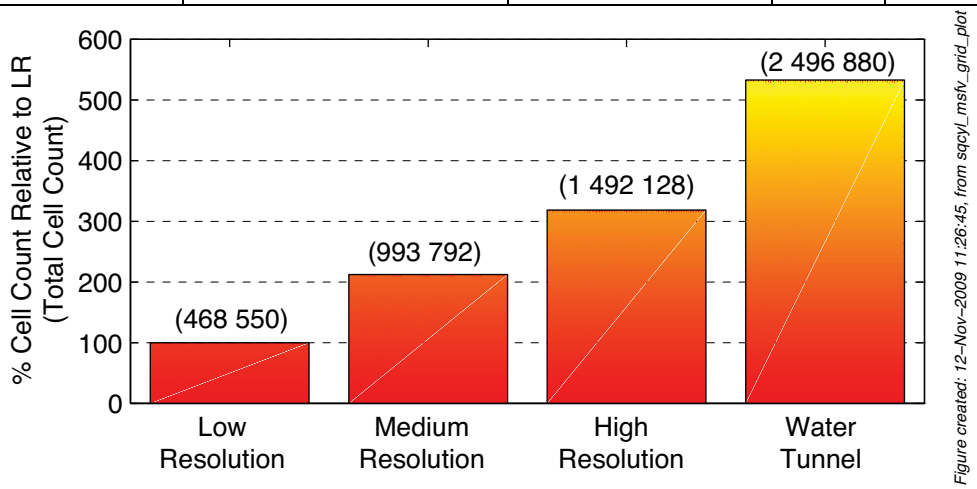


**Figure 5-12 – Total cell count for the four square cylinder models and their size relative to the low resolution mesh.**

These three parameters – $n$, $\Delta s_{start}$ and $\Delta_{end}$ – were selected so that there was a smooth transition from the small cells adjacent to the cylinder wall to the large cells with no, or at least very small, discontinuities as shown in Figure 5-13 and Figure 5-14.

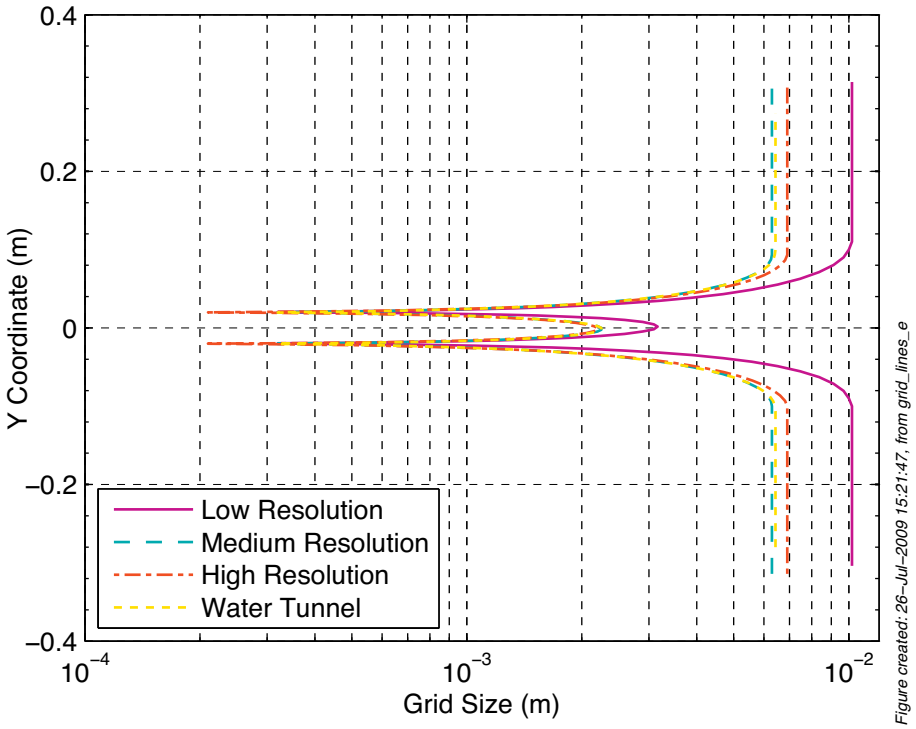


**Figure 5-13 – Lateral cell size as a function of *y* coordinate for the meshes.**

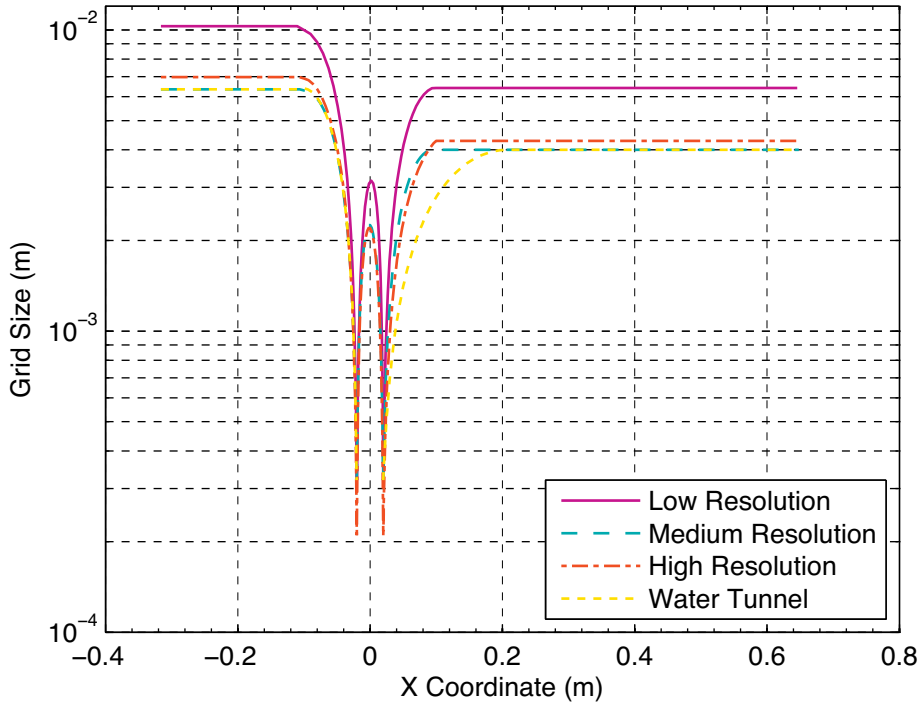


**Figure 5-14 – Streamwise cell size as a function of *x* coordinate for the meshes.**

As already mentioned above, the water tunnel mesh was based on the MR spanwise periodic mesh. However, due to the combination of the slightly reduced lateral domain

and the greatly extended spanwise domain in the water tunnel mesh, the number of cells in the near wake was reduced in conjunction with an increase in the spanwise direction.

### 5.3.2. Boundary and Initial Conditions

The inlet boundary condition was specified with a constant velocity, which was computed from the Reynolds number, of $U_\infty = 0.535$ m/s . No allowance was made for the free stream turbulence fluctuations or the development of the flow along the full water tunnel duct prior to the computational inlet. All the faces of the cylinder were defined as non-slip, impermeable walls. The spanwise, *z*-direction, boundary conditions were either defined as periodic, creating an infinite length cylinder, or non-slip, impermeable walls, thereby creating an approximation of the laboratory water tunnel. The outlet boundary was set as a constant pressure boundary. The lateral boundaries, in the *y*-direction, were defined as either zero friction walls for the spanwise periodic simulations or as non-slip, impermeable walls for the water tunnel simulation. For reference, these boundaries are shown on Figure 5-10 together with the dimensions of the models.

For CFD simulations of bluff body geometries and their associated shedding flows, there can be a significant computational requirement to develop from the constant input state into the unsteady, shedding regime. Therefore, to reduce the computational time of the start up transient, an artificial disturbance was introduced by starting the transient calculations as if the flow were steady. Then the solution from the un-converged steady state simulation was used as a "better" approximation of the initial conditions for the unsteady simulations.

### 5.3.3. Solver Parameters

All the unsteady runs were computed with a time step size of 1ms. Further, while balancing the use of computational resources, including CPU time and storage allocation, the models were allowed to run for a minimum of 40s of simulated time, that is 40 000 time steps. The convergence of the solver, detailed in Appendix A, was controlled by a maximum of 25 iterations, four orders of magnitude reduction in the residuals and a limit of the minimum residuals to $1\times10^{-18}$. A conjugate gradient solver with preconditioner was set for the velocity solver while and adaptive multigrid solver was used for the pressure corrector.

## 5.4. Convergence of the Solver During the Simulations

As with all numerical simulations, including the single-phase development studies summarised above and detailed in Appendix C, the level of numerical convergence of the solver must be examined prior to a detailed description of the computed solutions. All four of the simulations described in this chapter converged within the specified maximum of $n_{iter} = 25$ as shown in Figure 5-15.

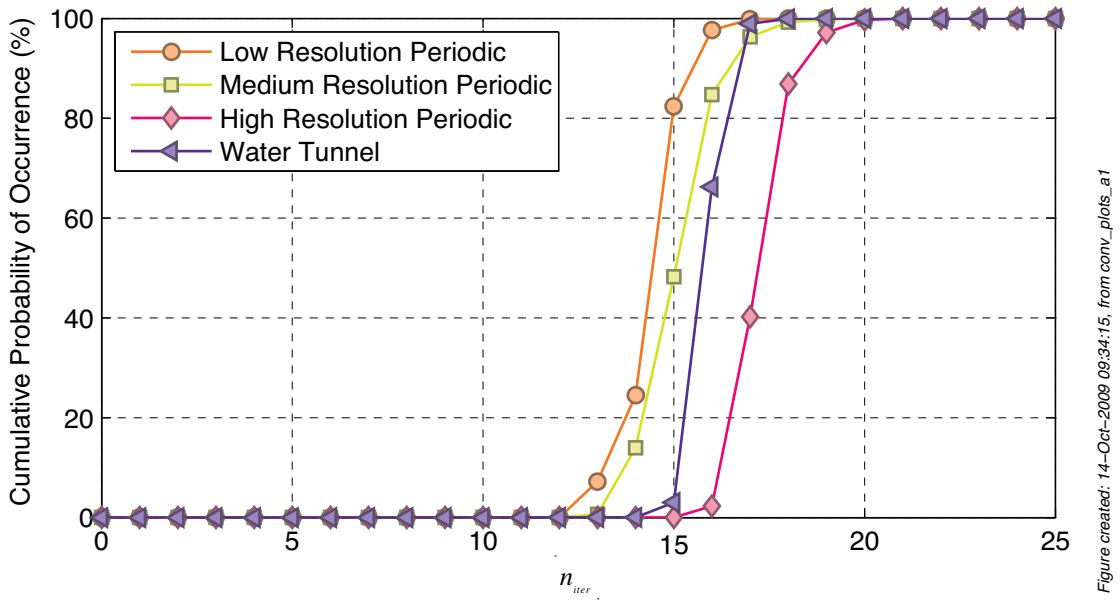


**Figure 5-15 – Cumulative distribution functions of $n_{iter}$ for the four simulations.**

Therefore, as the configuration of the models has been completely described (§5.3) and as the simulations converged for all time steps, the results of the simulations can be critically examined.

## 5.5. Observations of the Global Flow Field from the Spanwise Periodic Meshes

### 5.5.1. Three Dimensional Structures

The flow around the square cylinder is characterised by a predominantly uniform shear layer that is attached to the separation point on the leading edge of the cylinder. This shear layer then rolls up and over top of the cylinder towards the rear face* as shown in

* Because the flow is predominantly symmetric around the $y$=0 plane, the descriptions presented in this chapter, unless specifically noted, should be interpreted as equally applicable for the top, positive $y$, as the bottom, negative $y$, directions

Figure 5-16. Within the separated region between the shear layer and the top face of the cylinder there is a recirculation region visible in Figure 5-16 as the dark blue coloured vorticity surfaces attached to the grey cylinder face.

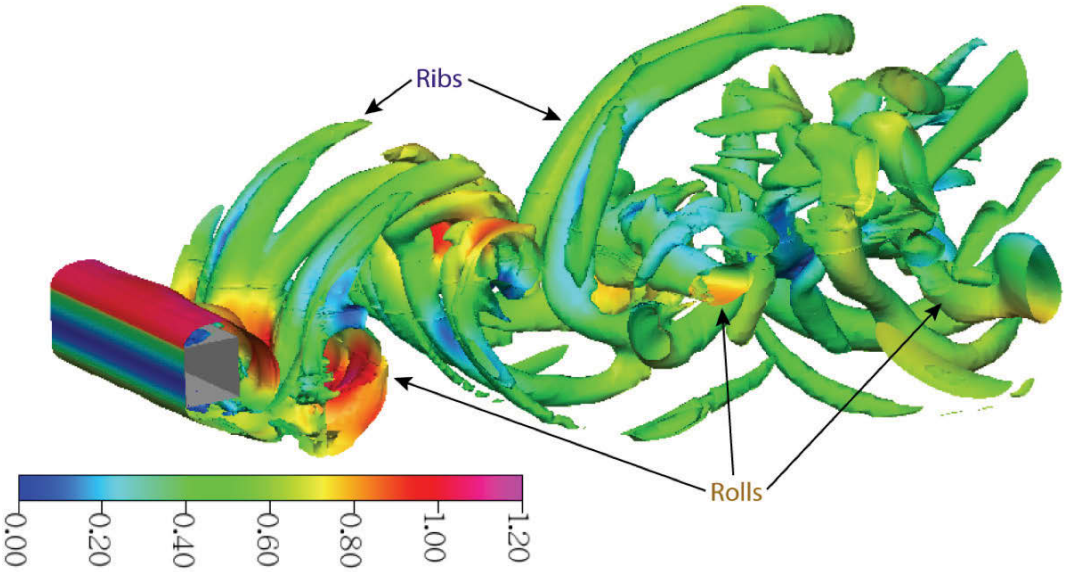


**Figure 5-16 – Flow visualisation of isosurfaces of vorticity magnitude at $|\omega|=25s^{-1}$ surfaces coloured by velocity magnitude from the high-resolution mesh at a simulation time of $t$=34.0s.**

As the separated shear layer extends beyond the downstream face of the cylinder, depending on the shedding phase, it either wraps around and down behind the cylinder, or continues in a gradual arc upwards towards the free stream. However, as shear layers are inherently unstable, the shear layer attached to the cylinder quickly breaks apart in to a series of streamwise ribs and spanwise rolls, indicated in Figure 5-16 and Figure 5-17.

The notations of "ribs" and "rolls" follows from the naming schema adopted by Dobre and Hangan (2004) who performed a series of hot wire laboratory experiments with the probes placed at

$$\frac{x}{d} = 26\,, \tag{5.10}$$

which they defined as within the intermediate wake.

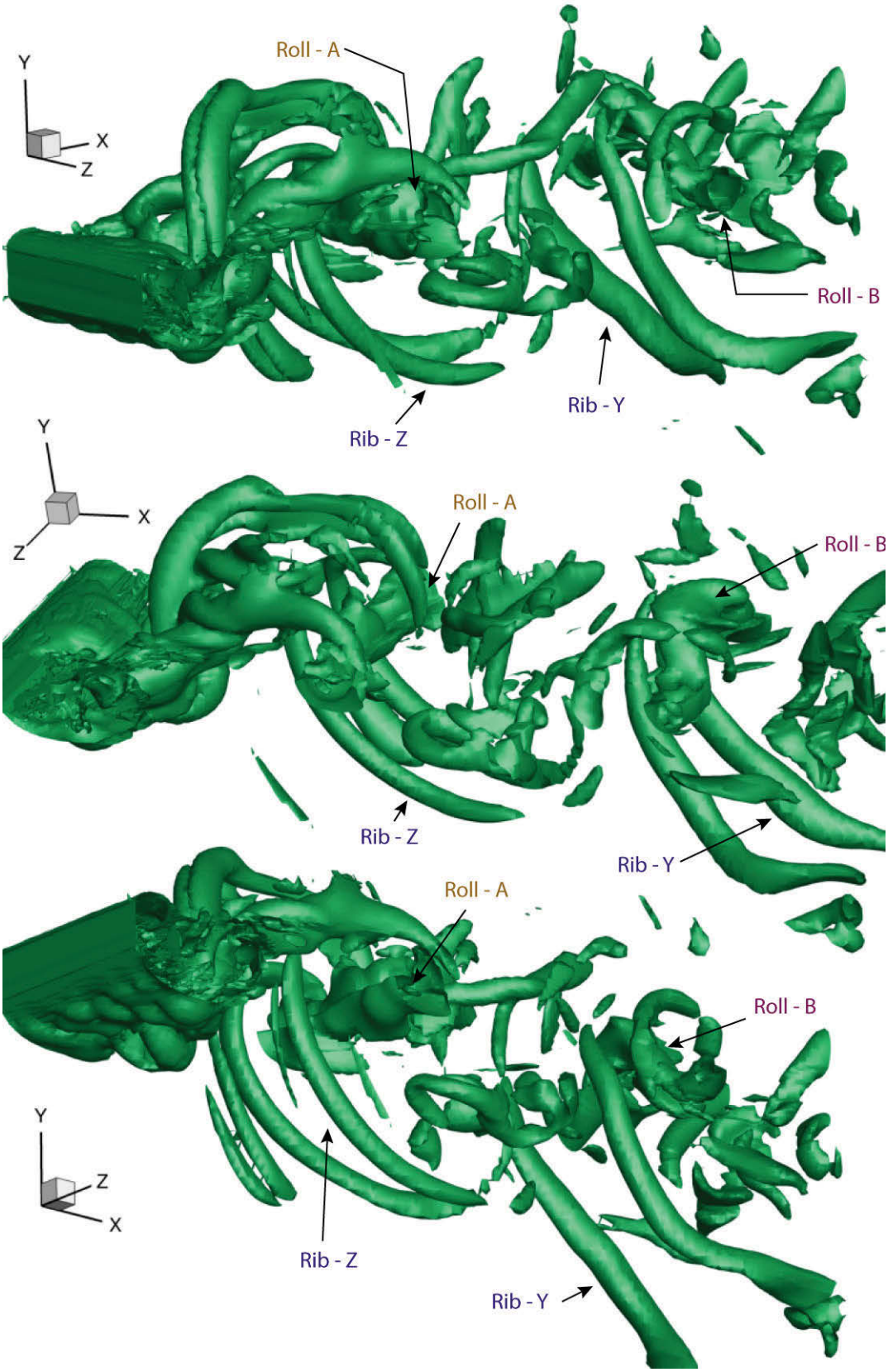


**Figure 5-17 – Three perspective views of the simulation time of *t*=8.6s from the high-resolution mesh with two ribs and two rolls identified and annotated.**

While Dobre and Hangan (2004) performed their experiments at the same $Re_d$ as the present work, their configuration was different in that their tunnel measured 0.12m in the lateral direction. No details of the spanwise dimension were given by the authors. With their 30mm square cylinder, this resulted in a reduced blockage ratio of 25% compared to the blockage ratio from the present work which is only 6.3%.

Both the ribs and rolls break up as they are transported downstream but from the single images* presented in Figure 5-16 and Figure 5-17 it is unclear as to the exact cause. Dobre and Hangan (2004) identified that there are "strong non-linear" interactions between these two structures that led to their decay and a corresponding increase in the homogeneity of the far wake. However, this effect is unlikely to be the cause because the computational domain used for these investigations does not extend into the wake region investigated by Dobre and Hangan (2004). Therefore, it is more likely that the observed break up of the ribs and rolls is due to a combination of grid size in the downstream region and the location of the outlet boundary. The present author has been unable to confirm if the decay in the current models is consistent with the results of Dobre and Hangan as they did not quantify their observed rate of the decay caused by the "strong non-linear interactions".

While the dominant flow is characterised by the formation and transport of ribs and rolls, there is an alternate, transient flow regime in which the ribs elongate and extend downstream, as shown in Figure 5-18. During this period, the formation of rolls is suppressed while any rolls already formed continue to be transported downstream. The alternate flow regime lasts for approximately one second and is spaced at intervals of ten to 15 seconds and to the knowledge of the present author, this alternate flow regime is not discussed elsewhere in the published literature.

* A number of time series animations are available on the DVDs that accompany this thesis, therefore it is suggested that these movies should be examined in conjunction with reading this chapter.

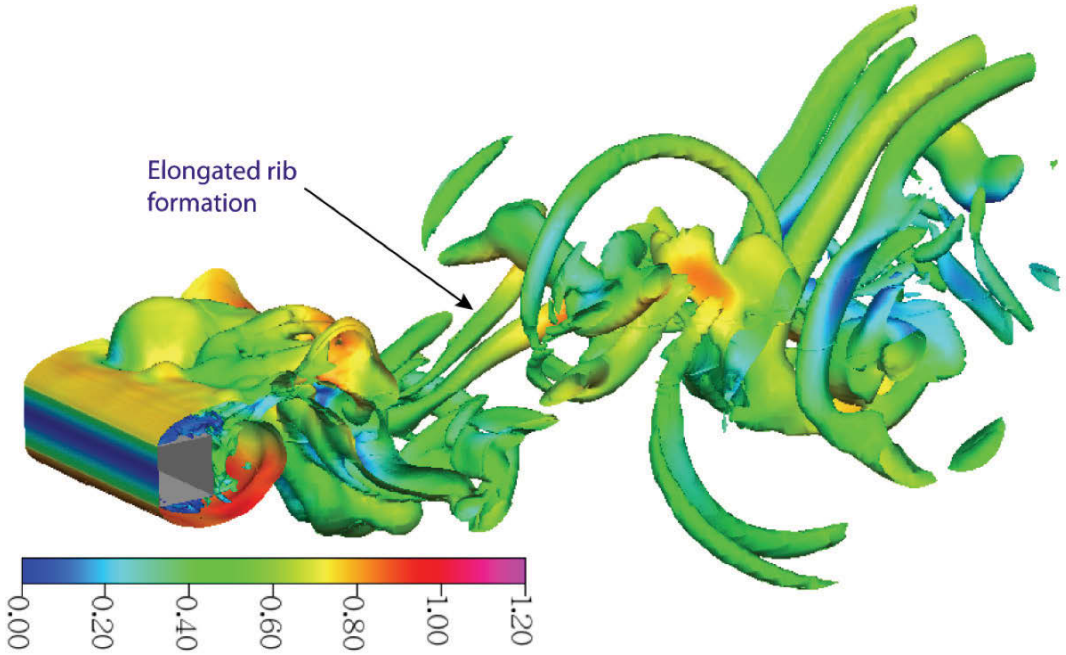


**Figure 5-18 – Flow visualisation of isosurfaces of vorticity magnitude at $|\omega|=25s^{-1}$ coloured by velocity magnitude, from the high-resolution model at a simulation time of $t$=35.0s.**

Song and Park (2009) undertook numerical investigations using Partially Averaged Navier-Stokes equations, in fact modified k-ω equations, on a grid similar, but marginally shorter in the spanwise direction, to the water tunnel configuration discussed above. They, as with the present work, used $\mathrm{Re}_d = 22 \times 10^3$ and, while they did not explicitly discuss the feature, a number of elongated ribs were visible in their results, as shown in Figure 5-19.

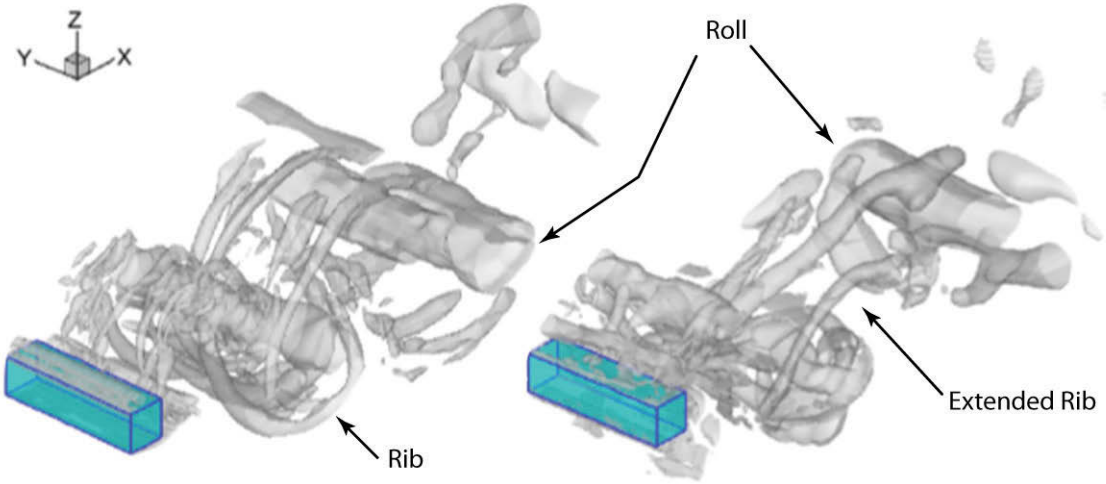


**Figure 5-19 – Q criterion vortex structures adapted from Song and Park (2009).**

Because there are significantly fewer published topological studies of the square cylinder than the right circular cylinder (Zdravkovich, 1997) it is unclear if this alternate flow regime is a real effect or a numerical artefact in the present work. For example, Dobre and Hangan (2004) only discuss the curved rib and roll mode. However, as the elongated flow features are visible in the published images of Song and Park (2009) it is likely that this alternate regime is a real flow feature not previously described.

### 5.5.2. Velocity Magnitude Distribution along the z=0 Plane

When the flow field is visualised by the velocity magnitude on a plane at $z$=0 the characteristic rolls and ribs are visible, as shown in Figure 5-20. However, the effect of the ribs on the flow field is subtle because the ribs are predominantly streamwise structures. Since they may not fall exactly on the selected plane their visibility as a velocity perturbation is not assured.

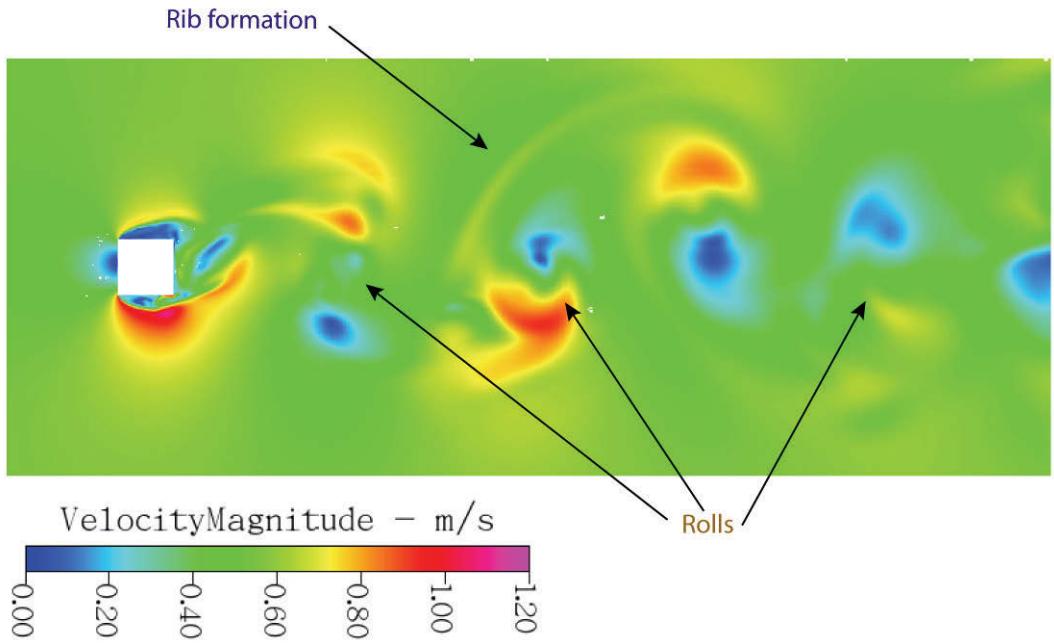


**Figure 5-20 – Flow visualisation on the $z$=0 plane from the high-resolution simulation, time $t$=34.4s.**

As noted above for the three-dimensional analysis, the flow regime periodically swaps to the alternate, elongated ribs regime, shown in Figure 5-18. This alternate flow pattern is also visible, and is plotted in Figure 5-21, as a region of uniform flow in the near wake. Because the elongated rib is both lengthened and not inline with the plane the flow field appears to be more uniform.

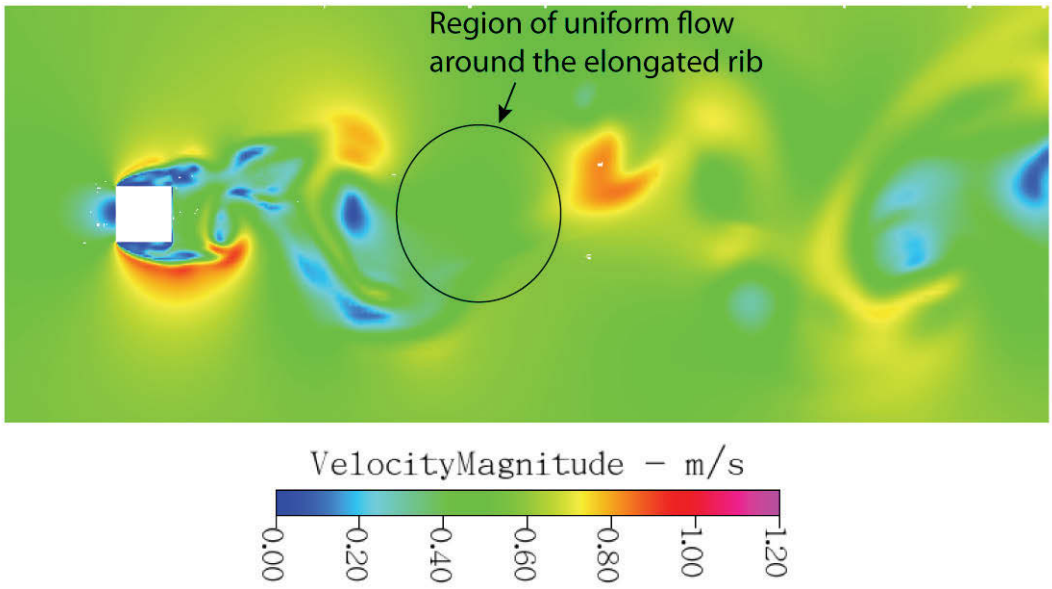


**Figure 5-21 – Flow visualisation of the velocity magnitude across a $z$=0 plane from the high-resolution model at a simulation time of 35.0s.**

In contrast to region of uniform flow identified in Figure 5-21, the near wake between the cylinder and the uniform region is highly irregular and disturbed, which is visible as convoluted three-dimensional isosurfaces shown in Figure 5-18. This disturbed region in the near wake is similar to a velocity magnitude plot published by Hoffman (2005), shown in Figure 5-22.

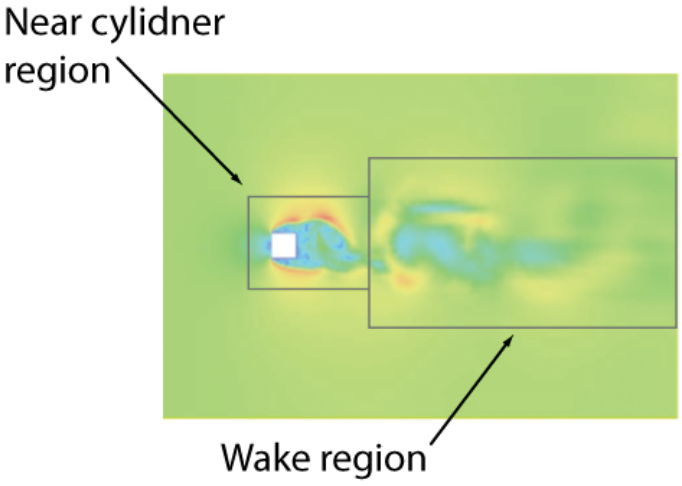


**Figure 5-22 – Flow visualisation on the centre plane of the fully developed flow computed by Hoffman (2005).**

Hoffman claimed that the flow shown in Figure 5-22 was the result of an adaptive DNS/LES simulation and is fully developed (Hoffman, 2005). However, by a visual

comparison with the present work, for example a comparison of the flow field shown in Figure 5-21 with that in Figure 5-22, Hoffman's flow field is not developed. That is, there is no vortex shedding that is characteristic of the wake in square cylinders at this $Re_d$. Therefore, the flow visualised in Figure 5-22 does not appear to be developed as it is different from either the visualisations in the present work, Figure 5-16 or Figure 5-20, and it does not match the flow schematic described by Dobre and Hangan (2004), shown in Figure 5-23.

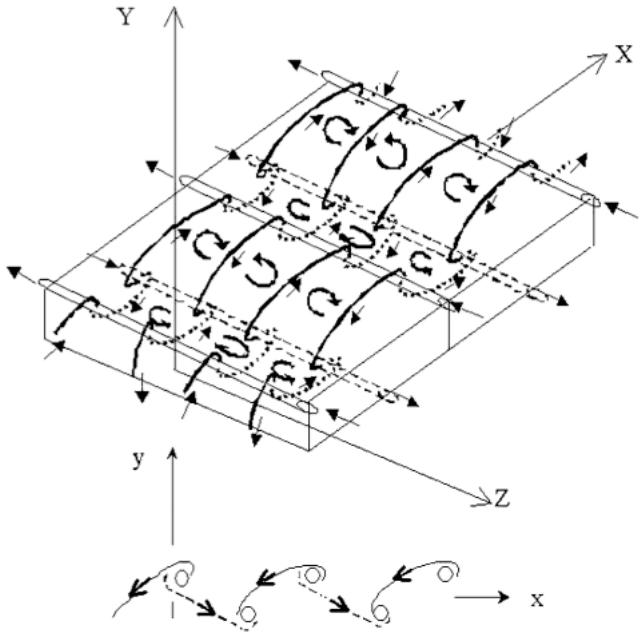


**Figure 5-23 – Idealised 3D wake topology from the horizontal perturbation model (Meiburg and Lasheras, 1988), reproduced from Dobre and Hangan (2004).**

The visualisations of both Dobre and Hangan (2004) and Song and Park (2009) lend strong credibility to the present results with excellent agreement of the large scale flow structures visible.

So far, the vorticity and velocity fields have been examined, almost, separately whereas they are in fact intimately linked via

$$\boldsymbol{\omega} = \nabla \times \mathbf{u} \,. \tag{5.11}$$

Therefore, simultaneously visualising the flow field with both the velocity magnitude and vorticity fields can provide additional observations to either support or refute the present simulations.

### 5.5.3. Vorticity and Velocity Magnitude Cut Planes

As has been discussed above there is an interaction between the ribs and rolls visualised by isosurfaces of vorticity and the velocity field. However, because of the compromises that were made when the mesh for these simulations was developed, there are some small artefacts in the computed vorticity, shown in Figure 5-24, which are restricted to the smallest cells with the largest size gradients. Further, as there is no visual indication of corresponding defects in the velocity field, the vorticity artefact must be due to the numerical inaccuracies of the post processing operations.

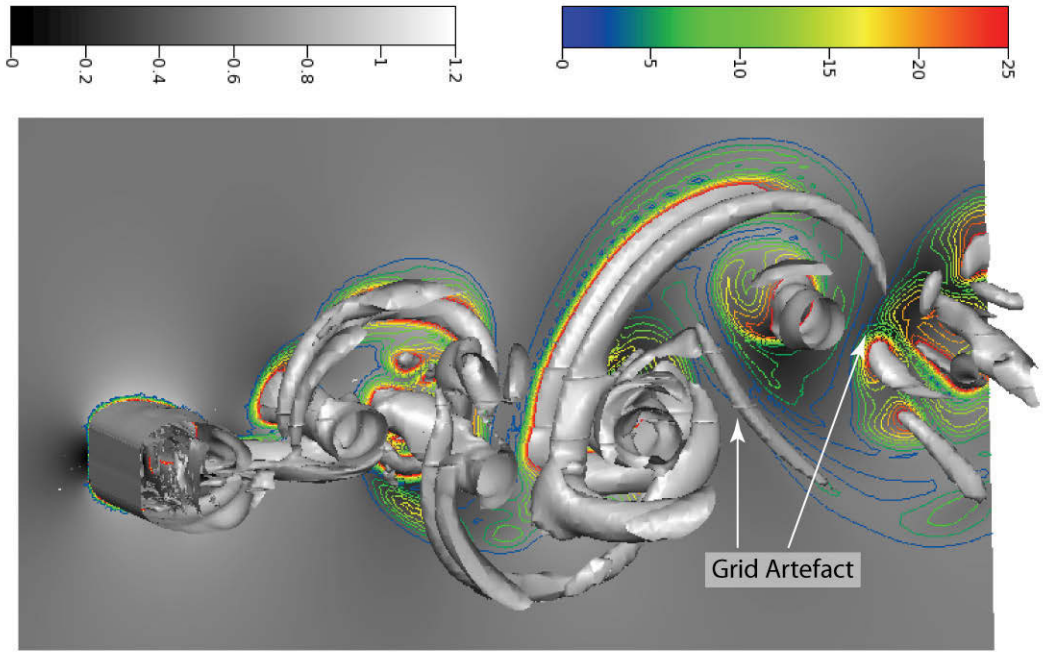


**Figure 5-24 – Cut plane at $z$=0 from the high-resolution model at $t$=35.0 showing velocity magnitude in grey scale and vorticity magnitude contours in colour and a three-dimensional view with an isosurface of $\omega=25s^{-1}$.**

The combined vorticity and velocity magnitude plots in both Figure 5-24 and Figure 5-25 show that the vorticity magnitude increases towards the centre of both the rolls and the ribs. Simultaneously for the roll that is cut across the plane, highlighted in Figure 5-25(b), the velocity magnitude drops to almost zero, indicating that, at this time instant, the roll core is almost stationary. This low velocity magnitude is most likely due to the chaotic fluctuations temporarily slowing the vortex core because the time series, shown in both Figure 5-16 and Figure 5-20 and in the animations on the DVDs attached to this dissertation, show that in general the vortices are transported

downstream. This temporary low speed region would also explain the apparent pause in the movement of the roll adjacent to the cylinder in Figure 5-20 before it moves downstream.

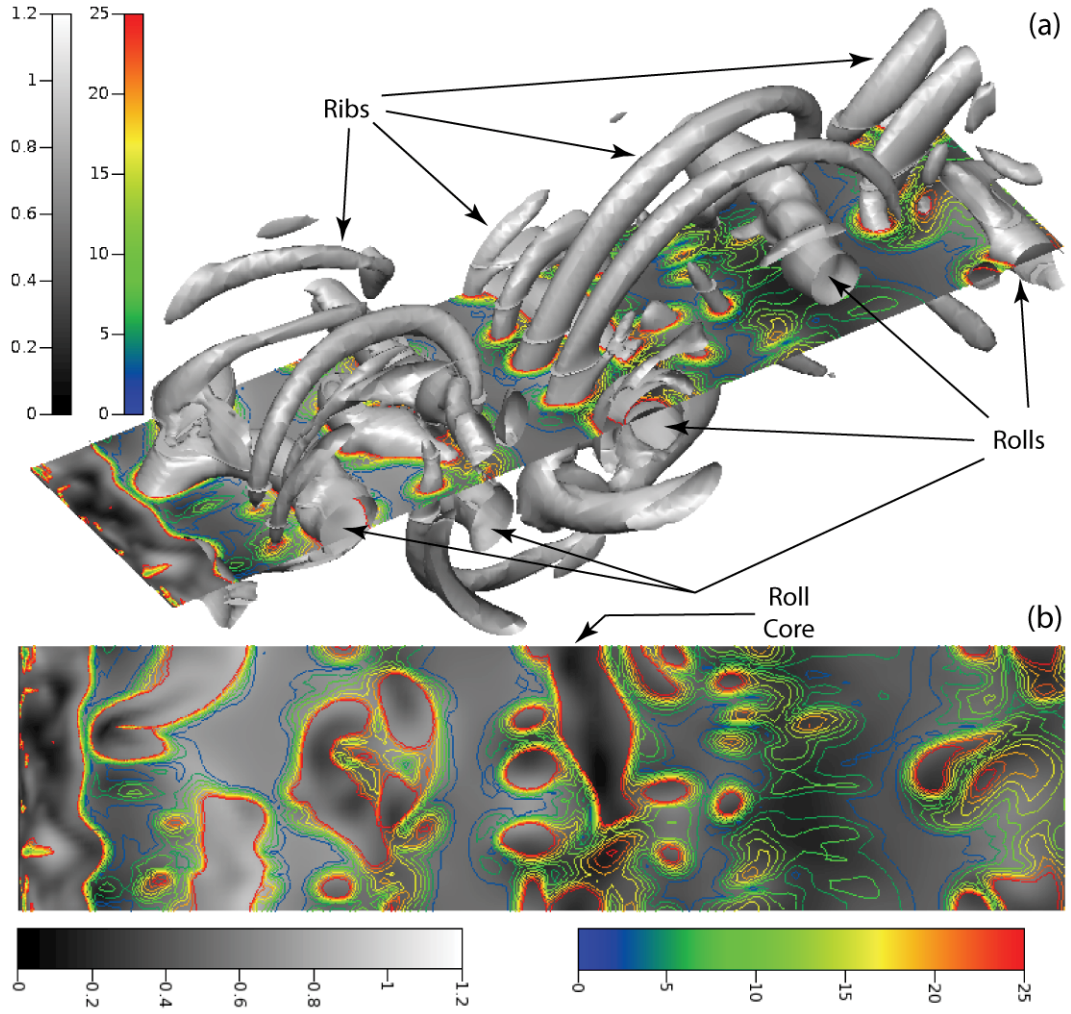


**Figure 5-25 – Cut plane at *y*=0 from the high-resolution model at *t*=34.6 showing velocity magnitude in grey scale and vorticity magnitude contours in colour (b) and a three-dimensional view with an isosurface of $|\omega|=25s^{-1}$ (a).**

Finally, in Figure 5-25, while the spanwise rolls appear independent of the domain width, they extend across the entire span, the ribs appear to be affected by the proximity to the spanwise periodic boundaries. For example, the collection of ribs above the cut plane in the downstream half of the domain appear to show significant variation across the domain with the central two ribs fully formed and wrapped over the spanwise roll. In contrast to the central ribs, the ribs that are located closest to the boundaries with a periodic specification appear stunted and malformed. If the domain were truly periodic, then there should be no noticeable affect from the location of the periodic boundaries on

the flow structures observed, in contrast to the images in Figure 5-25. Further, if the vortex field from the high-resolution, spanwise periodic simulations, shown in Figure 5-25, is compared with a similar visualisation from the water tunnel model shown in Figure 5-26 there are two points of note. First, that the spanwise rolls, as with the spanwise periodic models, cross the entire spanwise width of the domain. Second, that in contrast to the spanwise periodic simulations, the structure of the ribs is different. As would be expected because of the increased width of the domain there is a higher count of ribs that form across the domain. However, their structure, compared with the spanwise periodic models is more regular, even in the regions near the side walls.

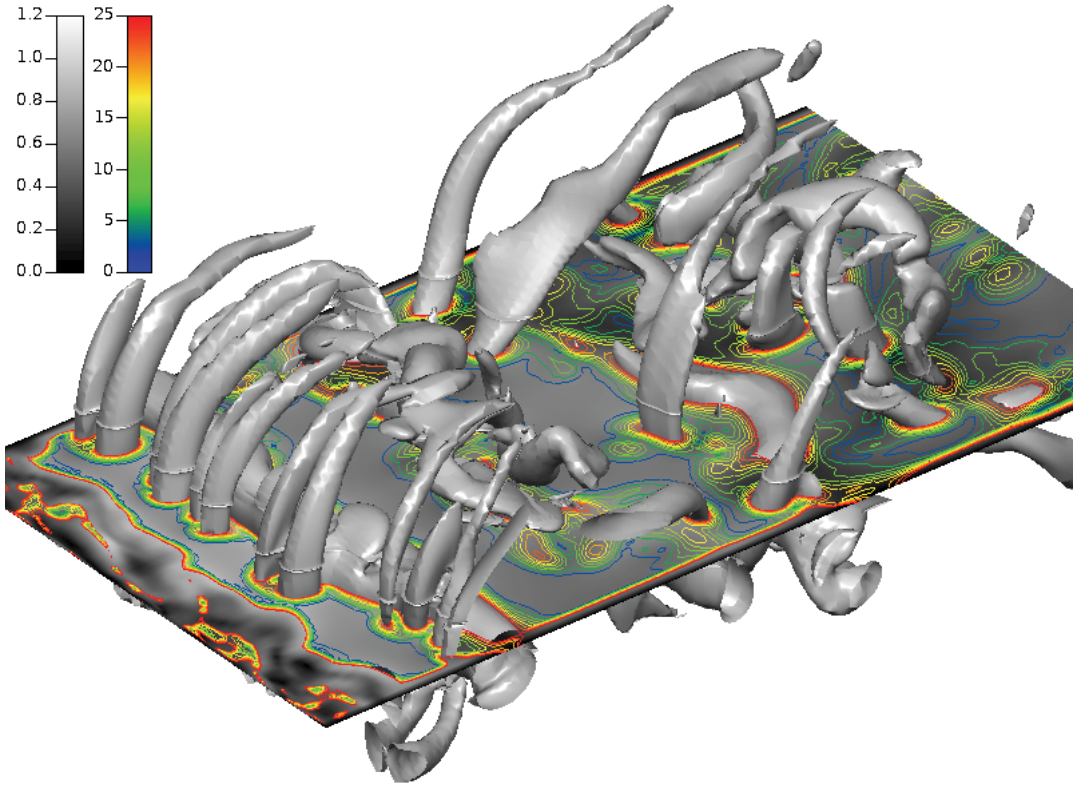


**Figure 5-26 – Flow visualisation of the vorticity magnitude (colour contours) and the velocity magnitude (greyscale) on the *y*=0 plane from the water tunnel simulation, time *t*=41s and the isosurfaces at $|\omega|=25s^{-1}$.**

These comparative, visual observations indicate that there is a potential problem with simulations that utilised the spanwise periodic boundary conditions; namely that the spanwise width is not large enough which, when combined with the assumption of periodicy, leads to the development of an unphysical flow field. That is, the spanwise width of the domain must be wide enough to allow the development of a large region of uncorrelated flow in the centre of the domain (O'Neill et al., 2004). Fortunately there is

a large body of work, for example the treatises of Tennekes and Lumley (1972) and Yaglom (1987), to provide direction for the computation of the velocity correlations as a function of both time and space.

## *5.6. Spanwise Velocity Correlations*

### 5.6.1. Description and Validation of the Sampling Technique Used in the Present Work

A correlation where the variables are separated in space but measured at the same time instants is referred to as a cross correlation (Orfanidis, 1996), with the correlation coefficients, $R_{lm}$, computed from

$$R_{lm}(r,t) = \frac{\overline{u_l(\mathbf{x},t)u_m(\mathbf{x}+r,t)}}{\sqrt{\overline{u_l'^2}\,\overline{u_m'^2}}} \tag{5.12}$$

in which $r$ is the spatial separation of point $m$ from point $l$ whose absolute position is denoted by $\mathbf{x}$, adapted from Pope (2001). Due to the application of the Cauchy-Schwarz inequality, $R_{lm}$ is limited to the range

$$-1 \le R_{lm} \le +1. \tag{5.13}$$

A special case, that is known as the autocorrelation, occurs when $r$ tends to zero, that is $l = m$, in which the maximum correlation occurs at zero time lag, $t = 0$.

The cross correlations computed from the present work were, necessarily, limited to discrete values of $r$ due to the discretisation of the computational mesh. However, in the time domain two sets of data were available to evaluate Equation (5.12), which related for the time step size, 1 kHz, and the frequency at which the total flow field data were saved at 10 Hz, respectively. Due to the restrictions on the data storage facilities, only 85 points were distributed throughout the computational domain that sampled at 1kHz. These 85 points were neither numerous enough, nor located in positions that would allow for, a spanwise correlation analysis. Hence, the data used in the correlation analysis presented in this section were sampled from the 10Hz, flow field data.

Because a 10Hz sampling rate is simultaneously 1% of the time step frequency and is only 5.6 times larger than the published shedding frequency of 1.8Hz (Lyn and Rodi, 1994, Lyn et al., 1995) there was a concern as to the accuracy of resultant correlations.

That is, the 10Hz sampling frequency may be too low to capture the high frequency events. Therefore, the autocorrelation function from the velocities sampled at 1kHz at the point probe located at (0.025, 0, 0) m was compared with data from the same location that was sampled at the lower, 10Hz, rate.

Despite the expected lower resolution, for both the *u* and *v*-velocity autocorrelation functions there is no appreciable difference at the common points between the 1kHz and 10Hz sample rates, shown in Figure 5-27 to Figure 5-29. There is a less than 2% difference in the *w*-velocity autocorrelation functions which is due to the comparatively small *w*-velocity. That is, because the *w*-velocities are so small, a comparatively

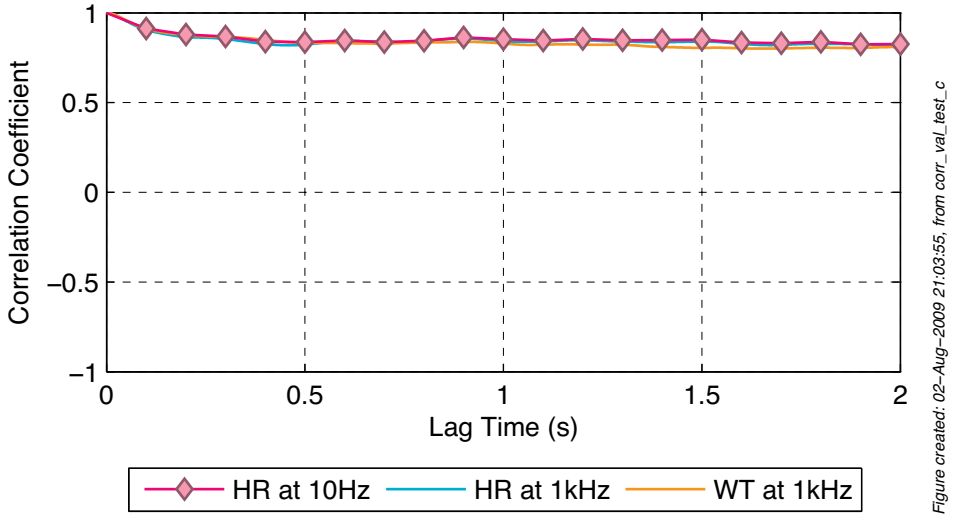


**Figure 5-27 – Autocorrelation function for a point located at (0.250, 0, 0)m showing the affect of a change of sample rates for the *u*-velocity.**

smaller difference in the sampled velocity can produce a significantly larger change in the autocorrelation function. These two observations are also valid for the comparison with the water tunnel results that were sampled at 1 kHz and are presented for comparison with the spanwise periodic models. Therefore, as there is essentially no change in the *u* and *v*-velocity autocorrelation and only a minor change in the *w*-velocity autocorrelation functions, it can be assumed that, despite the loss of detail, the major flow field features are still captured at a sample rate of 10 Hz. Hence, the spanwise correlations from the present work can be investigated at any point, not just the points for which a full data set is available.

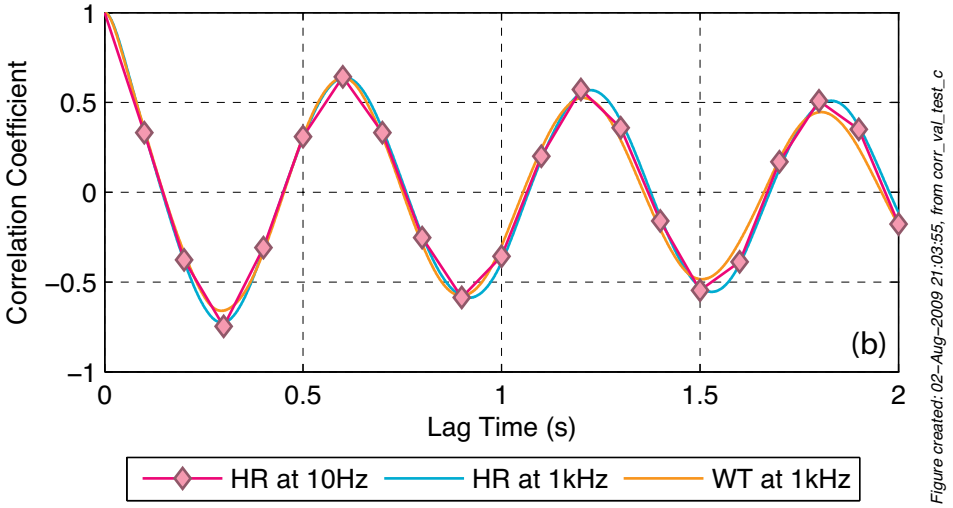


**Figure 5-28 – Autocorrelation function for a point located at (0.250, 0, 0)m showing the affect of a change of sample rates for the *v*-velocity.**

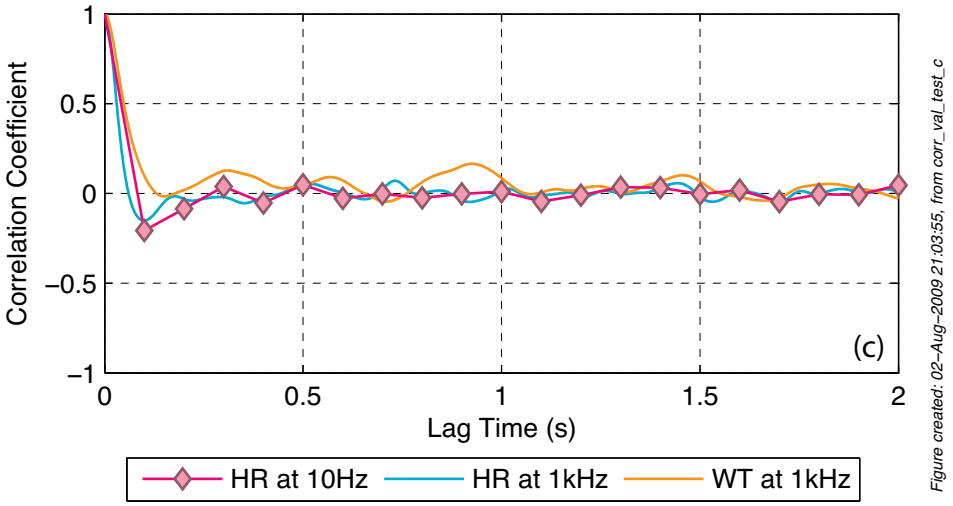


**Figure 5-29 – Autocorrelation function for a point located at (0.250, 0, 0)m showing the affect of a change of sample rates for the *w*-velocity.**

### 5.6.2. Correlation Analysis of the Data from the Present Work

It was noted above in the quantitative evaluation of the flow visualisations that different results were obtained from the simulations with alternative treatments of the spanwise domain. Therefore, to quantify any possible differences between the different spanwise simulations, the results from the simulations were sampled at 10 Hz along spanwise line probes, as shown schematically in Figure 5-30, and subjected to correlation analyses.

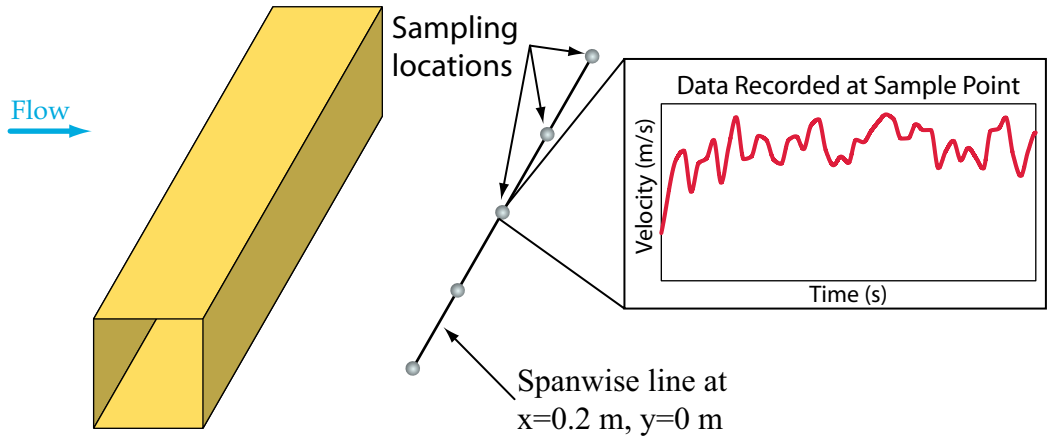


**Figure 5-30 – Schematic of the spanwise distribution of sampling points used in the correlation analysis.**

For the analyses presented in this section the reference point *l*, in Equation (5.12), was set at $z = 0$ while point *m* was varied to compute the distribution of $R_{lm}$. Therefore, the autocorrelation, $R_{lm} = R_{ll} = 1$, also occurs at $z = 0$. In total, six spanwise lines were sampled with one located upstream of the cylinder, one located downstream of the cylinder but above the boundary of the mean wake while the remaining four probes were distributed in the wake region, as shown in Figure 5-31 and detailed in Table 5-3.

**Table 5-3 – List of the locations of the spanwise line probes.**

| Sample Line | x (m) | y (m) |
|---|---|---|
| UC1 | -0.20 | 0.00 |
| SC1 | 0.20 | 0.16 |
| WC1 | 0.10 | 0.00 |
| WC2 | 0.20 | 0.00 |
| WC3 | 0.40 | 0.00 |
| WC4 | 0.60 | 0.00 |

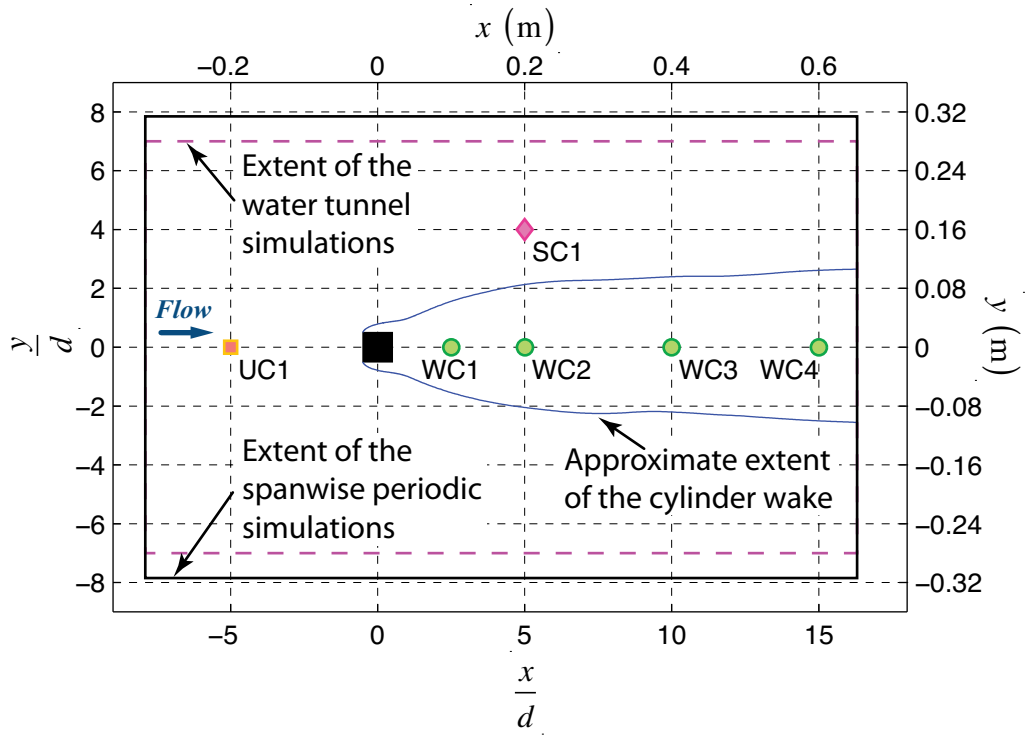


**Figure 5-31 – Location of the point probes chosen for the correlation analysis with the computational boundaries and an indicative location of the wake boundary.**

For the line probes within the wake region the correlations were also compared with those computed by Dobre and Hangan (2004), who took spanwise correlation measurements within the wake of a square cylinder flow at the same $\mathrm{Re}_d$ but for a cylinder that was longer in the spanwise direction. Dobre and Hangan (2004) computed their correlations in one direction only with the implicit assumption that they would be symmetrical around the centre of their tunnel; their zero point. In contrast, while the correlation functions computed from the present work were also computed relative to the $z$=0 plane, they were not assumed to be symmetrical around this plane. Hence, the single sided correlation functions of Dobre and Hangan (2004), when present on the graphs plotted below have been mirrored to match the two-sided data from the present work. Finally, the correlations published by Dobre and Hangan (2004) were computed from data that was measured at $x = 26d$ compared with the limit of $x \leq 15d$ for the present work. Therefore, due to the difference in the measurement locations, some differences would be expected.

The flows from both the spanwise periodic and the water tunnel simulations remain highly correlated for both the upstream line, UC1, and the lateral point, SC1, as shown

in Figure 5-32 and Figure 5-33, respectively. These correlation results were expected from an inspection of the flows namely, that as there is almost no disturbance in these regions the correlation function should be high. However, while a high correlation was expected, the correlation coefficients for the spanwise periodic models are all above 0.98 which indicates an almost perfect, and seemingly unphysical, similarity in the flow across the entire spatial and time sample windows.

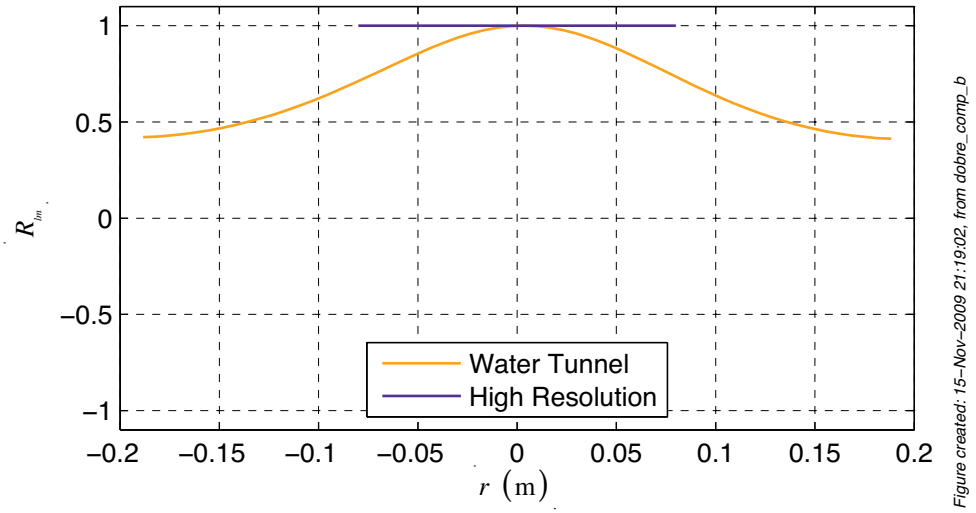


**Figure 5-32 – $R_{lm}$ correlation coefficients for both the water tunnel and the HR spanwise periodic simulations as a function of separation over the line UC1.**

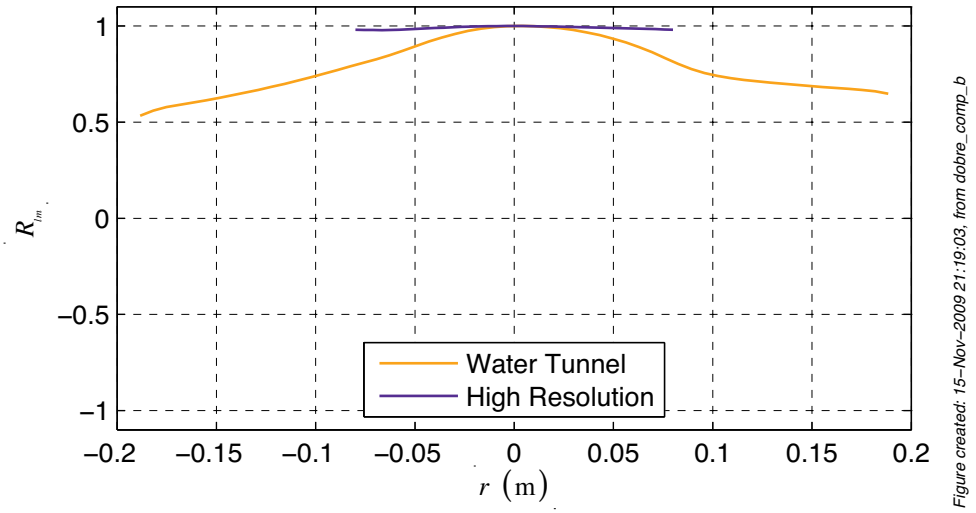


**Figure 5-33 – $R_{lm}$ correlation coefficients for both the water tunnel and the HR spanwise periodic simulations as a function of separation over the line SC1.**

In contrast to the spanwise periodic simulation, $R_{lm}$ for the water tunnel simulation dropped to 0.5 as $m$ approached the walls, which indicated a lower, but still positive,

correlation of the flows. Intuitively this result seems more realistic because $R_{lm} \geq 0.98$ seems to be impossibly high for a "real" flow.

Despite minor differences in the absolute value, both the shape and trend of $R_{lm}$ as a function of $r$ are consistent for all four points tested in the wake, that is points WC1 to WC4 as shown in Figure 5-34 to Figure 5-37, respectively. From the central peak at $r = 0$, the values of $R_{lm}$ for both the water tunnel and spanwise periodic simulations drop quickly to 0.5, which is inline with the experimental results of Dobre and Hangan (2004).

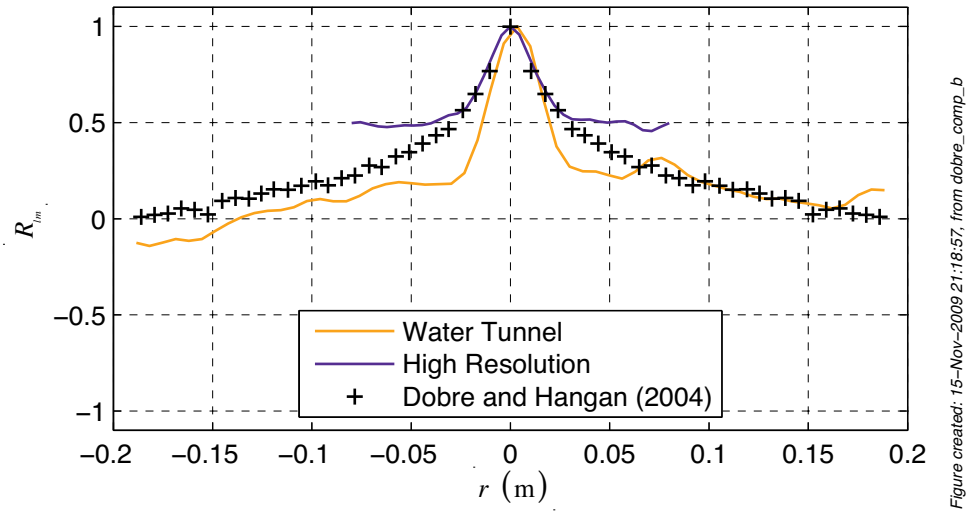


**Figure 5-34 – $R_{lm}$ correlation coefficients for both the water tunnel and the HR spanwise periodic simulations as a function of separation over the line WC1.**

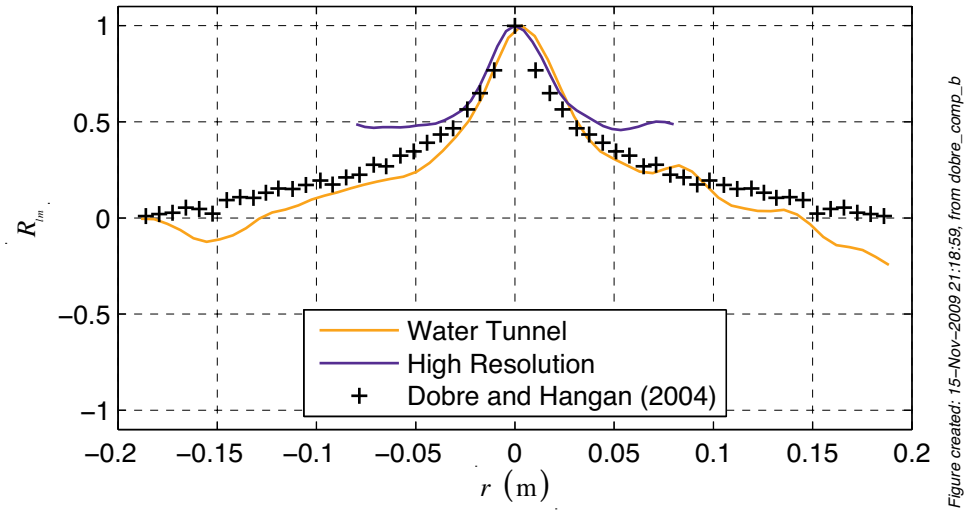


**Figure 5-35 – $R_{lm}$ correlation coefficients for both the water tunnel and the HR spanwise periodic simulations as a function of separation over the line WC2.**

However, with the sample line WC1, which was closest to the cylinder, as $r$ was further increased the results from the simulations diverged with the spanwise periodic results stable at $R_{lm} = 0.5$ for $r > 0.03$ m. In contrast to the stability of the spanwise periodic simulations, the results from both physical experiment and the present water tunnel simulation continued in a similar downward trend toward $R_{lm} = 0$, or no correlation.

As the sample location was moved downstream to points WC2, 3 and 4, in Figure 5-31, $R_{lm}$ for the water tunnel simulations is a consistent match with the experimental results from Dobre and Hangan (2004). However, the stable region of $R_{lm}$ that was observed in the results from WC1, shown in Figure 5-34, and to a lesser extent from WC2, shown in Figure 5-35, was reduced as the distance of the sample line from the cylinder was increased. It was noted that when the downstream sampling location reached $x = 15d$, or at WC4 as shown in Figure 5-37, there was no stable region and $R_{lm}$ as a function of $r$ was almost coincident with both the water tunnel simulation and the experimental results.

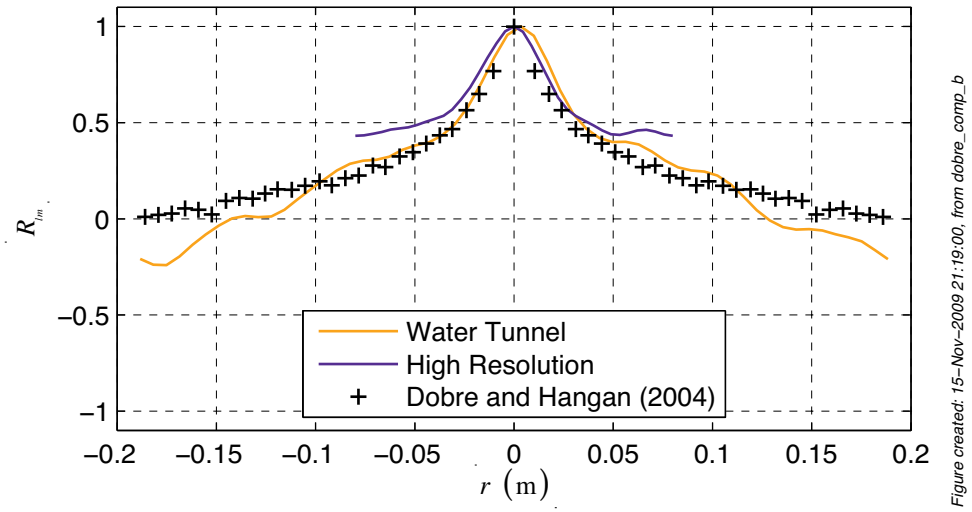


**Figure 5-36 – $R_{lm}$ correlation coefficients for both the water tunnel and the HR spanwise periodic simulations as a function of separation over the line WC3.**

Finally, it must be noted that the results from the present numerical simulations show a degree of asymmetry that was not expected from the authors conception of the flow, which was that there would be no left/right bias. As such, this result warrants subsequent investigation that was not the subject of this research. However, the effect is most likely due to a combination of the lower sampling rate and a sampling window that was too short.

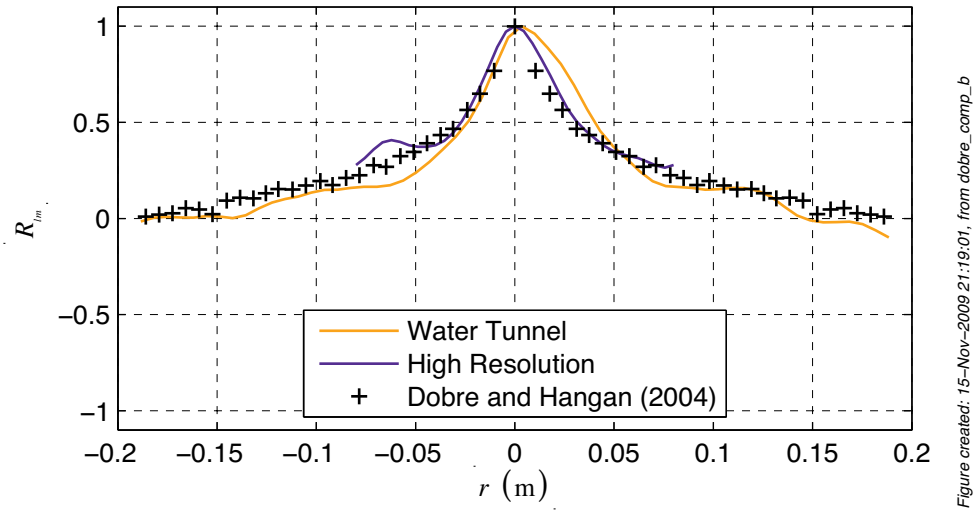


**Figure 5-37 – $R_{lm}$ correlation coefficients for both the water tunnel and the HR spanwise periodic simulations as a function of separation over the line WC4.**

There are two main observations presented above that are particularly relevant to the present work: firstly that for all the samples taken in the wake $R_{lm}$ dropped from one to 0.5 by $r \cong \pm 0.04m$; and, secondly, that for the samples in the wake closest to the cylinder, the spanwise periodic correlations remained stable at 0.5. These two results are both intimately linked and simultaneously important because the region of highly correlated flows for the spanwise periodic simulation in the centre of the domain was equal to half the spanwise width with no surrounding region of uncorrelated flow. This result violated a fundamental tenant of periodicy that there must be a sufficiently large region of uncorrelated flows within the domain (O'Neill et al., 2004).

Recommendations for the domain size vary from two to six times the integral length (O'Neill et al., 2004) and although the spanwise integral length was not computed for the present work, Dobre and Hangan (2004) estimated the spanwise integral length as approximately one cylinder diameter. Further, Dobre and Hangan also noted that this integral length was about half the "cross-wake extent" that indicated that the size of the large-scale flow structures is in the order of two cylinder diameters. Therefore, as the conclusions drawn by O'Neill et al (2004) were taken from the results of simulations of homogenous turbulence with no large scale structures such as ribs, rolls or a wake, it is the present author's opinion that the estimated size of the flow structures should also be considered when estimating the width of the domain. From the present work, it is unclear what the recommended number of structures should be but at a minimum, three structure widths would seem to be a reasonable lower limit. Therefore, for this

configuration, the flow structure criterion would define a minimum spanwise width of six cylinder diameters of uncorrelated flow, whereas the integral length benchmark would suggest a minimum uncorrelated extent of three cylinder diameters. In contrast, neither the spanwise periodic simulations of the present work nor the vast array of published numerical results based on the same assumptions met the six diameters of uncorrelated flow criterion.

## *5.7. Review of the Flow Visualisations*

With this visual examination of the flow field, visualised by both the vorticity and velocity magnitudes, and the spanwise correlation results it is clear that there is a difference in the simulated flow patterns between the spanwise periodic models and the water tunnel model. It is then a reasonable assumption that the simulated flow from the water tunnel model would be a better approximation of the experimental data of Lyn and Rodi (Lyn and Rodi, 1994, Lyn et al., 1995). However, as the vast majority of the numerical results that are available for validation are from models based on the spanwise periodic assumptions the remainder of the single fluid validation presented in this dissertation will deal with the observations from both spanwise periodic models and the water tunnel model simultaneously.

# 6. Single Phase Validation: Point and Integral Data

## *6.1. Introduction*

It has been shown in §5 that the assumptions that underpin the vast majority of the published simulations, whose results have become the de facto standard for square cylinder flow at $\mathrm{Re}_d = 22 \times 10^3$, are wrong in that the assumption of periodicy combined with an inadequate spanwise width resulted in the computation of unphysical flows. Despite the differences in the results of the simulations developed in the present research, the majority of the validation data available for comparison was developed from simulations using the spanwise periodic domain. Because of the ease of comparison between numerical simulations, in particular with respect to the inherent uncertainties of laboratory experiments, these data will predominantly be used in the following discussions, subject to the caveats already outlined. The present discussion will, therefore, proceed with a more "traditional" validation comprised of an analysis of the grid convergence followed by a critical examination of the statistical characteristics of a number of time domain parameters.

## *6.2. Grid Convergence*

### 6.2.1. Methodology

There are numerous rigorous mathematical methods available to undertake a grid convergence study that include the methods outlined in the treatise of Roach (1998b). A particular method, which is based on a Richardson extrapolation has been recommended by the editorial board of the ASME Journal of Fluids Engineering (Celik et al., 2008), was used to test the convergence of the different parameters as a function of the change of the grid size.

Despite the apparent rigour of a mathematical method, oscillatory convergence is a known limitation, which can lead to artificially high confidence bounds, and occurred for the majority of the parameters tested in the present work. Ideally, if oscillatory convergence were to be encountered during a grid convergence investigation, additional simulations on different meshes should be computed. These additional data should provide the further refinement necessary to quantify the oscillatory convergence.

Additional simulations were not undertaken due to the lack of computational wall time, instead a qualitative analysis of the statistical characteristics of the velocity from a point that was common to all the simulations was used to assure the present author, and by extension the reader, of the consistency of the simulations. It should be noted that this process was designed to assess the consistency of the results of the simulations but not the accuracy of the numerical results relative to other, published, studies.

### 6.2.2. Velocity Components as a Function of Time

A point probe that tracked all three velocity components as a function of time was located within the wake region at (0.078, 0, 0)m as shown in Figure 6-1. The boundary of the wake was defined as the locus of

$$U = 0.99U_{\infty} \tag{6.1}$$

in which $U$ is the time averaged velocity field and the constant, 0.99, was selected with consideration to boundary and mixing layer analyses (White, 1991).

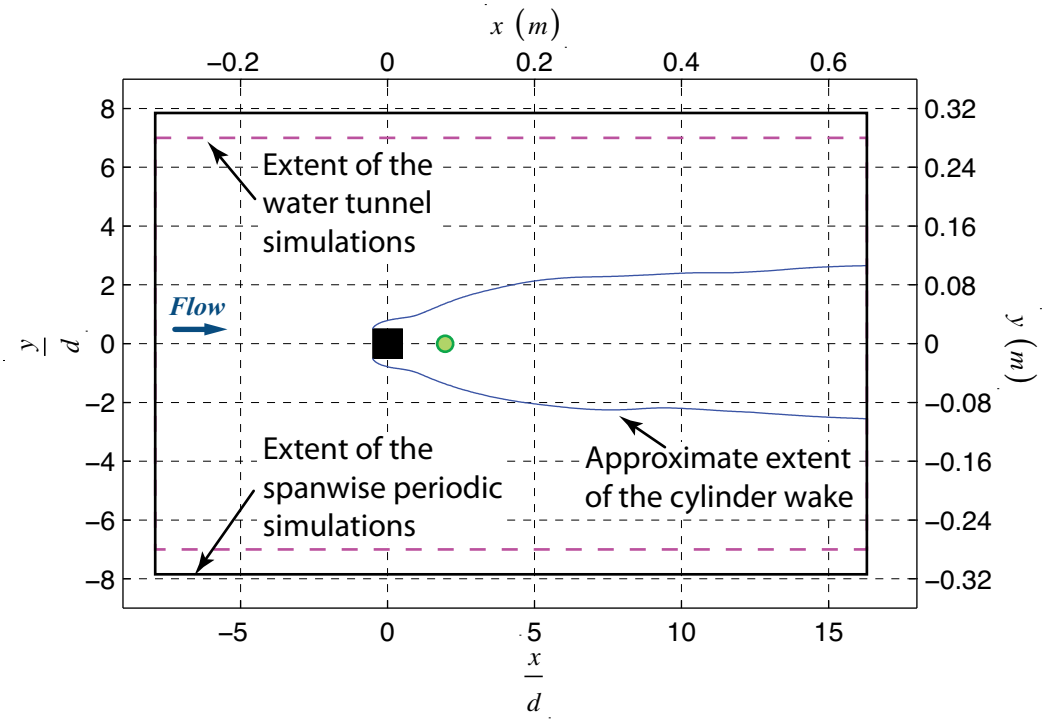


**Figure 6-1 – Location of the point probe in relation to the square cylinder and the approximate boundary of the wake region.**

The traces of the *u*-velocities as a function of time, as shown in Figure 6-2, are impossible to distinguish via a visual comparison. Both the mean and the amplitude of

the signal around the mean appear to be the same and all four signals include occasional "blips" such as that for the low-resolutionsimulation at $t \cong 17$ s. The corresponding plots of the *v* and *w*-velocities are not shown because they are also similar to each other.

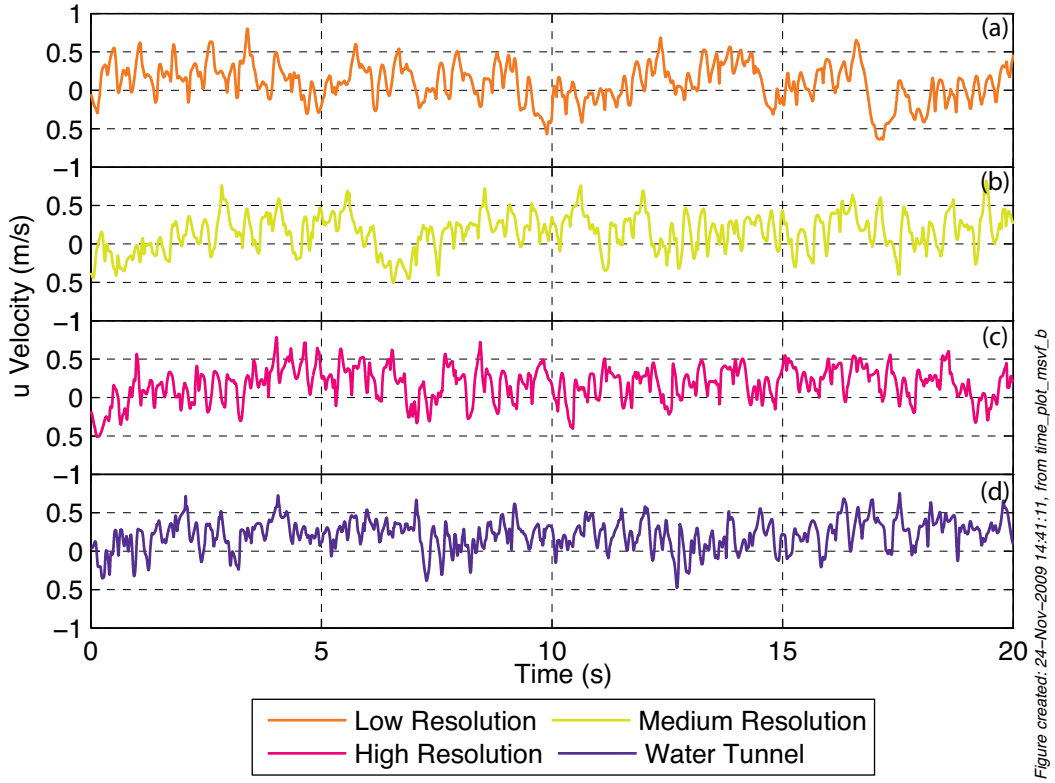


**Figure 6-2 – *u* velocity as a function of time for the point probe at (0.78,0,0)m.**

Therefore, as the visual comparison has indicated that the three velocity components from the four simulations are broadly consistent, a more rigorous approach was required to formally evaluate the similarities, and differences, between the simulations.

### 6.2.3. Statistical Characteristics of the Velocity Traces

As a first attempt to apply a more rigorous approach to the comparison of the velocity component data, the distribution functions were computed. In conjunction with the histograms, a number of fundamental statistical quantities such as the mean and standard deviation were evaluated for further comparison.

All the distribution functions are self similar, for example, the shape of the histogram for the *u*-velocities are skewed to the right with a peak at approximately 0.3 m/s, as shown in Figure 6-3. However, the distributions from the three velocity components are markedly different to each other with the *u*-velocity being right hand skewed, as

shown in Figure 6-3, the *v*-velocity functions being bi-modal, as shown in Figure 6-4, and the *w*-velocity functions peaked symmetric, as shown in Figure 6-5.

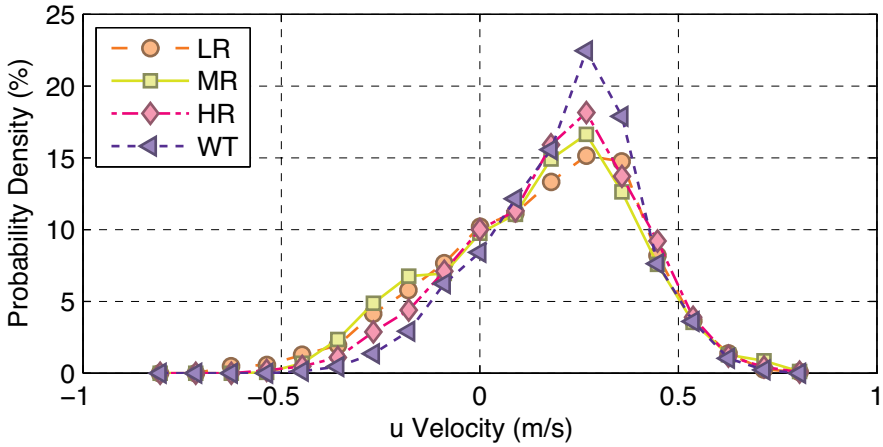


**Figure 6-3 – Distribution function of the *u*-velocities from the four simulations.**

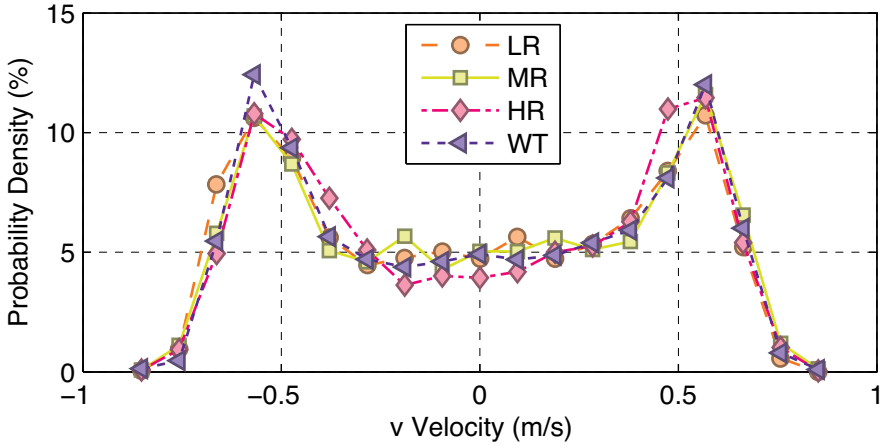


**Figure 6-4 – Distribution function of the *v*-velocities from the four simulations.**

To quantify the visual similarities of the histograms, the statistical characteristics of: global minimum; global maximum; mean, standard deviation, mode, median, skewness and kurtosis were computed for the *u-, v-* and *w*-velocity time series data across the four simulations. For the first four parameters, there is no discernable trend in the results across either the configurations or velocity components, as shown in Figure 6-6. For

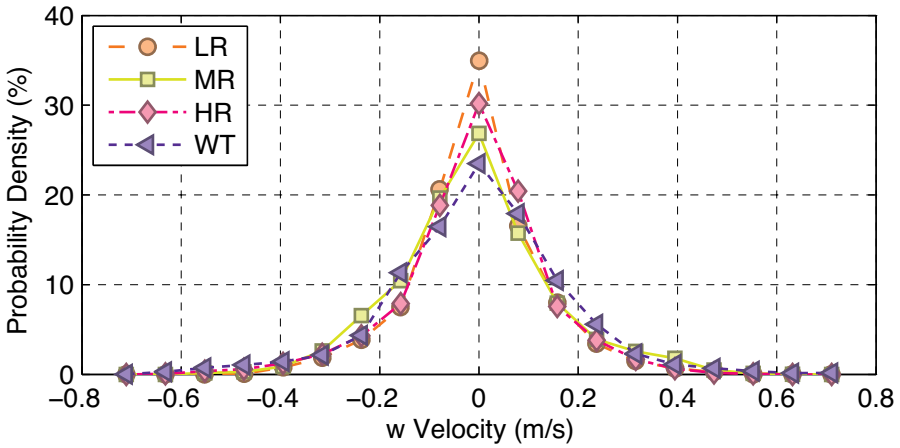


**Figure 6-5 – Distribution function of the *w*-velocities from the four simulations.**

example, the minimum velocities increase for the *u*-component but decrease for the *w*-component, despite the similarity in their absolute values, shown in Figure 6-6(a). Further, the maximum and standard deviations are consistent with a less than 10% variation within the individual velocity components computed, Figure 6-6(b) and (c), while the mean for the *u*-velocity shows an increasing trend as the model resolution is increased.

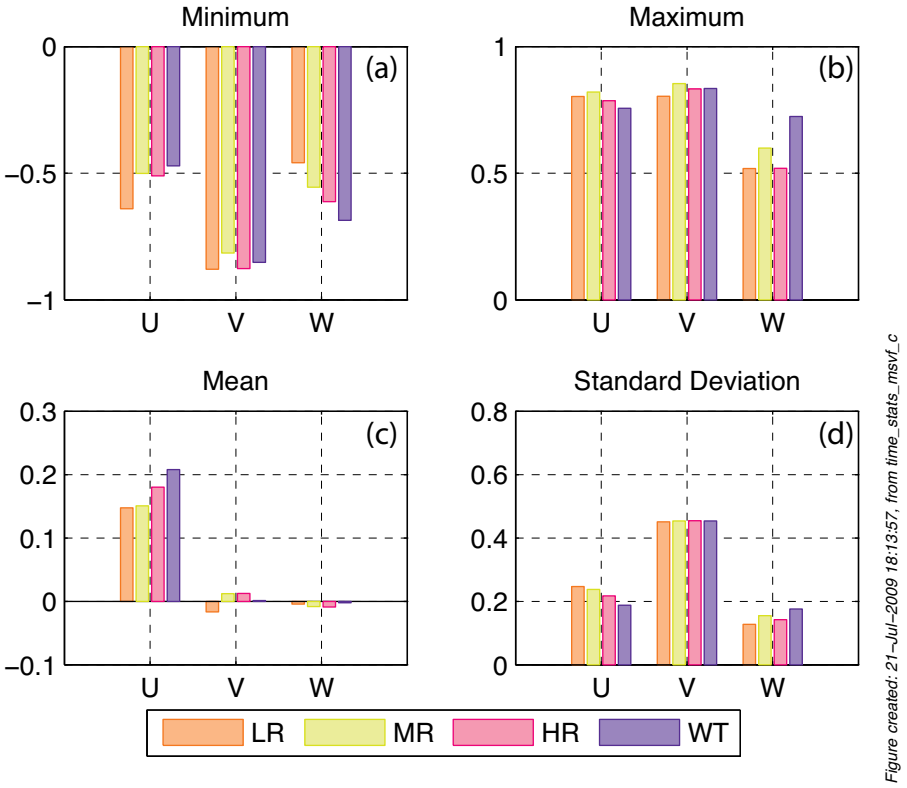


**Figure 6-6 – Minimum, maximum, mean and the standard deviation for the principle velocities from the point probe at (0.078, 0, 0)m, see Figure 6-1.**

With the exception of the mode, shown in Figure 6-7, the other four parameters are broadly consistent and show differences of less than 20% across the four simulations. However, because the mode is more indicative of a change in skewness of the distribution rather than a gross statistical variation, the discrepancy of the mode does not indicate a statistically significant difference in the time series data. Examination of the corresponding *u*-velocity skewness shows a large difference, for example from -0.5 to -0.3 or 40% relative to the LR grid, which supports the possibility of a skewed distribution. In contrast to the *u*-velocity results, the *w*-velocity mode variance is low compared with a correspondingly huge difference in the *w* skewness and as this result does not invalidate the previous explanation of the different modes, both results are statistically consistent.

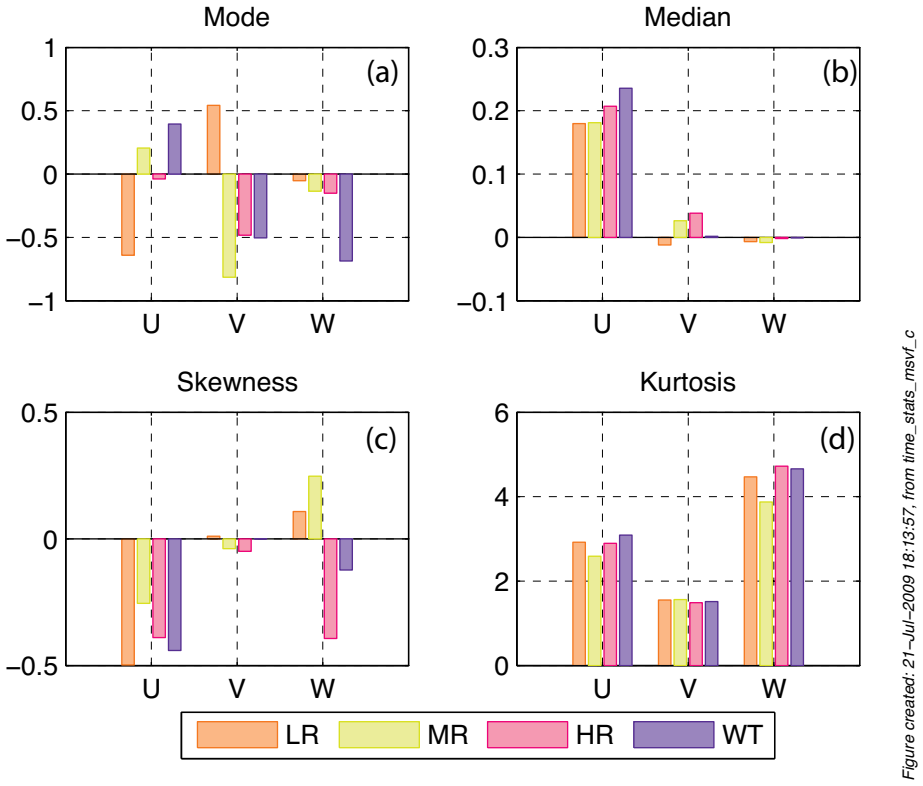


**Figure 6-7 – Mode, median, skewness and kurtosis for the principle velocities from the point probe at (0.078, 0, 0)m.**

### 6.2.4. Outcome of the Grid Convergence Study

The combination of the qualitative examination of the velocities as a function of time and the time domain statistics of the velocities has indicated that there is little difference between the results obtained from the three different resolution meshes. Therefore, the

results from the grids are converged, although, as discussed above, no precise confidence estimate is available for these results.

While the remainder of this chapter will be presented as if it were part of a validation study, and thus the results from the present simulations will be compared with published data, it is in fact more than a validation study. The comparisons can also serve as a more detailed grid convergence check than the brief grid convergence study performed in this section.

The data that was available, and was therefore used, for validation fell into three broad categories: time averaged velocity data; statistical spectral data and averaged integral parameters, such as the drag and lift coefficients. Therefore, the remainder of the chapter will be arranged to reflect these three broad classifications.

## *6.3. Spatial Domain Analysis of Time Averaged Data*

### 6.3.1. Motivation for Time Averaging

It is the opinion of the present author that the majority of the characteristics in bluff body flows, such as that discussed herein, are contained within the interactions that occur in simulation time and that most of this is lost when averages, be they spatial or temporal, are taken. However, it is also acknowledged that very few, if any, journals allow for the publication of the full colour flow visualisations that would be required to present arguments based on the time domain interactions. Hence, the necessity to reduce the time domain data to averaged values.

Although the time series data presented previously were discussed in the context of a grid convergence study, the same data, or more specifically, its time averaged values, are more relevant within a validation study. More specifically, because the majority of the published data sets detail time averaged quantities, the time domain data presented in §6.2 can be averaged for direct comparison. For example Lyn and Rodi (1994) and Lyn et al (1995) both presented their experimental data as time averaged values aligned in $z$=0 plane. However, the method of averaging the data, and in particular the computation of the fluctuating quantities could make a difference to the computed parameters.

### 6.3.2. Method to Compute the Online Averages

The averaged flow field results, in contrast to the point probe results, presented in this dissertation were not calculated as a post processing operation but rather directly within the solver as the run progressed. Further, the averages were computed using a three-stage process that was designed to, firstly, let the flow transition from the initial conditions into the fully developed regime. During the second stage, the averages were computed while the third stage calculated the fluctuating quantities based on second stage averages, shown diagrammatically in Figure 6-8.

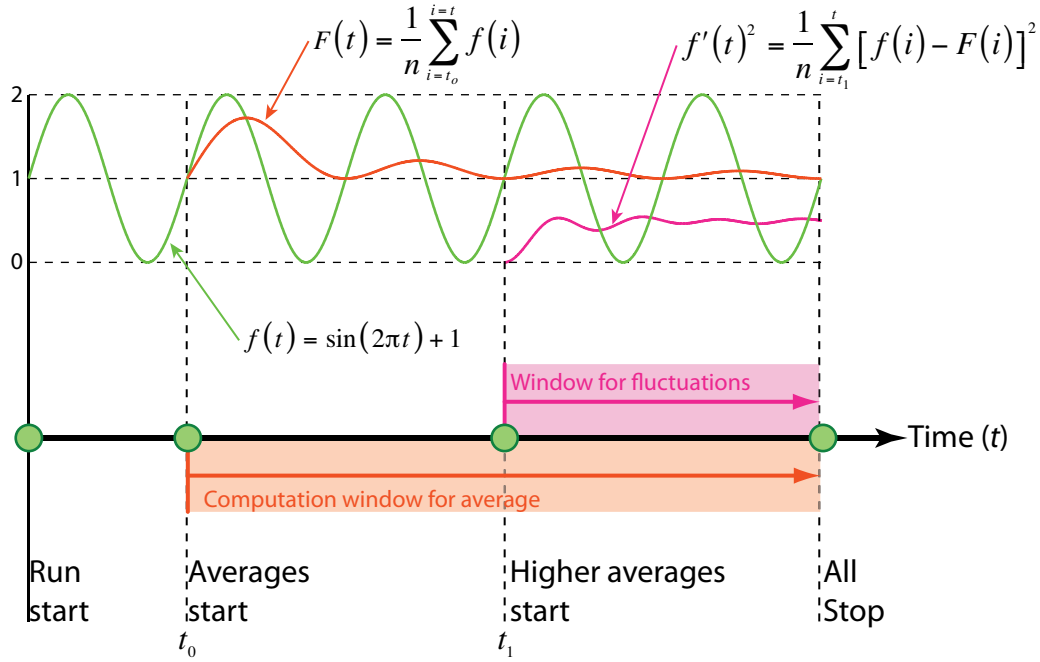


**Figure 6-8 – Diagram of the development of the averages and the three phases of online averaging.**

To illustrate this process, suppose that a general quantity, $f$, at a particular point within the domain is approximated as

$$f(t) = \sin(2\pi t) + 1. \tag{6.2}$$

As the simulation progressed and the flow developed into the shedding regime, $t_0$, the average* would be computed as

* The convention of the lower case, upper case and prime notations that represent the total, time average and the fluctuations, respectively, is in effect here and is fully detailed in §2.6.

$$F(t)=\begin{cases} 0 & \text{for } t<t_0 \\ \dfrac{1}{t-t_0}\displaystyle\int_{t_0}^{t} f(t)\,dt & \text{for } t \geq t_o \end{cases} . \tag{6.3}$$

Finally, when the averages had sufficiently stabilised, at $t = t_1$, the mean squared fluctuations,

$$\overline{f'(t)^2}=\begin{cases} 0 & \text{for } t < t_1 \\ \dfrac{1}{t-t_1}\displaystyle\int_{t_1}^{t} \left(f(t)-F(t)\right)^2 dt & \text{for } t \geq t1 \end{cases} , \tag{6.4}$$

can be computed. The source code for the Fortran 95 routine developed to compute this online average is included in Appendix D.

However, a close inspection of Figure 6-8 illustrates the limitation of this, and in fact any, average in that the final value of the average is dependent on the size of the window over which the averages were computed. Therefore, a method, or methods, is required to test the quality of the averages.

### 6.3.3. Methods to Test the Quality of the Average Statistics

Three approaches were developed that were based on the assumption that the average flow was symmetrical about the $y = 0$ plane. The first method was a visual technique that examined the visualisation of an averaged quantity displayed on a plane with a normal vector of $\mathbf{n} = [0,0,\pm 1]$. Clearly there are an infinite number of distinct planes with this normal vector; therefore, for the work described herein the $z = 0$ plane was used. To apply a more rigorous basis instead of a quick, visual examination of the averaged field, the second and third methods were based on data collected from the point probes. These data were available in real time while the simulation was being computed and, hence, were the primary indicators of the quality of the averaged statistics.

With the second method Equations (6.3) and (6.4) were evaluated using the simulation data, an example of which is shown in Figure 6-9. These results were evaluated for their consistency: for example if the average was less than five percent different from

half a second previously. Therefore, if the averages are stable, then the computation of the fluctuations can begin or if the fluctuations are stable then the simulation can stop.

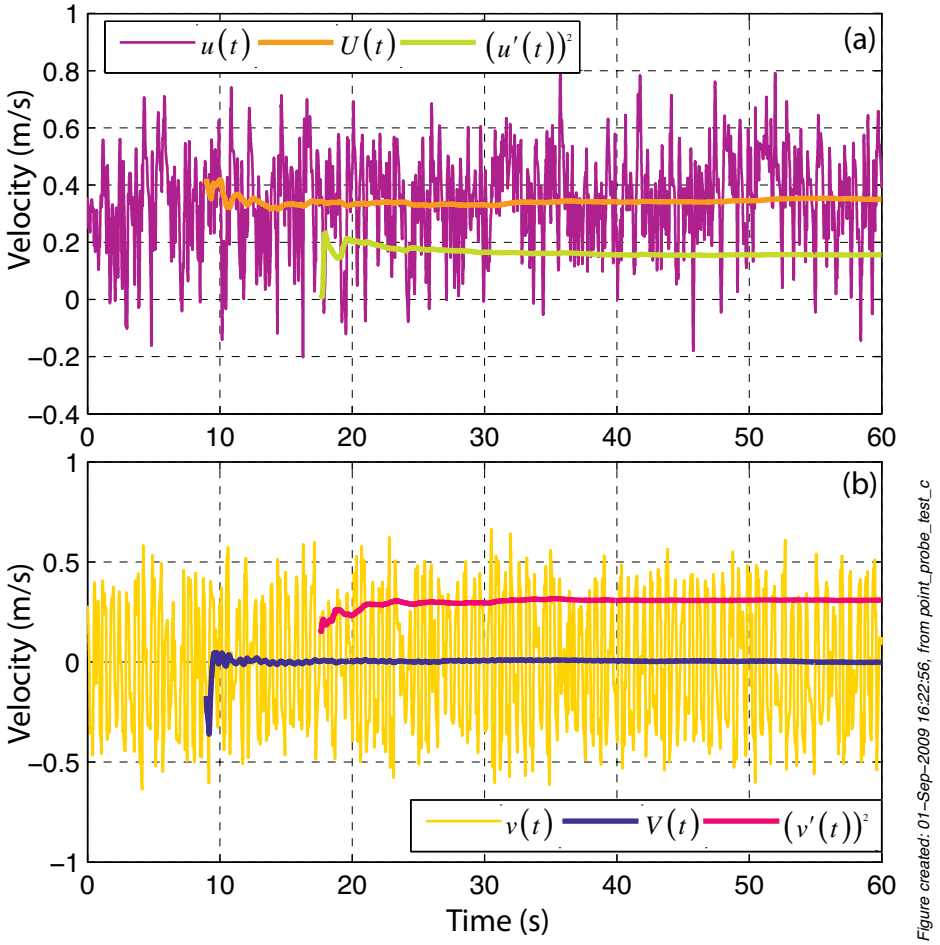


**Figure 6-9 – Example of the development of the averages and fluctuating statistics as a function of time.**

The third method, however, can be considered as a formalisation of the first, visual check. In this case suppose that we are interested in the *u*-velocities at points on the $z = 0$ plane and further consider that for every point above the $y = 0$ plane there is a corresponding mirror point below the plane, referred to as upper and lower, respectively. Next, the average velocities measured at the upper and lower points can be plotted as the abscissa and ordinate, respectively. Finally, for a perfectly symmetrical average, all the upper and lower pairs would have symmetrical velocities and would be coincident with the line defined by the coefficients

$$\begin{aligned} a &= 1 \\ b &= -1 \\ c &= 0 \end{aligned} \tag{6.5}$$

of a general two-dimensional line

$$ax_{lower} + bx_{upper} + c = 0\,. \tag{6.6}$$

Therefore, the perpendicular distance of the coordinates from this line can be used as a measure of the inaccuracy of the average. That is, the general form of the two-dimensional distance of a point a line is (Weisstein, 2008)

$$\mathfrak{D} = \frac{\left|ax_{lower} + bx_{upper} + c\right|}{\sqrt{a^2 + b^2}}, \tag{6.7}$$

then with our line Equation (6.7) becomes

$$\mathfrak{D} = \frac{\left|x_{lower} - x_{upper}\right|}{\sqrt{2}}, \tag{6.8}$$

which is shown in

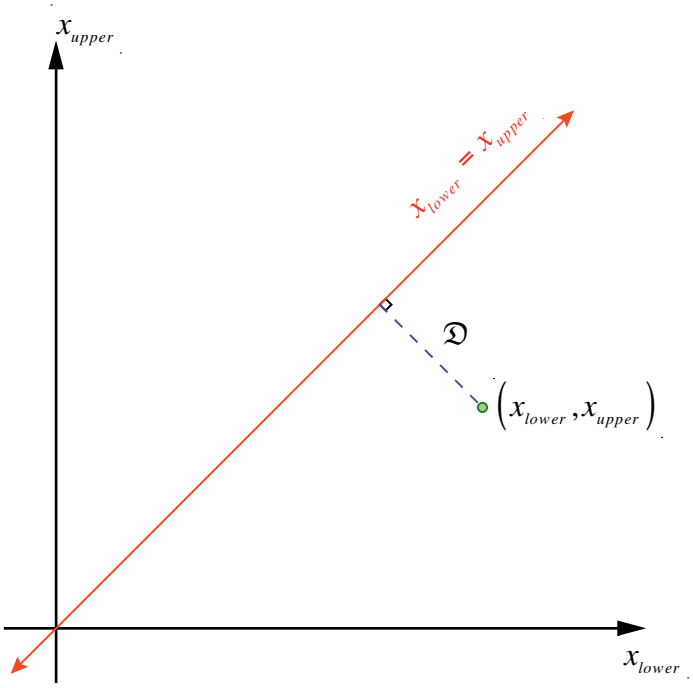


**Figure 6-10 – Definition sketch of the line and the perpendicular distance.**

### 6.3.4. Quality of the Averages from the Present Work

The length of the three stages of averaging for the four simulations described in the present work is detailed in Table 6-1. Because both the length of the averages and the location in simulations where the averages were computed was different in all four simulations, the quality of the averages must be critically examined.

**Table 6-1 – Details of the averaging stages from the present work.**

| Model | Length of Phase 1 (s) | Length of Phase 2 (s) | Length of Phase 3 (s) |
|---|---|---|---|
| Low Resolution | 11.731 | 9.388 | 29.809 |
| Medium Resolution | 8.974 | 8.659 | 42.367 |
| High Resolution | 30.001 | 6.994 | 7.005 |
| Water Tunnel | 10.797 | 5.189 | 24.016 |

As discussed in §6.3.3 the first method used to test the quality of the averages, which was defined as the level of symmetry around the $y = 0$ plane, was a visual examination of the average velocity field. For the present simulations, the time averages have converged, as shown in Figure 6-11 and Figure 6-12, because the flow field appears to be symmetrical.

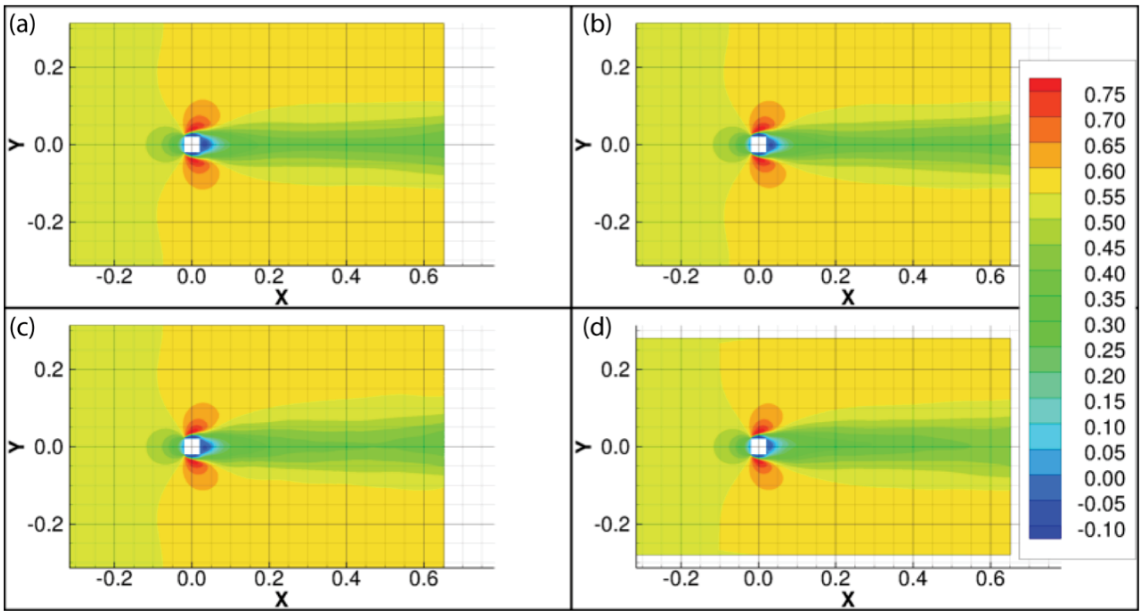


**Figure 6-11 – Visualisation of the time averaged *u*-velocity on the *z*=0 plane for the LR, MR, HR and WT simulations, subplot (a) – (d) respectively.**

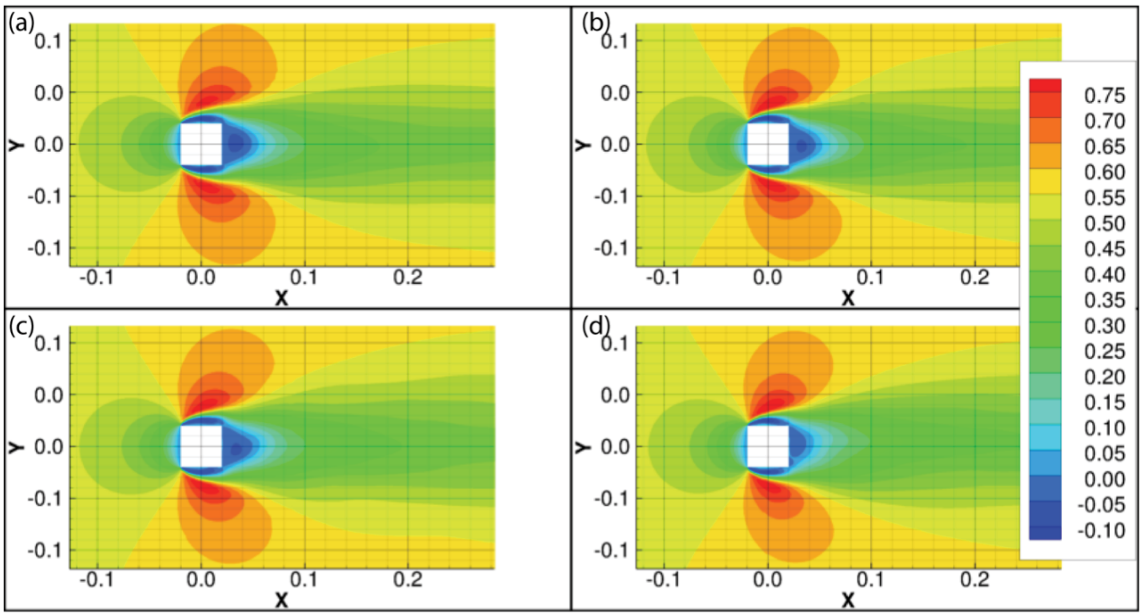


**Figure 6-12 – Magnification of the near cylinder regions of Figure 6-11.**

It should be noted that while there are differences in the structure of the time averaged flow fields between the simulations, these differences can be examined once the quality of the time-averages has been established. To continue with the second quality check, point probes four and eight, shown in Figure 6-13, were selected for detailed analysis.

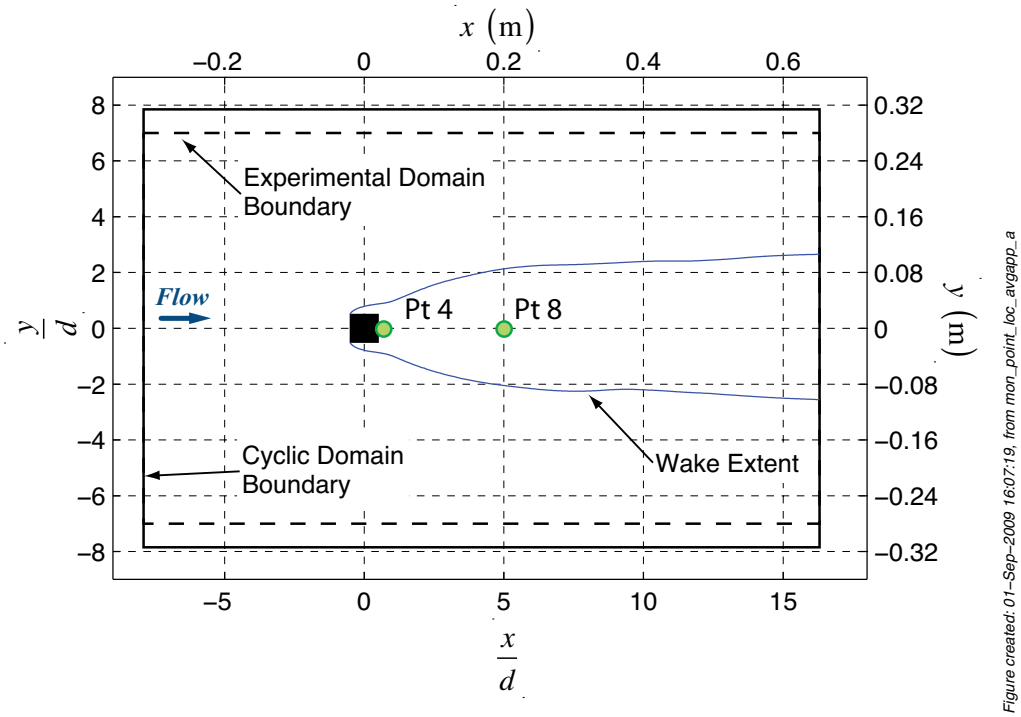


**Figure 6-13 – Sketch of the location of point probes four and eight relative to the domain boundaries and the indicative wake extent.**

Of these, the two extremities of the averages occurred in the low-resolution simulation with the longest averaging window and the high-resolution simulation with the shortest averaging window. Hence, with a longer window the data from the LR simulation should be the best to test the stability of the averages as a function of time.

Both the average and the fluctuations computed from point four of the LR simulation stabilised to within five percent of the their final values in less than five seconds of the average starting, as shown in Figure 6-14. However, the value of the fluctuating components is more unstable and is more dependent on the changes in the flow field, and hence the changes in the average, than the average itself. For example with the $v$-components at point four, shown in Figure 6-14(b) the average remains constant at approximately zero over the time interval of $t \geq 20$ s whereas the fluctuations respond to a change in the flow between $35 \leq t \leq 38$ s by dropping from 0.4 m/s to 0.35 m/s.

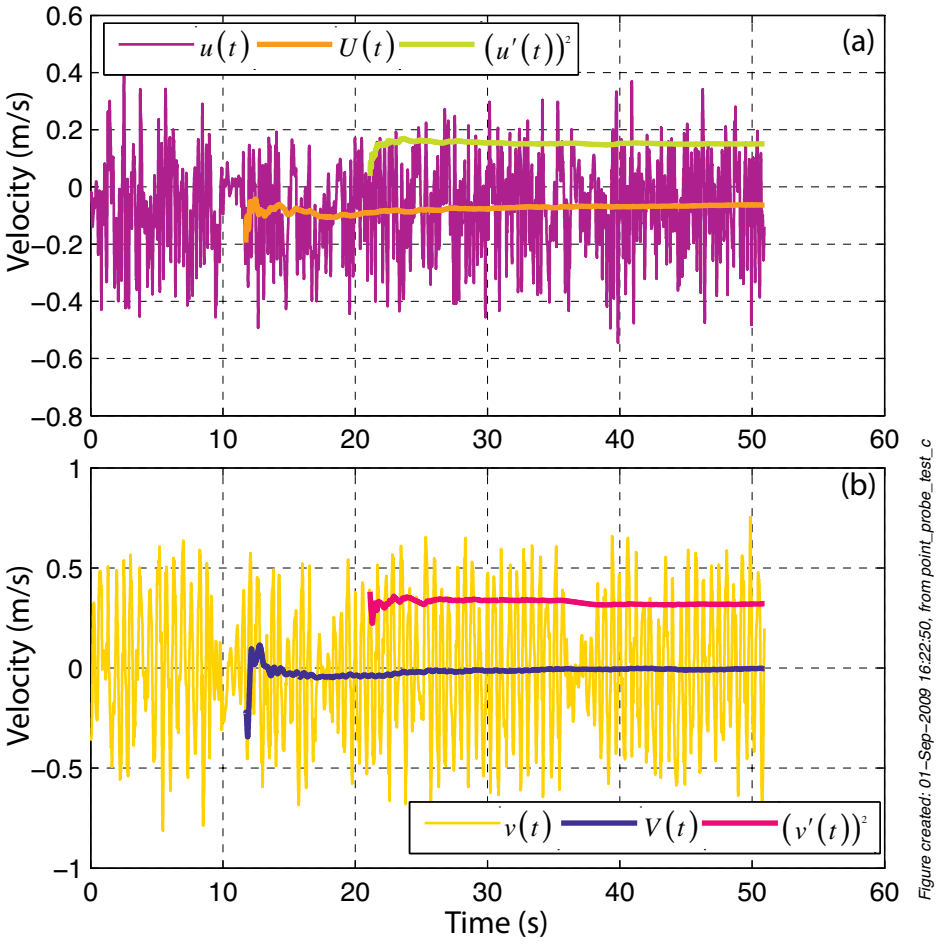


**Figure 6-14 – The development of the averages and mean squared fluctuations as a function of time for the LR simulation at point probe four.**

These results indicated that a minimum of five seconds is needed to stabilise the averages for these flows to better than five percent accuracy. Therefore, all the windows used in the present work for the water tunnel simulation, as detailed in Table 6-1, met this requirement.

The results from the high-resolution simulation support the conclusion that the averaging window must be at least five seconds long because the results also stabilise to within five precent within five seconds, as shown in Figure 6-15. Intriguingly, the *v*-velocity trace in Figure 6-15 appears to be transitioning in the several seconds before the simulation was terminated. It would have been interesting to continue the simulation and examine both the potentially alternate flow regime and the corresponding effect on the averages computed.

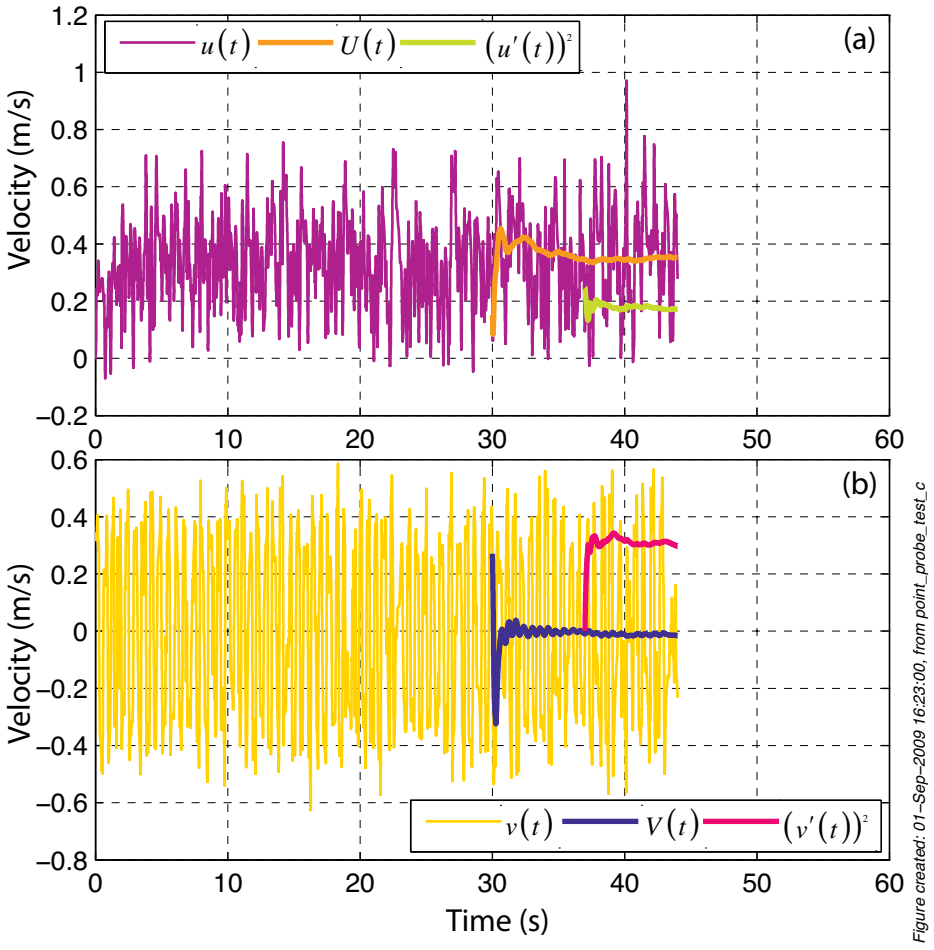


**Figure 6-15 – The development of the averages and mean squared fluctuations as a function of time for the HR simulation at point probe eight.**

As both the initial visual check and an examination of the point probe data has showed that the averages are converged, the final check was to perform the scatter analysis and examine the distribution of the distance from symmetry. From a visual inspection of the scatter plots, almost all of the points fall within 0.02 m/s of the symmetry line, as shown in Figure 6-16 for the medium-resolution simulation*, or to better than four percent error.

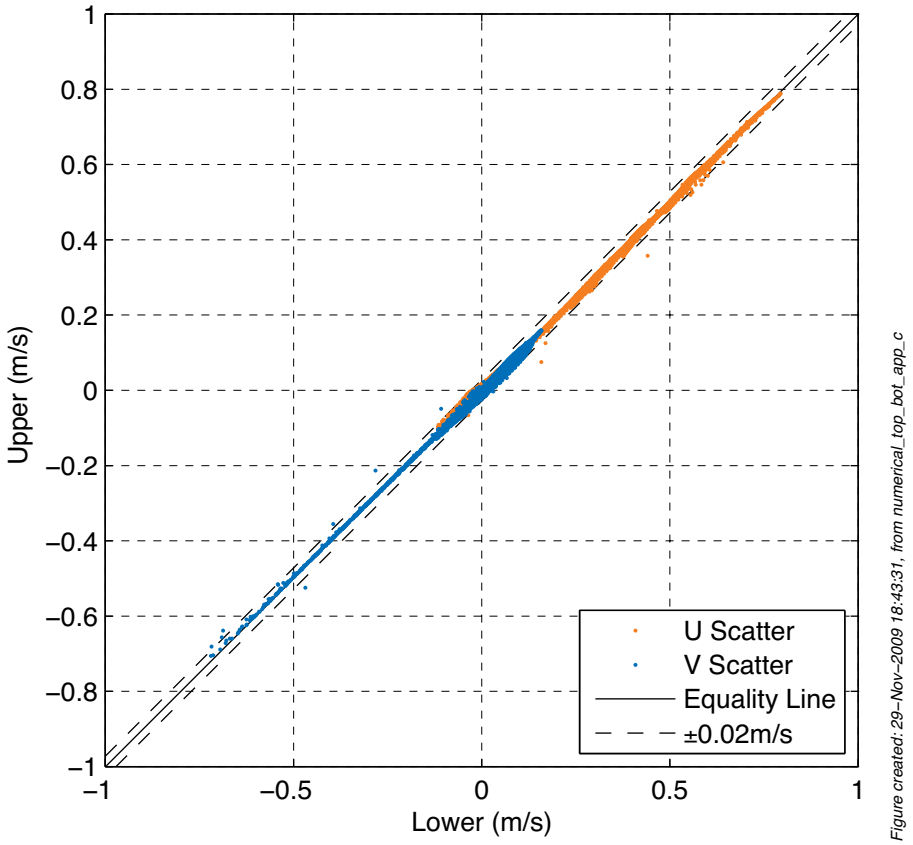


**Figure 6-16 – Scatter plot of the upper and lower points for the time averaged *u*- and *v*-velocities from the medium-resolution simulation.**

To quantify the results of the visual inspection of the scatter plot, the distance of the scatter points from symmetry, the $\mathfrak{D}$ parameter, can be examined with a plot of the histogram, as shown in Figure 6-17. For all four simulations, more than 55% of the points fall within 0.002 m/s, or $0.3\% \times U_{\infty}$, of symmetry. Because of the shorter length of the windows used to compute the high-resolution averages, there is a broader

* Only the scatter plot of the medium resolution simulation data is shown because the scatter plots from the three other simulations are, essentially, indistinguishable from each other. Hence, a single plot is enough to convey the thrust of the argument.

distribution of $\mathfrak{D}$, in particular for the *v*-velocities. Therefore, it is expected that the spread of the results from the high-resolution simulation would reduce if the data were averaged for longer.

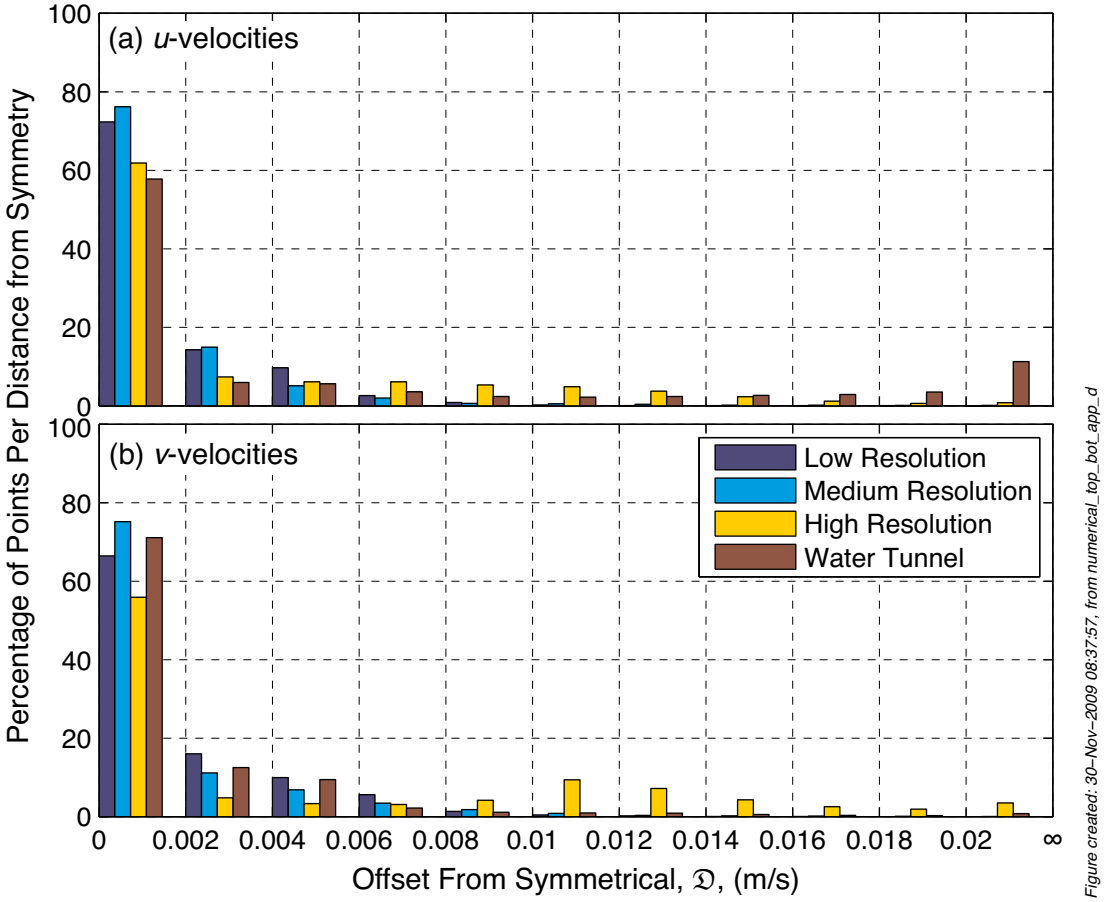


**Figure 6-17 – Histogram of $\mathfrak{D}$ for the *u*- and *v*-velocities from the four simulations.**

Intriguingly five percent of the points for the average *u*-velocities from the water tunnel simulation are at $\mathfrak{D} \geq 0.02$ m/s, which was unexpected given the length of the computation windows used. However, given that nearly 90% of the points are within $\mathfrak{D} \leq 0.01$ m/s this large outlier will be considered as an anomaly and not subjected to further analysis.

Therefore, as the three methods envisaged as checks of the quality of the averages all returned results that indicated high quality averages, the results from the present simulations can be compared with published experimental and numerical data. Further, as the grid comparison study discussed in §6.2 indicated that there was relatively little difference between the results from all four simulations, the future examinations can focus on the medium resolution spanwise periodic and water tunnel simulations.

### 6.3.5. Comparison with Averaged Experimental Data

The experimental data published by Lyn and Rodi (1994) and Lyn *et al* (1995) is based on Laser Doppler Anemometry data measured at approximately 500 points on the upper half of a $z = 0$ plane in a water tunnel. Further periods of up to one hour or "in terms of shedding cycles [a count of] $O\left(10^4\right)$" (Lyn and Rodi, 1994) were used to compute the averages. To compare the experimental and numerical data a similar approach to the scatter plots that were introduced above can be used. Whereas the previous method plotted upper and lower halves of a plane, the current approach can plot the experimental and numerical data instead, as shown in Figure 6-18.

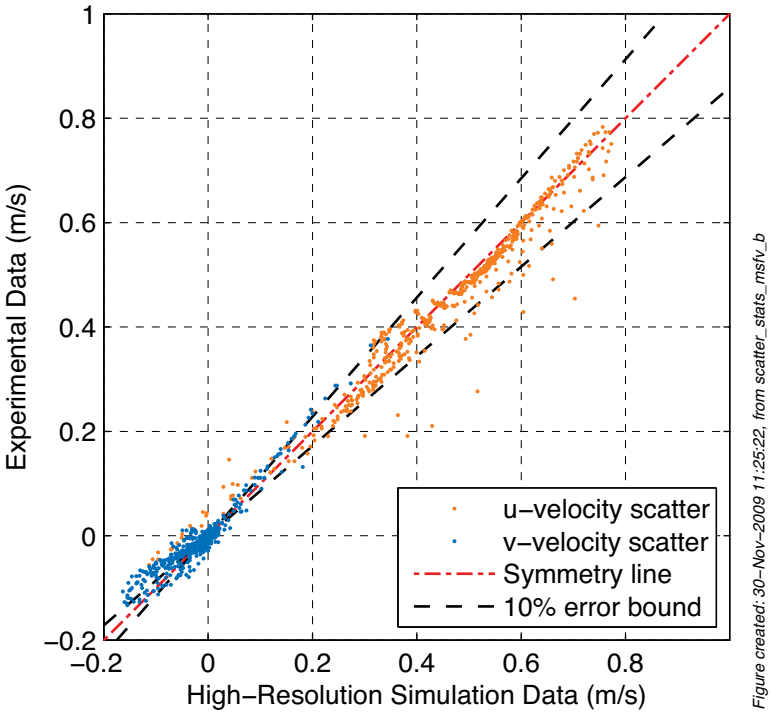


**Figure 6-18 – Point-by-point comparison of the high resolution simulation data from the present work with the experimental data of Lyn and Rodi (1994).**

As would be expected from the results discussed above, the *u* and *v*-velocity scatter plots from both the medium-resolution and water tunnel simulations, are similar when compared with the same experimental data, as shown in Figure 6-18 for the high-resolution and in Figure 6-19 for the water tunnel simulations respectively. For both simulations, the *u*-velocities consistently fall towards the numerical side of symmetry, which indicates that the simulation velocities are underestimated relative to the laboratory. In contrast to this result, the *v*-velocities are skewed towards the experimental data, which lead to the opposite conclusion: that the solver systematically

overestimated the *v*-velocities. Crucially, then, the question becomes: is this degree of scatter acceptable as a part of a validation study? An inspection of the scatter patterns alone cannot provide enough detail to answer that question, whereas the distribution of $\mathfrak{D}$ can provide an indication of the quality, and hence acceptability, of the simulations.

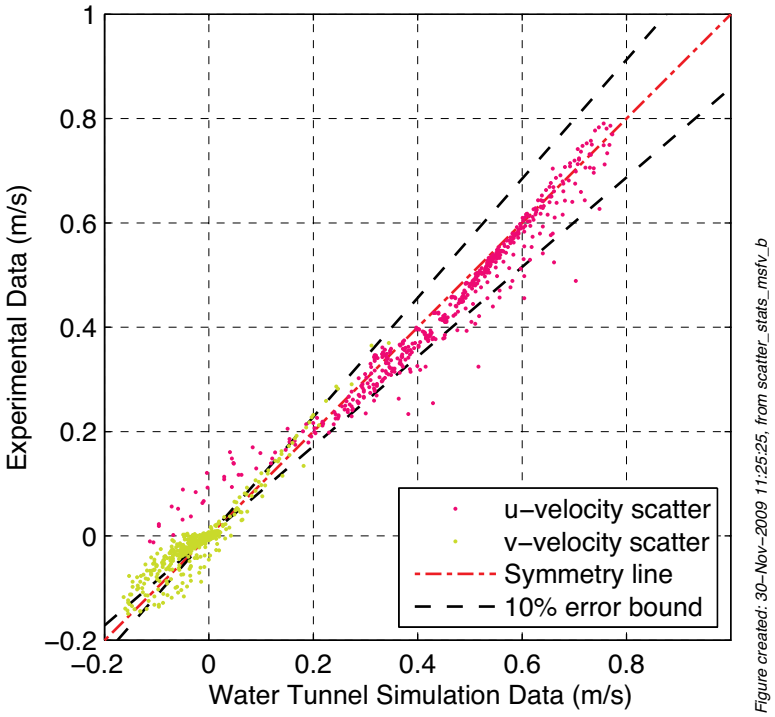


**Figure 6-19 – Point-by-point comparison of the water tunnel simulation data from the present work with the experimental data of Lyn and Rodi (1994).**

To aid an examination of the scatter suppose that Equation (6.8) were redefined as

$$\mathfrak{D} = \frac{\left| x_{sim} - x_{exp} \right|}{\sqrt{2}} \frac{1}{x_{sim}} \tag{6.9}$$

to express $\mathfrak{D}$ as a distance relative to the numerical point, which can then be interpreted as a percentage error. For example, the ten percent error bounds are shown in Figure 6-18 and Figure 6-19. Then, with the *u*-velocities over 90% of $\mathfrak{D}$ fall within the 10% error bound, as shown in Figure 6-20. Despite the good agreement of the *u*-velocity scatter, the *v*-velocity scatter is significantly higher with over 50% of $\mathfrak{D}$ greater than 10% and 25% greater than 100%. These *v* scatter are somewhat overestimated due to the low magnitude of simulation velocities that significantly magnify a very small absolute error.

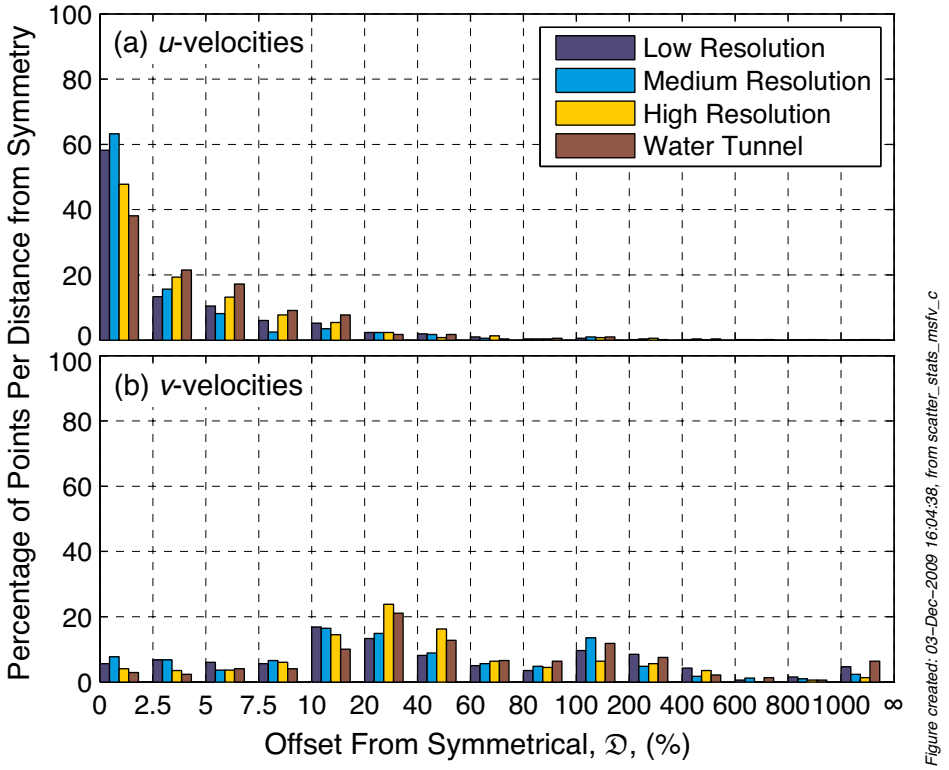


**Figure 6-20 – Histogram of $\mathfrak{D}$ as a function of the percentage error defined in Equation (6.9).**

The results from the comparison with the experimental data of Lyn and Rodi (1994) indicate that the *u*- and *v*-velocities, with a caveat related to the magnitude of the *v*-velocities, compare well. There is, however, a limitation to this approach in that there are two inherent errors in the experimental data: (1) the precision of the measurement of the boundary conditions and (2) the precision of the position of the LDA measurement window. Therefore, the simulations, to within the limits of the experimental uncertainty, are validated.

In contrast to experimental data, numerical data is, in some aspects, superior because the researcher has total control over all parameters in the study. Therefore, the intrinsic inaccuracies with experimental procedures can be overcome by comparing the present results with those obtained from similar numerical simulations.

### 6.3.6. Comparison with Averaged Numerical Data

Despite the volume of publications concerned with numerical simulation of the right square cylinder at $\mathrm{Re}_d = 22 \times 10^3$, the most comprehensive collection is that compiled by Voke (1996). Somewhat surprisingly, although not demonstrated within this

dissertation, the spread of numerical results has not decreased over the years since the publication of the DLES2 results. Therefore, the combined results from the DLES2 test case remain an appropriate data set for comparison with the present simulations. Voke (1996) selected eight results for detailed comparison and discussion yet acknowledged that one of the data sets had not been averaged for a sufficient window for the higher order statistics to have converged sufficiently, hence they have not been included in the comparisons with the present work. The time-averaged velocity statistics were compared along four lines within the $z = 0$ plane, shown in Figure 6-21, which coincided with the laboratory sampling plane and locations of Lyn and Rodi (1994).

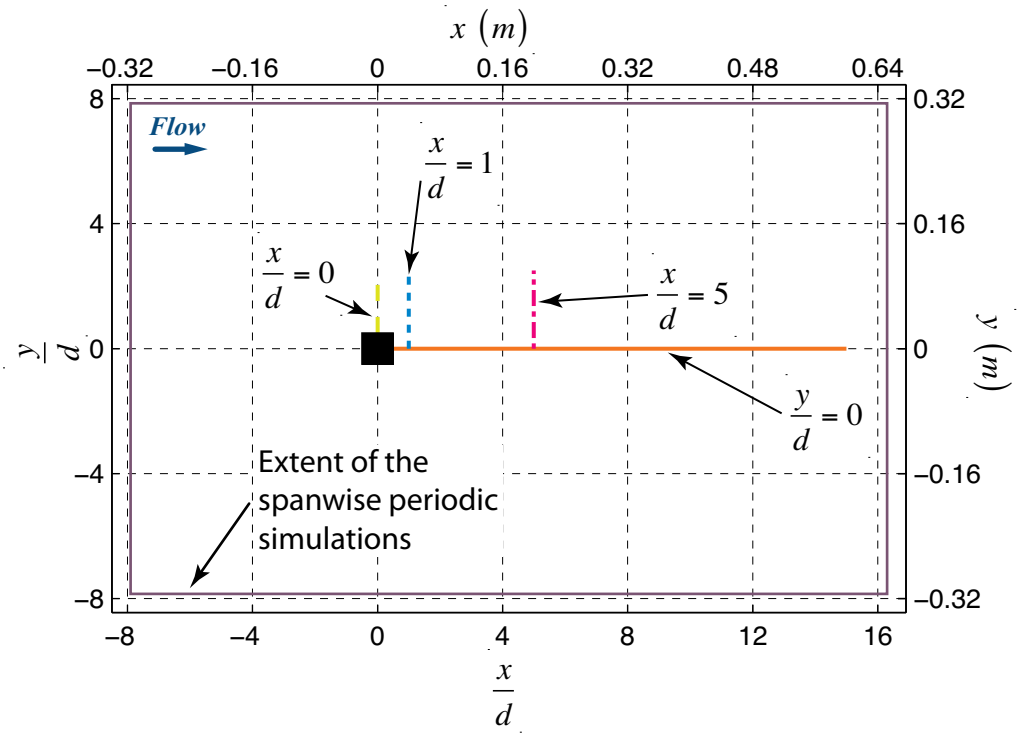


**Figure 6-21 – Location of the four comparison lines within the $z = 0$ plane used at the DLES2 conference described by Voke (1996).**

The *U*-velocities* from the four present simulations followed the general trend of the reference works, as shown in Figure 6-22 and in higher detail for the region close to the cylinder in Figure 6-23, and were consistent with each other. That is, from an initial velocity of zero at the downstream face of the cylinder, the *U*-velocities decrease to a

* The reader is reminded of the convention, introduced in §2.6, for labelling the time averaged, instantaneous and fluctuating velocities with capital letters, lower case letters and lower case letters with a prime, respectively. An over bar also indicates a time average quantity.

minimum at $x \cong 0.75d$ m before increasing to become positive near $x \cong 1.25d$ m. As $x$ was further increased, the time averaged velocity recovered to $U \cong 0.75U_\infty$ m/s for $x \geq 7d$ m.

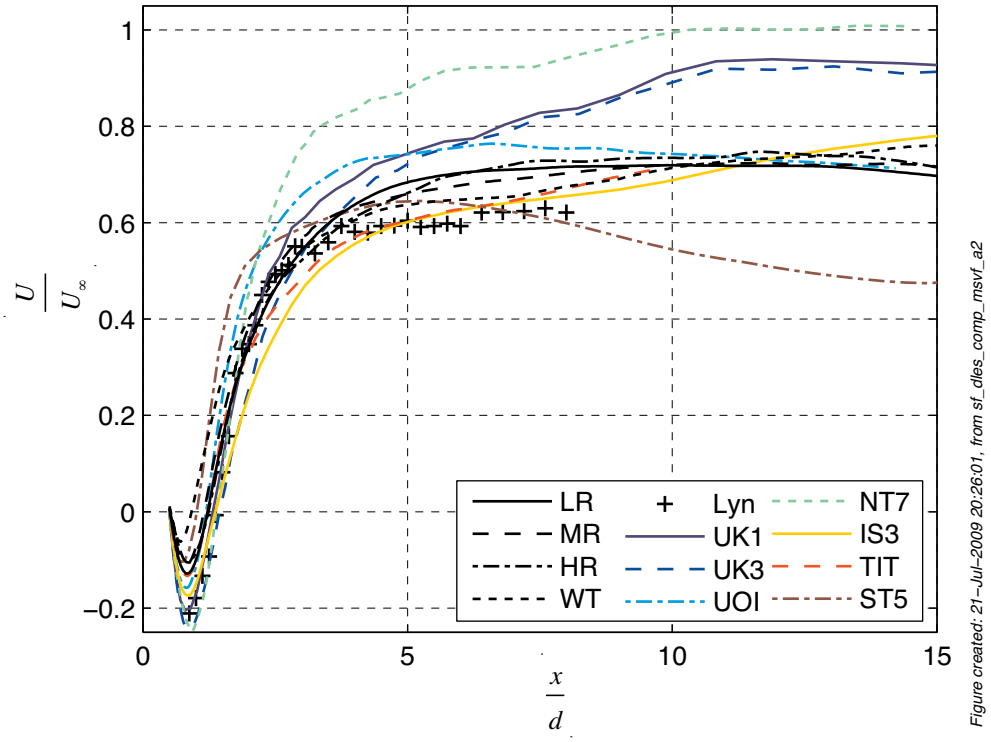


**Figure 6-22 – *U*-velocity plot along the y=0, z=0 line of the present results compared with results from the DLES2 workshop (Voke, 1996) and the experimental data of Lyn and Rodi (1994).**

In the region $x \geq 7d$ m the results from the present simulations are within the centre of the numerical data but are faster than the experimental results of Lyn and Rodi (1994). However, in the gradient region, over approximately

$$1.5 \leq \frac{x}{d} \leq 4, \tag{6.10}$$

where the *U*-velocities increase from small negative to large positive the present results are a good match to the experimental data. The recirculation zone, roughly $x \leq 1.5d$ m, adjacent to the downstream face of the cylinder from the water tunnel simulation is both shorter than the spanwise periodic simulations, 0.4m and 0.7m respectively, and with higher negative velocity, -0.03m/s and -0.1m/s, respectively. Further, all four simulations underestimated the length of the recirculation zone, $l_r$, defined as the

distance from the rear of the cylinder at which the *U*-velocity recovers from negative to positive.

The reason for the contrast of the under estimation of the negative velocities close to the cylinder and the corresponding over estimation further from the cylinder is unclear but the two are most likely intimately linked. A possibility is that the model is overlay dissipative, which would explain the near cylinder results. However, this conjecture does not support the higher velocity that was simulated further downstream because an overly dissipative model would be expected to also reduce the far field velocity.

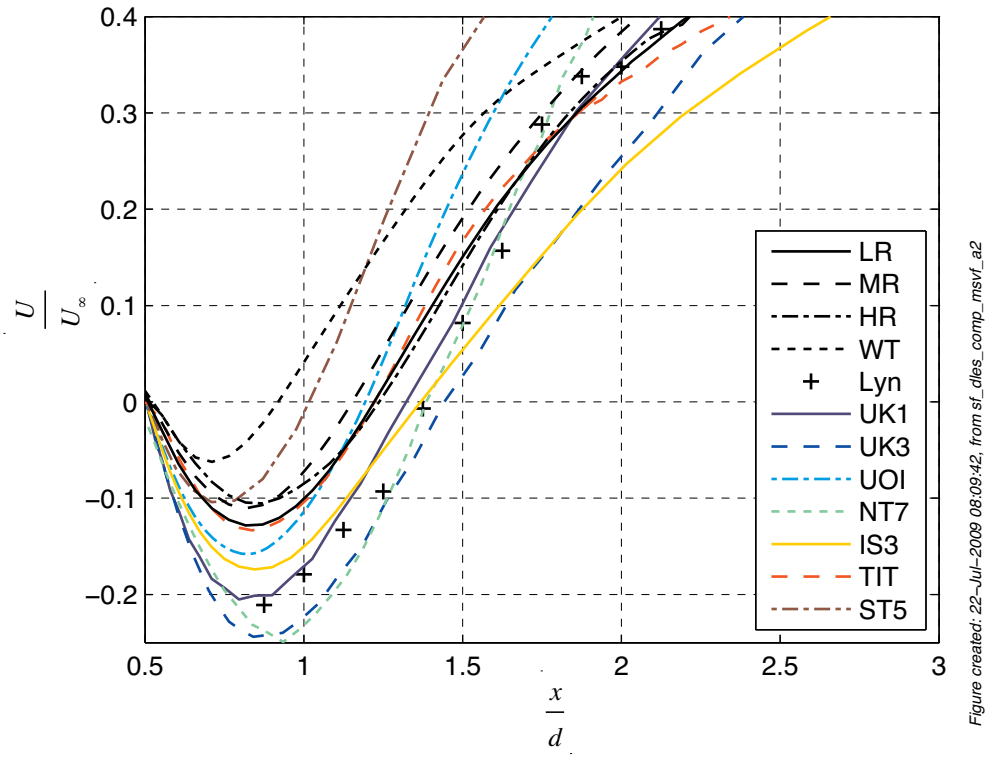


**Figure 6-23 – Magnification of the *U*-velocities in near cylinder region of Figure 6-22.**

Alternatively, the constant pressure outlet boundary may have been too close to the cylinder that could have forced the increase in the downstream velocity to overcome the applied pressure. This increased velocity closer to the outlet may have then propagated upstream and caused both the more positive recirculation velocity and shorter recirculation length. However, the preliminary studies, which are summarised in §5.2 and presented in detail in Appendix C, indicate that for this length to the outlet there should be no effect on the flow field at these distances from the cylinder. Nevertheless, as the preliminary studies were performed in two-dimensions their applicability to the

three-dimensional results is questionable. Therefore, a test of the length to the outlet boundary should be undertaken in three-dimensions but this was not computationally feasible.

The interpretation of the water tunnel results is complicated, as noted above, by the lower length of time for the averages, hence the incorrect recirculation zone results may be due solely to the lower window available for the computation of the average. While the *U*-velocity* results are generally encouraging, a major argument for using large eddy simulation instead of Reynolds-averaged models is in the computation of the fluctuating quantities.

When the $\overline{v'v'}$ fluctuations from the present simulations are compared with themselves along the $y = 0$ line, the results are remarkably consistent in the region of $x \geq 2d$ m, as shown in Figure 6-24. In contrast, over the range of $x \leq 2d$ m, the $\overline{v'v'}$ fluctuations

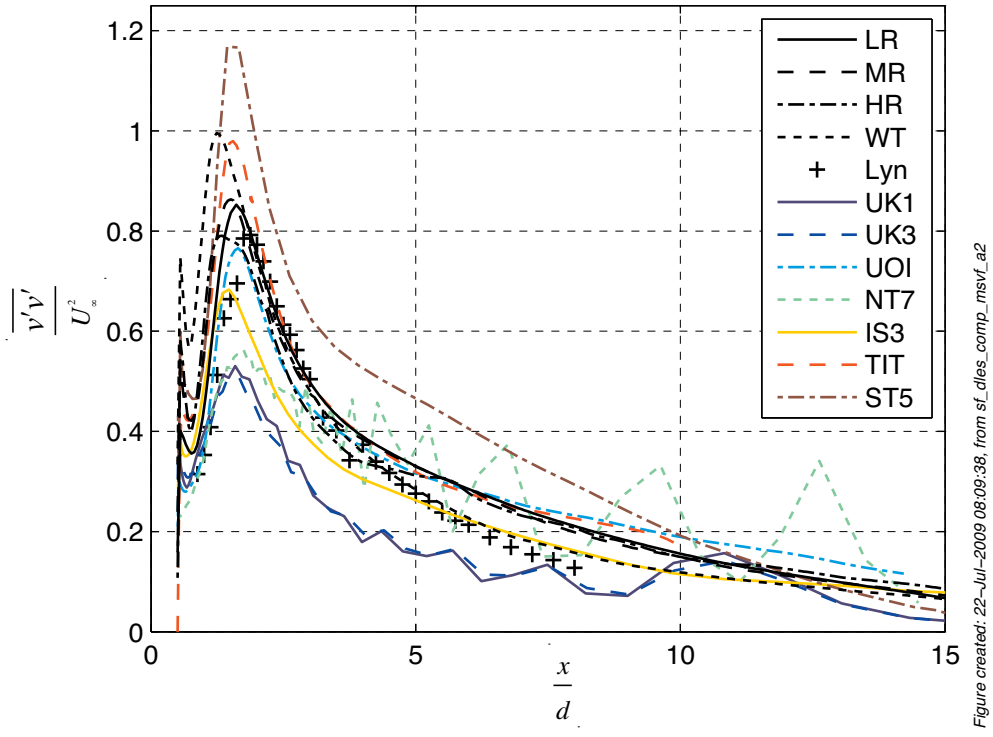


**Figure 6-24 – Centreline plot of the time average of the *v'v'* fluctuations.**

* Neither the *V* nor *W*-velocities were compared because the experiments of Lyn and Rodi (1994) only measured the *U*-velocity.

from the three spanwise periodic models are also consistent with each other, whereas the fluctuations from the water tunnel simulation are much higher than the equivalent spanwise periodic simulations. This is due to the shorter length of the averaging window used for the water tunnel simulations.

Close to the downstream face of the cylinder, over approximately

$$0.5 \le \frac{x}{d} \le 1.7\,, \tag{6.11}$$

the magnitudes of the $\overline{v'v'}$ fluctuations from the present simulations are both higher than the experimental results of Lyn and Rodi and the majority of the numerical data, as shown in Figure 6-25. Sufficient experimental data was not captured in

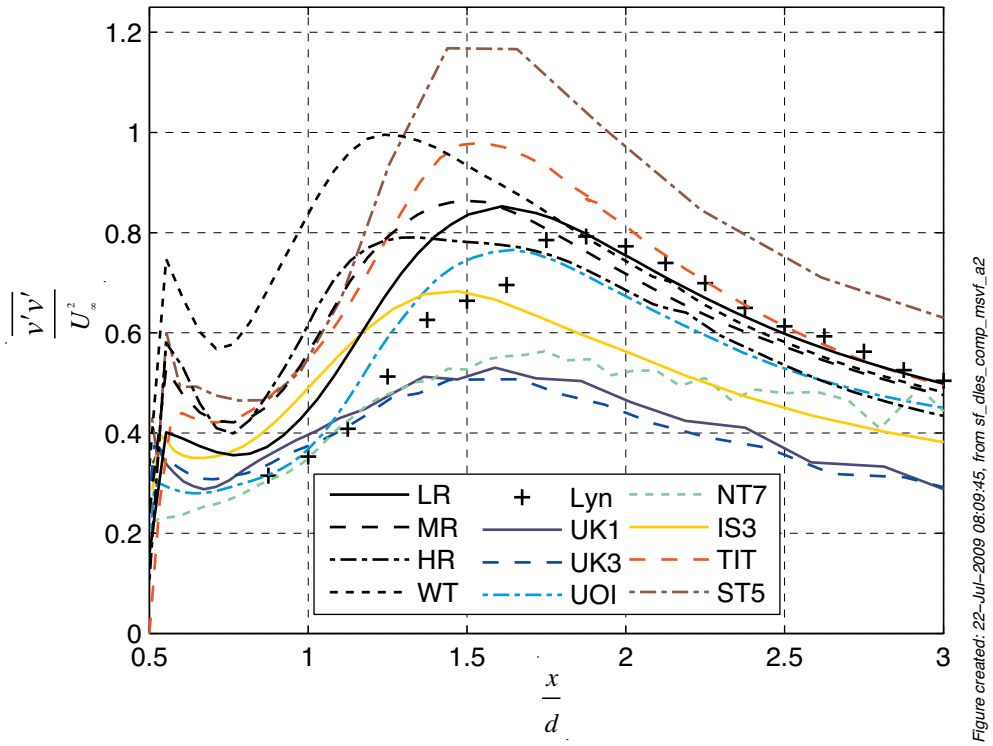


**Figure 6-25 – Zoom of the near cylinder results plotted in Figure 6-24.**

the very near wake region so that neither the shape nor the trends of the numerical data could be compared. However, over the region of

$$1.9 \le \frac{x}{d} \le 4 \tag{6.12}$$

the $\overline{v'v'}$ fluctuations are an excellent match with the experimental data and fall within the spread of the numerical data. At downstream distances greater than those of Equation (6.12) the $\overline{v'v'}$ fluctuations are consistently higher than the experimental data of Lyn and Rodi but towards the centre of the numerical data. The inconsistency of the $\overline{v'v'}$ results is, as with the *U*-velocities, puzzling as no single theory posited by the present author could explain the mix of overestimation close to the cylinder and towards the outlet combined with the excellent agreement between these two zones.

In contrast to the $\overline{v'v'}$ fluctuations, the $\overline{u'u'}$ fluctuations are within the spread of the numerical data yet consistently larger than the experimental results, as shown in Figure 6-26. Nevertheless, the general profile of the curves is consistent with a large peak near

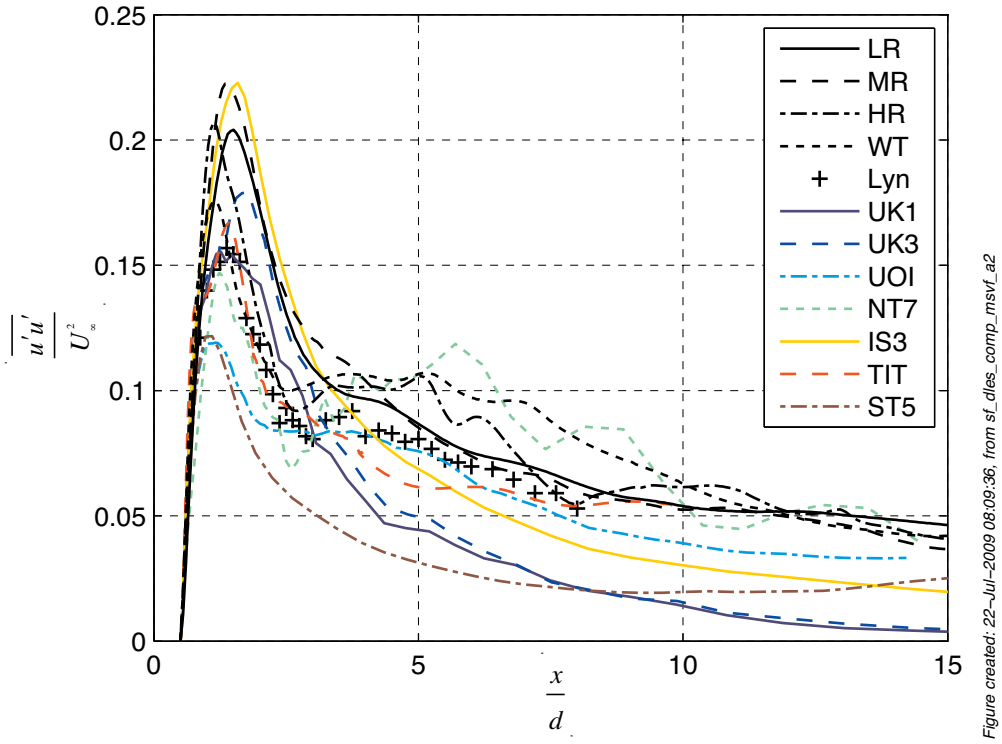


**Figure 6-26 – Centreline plot of the time average of the $u'u'$ fluctuations.**

$x \cong 1d$ m that quickly drops before a striking discontinuity at $x \cong 3d$ m. After the discontinuity the value of the $\overline{u'u'}$ fluctuations steadily decrease with the results from the present simulations close to those from the laboratory experiments.

The $\overline{w'w'}$ fluctuations from the present work are broadly consistent with the published numerical data as shown in Figure 6-27. That is, all the models have a peak

immediately adjacent to the cylinder, followed by a trough and a gradual rise and fall as $x$ is increased. The near wake trough and following peak in $\overline{w'w'}$ does not appear to be related to the location of the recirculation zone. As Lyn and Rodi (Lyn and Rodi, 1994) used a two-component LDA that was configured to measure the $u$- and $v$-velocities there is no experimental data for comparison.

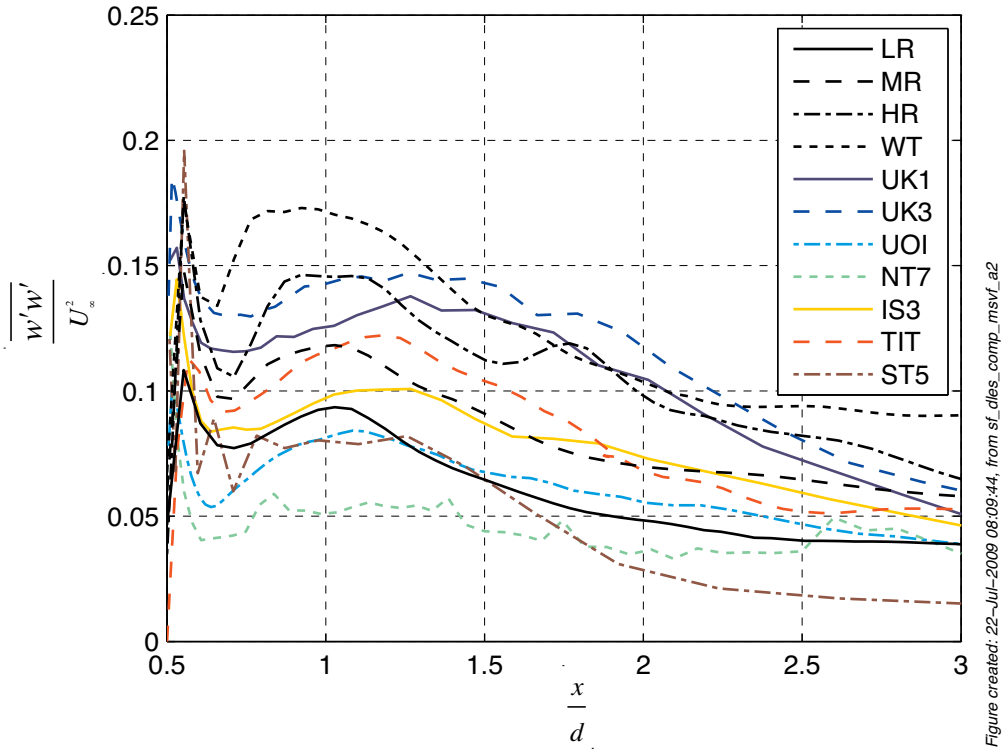


**Figure 6-27 – Centreline plot of the time average of the $w'w'$ fluctuations.**

In addition to the time averaged $u$-velocity and fluctuating components that were measured along the $y = 0$, $z = 0$ line, discussed above, measurements were also taken along three constant $x$ lines in the $z = 0$ plane at $x = 0$ m, $x = d$ m and $x = 5d$ m, as shown in Figure 6-21. Of the measurements taken by the experimenters (Lyn and Rodi, 1994) four were to be compiled for comparison at the DLES2 conference (Voke, 1996), namely:

1. The time averaged $u$-velocity, $U$, as shown in Figure 6-28;
2. The time averaged, squared $u$-velocity fluctuations, $\overline{u'u'}$, as shown in Figure 6-29;
3. The time averaged, squared v-velocity fluctuations, $\overline{v'v'}$, as shown in Figure 6-30, and;

4. The time averaged, squared w-velocity fluctuations, $\overline{u'v'}$, as shown in Figure 6-31.

When all 12 comparison plots (that is four parameters at three locations) were subjected to a visual analysis, it was noticed that the plots at common $x$ locations could be differentiated into two regions. The first region was characterised by recirculating flows and was located closer to the cylinder and the $y = 0$ plane while the second zone was associated with more uniform flows reminiscent of a deformed and accelerated free stream. Not surprisingly, the free stream zone was located further away from both the cylinder and the $y = 0$ plane. Within the recirculating zone, the values of all four parameters varied, sometimes significantly. In contrast, but with the notable exception of the NT7 simulation, the parameter values in the free stream zone were very similar between all the numerical and experimental results. The transition between the recirculating and free stream region occurred over the range $d \le y \le 1.25d$ m for both the $x = 0$ m and the $x = 1d$ m lines. While the transition for the $x = 5d$ m line was more difficult to define it was estimated to occur over the range $2d \le y \le 2.5d$ m. These two boundaries, which were estimated from the plots in Figure 6-28 to Figure 6-31, are in good agreement with the time-averaged extent of the wake discussed in §6.2.2 and shown in Figure 6-1.

As the flow in the free stream region is predominantly uniform, but perhaps turbulent, it is relatively "simple" to compute, hence the majority of the numerical experiments, including the present work, correctly simulated the averages and fluctuations in this region. In contrast, the recirculation/wake region is subjected to both turbulent fluctuations and the large-scale velocity variations that are associated with a von Kármán vortex street. This increased complexity is computationally "harder" to simulate, which explains the differences between the numerical simulations.

The time averaged $u$-velocity $(U)$ plots, shown in Figure 6-28, for the $x = 1d$ m and the $x = 5d$ m are unremarkable in that the results from the present simulations are consistent with the majority of the comparison simulations and the experimental values. However, for the region close to the cylinder on the $x = 0$ line there is a striking difference with a second recirculation zone computed in all of the present simulations

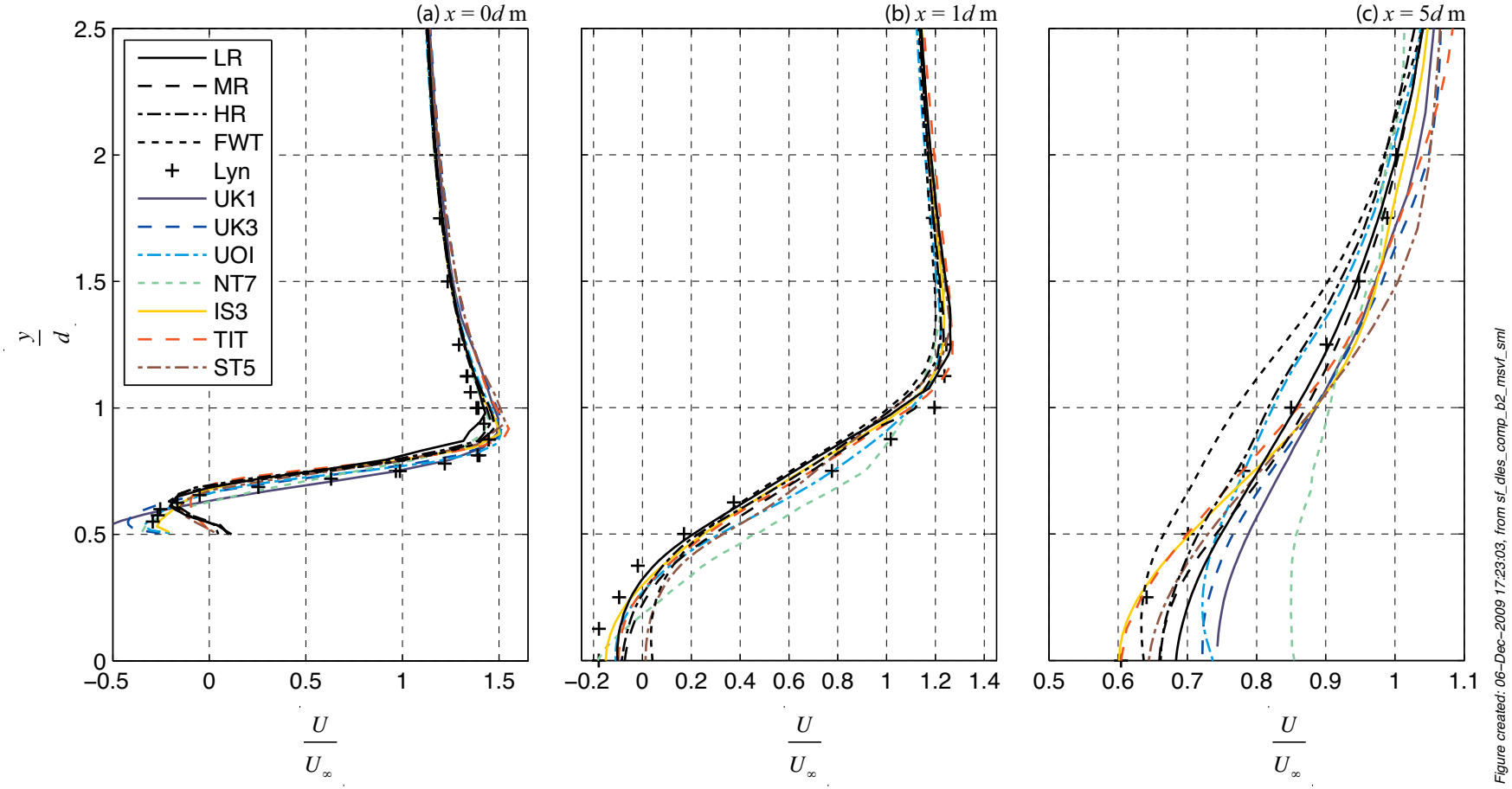


**Figure 6-28 – Time average *u*-velocities from the present simulations, the experimental data of Lyn and Rodi (1994) and the compiled results of Voke (1996) along constant *x* lines in the *z* = 0 plane.**

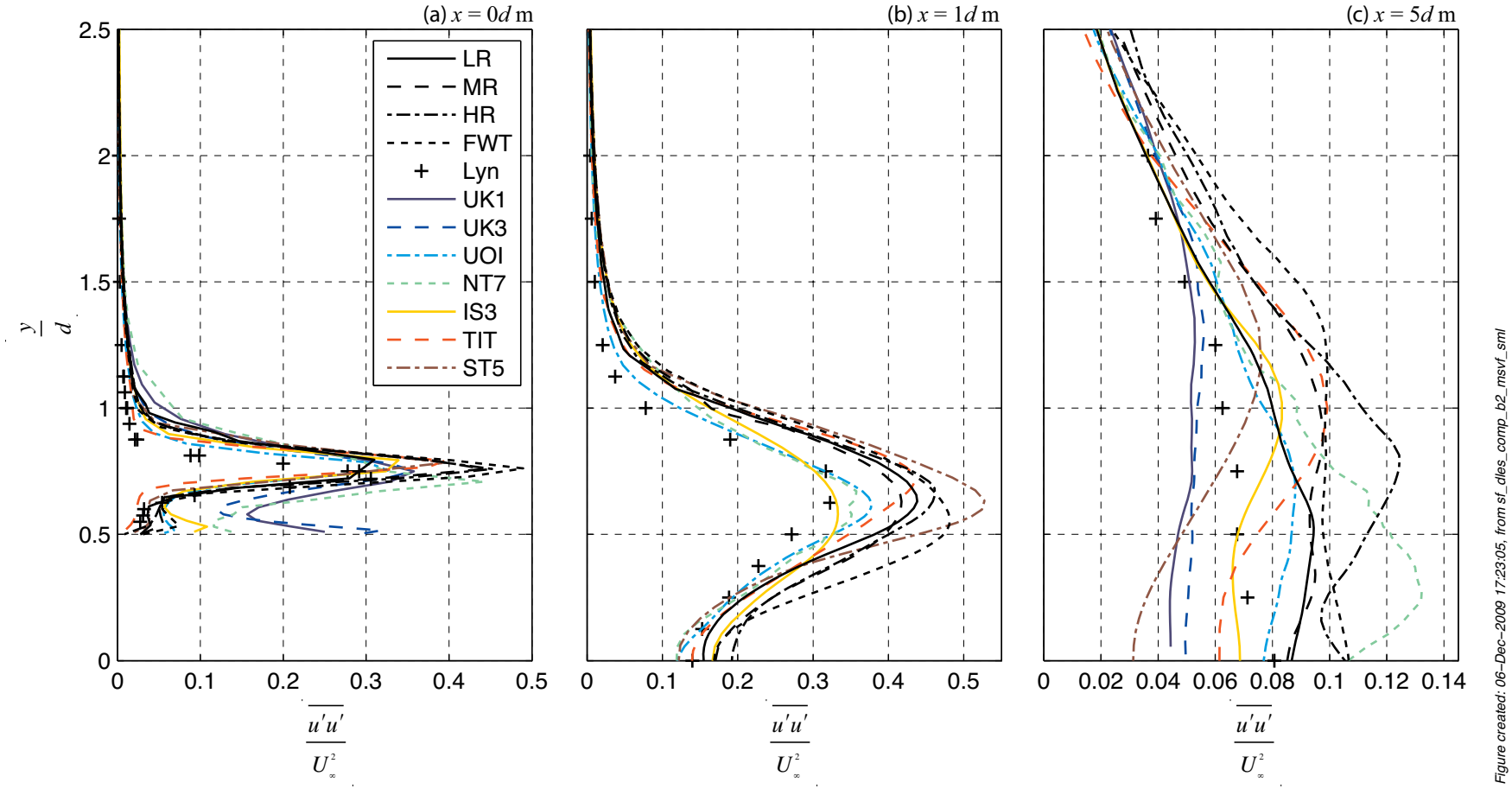


**Figure 6-29 – Time average *u'u'* fluctuations from the present simulations, the experimental data of Lyn and Rodi (1994) and the compiled results of Voke (1996) along constant *x* lines in the *z* = 0 plane.**

and two of the DLES2 simulations. In contrast, the remaining DLES2 simulations and the experimental data of Lyn and Rodi (1994) do not show the second recirculation zone. Voke (1996) does not discuss the near cylinder differences merely noting that the "agreement for $U$ is adequate". Alternatively, the experimental data close to the wall may be erroneous as the experimenters were forced to use specialist LDA apparatus to measure close to the wall (Lyn and Rodi, 1994, Lyn et al., 1995) and the values measured with LDA can be affected in regions close to the wall (Durst et al., 1995, Stoots et al., 2001). The remaining simulations from the literature provide no further clarification as they also show similar variation with respect to the recirculation region. Therefore, this inner recirculation zone will remain an anomaly subject to further research.

Interestingly, and in stark contrast to the values of $U$, the $\overline{u'u'}$ fluctuations from the present simulations over the line $x = 0$ are in remarkably good agreement with three of the DLES2 simulations and the experimental data. In addition, the simulations whose results were good approximations of $U$, were simultaneously in poor agreement with the experimental values of the $\overline{u'u'}$ fluctuations. Voke (1996) noted, when discussing these results that "…no simulation shows a clear advantage in all the quantities [examined]", which is supported by the disparity between the values of $U$ and the $\overline{u'u'}$ fluctuations from the present work. For $\overline{u'u'}$ fluctuations over the $x = 1d$ m line all the simulations have the same general shape as the experimental data but again, no single simulation, including the present work, correctly capture all aspects of the $\overline{u'u'}$ curve as a function of $y$. By the $x = 5d$ m line, despite an order of magnitude reduction in the magnitude of the, for $y < 1.5d$ m no simulation is in good agreement with the experimental data. It could however be argued that, by this distance downstream combined with the fluctuations being in the order of eight percent of the free stream velocity, these differences are negligible.

The results for both the $\overline{v'v'}$ and $\overline{u'v'}$ fluctuations are consistent with the $U$ and $\overline{u'u'}$ fluctuations in that no single simulation accurately captures all the features of the curves at all of the three locations investigated. Again, the results from the present simulations are within the spread of the DLES2 data and are a good agreement, subject to the caveat of experimental uncertainty, with the experimental data.

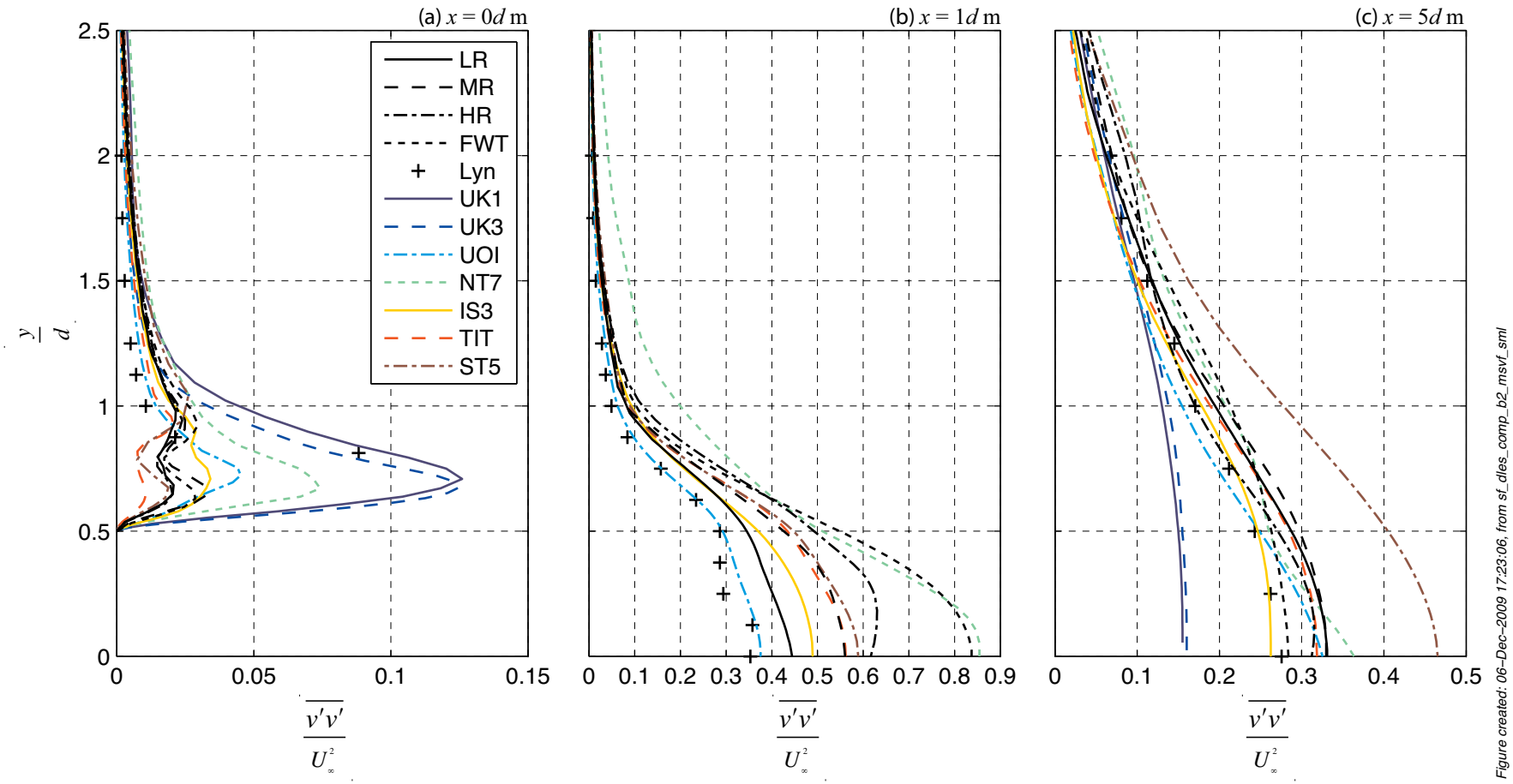


**Figure 6-30 – Time average *v'v'* fluctuations from the present simulations, the experimental data of Lyn and Rodi (1994) and the compiled results of Voke (1996) along constant *x* lines in the *z* = 0 plane.**

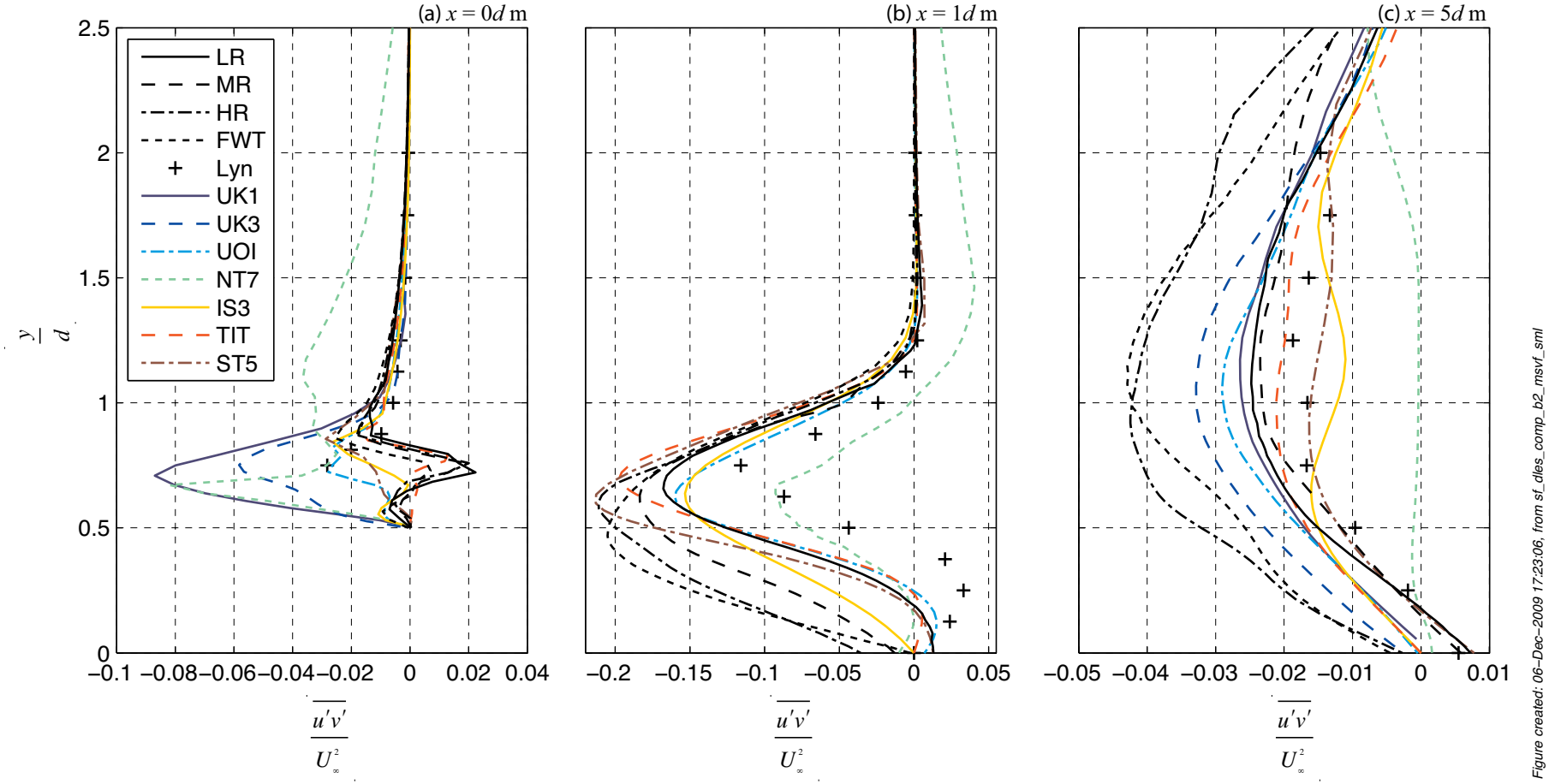


**Figure 6-31 – Time average *u'v'* fluctuations from the present simulations, the experimental data of Lyn and Rodi (1994) and the compiled results of Voke (1996) along constant *x* lines in the *z* = 0 plane.**

Therefore, of the one average and the three fluctuations examined despite some minor differences the results from the present simulations are in generally good agreement with DLES2 simulations and the experimental data of Lyn and Rodi (1994). Indeed an additional recirculation zone was identified on the top face of the cylinder, which was in contrast with several of the DLES2 simulations yet supported a further group of simulations. This feature was not observed in the experimental results but this may be due to experimental limitations rather than the recirculation being unreal. Further work will be required to resolve this dilemma. However, the results from the present simulations are in good agreement and the spectral quantities can be examined.

## *6.4. Spectral Analysis of Turbulence Statistics*

### 6.4.1. Introduction

Statistical spectral analysis allows for the transformation of time domain data into the frequency domain and is a valuable method of calculating the shedding frequency and various microscale lengths that are useful in describing turbulence. Values of the quantities obtained from the present work can then be used both for a comparison with published results and for checking the consistency of the models across different grid sizes. Of the many parameters it is possible to evaluate in the frequency domain, only three will be discussed in detail in this section:

1. Dominant frequency: although the dominant frequency, often normalised to the Strouhal number (*Sr*), is an important validation parameter, the results from a number of studies indicate that the dominant frequency is somewhat independent of the turbulence model (Voke, 1996, Rodi, 1997, Rodi et al., 1997, Sohankar et al., 1999).
2. Slope of the power spectral density (PSD) plot at high frequencies: this is an important validation of the models as there is a strong history of experimental data (Lumley and Yaglom, 2001, Yaglom, 2001) and theoretical work, e.g. Kolmogorov (1941), that predict what the shape of the PSD plot should be.
3. Turbulent length scales as related to the grid scales: it is important to evaluate the Kolmogorov lengths as they define the smallest scales of motion that direct numerical simulations must approximate. As the present simulations were

targeted as LES scales the mesh sizes used were envisaged to be an order of magnitude larger than the Kolmogorov lengths.

### 6.4.2. Specific Method of Computation

The first step to computing the frequency domain representations of the present data was to evaluate the peak-to-peak frequency of the *v*-velocity data by hand, which was approximately 1.67 Hz. Next, the frequency resolution for the Fourier transform was arbitrarily assumed to be one tenth of this frequency, or $\Delta f = 0.167$ Hz/sample. Further, the sampling frequency, $f_s$, was fixed at 1 kHz, which is the inverse of the time step size used for all four simulations. Therefore, as the window length, *n*, is related to the sampling frequency and frequency resolution by

$$\Delta f = \frac{f_s}{n}, \tag{6.13}$$

the nominal window length for the specified frequency resolution was 5988 points. However, the implementation of the digital Fourier transform within MATLAB is optimised for windows whose length is equal to a power of two (Mathworks, 2002), therefore the window length was increased to 8192, or $2^{13}$, with a resultant increase in the frequency resolution 0.122 Hz/sample. Further, with a window length of $2^{13}$ the approximate error in the frequency spectrum due the digital Fourier transform process alone was $\pm 0.06$ Hz/sample, which is plus or minus half the limit of measurement.

As the power spectral density is a statistical quantity it must be averaged over a number of realisations (Orfanidis, 1996). Therefore, 100 realisations of the power spectral density were calculated using a rectangular window $2^{13}$ samples long with the periodogram spectral estimation method in the Signal Processing Toolbox of MATLAB 2008a (The Mathworks, 2008) and were averaged. The windows were evenly distributed over the range

$$5 \le t \le 40 \text{ s}. \tag{6.14}$$

### 6.4.3. Power Spectra and Dominant Frequencies

All the power spectral densities as a function of frequency were computed from the *v*-velocities at eight points located along the wake centreline, i.e. the line $y = 0$, $z = 0$ for $x \ge 0.5d$ m. The plots were characterised by a plateau at frequencies below 3 Hz; a

distinct peak at approximately 1.6 Hz and a tail that decayed for frequencies above 3 Hz, as is shown in Figure 6-32 for the point $(0.078,0,0)$ m [*].

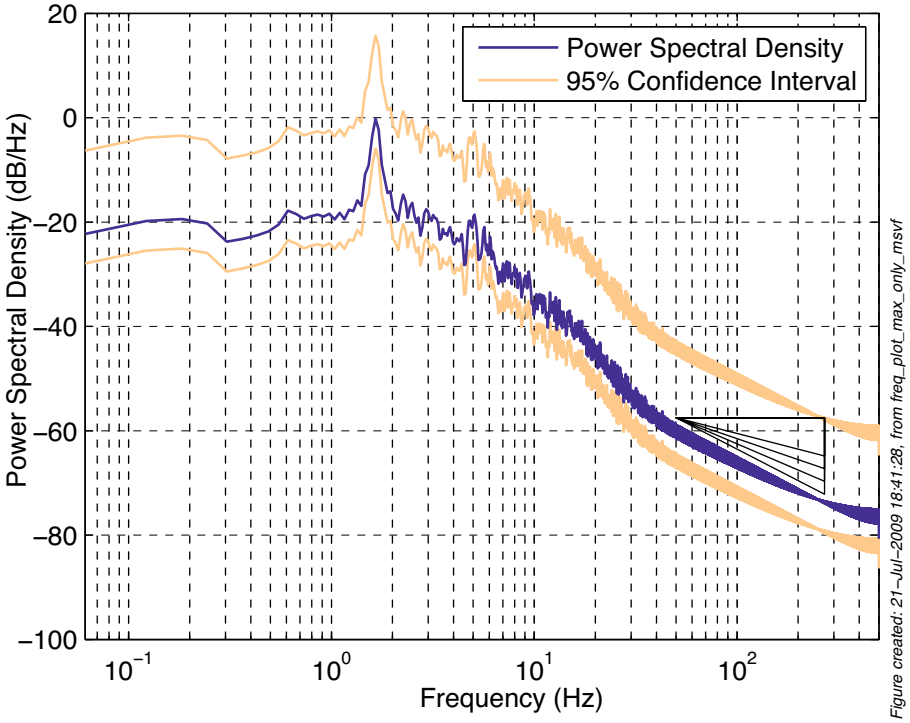


**Figure 6-32 – Power spectral density of the *v*-velocity for a point on the wake centreline at *x*=0.078 m from the high-resolution simulation.**

Intriguingly, at approximately 5 Hz a second smaller, less defined but distinct peak was observed to rise out of the decay slope. The present author is not aware of any discussion of the second peak and further investigation will be required to firstly confirm the veracity of the result but also the cause, specifically whether the peak is a harmonic of the dominant shedding or is due to an alternate unknown cause.

The peak shedding frequency, that is the frequency at which the tallest peak occurs, computed from the PSD calculations was 1.77Hz, 1.59Hz, 1.65Hz and 1.65Hz for the low, medium and high-resolution and the water tunnel simulations respectively. When converted to the non-dimensional Strouhal number defined as

$$Sr = \frac{d \times f}{U_\infty} \tag{6.15}$$

[*] More examples are not shown because the difference in the plots is sufficiently small that the presentation of additional plots would not add to the quality of the argument.

the results become: 0.132, 0.119, 0.123 and 0.120 with an error of ±0.004, respectively. These results from the present simulations are exceptionally close to the published numerical results that range from 0.066 to 0.161 but are clustered around 0.130, for example the numerical simulations of Sohankar et al. (1999) and the experimental results of Lyn and Rodi (1994) of 0.132.

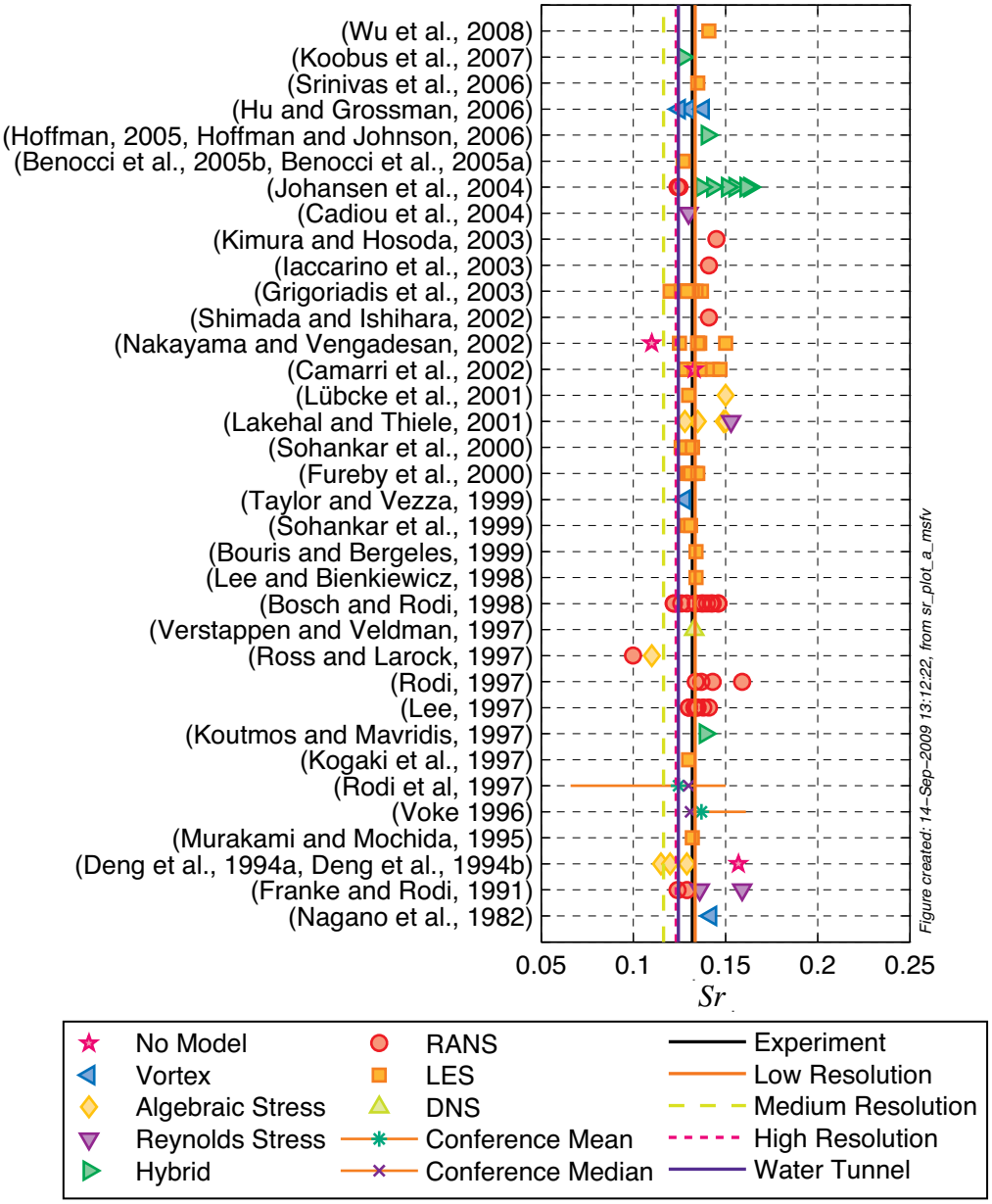


**Figure 6-33 – Comparison of Strouhal numbers from published data and the four simulations of present work.**

Interestingly, the results from the present simulations follow the trend discussed by Rodi *et al* (1997) in that the Strouhal number appears to have a low dependence on the

particular combination of turbulence model and numerical mesh, as is readily seen in Figure 6-33. It therefore follows that the Strouhal number is not a good parameter for validation studies. For example, the numerical studies of both Bosch and Rodi (1998) and Grigoriadis et al (2003), also shown on Figure 6-33, showed little dependence of *Sr* on either different grids or the numerical model used.

Further evidence of the insensitivity of *Sr* to the choice of the turbulence model is that all the RANS results shown in Figure 6-33 are also acceptably close to the laboratory result. Therefore, given the otherwise bad results when RANS computations are used, the apparent quality of the results for *Sr* indicates that *Sr* is very insensitive to the choice of numerical model.

### 6.4.4. Decay Slope Estimation

Theoretical studies based on dimensional arguments (Kolmogorov, 1941) indicate that the power spectral density should decay as

$$\text{PSD} \propto f^{-5/3} \tag{6.16}$$

for very large Reynolds numbers and in the inertial subrange, as shown in Figure 2-3 is a schematic plot of the relationship between the slope and inertial subrange. For comparison, four triangles with indicative power law slopes based on the assumption that

$$\text{PSD} \propto f^{\varkappa} \tag{6.17}$$

in which $\varkappa = \left\{-2, -5/3, -4/3, -1\right\}$, are shown in Figure 6-32. Using these reference triangles the slope of the power spectral density curve at high frequencies (herein the decay slope) is close to the theoretical minus five-thirds slope. However, a more rigorous examination in place of a visual inspection was developed to directly quantify the decay slope.

From a visual inspection of the data, the linear power-law region is between the frequency range $150 \le f \le 300$ Hz. The PSD coefficients and frequencies that resulted from the Fourier transform and averaging process described above were linearised by performing all the computations in $\log_{10}$ space and the regression model was applied to eight points along the wake centreline.

To describe the regression model suppose that the PSD as a function of frequency can be described as

$$PSD = Cf^{\varkappa} + D \tag{6.18}$$

in which $C$ and $D$ are constants. Then, taking the logarithm of Equation (6.18) and rearranging results in

$$\log(PSD - D) = \varkappa \log(f) + \log(C). \tag{6.19}$$

Now suppose that

$$Y = \log(PSD - D) \tag{6.20}$$

and

$$X = \log(f). \tag{6.21}$$

Equation (6.19) can now be generalised to

$$Y_i = \beta_0 + \beta_1 X_{i1} + \varepsilon_i. \tag{6.22}$$

at any frequency, $f_i$, where

$$\beta_0 = \log(c) \tag{6.23}$$

is the intercept when $X_i = 1$ and $\varepsilon_i$ is the error which is assumed to be normally distributed, $\varepsilon_i \sim N(0, \sigma^2)$, with a zero mean and a variance of $\sigma^2$. The estimator can then be computed by

$$\hat{\beta} = \left(X^T X\right)^{-1} X^T y, \tag{6.24}$$

in which the $^T$ is the matrix transpose operator and $X$ is the observed values matrix of the regressors. Terms with a hat indicate values estimated from the regression while terms without a hat represent an ideal value. An unbiased estimator of the variance of the errors can then be computed from

$$\hat{\sigma}^2 \coloneqq \frac{S}{n - p} \tag{6.25}$$

in which $n$ is the number of samples and $p$ is the apparent order of the regression. In this model $p = 2$, see Equation (6.22) and $n$=4195. $S$ is defined as the sum of the squared errors

$$S := \sum_{i=1}^{n} \hat{\varepsilon}_i^2 \,. \tag{6.26}$$

Confidence intervals on the estimator $\hat{\beta}_j$ can be calculated from the standard deviation

$$\hat{\beta}_j \pm \hat{\sigma}_j t_{\frac{\alpha}{2}, n-p} \tag{6.27}$$

in which the confidence level parameter $(\alpha)$ is defined as $100(1-\alpha)$ and the $t$ parameter is taken from a Student T table, or other suitable source, for the requisite degrees of freedom and level of confidence.

For the four simulations tested over the defined frequency band the power law decay slope fell within 0.35% of the theoretical slope, shown in Table 6-2. The perfect slope value of $-1.666\dot{6}$ fell within the 95% confidence bounds for all four models.

**Table 6-2 – Power law slope calculated via a linear regression of the point probe discussed in §6.4.3. The frequency range was for 4195 points over 150-300Hz.**

| Model | Slope | $\sigma_j$ | 95% Confidence Interval |
|---|---|---|---|
| LR | -1.6634 | 0.0049 | [-1.6742, -1.6525] |
| MR | -1.6678 | 0.0025 | [-1.6733, -1.6622] |
| HR | -1.6517 | 0.0090 | [-1.6716, -1.6318] |
| WT | -1.6545 | 0.0082 | [-1.6727, -1.6364] |

The standard deviation from the models increased inline with the model resolution from a low of 0.0030 to a high of 0.0090 for the LR and HR simulations, respectively. This is most likely due to the higher resolution model capturing more of the "physics" and thus showing a greater variability in the $v$-velocity as a function of time, which in turn flowed through to the slope estimation.

This regression model was applied to the other seven monitor points located close to the wake centreline. As with the results shown in Table 6-2 all eight points had approximately the same slope, which was very close to the theoretical decay slope, shown in Figure 6-34. Again, confidence bounds were computed but were so small as to be indistinguishable from the marker at the scale used in Figure 6-34 and were therefore not plotted.

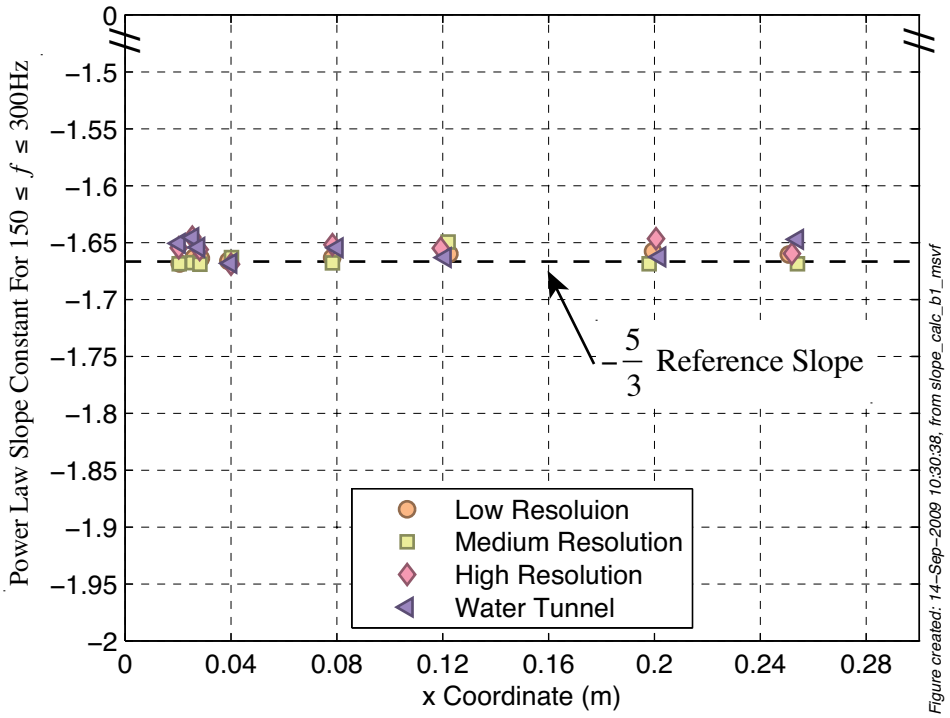


**Figure 6-34 – Indicative slope of the PSD traces in the power-law decay regions for eight points located in the wake along the $y = 0, z = 0$ line.**

A potential question with the present simulations is that in order to minimise the total cell count the mesh in the far field was increased in size. Further, since it is a trivial matter to show that if the cells become too large, or the change in cell size is too great, the apparent order of the computation scheme is reduced to first order (Pourquie et al., 1996, Roache, 1998a). Moreover, as first order models have been shown to be overly dissipative (Roache, 1998a), the power law decay slope would significantly increases from the -5/3 value. Therefore, a point of possible concern for the present simulations was that the size of the far field cells and/or the rate of change of the cell sizes might be too large. However, as may be seen in Figure 6-34, because the decay slope remains constant downstream through both the wake and increasing cell size, the simulation technique appears to have not increased dissipation. Therefore, as the slope of the

power spectral density curves is in good agreement with the theoretical predictions, the turbulent length scales, which are based on the spectral calculations, can be evaluated.

### 6.4.5. Turbulent Length Scales

The final parameter to be discussed in this section is the Kolmogorov microscale length defined as:

$$\eta \cong \left( \frac{\nu^3}{\bar{\varepsilon}} \right)^{\frac{1}{4}} \tag{6.28}$$

in which $\bar{\varepsilon}$ is the average dissipation rate. As the dissipation rate was not directly calculated in these simulations an experimental method described by Mallinson et al (2004) and designed for hot wire anemometry data was used. Mallinson et al tested three methods of computing the dissipation rate and hence $\eta$ and concluded that there was little difference in the results. Therefore, with the ready availability of the spectral data, their third method based on spectral calculations was adopted for the work described herein.

With the spectral method, the average dissipation (Pope, 2001) is

$$\bar{\varepsilon} = 15\nu \int_0^\infty \kappa^2 E(\kappa) d\kappa \tag{6.29}$$

in which $\kappa$ is the wave number given by

$$\kappa = \frac{2\pi f}{U_{ref}} \tag{6.30}$$

and $E(\kappa)$ is the power spectrum in wave number space that is related to the power spectrum in frequency space, $E(f)$, by the relation

$$E(\kappa) = \frac{E(f) U_{ref}}{2\pi} \tag{6.31}$$

Here $U_{ref}$ is a reference velocity scale, which was taken to be the time-averaged *u*-velocity at the point where the calculations were being performed. The Kolmogorov length calculations were performed using the same spectral averaging method as outlined above but were based on the *u*-velocity, so the reference velocity scale was assumed to be the mean of the *u*-velocity in the time domain. These computations were

performed over the same set of points as the power-law decay computations and the results are shown in Figure 6-35.

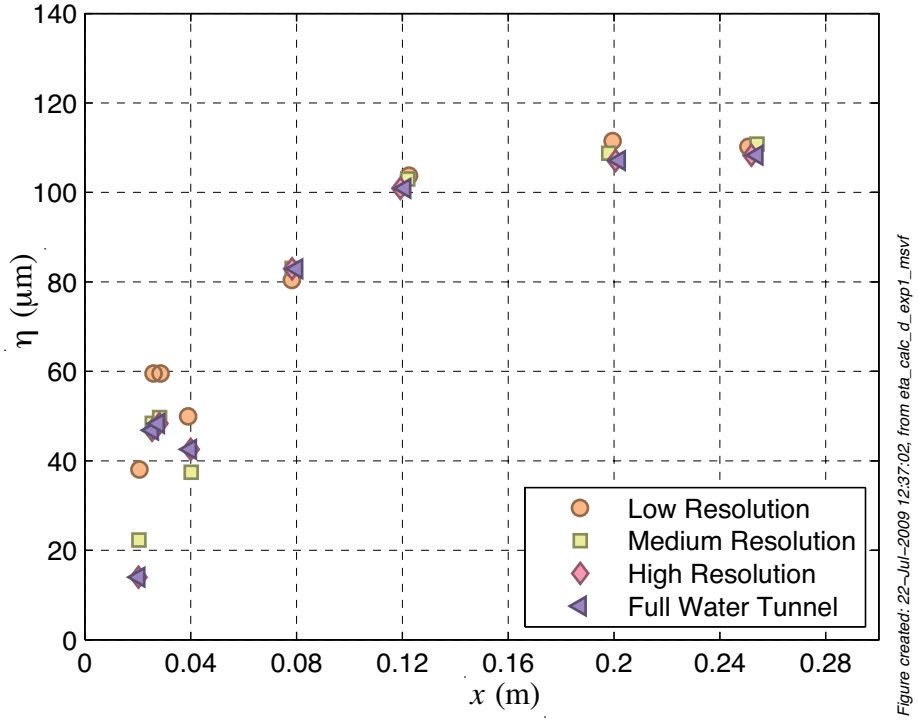


**Figure 6-35 – Kolmogorov lengths computed along the wake centre line.**

As an order of magnitude comparison, Dobre and Hangan (2004) estimated, albeit via a slightly different method, $\eta$ to be 64 μm at a point on the wake centreline at $x = 26d$ m, which is in good agreement with the 20-140 μm computed within the present work. Dobre and Hangan (2004) estimated $\eta$ using the inviscid approximation (Tennekes and Lumley, 1972) that assumes the dissipation rate to be

$$\varepsilon = \frac{(u')^3}{d} \tag{6.32}$$

in which "…$u'$ is the maximum streamwise velocity standard deviation at the measurement location and $d$ is the cross square cylinder width" (Dobre and Hangan, 2004). However, the limitation of this method, as discussed conceptually by Mallinson et al (2004) and examined with DNS data (Del Álamo and Jiménez, 2009, Moin, 2009) is that Taylor's hypothesis is implicitly used with the assumption that the velocity is constant over time, which is clearly incorrect for the flows observed at this location, for example see Figure 6-2. Despite the additional caveat when interpreting this result the similarity with the present work is very encouraging.

As $\eta$ is an estimate of the smallest scales of turbulence, and as the turbulence decays and the wake grows, $\eta$ should therefore first increase as the wake, and turbulence, intensity increases in the near wake, for example, as the $u'$ components increase in Figure 6-26. Then as the far wake decays, $\eta$ should further decrease in conjunction with the trend of the flow towards uniformity. These trends are visible in Figure 6-35 with an initial sharp increase in the near wake before levelling off at around $\eta$=130μm in the far wake. There is a discontinuity to this trend at x≅0.04m, which is close to the recirculation length where on the average the flow velocity tends to zero. The lower average *u*-velocity and corresponding lower level of fluctuations at this location is the most likely cause in the discontinuity of $\eta$ as it will lead to a lower power spectral density curve and hence, via the integral, a lower final value for $\eta$.

Because the present simulations have been shown to adequately represent the time-averaged and turbulent-spectral parameters the so-called integral quantities, such as the average drag and lift coefficients, which are dependant on the geometry of the object, and the Reynolds number can be examined.

## *6.5. Single Parameter Validation: Integral Quantities*

### 6.5.1. Quantities Considered

To continue the reductive validation process, whereby the examination began with visualisations of the flow field and reduced the complexity with the use of averages, the final step is to compare the integral quantities. For this study, six parameters were considered, namely the mean force coefficients, that is $C_D$ and $C_L$; the root mean squared force coefficients $C'_D$ and $C'_L$; the recirculation length, $l_r$ and the coefficient of base pressure, $C_p$. The following sub-sections will briefly discuss the results, in the above order.

### 6.5.2. Mean $C_D$ and $C_L$

The mean $C_D$ from the spanwise periodic models appear to converge to approximately 2.5 as the cell count is increased, with values of 2.42, 2.50 and 2.51 for the low, medium and high-resolution simulations respectively. In contrast to the results from spanwise periodic simulations, the mean $C_D$ from the water tunnel model is 25% higher at 2.66, as shown in Figure 6-36.

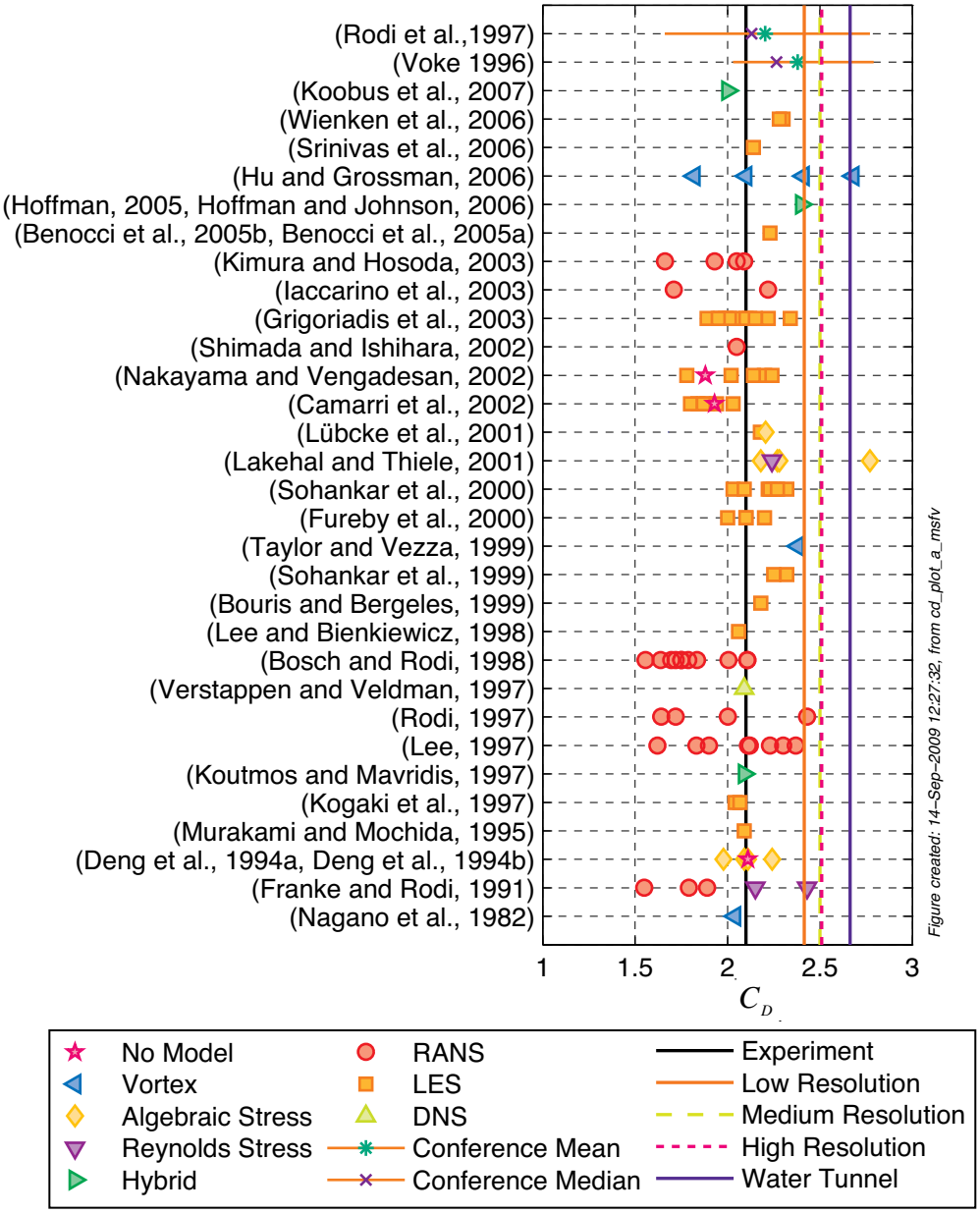


**Figure 6-36 – Comparison of mean drag coefficients from published data and the four simulations of present work.**

It is noted that while all four of these results are within the bounds of the published $C_D$ results, they are close to the upper limit and are 20% and 27% higher than the experimental $C_D$ of 2.1 (Lyn and Rodi, 1994) for the spanwise periodic and the water tunnel simulations, respectively.

The values of the mean $C_L$ for the present work are all within the bounds

$$-0.06 \le C_L \le 0.03\,, \tag{6.33}$$

which is acceptably close to zero, as shown in Figure 6-37. That is, over the simulation time windows used to compute $C_L$, the computed value will move slightly around zero as a function of the vortex shedding phase. Hence, small deviations from zero, as shown in the limits of Equation (6.33), are due to the location in the shedding cycle where the average computation stopped rather than to an incorrect non-zero mean.

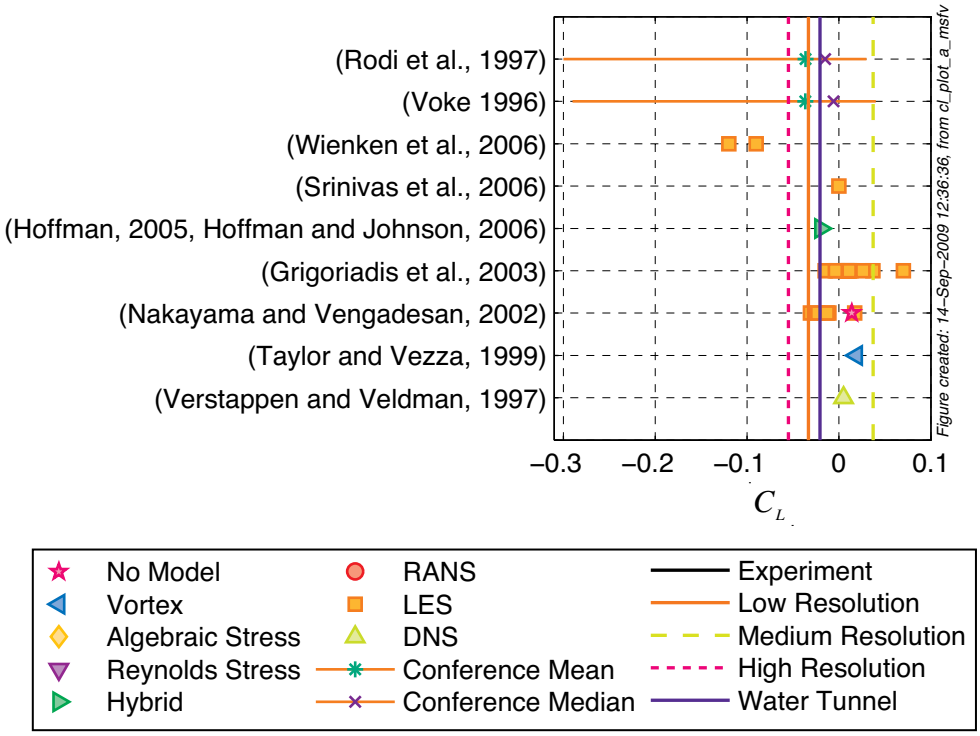


**Figure 6-37 – Comparison of mean lift coefficients from published data and the four simulations of present work.**

### 6.5.3. Root Mean Squared $C_D$ and $C_L$

The root mean squared drag, $C'_D$, results from the spanwise periodic simulations and as with $C_D$ were towards the higher end of the published results at 0.28, 0.31 and 0.26 for the low, medium and high-resolution simulations respectively, as shown in Figure 6-38. Somewhat surprisingly given the substantially higher $C_D$ that the benchmarks for the water tunnel simulation, the corresponding $C'_D$ was 40% lower than the medium resolution simulation. This lower $C'_D$ for the water tunnel simulation was near to the centre of the reference LES data and the combined conference LES results, as shown in Figure 6-38, which if taken by itself would indicate perfect validation. No results from laboratory experiments for $C'_D$ were available to the present author for comparison.

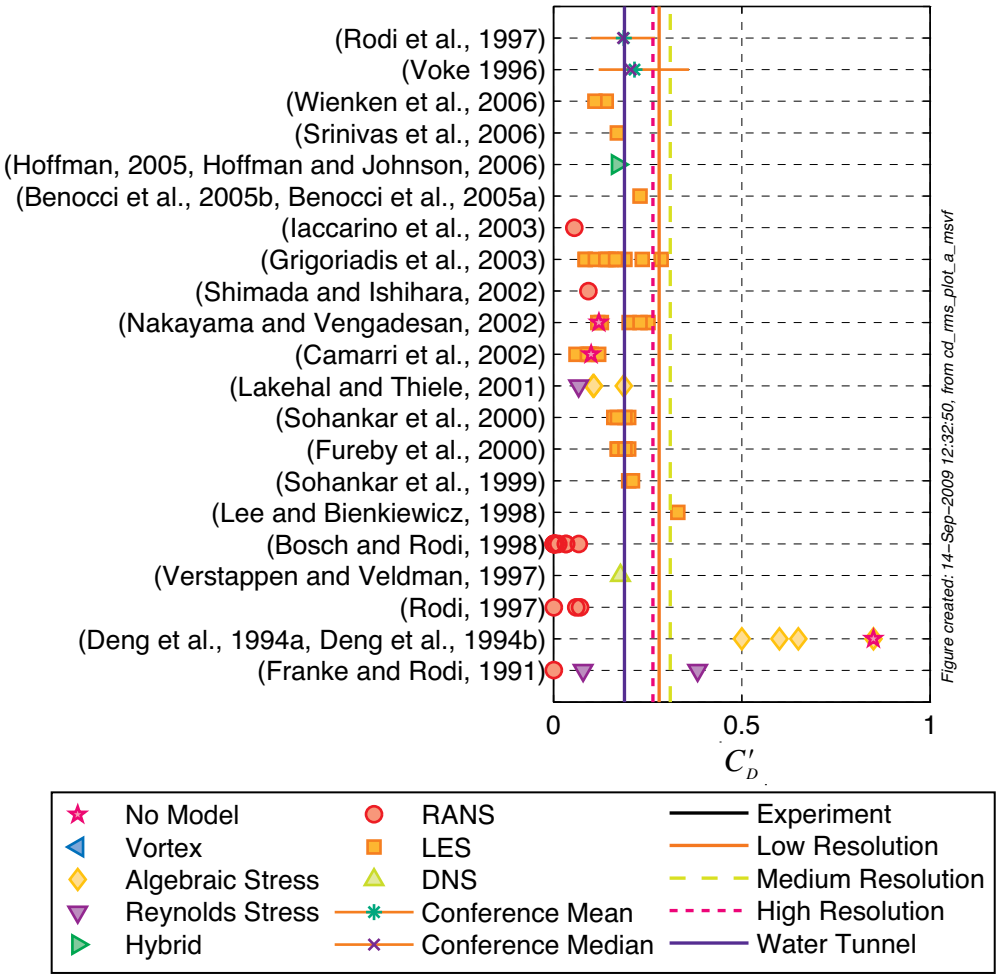


**Figure 6-38 – Comparison of root mean squared drag coefficients from published data and the four simulations of present work.**

As with $C'_D$ for the spanwise periodic simulations, $C'_L$ for the same simulations was also higher than, yet still within the bounds of, the majority of the comparison simulations, as shown in Figure 6-39, at 1.47, 1.59 and 1.60 for the low, medium and high-resolution simulations respectively. In contrast to the high results from the spanwise periodic models, and in parallel with the $C'_D$ results, $C'_L$ for the water tunnel simulation is both lower than the spanwise periodic results at 1.19 and closer to the Lyn and Rodi (1994) result of 1.3.

In addition to the laboratory result of 1.3 from Lyn and Rodi (1994), Cheng et al. (1992) published a $C'_L$ of 0.5 for an equivalent configuration as the present work, also shown in Figure 6-39. This result is particularly puzzling because it is some 60% lower than the Lyn and Rodi result around which the majority of the numerical results, including the present work, cluster. The present author cannot explain the discrepancy of this result

as the blockage ratios and turbulence intensity ratios were in the same ranges for both studies, with the only significant difference being that Lyn and Rodi performed their experiments in a water tunnel, while Cheng et al. utilised a wind tunnel.

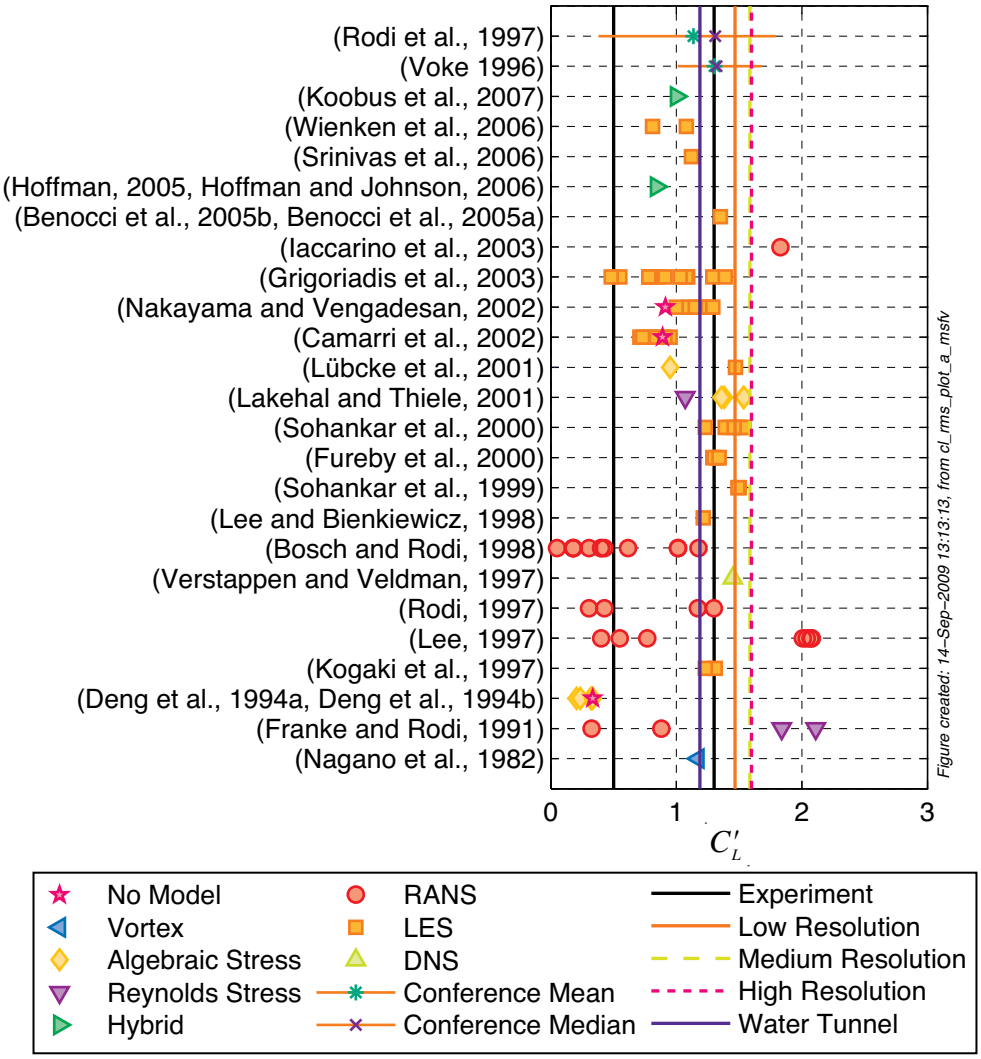


**Figure 6-39 – Comparison of root mean squared lift coefficients from published data and the four simulations of present work.**

It is interesting to again note the poor performance of RANS based solvers in resolving both the mean and, particularly, the RMS quantities. That is, while there is a spread of results for the mean $C_D$, the majority of the RANS results are lower than the experimental data, as shown in Figure 6-36. In turn this, if the results were taken out of context, could result in a non-conservative estimate of the drag forces. However, the RANS models, with the notable exception of a cluster of results from Lee (1997) which are overestimated by 50%, are unable to resolve the fluctuations, as shown in Figure 6-39. Therefore, with RANS models apparently unable to resolve either the drag or the

fluctuations to a reasonable degree, the axiom of "any answer is better than none" must be questioned. In contrast, the high order methods such as large eddy simulations and DNS, as well as the approach used in the present work all capture, to a varying extent, both the mean and fluctuations.

### 6.5.4. Recirculation Length

The recirculation length was computed from the averaged flow field data and was defined as the length from the downstream face of the cylinder to the point, $x_{lr}$, where

$$U(x) = 0 \quad \text{for} \quad x \gg \frac{d}{2} \tag{6.34}$$

and for the major recirculation zone. That is, secondary recirculation zones were observed very close to the cylinder but were ignored for these comparisons. $l_r$ from the present simulations was 1.38, 1.31 and 1.34 for the low, medium and high-resolution spanwise periodic simulations and 1.02 for the water tunnel simulation, as shown in Figure 6-40.

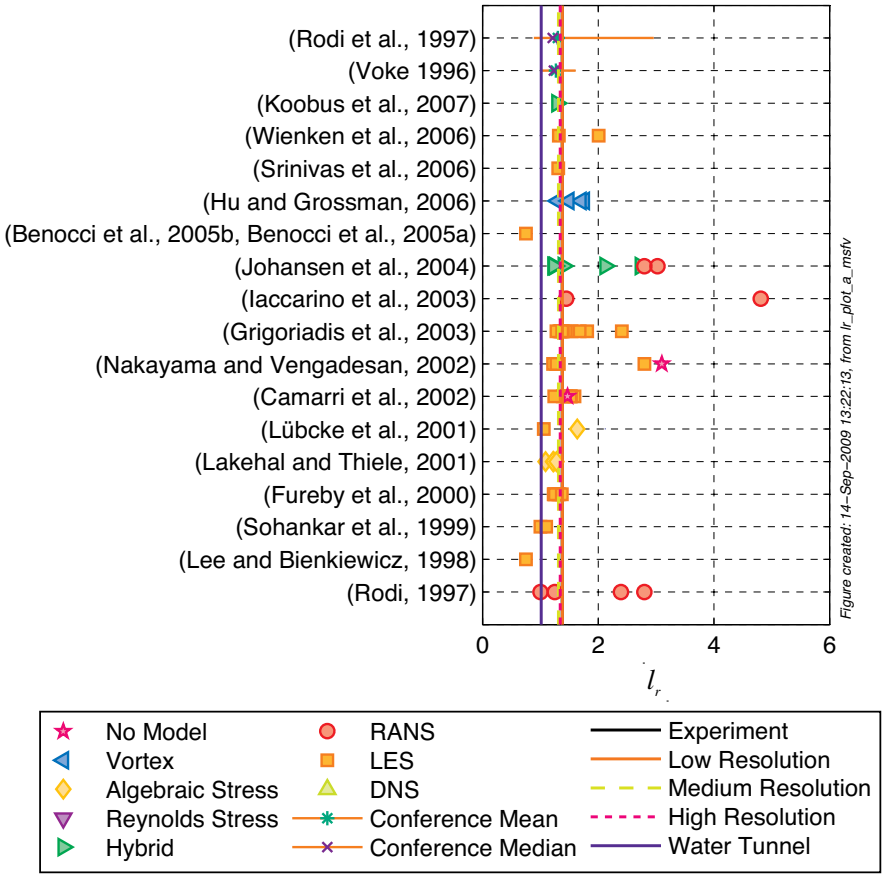


**Figure 6-40 – Comparison of recirculation lengths.**

These results from the spanwise periodic model compare favourably with the 1.38 measured by Lyn and Rodi (1994). However, $l_r$ computed from the water tunnel simulation is some 25% lower than the benchmark laboratory and numerical data.

### 6.5.5. Base Pressure Coefficient

The base pressure coefficient presented in this dissertation was computed as

$$C_P = \frac{\sum_{i=1}^{N_{nodes}} P_i}{\frac{1}{2}\rho v^2} \tag{6.35}$$

in which $P_i$ represents the time averaged pressure at a node $i$ on the downstream face of the cylinder. The results from the spanwise periodic models of -1.48, -1.55 and -1.54 for the low, medium and high-resolution models compares favourably with the spread of reference numerical results, as shown in Figure 6-41.

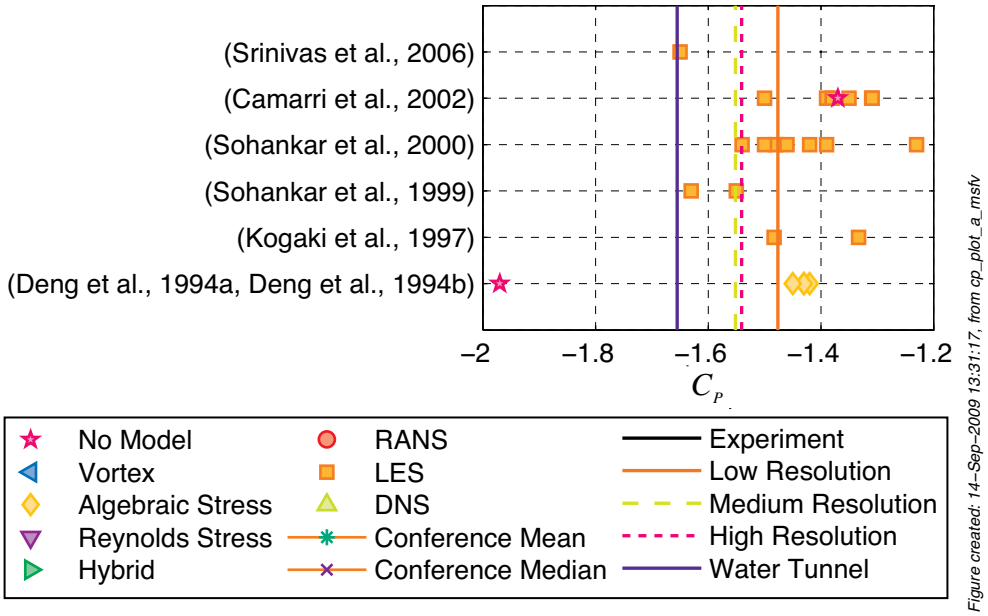


**Figure 6-41 – Comparison of coefficients of base pressure from published data and the four simulations of present work.**

However, $C_P$ from the water tunnel simulation is, with the exception of one result, lower than the benchmark data.

### 6.5.6. Discussion of the Single Parameter Results

In general, the results are acceptable for the purposes of this validation study. That is, as the work presented in this dissertation is designed to reduce the computational requirements for modelling it was anticipated that there might be a corresponding loss in accuracy.

The model results for the coefficient of base pressure and the recirculation length must be related in that the larger negative base pressure, or suction, which would probably draw the downstream recirculation region closer to the cylinder. Naturally, this would then also reduce the recirculation length.

The smaller recirculation length and higher base pressure coefficient could also explain the higher lift forces and the higher lift and drag RMS coefficients. In this case it is conjectured that the amount of energy contained in the recirculation region is approximately consistent with the reference data but is contained in a smaller volume. It then follows that the fluctuations, although at approximately the same dominant frequency as the reference data sets, would be more violent, hence the higher RMS values. Unfortunately, the relatively high value of the drag coefficient is not compatible with this hypothesis as a higher base pressure should balance the already high upstream pressure and therefore reduce the drag felt by the cylinder.

Alternatively the 2$^{nd}$ order upwind model may be overly dissipative, which would be a direct contrast to the spectral results presented in §6.4. Further investigation, rather than validation *per se*, will be required to quantify the causes, and possible remedies, for these variances.

## *6.6. Wall Time*

Although wall time is not, strictly speaking, a validation parameter, as a central hypothesis of the present work is that the subgrid models may be replaced by the use of a 2$^{nd}$ order upwind discretisation scheme that is faster than the alternative turbulence models, run times must be discussed. The difference in computational speeds was evaluated on the medium resolution grid with several different subgrid scale models. All the simulations were run within the CFD-ACE+ computation fluid dynamics solver and all used the default settings for the respective turbulence models as specified by the code developers. All the models were started from rest and the inlet velocity was

accelerated using a sinusoidal acceleration function over two seconds. The models were allowed to run for 2000 time steps, or 2s of model time, before being stopped and the wall time calculated.

Of the six models tested five were LES type models and one was a *k-ε* RANS type model. The models are listed in order of increasing computation complexity and are discussed below:

1. 2nd Order Upwind Model (2nd Order): the model used in the present work;
2. Smagorinsky based LES (LES Smag): the Smagorinsky subgrid scale model (Smagorinsky, 1963) is used for a LES simulation;
3. Detached Eddy Simulation (DES): a mixture of LES and RANS computations, which therefore requires a splitting algorithm to determine the appropriate solver to use in each zone before computing the turbulence quantities;
4. Dynamic LES Model (LES Dyn): the dynamic model used in this simulation is based on Lilly's modification (1992) of the dynamic Smagorinsky LES model proposed by Germano (1991) and evaluates the Smagorinsky stress tensor with a double filtering process;
5. Locally Dynamic LES Model (LES LD): utilises Menon's locally dynamic LES model (Menon and Kim, 1996);
6. *k-ε* with Renormalised Groups: this model is based on the Renormalised Group *k-ε* model of Yakhot and Orszag (1986) and is perhaps an unfair comparison because RANS models have a significantly higher computation workload than Smagorinsky type LES models but are designed to run on grids with smaller cell counts. Therefore, a RANS model should, by definition, run more slowly on a LES scale mesh than a LES type model.

The results of the model speed tests are shown in Figure 6-42 and three trends are visible, firstly that the 2nd Order LES model was significantly faster than all the other models. Second, that as the theoretical computation complexity increased so did the model run time and thirdly that the *k-ε* RANS model was slower than the majority of the LES type models.

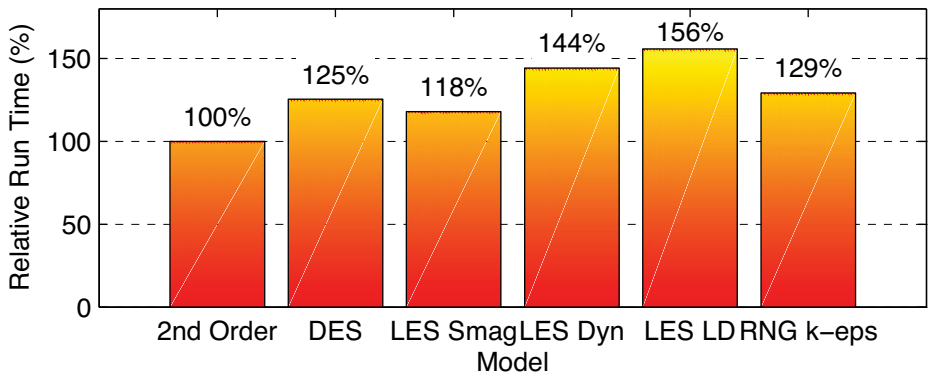


**Figure 6-42 – Comparison of model run speeds for different LES subgrid models and an indicative k-epsilon RANS model.**

However, despite the *k*-$\varepsilon$ performing worse than 2nd Order Upwind, DES and LES models it was still faster than both of the dynamic LES models. This is somewhat surprising as the author was expecting the RANS type models to perform far worse than any of the LES models. Instead, it would appear that the dynamic models were incurring a significant computational penalty for the required additional computations.

## 6.7. Discussion of the Single Phase Validation Studies

The validation studies presented in this, and the previous, chapter were primarily intended to show that the 2nd order upwind technique was capable of simulating the massively separated, turbulent flows around a bluff body at a Reynolds number of $\mathrm{Re}_d = 22 \times 10^3$. However, in addition to this pure validation exercise a number of new discoveries were made that simultaneously cast doubt on the reliability of previous numerical simulations and offer an alternative to improve future numerical experiments.

As a preparation exercise for the main validation study, which was discussed in §5.2, a number of two-dimensional simulations were undertaken to quantify the requirements for both the maximum mesh size adjacent to the cylinder and the minimum length from the cylinder to the outlet. The flow field, as visualised with velocity magnitudes, was interpreted to be "unphysical" in that instead of the expected von Kármán vortex street irregular blobs of fluid were ejected from the nominal wake, as shown in Figure 5-4. This interpretation cast significant doubt on the validity, and hence applicability, of the majority of the published data that was computed using two-dimensional meshes and was intended to be used for the validation of the three-dimensional simulations of the present work.

Despite the interpretation that the results from the two-dimensional simulations were unphysical, this was not the primary purpose of the two parametric studies. Instead these investigations were envisaged to test the effect of independently changing the distance from the cylinder to the outlet boundary and the length of the cell, normal to the cylinder, for the cell adjacent to the cylinder, as shown in Figure 5-2 and Figure 5-3. In this regard, a clear effect was observed as the value of the parameters was changed with a critical for both parameters after which the simulations were largely independent of the value of the parameter. To examine this the probability distribution functions were examined as shown in Figure 5-8 and Figure 5-9 for the $\mathfrak{L}$ and $\mathfrak{F}$ simulations, respectively. The simulations of $\mathfrak{L}$ were independent for $\mathfrak{L} \geq 400$ mm, while the results from the $\mathfrak{F}$ simulations were independent for $\mathfrak{F} \leq 500$ μm. Therefore, these results were used to guide the development of the three-dimensional meshes.

With these recommendations, two configurations of three-dimensional meshes were constructed. The first was designed to match the workshop specifications detailed by Rodi et al (1997) while the second was envisaged to represent the close circuit water tunnel used by Lyn and Rodi (1994). Interpretation of the flow field from the spanwise periodic simulations hinted that the spanwise width was too narrow. That is, the streamwise rib structures appeared to be compressed in the spanwise direction when compared to the same visualisations from the water tunnel simulations, as shown in a comparison of Figure 5-25 and Figure 5-26, respectively. An examination of the spanwise correlation coefficients, discussed in §5.6, confirmed the suspicion that the region of uncorrelated flows in the centre of the spanwise periodic domain was too small. Further, the simulations with the water tunnel largely ameliorated these problems for two reasons. Firstly, no periodic boundaries were required because this configuration exactly matched the experimental configuration and, secondly, irrespective of the match with the experimental configuration there was a large enough region of uncorrelated flow in the centre of the domain. Despite these problems discovered with the spanwise periodic simulations the vast majority of the numerical data available for validation is based on this configuration, therefore the validation that progressed and was discussed in §6 focused on the results from the spanwise periodic simulations.

The validation began with an examination of the grid independence, discussed in §6.2, but as a number of the parameters tested showed oscillatory convergence a formal mathematical procedure would be inappropriate (Celik et al., 2008). Instead a qualitative analysis of the velocity data as a function of time, presented in §6.2.2, and the reduced, statistical properties of the velocity components at a point, presented in §6.2.3, was performed. The interpretation of these two distinct forms of data indicated that the three spanwise periodic simulations were "converged" in that there was little difference between the simulations. In an apparent confirmation of the initial estimate of oscillatory convergence, there was no clear trend in the eight statistical properties examined across the simulations. Therefore, as the results from the simulations were "converged" the component of the validation study with the published data could proceed.

The majority of the data available for validation was time averaged and split between spatial data, that is the time averaged velocity along a line, and the so called "integral" quantities, such as the time averaged $C_D$ and $C_L$ as well as the recirculation length and peak frequency. Therefore, to convert the unsteady results from the present simulations an online average method was presented and validated in §6.3.2 and §6.3.3, respectively. In a similar trend to the results already discussed all of the integral parameters were close to, and within the spread of, the references. Further, there was no single trend from low to medium to high resolution for all the parameters.

Given that the technique has not only been successfully validated to simulate bluff body, transitional flows with single phases, but also revealed a significant limitation in many of the present simulations, as well as providing a strategy to ameliorate the defects, the method can be extended to two-phase, bluff body flows. However, as the extension to two-phase flows will introduce a number of new physical effects this extension should also be validated prior to using the method to investigate, general turbulent, two-phase flows.

# 7. Flows with a Free Surface

## *7.1. Introduction*

In a manner similar to the validation of the square cylinder discussed previously, two selection criteria were primarily used to decide if a particular configuration would be suitable for a validation exercise, namely:

1. Was the quality of the description of the geometric configuration sufficiently high to be reproducible?
2. Was there suitable physical and numerical data available for detailed comparison?

Initially the tow tank experimental results of Inoue et al (1993) appeared to meet these criteria. In addition to providing extensive data on the time averaged free surface elevation, four velocity profiles, both inside and adjacent to the wake region, were taken using a hot film probe that was submerged behind the cylinder.

Both Chen et al (2000) and Kawamura et al (2002) used the Inoue study as the basis for their Large Eddy Simulation, as detailed in Table 7-1. Both of these groups reported favourable results with different dimensions and boundary conditions. Therefore, with these positive results from simulations with different geometric configurations, the right circular cylinder that pierced a free surface was adopted as the configuration for the present validation study. As the present work was being finalised Yu et al (2008) published their results of a Large Eddy Simulation of the same configuration, which provided further validation data.

All research programs are subject to a certain degree of "evolution" as new results are published or, more likely, are simply discovered by the primary researcher. This investigation was no different in that a specific geometric configuration was initially chosen, yet subsequently, as the present research, and in particular the scope of the literature review, expanded, further published data were discovered and incorporated into the current project.

**Table 7-1 – Key parameters of the benchmark right circular cylinder studies to be used to validate the present work.**

| Paper | Type | Turbulence Model | Wall Function | $N_{cells}$ LR | $N_{cells}$ MR | $N_{cells}$ HR | Water Depth | Air Height | US Distance | DS Distance | Width from Cylinder | Topology Type |
|---|---|---|---|---|---|---|---|---|---|---|---|---|
| Inoue et al (1993) | Tow Tank | N/A | N/A | N/A | N/A | N/A | Not Known | N/A | N/A | N/A | 30D | N/A |
| Chen et al (2000) | LES | RNG Smagorinsky | None | - | - | 132,680 | 2D | Not Specified | 10D | 20D | 10D | Un-structured |
| Kawamura et al (2002) | LES | Smagorinsky | Yes but unspecified | 67,473 | 142,545 | 525,987 | 4D | Not Specified | 10D | 15D | 10D | Structured O-Type |
| Yu et al (2008) | LES | Smagorinsky | Van Driest | - | 1,647,459 | 3,395,651 | 4D | 4D | 20D | 20D | 20D | Structured O-Type |
| Present Work | Coarse DNS | N/A | None | 245,430 | 373,340 | 588,500 | 8D | 4D | ~14D | ~19D | ~14D | Structured O-Type |

With the geometric configuration apparently fixed, a number of preliminary studies were developed to test unknown variables such as the location of the side walls – variables that differed between all three of the numerical papers and the experimental investigation of Inoue. While these two-dimensional, preliminary studies were being undertaken the literature review continued in parallel and the extensive experimental data set of Hay (1947) was discovered by the present author.

Hay conducted an exhaustive program of tow tank tests that were designed to investigate the "resistance of simple geometrically-shaped formes towed through the water surface" (Hay, 1947). Unlike Inoue, Hay exhaustively described the experimental conditions that were of particular relevance for the present work, namely the dimensions of the tow tank. In line with the stated aim of the tow tank experiments, Hay made a staggering 900 measurements of drag coefficients for combinations of three variables:

1. The depth of immersion, $L$.
2. The diameter of the cylinder, $d$.
3. The speed of the cylinder through the otherwise quiescent tank.

Thus, this data set provides a superlative reference source for trends as well as definitive measurements of specific depth/diameter/speed combinations, as shown in Figure 7-1.

In addition to the phenomenal record of drag forces, Hay also shot over 730 photographs of these depth/diameter/speed combinations from three different angles. Two of the images were perpendicular to the direction of travel with one above the free surface looking down and the other below the free surface. The third set of images was taken from behind and to the side of the cylinder looking upstream at the wake. Hay then applied photogrammetry techniques to these images and made 1500 measurements of six different wave shape parameters. Specifically, wave shapes parameters were lengths such as the height of the bow wave and the distance to the top of the rooster tail from the cylinder.

There is no velocity profile data nor are there free surface contours at the smaller diameter, lower speeds investigated by Inoue. However, as the available Hay data is so extensive, the trends are readily apparent and, thus, results from the present work can still be compared. Therefore, the focus of the present work was varied slightly to

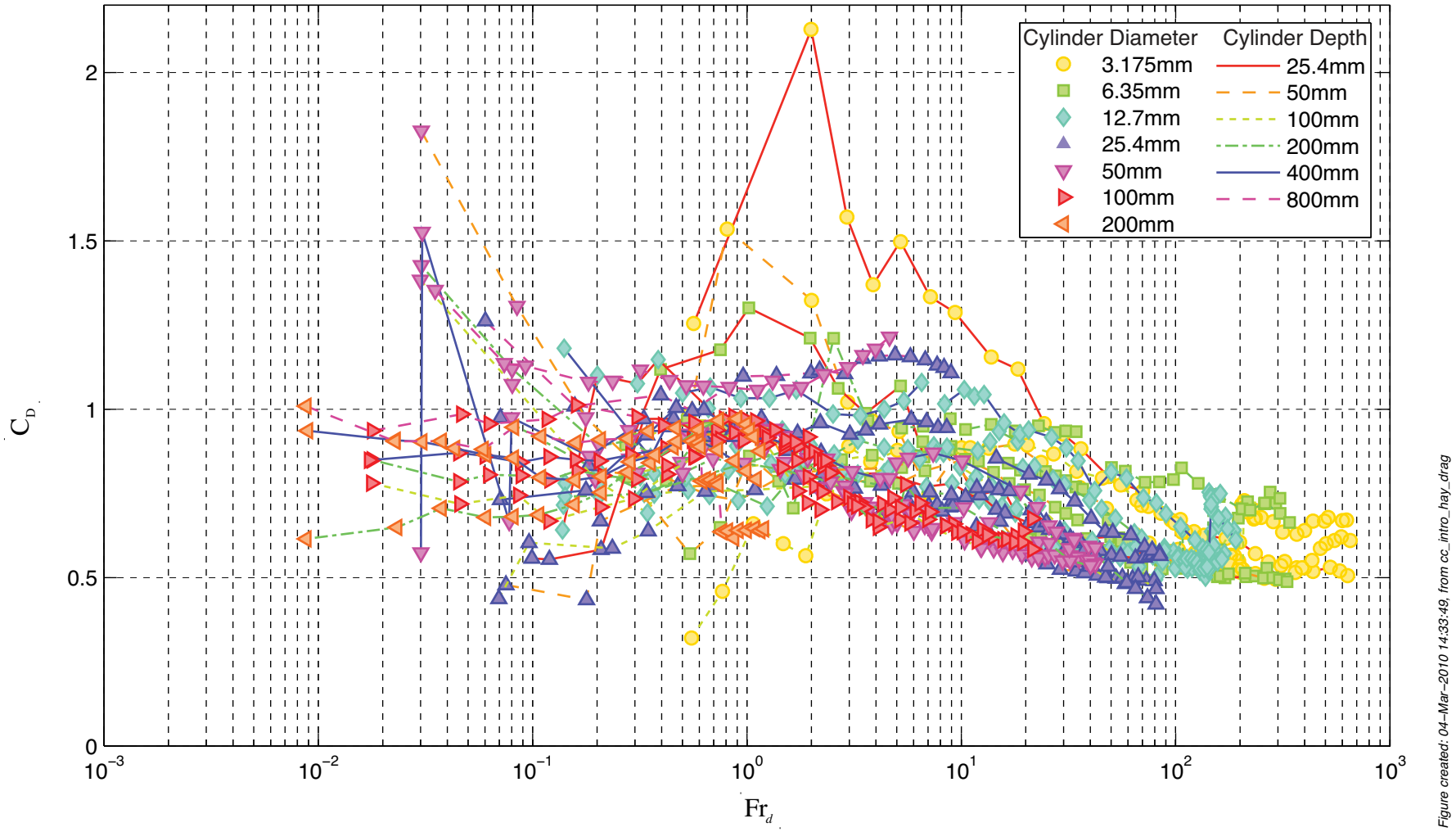


**Figure 7-1 – All 900 drag coefficients measured by Hay (1947) plotted as a function of Froude number relative to the diameter.**

remain with the diameter/speed configuration investigated by Inoue et al (1993), but with the computational geometry configured to match the fully described tank used by Hay (1947). However, there are a few caveats to be considered with the numerical simulation of tow-tank experiments.

## 7.2. The Cylinder Centred Inertial Frame of Reference

The tow tank that was used by Hay in his landmark investigations was located at the David Taylor Model Basin, Maryland, USA, shown schematically in Figure 7-2. In total seven diameters that ranged from 3.175 mm to 200 mm were dragged through the tow tank at speeds up to 4.6 m/s. Concurrently, the depth of immersion of the cylinder, relative to the at rest free surface, ranged from 25.4 mm to 800 mm.

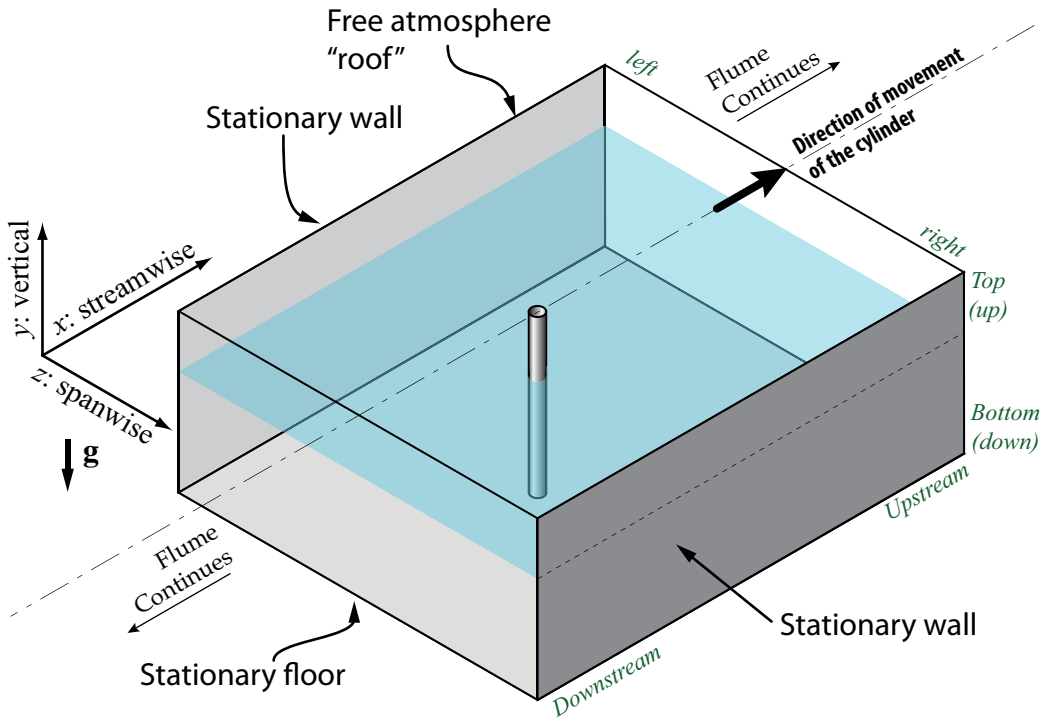


**Figure 7-2 – Diagram of a sub-section of the David Taylor Model Basin with the surface piercing circular cylinder and the free surface shown.**

For this present work because of a combination of limitations of the CFD-ACE+ computational fluid dynamics code and, despite the availability of state of the art computational resources, the lack of a sufficiently large computational facility made it impossible to directly simulate the tow tank utilised by Hay. Therefore, in order to reduce the size of the computational domain, the inertial frame of reference was changed such that instead of being based relative to the outside of the tank, it was

centred on the cylinder. This allowed the streamwise length of the computational domain to be reduced to only a 1/25$^{th}$ length of the full tunnel.

To reverse the inertial frame of reference, suppose that, instead of the cylinder moving through otherwise stationary fluid and walls, the cylinder was fixed within the computational geometry and the fluid and wall boundaries were accelerated around the cylinder, as shown in Figure 7-3 compared with Figure 7-2. This was an approach originally that was originally suggested by Leonardo di Vinci (Anderson, 1997).

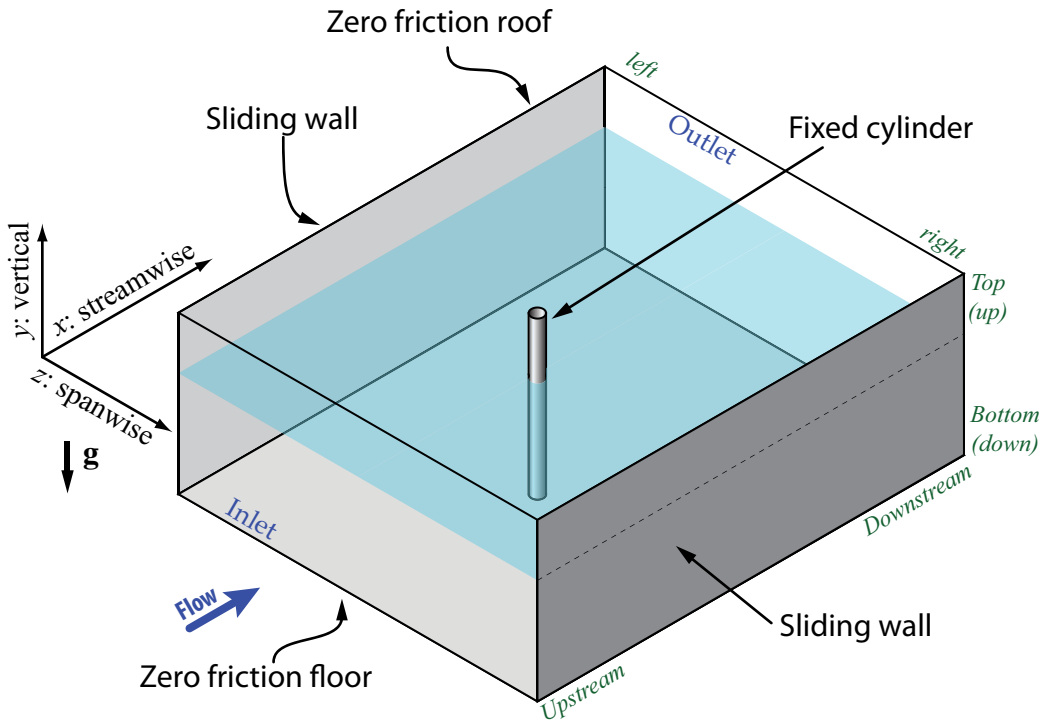


**Figure 7-3 – Diagram of the configuration of the cylinder centred reference frame.**

This change in the reference frame is not, however, a perfect solution because of the difference in the turbulence levels that the cylinder will experience in the alternate configurations. That is, if the cylinder were towed through quiescent fluids, as was the case for the laboratory experiments of Hay, the cylinder would encounter fluids with negligible turbulent fluctuations. Arguably, the turbulent fluctuations should be zero but it could reasonably be expected that due to the minor action of convection currents, or residual currents from previous experiments, there would be some small movement in the fluid. In contrast to the physical conditions, the numerical cylinder would experience turbulent fluctuations because, although the water would be injected into the numerical model with no turbulent fluctuations, the velocity is sufficiently high that turbulent fluctuations would develop upstream of the cylinder.

This effect should be sufficiently small such that any resultant error would be insignificant compared with that generated from the other numerical assumptions and methods. In order to maintain the highest similarity between Hay's experiments and the present numerical simulations and simultaneously minimise disturbances due to changed inertial frame of reference, the wall boundary and volume conditions that were to be imposed on the fluids needed to be carefully specified.

## 7.3. Cylinder Centred Boundary Conditions

Within the present simulations, five distinct boundary conditions had to be considered, namely:

1. The inlet.
2. The outlet.
3. The cylinder faces.
4. The spanwise walls.
5. The two boundaries at the vertical extents of the computational domain.

It was presumed that in the physical experiments the towing carriage was initially at rest and subsequently accelerated up to the test speed before the measurements were taken. As Hay did not publish information regarding the acceleration phase of his experiments, the present author assumed a velocity profile in time of the form

$$u_{inlet}(t) = \begin{cases} U_\infty \sin\left(\dfrac{\pi t}{4}\right)^2 & \text{for } 0 \le t \le 2 \\ U_\infty & \text{for } t > 2 \end{cases}, \tag{7.1}$$

in which $t$ is the time in seconds. This profile is shown for the non-dimensional case in Figure 7-4 and was uniformly applied over the entire inlet face at a given time instant, $t$.

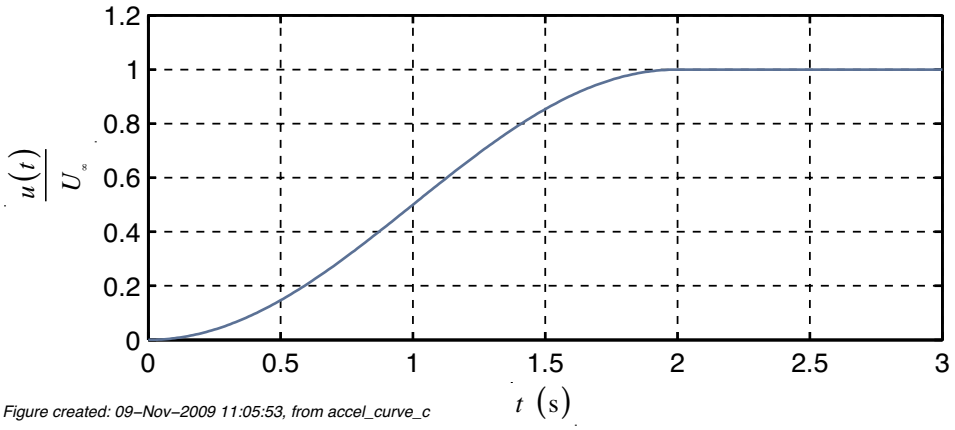


**Figure 7-4 – Plot of the normalised inlet velocity as a function of time.**

The outlet to the computational domain was set such that the fluid could flow freely out as the simulation progressed. In contrast to the physical experiments where the cylinder moved through the tank, the cylinder is stationary for the numerical simulations. Therefore, the cylinder faces were set as non-slip, stationary walls.

In the room centred frame of reference the spanwise walls are nominally described as non-slip walls that are fixed in space. However, within the cylinder centred inertial frame of reference the walls "appear" to move past the cylinder at the same rate as Equation (7.1). Therefore, these walls were specified to be non-slip walls that accelerated at the same rate as the inlet.

With the physical experiments conducted at the David Taylor Model basin the lower boundary would be a wall at the bottom of the tank while the upper boundary would be the roof of the facility. However, it was not feasible to simulate to these spatial extents so the vertical domain was artificially reduced and bounded with zero friction walls.

## *7.4. Cylinder Centred Volume Conditions*

In contrast to the room centred inertial frame of reference where the cylinder was accelerated through the nominally quiescent fluids, in the numerical simulations both the fluids, the air and the water, must be accelerated simultaneously with the sidewalls around the stationary cylinder. Therefore, to match the velocity profile specified at the inlet, the acceleration of the fluid volume as a function of time was calculated as the derivative of Equation (7.1), namely;

$$\frac{du_{inlet}}{dt}(t) = \begin{cases} \frac{U_\infty \pi}{4} \sin\left(\frac{\pi t}{2}\right) & \text{for } 0 \le t \le 2 \\ 0 & \text{for } t > 2 \end{cases} . \tag{7.2}$$

This acceleration as a function of time, as shown in Figure 7-5, was applied to every computational cell as a user defined gravitational acceleration in the streamwise direction. In addition to the applied streamwise acceleration, the gravitational acceleration due to the mass of the earth was set at a constant 9.81m/s that acted in the negative *y*-direction, as shown in Figure 7-2.

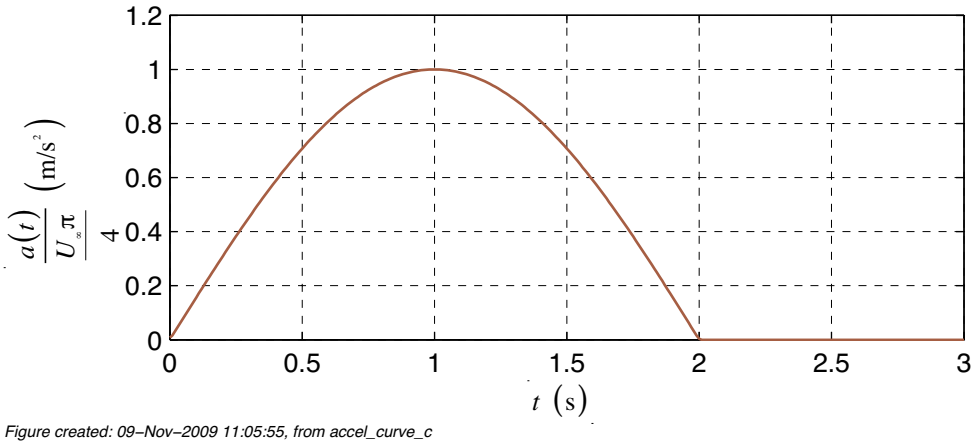


*Figure created: 09–Nov–2009 11:05:55, from accel_curve_c*

**Figure 7-5 – Plot of the normalised acceleration as a function of time.**

## *7.5. Non-Dimensional Numbers*

The final step to maximise consistency between the experiments of Inoue and those of Hay was to define a common non-dimensional parameter. In the simulation of turbulent free surface flows, both the Reynolds number and the Froude number are important as the first is used to characterise the turbulence while the second is used to characterise the free surface. To add further confusion there are two definitions of the Froude number and two possible length scales: the cylinder diameter and the depth of immersion.

For the present work and for most of the comparisons, including the step from the single fluid simulations, the interest is in the turbulent quantities. Therefore, the Reynolds numbers is the critical non-dimensional number that was defined relative to the cylinder diameter,

$$\mathrm{Re}_d = \frac{U_\infty d}{\nu_{water}} \tag{7.3}$$

in which $d$ is the diameter of the cylinder and $U_\infty$ is the velocity with which the cylinder was towed through the water. For the remainder of this dissertation if it is not specifically mentioned in the discussion the reference fluid is water. In contrast, if the air phase were chosen instead the resultant Reynolds number would be lower.

Finally, of the two definitions of the Froude number, unless specifically mentioned otherwise, this non-dimensional number was assumed to be

$$\mathrm{Fr}_d = \frac{U_{ref}^2}{gd} \tag{7.4}$$

in which $g$ is the magnitude of the gravitational vector. As with the square cylinder investigations a number of preliminary studies were undertaken to investigate some of the numerical and geometric assumptions that were presumed to influence the three-dimensional, two-phase simulations.

# 8. Two-Phase Preliminary Studies

## *8.1. Introduction*

Firstly it should be noted that two conclusions from the square cylinder investigations were assumed to be especially relevant to the circular cylinder studies, namely that both the location of the outlet boundary and the grid resolution in the region close to the cylinder surface would affect the computed flow field. For example, when the outlet boundary was located too close to the square cylinder, the computed flow field structures, and by extension the forces felt by the cylinder, were different from those found when the outlet boundary was located further from the cylinder. Further, as the distance from the cylinder to the outlet boundary was increased the flow field stabilised into a periodic shedding regime. Moreover, observations from the square cylinder studies indicated that as the cell size adjacent to the cylinder increased, poor solutions of the flow field resulted. Further, and in contrast to the square cylinder where the sharp corners provided well-defined separation points, the location of the separation points for the circular cylinder change as a function of Reynolds number (Zdravkovich, 1997). Therefore, it could be supposed that the affect of the grid size in the region close to the circular cylinder would be much more significant than is the case with the corresponding square cylinder flow and, hence, warrants further detailed investigation.

In fact, this effect was observed by Fröhlich and Rodi (2004) who numerically investigated finite height circular cylinders in single phase flows at a $\mathrm{Re}_d = 43 \times 10^3$ and described the consequence of insufficient resolution as "drastic". As they reduced the grid resolution, the drag coefficient similarly reduced from 0.88, consistent with published results that were collated by Fröhlich and Rodi, to 0.32. Further, although they did not include the streamline images to which they referred, they argued that, as the grid resolution was reduced, the flow patterns around the cylinder deviated from a "reasonable match" with experimental PIV data to a narrower wake with the "shear layers…shifted towards the symmetry plane" (Fröhlich and Rodi, 2004).

Therefore, in order to develop strategies to ameliorate these potentially adverse effects, a number of preliminary studies were performed on simplified models that reduced the complex, three-dimensional problem into a series of two-dimensional configurations. These simplifications reduced the required computational effort, thereby allowing for a

larger number of variations in a parametric study. The conclusions drawn from the data obtained from these parametric studies could then used to guide the development of the three-dimensional models.

Three studies were performed with the first investigation designed to determine the influence of different hydrostatic pressure distributions across the inlet and outlet boundaries. The second study was envisaged to explore the grid requirements adjacent to the cylinder, while the third was aimed at probing the affect of the location of the outlet boundary position downstream of the circular cylinder.

## *8.2. An Inquiry into the Influence of a Hydrostatic Pressure Variation at the Inlet and Outlet Boundaries*

### 8.2.1. Motivation for this Study

As the density ratio of the water and air used in the present studies was nearly 1000:1, the hydrostatic effect from the air phase at both the inlets and outlets is in most cases assumed to be negligible and, therefore, is often ignored. Hence, the first investigation in the preliminary studies of the two-phase flows was designed to test the effect of different inlet and outlet pressure boundary conditions that are, of course, merely alternate assumptions of the hydrostatic pressure distribution. The hydrostatic pressure distribution in a quiescent fluid is given by

$$p_h = p_0 + \rho g h\,, \tag{8.1}$$

in which $p_0$ is a pressure at the highest point in the region of interest. For example, in an open body of water, such as a lake or river, $p_o$ can be used to describe the pressure on the free surface that is due to atmospheric pressure, which can then change over time as different weather systems move over the water body. Therefore, while the hydrostatic component within the water phase, the second term on the right hand side of Equation (8.1), will be invariant, the pressure felt at any point in the water body will change because of the change in $p_0$.

Suppose that the hydrostatic pressure effect in the air phase is assumed to be negligible, then the pressure distribution over the air phase boundary faces will be uniform. Alternatively, if the hydrostatic pressure effect is assumed to be significant then the pressure distribution across the same boundary faces will be of the form described in

Equation (8.1). To test the validity of these alternate assumptions, a two-dimensional numerical model was designed to represent a vertical slice of an open channel that was flowing half full of water and air without an obstacle such as the right circular cylinder. Two tests were then conducted on this common computational mesh with the first based on the assumption of a hydrostatic pressure variation in the water boundary face only while the second was specified with a hydrostatic pressure variation across both the air and water boundary faces. For the remainder of this chapter these two tests will be referred to as the no air (NA) and with air simulations (WA).

### 8.2.2. Geometric Design, Grid Layout and Solver Configuration

In order to address the alternate hypotheses described above, a two-dimensional mesh envisaged to represent a vertical slice through an open channel was developed, as shown in Figure 8-1.

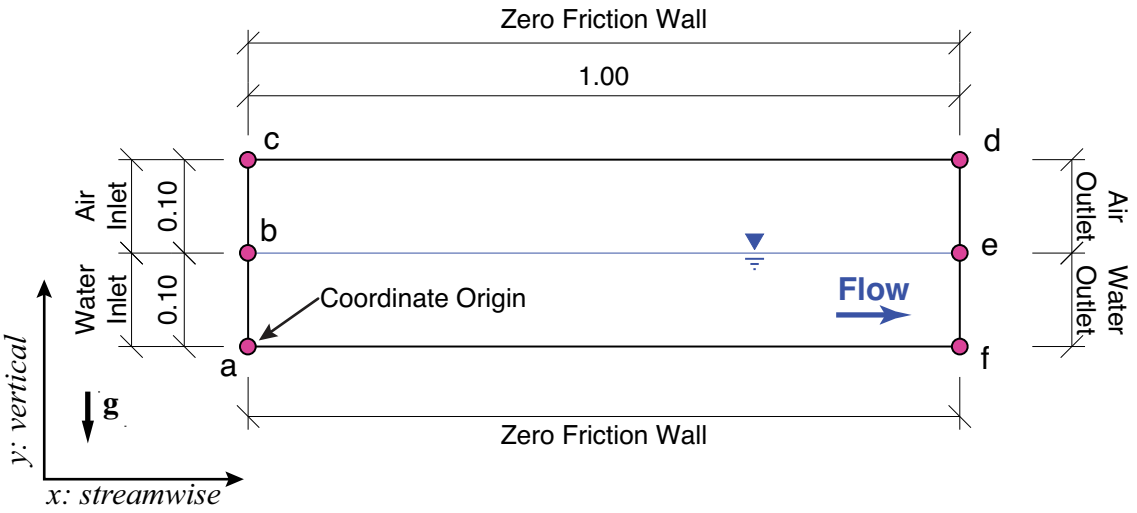


**Figure 8-1 – Sketch of the two-dimensional channel model and the edge and boundary layout used for testing the hydrostatic pressure assumption.**

Further, to maintain similarity with the surface piercing circular cylinder simulations, the Reynolds number, $\mathrm{Re}_h$, was defined as

$$\mathrm{Re}_h = \frac{U_\infty h}{\nu_{water}} = 27 \times 10^3, \tag{8.2}$$

in which $U_\infty$ is the inlet velocity and $h$ is the depth of the water phase. The computational mesh was created from one block that consisted of square cells with a side length 2.5mm. Due to a requirement with the CFD code that a single inlet (or outlet) be specified per phase, the inlet and outlet boundaries were split into a pair of

boundaries with one for the water and the other for the air, as illustrated in Figure 8-1. The edge layout and dimensions are also shown in Figure 8-1 while the number of nodes per edge is detailed in Table 8-1, which resulted in a computational mesh with 16 000 cells.

**Table 8-1 – Edge node count and spacing for the edges sketched in Figure 8-1.**

| Edge | Number of Nodes | Uniform Spacing (mm) |
|---|---|---|
| ab, bc, de, ef | 41 | 2.5 |
| cd, af | 401 | 2.5 |

As an initial condition the domain was split vertically* into water and air phases, as shown in Figure 8-1, but there was no corresponding split in the computational block. The time step was arbitrarily set to 100μs that, with $U_\infty = 0.27\text{m/s}$, resulted in a CFL number of 0.01. $U_\infty$ was specified as a constant velocity for both the air and water inlets, shown in Figure 8-1, as well as for the initial velocity within the entire computational domain. Both the outlet boundaries were set as constant pressure outlets† with the appropriate fluid should the flow appear to be entering rather than leaving the computational domain. The pressure distributions on all the inlets and outlets were based on the hydrostatic profile being tested with zero pressure assumed to act at the top of the domain.

The same second order upwind with limiter spatial differencing scheme as was proposed for the circular cylinder studies was implemented in these trials. Because the time step was so small, it was assumed that there would be relatively little change of the flow between successive time steps. Therefore, to reduce the computation requirements, the solver was restricted to a maximum of ten iterations; a maximum of

* The relative descriptors of "top" and "bottom" are defined relative to the gravitational vector along the vertical axis, shown in Figure 8-1, whereas "left" and "right" refer to the negative $x$ and positive $x$-directions, respectively.

† The description of a boundary as a "constant pressure boundary" is somewhat confusing because, as discussed above, the aim of these tests was to investigate boundaries with and without pressure gradients. However, while the pressure may vary in space, as in these tests, or indeed in time as well, as far as the solver is concerned the pressure is "constant" for a particular time step and spatial coordinate. This particularly confusing nomenclature is reminiscent of the, then, U.S. Secretary of Defence, Donald Rumsfeld's, perplexing, yet appropriate "unknown unknowns" press briefing (Rumsfeld, 2002).

three orders of magnitude of convergence or a minimum residual of $1\times10^{-8}$, whichever occured first. A conjugate gradient solver with preconditioner was specified for the velocity while an adaptive multi-grid solver was used for the pressure corrector.

### 8.2.3. Convergence of the Solver During the Simulations

Prior to discussing the results from the simulations, the convergence of the solver throughout the two simulations must be discussed to assure the reader of the *numerical* accuracy of the data. That is, irrespective of the computed flow being physically improbable it is required to demonstrate that the solver has converged. For this discussion, suppose that $n_{iter}$ represents the number of internal iterations per time step to convergence, then for all, with one notable exception, of the time steps computed the solver converged to the specified limits for both simulations, as shown in Figure 8-2.

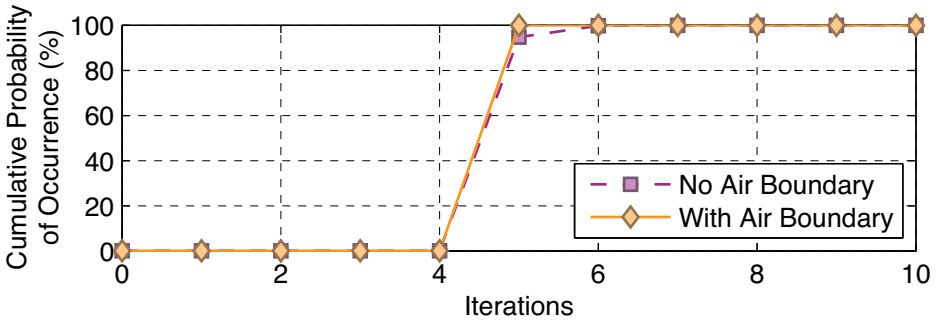


**Figure 8-2 – Cumulative probability distribution of $n_{iter}$ for both the no air and with air simulations.**

The one exception to the otherwise excellent convergence was for the last time step of the no air simulation where the solver diverged. Indeed for all of the WA simulation and for 95% of the NA simulation the convergence criteria were reached by $n_{iter} = 5$ with the remaining five percent of the no air time steps converged by $n_{iter} = 6$. Therefore, to the limits of the specified numerical precision, both the simulations have converged and the flow results can be examined in detail.

### 8.2.4. Observations and Discussions from the Hydrostatic Tests

As presented above, the initial conditions for both simulations was specified with a uniform velocity equal $U_\infty$ and an even air-water split as shown in Figure 8-3.

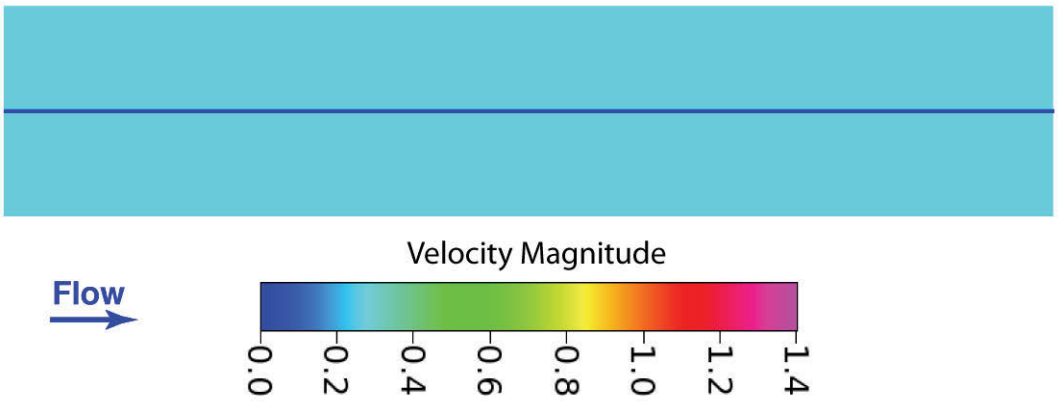


**Figure 8-3 – Snapshot of the flow field at time, $t = 0$, for both simulations with the domain coloured by the fluid velocity magnitude and the free surface a blue line.**

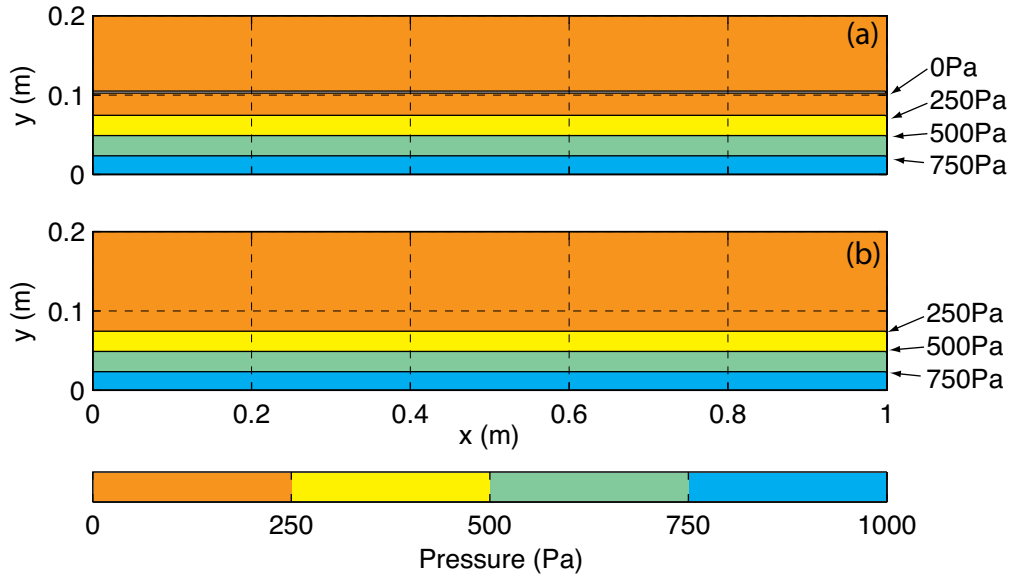


**Figure 8-4 – Snapshot of the pressure distribution at time, $t = 0$, for the no air (a) and the with air (b) simulations.**

Despite the complete specification of the boundary conditions, the initial pressure distribution within the domain was computed by the solver, with the results being shown in Figure 8-4. The vertical pressure gradient from the base of the domain to the free surface is indicative of the expected hydrostatic pressure variation within the water phase. Because the expected hydrostatic variation in the air phase is small relative to that in the water, any changes in the air region are not visible in Figure 8-4. By a similar argument, any small differences in the pressure within the water phases will be disguised by the relatively high pressure at the deepest point of the water phase.

Therefore, to explore the differences between the NA and WA initial conditions a pressure difference function within the two-dimensional domain, $\mathbf{x}$, was defined as

$$\Delta P(\mathbf{x})_{t=0.0s} = P(\mathbf{x})_{NA} - P(\mathbf{x})_{WA} + \rho_{air}\mathbf{g}h_{air}, \tag{8.3}$$

in which $h_{air} = 0.1$ is the height of the air column above the free surface and the subscripts *NA* and *WA* represent the no air and with air simulations, respectively. Because at a simulation time of $t = 0$ the solver had not computed the pressure gradient within the air phase for the no air simulation, the last term in Equation (8.3) was introduced such that $\Delta P(\mathbf{x}_{water})_{t=0.0s} \cong 0$ for the region of the domain that contained water. In contrast, for the with air simulation the solver had computed the hydrostatic pressure variation for the entire domain. Despite the difference in the hydrostatic profile in the air phase and the constant offset, there was only a very small difference in the hydrostatic profile for water phases, as shown in Figure 8-5. Therefore, at least for the initial time step, the pressure specification at the boundaries has propagated into the domain, instead of the solver computing a hydrostatic profile.

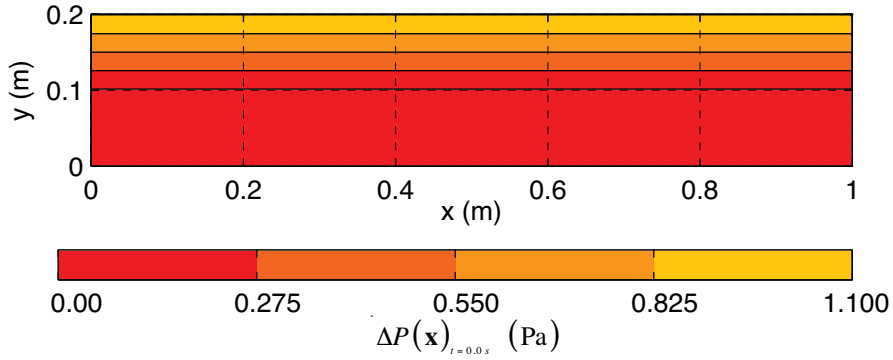


**Figure 8-5 – Contour plot of the pressure differential defined in Equation (8.3).**

By a simulation time of $t = 0.1$ s the velocity field had developed from the uniform initial conditions, shown in Figure 8-3, into the predominantly uniform flow field shown in Figure 8-6. Both the simulations developed velocity defects in the region of the air phase outlet but as the magnitude of the anomaly in the with air case was less than 0.1m/s, or one third of $U_\infty$, it will be neglected for the remainder of this analysis. However, in contrast to the with air case, the maximum velocity defect in the no air case was in the order of 1.3 m/s or nearly five times the free stream velocity as shown in the top right of Figure 8-6(a).

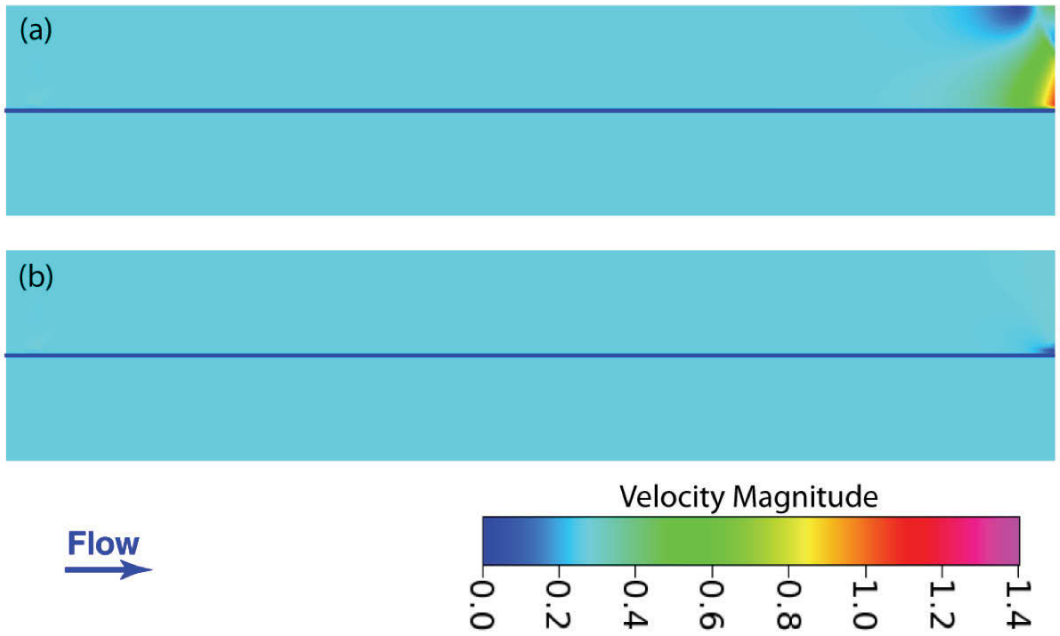


**Figure 8-6 – Visualisation of the velocity magnitude and the location of the free surface at a $t$ = 0.1s for the no air (a) and the with air (b) simulations.**

The main disadvantage of velocity magnitude visualisations is that there is no indication of the direction of the velocity, whereas velocity vectors can provide further information to quantify the flow features. In the present simulation with no hydrostatic pressure in the air phase boundaries, the velocity disturbance observed in Figure 8-6(a) was in fact a recirculation zone, as shown in Figure 8-7(a). That is, with the velocity vectors at the top of the domain observed to be pointing into the domain, air was being transported across what was nominally an outlet face and into the domain. Due to the interaction with the upstream flows, this incoming air was then turned around and accelerated out of the domain approximately parallel to the water surface. In contrast, no such recirculation was observed in the simulation with the hydrostatic pressure variation in the air outlet boundaries, as shown in Figure 8-7(b).

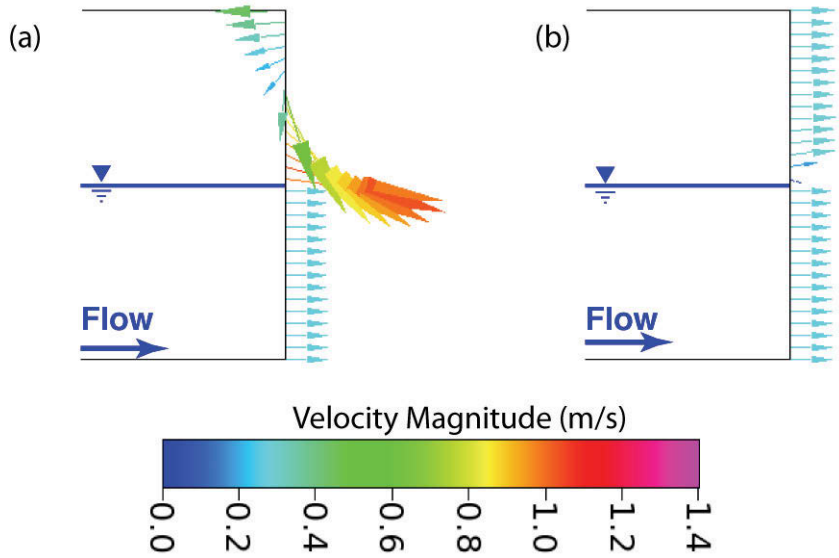


**Figure 8-7 – Velocity vectors coloured by their magnitude at the air and water outlets at time $t = 0.1$s for the no air and the with air cases, (a) and (b) respectively.**

It seems highly unlikely that a recirculation type flow feature such as that visible in Figure 8-6(a) and Figure 8-7(a) would occur naturally. Therefore, as a similar unphysical flow feature was not observed in the with air simulation it must be due to the non-hydrostatic boundary conditions in the no air simulation. With the benefit of hindsight, this conclusion should have been apparent, as the non-hydrostatic boundary is itself an unphysical assumption. Therefore, if the pressure is the driver of the recirculation it must be investigated later in the analysis of these experiments.

By $t = 0.1$s both the no air and with air simulations had developed hydrostatic pressure profiles across the air and water phases, as shown in Figure 8-8, whose differences were indistinguishable at the scale used in Figure 8-8.

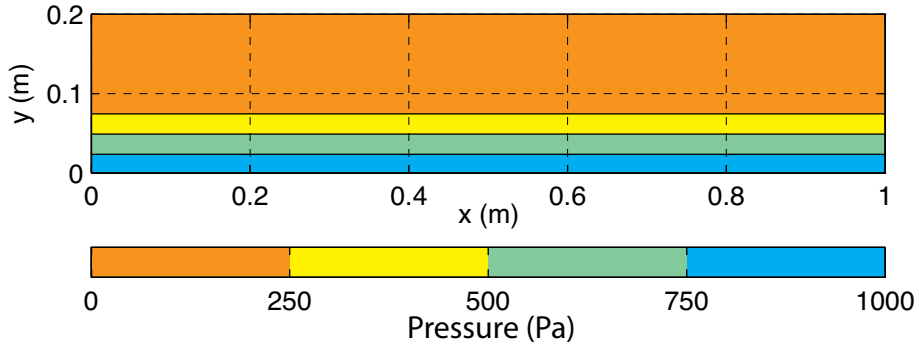


**Figure 8-8 – Indicative pressure distribution at $t = 0.1$ s for the two simulations.**

Therefore, to quantify the differences in the pressure field a difference function, similar to Equation (8.3), was defined as

$$\Delta P(\mathbf{x})_{t=0.1s} = P(\mathbf{x})_{NA} - P(\mathbf{x})_{WA} + c_{\Delta P} \tag{8.4}$$

in which $c_{\Delta P} = 0.3029\text{Pa}$ was defined such that

$$\Delta P(\mathbf{x})_{t=0.1s} \cong 0 \tag{8.5}$$

for the majority of the computational region. The exception to this generally uniform pressure difference was close to the outlet boundaries, where there was a positive pressure difference across the upper half of the air outlet and a negative pressure difference over the lower half, as shown in Figure 8-9. These pressure differences are indicative of, and in fact are, the drivers of the recirculation zone at the outlet. The difference in the pressure in the water phase is due to the hydrostatic effect described in Equation (8.1) where the high pressure at the lower side of the air outlet has increased $p_0$.

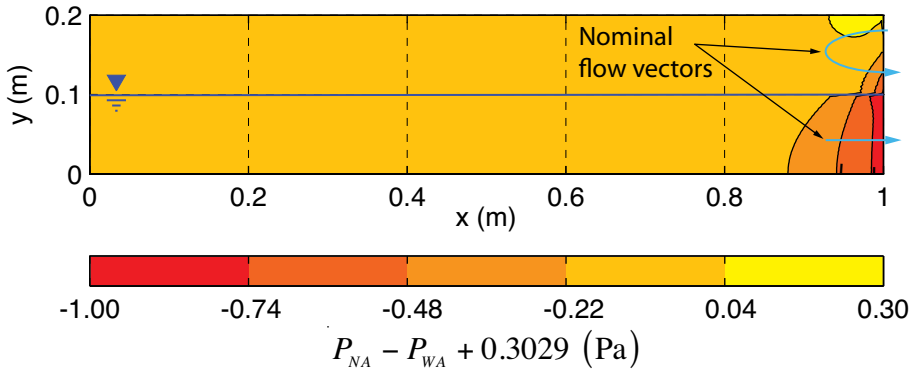


**Figure 8-9 – Contour plots of the pressure differential defined in Equation (8.4).**

Further, the constant pressure difference in the majority of the computational domain is a result of the solver enforcing continuity. That is, because of the recirculation zone at the outlet the air flows coming from upstream have to work harder to exit the domain. Therefore, as the pressure has been specified at the outlet, the upstream inlet was forced to increase the incoming pressure to overcome the constriction at the outlet. However, both the simulations computed the flows for simulation times greater than 0.1 s.

By $t = 5.1$ s the recirculation zone had both expanded, Figure 8-10(a) compared with Figure 8-6(a), and strengthened, Figure 8-11(a) compared with Figure 8-7(a), which

provided further support for the pressure imbalance explanation as the leading cause of the instabilities observed in the results from the no air simulation.

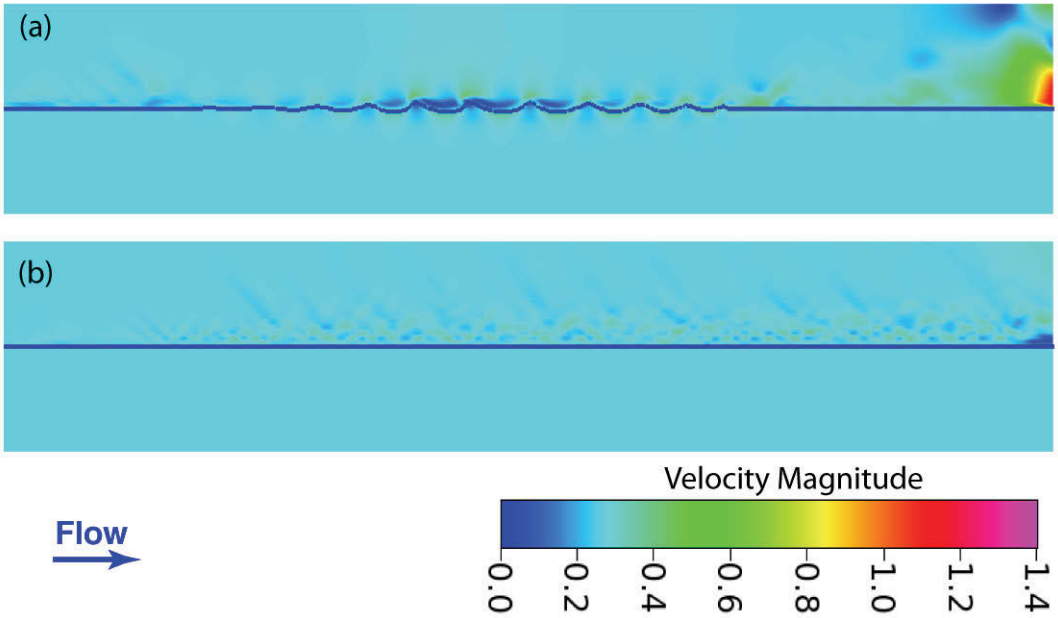


**Figure 8-10 – Snapshot of the flow field at *t*=5.1s for the no air (a) and the with air (b) simulations with the domain coloured by the velocity magnitude and the free surface by a solid blue line.**

In the no air simulation near the centre of the domain, at $x = 0.5\text{m}$, free surface waves developed to an amplitude in the order of 5mm and were associated with maximum velocities of 0.4m/s, as shown in Figure 8-10(a). In contrast, waves of this scale were not observed in the with air simulation, instead small amplitude, so small as to be invisible in Figure 8-10(b), and low velocity disturbances in the air phase were observed as shown in Figure 8-10(b). However, the formation of small ripples and associated velocites, such as those observed in the present work, were expected and further were assumed to be analogous to the "boils" observed in open channel and river flow (Nezu and Nakagawa, 1993, Sturm, 2001). From these observations that were made for $t \leq 5.1\,s$, the recirculation zone that was observed in the no air simulation should continue to expand upstream before stabilising and the associated recirculation zone would drive the formation of more unphysical free surface waves. However, because the computational solver used with the no air simulation diverged shortly after $t = 5.1\text{s}$ these projections could not be tested.

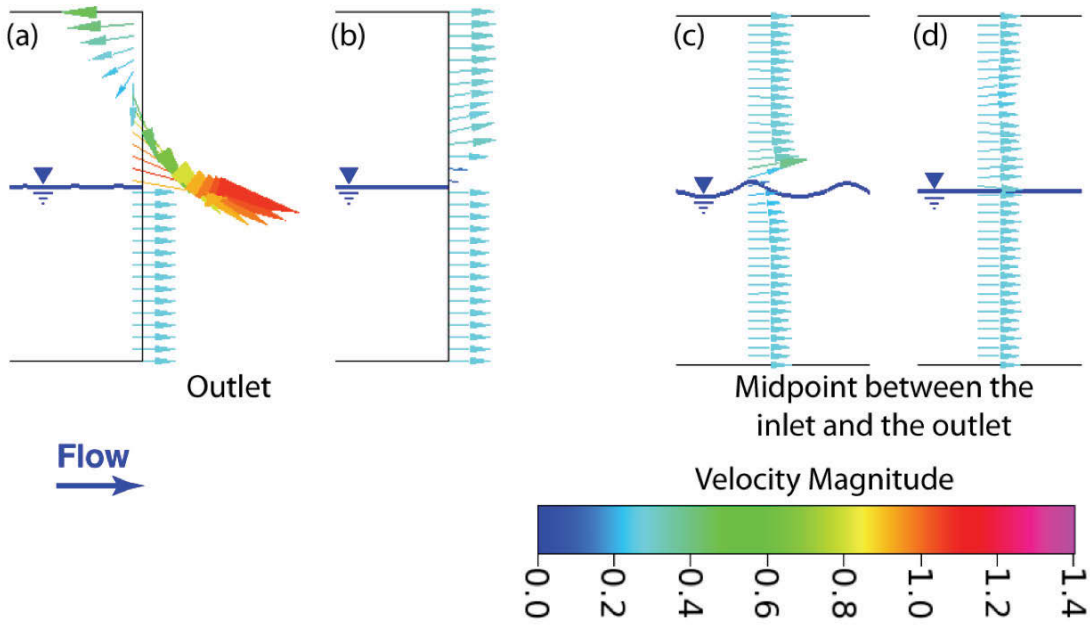


**Figure 8-11 – Velocity vectors along constant x lines for the no air simulation – subplots (a) and (c) – and the with air model – subplots (b) and (d).**

When the free surface waves formed, the maximum velocity of the fluid close to the free surface was in the order of double the inlet velocity. Because of this increased velocity, the free surface CFL would also be double that which had been originally assumed. Since the VOF model is known to be very sensitive to the rate of movement of the free surface (ESI CFD Inc., 2007a), which may differ significantly from the local velocity of the fluid, it is not surprising that the computations diverged.

To test the sensitivity of these free surface waves to changes in the solution scheme the numerical damping and relaxation parameters within the solver were both increased. However, despite the increased damping the unphysical waves still developed, which indicated that they are independent of the solution algorithm and numerical damping.

The with air simulation was arbitrarily stopped at $t = 40\text{s}$ because there was no appreciable change in the observed flow patterns.

With these observations that were made over 5.1 s and 40 s of simulation time for the no air and with air simulations, respectively, it can be concluded that the pressure imbalance that results from the incorrect specification at the air phase outlet boundary is the cause of the recirculation zone. That is, because of the relatively high-pressure difference in the region of the free surface, air will be driven out of the domain faster than it is supplied from the upstream channel and inlet. Therefore, to satisfy continuity,

air must be drawn in through the upper zone of the outlet boundary where there is a lower pressure differential: an affect that is sketched in Figure 8-12. Then, as the incoming flow from the outlet boundary moves upstream and interacts with the fluid flowing downstream from the inlet and because both the zero friction wall and the free surface act as a fixed boundaries, the flows will be directed down and towards the outlet. Hence, the returning flows have created the recirculation zone, observed in Figure 8-7(a). By extension, the upstream extent of the recirculation zone would be controlled by the energy balance between the fluid travelling downstream from the entrance and the fluid moving upstream from the inlet.

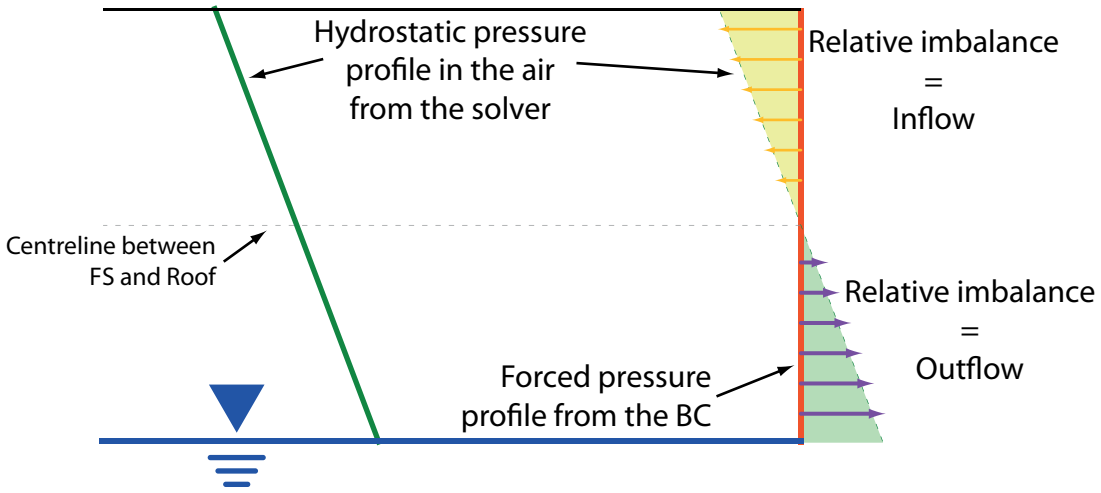


**Figure 8-12 – Sketch of pressure imbalances causing unphysical boundary flows.**

Several observations were made from both these simulations, namely that (1) a large, high speed recirculation zone located adjacent to the air phase outlet boundary developed early in the simulation and (2) that large and growing free surface waves developed in the domain. The recirculation zone was observed at the air phase outlet boundary at low simulation times and was characterised by velocities in the order of five times $U_{\infty}$. As the simulation progressed, the effects of this recirculation zone extended upstream and impinged on the free surface, which initiated large amplitude waves with high trough velocities. Both of these observed flow features are unphysical and neither the large recirculation zone nor the large free surface waves were observed in the simulation designed with a hydrostatic pressure variation in both the water and air phases. Therefore, these twin but interrelated phenomena ultimately caused the solver to diverge. It follows that the full hydrostatic pressure distribution must be specified at the outlet boundaries. In contrast to the outlet boundaries, for inlets that are specified as

constant velocity inlets, the solver adjusts the pressure as required. Having completed the first preliminary study and determined the appropriate boundary conditions at the inlet and outlet of the computational region, the details of the mesh needed for accurate solutions needed to be determined.

## 8.3. A Study of the Grid and Geometric Configurations

### 8.3.1. Motivation for these Studies

The remaining two preliminary studies are presented consecutively in §8.3 because they were both based on the same two-dimensional simplification of the three-dimensional tow tank, as shown in Figure 8-13(a). These two parametric studies were designed to, separately, quantify the affect of varying the distance to the outlet boundary from the cylinder, $\mathfrak{L}$, and changing the size of the cell adjacent to the wall, $\mathfrak{F}$, on the simulated flow fields. Both of these parameters is shown in Figure 8-13,

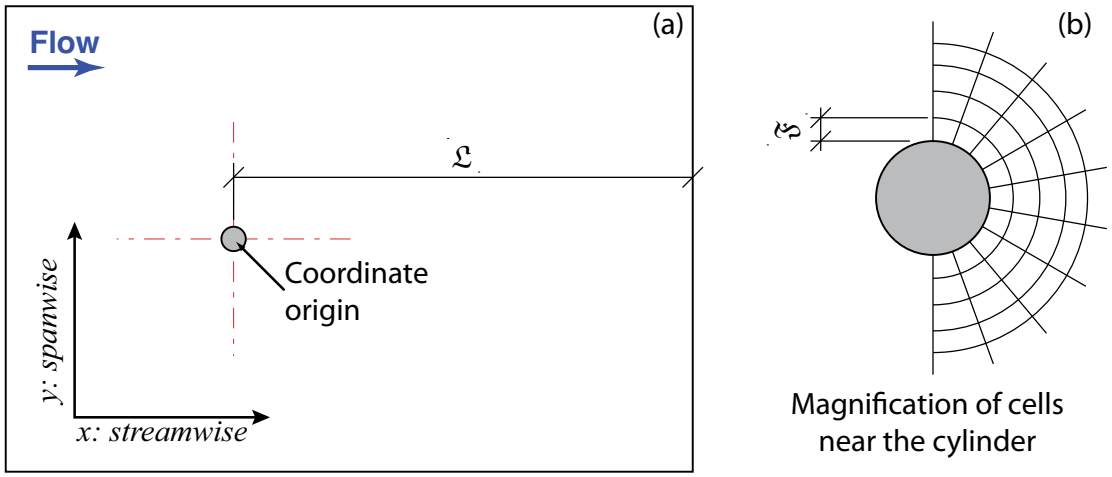


**Figure 8-13 – Sketch of the two-dimensional plane used in the geometry tests with the length to the outlet boundary, $\mathfrak{L}$, and the wall normal cell size, $\mathfrak{F}$, shown.**

Within each study a number of test simulations were conducted where the parameter under investigation was modified. For the $\mathfrak{L}$ tests, the distance was varied from 400mm to 2998mm in non-uniform increments. Separately, in the $\mathfrak{F}$ simulations the cell side length was varied from 50μm to 5mm in, similarly, non-uniform steps.

The Reynolds number, $\mathrm{Re}_d$, for these two studies was defined as

$$\mathrm{Re}_d = \frac{U_\infty d}{\nu} = 27 \times 10^3, \tag{8.6}$$

which was based on the cylinder diameter, $d$, and the free stream velocity, $U_\infty$. Because for a given velocity in the three-dimensional simulations with a free surface, the water phase would be at a higher Reynolds number, that is as $\nu_{water} \ll \nu_{air}$ then $\mathrm{Re}_{water} \gg \mathrm{Re}_{air}$, and hence be more turbulent, the fluid used in these two studies was water.

Finally, as the two parametric studies described in this section were each carried out simultaneously, there was no data on $\mathfrak{L}$ that could be used as an input for the parametric study of $\mathfrak{F}$ and vice versa. Hence, an arbitrarily small $\mathfrak{F}$ was used for the $\mathfrak{L}$ tests and, similarly, an intermediate $\mathfrak{L}$ was chosen to place the outlet boundary for the determination of $\mathfrak{F}$. With these common specifications for the basis of the parametric tests a computational domain was developed that, with suitable minor amendments, could be used as the foundation for the projected simulations.

### 8.3.2. Geometric Design and Grid Layout: Common Parameters

The computational mesh used as the basis for all the tests described in this section was designed to represent a horizontal slice of the David Taylor Model Basin, shown in Figure 8-13(a). With the fluid specified as water and $\mathrm{Re}_d = 27 \times 10^3$, the characteristic velocity was fixed at $U_\infty = 0.54$ m/s, which was the same as the three-dimensional simulations with a free surface. With the exception of the grid for the shortest $\mathfrak{L}$ simulation, all the grids consisted of six structured blocks and one unstructured block, as shown in Figure 8-14. The cells within the structured blocks adjacent to the outer walls, the inlet faces and the outlet faces were composed of uniform square cells while the two, inner structured blocks adjacent to the cylinder were developed as an O-Type topology, shown in Figure 8-15.

To create a smooth transition from the inner O-Topology blocks to the outer square cells a single unstructured domain, shown in Figure 8-15, was created. The unstructured domain was constructed with quadrilateral cells whose spacing was controlled using the paving algorithm available in the code (ESI CFD Inc., 2007c). Further, the cells adjacent to the structured blocks were fixed to the nodes to enforce a smooth boundary between blocks.

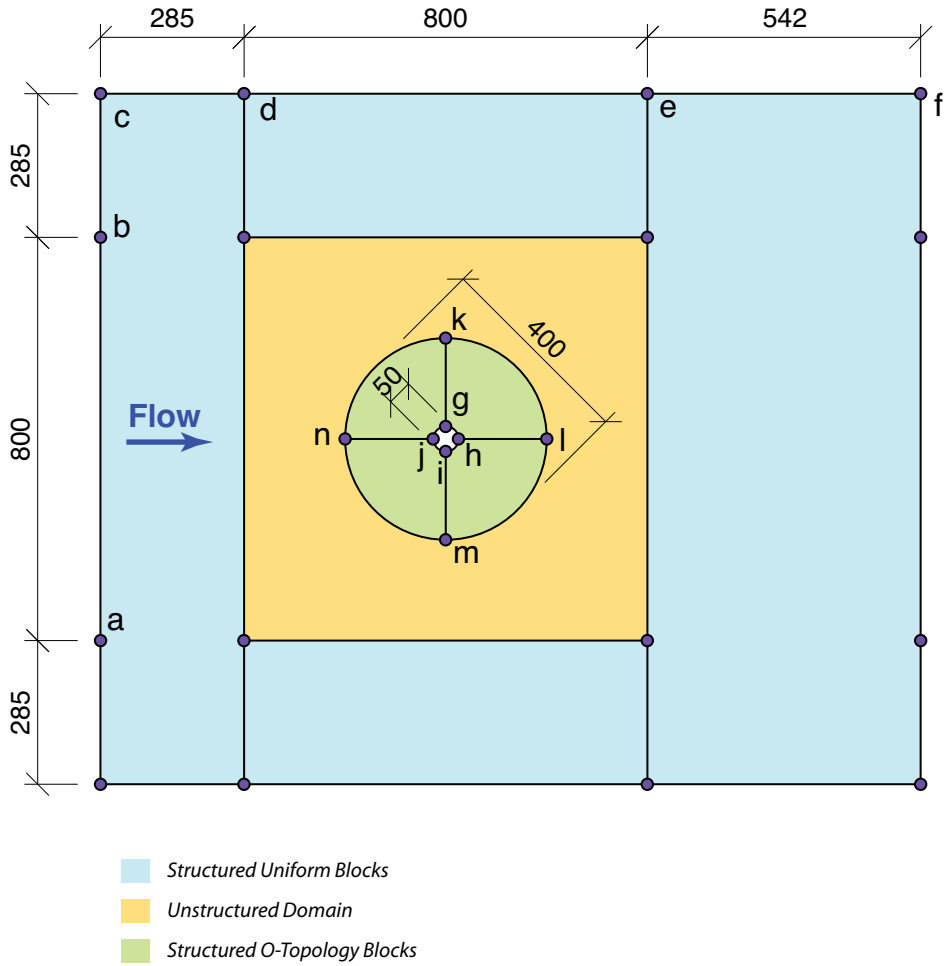


**Figure 8-14 – Dimensional sketch (in millimetres) and grid layout for the two-dimensional mesh used in testing the size of the inner cylinder cell.**

The nodes along the four radial edges that emanated from the central cylinder, for example edge gk as shown in Figure 8-14, were distributed using the hyperbolic tangent stretching function (Vinokur, 1980, Vinokur, 1983) described in §5.3, while the nodes along the remaining edges were uniformly distributed. A list of the number of nodes distributed along each edge is given in Table 8-2, with edge ends identified in Figure 8-14. For the four edges with a hyperbolic tangent spacing, the outer nodal space was fixed at 20mm for all the tests whereas the inner nodal space was varied, for the $\mathfrak{F}$ tests, as specified below.

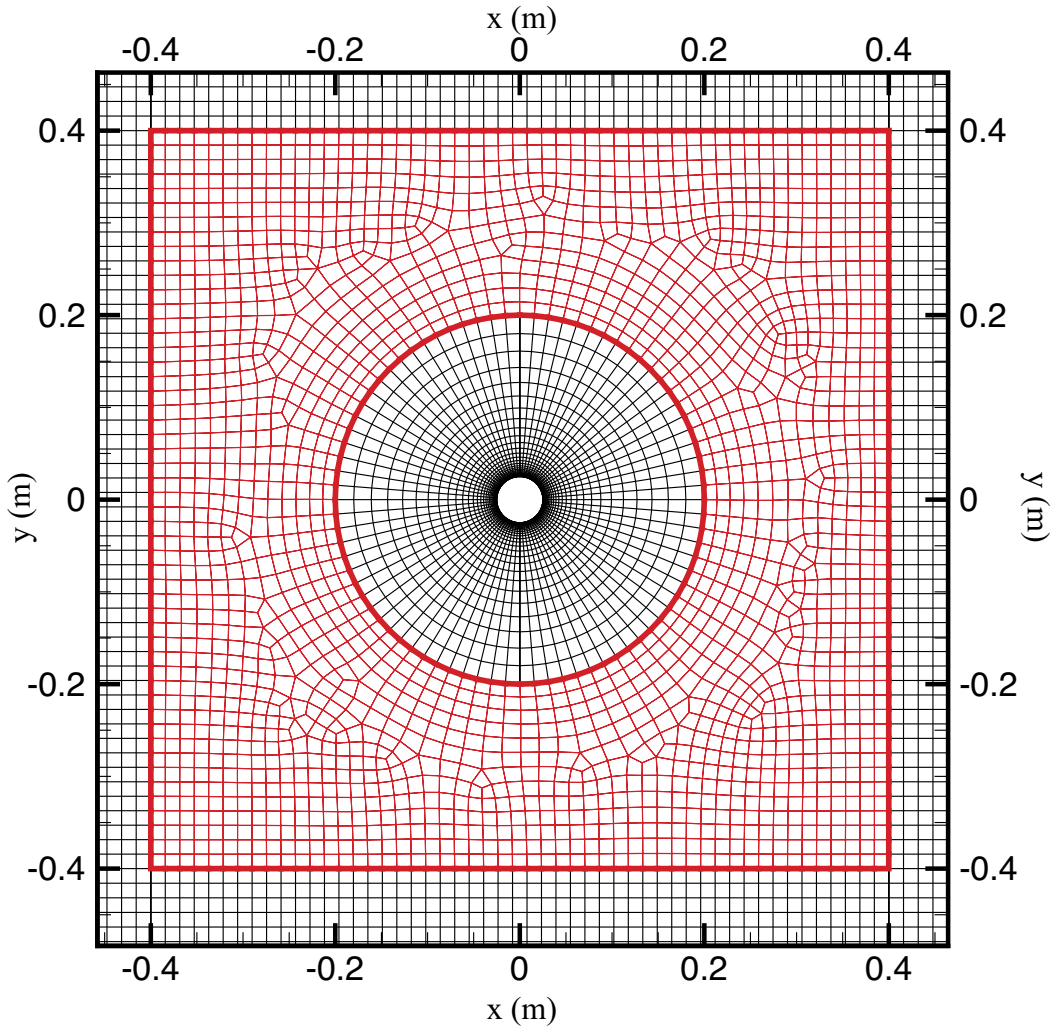


**Figure 8-15 – Magnification of the central structured O-Type domains adjacent to the cylinder and the transitional unstructured domain.**

**Table 8-2 – Edge list and node count for edges that are common for all the models, with nodes spaced uniformly (unless noted otherwise) across all the listed edges.**

| Edge/s | Number of Nodes |
|---|---|
| bc, cd | 19 |
| de | 52 |
| ml, lk, kn, nm, gh, ki, ij, jg | 21 |
| ef | 35 |
| jn, gk, hl, in – hyperbolic tangent distribution | 37 |

### 8.3.3. Geometric Design and Grid Layout: Test Specific Modifications

The only changes made to the base model described above in §8.3.2 for the $\mathfrak{F}$ tests were to the four radial edges identified as gk in Figure 8-14. The cell length at the end of the edge furthest from the cylinder was fixed at 20mm, while $\mathfrak{F}$ was set to 0.05 mm, 0.15 mm, 0.25 mm, 0.50 mm, 1.00 mm and 5.00 mm for the six simulations, respectively. For the five shortest $\mathfrak{F}$ simulations, the number of nodes along gk was constant at 37 whereas for the longest $\mathfrak{F}$ there were 19 nodes that resulted in a cell count of 12 000 and 9 750 cells respectively, as shown in Figure 8-16. Because of the six lengths of $\mathfrak{F}$ chosen, the distribution of the cells and cell sizes along the edge also changed for each computational test as shown in Figure 8-17.

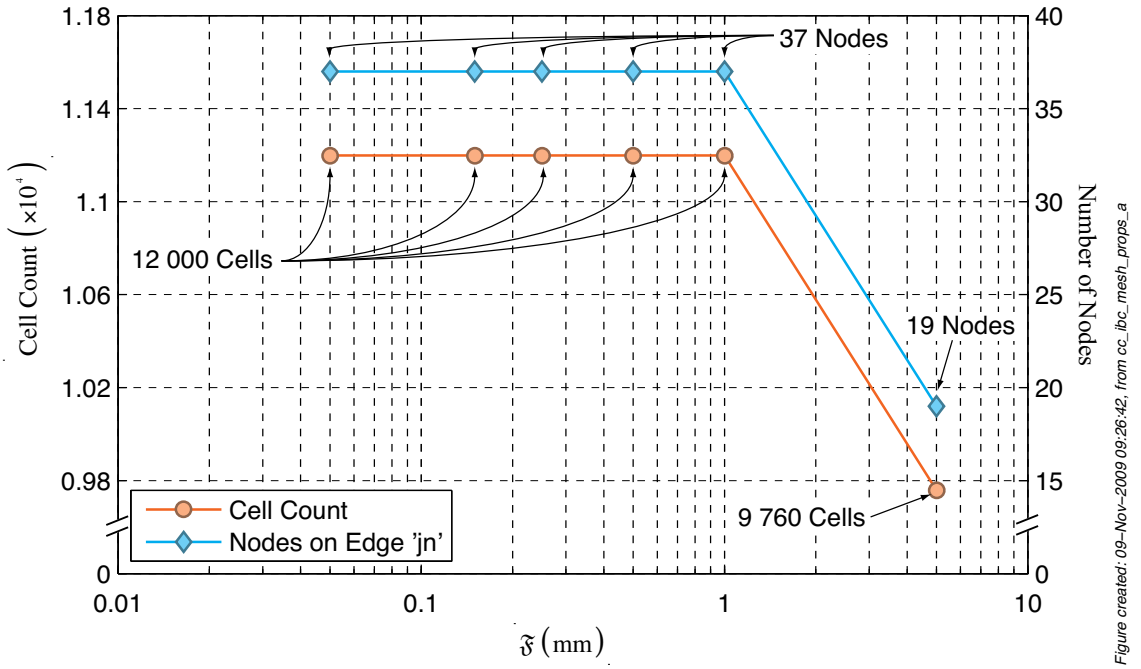


**Figure 8-16 – Cell count and number of nodes along edge jn for the six $\mathfrak{F}$ meshes.**

For all the $\mathfrak{L}$ tests, $\mathfrak{F}$ was fixed at 0.15mm and the length of the edge ef was changed to adjust $\mathfrak{L}$ as per the list in Table 8-3 and Figure 8-18. The number of nodes distributed along the edges was computed so that the nodal spacing in the downstream block was similar for all the tests.

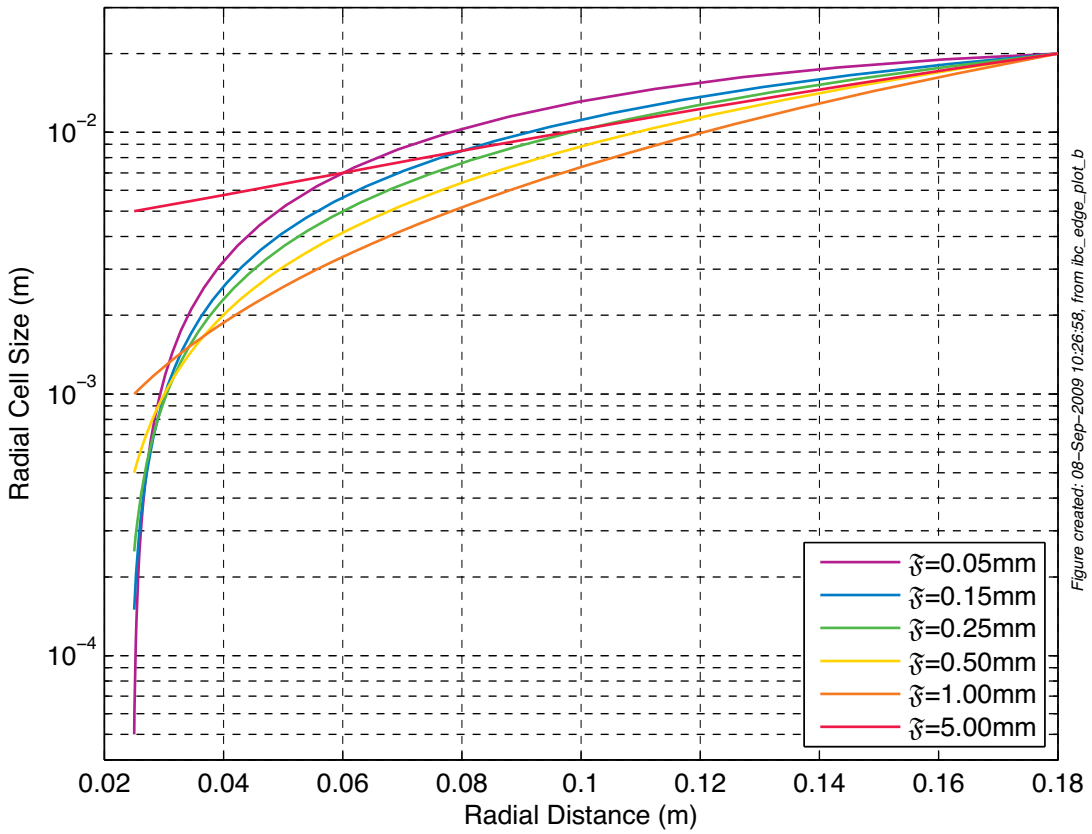


**Figure 8-17 – Plot of the radial cell size as a function of the radial distance for six tests of different wall normal cell sizes.**

**Table 8-3 – Length and number of the nodes for the variable length edge ef shown in Figure 8-14 for the length to the outlet boundary tests.**

| Length of Edge (mm) | ℒ (mm) | Number of Nodes | Cell Count |
|---|---|---|---|
| 0 | 400 | 0 | 8 240 |
| 285 | 685 | 19 | 9 810 |
| 542 | 942 | 35 | 11 200 |
| 799 | 1199 | 52 | 12 700 |
| 1056 | 1456 | 68 | 14 100 |
| 1313 | 1713 | 85 | 15 500 |
| 1570 | 1970 | 101 | 16 900 |
| 1827 | 2227 | 117 | 18 300 |
| 2084 | 2484 | 131 | 19 500 |
| 2341 | 2741 | 150 | 21 200 |
| 2598 | 2998 | 166 | 22 600 |

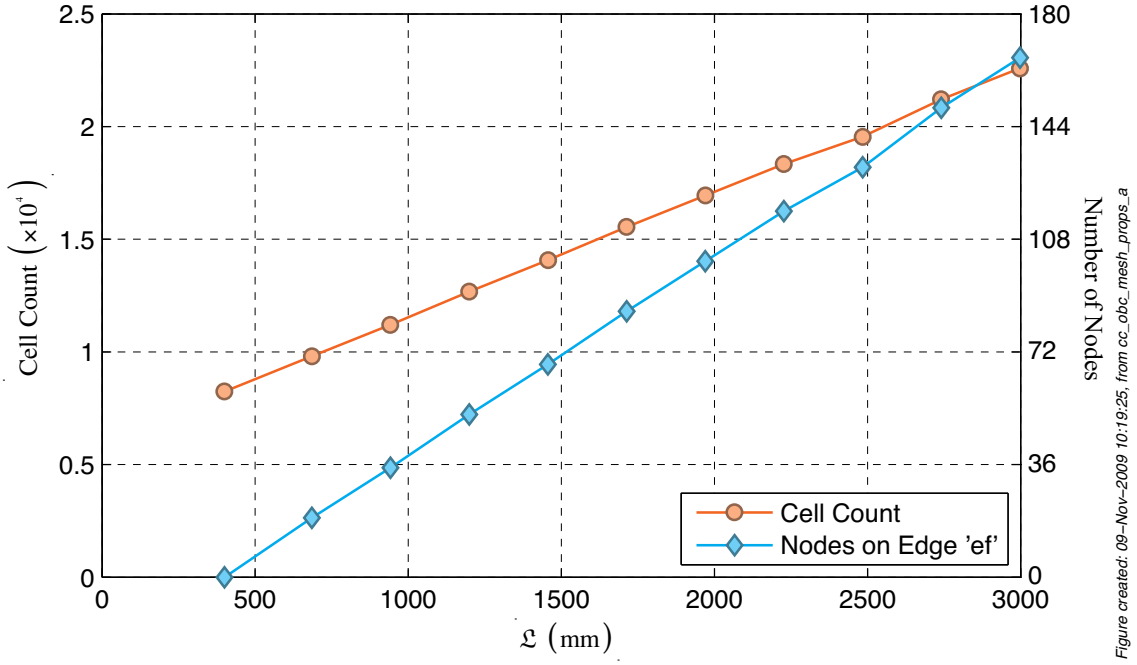


**Figure 8-18 – Cell count and number of nodes along edge ef for the 11 simulations of ℒ.**

### 8.3.4. Solver Configuration

With the geometry of the computational models fully described, the configuration of the numerical solver can be discussed. Because the time step of the simulations was set to 2.5 μs, it was assumed that there would be little change in the flow field between time steps. Therefore, to reduce the computational requirements, the solver specified to have converged at a maximum of ten iterations per time step or at three orders of magnitude reduction in the residuals or a minimum residual of $1\times10^{-8}$. The detail of the application of these convergence criteria is presented in Appendix A.

As with the simulations presented in §8.2, the same second order upwind with limiter spatial differencing scheme as proposed for the three-dimensional free surface models was used in these investigations. A conjugate gradient solver with preconditioner was used for the velocity while an adaptive multi-grid solver was used for the pressure corrector scheme.

Notwithstanding the two-dimensional approximations, these simplified models were thought to reasonably represent the situation below the water level of the three-dimensional models. Therefore, the boundary conditions in the present study matched those proposed for the three-dimensional models, as shown for the *xz*-plane in Figure

7-2. Further, because of the change in the inertial frame of reference proposed for the three-dimensional simulations, the spanwise walls were set as non-slip but moving walls. A full account of the change of the inertial frame of reference is presented in §7.3.

### 8.3.5. Point Probe Locations

After the grid geometry had been settled and solver parameters specified, seven point "probes" were distributed within the computational domain. These points were distributed between the downstream face of the circular cylinder and the shortest outlet length, $\mathfrak{L} = 400$ mm, at the locations shown in Figure 8-19, such that the data collected from these "probes" could be compared across all the simulations discussed in this section. The two velocity components (i.e. $u$ and $v$) and the pressure were recorded at all time steps for all the "probes".

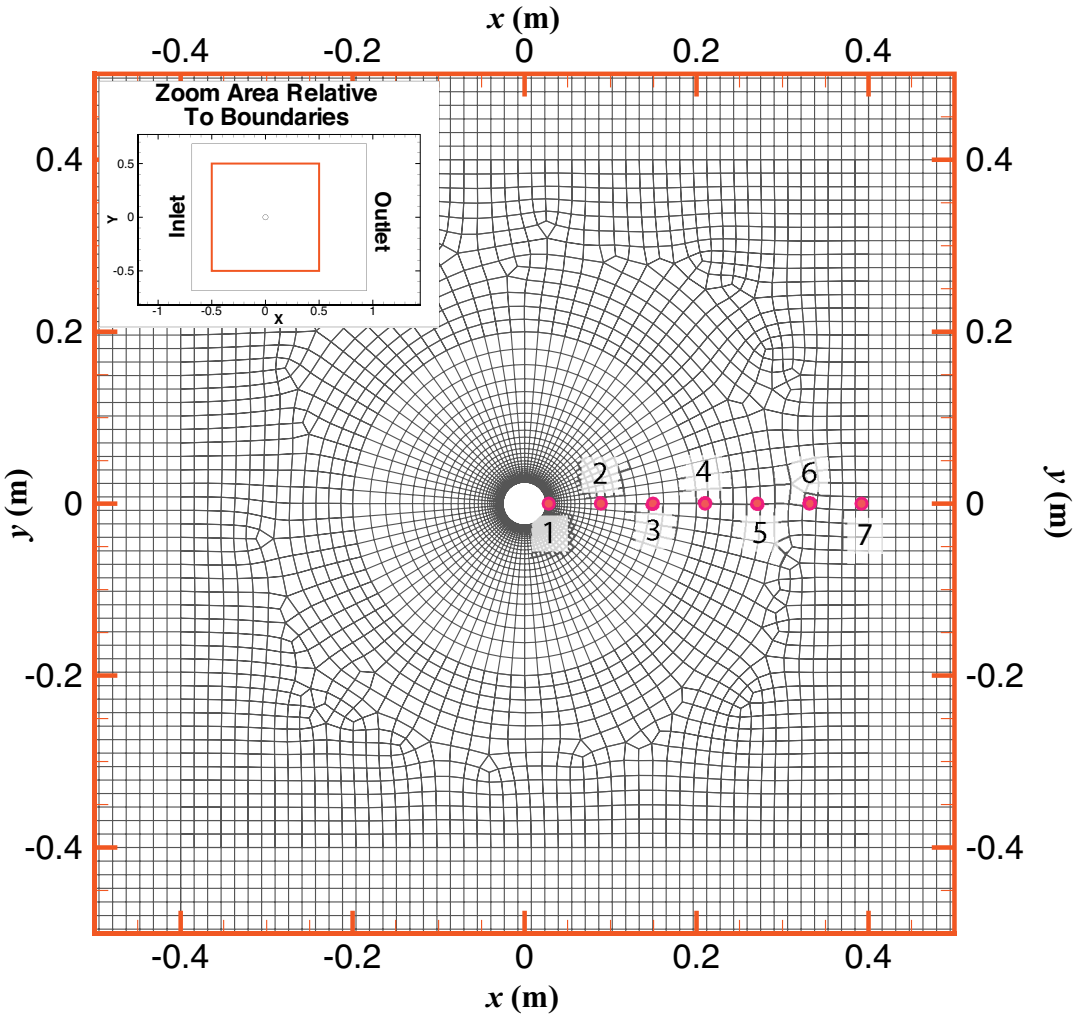


**Figure 8-19 – Plot of the point probe locations.**

### 8.3.6. Convergence of the Solver During the $\mathfrak{F}$ Simulations

Of the two studies described in §8.3, the $\mathfrak{F}$ simulations will be discussed first however, as with the studies presented above, prior to a detailed discussion of the results the convergence of the solver will be examined first. For the $\mathfrak{F}$ simulations all the time steps computed converged within six iterations for all of the four million time steps computed per simulation, as shown in Figure 8-20.

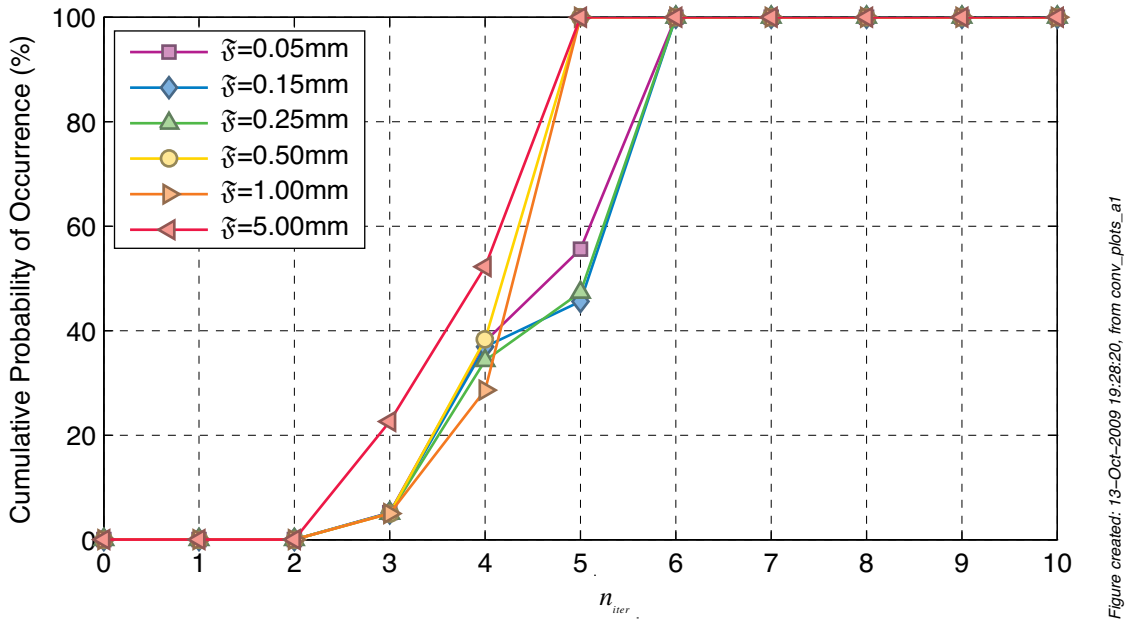


**Figure 8-20 – Cumulative probability distributions of $n_{iter}$ for the six $\mathfrak{F}$ simulations.**

Therefore, as all the simulations converged within six iterations the simulations were converged to the limits of the specified numerical accuracy. However, despite the apparent numerical convergence the computed flow field still requires critical examination.

### 8.3.7. Observations from the Parametric Tests of $\mathfrak{F}$

After a development period of around two seconds, which agreed with the initial acceleration described in §7.3, the drag and lift coefficients from the simulation with the largest cell size – $\mathfrak{F} = 5.00$ mm – stabilised at approximately 0.25 and zero, respectively, as shown in Figure 8-21(a). Because these coefficients stabilised at fixed values with no periodic fluctuations that are the hallmark of cyclical vortex shedding it is highly unlikely that any periodic shedding from the cylinder occurred during the simulations.

As $\mathfrak{F}$ was decreased to 1.00mm, some shedding was observed in the variation of the lift coefficients as a function of time, as shown in Figure 8-21(b). However, the RMS of the lift coefficient of approximately 0.25 from this simulation is still lower than the published value of 0.66±0.13 (Zdravkovich, 1997). The drag coefficient from the $\mathfrak{F} = 1.00$ mm simulation is very similar to that from the $\mathfrak{F} = 5.00$ mm simulation both of which are below the accepted drag value of 1.2 (Zdravkovich, 1997).

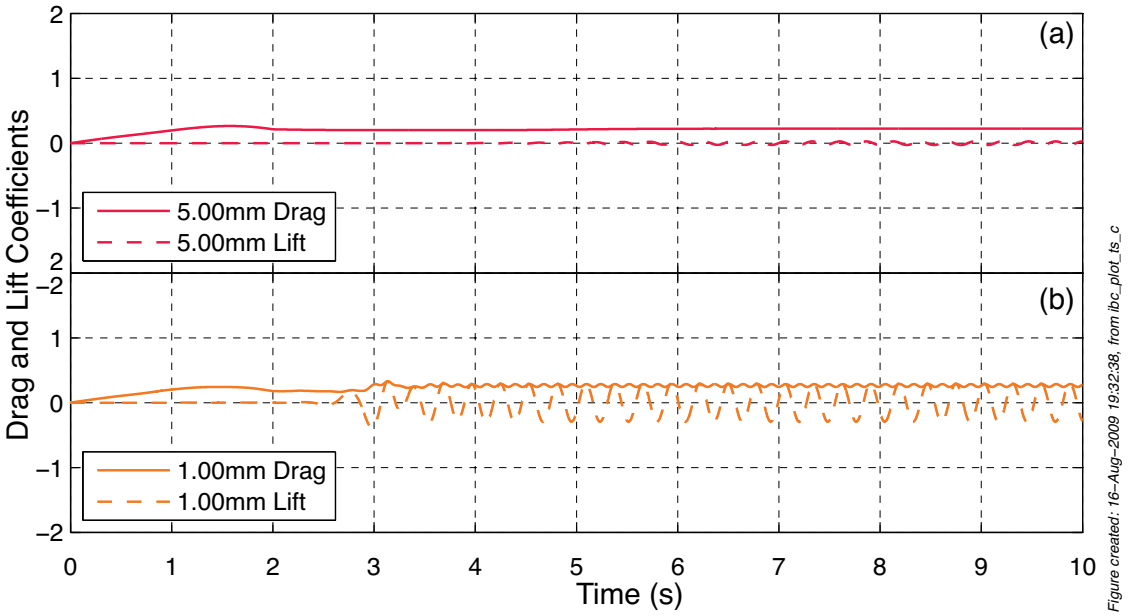


**Figure 8-21 – $C_D$ and $C_L$ as a function of time from the $\mathfrak{F}$ = 5mm and $\mathfrak{F}$ = 1mm simulations, (a) and (b) respectively.**

Despite a lack of clear evidence of periodic shedding in the plot of $C_D(t)$ and $C_L(t)$ from the $\mathfrak{F}$=5.00mm simulation, as shown in Figure 8-21(a), a small periodic shedding flow pattern was computed further downstream in the wake, as shown in Figure 8-22. The lack of shedding at the cylinder is because $\mathfrak{F} = 5.00$ mm is too large to capture the boundary layer around the cylinder, visible in Figure 8-22 by the relatively large region of low-speed blue and green coloured flow that completely surrounds the cylinder. Therefore, as the simulation could not capture the boundary layer adequately it could not possibly capture the separation points accurately and, by extension, develop realistic flow patterns.

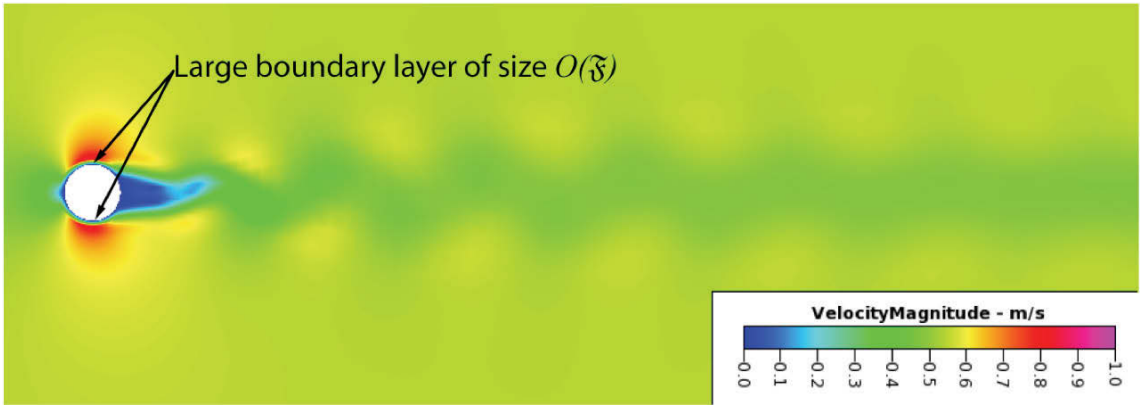


**Figure 8-22 – Velocity magnitude of the flow field from the $\mathfrak{F}$ = 5mm simulation.**

In contrast, as shown in Figure 8-23, with $\mathfrak{F}$ reduced to 0.50mm, fully developed vortex shedding and the associated von Kámán vortex street are observed. This observation provides further support to the well-known numerical requirement that unless the boundary layer is adequately resolved the flow field will not be computed correctly.

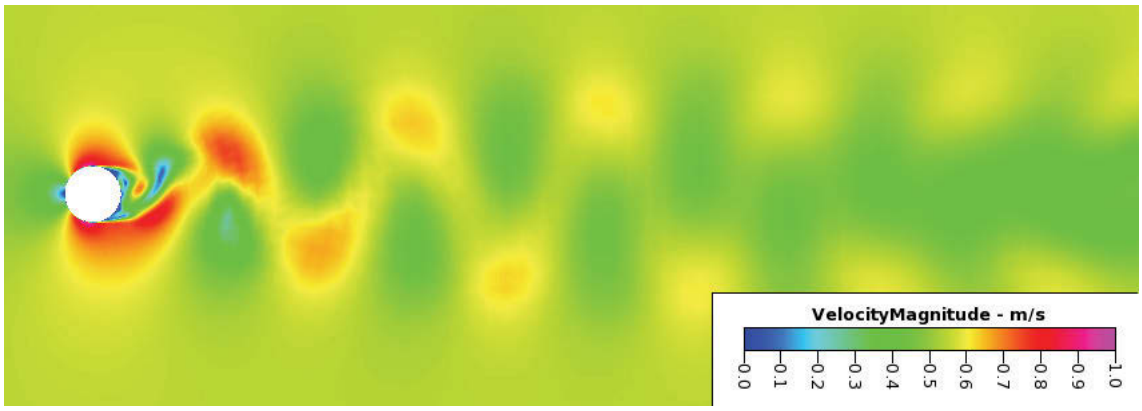


**Figure 8-23 – Velocity magnitude of the image from the $\mathfrak{F}$ = 0.50mm simulation.**

As would be expected with a flow field that is characterised by periodic vortex shedding, such as that shown in Figure 8-23, fluctuations in the corresponding lift and drag coefficients were observed and are shown in Figure 8-24. The RMS lift coefficient from the $\mathfrak{F} = 0.50$ mm simulation was 0.54 that is within the range of published data of 0.66±0.13 (Zdravkovich, 1997), albeit very close to the lower bound. Despite the potential agreement of the RMS lift coefficient, the drag coefficient value of approximately 0.6 is well below the published value of 1.2 (Zdravkovich, 1997). Both of these values are, however, improvements on the results computed from the $\mathfrak{F} = 5.00$ mm and $\mathfrak{F} = 1.00$ mm simulations discussed above.

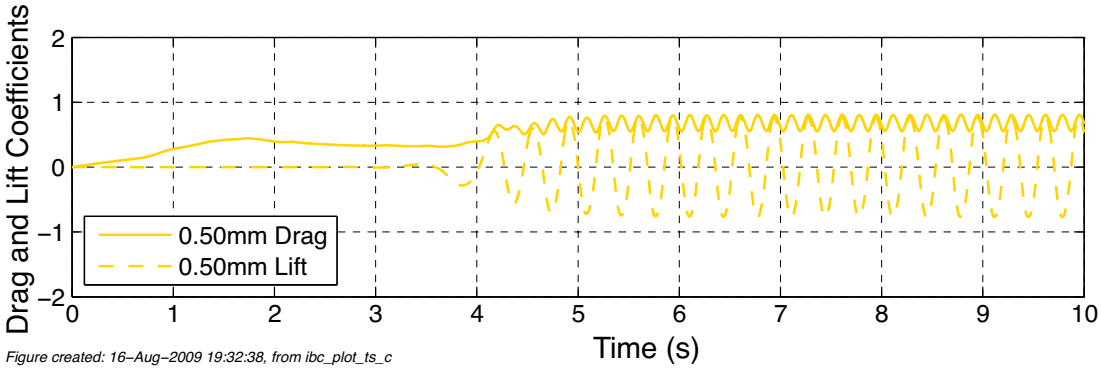


**Figure 8-24 – $C_D$ and $C_L$ as a function of time from the $\mathfrak{F}$ = 0.50mm simulation.**

As can be seen by comparing the simulated flow fields from the $\mathfrak{F} = 0.50$ mm, Figure 8-23, simulation with that from the $\mathfrak{F} = 0.05$ mm simulation, Figure 8-25, the shedding pattern is intensified and both the velocities and width of the wake increased. It should be noted that while the velocity magnitudes shown in Figure 8-25 were taken from the $\mathfrak{F} = 0.05$ mm simulation, the results from the $\mathfrak{F} = 0.25$ mm and the $\mathfrak{F} = 0.15$ mm simulations were sufficiently similar that they are not presented.

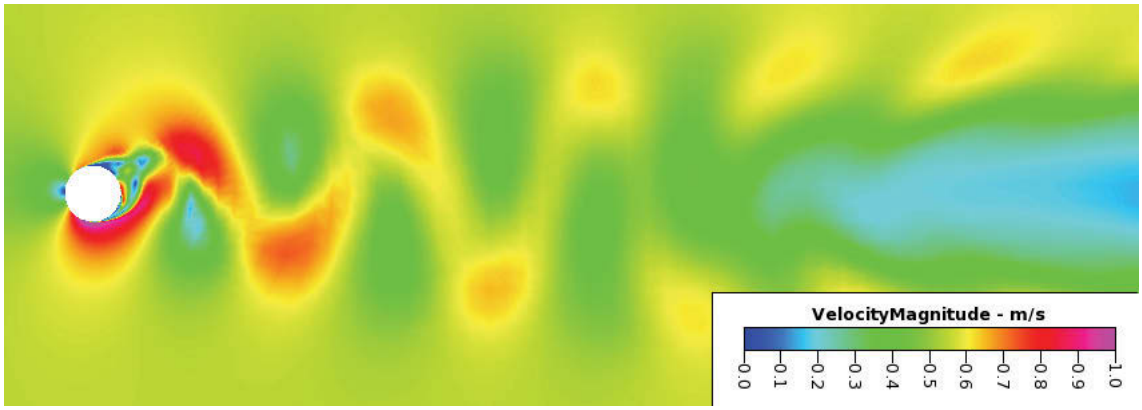


**Figure 8-25 – Velocity magnitude of the flow field from the $\mathfrak{F}$ = 0.05mm simulation.**

The intensification of the shedding is similarly reflected in the drag and lift coefficients of the three, shortest $\mathfrak{F}$ simulations, as shown in Figure 8-26, where the mean drag has increased to approximately 1.15 and the RMS lift has increased to 0.82. These force coefficients measurements are consistent across the three simulations with the shortest wall normal lengths and are approximately 5% below the published drag and 4% above the published RMS lift results (Zdravkovich, 1997), respectively. Despite the close agreement with the mean drag and the RMS lift to published data, the trend of the $C_L$ and $C_D$ as the mesh size in the vicinity of the obstacles is reduced is more important.

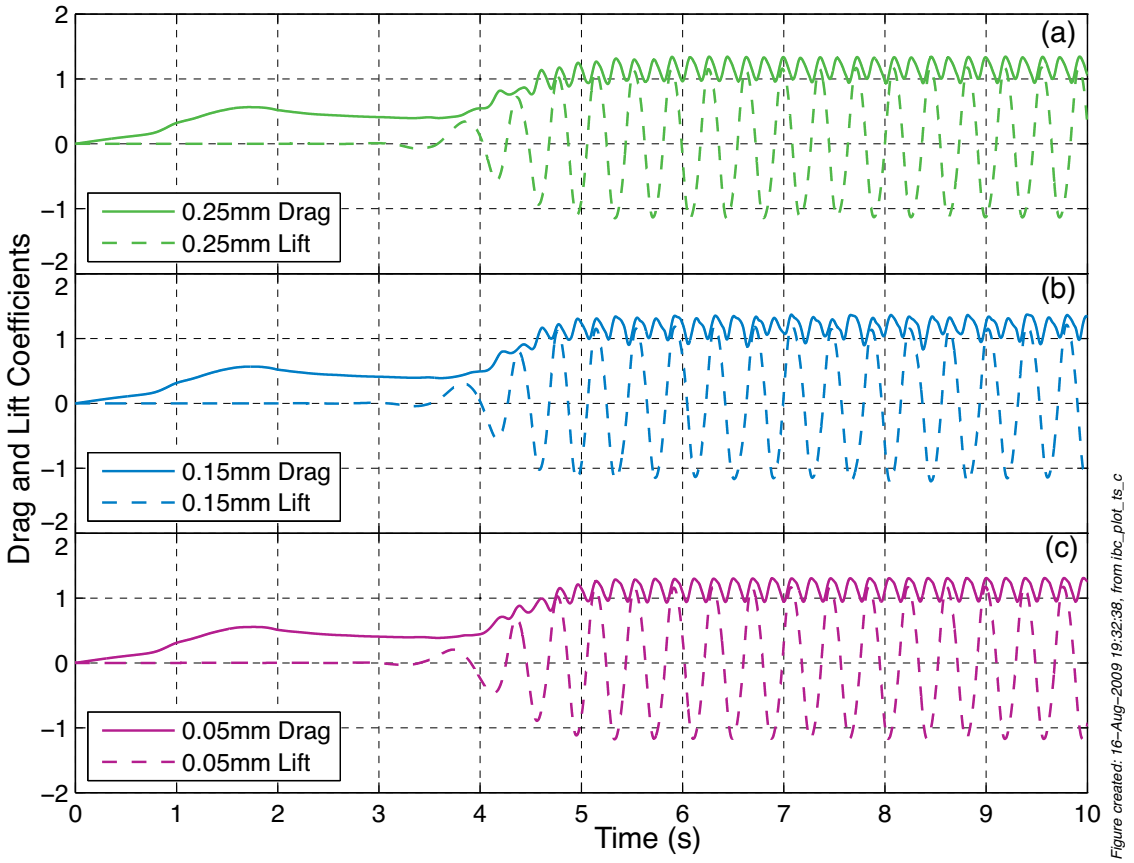


**Figure 8-26 – $C_D$ and $C_L$ as a function of time from the $\mathfrak{F}$ = 0.25mm (a), $\mathfrak{F}$ = 0.15mm (b) and $\mathfrak{F}$ = 0.05mm (c) simulations.**

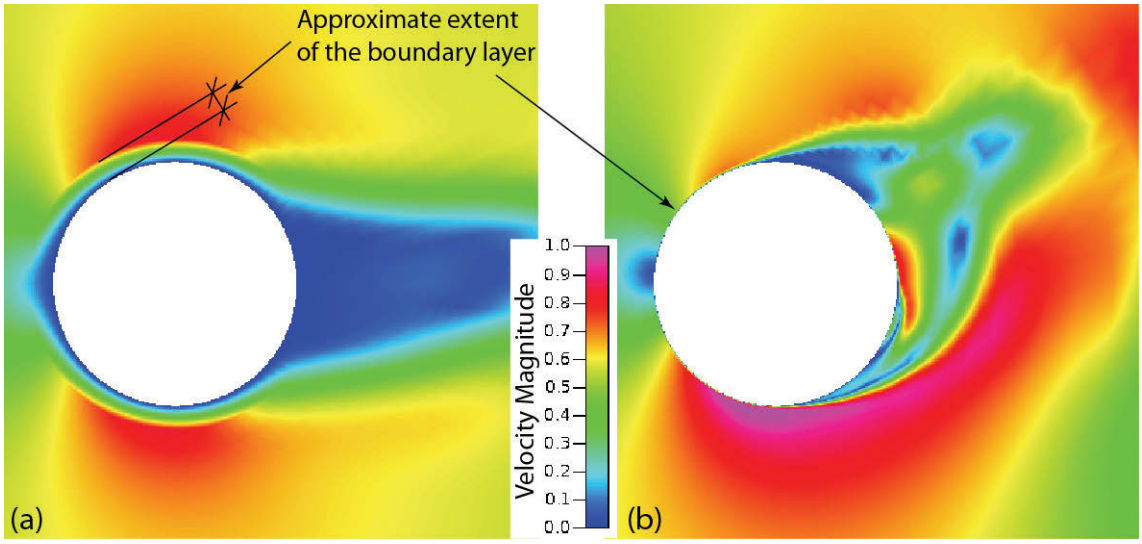


**Figure 8-27 – Zoom of the velocity magnitude in the region close to the cylinder for (a) $\mathfrak{F}$=5.00mm and (b) $\mathfrak{F}$=0.05mm simulations, respectively.**

The flow fields from the region near the cylinder at the two extreme values of $\mathfrak{F}$ are compared in Figure 8-27. The boundary layer extent in the $\mathfrak{F}$ = 5.00 mm simulation is

large and extends through the entire cell adjacent to the cylinder wall, as shown in Figure 8-27(a), whereas in the region upstream from separation for the $\mathfrak{F} = 0.05$ mm simulation the boundary layer is almost invisible at the scale used in Figure 8-27(b).

To allow for a quantitative discussion of the trends of $\overline{C_D}$ and $C_L'$ they are plotted as a function of $\mathfrak{F}$ in Figure 8-28. There are three regions of this plot, which have been alluded to in the structure of the discussion above. The first region correlated to the longest wall normal cell lengths, $\mathfrak{F} \geq 1.00$ mm, characterised by low mean drag and RMS lift values and although there may be separation of the flow around the cylinder there is little, or no, vortex shedding from the cylinder itself.

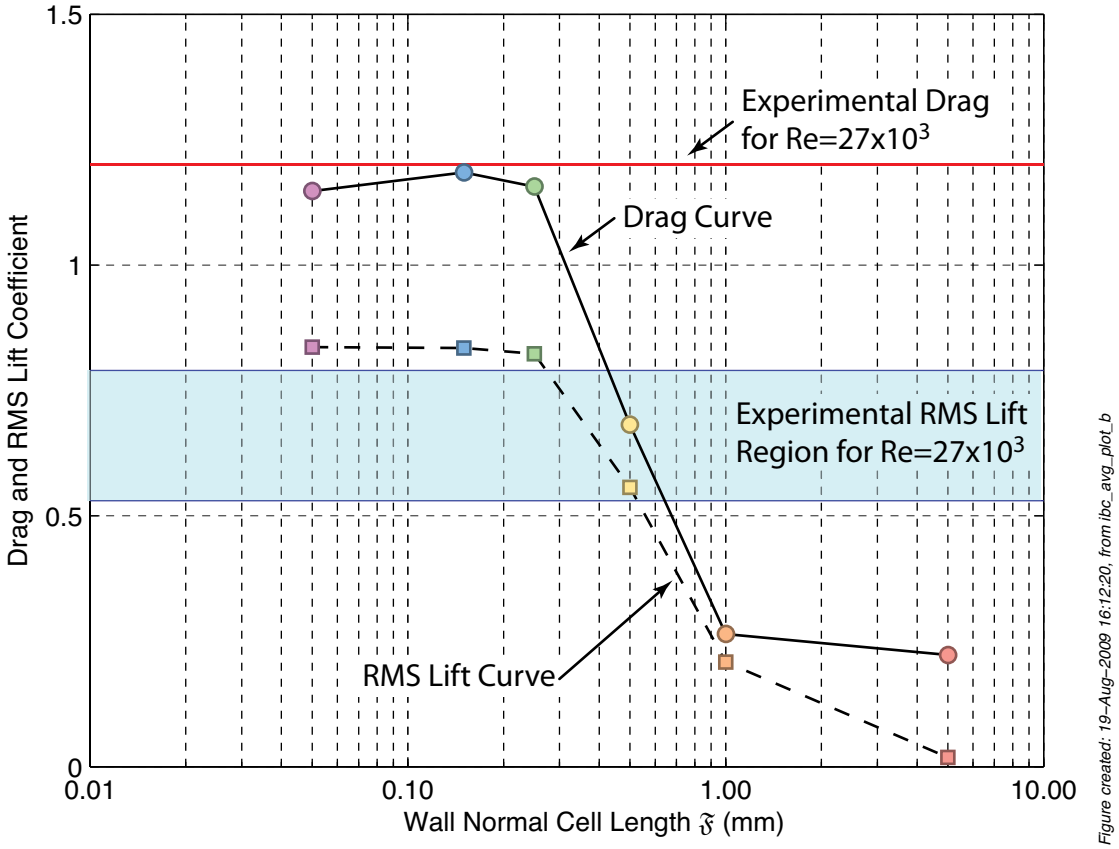


**Figure 8-28 – Average $C_D$ and RMS $C_L$ as a function of $\mathfrak{F}$.**

Conversely at the shortest wall normal cell lengths, $\mathfrak{F} \leq 0.25$ mm, the values of the mean drag and RMS lift plateau as $\mathfrak{F}$ is decreased. Between these upper and lower bounds there is a sharp transition region where the flow is, qualitatively, closer to that calculated with the simulations with a shorter $\mathfrak{F}$, for example the flow shown in Figure 8-23 appears closer to that in Figure 8-25 rather than Figure 8-22. Concurrently, the mean drag and RMS lift coefficients in this transition were midway between the values

for the longer and shorter wall normal regions. As only one simulation in the present study fell within the transition region, the shape of the curve between the longer and shorter zones cannot be determined with any certainty. However, as already mentioned above, the final shape of the curve is of less importance than the trend of the force coefficients because these results are from a two-dimensional study whereas the simulations with the cylinder that penetrates a free surface will be three-dimensional. It is important, though, that the three-dimensional model be constructed in such a way that the cells closest to the cylinder are sufficiently small as to be in the shortest wall normal length $\mathfrak{F}$, plateau region in Figure 8-28, such that the boundary layer is adequately resolved.

Finally, as discussed above in the description of the model configuration, §8.3.1, that because the wall normal cell length and the distance to the outlet boundary studies were performed in parallel, the wall normal cell length for the outlet tests was arbitrarily specified as $\mathfrak{F} = 0.15$ mm. From the discussion of the results presented above and, in particular, by an inspection of Figure 8-28 it is seen that this assumption is valid as $\mathfrak{F} = 0.15$ mm falls within the lowest, plateau region where the mean drag and RMS lift coefficients are unaffected by changes in the wall normal cell size.

### 8.3.8. Convergence of the Solver During the $\mathfrak{L}$ Tests

As has been the procedure for the work presented so far in this dissertation, before the results from a group of simulations can be examined, the numerical convergence of the solver must be scrutinised in order to assuage concerns that the limits of numerical convergence have not been met. The cumulative probability distribution functions of $n_{iter}$ for the eleven $\mathfrak{L}$ simulations were similar with all of the available time steps converged within six iterations, as shown in Figure 8-29. Therefore, the simulations have been shown to have converged to the specified level of numerical accuracy such that the flow results can be critically examined.

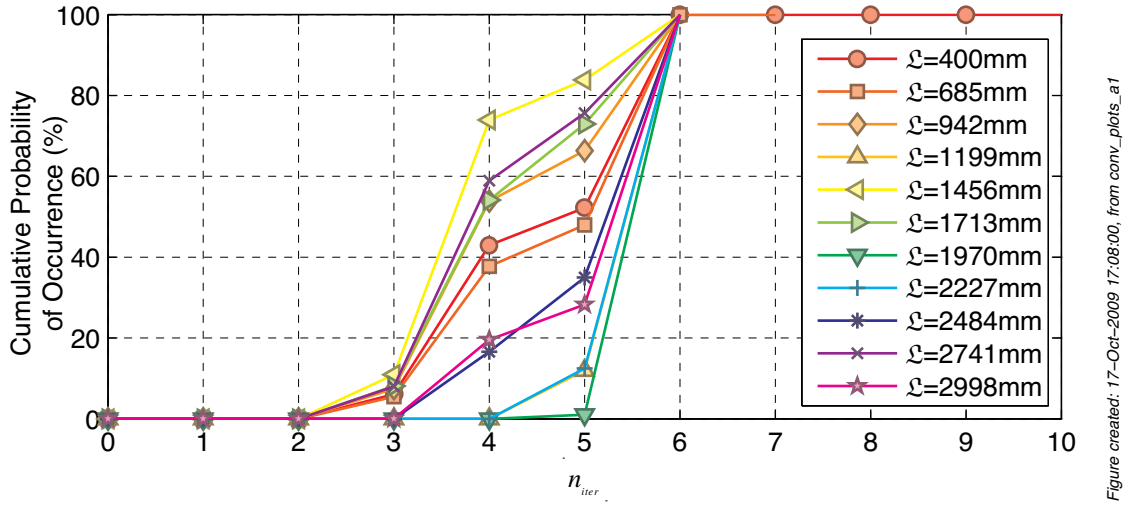


**Figure 8-29 – Cumulative probability distributions of $n_{iter}$ for the 11 ℒ simulations.**

## 8.3.9. Observations from the Parametric Tests of ℒ

As shown in Figure 8-30, all the simulations of ℒ developed a characteristic von Kármán vortex street in the wake region with examples from the ℒ = 400mm, ℒ = 1199mm and ℒ = 2998mm simulations. While the three images are from different simulation times they show the broad similarity of the flow fields because they were all imaged after the simulations had developed and are approximately in phase. For example, the location of the shed vortices and their transport downstream is generally consistent with the approximate locations of the shed vortices within the wake as is clearly seen in Figure 8-30.

In the immediate vicinity of the cylinder, all three simulations appear to be broadly similar in that there is a region of high-speed flow that rolls off from the top of the cylinder, which then overtakes a slow speed region attached to the rear and bottom of the cylinder. This high-speed roll off region then forms the next shed vortex made visible by its high-speed region in the wake.

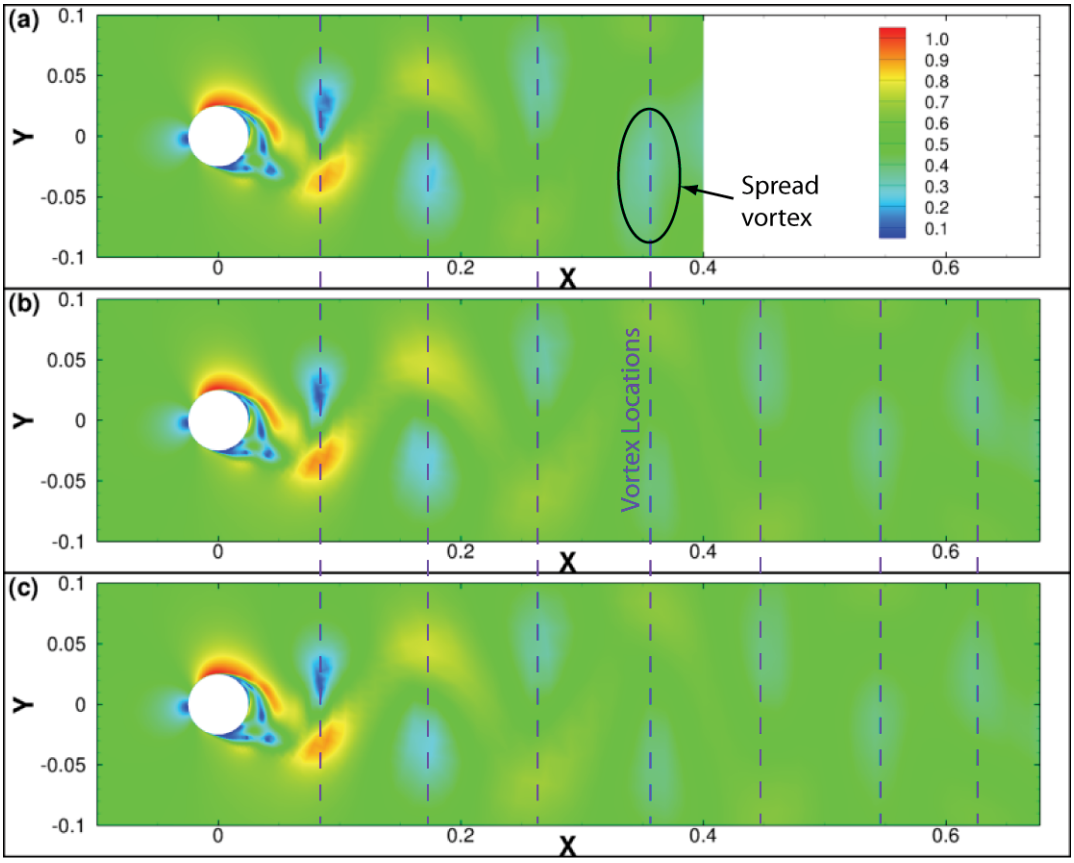


**Figure 8-30 – The von Kármán vortex street visualised with the velocity magnitude for the $\mathfrak{L}$ = 400mm (a), $\mathfrak{L}$ = 1199 (b) and $\mathfrak{L}$ = 2998 (c) simulations.**

In addition, all the vortices, with the exception of the vortex closest to the outlet in the $\mathfrak{L} = 400$ mm simulation, Figure 8-30(a), have the same magnitude and size. However, the outlet boundary in the $\mathfrak{L} = 400$ mm simulation appears to have an effect on the vortex street because the vortex that is closest to the outlet is both larger in size and has a higher velocity magnitude than the corresponding vortices in the other simulations.

Because the velocity fields shown in Figure 8-30 are approximately in phase and, visually at least, overlap for the range

$$-0.2 \leq x \leq 0.4 \tag{8.7}$$

the velocity magnitudes from different simulations can be subtracted to quantify the magnitude of the difference between the vortex spread..

When the velocity field for $\mathfrak{L} = 1199$ mm simulation was subtracted from the field extracted from the $\mathfrak{L} = 2998$ mm simulation, there is a region of high difference close to the cylinder that was surrounded by a larger region of low difference, as shown in Figure 8-31(a). The high difference region is not necessarily indicative of an effect

from the boundary but, more likely, is due to rather smaller errors in the phase of the local velocity field. That is, because the wake close to the cylinder is characterised by comparatively high velocities in a relatively compact area, small differences in the phase can account for the large differences which are visible in Figure 8-31(a). Outside of these regions that are close to the cylinder, the differences in the flow field are less than 0.01m/s, which indicates that the both the flows are in phase and that there is no effect from the reduction of $\mathfrak{L}$ to 1199mm from 2998mm.

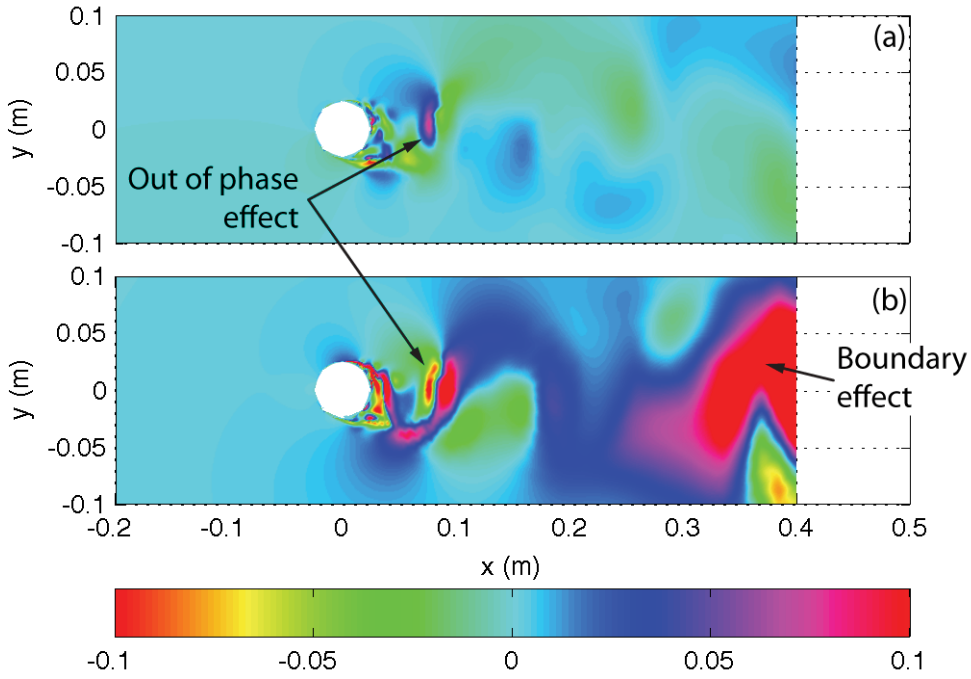


**Figure 8-31 – Difference in the velocity fields between the $\mathfrak{L}$ = 2998 mm and the $\mathfrak{L}$ = 1199 mm simulations; and the $\mathfrak{L}$ = 2998 mm and the $\mathfrak{L}$ = 400 mm simulations, (a) and (b) respectively.**

In contrast to the excellent agreement of the results from the longer $\mathfrak{L}$ simulations, when the flow field from the $\mathfrak{L} = 400$ mm simulation was subtracted from the $\mathfrak{L} = 2998$ mm simulation the far field differences were up to 0.1m/s, as shown in Figure 8-31(b), or ten times the maximum difference between the $\mathfrak{L} = 1199$ mm and the $\mathfrak{L} = 2998$ mm simulations. There were two high defect regions observed with the first located close to the cylinder which was, as with the discussion of the $\mathfrak{L} = 1199$ mm simulation above, due to the slight errors in phase. However, the second high defect region was much larger and was located adjacent to the outlet boundary and is therefore due to the presence of the boundary. Given that the outlet boundary has an effect on the velocity field which is reduced as the boundary is moved further from the cylinder, it should

then be possible to further examine this affect with a statistical analysis of the point probe data.

All the simulations started from the same initial conditions and were subject to the same development, namely quiescent fluids and a two second acceleration, respectively. This effect was observed in the velocity data that was recorded at the seven point "probes", as shown in Figure 8-32 and Figure 8-33 for the *u*- and *v*-velocities. In addition, these coincident velocity traces were continued beyond the initial two second start-up period until approximately four seconds of simulation time after which the traces diverged.

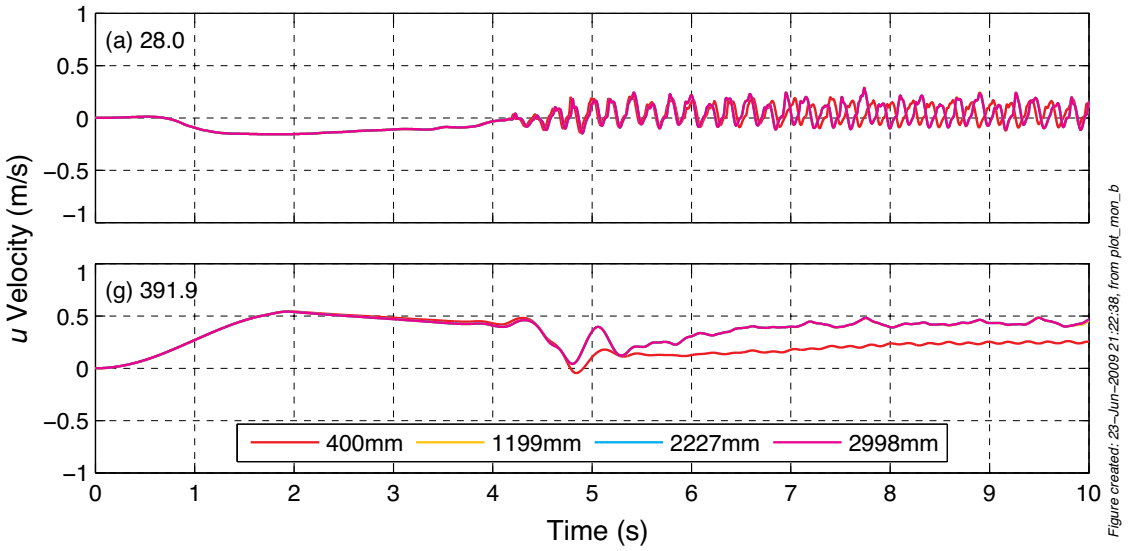


**Figure 8-32 – Plot of the four of the length test *u*-velocities as a function of time for the seven point probes.**

As the simulations progressed, the flow field developed from the quiescent initial conditions into the fully developed shedding regime and the wake had not fully extended to the outlet boundary. Therefore, any reflections from the outlet boundary had not had sufficient time to move upstream and affect the flow around the cylinder. This result can be interpreted as supportive of the common practice to allow computational fluid dynamics computations to run for a sufficient time such that multiple "flow lengths" can pass and allow the effect of any boundary conditions to propagate into and throughout the domain.

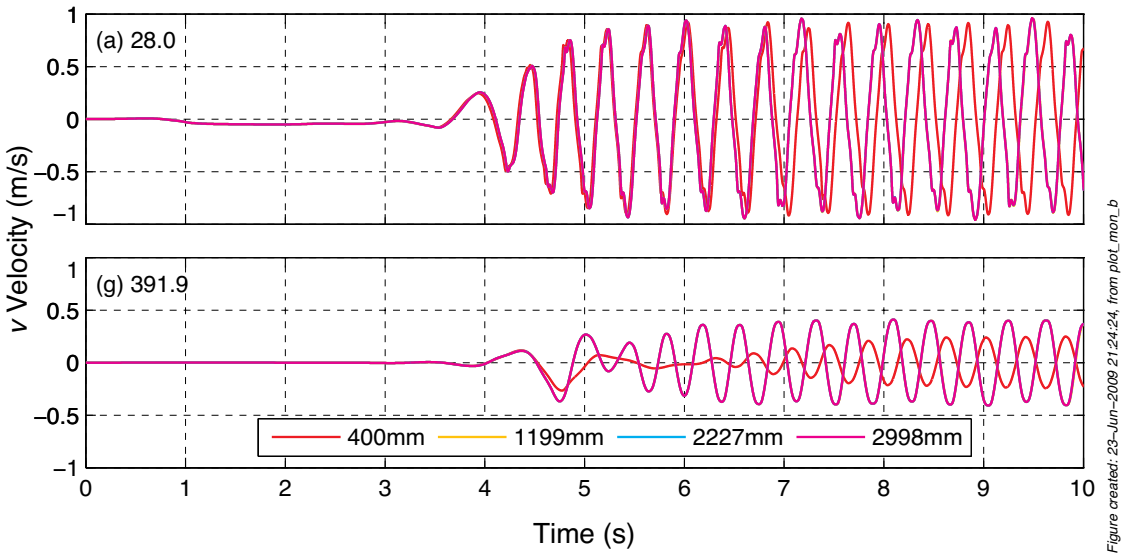


**Figure 8-33 – Plot of the four of the length test *v*-velocities as a function of time for the seven point probes.**

In addition, the results from the three longest $\mathfrak{L}$ simulations plotted are remarkably consistent for their entire run time. In contrast, the traces from the $\mathfrak{L} = 400$ mm simulation, at the point probed furthest from the cylinder, and hence closest to the outlet boundary, differ noticeably from the other three traces*. Given that a visual inspection of both the flow field and velocity traces for the simulations of $\mathfrak{L} \geq 1199$ mm revealed little difference in the respective data, it could be concluded that the outlet boundary is sufficiently far downstream to have little effect on the flow field in the vicinity of the cylinder. Therefore, the mean of the *u*-velocity and the RMS of the *v*-velocity can be used to quantify the differences in the velocities due to changing the location of the outlet boundary.

Both the mean and RMS of a fluctuating variable are statistical properties that are valid over a given window of the data, therefore for the present work these parameters were computed over the time window

$$5 \leq t \leq 10 \text{ s}. \tag{8.8}$$

Since both the mean *u*-velocities and the RMS *v*-velocities for the simulations with $\mathfrak{L} \geq 1970$ mm were identical to three significant figures, the velocity fields were

* Only two point probe traces are shown in Figure 8-32 and Figure 8-33 because at the closest point probe, the traces are visually similar, whereas by the furthest point probe there is a noticeably difference. Over this range the longer $\mathfrak{L}$ simulation data remain coincident while the $\mathfrak{L} = 400$ mm traces steadily diverge.

assumed to be converged for the longer Ł. It is interesting to note that the mean and RMS values for the three point probes closest to the cylinder differed by less than 1% from the values obtained from the longer Ł simulations while the remaining four points are within 4% of the benchmark values, as shown in Figure 8-34 for the *x*=28mm probe only.

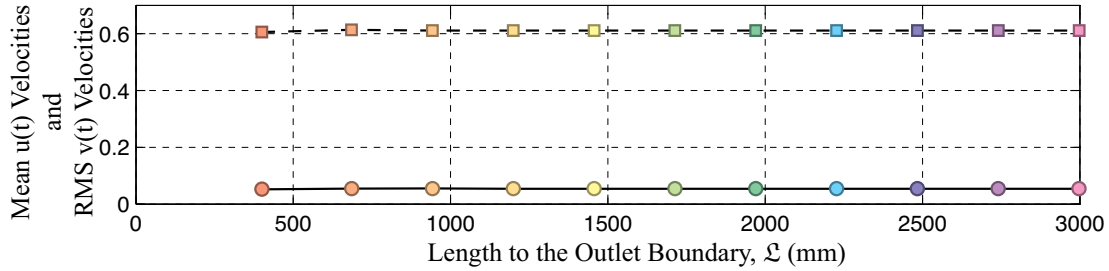


**Figure 8-34 – Plot of *U*-velocities (circle symbols and solid lines) and the RMS *v*-velocities as a function of Ł for point probe located at x=28mm.**

Therefore, there is no noticeable effect from the outlet at the points for $x \le 150$ mm. However, as the point probe approached the outlet boundary both the mean and RMS decreased for the shorter Ł simulations relative to the longer Ł simulations, as shown in Figure 8-35.

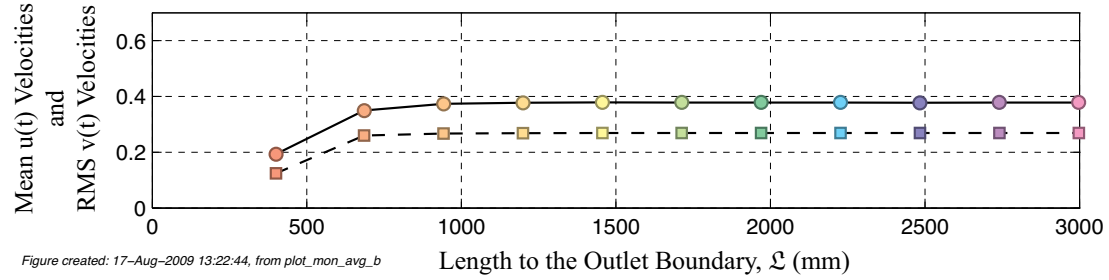


**Figure 8-35 – Plot of *U*-velocities (circle symbols and solid lines) and the RMS *v*-velocities as a function of Ł for the point probes located at x = 200mm.**

While the plot of the mean *u*-velocities and the RMS *v*-velocities in Figure 8-35 indicated that the proximity of the outlet boundary adversely affects the flow field, the effect should be quantified to provide guidance as to the minimum separation distance required. Therefore, to further quantify the magnitude of this affect the error in the mean, and RMS, was computed as

$$\mathfrak{U}_{Pt} = \left| \frac{U_{Pt} - U_{BM}}{U_{BM}} \right| \tag{8.9}$$

in which $\mathfrak{U}_{Pt}$ is the error at a given point, $U_{Pt}$ is the mean (or RMS) computed at a given monitor point over the window defined in Equation (8.8) and shown in Figure 8-34 and Figure 8-35. The quantity $U_{BM}$ is the benchmark value of the mean, or RMS, for a particular monitor point that was computed from the simulations with $\mathfrak{L} \geq 1970$ mm as discussed above.

For all point probes, as the distance of the probe from the outlet boundary was increased the error, $\mathfrak{U}_{Pt}$, decreased, as shown in Figure 8-36 and Figure 8-37. This trend is particularly apparent for point probes six and seven that both started with $\mathfrak{U}_{Pt}$ in the order of 50% when they were located less than 100mm from the outlet boundary. This high $\mathfrak{U}_{Pt}$ then dropped rapidly so that when the distance to the outlet was greater than 600mm the error, relative to the large $\mathfrak{L}$ simulations, was less than one percent. While the point probes that were closer to the cylinder, for example probes one and two, start from considerably lower errors that are in the order of four percent, they also reduced to less than one percent error when the distance to the outlet was greater than 600mm.

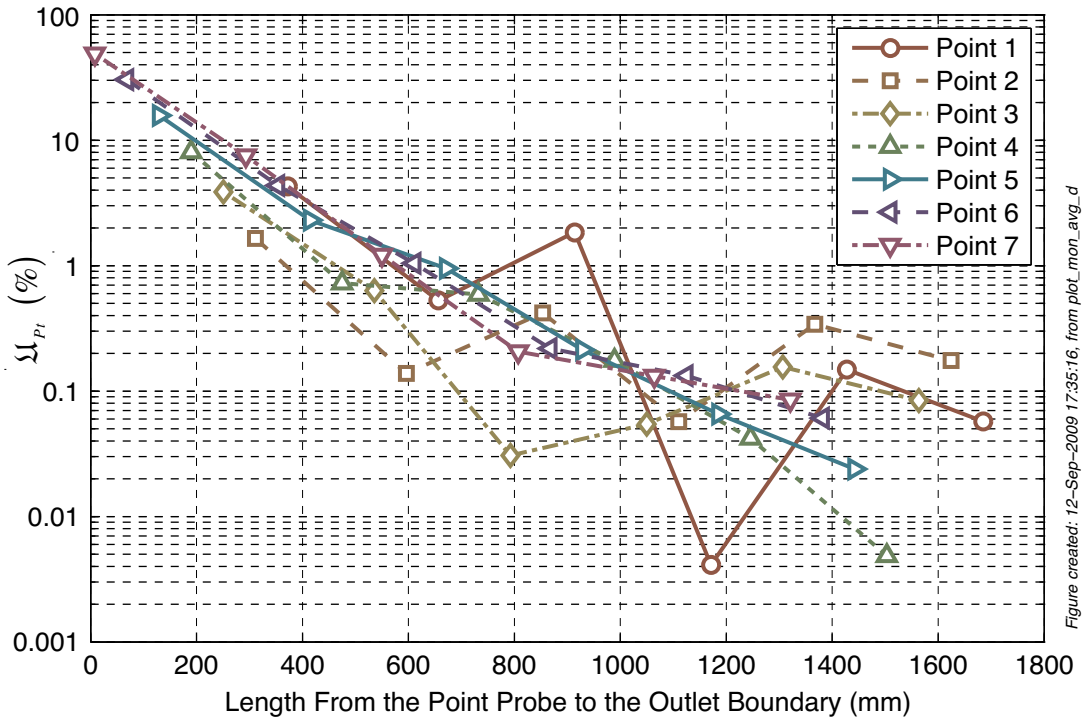


**Figure 8-36 – $\mathfrak{U}_{Pt}$ for the mean *u*-velocity as a function of the distance of the point probes from the outlet boundaries.**

These observations suggest that for the flow field to converge the outlet boundary must be placed further than 600mm, not from the cylinder, but from the region of interest in the flow. With this limitation under consideration, there should be little effect on the lift and drag values on the cylinder because at a minimum $\mathfrak{L}$ value of 400 mm the cylinder is close to the 600mm limit. Significantly as was observed both above for circular cylinder and in the square cylinder preliminary studies described in Appendix C, the force coefficients are not too sensitive to changes in the numerical configuration.

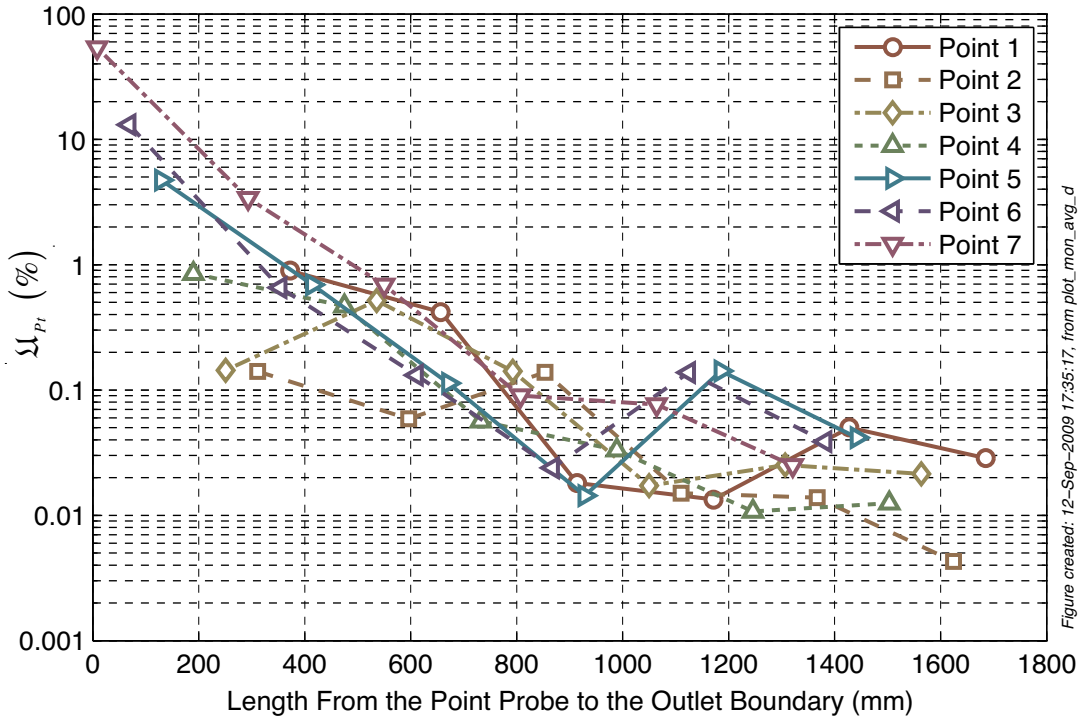


**Figure 8-37 – $\mathfrak{U}_{Pt}$ for the RMS *v*-velocity as a function of the distance of the point probes from the outlet boundaries.**

In fact, there is so little difference in the lift and drag coefficients as a function of time for all $\mathfrak{L}$ values that when plotted together they appear collinear. All the traces are therefore characterised by the same regions being: a development phase during the first four seconds that was then followed by a quickly developing quasi steady regime of periodic vortex shedding, as shown in Figure 8-38.

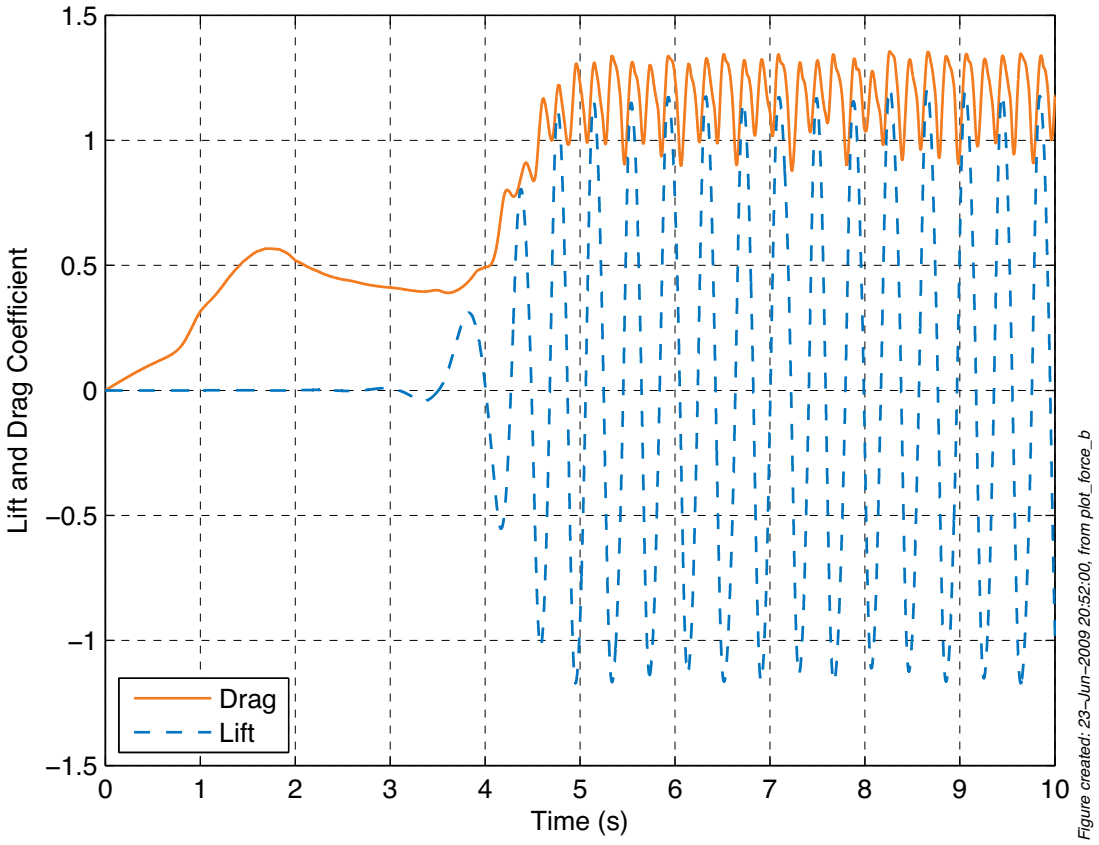


**Figure 8-38 – $C_D$ and $C_L$ as a function of time from the $\mathfrak{L}$ = 685mm simulation.**

Little difference is seen in the lift and drag coefficients as a function of time hence, only $C_D(t)$ and $C_D(t)$ is shown for the $\mathfrak{L} = 685$ mm simulation. However, given the inaccuracies inherent in a visual comparison, to facilitate a rigorous comparison the coefficients were averaged over the same window as above and plotted as a function of $\mathfrak{L}$. The mean drag and the RMS lift coefficient at the shortest $\mathfrak{L}$ are both 10% lower than the equivalents from the simulations with a longer $\mathfrak{L}$, as shown in Figure 8-39. Further, the values of the mean drag and RMS lift coefficients plateau as $\mathfrak{L}$ is increased beyond 942mm.

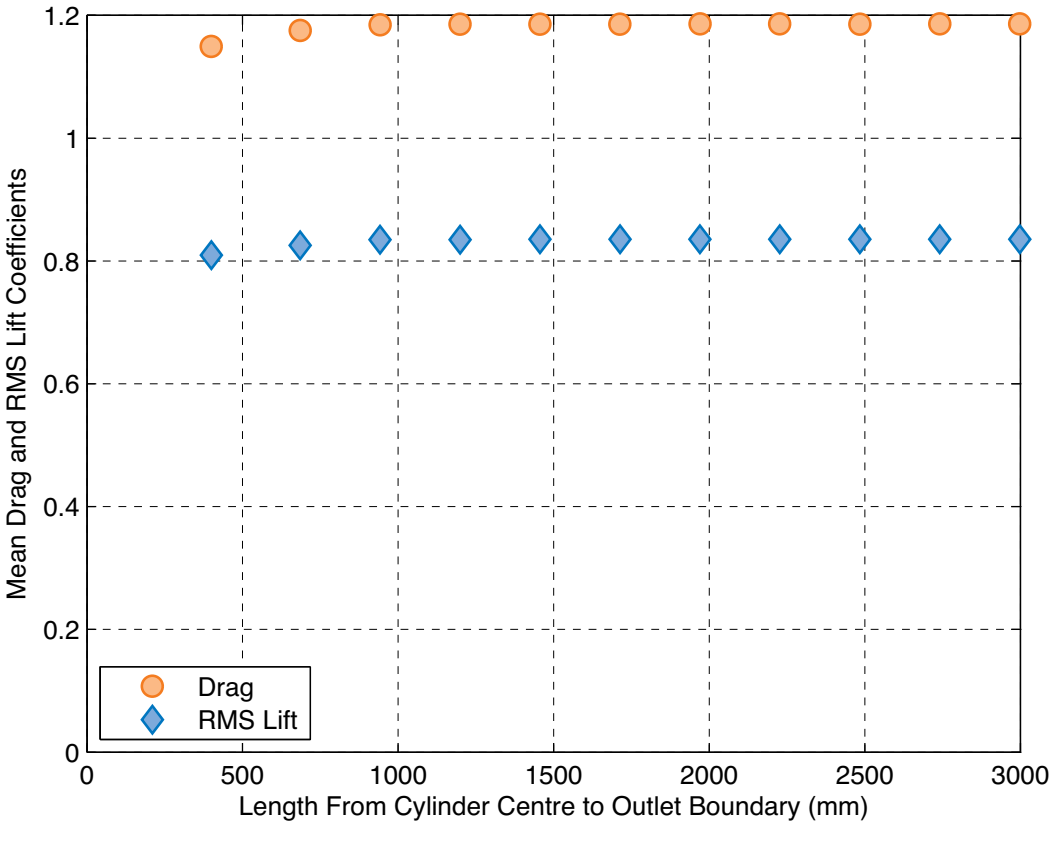


**Figure 8-39 – Plot of the mean drag and the RMS lift coefficients as a function $\mathfrak{L}$.**

## 8.4. Recommendations for the Development of the Three-Dimensional Models from the Two-Phase Preliminary Studies

From these three two-dimensional studies three recommendations can be made to guide the development of the three-dimensional models:

1. That the hydrostatic pressure distribution must be applied across both the air and water outlet faces;

2. That the distance on the outlet from the flow region *of interest* should be at least 600 mm, and;

3. That $\mathfrak{F} \leq 25$ mm.

Of these, the second recommendation is potentially the most interesting and because it was not specifically being tested, was a somewhat serendipitous discovery. The test

was designed to investigate the effect of the distance from the cylinder to the outlet but instead showed that the distance from the flow region *of interest* is more important. For example with the three-dimensional simulations that are designed to compute flow features that extend a significant downstream from the cylinder, such as the rooster tail, the length of these features should become the reference length to set the location of the outlet.

With these preliminary studies conducted and analysed development and investigation of the three-dimensional computational models can be discussed. As has been the practice of this dissertation the particular combinations, in this case the combination of a three-dimensional grid, a free surface model and the numerical solver to approximate the turbulent decay, must be fully validated before a thorough investigation can proceed with confidence.

# 9. Three-Dimensional, Two-Phase Simulations: Configuration and the Simulated Free Surface Shape

## 9.1. Introduction

As discussed in §7 for the three-dimensional tow tank simulations, the inertial frame of reference was transformed such that the cylinder remained fixed and the other computational elements were instead translated, as shown in Figure 9-1. In the present research, two Reynolds numbers were numerically investigated, namely $\mathrm{Re}_d = 27 \times 10^3$ and $\mathrm{Re}_d = 54 \times 10^3$, with the first being similar to that used in both the square cylinder validation study and the studies based on Inoue's tow tank experiments (1993). The second, larger Reynolds number, was envisaged as an extension to push the limits of the proposed computational technique and yet remain within the extensive data reported by Hay (1947).

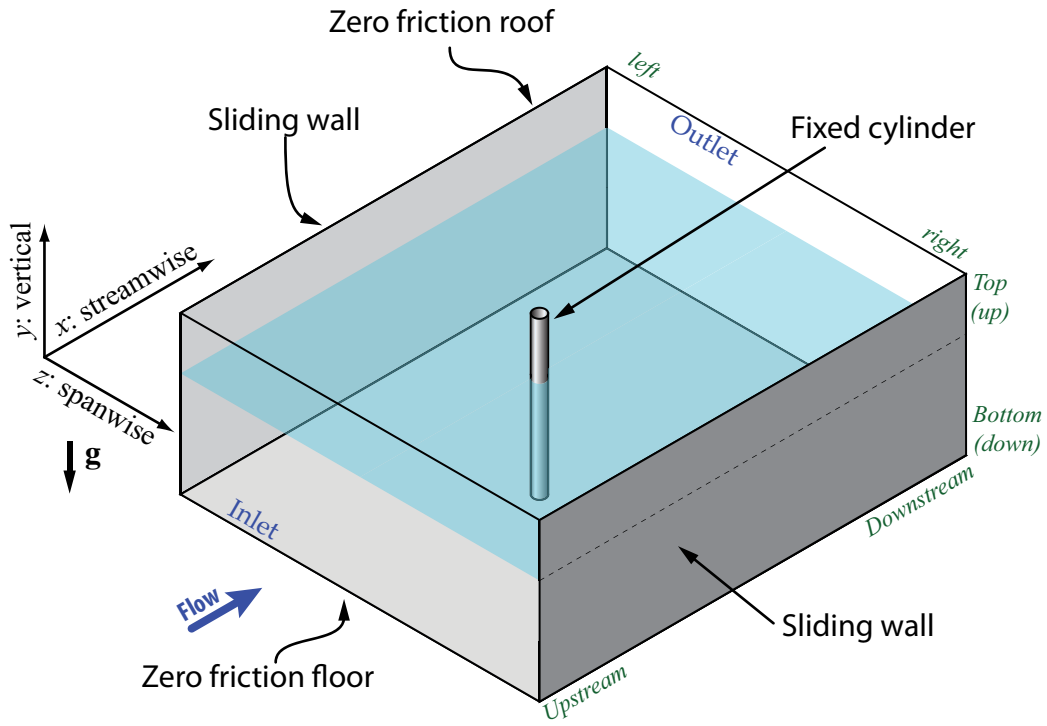


**Figure 9-1 – Sketch of the cylinder centred domain, repeated from Figure 7-3.**

As well, two different depths of immersions of the cylinder, relative to the elevation of the initial rest free surface were investigated. Their exact configuration will be discussed shortly. As with all CFD research, the square cylinder work presented within this dissertation was no exception, the geometric and solver configurations must be

specified prior to any critical examination of numerical results. By convention, a validation would then follow with an application of the technique to an additional problem/s to finish. Despite the present research being conducted using this process, the results will be presented differently because the validation data was such an excellent match with the validation studies that it could simultaneously be used as part of the investigations.

## *9.2. Configuration of the Simulations*

### 9.2.1. General Geometric Configuration

The tow tank used by Hay (1947) was located at the David Taylor Model Basin, Maryland, U.S.A. and measured 1.37m wide by 1.52m deep by 40.54m long. Clearly, a cross-section of $1.37 \times 1.52\text{m}$ could not be simulated, to sufficient detail, for the full 40.54 m, hence the need to translate the inertial frame of reference while simultaneously reducing the length. As the present researcher assumed that the full width of the tank should be simulated it remained to define both the horizontal and vertical extents of the computational domain.

With respect to the horizontal extent of the computational domain, there were two boundaries to be placed, namely the outlet and the inlet. To aid in the placement of the outlet, three criteria were examined:

(1) Recommendations from the preliminary length to the outlet test, the "$\mathfrak{L}$" parameter.

(2) Estimation of the flow field features to be captured.

(3) Grid development requirements.

The first criterion can be succinctly expressed by the inequality

$$\mathfrak{L} \geq 600\text{mm}. \tag{9.1}$$

With respect to the second criterion, Hay (1947) observed that the top of the rooster tail had the longest downstream extent, which for the present conditions would be expected to occur at approximately 250 mm. Therefore, as it was observed in the preliminary studies that there should be a buffer of at least 600 mm from the flow region of interest, the outlet should be at least 850 mm from the cylinder.

With due consideration to these three criteria, the outlet was placed at

$$\mathfrak{L} = 942\text{mm}\,, \tag{9.2}$$

which exceeded both the first and second requirements and simplified some aspects of the third, as shown in Figure 9-2.

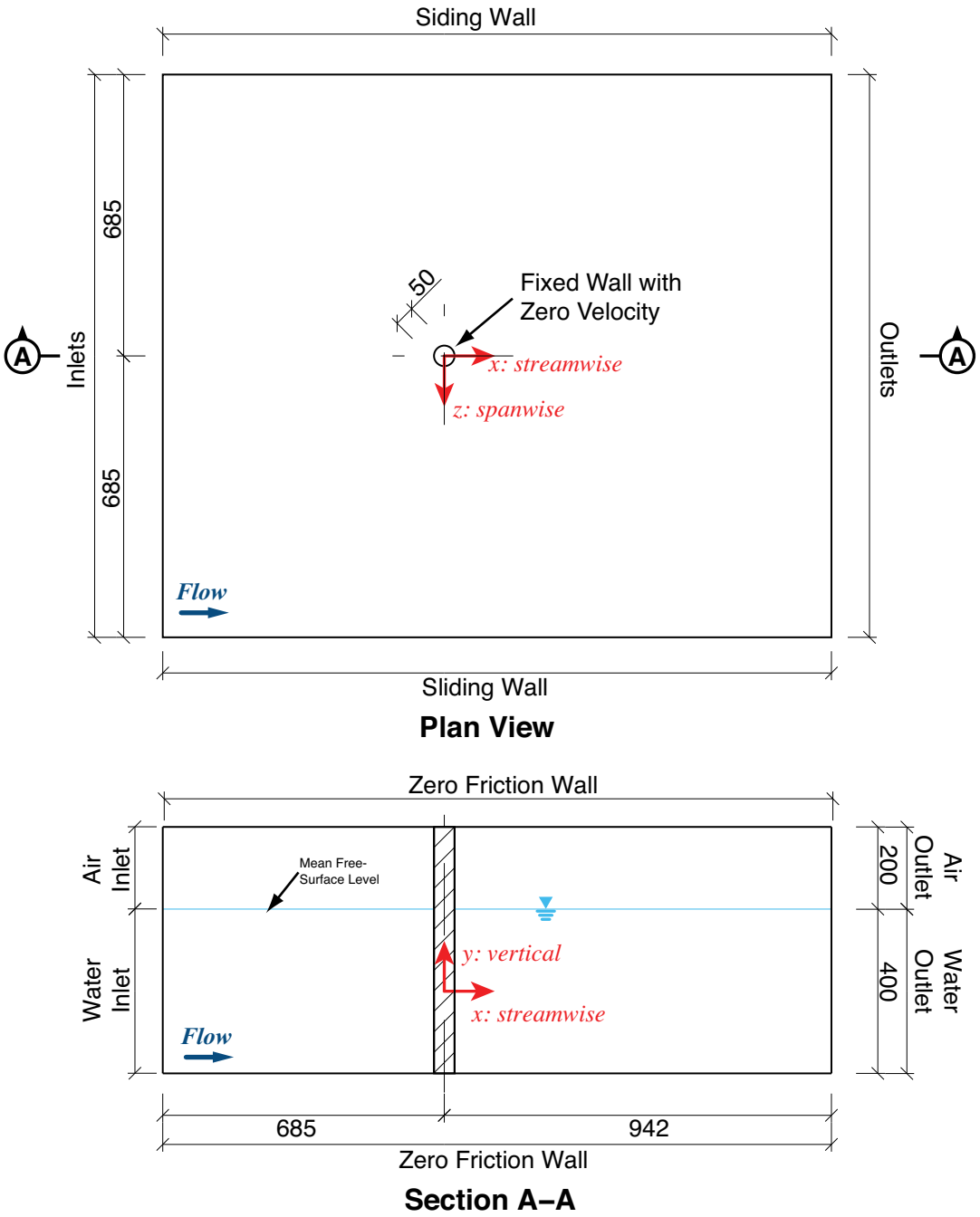


**Figure 9-2 – Sketch of the geometry, boundary conditions and coordinate origin used in the circular cylinder investigations, all dimensions are in millimetres.**

In contrast to the outlet, no specific test or tests were undertaken to determine the effect of the location of the inlet relative to the cylinder. Therefore, based on the criterion expressed in Equation (9.1) and with the supposition that the upstream region of interest is very close to the cylinder then the upstream length should be greater than 600 mm. Finally, the upstream boundary was placed at 685 mm from the centre of the cylinder, which exceeded the criterion of Equation (9.1). Further, this distance "squared" the upstream portion of the domain with the distance from the cylinder to the side walls and thus significantly simplified the creation of the grid.

In the absence of definitive data in the form of preliminary tests or reference studies the upper and lower walls were located such that it could be assumed that their location would have no effect on the free surface. Therefore, they were placed 200 mm above and 400 mm below the elevation of the still water level. No data was available concerning the upper wall but the depth exceeded both the depth of velocity measurements by Inoue (1993) and the numerical simulations of Chen (2000), Kawamura (2002) and Yu (2008).

### 9.2.2. Configuration of the Computational Meshes

Four separate computational meshes were constructed for the two distinct cylinder configurations. In the first instance, referred to as the "full depth" simulation, the cylinder extended the entire distance from the upper to the lower zero friction walls. Whereas in the alternate configuration, referred to as the "cut off" simulation, the cylinder extended from the top wall but stopped 200 mm from the lower wall, that is the cylinder stopped at the coordinate origin in Figure 9-2. This allowed for water, or perhaps even air, to flow under as well as around the cylinder.

Three different resolution meshes of the full depth configuration were created to allow for a mesh refinement study. In contrast, only a single mesh that was based on the medium resolution full depth configuration was created for the cut off configuration, as shown in Table 9-1.

**Table 9-1 – Matrix of meshes constructed per configuration of cylinder depth.**

| | Full Depth | Cut Off |
|---|---|---|
| **Low Resolution** | ✔ | ✗ |
| **Medium Resolution** | ✔ | ✔ |
| **High Resolution** | ✔ | ✗ |

The layout of the edges and the node counts used in the construction of the full depth configuration is shown in Figure 9-3 and Table 9-2, respectively, while Figure 9-4 and Table 9-3 contain the same data for the cut off configuration.

Notes:
For the edges not specifically indicated, the number of nodes and the end spacing can be inferred from the following conditions:
-the cylinder possesses π/2 rotational symmetry around the y-axis;
-the model is mirror-symmetric around the z=0 plane;
-horizontal edges are vertically consistent;
-vertical edges are horizontally consistent

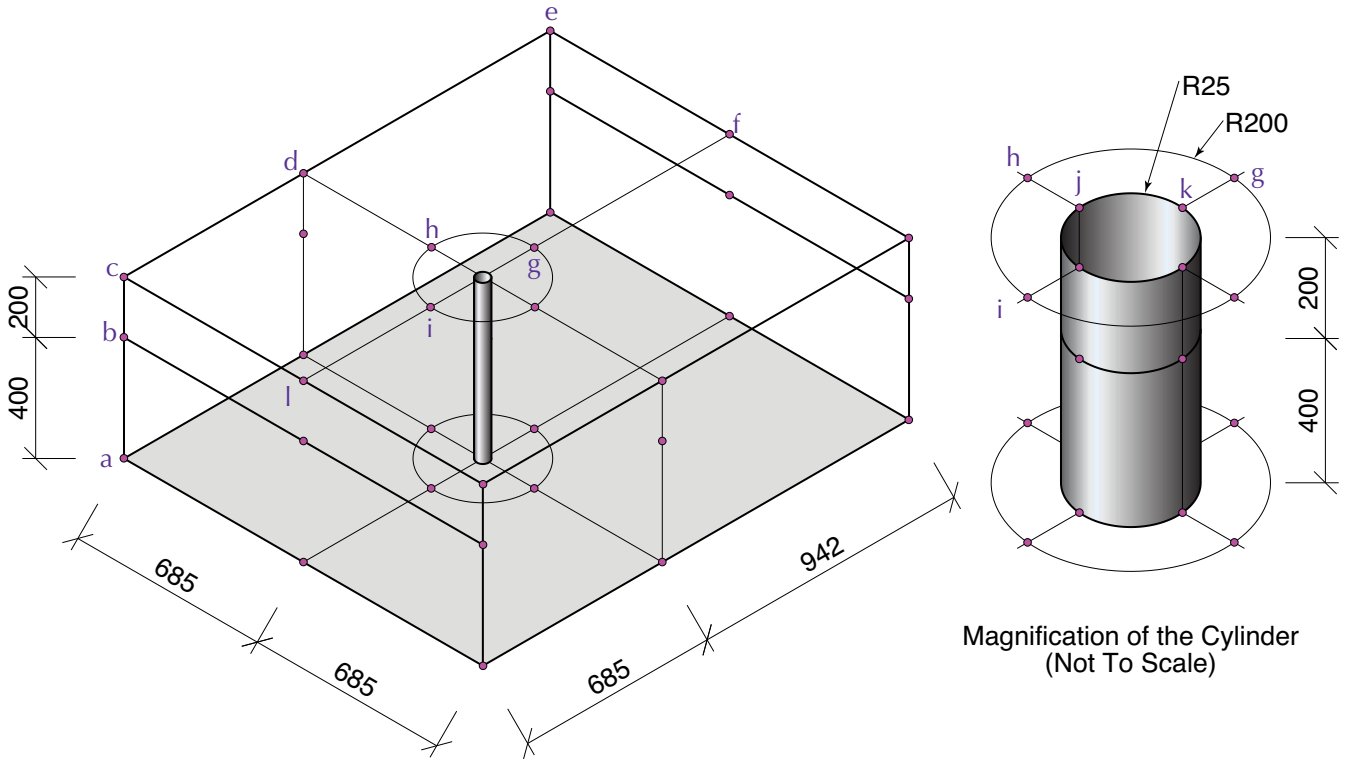


**Figure 9-3 – Geometry and edge sketch for full depth configuration with all dimensions in millimetres.**

**Table 9-2 – Edge details for the full depth cylinder configuration. Dist = Distribution type; HT = Hyperbolic tangent distribution; U = Uniform distribution.**

| Edge | End | Low Resolution | | Medium Resolution | | High Resolution | | Dist |
|---|---|---|---|---|---|---|---|---|
| | | Spacing (mm) | Nodes | Spacing (mm) | Nodes | Spacing (mm) | Nodes | |
| lc | l | 50.00 | 11 | 50.00 | 11 | 40.00 | 14 | HT |
| | c | 80.00 | | 80.00 | | 64.00 | | |
| dc | d | 50.00 | 11 | 50.00 | 11 | 40.00 | 13 | HT |
| | c | 80.00 | | 80.00 | | 64.00 | | |
| de | d | 50.00 | 13 | 50.00 | 13 | 40.00 | 16 | HT |
| | e | 120.00 | | 120.00 | | 96.00 | | |
| ef | f | 60.00 | 9 | 60.00 | 9 | 48.00 | 11 | HT |
| | e | 100.00 | | 100.00 | | 80.00 | | |
| bi | b | 22.00 | 12 | 22.00 | 15 | 17.60 | 19 | HT |
| | i | 58.00 | | 58.00 | | 40.00 | | |
| hd | h | 22.00 | 12 | 22.00 | 15 | 17.60 | 19 | HT |
| | d | 56.00 | | 56.00 | | 40.00 | | |
| gf | g | 22.00 | 12 | 22.00 | 15 | 17.60 | 19 | HT |
| | f | 130.00 | | 130.00 | | 95.00 | | |
| jh | j | 0.20 | 30 | 0.15 | 37 | 0.10 | 37 | HT |
| | h | 20.00 | | 20.00 | | 0.16 | | |
| jk | - | 1.77 | 21 | 1.77 | 21 | 1.41 | 26 | U |
| | - | | | | | | | |
| hg | - | 14.14 | 21 | 14.14 | 21 | 11.31 | 25 | U |
| | - | | | | | | | |
| bc | b | 2.00 | 27 | 2.00 | 31 | 1.60 | 39 | HT |
| | c | 20.00 | | 12.00 | | 9.60 | | |
| ba | b | 2.00 | 47 | 2.00 | 55 | 1.60 | 69 | HT |
| | a | 20.00 | | 20.00 | | 16.00 | | |

Notes:
For the edges not specifically indicated, the number of nodes and the end spacing can be inferred from the following conditions:
-the cylinder possesses π/2 rotational symmetry around the y-axis;
-the model is mirror-symmetric around the z=0 plane;
-horizontal edges are vertically consistent;
-vertical edges are horizontally consistent

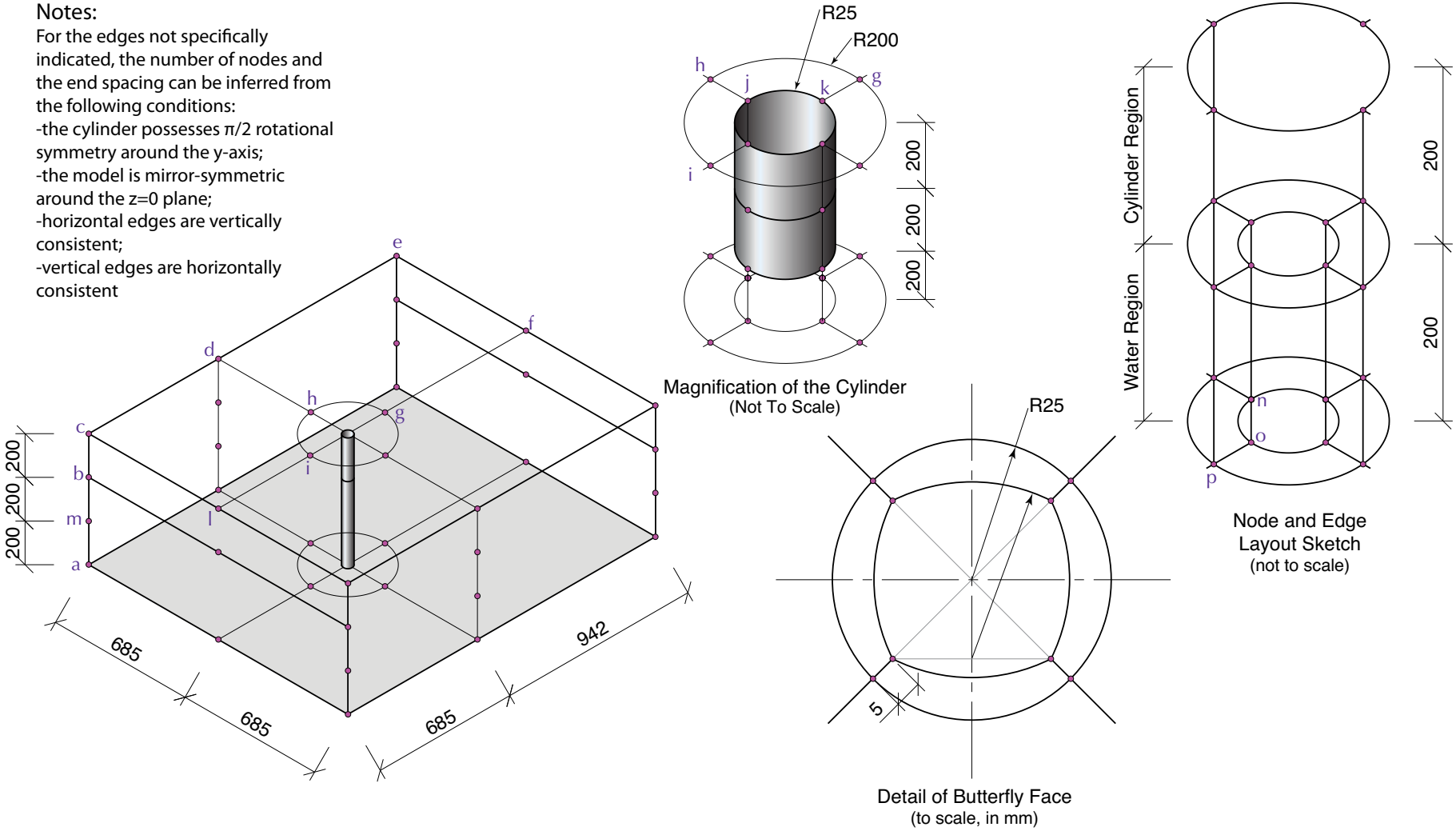


**Figure 9-4 – Geometry and edge sketch for the cut off cylinder configuration with all dimensions in millimetres.**

**Table 9-3 – Edge details for the cut off cylinder configuration. Dist = Distribution type; HT = Hyperbolic Tangent distribution; U = Uniform distribution.**

| Edge | End | Spacing (mm) | Nodes | Distribution |
|---|---|---|---|---|
| am | a | 15 | 20 | HT |
| | m | 2 | | |
| mb | m | 2 | 51 | HT |
| | b | 2 | | |
| bc | b | 2 | 31 | HT |
| | c | 12 | | |
| cl | c | 80 | 11 | HT |
| | l | 50 | | |
| cd | c | 80 | 11 | HT |
| | d | 50 | | |
| de | d | 50 | 13 | HT |
| | e | 120 | | |
| ef | e | 100 | 11 | 9 |
| | f | 60 | | |
| dh | d | 56 | 15 | HT |
| | h | 22 | | |
| fg | f | 130 | 15 | HT |
| | g | 22 | | |
| li | l | 58 | 15 | HT |
| | i | 22 | | |
| ih | | N/A | 21 | U |
| | | N/A | | |
| hj | h | 20 | 37 | HT |
| | j | 0.15 | | |
| kj | j | N/A | 21 | U |
| | k | N/A | | |
| no | n | N/A | 21 | U |
| | o | N/A | | |
| po | p | 0.15 | 11 | HT |
| | o | 0.8 | | |

The application of these nodes per edge, edge end spacing and distribution functions resulted in nodal spacing that varied smoothly across the edges as shown in Figure 9-5 and total cell counts for the four meshes as detailed in Table 9-4.

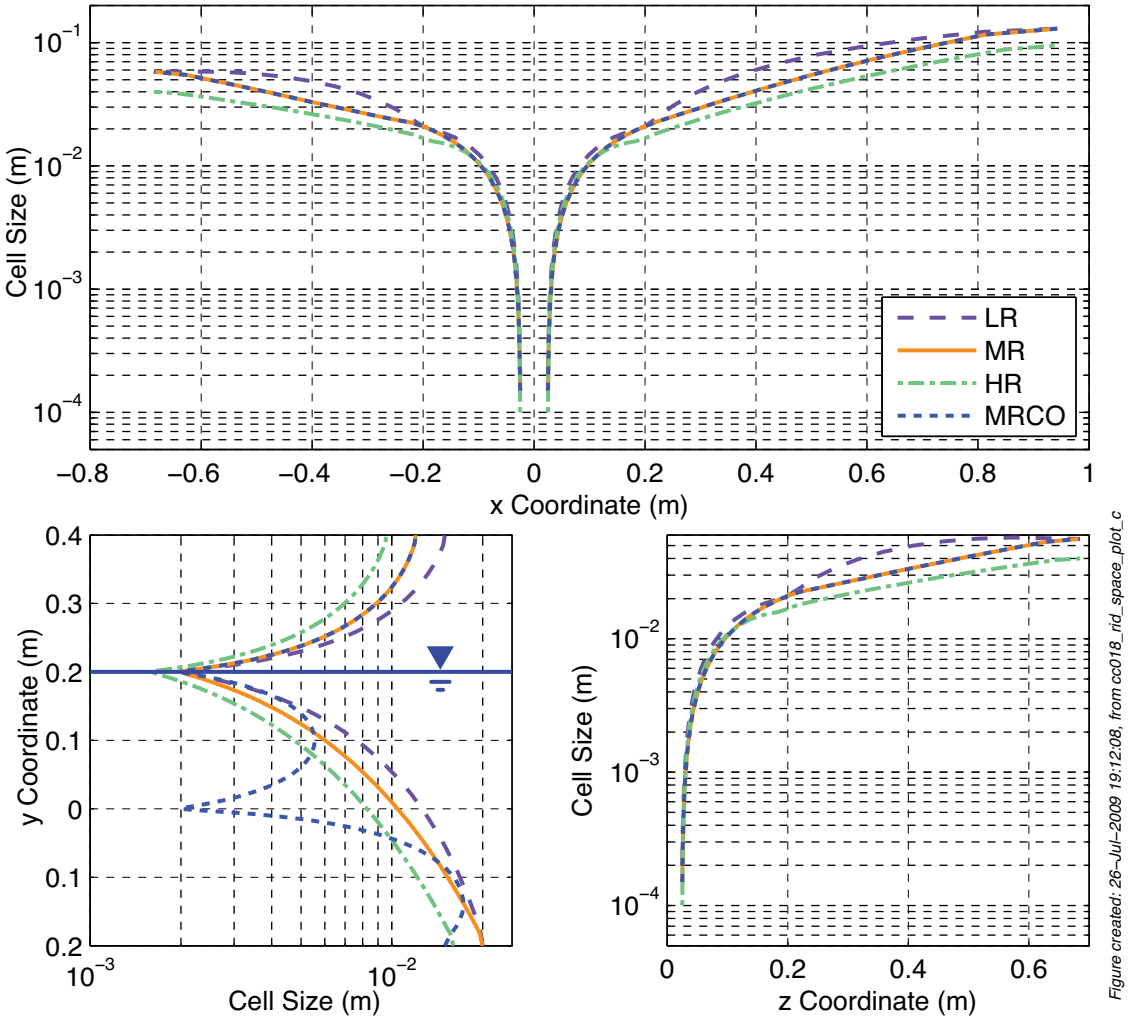


**Figure 9-5 – Plots of the cell size along lines that contain the point (0,0,0) and are parallel to the *x*-, *y*-, and *z*-axes (a), (b) and (c) respectively. Due to the mirror-symmetry around the *z*=0 plane, only the positive *z*-axis is shown in (c).**

**Table 9-4 – Total cell count for the three grids.**

| Full Depth Low Resolution | Full Depth Medium Resolution | Full Depth High Resolution | Partial Depth Medium Resolution |
|---|---|---|---|
| 245 430 | 373 340 | 588 500 | 418 800 |

To assist in the blending from the inner circular grid to the rectangular boundary, the four, radial edges in the outer region, highlighted in Figure 9-6, were set as orthogonal edges. That is, any mesh lines into any of those four edges were forced to join the edge at right angles.

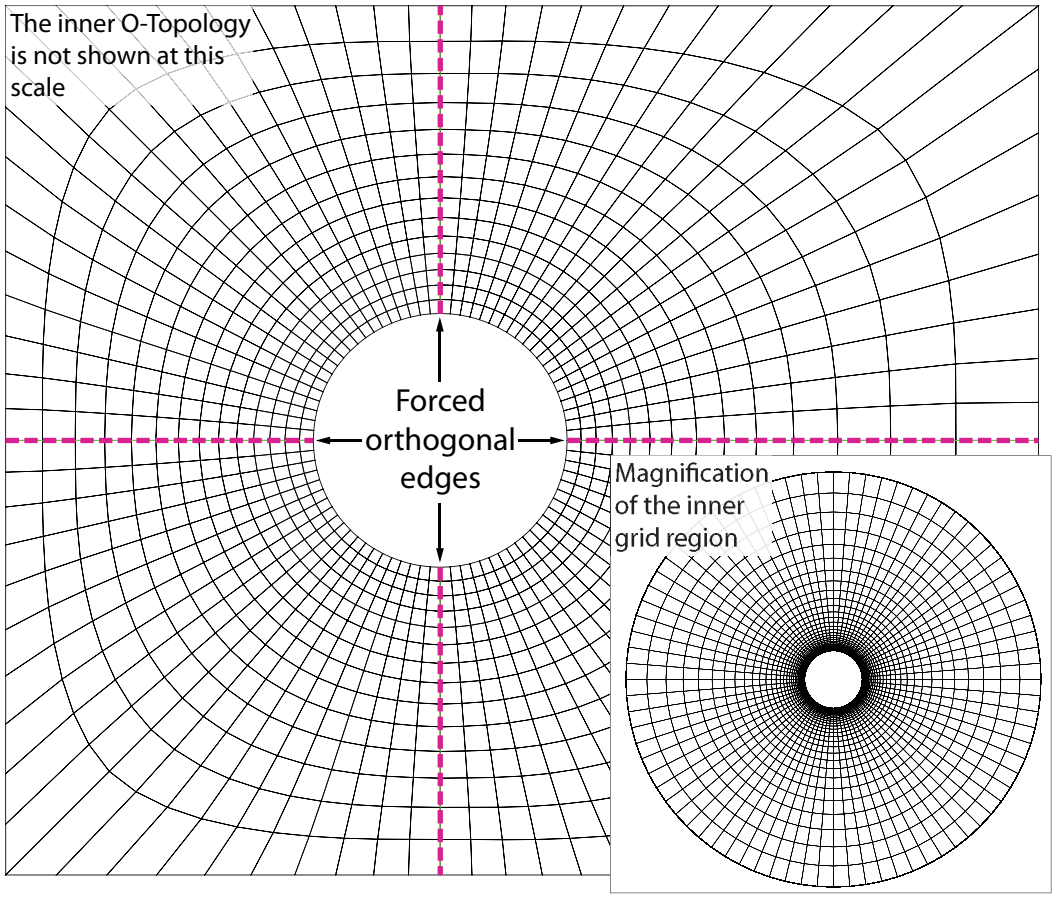


**Figure 9-6 – View of a *y*-plane taken from the medium resolution model with the dashed, purple lines showing the forced orthogonal edges.**

With the specific geometric configuration described and the block and edge layout used to discretise the domain also presented, the discussion can turn to the time step and solver specifications implemented with the present work. Please note that the boundary conditions have already been discussed in §7.3.

### 9.2.3. Time Step and Solver Configuration

The time step that was used for the simulations described in the present work was set using the Courant-Friedrichs-Lewy (CFL) condition (Courant et al., 1967),

$$N_{CFL} = \frac{U_{ref}\Delta t}{\Delta x}, \tag{9.3}$$

as a guide. However, despite the original definition of

$$N_{CFL} \leq 1 \tag{9.4}$$

for stability, numerical experiments conducted in preparation for this work, not discussed in this dissertation, indicated that for the VOF model

$$N_{CFL} \ll 0.1 \tag{9.5}$$

was more appropriate and which is in agreement with the recommendations of the code developer (ESI CFD Inc., 2007a). Hence, the time steps that were used were all less than 16 μs as detailed in Table 9-5.

**Table 9-5 – Time step size for the different resolution and speed combinations.**

| **$Re_d$=27×10$^3$** | **$Re_d$=54×10$^3$** | | |
|---|---|---|---|
| **Medium Resolution** | **Low Resolution** | **Medium Resolution** | **High Resolution** |
| 16 μs | 10 μs | 8 μs | 5 μs |

With the time step set as shown in Table 9-5, the spatial discretisation was configured to use the same second order upwind with limiter scheme with zero blending as used previously in this dissertation. A conjugate gradient squared solver with preconditioner (Saad, 1996) was used as the velocity solver while an adaptive multigrid solver (Lonsdale, 1993) was used for the pressure correction. To reduce the occurrence of free surface artefacts such as the generation of small, isolated regions of air within the predominantly water phase, and vice versa, a flotsam and jetsam filter was used (ESI CFD Inc., 2007a) at the end of each time step.

The iterative cycle was controlled by three parameters: (1) a maximum iterative count per time step of ten iterations, (2) a convergence criteria of $10^{-3}$, or three orders of magnitude reduction in the "error" and (3) a minimum residuals of $10^{-6}$. Details of the interactions and meanings of these parameters is detailed in Appendix A. Prior to an examination of the flow features to validate the numerical approach, the convergence of the solver must be inspected to ensure the minimum level of numerical accuracy, the solver precision, has been reached.

## 9.3. Convergence and Stability of the Numerical Solver

As with all numerical simulations that rely on an iterative solver the convergence of the solver must be examined. For all three simulations at $Re_d=54\times10^3$ over 99% of the time steps converged, whereas for the simulation at $Re_d=27\times10^3$ the convergence rate dropped to 92%, as shown in Figure 9-7.

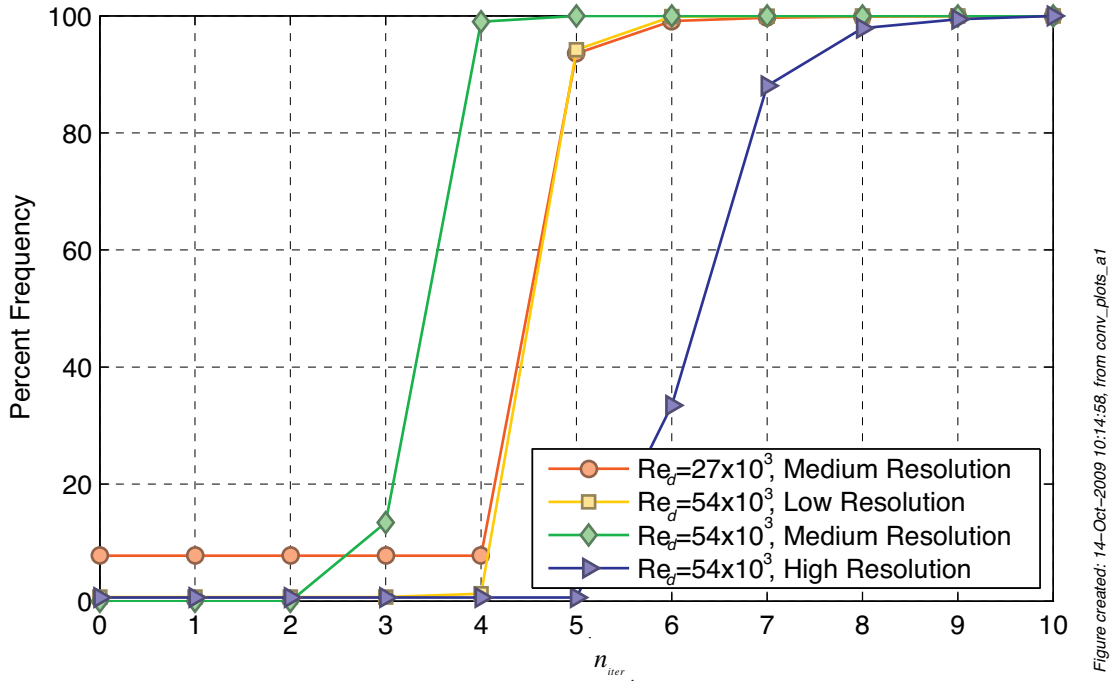


**Figure 9-7 – Cumulative probability distributions of $n_{iter}$ for the four free surface piercing simulations.**

Therefore, as the numerical solver converged for the vast majority of time steps across all the simulations, the results can be deemed correct to the specified level of numerical accuracy. Because numerical convergence does not guarantee that the solution is a correct representation of the intended physical configuration, the results must still be critically examined.

## 9.4. Visual Examination of the Simulated Free Surfaces

### 9.4.1. Case 1: Full Depth, $Re_d = 27\times10^3$

As has been the procedure of this dissertation the analysis of the results will start from the most general, for example a qualitative examination of the shape of the free surface, followed by successive refinements towards velocity measurements at specific locations. Of the results introduced for comparison only Hay and Yu et al presented

oblique angle images of the free surface that were suitable for visual comparison with the present work.

As discussed in §1.9 the most extensive visual record of the free surface elevation was that published by Hay (1947) yet Inoue et al (1993), which the present simulations match for Reynolds number, did not investigate a combination studied by Hay. Therefore, by extension, the velocities in the present $\mathrm{Re}_d = 27 \times 10^3$ simulations do not exactly match that of Hay. The two configurations photographed by Hay that are closest to the present work were at speeds of 0.3 m/s and 0.6 m/s, as shown in Figure 9-8(b) and (c), respectively. Hence, as the free stream velocity in the current work was 0.54 m/s, it would be reasonable to assume that the results from the present simulations would be closest to the 0.6 m/s observations from Hay. This is in fact the case, where the results from the present work, as shown in Figure 9-8(a), are in excellent agreement with the 0.6 m/s Hay image, as shown in Figure 9-8(c),

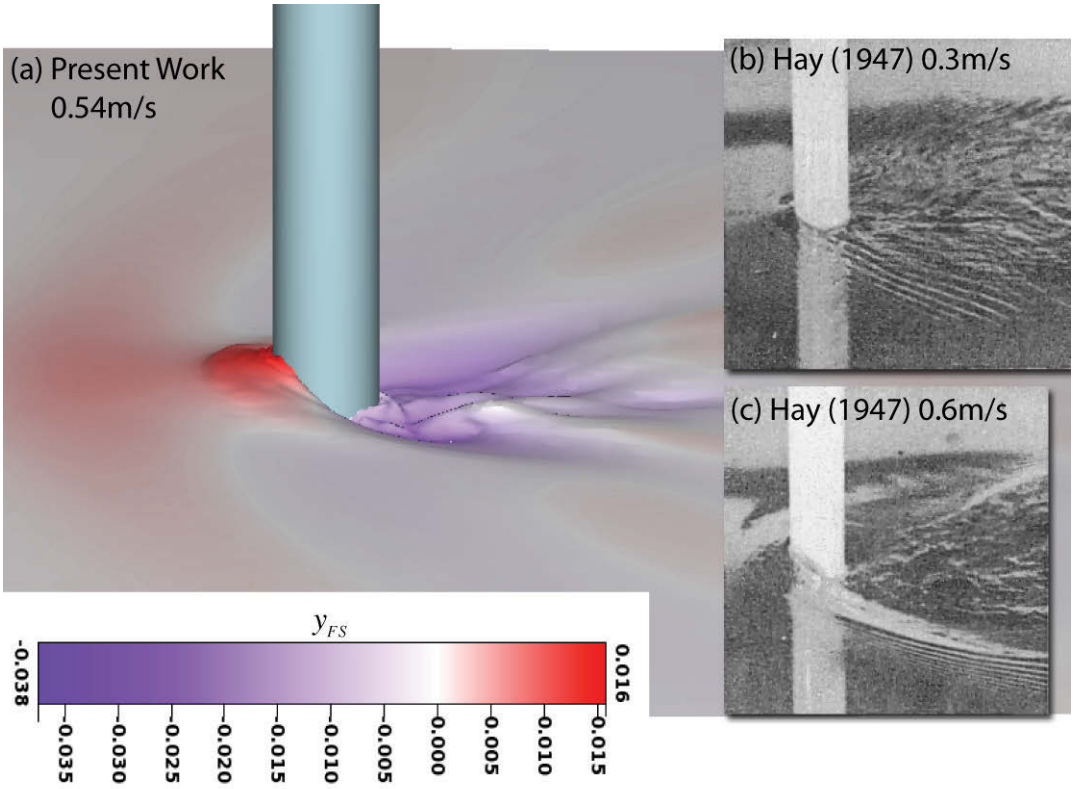


**Figure 9-8 – Medium Resolution Grid, Low Speed Oblique Comparison with Experimental Photographs of the Free Surface in the Near Wake of the Cylinder**

Specifically, both the 0.6 m/s Hay image and image of the instantaneous free surface elevation from the present work have the same large-scale features, including

1. A small bow wave, in the order of 15mm high (scaled from the colour plot);
2. Transformation of the bow wave in the near field to a Kelvin wake in the far field;
3. A disturbed wake region with small wake waves but no obvious large scale rooster tail;

In addition to the excellent agreement with the Hay data visible in Figure 9-8, the side view of the wake from the present simulations and the 0.6 m/s Hay data, as shown in Figure 9-9(a) and (c), are also in, again, excellent agreement. The shapes of the bow waves in these two results are remarkably similar but the wake region in the Hay data, Figure 9-9(c), is noticeably extended downstream compared to the present results, Figure 9-9(a). However, a degree of caution must be used when interpreting this last observation because there are a number of shadows in the Hay image that make a visual comparison of the wake extent difficult.

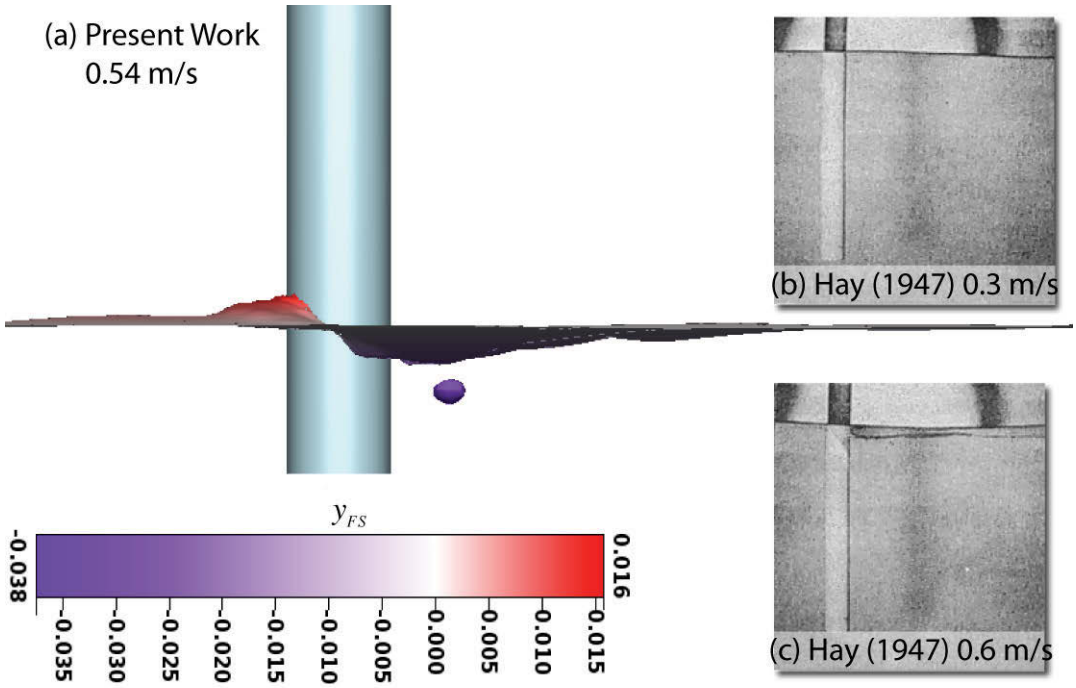


**Figure 9-9 – Medium Resolution Grid, Low Speed Side View Comparison with Experimental Photographs of the Free Surface in the Near Wake of the Cylinder**

While the present simulation does accurately, at least visually, capture the large-scale features of the free surface, it does not capture the small capillary waves that are visible in the photographs of the extended bow wave and near wake, for example Figure 9-8(c). This lack of resolution is due to the numerical limitations of the grid, which was large

compared to the wavelength of these capillary wave features. In defence of the present simulations, it must be noted that to barely capture* these capillary waves the cell sizes would need to be in the order of 0.1 mm, which when extended to the entire domain would have resulted in an impossibly high cell count. Therefore, more of these fine wave structures should be resolved if the resolution in the region of the free surface were to be increased. This projection is supported with the simulation of additional free surface waves that are visible in the results of Yu et al (2008), as shown in Figure 9-10, who utilised $O\left(1.6\times10^{6}\right)$ cells relative to the $O\left(373\times10^{3}\right)$ cells in the present work. Yet, even with these additional cells Yu et al (2008) do not fully simulate the free surface as observed by Hay.

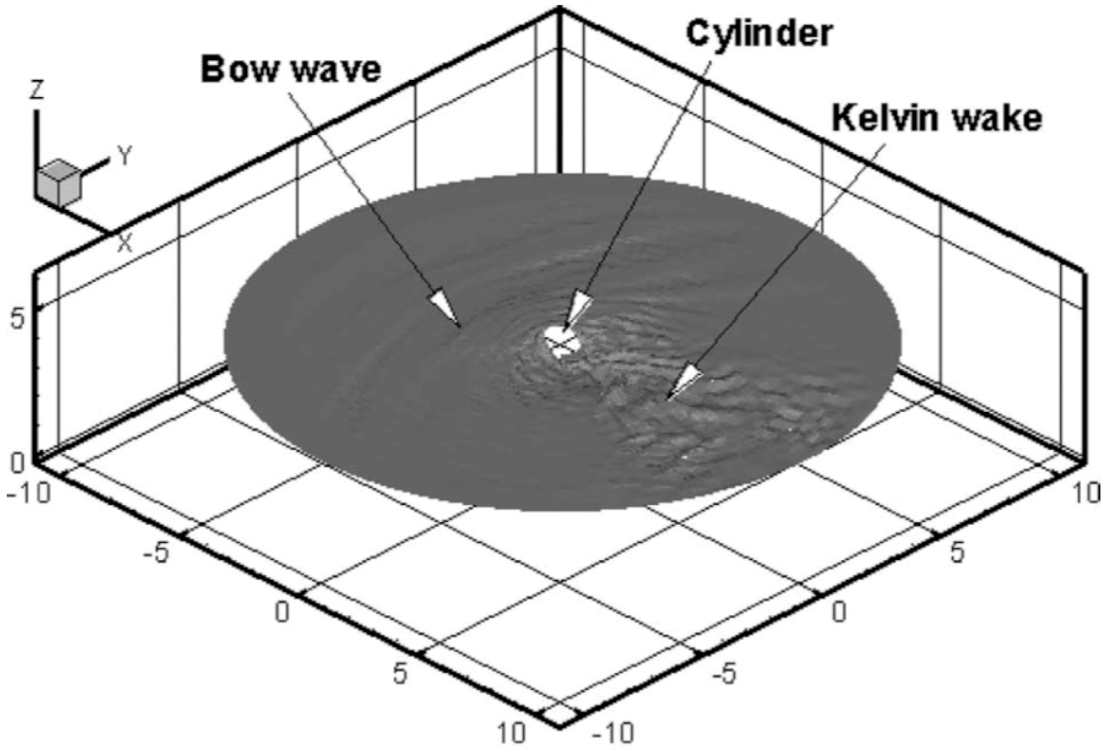


**Figure 9-10 – Shape of the instantaneous free surface from Yu et al (2008).**

Therefore, as the increased cell count has resulted in increased resolution of the free surface wave features it could be suggested that neither of these simulations have yet reached mesh independence with respect to these surface waves. It would be natural

* Based on the commonly held interpretation that a minimum of five points are needed to resolve a wave (Fletcher, 1991, Orfanidis, 1996, Roache, 1998a) and that the wavelength of the capillary waves are in the order 0.5 mm.

then to suppose that, as with an integral quantity such as the drag coefficient, there is a point of mesh independence for the free surface simulation. This appears unlikely because, unlike a drag coefficient or averaged velocity, there is a continuum of free surface features that must be simulated. To support this proposition, suppose that we consider the local radius of the free surface as the defining parameter that must be simulated with the VOF method, then the radius must vary over the range

$$0 < \left|\mathbf{r}_{surface}\right| \leq \infty . \tag{9.6}$$

At the largest radii where the free surface is essentially flat, the radius tends to infinity and the free surface is relatively simple to simulate with large cells. In contrast, at the smallest radii, of bubbles and droplets, the radii that must be simulated continually decrease in radius to be limited only by the molecular size of the fluid in question. Hence, $1/5^{th}$ of a bubble that is only a few times the molecular scale is almost impossible to simulate to the scales of the work discussed in this dissertation and, by extension, VOF must be considered as impossible to achieve mesh convergence.

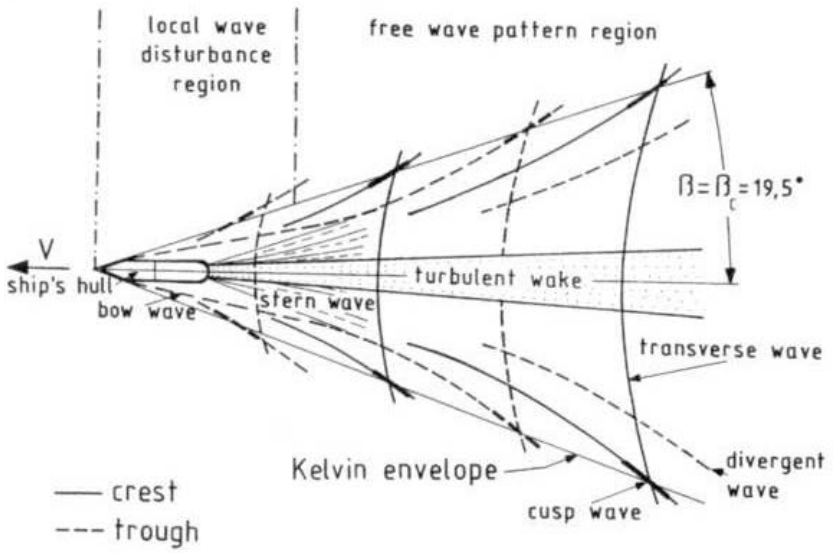


**Figure 9-11 – Sketch of the structure of a ship wake reproduced from ESA (*'Ship Wakes,'* 2009).**

To diverge from the current discussion momentarily, it appears that the Kelvin wake region identified by Yu et al (2008), for example the annotations visible in Figure 9-10, is incorrectly labelled. Specifically, if standard nomenclature from the study of ship wakes (which appears to be the de facto standard) is to be adopted then what Yu et al (2008) have identified as a Kelvin wake would be better labelled as turbulent wake

within the centre of the Kelvin envelope (*'Ship Wakes,'* 2009), as shown in Figure 9-11. It should be noted that while the transverse and diverging waves appear to meet at their respective cusps, they are in fact out of phase by one quarter of a wavelength.

Then, given that all the measurements for both the experiments and numerical simulations discussed in this dissertation were made within the local wave disturbance region, identified in Figure 9-11, it is highly unlikely that a fully developed Kelvin wake would have been observed. More likely, the observations would record the turbulent structures that are the precursor of the developed, large-scale Kelvin wake.

Returning to the current discussion, the excellent agreement of the results from the present work with the photographic records of Hay has been based on qualitative comparisons. To add a degree of rigor to these comparisons Inoue et al (1993), Chen et al (2000), Kawamura et al (2002) and Yu et al (2008) all published measurements of the time averaged free surface, which can be contrasted with the present results.

To develop the time averaged free surface elevation, recall that the VOF function, $F$, is defined over the range

$$0 \le F \le 1 . \tag{9.7}$$

Then the discrete time average for a general location in the computational domain, $\mathbf{x}$, is

$$\bar{F}(\mathbf{x}) = \frac{1}{n_{steps}} \sum_{m=1}^{n_{steps}} F(\mathbf{x}, t_m) \tag{9.8}$$

in which $F(\mathbf{x}, t_m)$ is the value of $F$ at point $\mathbf{x}$ and time $t_m$. Again, by extension $\bar{F}$ is only valid over the range

$$0 \le \bar{F} \le 1 \tag{9.9}$$

therefore a value outside this range should be treated as an indicator of an error in the numerical method. The location of the time averaged free surface was then assumed to be at the locus of

$$\bar{F}(\mathbf{x}) = 0.5 . \tag{9.10}$$

To highlight the size of the, generally small, free surface waves relative to the initial elevation of the free surface the elevation coordinate, $y$, was transformed as

$$y_{FS} = y - 0.2 . \tag{9.11}$$

There is a high degree of symmetry in the elevation of $\bar{F}$ around the *xz*-plane, as shown in Figure 9-12 and three symmetrical features, high and low points, in the wake were specifically identified. The high and low points are connected to the centre of the cylinder with radial lines, which form angles of 48°, 36° and 27° with the *xz*-plane for the "low and trough", "high and ridge" and "low" features, respectively. As was discussed above none of these angles are close to the 19° angle typical of a developed Kelvin wake (*'Ship Wakes,'* 2009), which supports the conjecture that the region under investigation in the present work is within the locally disturbed region instead of the developed Kelvin wake

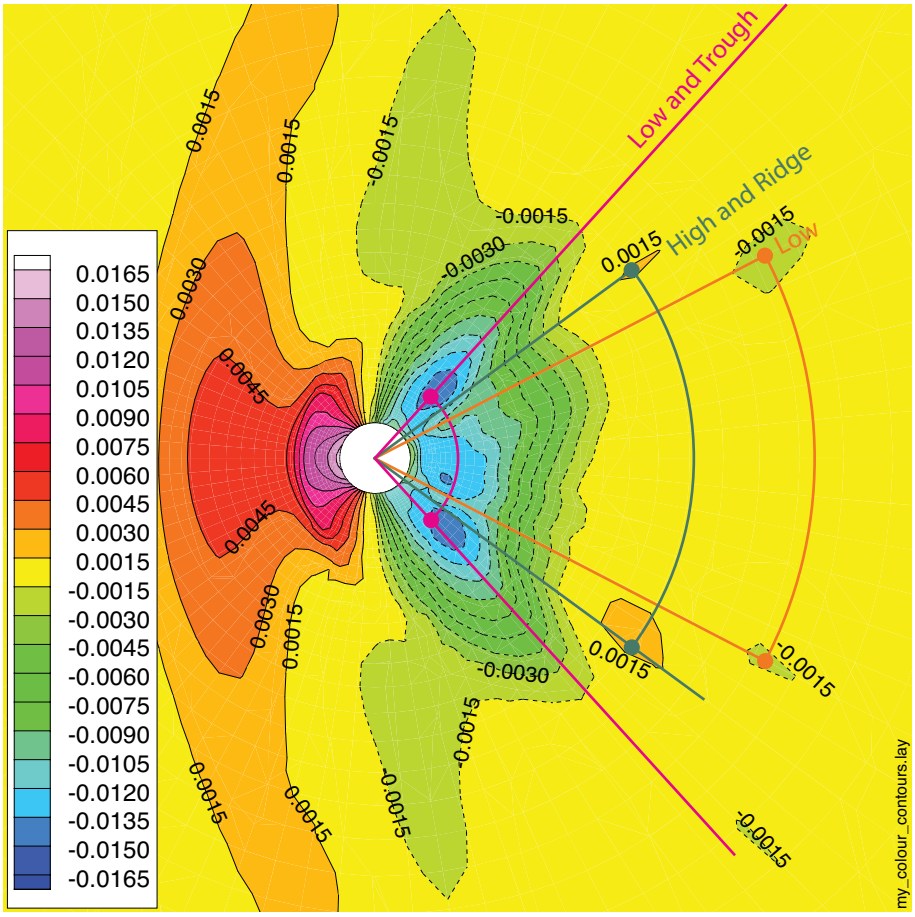


**Figure 9-12 – Contour plot of the time-averaged $y_{FS}$ (in metres) from the present work with annotations highlighting particular features.**

In contrast to the developed Kelvin wake, where the dominant wave pattern is the 19° "shockwave", within the local disturbance region there are a number of different waves that can be thought of as precursors to the far field wake. The predominant initiator waves are known to form at angles close to 35° (Yang, 2007), which is in remarkably close agreement to the "high and ridge" feature marked on Figure 9-12 that was

measured at close to 36°. Thus, this interpretation of the wave shapes from the present work support the projection introduced above that the region of the present simulation is within the local disturbance region. In addition, the region identified by Yu et al (2008) as a Kelvin wake is at best incorrectly labelled, but at worst is an artefact from an unreliable computation. While the image of the time averaged $y_{FS}$ shown in Figure 9-12 is an interesting plot, by itself there is little validation value. Therefore, the time averaged $y_{FS}$ values from the present work must be compared with other published studies, preferably both experimental and numerical.

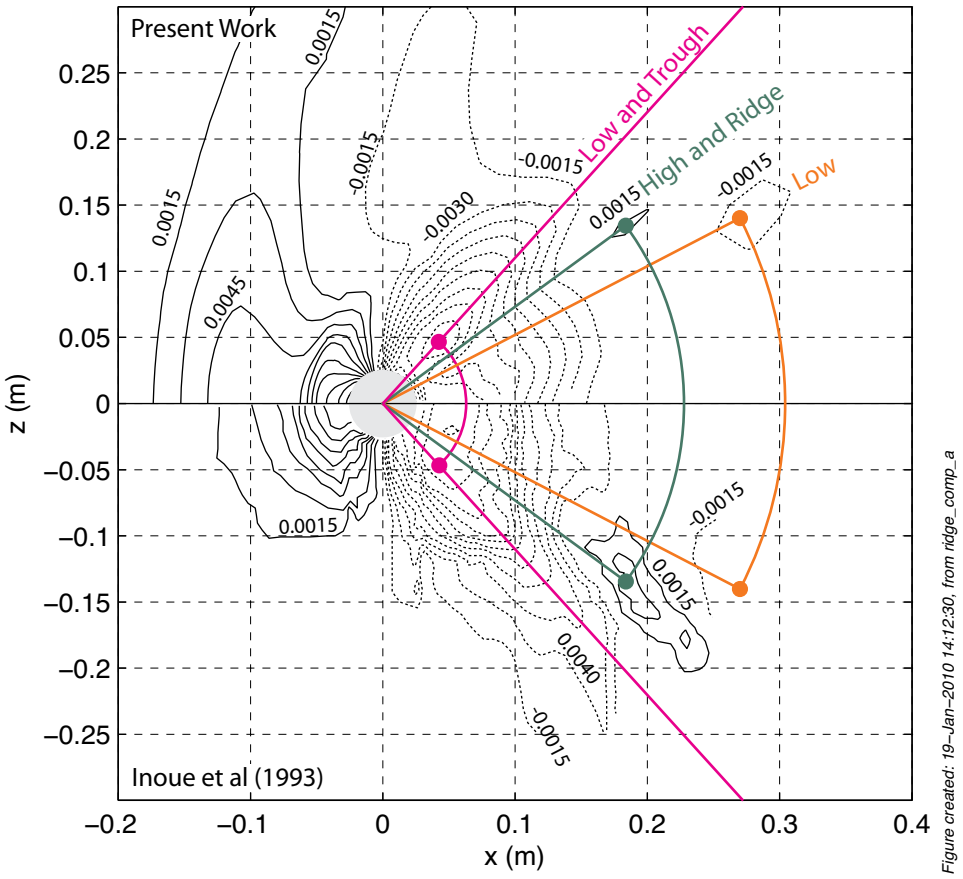


**Figure 9-13 – Contour plot comparison of the time-averaged $y_{FS}$ from the present work and the tow tank results of Inoue et al (1993).**

The shape of the free surface from the present work is in excellent agreement with that measured experimentally* in a tow tank by Inoue et al (1993), as shown in Figure 9-13. All three of the features identified from the present work, Figure 9-12, are not only

* All the contours presented within this thesis that are reproduced from other publications were digitised from the respective papers and therefore may, consequently, contain some inaccuracies.

present in both their work and Inoue's but are of remarkably similar magnitudes and radial distances from the cylinder.

As there is an excellent comparison between the present work and experimental data, we can now examine the alternate numerical results. Because the results of Yu et al (2008) are simultaneously the most recently published and used the largest cell count, for similar domain sizes, it would be expected that their results would be the most accurate. Interestingly, this is not the case as their time averaged $y_{FS}$ data are distinctly different from the present work, as shown in Figure 9-14. Specifically, none of the features observed in the wake from either the present study and the experimental data, as shown in Figure 9-12 and Figure 9-13 respectively, are visible in Yu et al (2008).

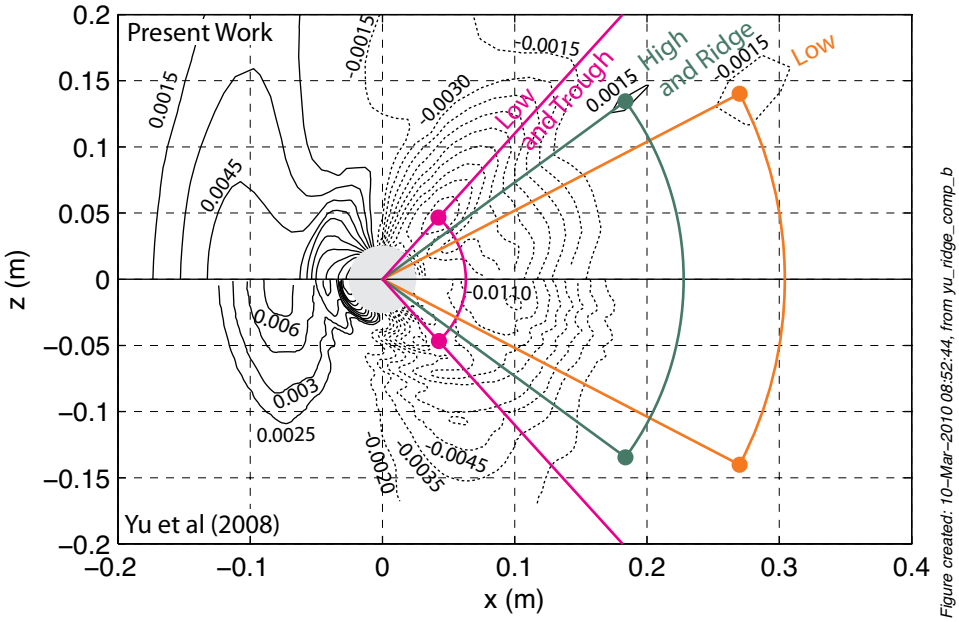


**Figure 9-14 – Contour plot comparison of the of the time-averaged $y_{FS}$ from the present work and the tow tank simulation of Yu et al (2008).**

It is possible that they did not average their simulation for long enough to obtain a suitable average. However, this is very unlikely though as it is stated in their paper that they averaged for 12 shedding periods, or 60 non-dimensional time units, and the averages were not started until 60 non-dimensional time units had elapsed (Yu et al., 2008). Alternatively, either their numerical method or domain configuration may not have been capable of capturing the free surface correctly. Because the authors published no detailed comparisons of the free surface, such as contour plots similar to Figure 9-13 or Figure 9-14, and only stated that the bow wave height "agrees well" with

experimental data it seems much more likely that there were problems with their code or configuration. Therefore, no further comparison with the Yu et al data will be undertaken in this dissertation.

Despite the very poor results of Yu et al (2008) the time averaged $y_{FS}$ contours published by Kawamura et al (2002) are in excellent agreement with both the present work and the experimental data of Inoue et al (1993). These two results are somewhat of a surprise as the more recent code and larger cell count utilised by Yu would be expected to result in a better simulation. Further both Kawamura and Yu claim to have used exactly the same Smagorinsky LES model and have similar domains so they appear to differ only in the choice of cell count and domain shape.

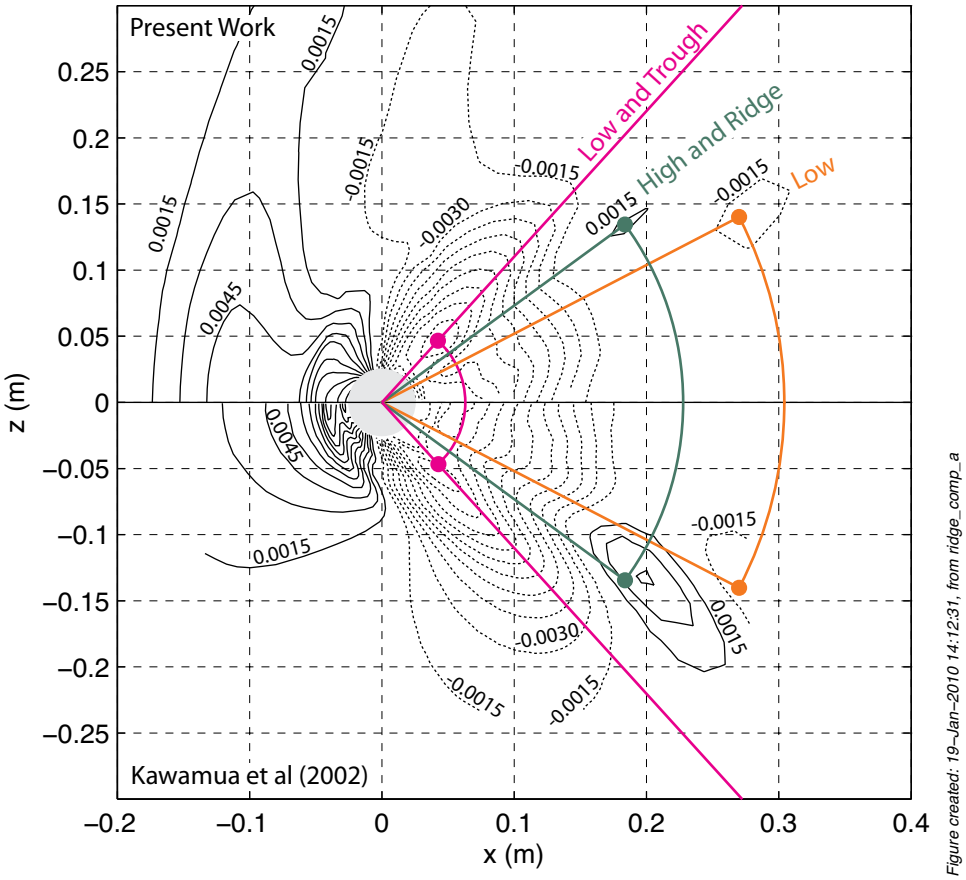


**Figure 9-15 – Contour plot comparison of the time-averaged $y_{FS}$ from the present work and the tow tank results of Kawamura et al (2002).**

As Chen et al (2000) did not publish contours of the free surface no comparison is possible but they did publish a plot of the time averaged $y_{FS}$ along the $x = 0.035\text{m}$ plane for $z \geq 0$, as shown in Figure 9-16. As can be seen, Chen's results are also in

good agreement with the experimental results of Inoue. As expected from the visual comparison of the $y_{FS}$ contours that were discussed above, both Kawamura's results and the present simulations are also in excellent agreement with the experimental data.

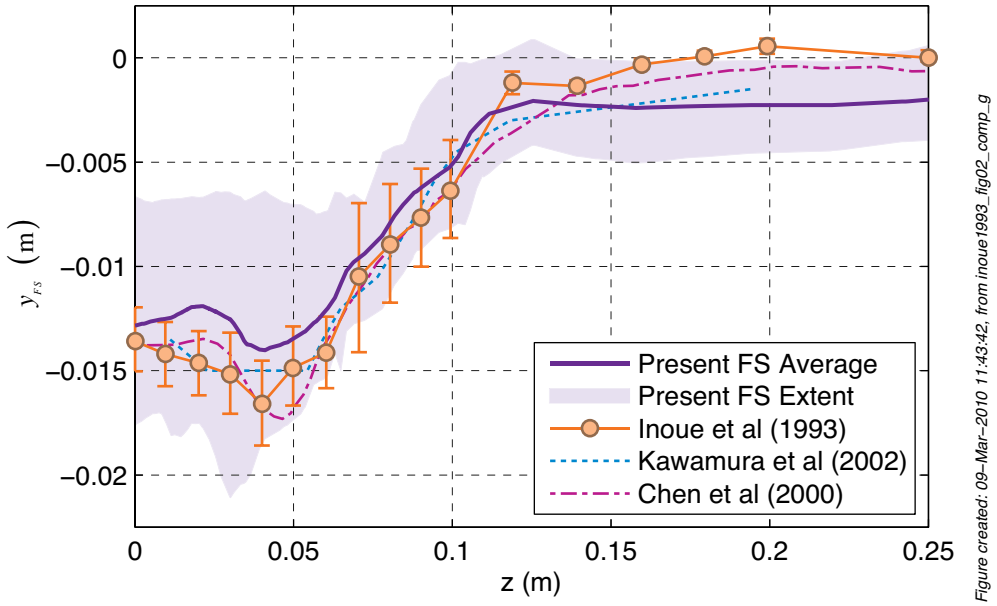


**Figure 9-16 – $y_{FS}$ as a function of $z$ for $x$ = 0.035 m with the error bars from the present work indicative of the spread rather than a measurement error.**

While it could be argued that a number of the data points from the present simulation in the region of

$$0 \le z < 0.05\text{m} \tag{9.12}$$

are outside of the error bounds for the experimental data as the magnitude of these differences is $O(1\text{mm})$ they can be safely assumed to be within the bounds of the accuracy of the present simulations. The method used to compute the average free surface in the present work can not compute an error estimate, instead the region enclosed by

$$0.05 \le \bar{F} \le 0.95 \tag{9.13}$$

is shown in Figure 9-16. Interestingly, the average free surface elevation over the range

$$0 \le z \le 0.1\text{m} \tag{9.14}$$

from the present work is closer to the lower bound of the shaded region. This could indicate that the average may have been started too early, while the free surface was still dropping to its average elevation. Alternatively, and more likely, the larger spread to the

higher elevations was a result of splashing around the cylinder. Irrespective, $y_{FS}$ from the present simulations is in excellent agreement with the other experimental and numerical studies.

In addition to the free surface measurements Inoue et al (1993) also measured four average velocity profiles as a function of depth at different locations, shown in Figure 9-17, using a hot film probe. Instead of a single component measurement, this probe would most likely have measured a value closer to the velocity magnitude (Bruun, 1995) comprised of the intended component smeared with influences from the remaining two. Therefore, it was assumed that, because of the smearing inherent in hot film anemometry, the most appropriate results from the present work would be the magnitude of all three velocity components.

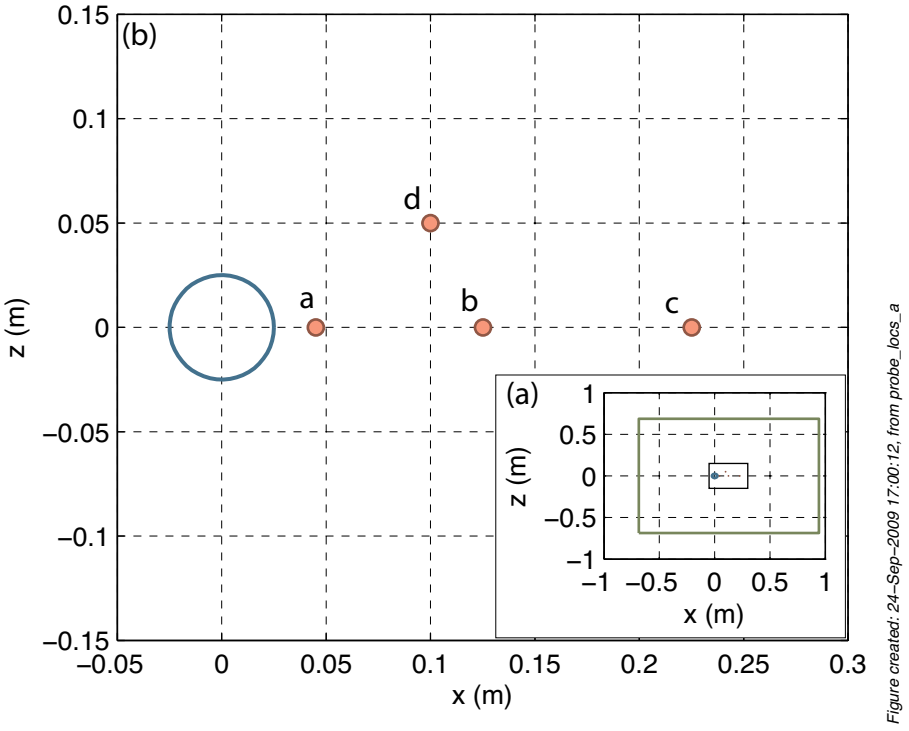


**Figure 9-17 – Plot of the horizontal location of the vertical traverse lines used by Inoue et al (1993) to measure the velocity relative to the entire computational domain of the present work (a) and a magnification of the cylinder region (b).**

Surprisingly, given the detail that the measurements of the free surface were presented by Inoue, error estimates of the velocity magnitudes were not included in the published data. Perhaps this was a limitation of either the hot film probe or the data-logging

equipment used in the experiments. In contrast to the experimental data, Kawamura et al (2002) did publish error estimates of their velocity profiles.

For the three stations that were located on the $z = 0$ plane, marked as points "a", "b" and "c" in Figure 9-17, the results from the present work for the velocities below the surface are in excellent agreement with the experimental and numerical results, as shown in Figure 9-18. Kawamura et al (2002) did not publish their velocity profiles in the air phase. However, if the trend of their results were to continue, the extrapolated velocity profile would differ from the present work. This discrepancy is probably due to the boundary conditions, which may not have accelerated the air phase as discussed in §7.3 for the present work. None of the papers adequately discussed their boundary conditions so this conjecture cannot be examined.

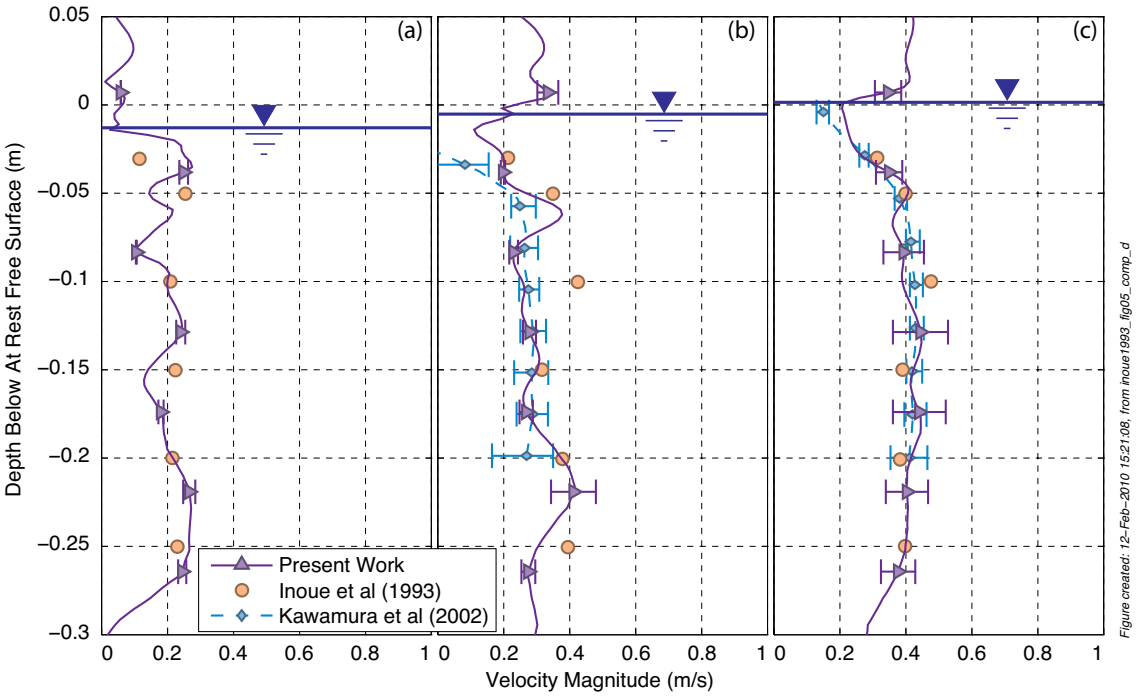


**Figure 9-18 – Average velocity as a function of $y_{FS}$ for the vertical station marked as "a", "b" and "c" shown in Figure 9-17 for subplots (a), (b) and (c), respectively.**

The final station, labelled as "d" in Figure 9-17, was located to the side of the $z = 0$ plane and the results from the present work are an almost perfect match to the numerical results described by Kawamura et al (2002). Both numerical results match the experimental data for $y_{FS} \geq -0.05\,(\mathrm{m})$ but otherwise the numerical results are consistently overestimated by approximately 15% relative to the experimental data.

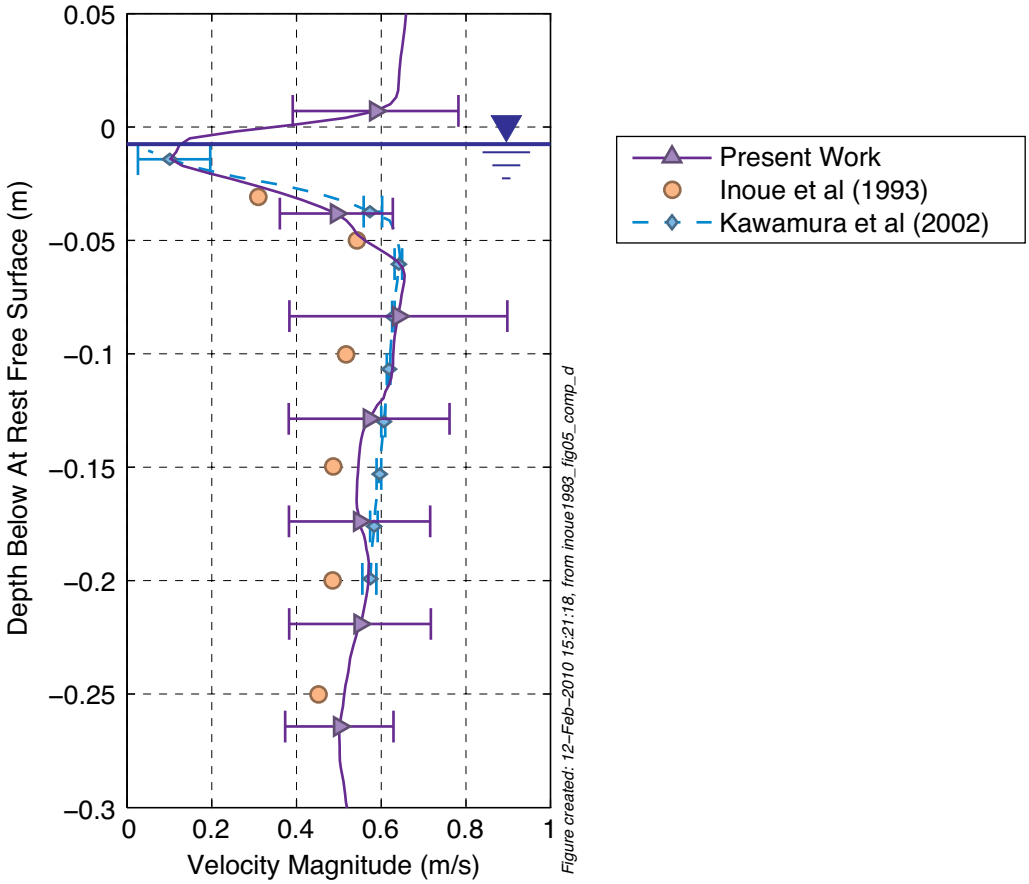


**Figure 9-19 – Average velocity as a function of $y_{FS}$ for the vertical station marked "d" in Figure 9-17.**

Based on a visual examination of the shape of the free surface there is an excellent agreement with the tow-tank results of both Hay (1947) and Inoue et al (1993) and the numerical date published by Kawamura et al (2002). Therefore, the validation and investigation can continue with the second case, the full depth cylinder at the higher Reynolds number of $\mathrm{Re}_d = 54 \times 10^3$.

### 9.4.2. Case 2: Full Depth, $\mathrm{Re}_d = 54 \times 10^3$

At this higher Reynolds number the only source of validation data for the shape of the free surface is from the extensive study described by Hay (1947), which is predominantly comprised of photographic images of the free surface. Further, for the reasons discussed above and as this Reynolds number was double the lower speed configuration that was discussed previously, the free stream velocity was 1.08 m/s, which is midway between the 0.91 m/s and 1.22 m/s studied by Hay. Therefore, the

flow features from the present work would be expected to contain features resembling aspects of both the higher and lower velocity results in Hay's study.

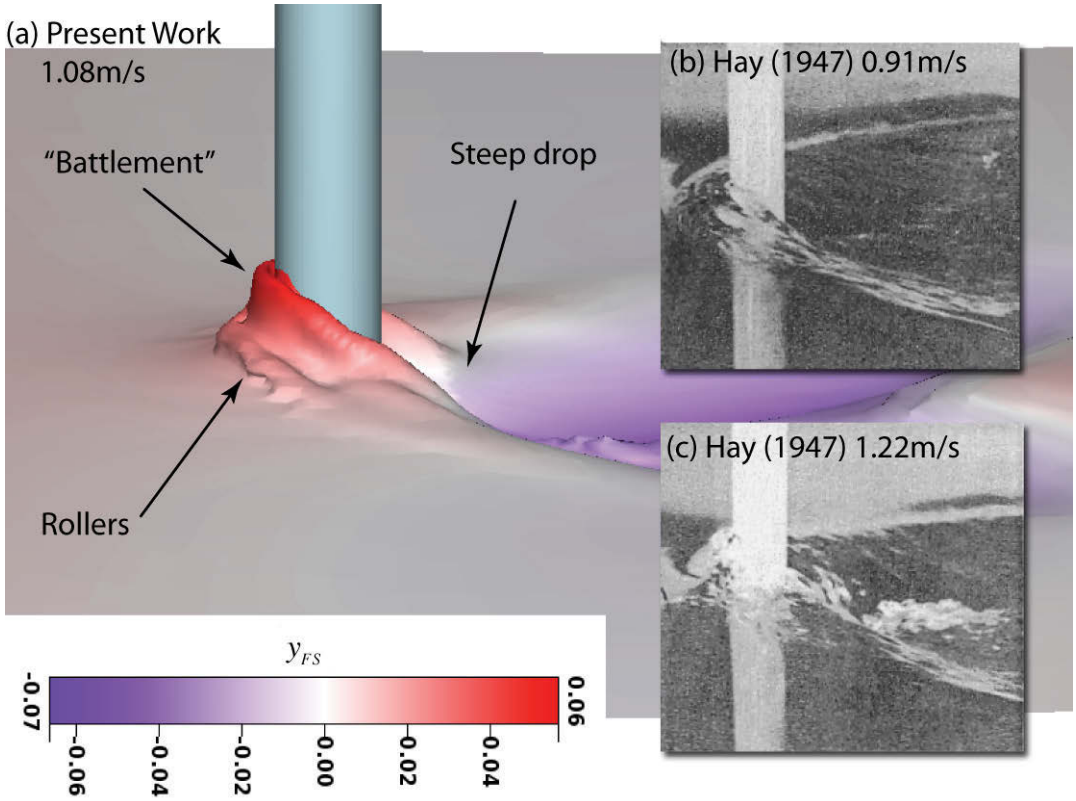


**Figure 9-20 – Medium Resolution Grid, High Speed Oblique Comparison with Experimental Photographs of the Free Surface in the Near Wake of the Cylinder**

As visible in a comparison of Figure 9-20 and Figure 9-21, the results from the present simulations appear to be a better approximation of the 1.22 m/s experiment in preference to the 0.941 m/s test. An examination of two key flow features was used to obtain this conclusion, namely:

1. As the flow wraps around the cylinder the drop into the draw down hole is relatively steep and there is a rooster tail* formed as shown in a comparison of the sub-images of Figure 9-20.

2. The shape of the bow wave from the present work is characterised by a lower roller section that spreads upstream of the cylinder and a battlement, that is a tall, and thin structure reminiscent of medieval English castles, type structure

* "Rooster tail", as defined and visualised by Brocchini and Peregrine (2001), will be used to describe the wake structure that extends downstream along the free surface and is symmetrical around the centreline. This structure is also known as a "roach" (Breslin and Skalak, 1959).

attached to the upstream edge of the cylinder. These features are visible in the 4ft/s experiment, in particular Figure 9-21(c), but not the 3ft/s experiment.

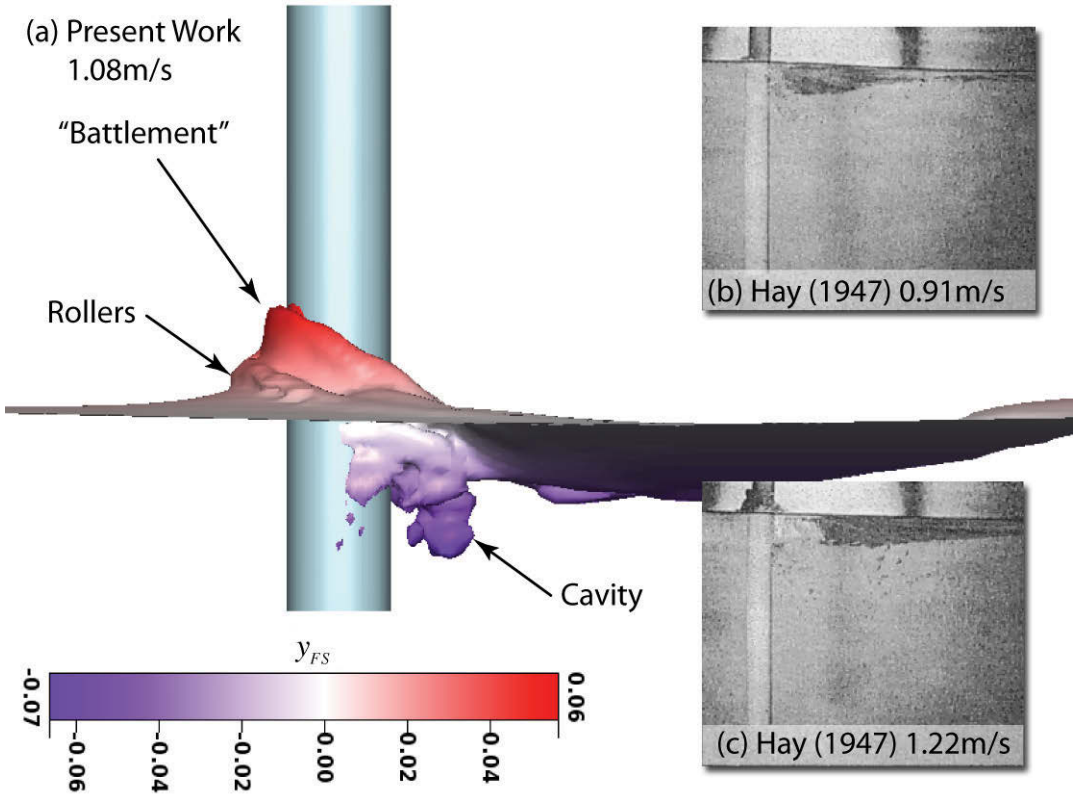


**Figure 9-21 – Medium Resolution Grid, High Speed Side View Comparison with Experimental Photographs of the Free Surface in the Near Wake of the Cylinder**

The observations from the simulations for which the cylinder extended across the entire vertical extent of the computational domain at both $\mathrm{Re}_d = 27 \times 10^3$ and $\mathrm{Re}_d = 54 \times 10^3$ support the conclusion that the present numerical approach can correctly capture the large-scale flow features. Therefore, the final configuration where the cylinder did not completely extend to the lower boundary of the domain can be examined.

### 9.4.3. Case 3: Partial Depth, $\mathrm{Re_d} = 54 \times 10^3$

As with the other high speed simulation discussed in §9.4.2 the only source of data available for comparison of the shape of the free surface from the present simulation is from Hay's monograph (Hay, 1947). Again, as the Reynolds number for the present work was defined relative to the cylinder diameter, the present results are mid-way between the two nearest photographs from Hay. Therefore, it would also be expected that the shape of the present free surface be also mid-way between the two extremities.

In contrast to these expectations, and in line with the previous high-speed results, the present results more closely match the image from the higher speed configuration of Hay, as shown in Figure 9-22 and **Error! Not a valid bookmark self-reference.**.

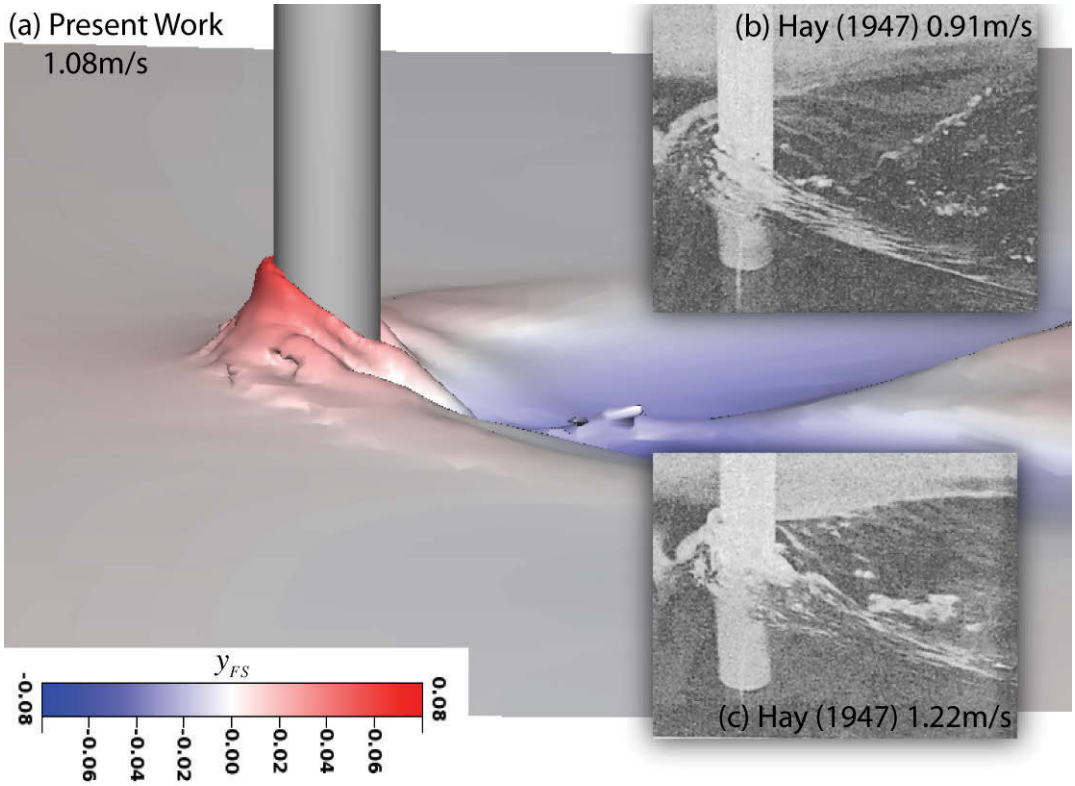


**Figure 9-22 – Oblique Comparison of the Free Surface Close to the Cylinder from the Present Partial Depth Simulation to the Experiments of Hay (1947).**

This conclusion was based on observations of the same two features as the full depth, high-speed simulation, namely the steep drop into the wake draw down and the taller bow wave shape. Interestingly, these two features appear to be of similar size in both simulations, which indicates that both the height of the bow wave and the depth of the wake draw down hole are independent of the depth of the cylinder below the at rest free surface. Precise measurements of these features, rather than the qualitative comparisons in this chapter, will quantify this possibility.

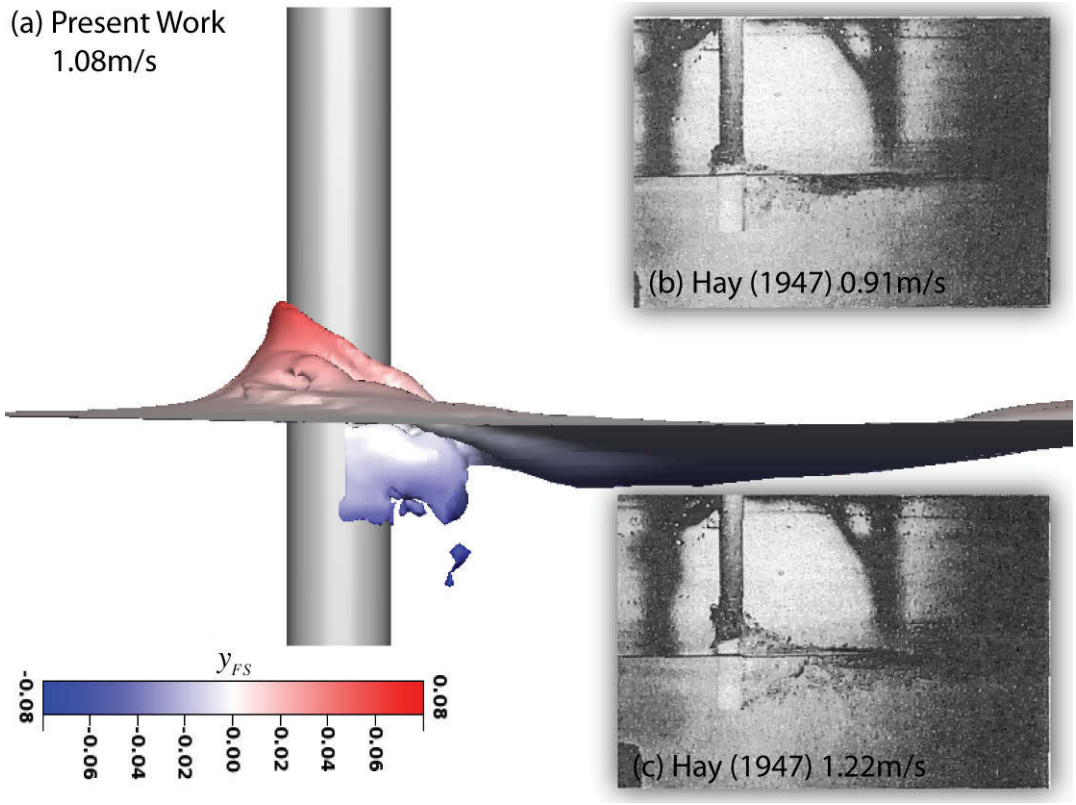


**Figure 9-23 – Side View Comparison of the Free Surface Close to the Cylinder from the Present Partial Depth Simulation to the Experiments of Hay (1947).**

# 10. Three-Dimensional, Two-Phase Simulations: Point, Time Domain and Spectral Results

## *10.1. Wave Shape Parameters*

### 10.1.1. Introduction

Following from the excellent agreement of the shape of the free surface discussed previously a detailed comparison of four of the six wave shape parameters measured by Hay (1947) can be performed. As already introduced in §1 these distances were measured by Hay using photogrammetry and the two parameters not subject to investigation in the present work, namely $D_2$ and $L_2$, were ignored because the ambiguity in their definition. In contrast to this ambiguity, the remaining four parameters can be simply defined and measured from easily identifiable features, as shown in Figure 10-1.

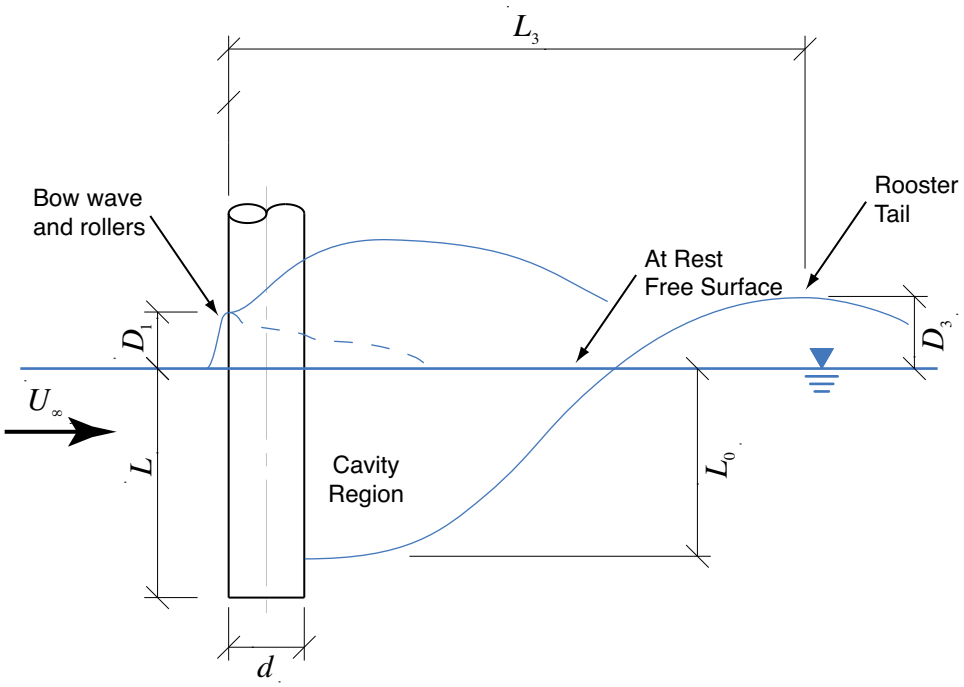


**Figure 10-1 – Sketch of the key lengths measured by Hay (1947).**

### 10.1.2. Bow Wave Height – $D_1$

At the end of the previous chapter it was suggested that, based on the observations of the present simulations, the bow wave height was independent of the depth immersion of the circular cylinder. Fortunately to extend from the limited test cases simulated in

the present work the extensive data set collected by Hay (1947) provides additional data to test this hypothesis, independent of the present results. Hay did not investigate these phenomena in detail, probably because he was more interested in the drag of the cylinders when towed, for which there is an extensive discussion (Hay, 1947).

To investigate these effects the data were plotted as a function of the Froude number* based on the diameter of the cylinder,

$$Fr_d = \frac{U_{ref}^2}{gd}, \tag{10.1}$$

instead of the Reynolds number†. The data support the hypothesis because for a given combination of Froude number and cylinder diameter, for the majority of the measurements $D_1$ is within 5%‡, as shown in Figure 10-2.

The notable exception to this trend occurs for the cylinders with

$$d \leq 6.35 \text{ mm} \tag{10.2}$$

and for

$$Fr_d \geq 100 \tag{10.3}$$

where the spread is in the order of 50%. However, from an inspection of the images of these flows there is huge splashing that would make an accurate measurement nearly impossible. Hence, significant caution should be taken interpreting these results for small $d$ at high $Fr_d$.

---

* This definition of the Froude number would traditionally be referred to as the square of the Froude number. However, this definition appears to be more "natural" to the present author as it is derived directly from an understanding of the physical systems being interpreted.

† The alternate analysis pathway based on the Reynolds number relative to the diameter resulted in an identical conclusion, yet because the Froude number is more commonly used when discussing free surface flows it will be the non-dimensional number predominantly used within this section.

‡ Although Hay did not specifically discuss the errors in the measurements of the free surface, these results would be close to the limit of the photogrammetry technique used.

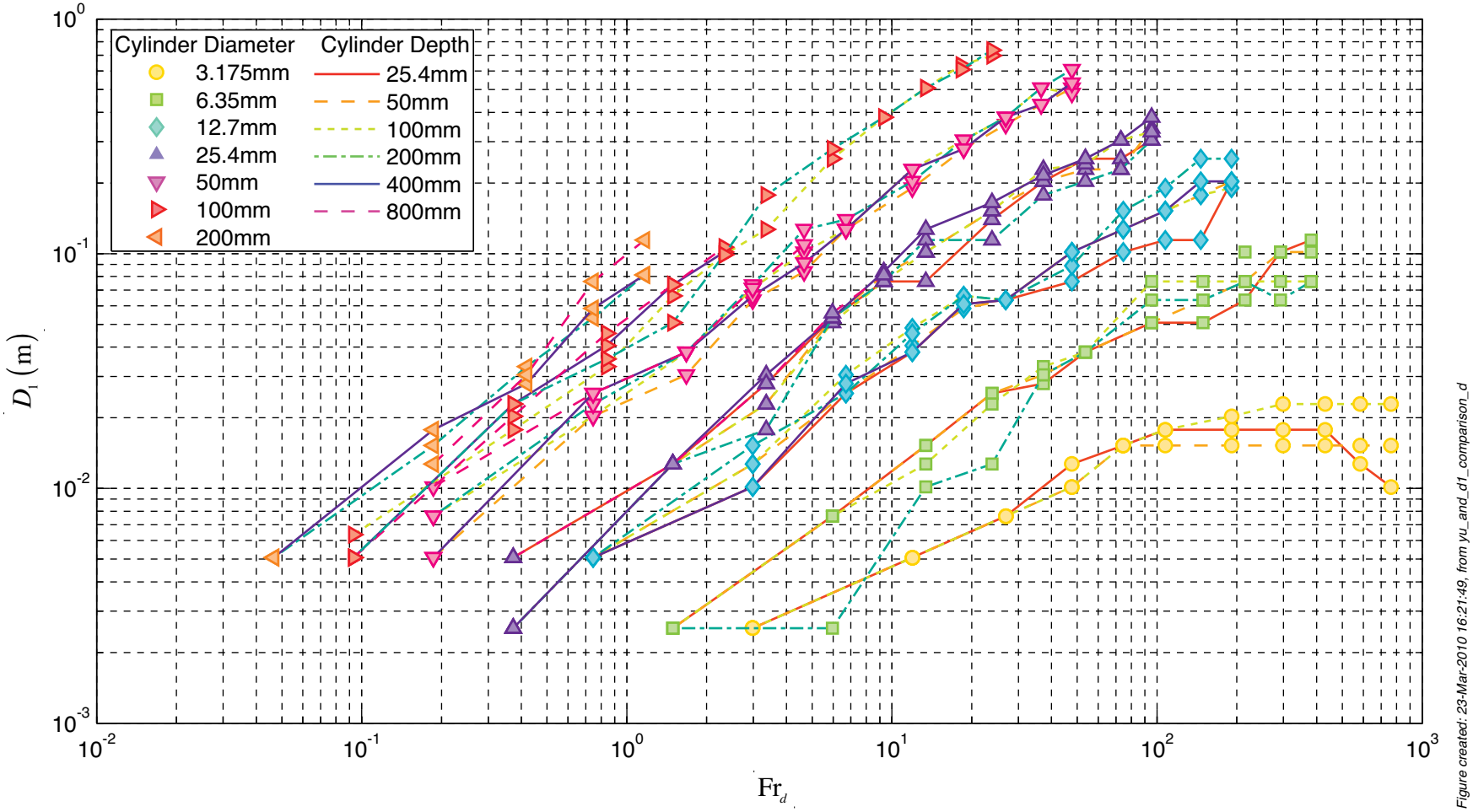


*Figure created: 23-Mar-2010 16:21:49, from yu_and_d1_comparison_d*

**Figure 10-2 – Bow wave height as a function of Froude number from all the measurements of Hay (1947).**

Indeed by extension as the spread for all the results from the $d = 6.35$ mm results is large, care should be taken with that entire curve, for example the $L = 200$ mm curve deviates significantly from the other results and would warrant further investigation.

With this functional dependence of $D_1$ in mind the present results are an excellent fit with both the Hay data and that of Wikramasinghe and Wilkinson (1997)* as shown in Figure 10-3. Further, as a number of measurements were made in the present study they were averaged with error bars representing the standard deviation. As the reader would note, though, there are no error bars visible in Figure 10-3, which is because the magnitude of the standard deviation was less than the size of the point markers.

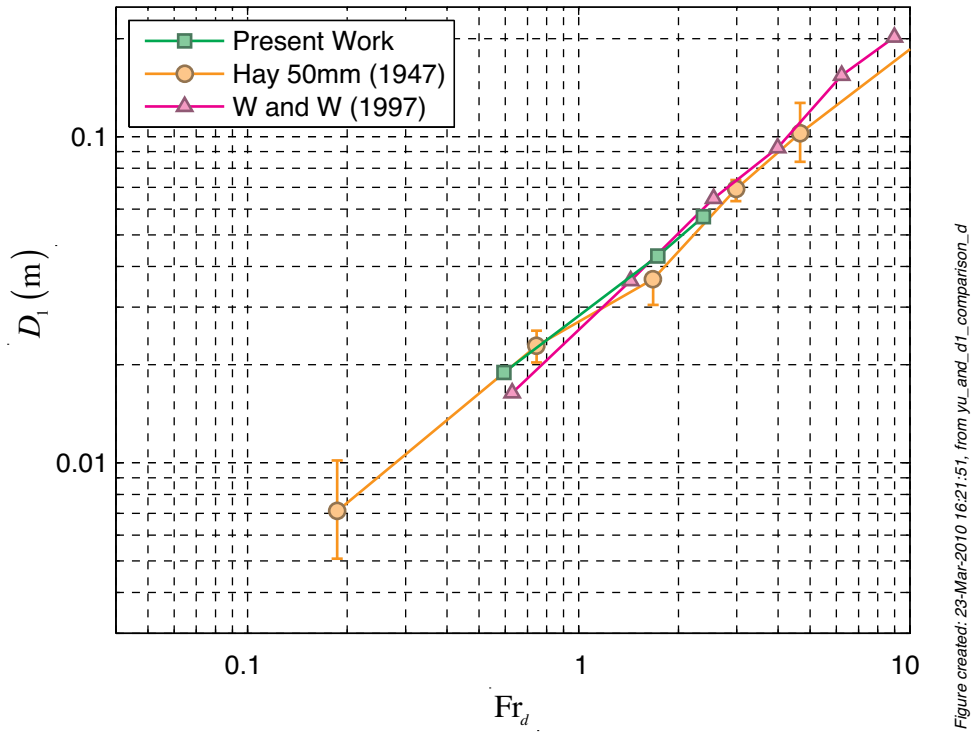


**Figure 10-3 – Plot of the $D_1$ as a function of $Fr_d$ for the present work, Hay (1947) and Wikramasinghe and Wilkinson (1997)**

In contrast, the error bars of the Hay data in Figure 10-3 do not represent the experimental standard deviation. Instead, all the measurements for a given $Fr_d$ in the 50 mm diameter experiments made by Hay were averaged and displayed as the point on Figure 10-3. The spread of the error bars is, rather than the standard deviation, the

* The data of Wikramasinghe and Wilkinson (1997) was published in Yu et al (2008) and reproduced here. Their original paper was not available to the present author.

bounds of the Hay data. This simplified the plot by reducing the number of overlapping markers to display.

### 10.1.3. Cavity Depth – $L_0$

The second wave shape parameter from the present work to be compared with that measured by Hay is $L_0$, as shown in Figure 10-1. Hay observed that the cavity depth increased as a function of the velocity until $Fr_L \cong 3$, whereupon the bottom of the cavity coincides with the end of the cylinder. That is, when

$$L_0 = L \tag{10.4}$$

the cylinder is fully ventilated and $L_0$ remains essentially constant with only minor increases in depth due to the downward flows under the cylinder. This behaviour is visible when the depth of the cavity is normalised by length and plotted against Froude number,

$$\frac{L_0}{L} \propto C_{L_0} \frac{U_{ref}^2}{gL} \tag{10.5}$$

in which $C_{L_0}$ is a constant of proportionality, as shown in Figure 10-4.

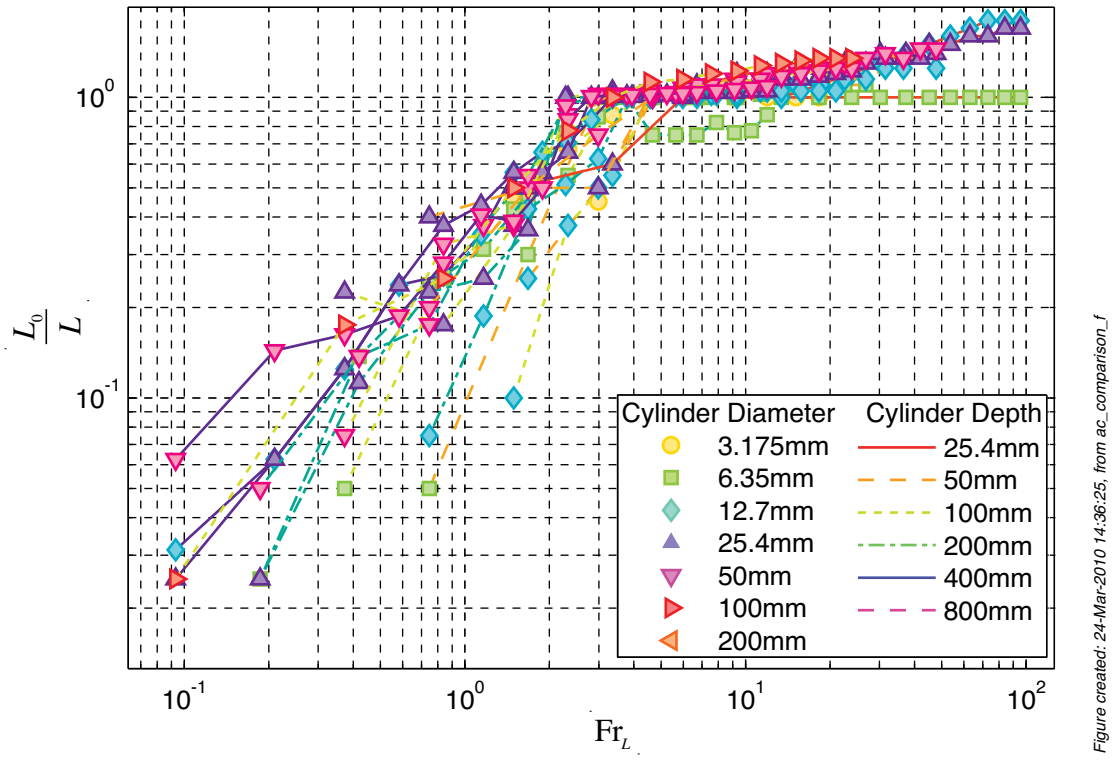


**Figure 10-4 – Plot of $L_0/L$ as a function of $Fr_L$, from Hay's (1947) Figure 92.**

Further, Hay suggested that for the subcritical flow range $C_{L_0}$ as being between 1/2 and 1/3. In contrast, as the results from the present work were obtained using a zero friction wall at the base of the domain, the length $L$ is undefined and the lengths $L_0$ measured by Hay (1947) were plotted as dimensional quantities – the same as data from the current simulations. Interestingly, Hay's predictions of the slope in the subcritical regime still hold for Froude numbers relative to the cylinder diameter, *d*, as shown in Figure 10-5.

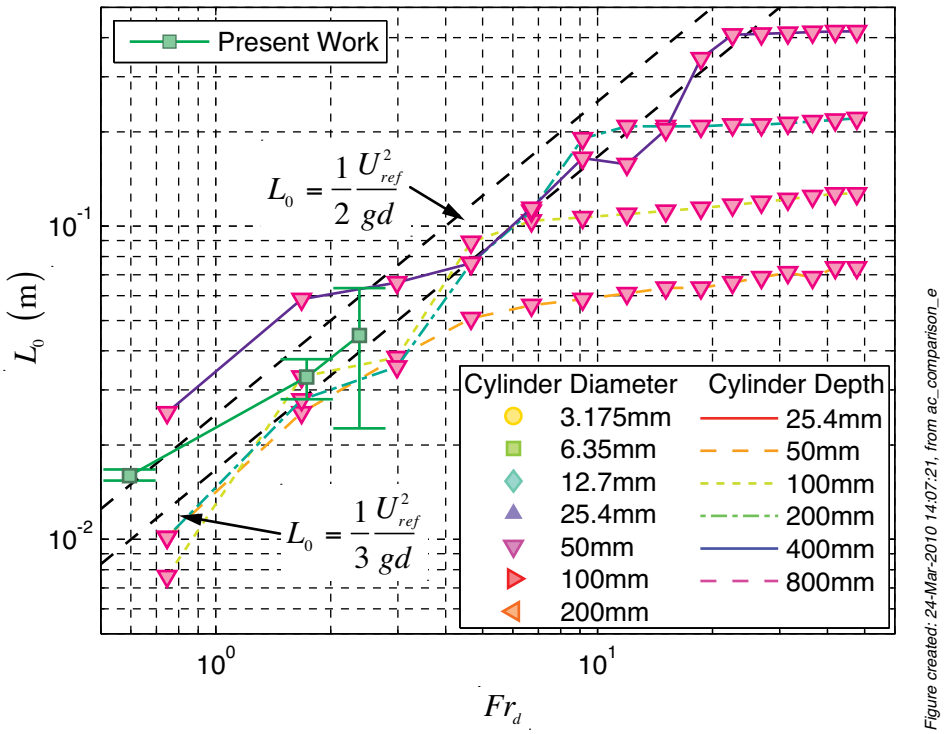


**Figure 10-5 – Plot of the depth of the ventilated cavity as a function of $Fr_d$.**

Despite the large error in the measurements from the present simulations, the data is an excellent agreement with the Hay data. Neither Chen at al (2000) nor Kawamura et al (2002) published their measurements of $L_0$.

The spread in the measurements from the present simulations that were made at the highest Froude number, shown in Figure 10-5 ranges from $L_0 = 0.022$ m to $L_0 = 0.063$ m with a mean at $L_0 = 0.044$ m. This differentiation is not due to a lack of accuracy in the measurements themselves but rather the fluctuations of the cavity as a function of time. Still, the spread of the data is predominantly within the bounds of Hay's work but it poses an interesting question, namely would the plots of Hay be as "clean" had he been able to take more measurements? Hay acknowledged the

possibility of errors while he discussed the break at $\mathrm{Fr}_L \cong 3$, as he only took a single image per combination of speed, depth and diameter (Hay, 1947). The size of the present data set is too small to investigate this supposition but it should be kept in mind for further work.

### 10.1.4. Rooster Tail Height – $D_3$

From the measurements of Hay (1947) the length to the peak of the rooster tail, $D_3$, displays a similar trend to $L_0$ in that the measurements appear to increase as a function of $Fr_d$ before they remain relatively constant beyond a critical Froude number. Intriguingly the data points for the all the measurements below the critical Froude number seem to fit the function

$$D_3 = \frac{Fr_d^{1.5}}{250} \tag{10.6}$$

as shown in Figure 10-6. The data available from Hay (1947) in the sub-critical range by itself is too sparse to make definitive predictions of the functional form of $D_3$.

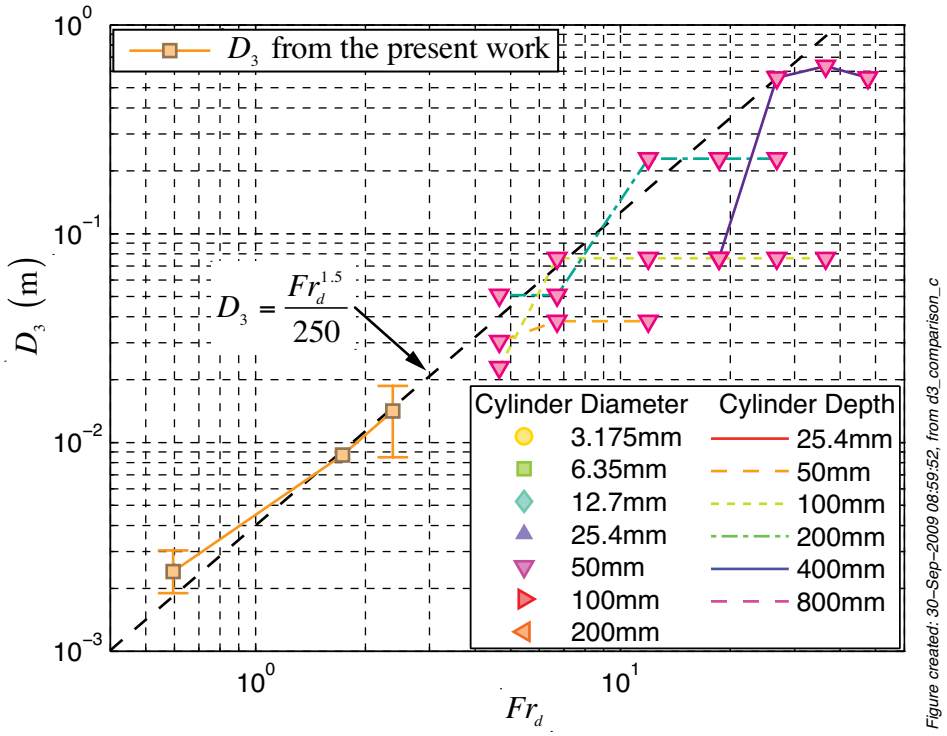


**Figure 10-6 – Plot of the height of the rooster tail as a function of $Fr_d$.**

However, the addition of the three data points from the present work would appear to strengthen the argument for the functional form described by Equation (10.6) because

the present data fit almost perfectly. As with the parameters presented above, the error bars are indicative of the spread of repeated measurements rather than representative of the precision of a single measurement. Irrespective of the definitive functional form of $D_3$ at subcritical Froude numbers, the present data fits within the trend of the Hay data hence, the present computational method appears to be adequately computing this parameter.

### 10.1.5. Rooster Tail Length – $L_3$

During the analysis of the $L_3$ parameter, the present author noticed that, of the images of the two-inch cylinders taken by Hay, three were suitable for measurement of $L_3$ but were not included in his published tables of other $L_3$ measurements. The reason for this lack of measurement is unclear because although Hay ignored a number of measurements due to factors such as bad lighting or shadows that obscured a particular feature, these $L_3$ lengths were clearly visible. Subsequently, these three measurements were scaled from the images published by Hay, as shown in Figure 10-7 and which is discussed in detail in Appendix E.

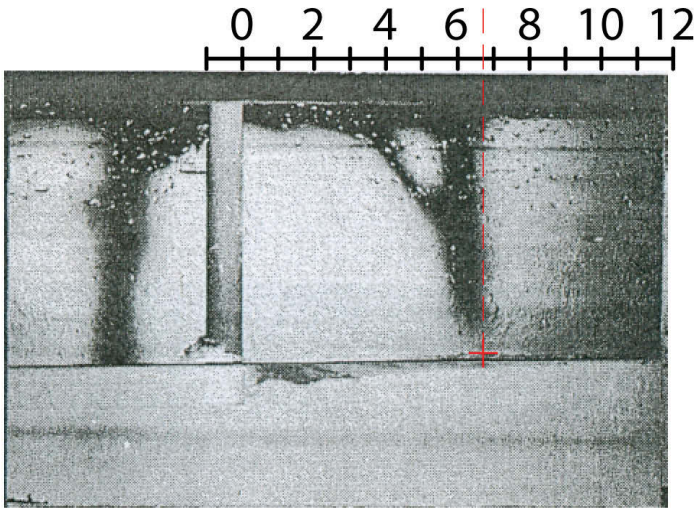


**Figure 10-7 – Example of the scaled measurements made from Hay's images.**

In his monograph Hay (1947) normalised his measured $L_3$ results by $L$, and noted that the points fell close to

$$\frac{L_3}{L} = \frac{Fr_d}{2}. \tag{10.7}$$

However, as $L$ is subject to debate in the present work, Hay's measurements of $L_3$ were plotted without normalisation, as shown in Figure 10-8. The results from the present work, which were made at lower $\mathrm{Fr}_d$ than those of Hay, are a very poor match to Hay's measurements.

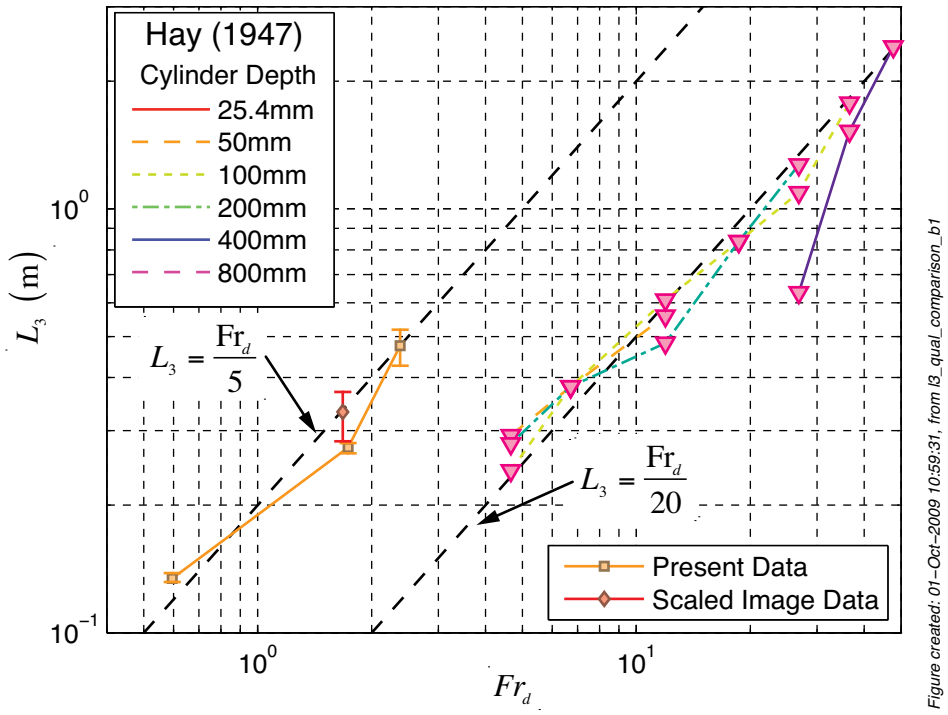


**Figure 10-8 – Plot of the length to the peak of the rooster tail, $L_3$ for $d$=50mm.**

In the alternate, non-dimensional plots the 50mm diameter data of Hay data can be approximated by

$$L_3 = \frac{\mathrm{Fr}_d}{20} \quad \text{for} \quad \mathrm{Fr}_d \geq 4.5 \tag{10.8}$$

rather than the 0.5 coefficient of Equation (10.7).

The new photogrammetric measurements, which were all obtained for the same $Fr_d$, when plotted on the same graph deviate significantly from the trend described by Equation (10.8), also shown in Figure 10-8. This result is interesting in itself as these three data points could represent an alternate flow regime that is only present at low $Fr_d$. Again, the error bars in Figure 10-8 represent the spread of the three measurements rather than the precision of individual measurements. However, without further data points the alternate flow regime at low $Fr_d$ was purely speculative.

When the results from the present simulations were plotted in conjunction with both the original measurements of Hay and the newly scaled Hay data, they were an excellent fit with the new measurements rather than a continuation of the original measurements. This is particularly exciting because these new data from the present simulations appear to confirm the presence of an alternate flow regime at low $Fr_d$ with a functional form of

$$L_3 = \frac{\mathrm{Fr}_d}{5} \quad \text{for} \quad \mathrm{Fr}_d \le 2.3 \quad . \tag{10.9}$$

It is unclear what the mechanism would be that could generate a longer $L_3$ at lower $Fr_d$, particularly as the aim of this section is validation rather than investigation, but this topic should be the subject of both further numerical and experimental work. For the current validation exercise, the $L_3$ parameter was validated not because of its consistency with the tabulated Hay measurements but because of the agreement with the new measurements taken from the photographic images published by Hay.

## *10.2. Spectral Validation*

As was introduced in §6.4, results from a spectral analysis can provide an indication of the turbulent decay and, hence, if the computational method is correctly accounting for the energy dissipation. Therefore, as the free surface has been shown to have a dissipative effect on vortex shedding (Kawamura et al., 2002) two points were selected that were as far away from the free surface as allowed within the current computational domain. These points were located on the $z$=0 plane at 5.8 cylinder diameters downstream at $y = -0.102$m and $y$=0.370m to be representative of the water and air phases, respectively.

The power spectral densities were computed using a similar method as was discussed in §6.4.2 with an assumed development time of two seconds and a rectangular window 262 145 points long. These parameters, with the sampling frequency of 125kHz resulted in a frequency resolution, or bandwidth, of 0.48Hz/sample.

The resultant power spectral densities from the $\mathrm{Re}_d = 54 \times 10^3$ simulation on the medium resolution grid were comprised of a range of energetic frequencies below ten hertz, with a constant slope for frequencies above ten hertz, as shown in Figure 10-9. A dominant shedding frequency of 4.8Hz and 4.3Hz was observed for the water and air,

respectively. As would be expected, the shedding is more defined in the water phase with the peak rising almost 10 dB/Hz higher than the low frequency plateau. In contrast to the result from the water phase, the power of the peak shedding frequency in the air is in the order of 3 dB/HZ higher than the next, low frequency peak.

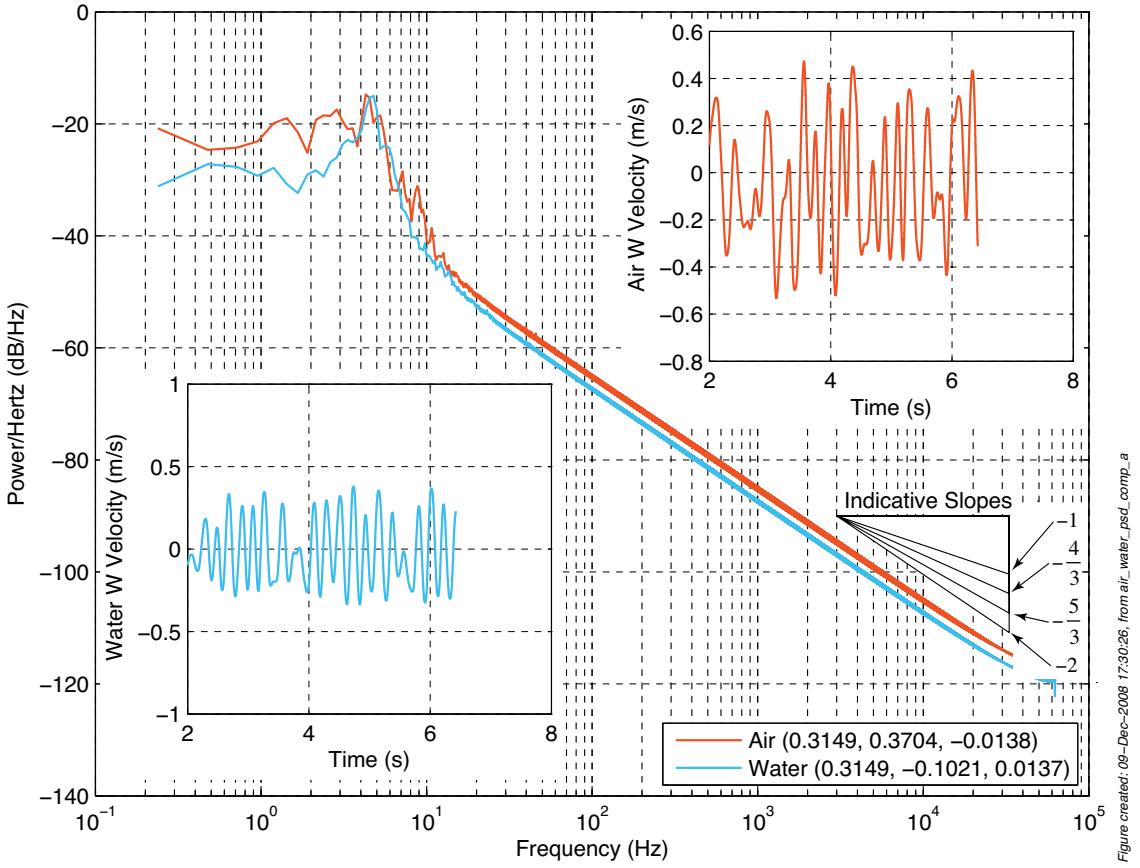


**Figure 10-9 – Power spectral density plots for the $Re_d = 54\times10^3$ simulation.**

This result of the differences in the power at low frequencies was expected because the gas phase is flowing at a much lower Reynolds number than the liquid phase. Therefore, the flows are less energetic and the shedding more easily contaminated with low frequency noise.

Similar power spectral density functions were computed for the same two monitor points whose results are shown in Figure 10-9 from the $Re_d = 27\times10^3$ medium resolution simulation but are not shown because, qualitatively, they are very similar to those shown in Figure 10-9. However, with the assumption introduced above, that the results from the points located in the air and water phases are representative of the local Reynolds number, that is the Reynolds number based on the respective viscosity, four combinations of Strouhal number and Reynolds number can be computed. Three of

these four Strouhal numbers compare very well with the single-phase reference data compiled from the meta-analyses of Drescher (1956) and Etkin (1957), as shown in Figure 10-10.

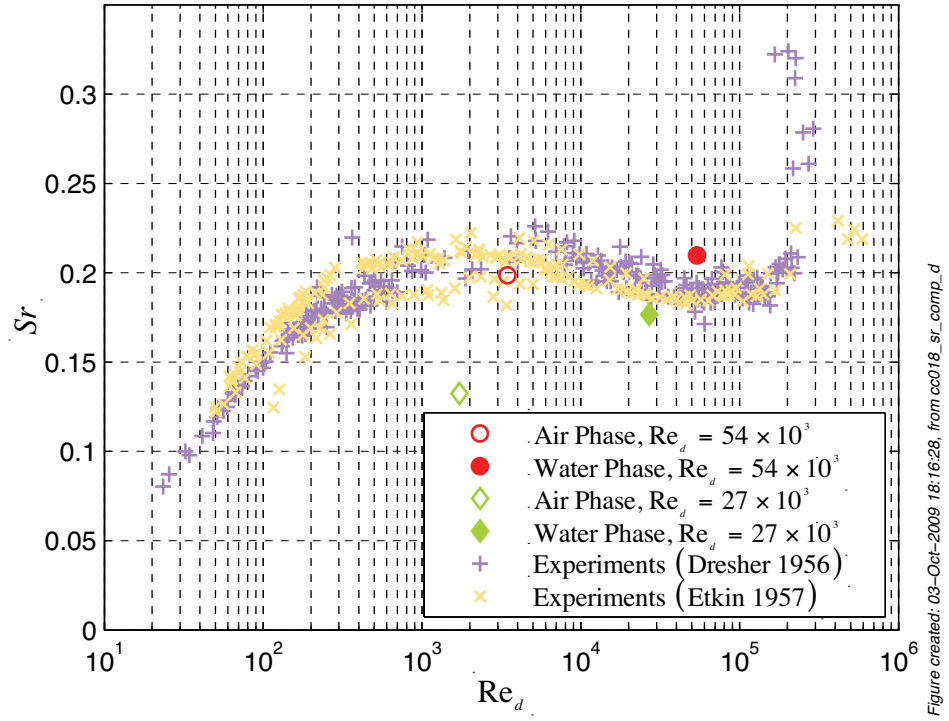


**Figure 10-10 – Strouhal numbers from the present simulations compared with results from two meta-analyses of single-phase experimental studies.**

While the Strouhal number from air-phase monitor point in the $\mathrm{Re}_d = 27 \times 10^3$ simulation is 35% lower than the reference data there are a number of reasons why this single result will not invalidate the simulations as a whole. Firstly, the corresponding measurement from the water phase is a close agreement with the experimental data. Second, there is an explicit assumption that allows the present data to be compared with single-phase results, namely that the free surface does not affect the flow at these two monitor points. This assumption may be wrong at this lower Reynolds number in the air-phase. Finally, to ensure the maximum distance from the free surface, the monitor points were located close the zero-friction top and bottom walls, which may also cause an effect in the air phase at this lower Reynolds number.

In addition to the dominant shedding frequency analysis presented above, the power spectral density plots can also be used to estimate the turbulent decay rate as a function of wave number (Tennekes and Lumley, 1972, Wilcox, 1998). For these four monitor

points the slope of the PSD plot did decay at the requisite -5/3 power law to describe the inertial sub-range, as shown in Figure 10-9, which was derived from dimensional arguments (Kolmogorov, 1941).

If unquestioning acceptance of the -5/3 power law were sufficient to validate the present simulations then no further comment would be required (Rogallo and Moin, 1984). Further, as the inertial sub-range is defined by the extent of the -5/3 decay slope, then for the present simulations it would start at approximately 10Hz, which seems to be too low a frequency. Further, the constant slope region is almost too constant over nearly five frequency decades that, again, seems to be an unlikely result that is too perfect for comfort. It would appear that the oft forgotten assumptions of Kolmogorov's work, namely homogeneity, do not always apply and in these situations the -5/3 law may not apply (Batchelor and Towsend, 1949, Jiménez, 2006). Therefore, the unquestioning application of the -5/3 law to all turbulent flows should be treated with caution.

Despite the caveats and cautions noted for the slope of the power spectral density plot for frequencies above ten hertz, the results from the spectral analysis support the validation of the proposed computational technique. That is the peak shedding results, notwithstanding the single discrepancy from the air-phase of the lowest Reynolds number tested, were very close to the benchmark single-phase results.

## *10.3. Computational Run Time Tests*

Although not technically a component of a validation study the computational run time is nevertheless important, as one of the major precepts of this thesis is that, in addition to equivalent accuracy, the 2$^{nd}$ Order method must be faster than alternate methods. This test was conducted in a similar manner to that described in §6.6 for the right square cylinder simulations and used identical turbulence models as described there but applied to the configuration of a right circular cylinder piecing a free surface.

The results were generally consistent with those of the single-phase, square cylinder in that the 2$^{nd}$ Order method was faster than the five alternatives tested, as shown in Figure 10-11. In this case the 2$^{nd}$ order model was 16% faster than the DES method and 19% faster than the Large Eddy Simulation with a Smagorinsky model.

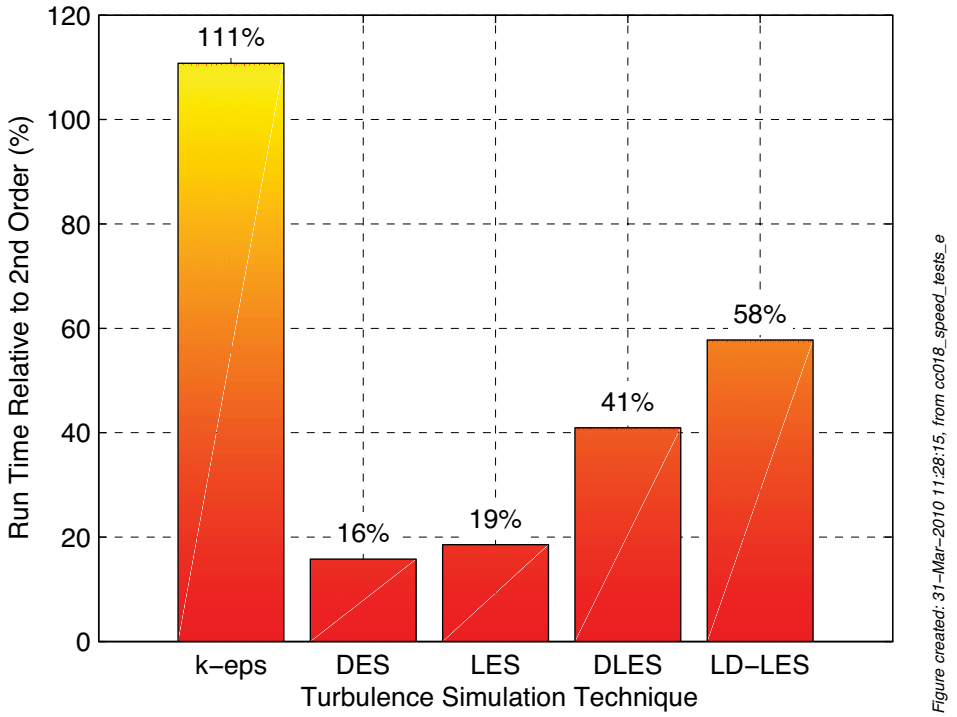


**Figure 10-11 – Comparison of computational run times for the 2nd order model with alternate turbulence models.**

Because of the potential savings of the RANS calculations the DES model's run time should be closer to that of the 2nd order model. However, on the present grid, which is at the lower end of LES resolution, the increased computational cost of deciding which cells are LES or RANS is probably greater than the RANS savings.

While it was not the aim of these run time tests to compare the quality of the results, the present author has supposed that the results would follow similar patterns to those of the square cylinder. That is, that *k*-*ε* simulations would produce poor results while the remaining methods should result in acceptable results. The data available for validation partially supports this proposition in that of the three published large eddy simulations two produced good results and one poor. There are no k-eps simulations of this configuration to compare.

It is particularly interesting that the present simulations are not only at least 16% faster than the nearest alternative but in terms of the free surface shape and velocities has produced much better results. However, the astute reader would have noted that, unlike the square cylinder validations, the drag force on the circular cylinder has not yet been analysed.

# 11. Three-Dimensional, Two-Phase Simulations: Drag Forces Experienced by the Cylinder

## *11.1. Introduction*

In addition to investigating the shape of the free surface, the results of which are presented in §9, and measuring a number of wave shape parameters, that are discussed in §10, Hay (1947) also measured the drag force that is exerted on cylinders during his experiments on the forces and fluid movements generated when right circular cylinders that penetrate a free surface are towed at constant velocities. For each combination of depth of immersion relative to the still water level, cylinder diameter and towing speed he gave only a single value of force, with no explanation of the exact meaning of this number. Despite Hay not clarifying whether his results were time averaged or a single instantaneous measurement, in the present work Hay's results have been assumed to be averages and are, therefore, compared with average results from the current simulations.

To ensure that the force measurements from the present work are analogous to those taken by Hay the forces were integrated over the entire cylinder face with no attempt to split the components into wetted and dry areas. The present author is not aware of the height of the circular cylinders above the free surface in Hay's experiments but, the contribution of the air phase to the total force should be quite small. Suppose that the force, $F_{Sectional}$, on a section of cylinder due to profile effects is proportional to the pressure due to motion, that is,

$$F_{Sectional} \propto \rho U_{\infty}^{2} dL, \tag{11.1}$$

it follows from Equation (11.1) that because the density of air is in the order of one $800^{th}$ of that of water, then the sectional forces should also be proportionally smaller in the air phase. This means that the increase in the drag force due to the part of the cylinder exposed to air is about 0.1% of the force exerted by the water on a cylinder of the same length. Therefore, the difference between the heights of cylinders from the free surface used by Hay (1947) and those employed in the present simulations have a negligibly small effect on comparisons of total drag force obtained in the two studies.

For consistency, all the force measurements from the present simulations, and the resistance measurements from Hay, will be presented as drag coefficients, defined as

$$C_D = \frac{F_D}{\frac{1}{2}\rho_{water} U_\infty^2 L d}, \tag{11.2}$$

in which $F_D$ is the total drag force and $L$ is the depth of immersion of the cylinder relative to the still water level.

It is now therefore possible to discuss the development of the drag force as a function of time during the acceleration period, compare average values with those obtained experimentally by previous researchers and attempt to develop an understanding of the extra drag caused by the presence of waves generated by the motion.

## 11.2. Forces on the Cylinders

All of the drag coefficients from the present work exhibit a development period over the first two seconds, as shown in Figure 11-1, which is the direct result of the acceleration function used in the present work (described in §7.3).

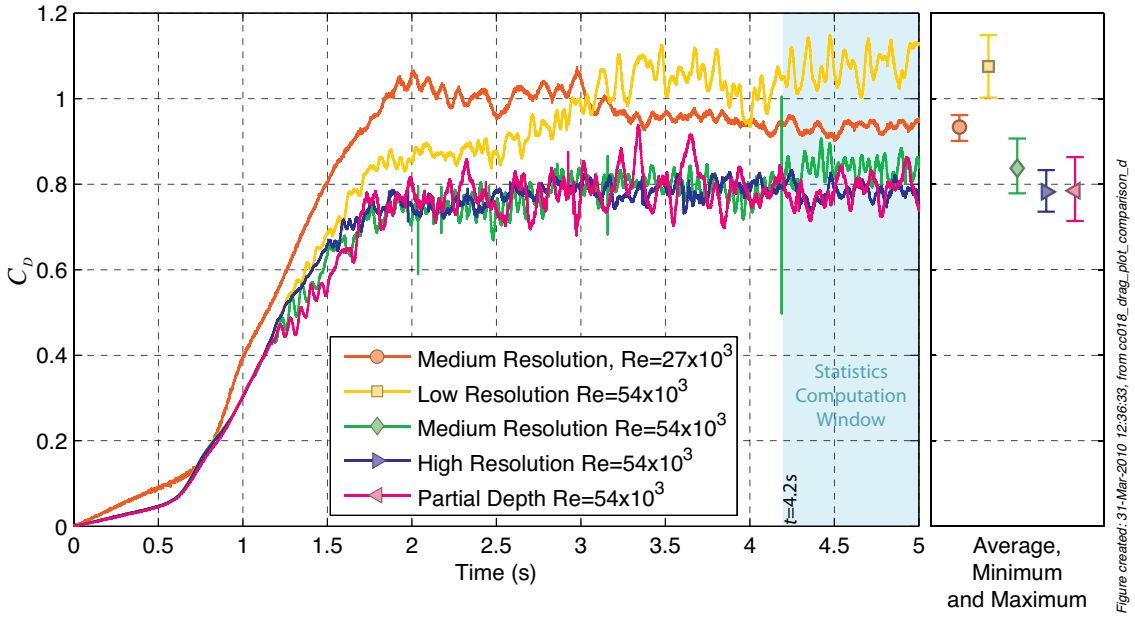


**Figure 11-1 – Drag coefficients as a function of time for the simulations at $Re_d$=27×10³ and $Re_d$=54×10³.**

The average drag from the low-resolution simulation at $\mathrm{Re}_d = 54 \times 10^3$ is noticeably higher than the medium and high-resolution simulations being 1.076, 0.838 and 0.782

respectively. If these values are used as the basis for a grid convergence estimate of the average drag by the method recommended by the ASME Journal of Fluids Engineering (Celik et al., 2008), then the grid converged drag is 0.776±0.008, which is in reasonable agreement with the medium resolution data and very close to the high-resolution result. Too few simulations were run to allow a similar calculation for the $\mathrm{Re}_d = 27 \times 10^3$ configuration.

As shown in Figure 11-2, all three of the averaged drag coefficient values, namely the $\mathrm{Re}_d = 27 \times 10^3$ full depth simulation and the full and partial depth simulations at $\mathrm{Re}_d = 54 \times 10^3$, are in excellent agreement with the Hay drag data.

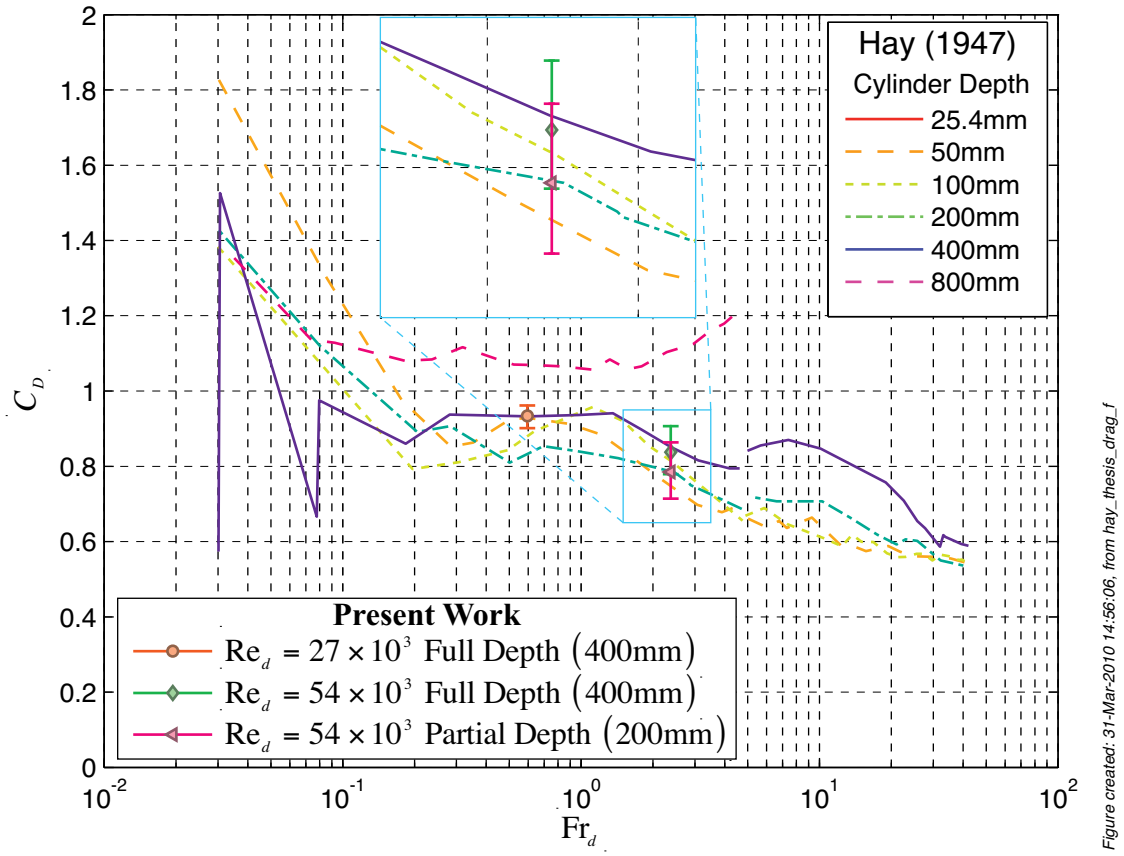


**Figure 11-2 – Comparison of the drag coefficients from the present simulations, with magnification of the present results, and the two inch measurements with different drafts from Hay (1947).**

The result of the averaged drag for the partial depth simulation at $\mathrm{Re}_d = 54 \times 10^3$, which for increased clarity is shown in the magnification inside Figure 11-2, is an almost perfect match for the 200mm depth measurements made by Hay. This is an

exceptionally good result as both Hay's 200mm results and the present partial depth simulations were computed at the same depth of immersion.

The second of the results, shown in the magnification subplot of Figure 11-2, is from the present full depth simulation that is 400mm from the still water level to the lower boundary. As can be seen in Figure 11-2 the present result is, again, an excellent match with the equivalent depth of immersion results made by Hay (1947).

In general, Hay's drag coefficient data are relatively constant, being between 0.8 and 1.0, over the range $0.1 \le \mathrm{Fr} \le 2$, as shown in Figure 11-2. For larger Froude numbers, the magnitude of the drag coefficient dropped from these values to approximately 0.6 at the highest speed measured by Hay, which was at $\mathrm{Fr} \cong 14$. At the lowest Fr measured the values of $C_D$ fluctuate widely but, as was noted by Hay, these measurements were at the lower accuracy limit of the equipment and, hence, "are probably an error" (Hay, 1947).

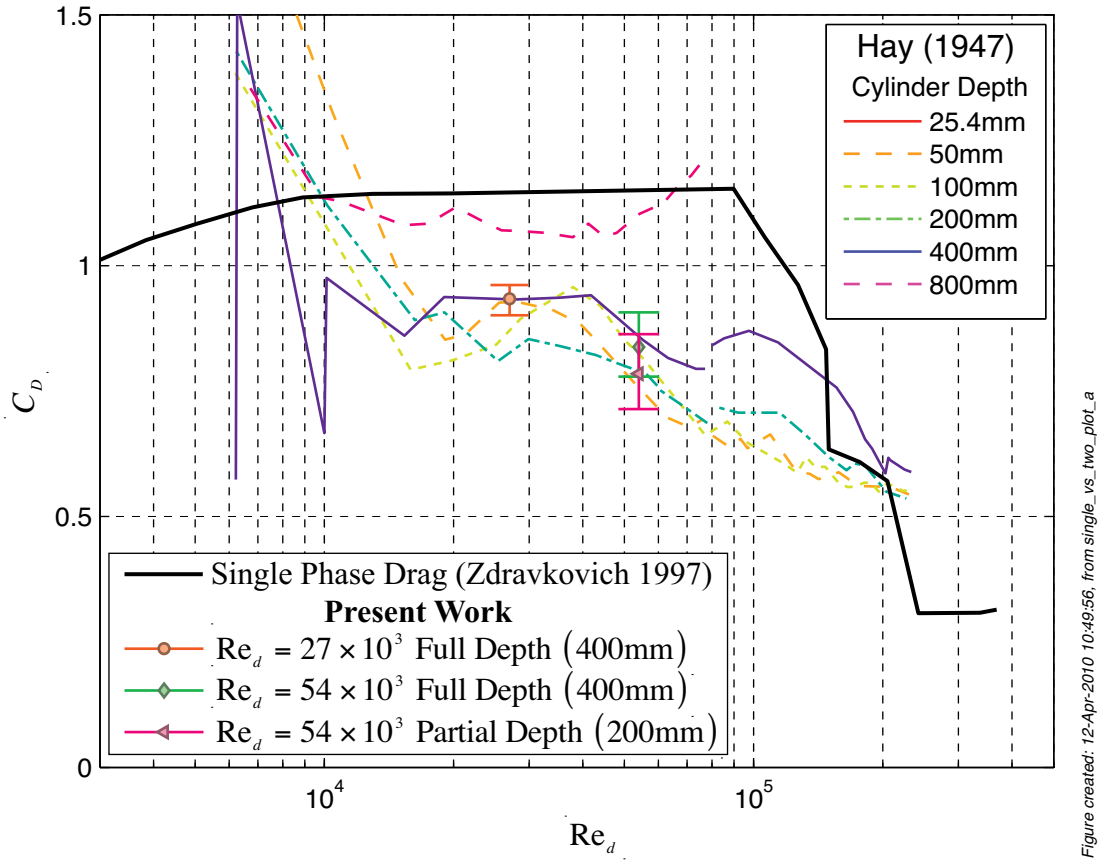


**Figure 11-3 – Comparison of the two-phase drag coefficients from the present work and Hay (1947) with that of a single-phase circular cylinder.**

Hay's discussion of the change of $C_D$ as a function of Re, as shown in Figure 11-3, is limited to 4 points, namely:

1. Resistance is reduced when the flow is allowed to become three-dimensional and "move towards the ends".
2. As the depth to diameter ratio is increased, the drag tends towards that of an equivalent diameter two-dimensional, single-phase cylinder.
3. The scatter indicates that that there is not a "simple" function of Re.
4. Distinct changes in the $C_D$ curve occur because of changes in the flow regime.

From these four points Hay concluded that the Reynolds number does have an "appreciable effect" on the flow pattern but continued the bulk of his analysis of $C_D$ on the assumption that Fr is the independent variable. He concluded that definite trends can be observed and further suggested a number of empirical relationships to describe the shape and trends of the measurements plotted against various non-dimensional groups.

It is clear from Figure 11-3 that the overall drag coefficient for a towed right cylinder which pierces a free surface obtained from Hay's experiments and the present numerical work, is lower that the equivalent drag coefficient at the same Reynolds number in single phase. This is contrary to expectations as it is usually thought that the generation of waves leads to a large increase in drag.

## *11.3.* Drag due to the Presence of the Free Surface

Hay's reslts were no re-investigated for a long period of time until Chaplin and Teigen (2003) presented what they described as a "re-analysis" of Hay's data with a particular emphasis on wave drag. They proposed that the wave making drag force, or the free surface effect, could be separated from the total drag by proposing that the effects of the free surface expressed as the force, $F_{FS}$, could be determined subtracting a "two-dimensional" drag force obtained in a single phase fluid, $F_{SF}$, from the total drag measurement obtained by Hay (1947), viz,

$$F_{FS} = F_D - F_{SF} . \tag{11.3}$$

In this case, “two-dimensional” flows are those that would be observed around cylinders that are fully submerged either a large distance from the free surface or in the completed absence of a free surface, such as would be found in a water tunnel. They further suggested that a surface resistance coefficient be defined as

$$C_{FS} = \frac{F_{FS}}{\frac{1}{2}\rho_{water} d^2 U_\infty^2}. \tag{11.4}$$

Their unexplained use of the area being equal to $d^2$ seems strange given that in all other cases familiar to the present author, the wetted frontal area of the cylinder relative to still water level has been used. Therefore, for the present work the area will remain equal to the wetted frontal area, $Ld$, of the submerged cylinder relative to the still water level, that is Equation (11.4) becomes,

$$C_{FS} = \frac{F_{FS}}{\frac{1}{2}\rho_{water} LdU_\infty^2}. \tag{11.5}$$

Next Chaplin and Teigen (2003) argued that $F_{SF}$ should be calculated in the “absence of the free surface”, which they directly computed from the integration of pressure tapping readings in their experiments. These measurements were taken completely submerged and with large splitter plates in place in an attempt to force the flow to be two-dimension and are arbitrarily taken as the values at a non-dimensional depth of -3 in Figure 11-4.

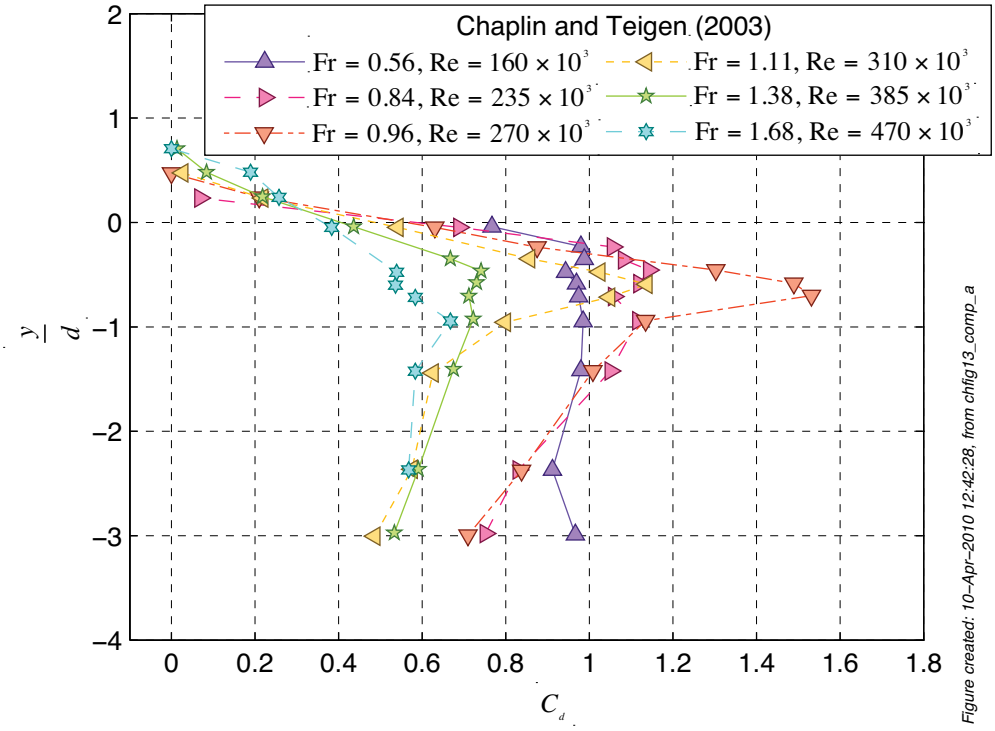


**Figure 11-4 – Sectional drag coefficients from Chaplin and Teigen (2003).**

Additional measurements were taken at different depths of immersion relative to the still water level, without splitter plates, to develop the remainder of the curves shown in Figure 11-4.

When they then computed the integral

$$C_D = \frac{1}{L}\int_{-L}^{\eta} C_d \, dy \tag{11.6}$$

in which $\eta$ is the maximum elevation of the bow wave and $C_d$ is the sectional drag coefficient shown in Figure 11-4, their resultant values of $C_D$ were similar to those measured by Hay. That is they were, with the exception of the measurements at the two highest Reynolds numbers, below the equivalent single fluid drag coefficients, as shown in Figure 11-5.

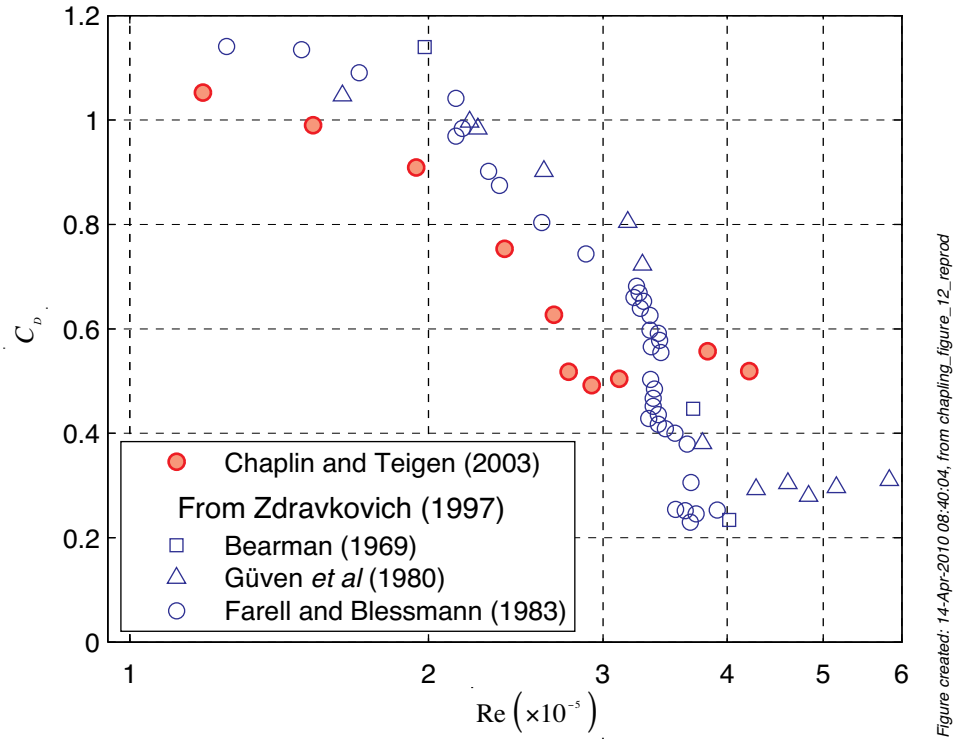


**Figure 11-5 – $C_D$ values computed by Chaplin and Teigen (2003) with additional data reproduced from Zdravkovich (1997).**

The method described in Equation (11.6) is very similar to that used in the present work, namely that $C_D$ can be computed from the forces that act on the entire area of the cylinder yet are normalised by the wetted frontal area relative to the still water level. Chaplin and Teigen (2003), in contrast to the present work, stopped their integration at the maximum height of the bow wave yet, as argued above, the contribution of the air phase is tiny. Therefore, the difference in the magnitude of $C_D$ from Chaplin and Teigen's data to the present will also be very small.

Interestingly, in order to evaluate $C_{FS}$ in Equation (11.3) Chaplin and Teigen (2003) then chose to use their measured values of $C_d$ at a particular depth as $C_{SF}$. As shown in Figure 11-6, because $C_{SF}$ is significantly less than $C_D$, positive values of the wave drag coefficient $C_{FS}$ resulted.

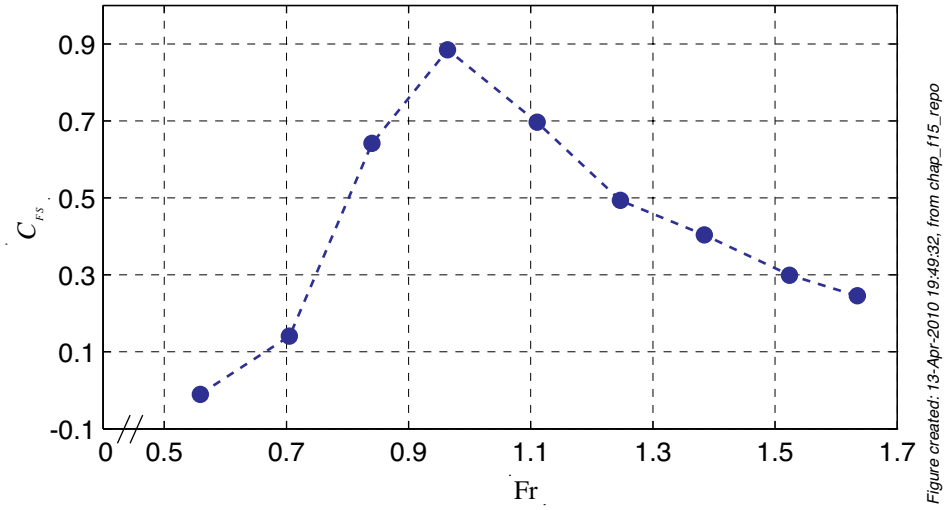


**Figure 11-6 – $C_{FS}$ as a function of Fr, reproduced from (Chaplin and Teigen, 2003).**

It seems to the present author though that both Hay and Chaplin and Teigen missed the most interesting point, already mentioned above: that for certain configurations the drag of a right circular cylinder, which pierces a free surface, *is* less than that of the same cylinder moving at the same Reynolds number but which is fully submerged in a single fluid. This would appear to be remarkably similar to the empirical usage, hitherto not satisfactory explained, of the use of a sharp transom to reduce the drag experienced by a ship. Following this logic, Chaplin and Teigen's positive values of $C_{FS}$ are not tenable as an examination of Figure 11-5 indicates that $C_{FS}$ should be negative for all but two of their points. It should also be noted that the majority of Hay's and the present data would also yield negative values of $C_{FS}$. Clearly then, evidence must be presented in support of this supposition.

## *11.4. Pressure Effects Due to the Presence of a Free Surface*

When Chaplin and Teigen (2003) computed their "deep" $C_d$ with the splitter plates in place they assumed that the combination of the depth of their measurement and the presence of the splitter plates would ensure the two-dimensionality of the flows. This, however, seems unlikely. First, based on his extensive and exhaustive study, Hay (1947) concluded that while the drag tends to that of the two-dimensional case as the draft was increased, there were three-dimensional effects. Hence, it is unlikely that the depths used by Chaplin and Teigen are deep enough to ensure two-dimensionality of the flow. Second, while the values of $C_D$ calculated by Chaplin and Teigen are close to

that of a single fluid, they are generally less than equivalent single fluid values, as shown in Figure 11-5. Hence, in order for $C_D$ to tend towards $C_{SF}$, $C_d$ must also tend towards $C_{SF}$ as the depth is increased. This effect is not observed in Chaplin and Teigen's results, as shown in Figure 11-4.

Neither Chaplin and Teigen nor Hay had sufficient data, data that is available from the present CFD simulations, to explain these anomalies. To start this analysis suppose that the friction drag is negligible at these Reynolds numbers – as it is, at least, for cylinders that are completely immersed in single fluids (Zdravkovich, 1997) – then the drag forces experienced by the cylinder are due only to the action of pressure, which in turn is dependent on the wake downstream of the cylinder.

To start the analysis of the influence that the free surface can exert on the pressure distribution it would be logical to first examine the case of a fully submerged right circular cylinder. Therefore, a simulation based on the previously validated medium resolution grid, was performed with water only, that is no free surface and, as expected a high positive pressure at the leading edge that was coupled with a low negative pressure at the trailing edge was observed as shown in Figure 11-7. By way of further explanation, Figure 11-7 shows the pressure on the cylinder as if it were unwrapped, such that the points with $\theta = 0$ represent the leading edge and, by extension, points at $\theta = \pm\pi$ are on the trailing edge. Although pressure is a scalar quantity, the negative pressure on the downstream face of the cylinder can be considered to act as a suction force, which, instead of reducing, actually reinforces the positive forces on the leading edge to increase the drag force.

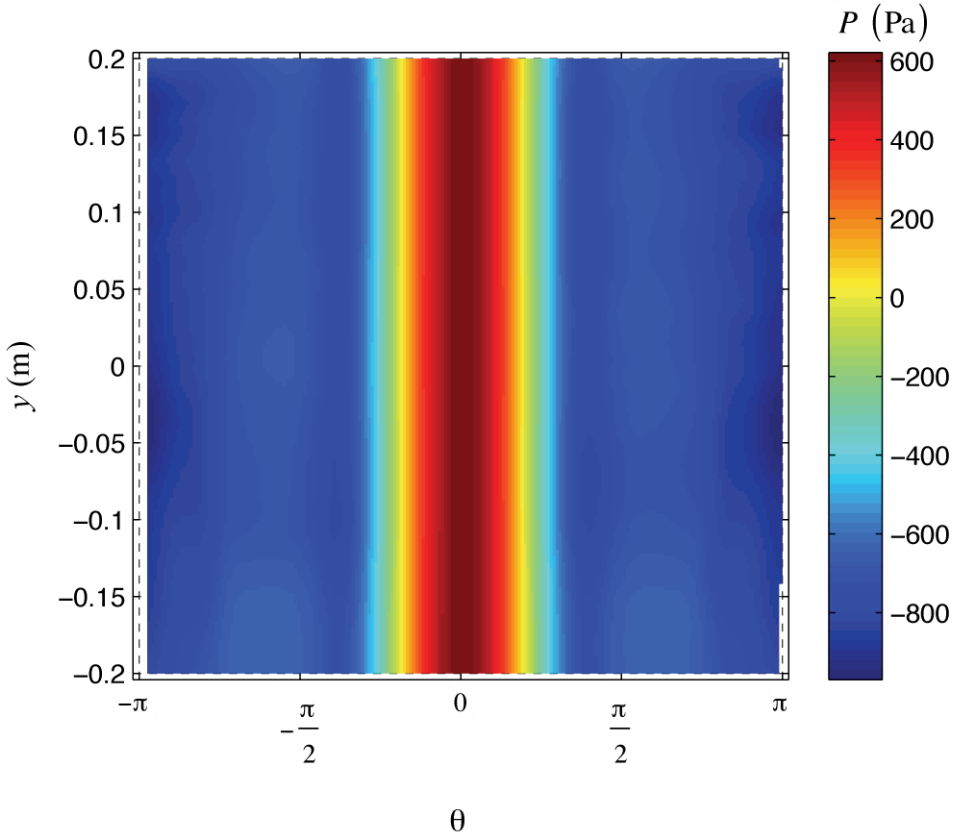


**Figure 11-7 – Average pressure distribution on the face of a, nominally, two-dimensional cylinder from a three-dimensional simulation.**

In contrast to the uniformity of the results from the single-fluid simulations, the pressure distribution from the two-fluid simulation, shown in Figure 11-8, is clearly non-uniform. The average free surface is indicated as a solid line and the still water level was at $y = 0.2\text{m}$. It can be clearly seen in Figure 11-8 that the pressure does not drop below the reference pressure anywhere as is the case in Figure 11-7. This is due to the fact that there is a fall in the surface in the wake of the cylinder and that a cavity filled with air, essentially at atmospheric pressure, means that the pressure in the separated region is essentially atmospheric. As expected, below the free surface the pressure rises with depth. This means that the pressure difference between the front and rear of the cylinder when it moves normal to and astraddle the free surface, determined from the data shown in Figure 11-8, is less than that when the pressure difference is obtained from the data shown in Figure 11-7 for a fully submerged cylinder. It follows that the drag force on a cylinder which pierces the free surface is less than the resistive force on a completely submerged cylinder well below the surface.

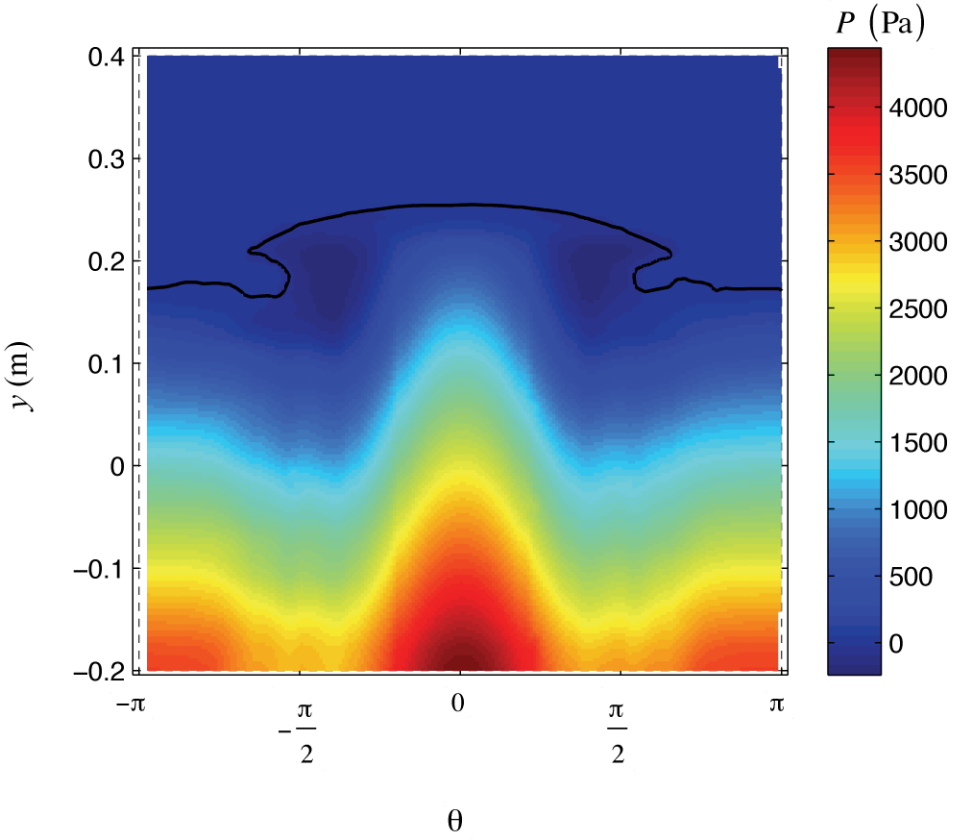


**Figure 11-8 – Average pressure distribution on the face of a three-dimensional cylinder with a free surface, which is marked with the solid line. Note that the still water level is at y=0.2m in this plot.**

While a visual examination of the pressure distribution as a function of $y$ and $\theta$ has indicated that there is an effect of the free surface on the vertical pressure distribution, the next step would be to investigate the sectional drag coefficient over a nominal vertical slice $\Delta y$, namely

$$C_d(y) = \frac{\Delta y \int_{-\pi}^{+\pi} P(\theta, y) \cdot \hat{\mathbf{n}}_x \, ds}{\frac{1}{2} \rho \Delta y d U_\infty^2} \tag{11.7}$$

in which $\hat{\mathbf{n}}_x$ is the component of the surface normal vector in the $x$-direction and $s$ is the circumference of the circle. The results from the present work are simultaneously close to and yet disparate with those of Chaplin and Teigen (2003), as shown in Figure 11-9. It should be noted that Chaplin and Teigen (2003) defined their Froude number as

$$\mathrm{Fr}_d = \frac{v}{\sqrt{gd}}, \tag{11.8}$$

or the square root of that used in the present work, so the Froude number listed in both Figure 11-4 and Figure 11-9 is their form. The reason for this duality is that with free surface flows two parameters are of interest: the Reynolds number and the Froude number, both of which cannot be simultaneously scaled, hence the work is both close to their Froude numbers but at significantly lower Reynolds numbers. Despite this scaling problem the results from the present work are clearly close to those of Chaplin and Teigen and, subject to the scaling caveat already discussed, can be assumed to be correct.

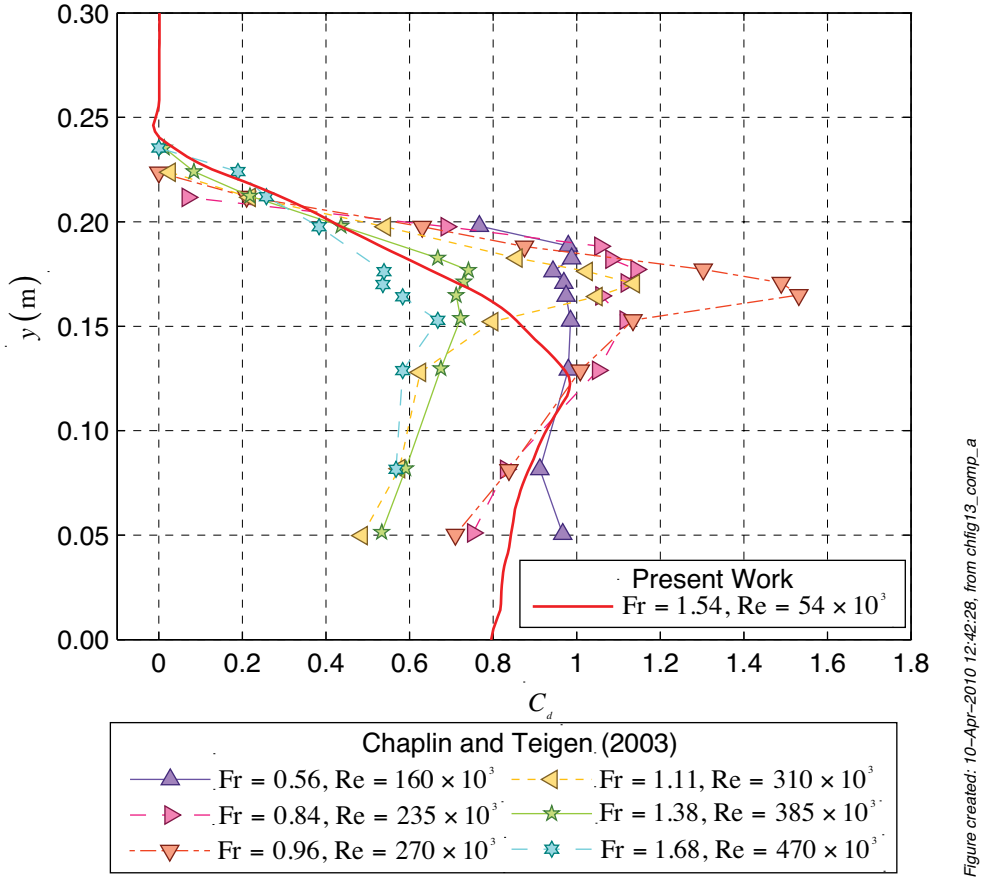


**Figure 11-9 – Reproduction of Figure 11-4 transposed into the present vertical coordinates with the sectional drag from the present work included.**

From an examination of Figure 11-9 it can be noted that all of the values of $C_d$ are lower than the nominal drag for a fully submerged cylinder, which is $C_D = O(1.2)$. However, as Hay (1947) noted that the drag returned to that of the fully submerged $C_{SF}$

as the depth was increased, then so must $C_d$ also tend to $C_{SF}$ as the depth is increased. Clearly this effect has not been observed, because the depths to which measurements were taken was not enough, in either the present work or that described by Chaplin and Teigen (2003). Therefore, the free surface must be exerting an influence on the pressure distribution around the cylinder.

Hence, having shown that the drag coefficient can be reduced when a circular cylinder pierces a free surface, the investigation can now turn to a meaningful definition of wave drag.

## 11.5. Alternative Wave Drag Values

In view of the difficulties mentioned above with the definition of the drag coefficient, defined in Equation (11.4), the drag force defined in Equation (11.5),

$$C_{FS} = \frac{F_{FS}}{\frac{1}{2}\rho_{water} L d U_\infty^2} \quad , \tag{11.9}$$

repeated here for clarity, will be used. $C_{FS}$ can be evaluated from Equation (11.3), also repeated here for clarity,

$$C_{FS} = C_D - C_{SF} \, , \tag{11.10}$$

provided $C_{SF}$ is evaluated from results obtained from the literature for fully submerged cylinders for example Zdravkovich (1997) rather than the "deep water measurement" of Chaplin and Teigen (2003). The values of $C_D$ used in Equation (11.10) are either those obtained in the present research or those presented by Hay (1947), as well the values of $C_D$ calculated by Chaplin and Teigen (2003) by their integral method, as shown in Equation (11.6).

Therefore, using the single fluid drag published in the meta-analysis of Zdravkovich (1997), as shown in Figure 11-10, the majority of $C_{FS}$ values obtained from Hay's and Chaplin and Teigen's data as well as all the $C_{FS}$ values calculated from the present results are negative. It is not surprising that the values of $C_{FS}$ from the present work match those of Hay – they are after all a good match for the raw values of $C_D$, as may be seen in Figure 11-2 and Figure 11-3.

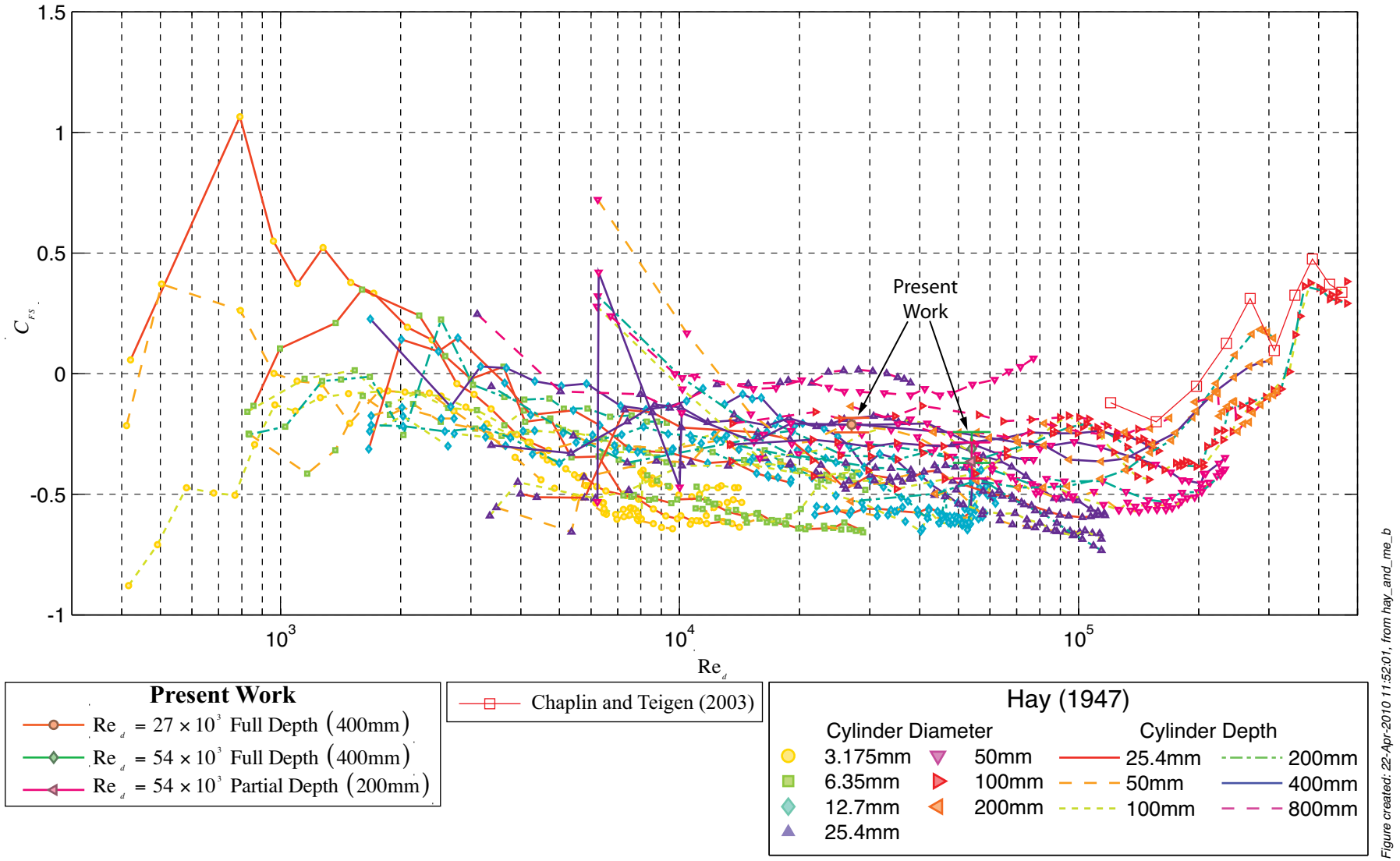


**Figure 11-10 – Recomputed values of $C_{FS}$ from Hay (1947), Chaplin and Teigen (2003) and the present work.**

It was a pleasant surprise to the present author that the re-computed values of $C_{FS}$ from Chaplin and Teigen were such an excellent match to those of Hay. Not only are the values of $C_{FS}$ in excellent agreement but the jagged shape of the curve also matches the distribution of the Hay data. Further Chaplin and Teigen's measurements were made on a 200mm diameter cylinder – as were the measurements of Hay shown on Figure 11-10 with left facing orange triangles – which are again the measurements against which the comparisons with Hay were made.

Therefore, the present author is confident in the alternative method of calculating $C_{FS}$ and that for the Reynolds numbers investigated in the present work, $C_{FS}$ should be negative. Based on an inspection of Figure 11-10, as Re is increased the value of $C_{FS}$ is similarly increased. This is due to the reduction in the magnitude of the single phase fluid drag because the separation points move towards the back of the cylinder when the flow becomes turbulent.

In particular the results from the partial depth simulation are exciting given that the depth of the cylinder is well defined and clear from the base of the computational domain and the results is an almost perfect match to Hay's measurements. Therefore, this remarkable agreement between the experimental results for the drag coefficient found in the literature and those obtained in the present study, combined with the previous examinations of the details of the flow confirm that the current simulation technique is capable of accurately computing all the features of the free surface flows and their effect on a body which pierces the free surface.

It is, therefore, now clear that the MILES/VOF method implemented to simulate turbulent free surface flows is the most appropriate tool. This conclusion was arrived at through not only the extensive validation studies undertaken but through the prediction of new flow features that matched those subsequently extracted from experimental data.

# 12. Conclusion

A combined MILES/VOF numerical Computational Fluid Dynamics (CFD) code has been developed. The code was extensively validated using flows both without and with free surfaces to test, respectively, the turbulence and the free surface models. While the work progressed from the relatively simple to the more complex, the conclusions will not be discussed in that order.

Two separate, two-dimensional investigations using wall-bounded simulations without free surfaces were conducted; namely one with a square obstruction and the other with a circular obstruction. The results from these two-dimensional simulations provided guidance for both the development of the three-dimensional computational meshes and the application of correct boundary conditions, particularly the boundary conditions at the outlet of the computational domain. However, a number of conclusions in addition to the desired recommendations were drawn from these simulations; of which the most significant relates to the general applicability of two-dimensional simulations at the Reynolds numbers investigated.

In relation to the location of the outlet boundary, it was found that the axiom that the boundary must be placed far enough away from the obstruction is too specific. Instead, a study of how the mean and RMS velocities, measured at fixed locations in the wake, changed as the boundary outlet boundary was moved further downstream showed that, to reduce their errors to less than 2% of the very long case, the outlet should be at least 400mm from the specific point on interest. Therefore, the axiom should be that the boundary must be sufficiently far away from the region of interest; which may extend much further into the wake than the bluff body itself.

From a visual examination of the flow fields from both these simulations, it was observed that the standard von Kárman vortex street was not formed. Rather, high-speed vortices were intermittently ejected perpendicular to the nominal vortex street. Since these vortices had not been reported in any of the laboratory or numerical simulations, it is apparent that they were unphysical.

This then raised the question as to why previous two-dimensional simulations, which added additional dissipation with a turbulence model such as the k-ε model, had resulted in acceptable values for the parameters chosen for comparison in the validation

process? When both the present two-dimensional simulations without a free surface were time averaged, the averaged parameters, such as the RMS lift and averaged drag, were within 1% of the published data. Further, there was no visible effect on the time averaged flow field that could be attributed to the unphysical vortices.

It is, perhaps, not so large a jump of the imagination to suppose that the numerically generated instantaneous flow fields have not previously been extensively investigated, hence unphysical flow features have not been observed, let alone reported. Clearly then, extreme care must be used with two-dimensional simulations because in the two cases studied in this work, the time averages were in good agreement with published time averaged results, in stark contrast to the unphysical instantaneous flow field. Two-dimensional simulations can be used with confidence to predict average trends and assist in the development of three-dimensional computational meshes.

The three-dimensional validation studies without a free surface were undertaken with the configuration of a right square cylinder mounted in cross flow with spanwise periodic boundaries. The results were mixed but positive. For example, the time averaged drag coefficient was in the order of 25% higher in the present work while both the recirculation length and the shedding frequency were both within 1% of the best estimates from the published literature.

Further, the time averaged velocities through the domain were similarly mixed in that some regions were in better agreement with published data than others. It is, however, a significant consolation that every other published dataset, both numerical and experimental, that was examined as part of this research showed similar variations being unable to simultaneously accurately predict every parameter. On balance, the time averaged velocity distributions from the present simulations were towards the middle of the spread of the published data while, simultaneously, the majority of the integral parameters, such as the drag coefficient, were in good agreement with the same published data.

While Power Spectral Density (PSD) plots have previously been extensively used in turbulence studies, a new method based on linear regressions was developed and applied to the results of the present simulations. In contrast to previous methods where the slope of the PSD curve was estimated visually, this new method provided an increased level of rigour by explicitly estimating the slope using a linear regression

function. The first step in the method is to compute the turbulent energy spectrum, otherwise known as the PSD, using a Digital Fourier Transform (DFT) after which the regression is applied to data at higher wave numbers. All the results from the present simulations were within 0.6% of the theoretically derived value of $-5/3$ and were computed with confidence intervals in the order of $\pm 0.02$. This excellent agreement was not isolated in a particular region of the grid but was observed throughout the wake.

Secondly, using similar spectral methods based on the DFT, the Kolmogorov length scale was computed and was found to be within an order of magnitude agreement with the only available data. That is, the values ranged from $\eta = 15\mu\text{m}$, computed near the downstream face of the cylinder to a maximum of approximately $\eta = 110\mu\text{m}$ at $7d$ downstream from the cylinder. Suppose that from this furthest point the turbulence intensity and the wake itself would decay as the flows moved further downstream, therefore the value of $\eta$ would be expected to simultaneously decrease. This is precisely what was found with the published value of $\eta$ measured at $26d$ being $64\mu\text{m}$, which is clearly in line with the reasoning presented above.

So far, the numerical calculations have been compared only with published results that had been time averaged; yet, as noted above the systematic averaging of potentially unphysical flows could reduce the quality of the results. Therefore, an examination of the flow field was undertaken with a number of flow visualisation techniques that indicated that there were a number of distinct structures across the domain. This raised two interesting questions:

1. Was the assumption of spanwise periodicy valid?
2. Was the span between the periodic boundaries, assuming that spanwise periodicy is valid, large enough?

To answer these two questions, the correlation coefficients between flow velocities measured at stations across the domain was computed. The result was that there was a very high correlation across the spanwise periodic domain with the lowest value of the correlation coefficient observed at +0.5. This is contrary to the established practice to provide a suitably large region of uncorrelated flow in the centre of the periodic domain. Therefore, the assumption of spanwise periodicy over a domain width of $4d$ was found to be invalid and the full width of the laboratory water tunnel should be simulated

instead. Naturally, there are potential repercussions from this conclusion on all the studies previously based on the assumption of spanwise periodicy across a domain 4*d* wide.

When a simulation using the dimensional of the actual water tunnel, which is wall bounded with a spanwise width of 9.75*d*, was run, the time averaged results had similar trends to those discussed above for the spanwise periodic simulations. Interestingly, the flow visualisations revealed noticeably different flow structures and large regions of uncorrelated flow. Therefore, for this configuration, the laboratory water tunnel configuration should have been used for all the computations based on this particular experiment.

To extend this discussion of the different structures in the flow, all the previous work, which includes the experimental investigations, averaged the data on the centre plane of the domain. However, it is evident from a visual examination of the data from the present work, that the flow structures do not align with the centre plane. Given this clear visual evidence of structures within the flow, it is highly likely that there would be a variation in the values of the time averages across the span of the domain, which should be investigated in the near future. Unequivocal visual evidence, such as with these structures, suggest that any future examinations must simultaneously investigate both the time-averaged values and the instantaneous flow field and supports the proposition that the MILES approach is superior.

At the beginning of this research it was assumed that, because the gradient of the hydrostatic pressure in the air phase is approximately two orders of magnitude smaller than the gradient of the hydrostatic pressure in water, ignoring the hydrostatic pressure gradient in the air phase would produce no adverse results. Prior to the development of the three-dimensional simulations with a free surface, this assumption was investigated using a number of two-dimensional simulations of a vertical slice of an open channel.

In fact, exactly the opposite was discovered! When the hydrostatic pressure gradient in the air phase was ignored, unphysical flow features developed. These unphysical flows were manifested as high-speed air flows in the order of seven times the free stream water velocity which first developed at the exit from the computational domain and then propagated upstream. As this high-speed zone extended upstream, large waves developed and grew so that finally the calculations diverged. Therefore, in contrast to

the initial assumption, the hydrostatic pressure gradient must be included as part of the boundary conditions in the air-phase at the inlet and outlet of the computation region. In situations where the flow is nominally open to the atmosphere, this may significantly increase the complexity of the simulations.

To validate the MILES/VOF solver for three-dimensional turbulent flows around a bluff body with a free surface, the configuration of a right circular cylinder that pierced the surface was used. The long axis of the cylinder was parallel to the gravitational vector and the domain was designed to represent a tow tank. Due to the limits of the computational resources, the entire tow tank was not simulated, instead the inertial frame of reference was moved to the centre of the cylinder so that rather than the cylinder being towed through the fluids, the fluids were moved around the cylinder. To closely approximate the conditions present in the tow tank, the fluids at the inlet were injected with no turbulent fluctuations and the sidewalls were moved at the same rate as the inlet velocities.

Three flow features were identified that were visible in both the present work and tow tank data and were named for their shapes, namely: a “low and trough”, a “high and ridge” and an isolated “low” point. Interestingly, whilst these three features were found in both the present work and the laboratory data, they were not present in the results from a recent LES simulation that simultaneously utilised a recognised Smagorinsky LES model and many more cells than the present work. Given that the present method can compute the shape of the free surface to a better approximation than more “established” techniques, this is more support for the efficacy of the MILES/VOF method.

The time averaged velocity magnitudes along four vertical test stations were in excellent agreement with published results from both laboratory and numerical experiments. 21 of the points available for comparison with the laboratory experiments were within 2% of the published values, which is within the bounds of experimental uncertainty. The remaining three points were near to 10% of the experimental data, which is still within excellent agreement. Again, these excellent results support the conclusion that the MILES/VOF solver proposed in this work is capable of simulating turbulent bluff body flows with a free surface.

In addition to the evident success of the visual examination of the shape of the free surface, further rigour was added through a comparison of measurements of the shape of the free surface. These measurements were compared with the extensive data set of Hay (1947) and, of the four parameters tested, three were within excellent agreement of Hay's data set.

Through this study a potentially new flow regime was identified with the length of the rooster tail double the length measured by Hay (1947) at slightly higher Froude numbers, for example $\mathrm{Fr}_d \cong 1.5$ compared with $\mathrm{Fr}_d \cong 5$. Initially this was identified as a possible error in the present simulations yet, when the raw images taken by Hay (1947) were checked the new flow feature was also present in three of his photographs. It is unclear why Hay (1947) in his exhaustive study did not document these three measurements and it is interesting to note that the present work is a near perfect match for the "new" data. Since the new flow regime was first identified during the analysis of the numerical results generated as part of the work for this dissertation and then "discovered" to be part of large body of data generated by Hay (1947), this prediction is therefore a real validation of the numerical method proposed in this thesis.

Further, Hay (1947) made over 900 measurements of the drag forces experienced by the cylinder as it was being towed and noted that most of the drag coefficients, when examined as a function of Reynolds number, were lower than the corresponding drag on a fully submerged cylinder. He performed little additional analysis of the drag as a function of Reynolds number, rather preferring to investigate the changes as a function of Froude number. Chaplin and Teigen (2003) re-examined the drag coefficients in an attempt to isolate a "wave" or "free surface" drag component. Strangely, instead of choosing a value from the literature for a fully submerged cylinder, they chose to use a representative value of the "single fluid" drag measured deep within their tow tank. As has been shown in the present work, the free surface does exert a considerable influence deep into the flow which resulted in Chaplin and Teigen's "single fluid" drag value as less than that of a fully submerged cylinder. As a result, the outcome of their analyses was that the values of their free surface coefficients was positive. This logic seems strange as Hay noted, in agreement with the present work, that the drag was lower than that found in the fully submerged case.

The denser information generated by the numerical work allowed the reasons for the reduction in the drag coefficient in the presence of the free surface to be elucidated. It is due to the fall of the free surface and the presence of an air bubble in the wake of the cylinder, thereby not allowing the pressure to reduce much below atmospheric pressure. Therefore, an alternative definition of the "free surface coefficient" proposed by Chaplin and Teigen was developed; namely, that the fully submerged value of the drag coefficient should be used as the reference case, which, when tested against Hay's data and the results from the present simulations, resulted in negative values of the coefficient. In addition, when the data published by Chaplin and Teigen (2003) was re-evaluated using the new definition they aligned with both Hay's data and the present simulations. It follows that this is the "correct" method of determining the free surface effect, because it simultaneously matches the conceptual requirement that the values should be negative and, when both Hay's and the present data were processed, all the values are in excellent agreement.

The present method is therefore not merely capable of simulating the flow around bluff bodies with the presence of a free surface but actually produces results which predict the shape of the frees surface and the velocity distributions more accurately that alternative methods.

A number of tests were conducted using one common computational mesh in order to evaluate the speed of the new solver relative to the alternate methods. All the boundary conditions, initial conditions and the parameters needed to run the simulations were fixed but, the solver configuration was changed to test different numerical and turbulence methods. The MILES/VOF solver was at least 16% faster than any of the other methods tested.

Because of the great success of the new MILES/VOF solver more areas of future research were discovered. While the results from the validation of flows without a free surface are quite acceptable, they are not as good as the results from the three-dimensional simulations with a free surface. This is because the grid used to simulate the flows around a square cylinder without a free surface was chosen to match that of a published study and is not the grid of choice if it had been constructed within this work. Therefore, further work, perhaps using the prediction of the three-dimensional

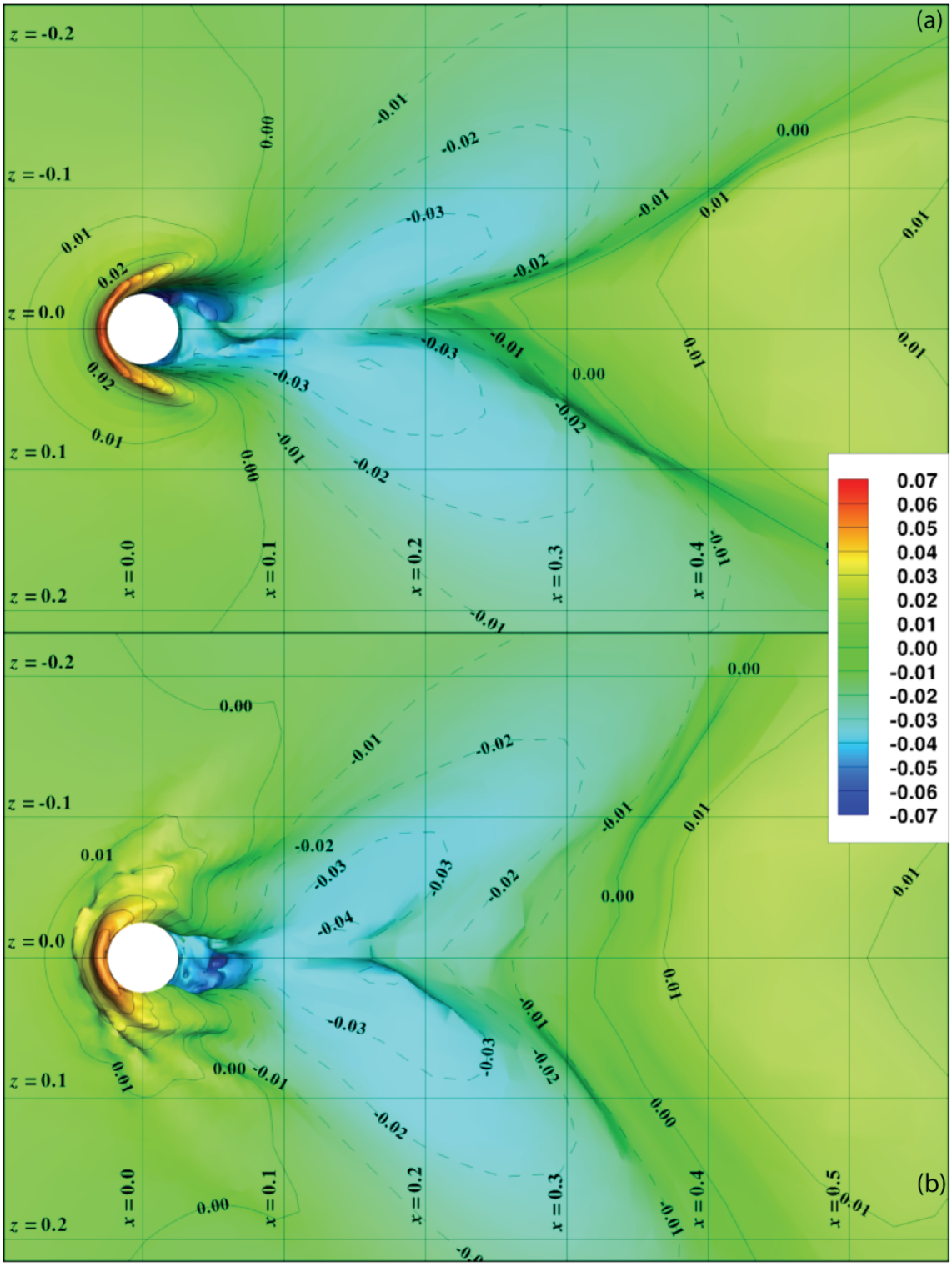


**Figure 12-1 – Comparison of the elevation of the free surface using no surface reconstruction and the PLIC method, (a) and (b) respectively.**

turbulence statistics in a different configuration, for example that described by Antonia and Browne (1986), would provide sufficient evidence to ensure the validity of the proposed MILES method.

Undoubtedly the most interesting future directions are with the free surface simulations. At the outset of the research described in this dissertation, it was argued that the VOF method with the PLIC surface reconstruction and surface tension was required for accurate simulation of the free surface. However, since that time, additional improvements have been proposed, such as the STACS scheme (Srinivasan and Wang, 2007), which could be tested. Alternatively, it is entirely possible that increased precision in the simulation of the free surface may not be required for these length scales. As may be seen in Figure 12-1, preliminary tests with no surface reconstruction and no surface tension, the so-called FOAM method, have shown promising results,

As discussed in above the power spectral density computed from the present work was in almost perfect agreement with the theoretical value derived from dimensional arguments. The present author must admit some discomfort with such excellent results and, hence, a degree of concern exists as to the validity of the result. There are a number of paths that should be investigated, including the specific digital Fourier transform algorithm used through to the quality of the MILES solver itself.

Finally, one of the most exciting discoveries of this research is the new, and in the opinion of the present author, the "correct" method to split the total drag that is experienced by a body subjected to flows with a free surface into the "free surface" and the "two-dimensional" components. Much more work is needed in this area as it may lead to better design and understanding of diverse fields such as ship dynamics and stirring rod type mixing.

It follows that the numerical solver based on a MILES/VOF formulation developed and extensively validated in this research can be used for the numerical simulation of free surface flows and is sufficiently accurate to open new areas of research and discovery.

# 13. Bibliography

Adobe Systems Incorporated 2007, *Adobe Photoshop CS3* (computer program), Adobe Systems Incorporated, San Jose, CA, USA. (10.0.1)

Amsden, A. A. and Harlow, F. H. 1970, *The SMAC Method: A Numerical Technique for Calculating Incompressible Fluid Flows*, Los Alamos National Laboratory, Los Alamos, New Mexico, USA.

Anderson, J., D Jr 1997, *A History of Aerodynamics and its Impact on Flying Machines*, Cambridge University Press, Cambridge, United Kingdom.

Antonia, R. A. and Browne, L. W. B. 1986, 'Anisotropy of the Temperature Dissipation in a Turbulent Wake', *Journal of Fluid Mechanics*, vol. 163, pp. 393-403.

*ANUGA* 2008, (computer program), Geoscience Australia and ANU, Canberra, Australia. (1.0 beta_5638)

Avis, C. 2001, *Sewer Overflows in Sydney and Erosion and Sediment Control for Stormwater Runoff Regulation*, University of Technology, Sydney, Sydney, Australia.

Bai, W. et al. 2009, 'Finite Volume Simulation of Viscous Free Surface Waves Using the Cartesian Cut Cell Approach', *International Journal For Numerical Methods In Fluids*. DOI: 10.1002/fld.2079

Barth, T. J. and Jespersen, D. C. 1989, The Design and Application of Upwind Schemes on Unstructured Meshes In *27th Aerospace Science Meeting and Exhibition*, AIAA, Reno, Nevada, USA.

Bastiaans, R. J. M., Vreman, A. W. and Pitsch, H. 2007, *DNS of Lean Hydrogen Combustion with Flamelet-Generated Manifolds*, Stanford University, Stanford.

Batchelor, G. K. and Towsend, A. A. 1949, 'The Nature of Turbulent Motion at Large Wave-Numbers', *Proceedings of the Royal Society A*, vol. 199, pp. 238-255. DOI: 10.1098/rspa.1949.0136

Bate, M. 2008, *'Star Cluster Formation in 3D'*, Available at: http://www.astro.ex.ac.uk/people/mbate/Cluster/cluster3d.html (7th October 2008)

Bearman, P. W. 1969, 'On Vortex Shedding from a Circular Cylinder in the Critical Reynolds Number Region', *Journal of Fluid Mechanics*, vol. 37, pp. 577-587.

Bearman, P. W. and Obasaju, E. D. 1982, 'An Experimental Study of Pressure Fluctuations on Forces and Oscillating Square-Section Cylinders', *Journal of Fluid Mechanics*, vol. 119, pp. 297-321.

Beecham, S., C. 1991, *Hydraulic Performance of Storm Sewage Overflow Chambers*. PhD Thesis, University of Manchester, Manchester.

Bekki, K. 2004, 'Star Clusters and Galactic Chemodynamics: Implosive Formation of Super Star Clusters', *Publications of the Astronomical Society of Australia*, vol. 21, pp. 167-170.

Benocci, C. et al. 2005a, 'Large eddy simulation of turbulent flows via domain decomposition techniques. Part 1: theory', *International Journal for Numerical Methods in Fluids*, vol. 48, no. 4**,** pp. 367-395.

Benocci, C. et al. 2005b, 'Large eddy simulation of turbulent flows via domain decomposition techniques. Part 2: applications', *International Journal for Numerical Methods in Fluids*, vol. 48, no. 4**,** pp. 397-422.

Bergmann, T. et al. 2007, 'One-Dimensional Hybrid Approach to Extensive Air Shower Simulation', *Astroparticle Physics*, vol. 26, no. 420-422.

Bird, R. B., Stewart, W. E. and Lightfoot, E. N. 2002, *Transport Phenomena*, John Wiley and Sons, Hoboken, NJ, USA.

Boris, J. P. 2007, 'More for LES: A Brief Historical Perspective of MILES', In *Implicit Large Eddy Simulation: Computing Turbulent Fluid Dynamics*, (eds) Grinstein, F. F., Margolin, L. G. and Rider, W. J., Cambridge University Press, Cambridge, United Kingdom.

Bosch, G. and Rodi, W. 1998, 'Simulation of Vortex Shedding Past a Square Cylinder with Different Turbulence Models', *International Journal For Numerical Methods In Fluids*, vol. 28, pp. 601-616.

Bouris, D. and Bergeles, G. 1999, '2D LES of Vortex Shedding from a Square Cylinder', *Journal of Wind Engineering and Industrial Aerodynamics*, vol. 80, no. 1-2**,** pp. 31-46.

Breslin, J. P. and Skalak, R. 1959, *Exploratory Study of Ventilated Flows About Yawed Surface-Piercing Struts*, National Aeronautics and Space Administration, Washington, DC, U.S.A.

Brocchini, M. and Peregrine, D. H. 2001, 'The Dynamics of Strong Turbulence at Free Surfaces. Part 1 Description', *Journal of Fluid Mechanics*, vol. 449, pp. 225-254.

Bruun, H. H. 1995, *Hot-Wire Anemometry: Principles and Signal Analysis*, Oxford University Press, New York, NY, U.S.A.

Buick, J. M. 1997, *Lattice Boltzman Methods in Interfacial Wave Modelling*. University of Edinburgh,

Cadiou, A., Hanjalić, K. and Stawiarski, K. 2004, 'A two-scale second-moment turbulence closure based on weighted spectrum integration', *Theoretical and Computational Fluid Dynamics*, vol. 18, no. 1**,** pp. 1-26.

Camarri, S. et al. 2002, 'Large-Eddy Simulation of A Bluff-Body Flow on Unstructured Grids', *International Journal For Numerical Methods In Fluids*, vol. 40, no. 11**,** pp. 1431-1460.

Celik, I. B. et al. 2008, 'Procedure for Estimation and Reporting of Uncertainty Due to Discretization in CFD Applications', *Journal of Fluids Engineering*, vol. 130. DOI: 10.1115/1.2960953

Chadwick, M. and Hardwick Jones, R. 2008, Models and Scales and WMA Water (Personal Communication)

Chaplin, J. R. and Teigen, P. 2003, 'Steady flow past a vertical surface-piercing circular cylinder', *Journal of Fluid Structures*, vol. 18, pp. 271-285.

Chen, L. et al. 1999, 'The Developmen of a Bubble Rising in a Viscous Liquid', *Journal of Fluid Mechanics*, vol. 387, pp. 61-96.

Chen, T., Chwang, A. T. and Zhang, D. 2000, 'Large-Eddy Simulation for a Free-Surface Turbulent Flow Past Vertical Cylinders', In *Tenth International Offshore and Polar Engineering Conference,* Seatle, WA, USA, pp. 60-67.

Cheng, C. M., Lu, P. C. and Chen, R. H. 1992, 'Wind Loads on Square Cylinder in Homogenous Turbulent Flows', *Journal of Wind Engineering and Industrial Aerodynamics*, vol. 41, no. 1-3**,** pp. 739-749.

Chung, T. J. 2002, *Computational Fluid Dynamics*, Cambridge University Press, Cambridge.

Clements, R. R. 1973, 'An Inviscid Model of Two-Dimensional Vortex Shedding', *Journal of Fluid Mechanics*, vol. 57, no. 2**,** pp. 321-336.

Coastal and Hydraulics Laboratory 2008a, *RMA-2* (computer program), U.S. Army Corps of Engineers,,

Coastal and Hydraulics Laboratory 2008b, *RMA-10* (computer program), U.S. Army Corps of Engineers,,

Constantin, P. and Foias, C. 1988, *Navier-Stokes Equations*, University of Chicargo Press, Chicargo, Il, USA.

Courant, R., Friedrichs, K. and Lewy, H. 1967, 'On the Partial Difference Equations of Mathematical Physics', *IBM Journal*, pp. 215-234.

Crank, J. and Nicolson, P. 1947, 'A Practical Method for Numerical Evaluation of Solutions of Partial Differential Equations of the Heat-conduction Type', *Proceedings of the Cambridge Philosophical Society*, vol. 43, pp. 50-67.

Deardoff, J. W. 1970, 'A Numerical Study of Three-dimensional Turbulent Channel Flow At Large Reynolds Numbers', *Journal of Fluid Mechanics*, vol. 41, no. 2**,** pp. 453-480.

Del Álamo, J. C. and Jiménez, J. 2009, 'Estimation of Turbulent convection Velocities and Corrections to Taylor's Approximation', *Journal of Fluid Mechanics*, vol. 640, pp. 5-26. DOI: 10.1017/S0022112009991029

Delft Hydraulics Software 2008a, *DELFT 3D* (computer program), Deltares, (2008)

Delft Hydraulics Software 2008b, *SOBEK River* (computer program), Deltares, (2008)

Delft Hydraulics Software 2008c, *SOBEK Urban* (computer program), Deltares, (2008)

Deng, G. B. et al. 1994a, '2-D Computations of unsteady flow past a square cylinder with the Baldwin-Lomax Model', *Journal of Fluids and Structures*, vol. 8, no. 7**,** pp. 663-680.

Deng, G. B. et al. 1994b, 'Incompressible flow calculations with a consistent physical interpolation finite volume approach', *Computers & Fluids*, vol. 23, no. 8**,** pp. 1029-1047.

*'Detached Eddy Simulation'*, 2009, Available at: http://www.cfd-online.com/Wiki/Detached_eddy_simulation_(DES) (10th March 2009)

Dhi Group 2008a, *MIKE 3* (computer program), Hørsholm, Denmark. (2008)

Dhi Group 2008b, *MIKE 11* (computer program), Hørsholm, Denmark. (2008)

Dhi Group 2008c, *MIKE 21* (computer program), Hørsholm, Denmark. (2008)

Dobre, A. and Hangan, H. 2004, 'Investigation of the three-dimensional intermediate wake topology for a square cylinder at high Reynolds number', *Experiments in Fluids*, vol. 37, no. 4**,** pp. 518-530.

Drazin, P. G. and Riley, N. 2006, *The Navier-Stokes Equations: A Classification of Flows and Exact Solutions*, Cambridge University Press, Cambridge, UK.

Drescher, H. 1956, 'Messung der auf querangeströmte Zylinder ausgeübten zeitlich veränderten Drücke', *Zeitschrift Fur Flugwissenschaften Und Weltraumforschung*, vol. 4, no. 1**,** pp. 17-21.

Durbin, P. A. 1995, 'Separated Flow Computations with the k-ε-$v^2$ Model', *AIAA Journal*, vol. 33, no. 4**,** pp. 659-664.

Durst, F., Jovanović, J. and Sender, J. 1995, 'LDA Measurements in the Near-Wall Region of a Turbulent Pipe Flow', *Journal of Fluid Mechanics*, vol. 295, pp. 305-335. DOI: 10.1017/S0022112095001984

Esi Cfd Inc. 2007a, *CFD-ACE+ Module Manual*, ESI Group, Huntsville, Alabama, USA.

Esi Cfd Inc. 2007b, *CFD-ACE+ User Manual*, ESI Group, Huntsville, Alabama, USA.

Esi Cfd Inc. 2007c, *CFD-GEOM Manual*, ESI Group, Huntsville, Alabama, USA.

Etkin, B., Korbacher, G. K. and Keefe, R. T. 1957, 'Acoustic Radiation from a Stationary Cylinder in a Fluid Stream (Aeolian Tones)', *The Journal of the Acoustical Society of America*, vol. 29, no. 1.

Faram, M. and Harwood, R. 2002, 'Assessment of the Effectiveness of Stormwater Treatment Chambers using Computational Fluid Dynamics', In *Global Solutions For Urban Drainage, The Ninth International Conference On Urban Drainage,* (eds) Strecker, E. and Huber, W., Lloyd Centre Doubletree Hotel, Portland, Oregon.

Farell, C. and Blessmann, J. 1983, 'On Critical Flow Around Smooth Cylinders', *Journal of Fluid Mechanics*, vol. 136, pp. 375-391.

Fletcher, C. A. J. 1991, *Computational Techniques for Fluid Dynamics*, 2nd edn, Springer-Verlag, New York, NY, U.S.A.

Franke, R. and Rodi, W. 1991, 'Calculation of vortex shedding past a square cylinder with various turbulence models', In *Turbulent Shear Flows 8,* (eds) Durst, F., et al., Springer-Verlag, Munich, Germany, pp. 189-204.

Fröhlich, J. and Rodi, W. 2004, 'LES of the Flow Around a Circular Cylinder of Finite Height', *International Journal of Heat and Fluid Flow*, vol. 25, pp. 537-548.

Fureby, C. et al. 2000, 'Large Eddy Simulations of the Flow Around a Square Prism', *AIAA Journal*, vol. 38, no. 3**,** pp. 442-452.

Gaston, M., Reizes, J. and Evans, G. 2002, 'Numerical Modelling of Multiple Three Dimensional Gas Bubbles Rising in a Quiescent Liquid Using a Volume of Fluid Method', In *Second Internation Conference on Computational Fluid Dynamics,* (eds) Armfield, S., Morgan, P. and Srinivas, K., Springer, Sydney, NSW, Australia.

Germano, M. et al. 1991, 'A Dynamic Subgrid-Scale Eddy Viscosity Model', *Physics of Fluids*, vol. 3, no. 7**,** pp. 1760-1765.

Grigoriadis, D. G. E., Bartzis, J. G. and Goulas, A. 2003, 'LES of the flow past a rectangular cylinder using the immersed boundary concept', *International Journal for Numerical Methods in Fluids*, vol. 41, no. 6**,** pp. 615-632.

Grinstein, F. F., Margolin, L. G. and Rider, W. J. 2007, 'Introduction', In *Implicit Large Eddy Simulation: Computing Turbulent Fluid Dynamics*, (eds) Grinstein, F. F., Margolin, L. G. and Rider, W. J., Cambridge University Press, Cambridge, United Kingdom.

Güven, O., Farell, C. and Patel, V. C. 1980, 'Surface Roughness Effects on the Mean Flow Past Circular Cylinders', *Journal of Fluid Mechanics*, vol. 98, pp. 673-701.

Harlow, F. H. and Amsden, A. A. 1970, 'A Simplified MAC Technique for Incompressible Fluid Flow Calculations', *Journal of Computational Physics*, vol. 6, pp. 322-325.

Harlow, F. H. and Welch, J. E. 1965, 'Numerical Calculation of Time-Dependent Viscous Incompressible Flow of Fluid With a Free Surface', *Physics of Fluids*, vol. 8, pp. 2182-2189.

Harwood, R. 2002, 'CSO Modelling Strategies Using Computational Fluid Dynamics', In *Global Solutions For Urban Drainage, The Ninth International Conference On Urban Drainage,* (eds) Strecker, E. and Huber, W., Lloyd Centre Doubletree Hotel, Portland, Oregon.

Harwood, R. and Saul, A. 1996, CFD and Novel Technology in Combined Sewer Overflow In *7th International Conference on Urban Storm Drainage*, (eds) Sieke, F. and Verworn, H.-R., Hannover, Germany, pp. 1025-1030.

Harwood, R. and Saul, A. 2001, 'Modelling the Performance of Combined-Sewer Overflow Chambers', *Water and Environment Journal*, vol. 15, pp. 300-304.

Harwood, R. and Saul, A., J., Prof 1999, 'The Influence of CSO Chamber Size on Particle Retention Efficiency Performance', In *8th International Conference on Urban Storm Drainage,* Sydney, NSW, Australia.

Hay, A. D. 1947, *Flow About Semi-Submerged Cylinders of Finite Length*, Princeton University, Princeton, NJ, USA.

Hirt, C. W. and Nichols, B. D. 1981, 'Volume of Fluid (VOF) Method for the Dynamics of Free Boundaries', *Journal of Computational Physics*, vol. 39, pp. 201-225.

Hirt, C. W., Nichols, B. D. and Romero, N. C. 1975, *SOLA - A Numerical Solution Algorithm for Transient Fluid Flows*, Los Alamos Scientific Laboratory, Los Alamos, New Mexico, USA.

Hoffman, J. 2005, 'Computation of Mean Drag for Bluff Body Problems Using Adaptive DNS/LES', *SIAM Journal on Scientific Computing*, vol. 27, no. 1**,** pp. 184-207.

Hoffman, J. and Johnson, C. 2006, 'Stability of the dual Navier-Stokes equations and efficient computation of mean output in turbulent flow using adaptive DNS/LES', *Computer Methods in Applied Mechanics and Engineering*, vol. 195, no. 13-16**,** pp. 1709-1721.

Hornsby Shire Council 1997, *Sustainable Water Best Practices*, Hornsby Shire Council, Sydney, NSW, Australia.

Hornsby Shire Council 2009, *'Catchments Remediation Program'*, Available at: http://www.hornsby.nsw.gov.au/environment/index.cfm?NavigationID=1536 (7th April 2009)

Horrocks, G. 2001, *A Numerical Study of a Rotary Valve internal Combustion Engine*. PhD, University of Technology Sydney, Sydney, NSW, Australia.

Hu, G. and Grossman, B. 2006, 'The computation of massively separated flows using compressible vorticity confinement methods', *Computers & Fluids*, vol. 35, no. 7**,** pp. 781-789.

Iaccarino, G. et al. 2003, 'Reynolds averaged simulation of unsteady separated flow', *International Journal of Heat and Fluid Flow*, vol. 24, no. 2**,** pp. 147-156.

Inoue, M., Baba, N. and Himeno, Y. 1993, 'Experimental and Numerical Study of Viscous Flow Field around an Advancing Vertical Circular Cylinder Piercing a Free-Surface', *Journal of Kansai Society of Naval Architects of Japan*, no. 220**,** pp. 57-64.

Jasond 2007, *'Structured Mesh Generation'*, Available at: http://www.cfd-online.com/Wiki/Structured_mesh_generation (5th July 2009)

Jiménez, J. 2006, 'Some Contributions and Challenges of Computational Turbulence Research', In *IUTAM Symposium on Computational Physics and New Perspectives in Turbulence,* vol. 4, (ed.) Kaneda, Y., Springer, Nagoya University, Nagoya, Japan, pp. 3-10.

Johansen, S. T., Wu, J. and Shyy, W. 2004, 'Filter-based unsteady RANS computations', *International Journal of Heat and Fluid Flow*, vol. 25, no. 1**,** pp. 10-21.

Jones, W. P. and Launder, B. E. 1972, 'The Prediction of Laminarization with a Two-Equation Model of Turbulence', *International Journal of Heat and Mass Transfer*, vol. 15, pp. 301-314.

Kawamura, T. et al. 2002, 'Large Eddy Simulation of a Flow Past a Free Surface Piercing Circular Cylinder', *Journal of Fluids Engineering*, vol. 124, no. 1**,** pp. 91-101.

Kimura, I. and Hosoda, T. 2003, 'A Non-Linear k-ε Model with Realizability for Prediction of Flows Around Bluff Bodies', *International Journal For Numerical Methods In Fluids*, vol. 42, pp. 813-833.

Kogaki, T., Kobayashi, T. and Taniguchi, N. 1997, 'Large eddy simulation of flow around a rectangular cylinder', *Fluid Dynamics Research*, vol. 20, no. 1-6**,** pp. 11-24.

Kolmogorov, A. N. 1941, 'Local Structure of Turbulence in Incompressible Viscous Fluid for Very Large Reynolds Number', *Izvestia Academy of Sciences, USSR, Physics*, vol. 6, no. 1 and 2**,** pp. 299-303.

Koobus, B. et al. 2007, 'Parallel simulation of three-dimensional complex flows: Application to two-phase compressible flows and turbulent wakes', *Advances in Engineering Software*, vol. 38, no. 5**,** pp. 328-337.

Kothe, D. B. et al. 1996, Volume Tracking of Interfaces Having Surface Tension in Two and Three Dimensions In *34th AIAA Aerospace Sciences Meeting*, Reno, Nevada, USA.

Koutmos, P. and Mavridis, C. 1997, 'A computational investigation of unsteady separated flows', *International Journal of Heat and Fluid Flow*, vol. 18, no. 3**,** pp. 297-306.

Lakehal, D. and Thiele, F. 2001, 'Sensitivity of turbulent shedding flows to non-linear stress-strain relations and Reynolds stress models', *Computers And Fluids*, vol. 30, no. 1**,** pp. 1-35.

Launder, B. E. and Sharma, B. I. 1974, 'Application of the Energy Dissipation Model of Turbulence to the Calculation of Flow Near a Spinning Disc', *Letters in Heat and Mass Transfer*, vol. 1, no. 2**,** pp. 131-138.

Launder, B. E. and Spalding, D. B. 1974, 'The Numerical Computation of Turbulent Flows', *Computer Methods in Applied Mechanics and Engineering*, vol. 3, pp. 269-289.

Lee, B. E. 1975, 'The Effect of Turbulence on the Surface Pressure Field of a Square Prism', *Journal of Fluid Mechanics*, vol. 69, Part 2, pp. 263-282.

Lee, S. 1997, 'Unsteady aerodynamic force prediction on a square cylinder using k-ε turbulence models', *Journal of Wind Engineering and Industrial Aerodynamics*, vol. 67-68, pp. 79-90.

Lee, S. and Bienkiewicz, B. 1998, 'Finite element implementation of large eddy simulation for separated flows', *Journal of Wind Engineering and Industrial Aerodynamics*, vol. 77-78, pp. 603-617.

Leonard, A. 1974, 'Energy Cascade in Large-Eddy Simulations of Turbulent Fluid Flows', *Advances in Geophysics*, vol. 18A, pp. 237-248.

Lilly, D. K. 1992, 'A Proposed Modification of the Germano Subgrid-Scale Closure Method', *Physics of Fluids*, vol. 4, no. 3**,** pp. 663-635.

Lonsdale, R. D. 1993, 'An Algebraic Multigrid Solver for the Navier-Stokes Equations on Unstructured Meshes', *International Journal For Numerical Methods In Heat and Fluid Flow*, vol. 3, no. 1**,** pp. 3-14. DOI: 10.1108/eb017512

Losasso, F., Fedkiw, R. and Osher, S. 2006, 'Spatially Adaptive Techniques for Level Set Methods and Incompressible Flo', *Computers and Fluids*, vol. 30, pp. 775-793.

Lübcke, H. et al. 2001, 'Comparison of LES and RANS in Bluff Body Flows', *Journal of Wind Engineering and Industrial Aerodynamics*, vol. 89, pp. 1471-1485.

Lumley, J. L. and Yaglom, A. M. 2001, 'A Century of Turbulence', *Flow Turbulence and Combustion*, vol. 66, pp. 241-286.

Lyn, D. A. et al. 1995, 'A laser-Doppler velocimetry study of ensemble-averaged characteristics of the turbulent near wake of a square cylinder', *Journal of Fluid Mechanics*, vol. 304, pp. 285-319.

Lyn, D. A. and Rodi, W. 1994, 'The flapping shear layer formed by flow separation from the forward corner of a square cylinder', *Journal of fluid Mechanics*, vol. 267, pp. 253-376.

Mallinson, S. G. et al. 2004, 'Analysis of Hot-wire Anemometry Data Obtained in a Synthetic Jet Flow', *Experimental Thermal and Fluid Science*, vol. 28, pp. 265-272.

Mathworks 2002, *MATLAB 6.5* (computer program), The Mathworks Incorporated, Natick, Massachusetts, USA. (6.5.0.180913a Release 13)

Meiburg, E. and Lasheras, J. C. 1988, 'Experimental and Numerical Investigation of the Three-Dimensional Transition in Plane Wakes', *Journal of Fluid Mechanics*, vol. 190, pp. 1-37.

Menon, S. and Kim, W. W. 1996, High Reynolds Number Flow Simulations Using the Localized Dynamic Subgrid-Scale Model In *34th Aerospace Sciences Meeting*, AIAA, Reno, NV, U.S.A.

Moffa, P. E. et al. 1983, 'Urban Runoff and Combined Sewer Overflow', *Journal of the Water Pollution Control Federation*, vol. 55, no. 6**,** pp. 676-679.

Moin, P. 2009, 'Revisiting Taylor's Hypothesis', *Journal of Fluid Mechanics*, vol. 640, pp. 1-4. DOI: 10.1017/S0022112009992126

Monaghan, J., J. 1988, 'An Introduction To SPH', *Computer Physics Communications*, vol. 48, pp. 89-96.

Monaghan, J., J., Thompson, M., C. and Hourigan, K. 1994, 'Simulation of Free Surface Flows with SPH', In *ASME Symposium on Computational Methods in Fluid Dynamics,* Lake Tahoe, California, USA.

Murakami, S. and Mochida, A. 1995, 'On turbulent Vortex Shedding flow Past 2D Square Cylinder Predicted by CFD', *Journal of Wind Engineering and Industrial Aerodynamics*, vol. 54/55, pp. 191-211.

N.A.S.A. 2004, *'Hubble2005-01-barred-spiral-galaxy-NGC1300.jpg'*, Available at: http://en.wikipedia.org/wiki/Image:Hubble2005-01-barred-spiral-galaxy-NGC1300.jpg (11th October 2008)

N.A.S.A. 2008, *'WMAP 2008.png'*, Available at: http://en.wikipedia.org/wiki/Image:WMAP_2008.png (11th October 2008)

Nagano, S., Naito, M. and Takata, H. 1982, 'A numerical analysis of two-dimensional flow past a rectangular prism by a discrete vortex model', *Computers And Fluids*, vol. 10, no. 4**,** pp. 243-259.

Nakamura, Y. 1993, 'Bluff-body aerodynamics and turbulence', *Journal of Wind Engineering and Industrial Aerodynamics*, vol. 49, no. 1-3**,** pp. 65-78.

Nakayama, A. and Vengadesan, S. N. 2002, 'On the influence of numerical schemes and subgrid-stress models on large eddy simulation of turbulent flow past a square cylinder', *International Journal for Numerical Methods in Fluids*, vol. 38, no. 3**,** pp. 227-253.

Nezu, I. and Nakagawa, H. 1993, *Turbulence in Open-Channel Flows*, International Association for Hydraulic Research, Rotterdam, The Netherlands.

O'neill, P. L. et al. 2004, 'Autocorrelation Functions and the Determination of Integral Length with Reference to Experimental and Numerical Data', In *Fifteenth Australasian Fluid Mechanics Conference (CD-ROM),* (eds) Behnia, M., Lin, W. and McBain, G. D., University of Sydney, University of Sydney, Sydney, NSW, Australia.

Okajima, A. 1982, 'Strouhal Numbers of Rectangular Cylinders', *Journal of Fluid Mechanics*, vol. 123, pp. 379-398.

Orfanidis, S. J. 1996, *Introduction to Signal Processing*, Prentice Hall, Englewood Cliffs, New Jersey, USA.

Patankar, S. V. 1980, *Numerical Heat Transfer and Fluid Flow*, McGraw-Hill, New York, NY, USA.

Patankar, S. V. and Spalding, D. B. 1972, 'A calculation procedure for heat, mass and momentum transfer in three-dimensional parabolic flows', *International Journal of Heat and Mass Transfer*, vol. 15, no. 10**,** pp. 1787-1806.

Perić, M., Kessler, R. and Scheuerer 1988, 'Comparions of Finite-Volume Numerical Methods with Staggered and Colocated Grids', *Computers and Fluids*, vol. 16, no. 4**,** pp. 389-403.

Pope, S. B. 2001, *Turbulent Flows*, Cambridge University Press, Cambridge, UK.

Pourquie, M., Breuer, M. and Rodi, W. 1996, 'Computed Test Case: Square Cylinder', In *Direct and Large Eddy Simulation II,* (eds) Chollet, J.-P., Voke, P. R. and Kleiser, L., Kluwer Academic Publishers, Grenoble, France.

Prandtl, L. 1925, 'Über die ausgebildete Turbulenz', *ZAMM*, vol. 5, pp. 136-139.

Reynolds, O. 1883, 'An Experimental Investigation of the Circumstances which Determine Whether the Motion of Water Shall be Direct or Sinuous, and of the Law of Resistance in Parallel Channels', *Philosophical Transactions of the Royal Society of London*, vol. 174, pp. 935-982.

Reynolds, O. 1895, 'On the Dynamical Theory of Incompressible Viscous Fluids and the Determination of the Criterion', *Philosophical Transactions of the Royal Society of London, Series A*, vol. 186, pp. 123-164.

Rhie, C. M. and Chow, W. L. 1983, 'Numerical Study of the Turbulent Flow Past and Airfoil with Trailing Edge Separation', *AIAA Journal*, vol. 21, no. 11**,** pp. 1525-1532.

Rider, W. J. and Kothe, D. B. 1998, 'Reconstructing Volume Tracking', *Journal of Computational Physics*, vol. 141, pp. 112-152.

Rider, W. J. et al. 1995, 'Accurate Solution Algorithms for Incompressible Multiphase Flows', *AIAA Paper 95-0699*.

Roache, P., J 1998a, *Fundamentals of Computational Fluid Dynamics*, Hermosa Publications, Albuquerque, New Mexico, USA.

Roache, P., J 1998b, *Verification and Validation in Computational Science and Engineering*, Hermosa Publications, Albuquerque, New Mexico, USA.

Rocla 2009, *'Water Quality: CDS Technologies: CDS Units'*, Available at: http://www.rocla.com.au/Popup_CDS_Units_Gallery.php?id=523&category=cdsunits (26th April 2009)

Rodi, W. 1997, 'Comparison of LES and RANS calculations of the flow around bluff bodies', *Journal of Wind Engineering and Industrial Aerodynamics*, vol. 69-71, pp. 55-75.

Rodi, W. et al. 1997, 'Status of Large Eddy Simulation: Results of a Workshop', *Journal of Fluids Engineering*, vol. 119, pp. 248-262.

Rogallo, R. S. and Moin, P. 1984, 'Numerical Simulation of Turbulent Flows', *Annual Review of Fluid Mechanics*, vol. 16, pp. 99-137.

Rott, N. 1990, 'Note on the History of the Reynolds Number', *Annual Review of Fluid Mechanics*, vol. 22, pp. 1-11.

Rumsfeld, D. H. 2002, *'U.S. Department of Defense News Briefing - Secretary Rumsfeld and General Myers'*, Available at: http://www.defenselink.mil/transcripts/transcript.aspx?transcriptid=2636 (8th September 2009)

Saad, Y. 1996, *Iterative Methods for Sparse Linear Systems*, PWS Publishing Company, Boston, MA, USA.

Sagaut, P., Deck, S. and Terracol, M. 2006, *Multiscale and Multiresolution Approaches in Turbulence*, Imperial College Press, London, UK.

Saul, A., J., Prof and Delo, E., A. 1983, 'Flood Control in Storm Sewers Using a High-Sided-Weir Storage Chamber', In *Hydraulic Aspects of Floods and Flood Control,* City University, London, England.

Scardovelli, R. and Zaleski, S. 1999, 'Direct Numerical Simulation of Free-Surface and Interfacial Flow', *Annual Review of Fluid Mechanics*, vol. 31, pp. 567-603.

Schaap, W. 2007, *'2dfdtfe.gif'*, Available at: http://en.wikipedia.org/wiki/Image:2dfdtfe.gif (11th October 2008)

Sethian, J. A. 1999, *Level Set Methods and Fast Marching Methods: Evolving Interfaces in Computational Geometry, Fluid Mechanics, Computer Vision and Materials Science*, Cambridge University Press, Cambridge UK.

Shaanan, S., Ferziger, J. and Reynolds, W. C. 1975, *Numerical Simulation of Turbulence in the Presence of Shear*, Department of Mechanical Engineering, Stanford University, California.

Shao, S. 2009, 'Incompressible SPH Simulation of Water Entry of a Free-Falling Object', *International Journal For Numerical Methods In Fluids*, vol. 59, pp. 91-115. DOI: 10.1002/fld.1813

Shepel, S. V. and Smith, B. L. 2009, 'On Surface Tension Modelling Using the Level Set Method', *International Journal For Numerical Methods In Fluids*, vol. 59, pp. 147-171. DOI: 10.1002/fld.1804

Shimada, K. and Ishihara, T. 2002, 'Application Of A Modified k-ε Model To The Prediction Of Aerodynamic Characteristics Of Rectangular Cross-Section Cylinders', *Journal of Fluids and Structures*, vol. 16, no. 4**,** pp. 465-485.

Shin, S. and Juric, D. 2002, 'Modelling Three-Dimensional Multiphase Flow Using a Level Contour Reconstruction Method for Front-Tracking Without Connectivity', *Journal of Computational Physics*, vol. 163, pp. 427-470.

Shin, S. and Juric, D. 2009, 'A Hybrid Interface Method for Three-Dimensional Multiphase Flows Based on Front Tracking and Level Set Techniques', *International Journal For Numerical Methods In Fluids*, vol. 60, pp. 753-778. DOI: 10.1002/fld.1912

*'Ship Wakes'*, 2009, Available at: http://earth.esa.int/applications/ERS-SARtropical/oceanic/shipwakes/intro/ (15th October 2009)

Shon, H. K., Vigneswaran, S. and Snyder, S. A. 2006, 'Effluent Organice Matter in Wastewater: Constituents, Effects and Treatment', *Critical Reviews in Environmental Science and Technology*, vol. 36, pp. 327-374.

Smagorinsky, J. 1963, 'General Circulation Experiments with Primitive Equations. 1. The Basic Experiment', *Monthly Weather Review*, vol. 91, pp. 99-164.

Sohankar, A., Davidson, L. and Norberg, C. 1999, 'A Dynamic One-Equation Subgrid Model for Simulation of Flow Around a Square Cylinder', In *4th International Symposium on Engineering Turbulence Modelling and Measurements,* (eds) Rodi, W. and Laurence, D., Elsevier Science Publishers, Ajaccio, Corsica, France, pp. 227-236.

Sohankar, A., Davidson, L. and Norberg, C. 2000, 'Large Eddy Simulation of Flow Past a Square Cylinder: Comparison of Different Subgrid Scale Models', *Journal of Fluids Engineering*, vol. 122, no. 1**,** pp. 39-47.

Song, C.-S. and Park, S.-O. 2009, 'Numerical Simulation of Flow Past a Square Cylinder using Partially-Averaged Navier-Stokes Model', *Journal of Wind Engineering and Industrial Aerodynamics*, vol. 97, pp. 37-47.

Spalart, P. R. and Allmaras, S. R. 1992, A One-Equation Turbulence Model for Aerodynamic Flows, AIAA Paper 92-439, Reno, Nevada, USA.

Spalart, P. R. et al. 1997, 'Comments on the Feasibility of LES for Wings and on the Hybrid RANS/LES Approach', In *Advances in DNS/LES - Proceedings of the First AFOSR International Conference on DNS/LES,* (eds) Liu, C. and Liu, Z., Greyden Press, Columbus, Ohio, USA, Louisian Tech University, Louisiana, USA.

Sreenivasan, K. R. 1999, 'Fluid Turbulence', *Reviews of Modern Physics*, vol. 71, no. 2**,** pp. S383-S395.

Srinivas, Y. et al. 2006, 'Large-Eddy Simulation of High Reynolds Number Turbulent Flow Past a Square Cylinder', *Journal of Engineering Mechanics*, vol. 132, no. 3**,** pp. 327-335.

Srinivasan, V. and Wang, D. M. 2007, 'Numerial Simulation of Free Surface Flows Using STACS-VOF Method', In *ASME/JSME 2007 5th Joint Fluids Engineering Conference,* vol. 2, ASME, San Diego, California, U.S.A., pp. 347-356.

Stoots, C. et al. 2001, 'A Large-Scale Matched Index of Refraction Flow Facilty for LDA Studies Around Complex Geometries', *Experiments in Fluids*, vol. 30, no. 4**,** pp. 391-398. DOI: 10.1007/s003480000216

Stovin, V. et al. 2002a, 'Parametric Studies on CFD Models of Sewerage Structures', In *Global Solutions For Urban Drainage, The Ninth International Conference On Urban Drainage,* (eds) Strecker, E. and Huber, W., Lloyd Centre Doubletree Hotel, Portland, Oregon.

Stovin, V., Grimm, J. and Saul, A. 2002b, 'Fine Sediment Retention in Storage Chambers: An Assessment of Time-Dependent Effects', *Water Science and Technology*, vol. 45, no. 7**,** pp. 123-131.

Stovin, V. and Saul, A. 1998, 'A Computational Fluid Dynamics (CFD) Partical Tracking Approach to Efficiency Prediction', *Water Science and Technology*, vol. 37, no. 1**,** pp. 285-293.

Stovin, V. and Saul, A. 2000, 'Computational Fluid Dynamics and The Design of Sewage Storage Chambers', *Water and Environmental Management*, vol. 14, no. 2**,** pp. 103-110.

Stovin, V. R. and Saul, A. J. 1996, 'Efficiency Prediction for Storage Chambers Using Computational Fluid Dynamics', *Water Science and Technology*, vol. 33, no. 9**,** pp. 163-170.

Sturm, T., W 2001, *Open Channel Hydraulics*, McGraw-Hill, New York, New York, USA.

Surendran, D. 2006, *'Proton Shower'*, Available at: http://astro.uchicago.edu/cosmus/projects/aires/ (5th October 2008)

Sussman, M. and Fatemi, E. 1999, 'An Efficient Interface-Preserving Level Set Redistributing Algorithm and its Application to Interfacial Incompressible Flows', *SIAM Journal on Scientific Computing*, vol. 20, pp. 1165-1191.

Sussman, M., Smereka, P. and Osher, S. 1994, 'A Level Set Approach for Computing Solutions to Incompressible Two-Phase Flow', *Journal of Computational Physics*, vol. 114, pp. 146-159.

Sussman, M. et al. 2007, 'A sharp interface method for incompressible two-phase flows', *Journal of Computational Physics*, vol. 221, pp. 469-505.

Tang, B., Li, J. F. and Wang, T. S. 2008, 'Some Improvements on Free Surface Simulation by the Particle Finite Element Method', *International Journal For Numerical Methods In Fluids*. DOI: 10.1002/fld.1937

Taylor, G. I. 1935, 'Statistical Theory of Turbulence', *Proceedings of the Royal Society, London*, vol. A151, p. 421.

Taylor, I. and Vezza, M. 1999, 'Prediction of unsteady flow around square and rectangular section cylinders using a discrete vortex method', *Journal of Wind Engineering and Industrial Aerodynamics*, vol. 82, no. 1-3**,** pp. 247-269.

Tennekes, H. and Lumley, J. L. 1972, *A First Course In Turbulence*, MIT Press, Cambridge, Massachusetts, USA.

The Mathworks 2008, *MATLAB* (computer program), The Mathworks, (7.6.0.324 (2008a))

Thompson, B. 2006, *Combined Sewer Overflows (CSOs)*, Thompson RPM, Stockton on Tees, UK.

*TUFLOW* 2008, (computer program), BMT WBM Pty Ltd, Sydney, Australia. (2008-08-AA)

U.S. Army Corps of Engineers 2008, *HEC-RAS* (computer program), (4.0)

United States Environmental Protection Agency 2004, *Report to Congress: Impacts and Control of CSOs and SSOs*, US EPA, Office of Water, Washington DC, USA.

Van Doormal, J. P. and Raithby, G. D. 1984, 'Enhancements of the SIMPLE Method for Predicting Incompressible Flows', *Numerical Heat Transfer, Part A: Applications*, vol. 7, no. 2**,** pp. 147-163.

Verstappen, R. W. C. P. and Veldman, A. E. P. 1997, 'Direct Numerical Simulation of Turbulence at Lower Costs', *Journal of Engineering Mathematics*, vol. 32, no. 2**,** pp. 143-159.

Versteeg, H. K. and Malalasekera, W. 1996, *An Introduction to Computational Fluid Dynamics: The Finite Volume Method*, Pearson Education Limited, Harlow, UK.

Vinokur, M. 1980, *On One-Dimensional Stretching Functions for Finite Difference Calculations*, NASA Ames Research Center, Moffett Field, California, USA.

Vinokur, M. 1983, 'On One-Dimensional Stretching Functions for Finite-Difference Calculations', *Journal of Computational Physics*, vol. 50, pp. 215-234.

Violeau, D. and Issa, R. 2007, 'Numerical Modelling of Complex Turbulent Free-Surface Flows with the SPH Method: An Overview', *International Journal For Numerical Methods In Fluids*, vol. 53, pp. 277-304. DOI: 10.1002/fld.1292

Voke, P. R. 1996, 'Flow Past A Square Cylinder: Test Case LES2', In *Direct and Large Eddy Simulation II,* (eds) Chollet, J.-P., Voke, P. R. and Kleiser, L., Kluwer Academic Publishers, Grenoble, France.

Walker, T. A. et al. 1999, *Removal of Suspended Solids and Associated Pollutants by a CDS Gross Pollutant Trap*, Cooperative Research Centre for Catchment Hydrology, Melbourne, Australia.

Weisstein, E. W. 2008, *'Point-Line Distance - 2-Dimensional'*, Available at: http://mathworld.wolfram.com/Point-LineDistance2-Dimensional.html (22nd November 2008)

White, F. M. 1991, *Viscous Fluid Flow*, 2nd edn, McGraw-Hill, Singapore.

Wienken, W., Stiller, J. and Keller, A. 2006, 'A Method to Predict Cavitation Inception Using Large-Eddy Simulation and its Application to the Flow Past a Square Cylinder', *Journal of Fluids Engineering*, vol. 128, no. 2**,** pp. 316-325.

Wikramasinghe, D. and Wilkinson, R. H. 1997, *Wakes and Waves Generated by Surface Piercing Cylinders*.

Wilcox, D. C. 1998, *Turbulence Modeling for CFD*, 2nd edn, DCW Industries, La Canada, California, USA.

Wojtenko, I., Stinson, M. and Field, R. 2002, 'High-Rate Disinfection of Combined Sewer Overflow', In *Global Solutions For Urban Drainage, The Ninth International Conference On Urban Drainage,* (eds) Strecker, E. and Huber, W., Lloyd Centre Doubletree Hotel, Portland, Oregon.

Wong, T. H. F. (ed.) 2005, *Australian Runoff Quality: A Guide to Water Sensitive Urban Design*, The Institution of Engineers Australia, Canberra, Australia.

Wu, X. and Moin, P. 2008, 'A Direct Numerical Simulation Study on the Mean Velocity Characteristics in Turbulent Pipe Flow', *Journal of Fluid Mechanics*, vol. 608, pp. 81-112.

Wu, Y., Sun, X. and Shen, S. 2008, 'Computation of wind-structure interaction on tension structures', *Journal of Wind Engineering and Industrial Aerodynamics*, vol. 96, no. 10-11**,** pp. 2019-2032.

Yaglom, A. M. 1987, *Correlation Theory of Stationary and Related Random Functions, Volume 1: Basic Results*, Springer Verlag.

Yaglom, A. M. 2001, 'The Century of Turbulence Theory: The Main Achievements and Unsolved Problems', In *New Trends in Turbulence*, (eds) Lesieur, M., Yaglom, A. M. and David, F., Springer, Berlin, Germany, pp. 1-52.

Yakhot, A. et al. 1992, 'Development of Turbulence Models for Shear Flows by Double Expansion Technique', *Physics of Fluids*, vol. 4, no. 7**,** pp. 1510-1520.

Yakhot, V. and Orszag, S. A. 1986, 'Renormalization Group Analysis of Turbulence. I. Basic Theory', *Journal of Scientific Computing*, vol. 1, no. 1**,** pp. 3-51.

Yang, S. 2007, *'Ship Kelvin Wake'*, Available at: http://www.wikiwaves.org/index.php/Ship_Kelvin_Wake (9th March 2010)

Yu, G., Avital, E. J. and Williams, J. J. R. 2008, 'Large Eddy Simulation of Flow Past Free Surface Piercing Circular Cylinders', *Journal of Fluids Engineering*, vol. 130.

Zdravkovich, M. M. 1997, *Flow around circular cylinders: a comprehensive guide through flow phenomena, experiments, applications, mathematical models, and computer simulations*, Oxford University Press, Oxford.

Zemach, Z. Unpublished Manuscript, *Notes on the Volume of a Ruled Hexahedron Behind a Truncating Plane.*

# Appendix A: Details of the Numerical Convergence Procedure within CFD-ACE+

## *A.1. Introduction*

There are numerous methods of computing the solver residuals that result from iterative numerical methods, some of which have been described in monographs such as Roach (1998) or Chung (2002). However, as the specific method used within CFD-ACE+ is not described in either of those reference works this appendix aims to present an illustrated explanation the CFD-ACE+ algorithm. The descriptions in this appendix are, necessarily, based heavily on the CFD-ACE+ user manual (ESI CFD Inc., 2007) and an explanatory fact sheet titled "Has your simulation converged?" (Thoms, 2004) published by ESI CFD, a division of ESI Group and the developer of CFD-ACE+, and therefore these documents will generally not be referenced further. However, additional references will be provided as required.

## *A.2. How the Residuals Are Computed within CFD-ACE+*

The residuals computed in CFD-ACE+ "represent the absolute error of a particular solver variable" (Thoms, 2004), where the individual error for each cell, $\Upsilon_{cell}$, is a real valued number defined over

$$-\infty < \Upsilon_{cell} < \infty, \tag{A.1}$$

and is defined as the difference of the particular variable, $\phi$, between iterative cycles. Therefore, the total residual that is displayed by the solver is defined as

$$\Psi = \sum_{Cells} \left| \Upsilon_{cell} \right|. \tag{A.2}$$

Consequently the value of the final residual, $\Psi$, will depend on the scale of the variable being solved. An example from the ESI fact sheet is that "values for velocity are often on the order of 1-100 m/s while values for enthalpy may be on the order of $300 \times 10^3$ J/kg" (Thoms, 2004). Thoms further argues that with the residual definition presented in Equation (A.2) the absolute value of the residuals is not important for the convergence cycle rather the order of magnitude reduction. That is, using the enthalpy example from ESI a three orders of magnitude reduction of $\Psi$ would be a reduction of

enthalpy from 300 000 J/kg to 300 J/kg, which is more important than the raw value of 300 000 J/kg or 300 J/kg. Further, it is then the responsibility of the user to determine what is the appropriate order of reduction for the model under consideration.

## *A.3. User Specified Control of Residual Limits and the Iterative Cycle*

Within CFD-ACE+ there are three parameters that relate to the iterative cycle and that can be controlled by the user, namely: (1) the maximum iterative count; (2) the convergence criterion and (3) the minimum residual criterion. The first parameter is an integer that specifies the maximum number of iterations the solver can complete before skipping to the next iteration. That is if the user enters a maximum iterative count of ten then that is the most iterations per time step that the solver can compute.

The second criterion or the convergence criterion, arbitrarily designated $\Theta$, is a real number that is valid over the range

$$0 < \Theta < 1. \tag{A.3}$$

However, by convention $\Theta$ tends to be an integer in logarithmic base ten space such that

$$\Theta = 10^{\chi}, \tag{A.4}$$

where $\chi$ is an integer over the interval

$$\chi \leq -1. \tag{A.5}$$

For example, if $\chi$ were set to minus three then $\Theta$ would become 0.001. The $\chi$ notation of log space is a convenient analogy because $\Theta$=0.001 is also referred to as requiring at least three orders of magnitude of convergence.

It must be noted that the reduction of orders is computed from the highest value of the residual. That is, if the value of $\Psi$ at the second iteration is higher than in iteration one; then the magnitude at the second iteration will become the upper limit from which the order of magnitude reduction is computed.

Finally, the third criterion, arbitrarily designated $\Xi$, specifies that when the residuals are less than or equal to a user specified value then the second criterion is no longer applied. That is, if the inequality

$$\Upsilon_{\phi} \leq \Xi \tag{A.6}$$

is met for all $\phi$ then the current iterative cycle will terminate. The fundamental assumption is that the solution is converged if the residuals are sufficiently small irrespective of the orders of magnitude reduction. $\Xi$ is a real number defined over the interval

$$0 < \Xi < \infty \tag{A.7}$$

but arbitrarily large values would be counterproductive as they could stop the iterative cycle before the solution had adequately converged.

## A.4. An Example of Iterative Convergence Control

To illustrate the above discussion the plot shown in Figure A-1 is a sample of the raw residuals, $\Psi$, generated from the 2998mm outlet boundary test discussed in §8.3. For this model the maximum iterations criterion was set to ten while $\Theta = 10^{-3}$ and $\Xi = 10^{-8}$ were used. Of note is the consistently downward convergence of the *u* and *v*-velocity residuals, especially in comparison to the pressure residual that displays a peak at the second iteration. It is this peak at iteration two that will be the reference for the convergence.

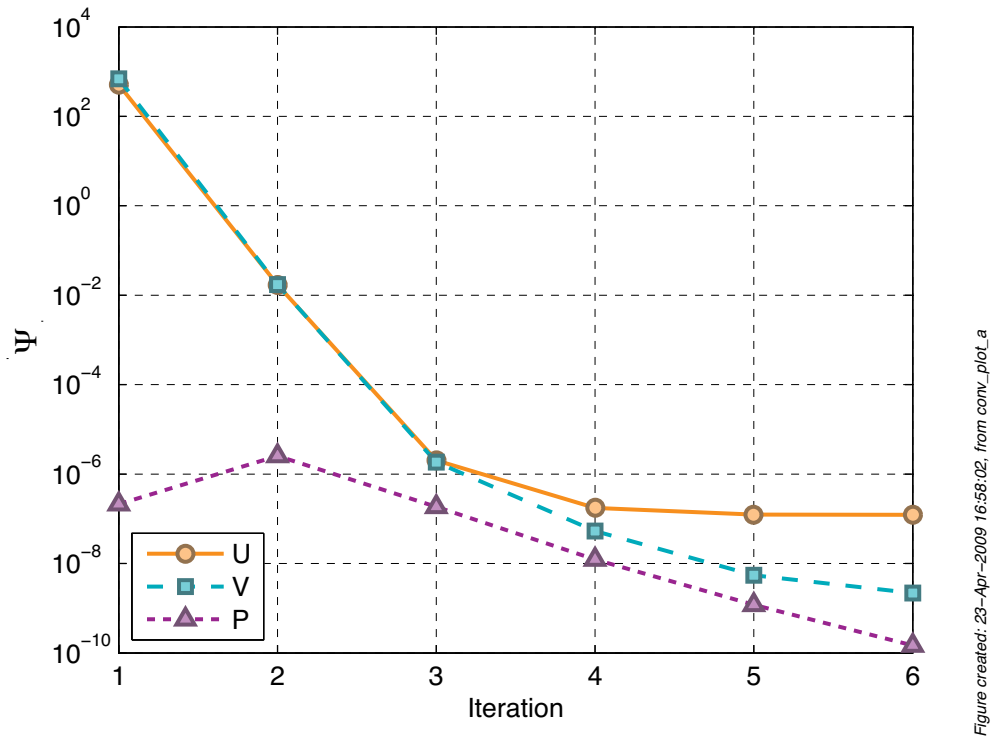


**Figure A-1 – Sample plot of numerical residuals from one time step of an unsteady computation.**

Also of note is the absolute magnitude of the plotted residuals. For this model there were 22 596 cells and the characteristic velocity was 0.54 m/s. Therefore, although the total residual for both the *u* and *v*-velocities is approximately 500 m/s that equates to an average error per cell of around $2.3\times10^{-2}$ m/s or less than 4.3% of the characteristic velocity. It could be argued that by itself an average error of 4.3% would be acceptable however by the third iteration the average error per cell has reduced to $9.0\times10^{-11}$ m/s or $1.7\times10^{-8}\%$ of the characteristic velocity. Clearly by the third iteration the velocities have converged.

When the residuals are normalized by the maximum residual, as shown in Figure A-2, the pressure residual is observed to be the driver of convergence. That is, of the three user defined criteria, neither the maximum iterative count nor the minimum residual specifications are met but rather the greater than three orders of magnitude of the pressure residual is the control. The residuals of both the *u* and *v*-velocity components converge to below the three orders requirement by the second iteration and then exceed the minimum residual limit by the third.

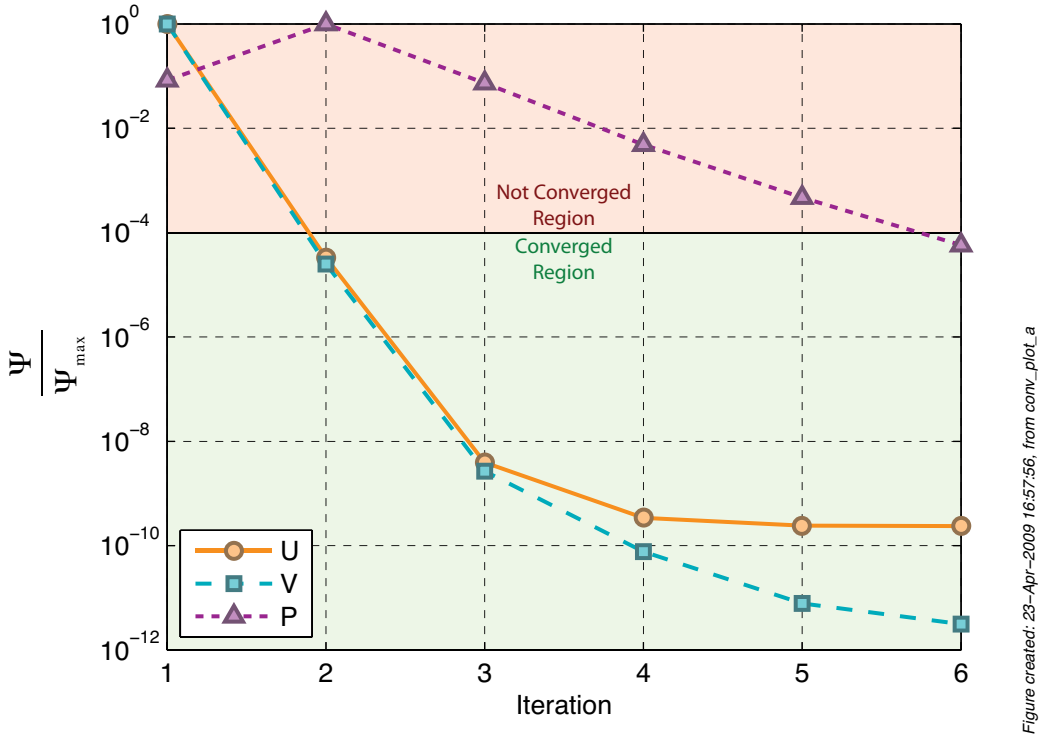


**Figure A-2 – Plot of the residuals from Figure A-1 normalised by their highest value together with the region of not converged and converged regions.**

## *A.5. Notes and Observations on Convergence*

Finally, it must be noted that the CFD-ACE+ manual states that "the solver quits the iterative procedure if any of the two criteria [listed in §A.3] is satisfied" (ESI CFD Inc., 2007). However, in the author's experience, and illustrated in the example in §A.4, the convergence criteria is the major driver of stopping before the maximum iterative limit is reached. Then, when the maximum iterative limit is reached, the solver always breaks and moves to the next cycle. These inconsistencies have been reported to the developer and are probably just one of the many typographic errors in the user manual that have been identified by the author and other UTS researchers in recent years.

# Appendix B: Hyperbolic Tangent Stretching Function

## *B.1. Derivation*

The derivations presented in this appendix follow closely from the original papers by Vinokur (1980, 1983) and an online explanatory note by "jasond" (2007). Let $\boldsymbol{\xi}$ be a discrete index vector defined for

$$\boldsymbol{\xi} = 0,2,3,\ldots n-3, n-2, n-1 \tag{A.1}$$

in which $n$ is the number of nodes to be distributed across an edge of length $l$, as shown in Figure B-1.

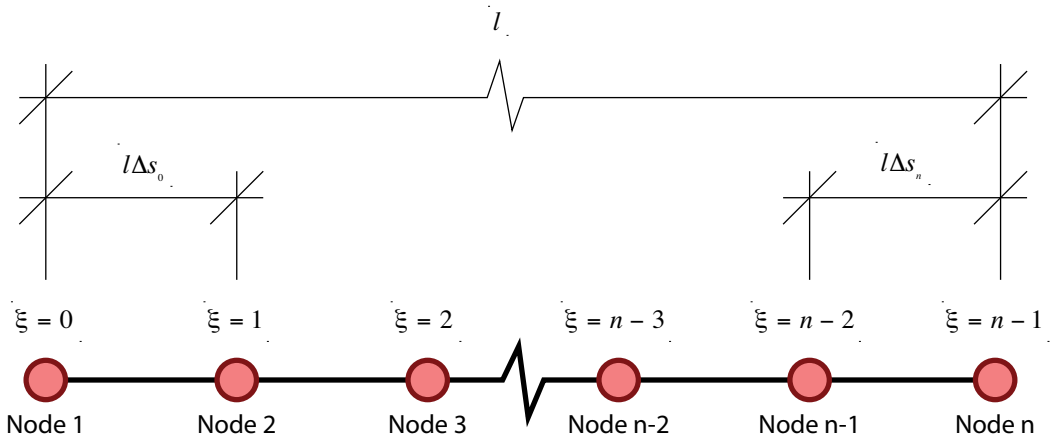


**Figure B-1 – Sketch of the coordinate notation used.**

However, for ease of computation a parametric space, $s(\boldsymbol{\xi})$, can be defined over the unit interval

$$0 \le \mathbf{s}(\boldsymbol{\xi}) \le 1 \tag{A.2}$$

such that the coordinates of the nodes along the line is

$$\mathbf{x}(\boldsymbol{\xi}) = \mathbf{s}(\boldsymbol{\xi}) l \,. \tag{A.3}$$

With these conventions, Vinokur further defined the constants

$$A = \frac{\sqrt{\Delta \mathbf{s}_{end}}}{\sqrt{\Delta \mathbf{s}_{start}}} \tag{A.4}$$

and

$$B = \frac{1}{n\sqrt{\Delta \mathbf{s}_{start}\Delta \mathbf{s}_{end}}} \tag{A.5}$$

in which $\Delta \mathbf{s}_0$ and $\Delta \mathbf{s}_n$ are the first and last node spaces, respectively. In conjunction with the number of nodes to be distributed across the edge, these end node spaces must be explicitly defined by the user. With these two additional definitions, Vinokur proposed the stretching function

$$\mathbf{s}(\xi) = \frac{\mathcal{Q}(\xi)}{A + (1 - A)\mathcal{Q}(\xi)} \tag{A.6}$$

in which

$$\mathcal{Q}(\xi) = \frac{1}{2}\left[1 + \frac{\tanh\left[\delta\left(\frac{\xi}{n-1} - \frac{1}{2}\right)\right]}{\tanh\left(\frac{\delta}{2}\right)}\right]. \tag{A.7}$$

The stretching factor, $\delta$, is found from solving the transcendental equation

$$\frac{\sinh(\delta)}{\delta} = B\,. \tag{A.8}$$

It must be noted that while the Equations (A.6) and (A.7) can be computed explicitly, an iterative solver must be employed to compute $\delta$ from Equation (A.8).

## *B.2. Sample MATLAB Code to Compute the Nodal Coordinates*

```
% Hyperbolic tangent tests
clear all
close all

% Inputs
l = 1; % length of the edge in metres
n = 51; % number of nodes but this is from n=1, for computations below
% need from n=0, hence redefine n
d1 = 0.001; % end 1 nodal spacing in metres
d2 = 0.005; % end 2 nodal spacing in metres

% Constants
xi = 0:1:n-1;
a = sqrt(d2) / sqrt(d1);
b = 1 / ((n-1) * sqrt(d1 * d2));

% Iterate for delta
% initial guess based on inverse sinh
delta = log(b + sqrt(b ^ 2 - 1));
```

```
iterCount = 1;
maxIters = 500;
endTolerance = 0.0001;
while iterCount <= maxIters && abs(sinh(delta) / delta - b) >=
endTolerance
    % Project deltaNew via Newton's method.
    delta = delta - (sinh(delta) / delta - b) /...
        (cosh(delta) / delta - sinh(delta) / delta ^ 2);

    % increase the iterative count
    iterCount = iterCount + 1;
end
display(iterCount)
clear maxIters endTolerance iterCount

qXi = 0.5 * (1 + tanh(delta * (xi / (n-1) - 0.5)) / tanh(delta / 2));
sXi = uXi ./ (a + (1 - a) * uXi);
nCoord = sXi * l;

clear sXi uXi
```

# Appendix C: Square Cylinder Two-Dimensional Tests

## C.1. Introduction

Despite a number of specifications that the computers were required to meet for submission of results at the 1995 workshop (Rodi et al., 1997), several parameters, for example the placement of the outlet boundary, were instead given as minimum distances. Similarly, the fine details of the mesh construction were left to the researchers to decide what was appropriate. Therefore, prior to developing the three-dimensional meshes discussed in §5 and §6 two parameter studies were designed to test the effect of changing two unspecified parameters, namely the (1) distance to the outlet boundary from the downstream cylinder face ($\mathfrak{L}$), shown in Figure C-1 and (2) the wall normal length of the cell adjacent to the square cylinder ($\mathfrak{F}$), shown in Figure C-2.

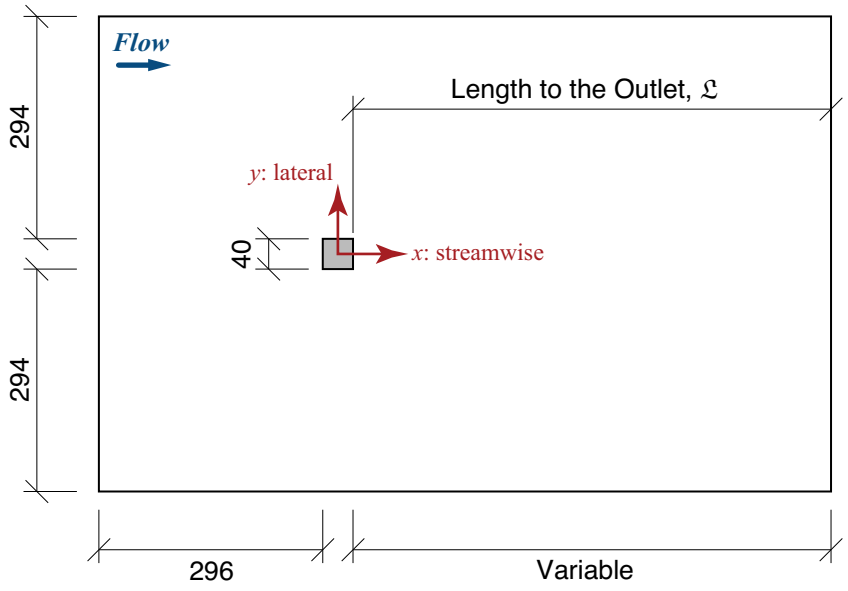


**Figure C-1 – Definition sketch of the length to the outlet boundary, $\mathfrak{L}$, parameter.**

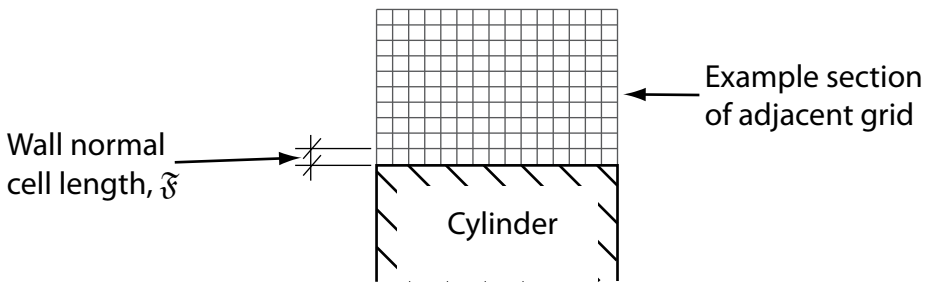


**Figure C-2 – Definition sketch of the wall normal cell length, F, parameter**

## C.2. Common Configuration for all the Parameter Studies

### C.2.1. Geometry and Mesh

To simultaneously further simplify the flow physics, that is, to isolate the effect of specific parameters, and to allow for faster run times, hence, to gather more data from and increased number of tests in a parameter study, the already reduced geometric configuration was reduced to two-dimensions, as shown in Figure C-3. With suitable modifications, such as the length of $\mathfrak{L}$ and $\mathfrak{F}$, this two-dimensional geometry was then used as the basis for the two parametric studies discussed below.

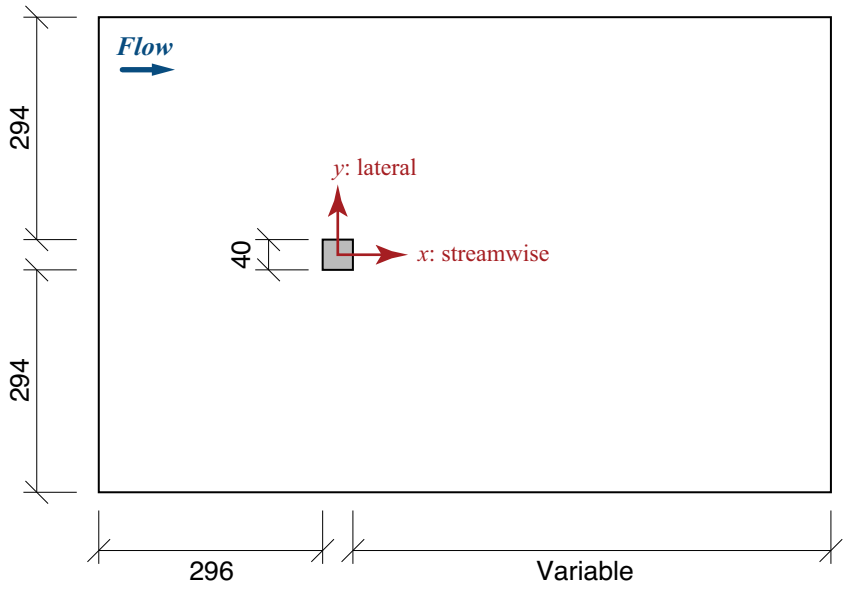


**Figure C-3 – Sketch of the common mesh configuration with the coordinate origin and axis direction names, all dimensions in millimetres.**

The geometrical domain, shown in Figure C-3, was split into four regions defined by 32 edges, shown in Figure C-4, which, subsequently, formed four blocks consisting of structured rectangular cells. The specifications of the edges that were common across all the tests described in this Appendix are listed in Table C-1, while the resultant of these parameters on the cell size distribution is shown in Figure C-5 and Figure C-6 for the $y$- and $x$-directions respectively. However, the edges hi and bc were modified, as discussed below, for the $\mathfrak{L}$ and $\mathfrak{F}$ studies, respectively. The distribution of the cell sizes for the $\mathfrak{F} = 0.3$ mm is shown in Figure C-5 and Figure C-6 for the $x$ and $y$-directions, respectively.

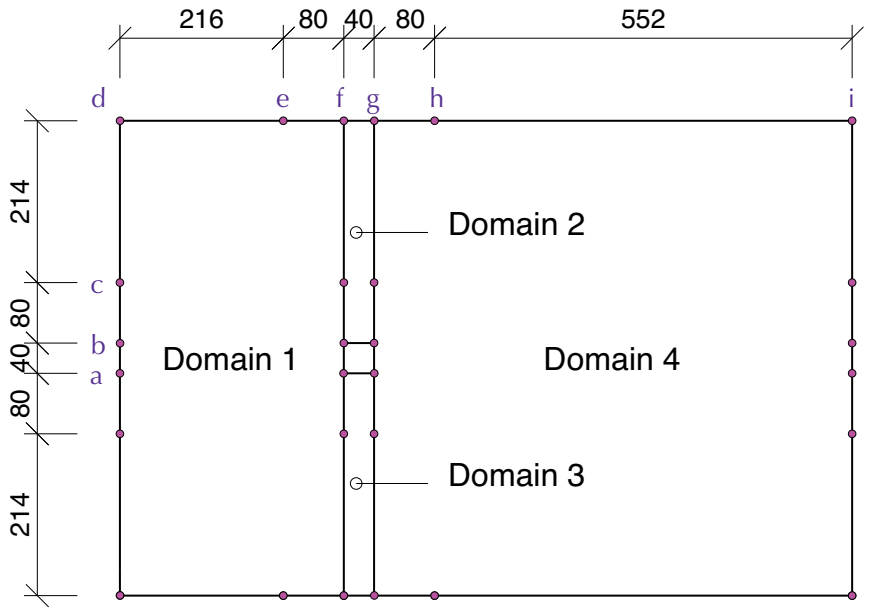


**Figure C-4 – Sketch of the template node and edge layout with dimensions in mm. The edges not identified are either mirror-symmetric around $y = 0$ or can be projected for block symmetry.**

**Table C-1 – Node count and distribution type for the edges sketched in Figure C-4.**

| Edge | End | Spacing (mm) | Nodes | Distribution |
|---|---|---|---|---|
| ab, fg | Symmetrical | 0.32 | 33 | Hyperbolic tangent |
| bc, ef | b, f | 0.32 | 29 | Hyperbolic tangent |
| | c, e | 6.29 | | |
| de | - | 6.35 | 35 | Uniform |
| | - | | | |
| cd | - | 6.29 | 35 | Uniform |
| | - | | | |
| gh | g | 0.32 | 41 | Hyperbolic tangent |
| | h | 4.00 | | |
| hi | - | 4.00 | 139 | Uniform |
| | - | | | |

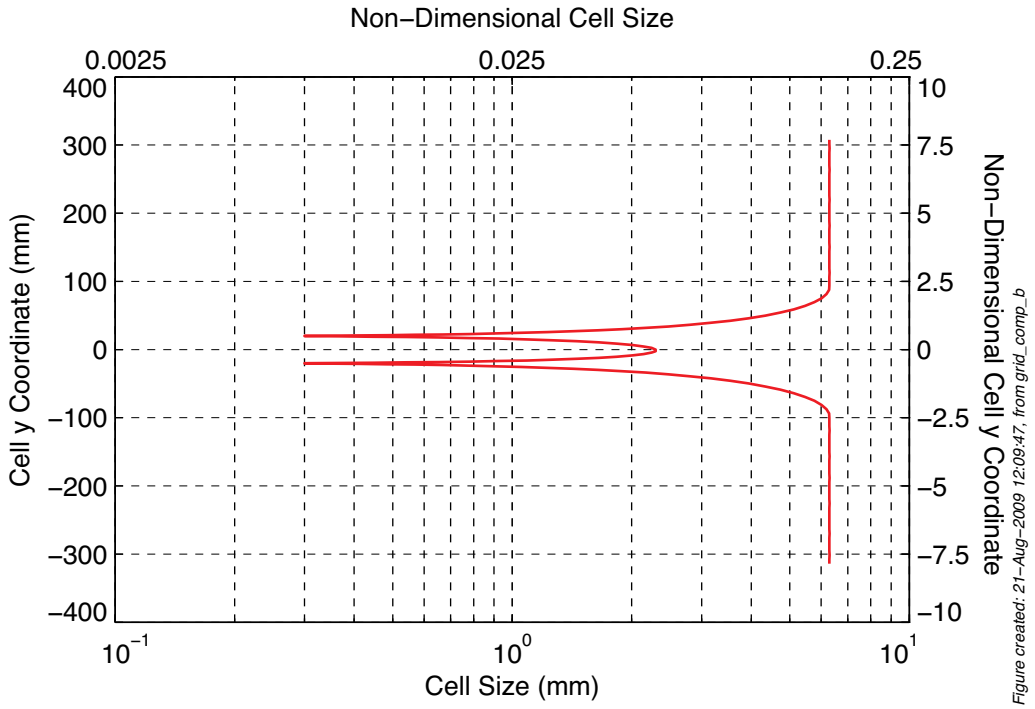


**Figure C-5 – Plot of the cell size in the *y*-direction as a function of the *y*-coordinate.**

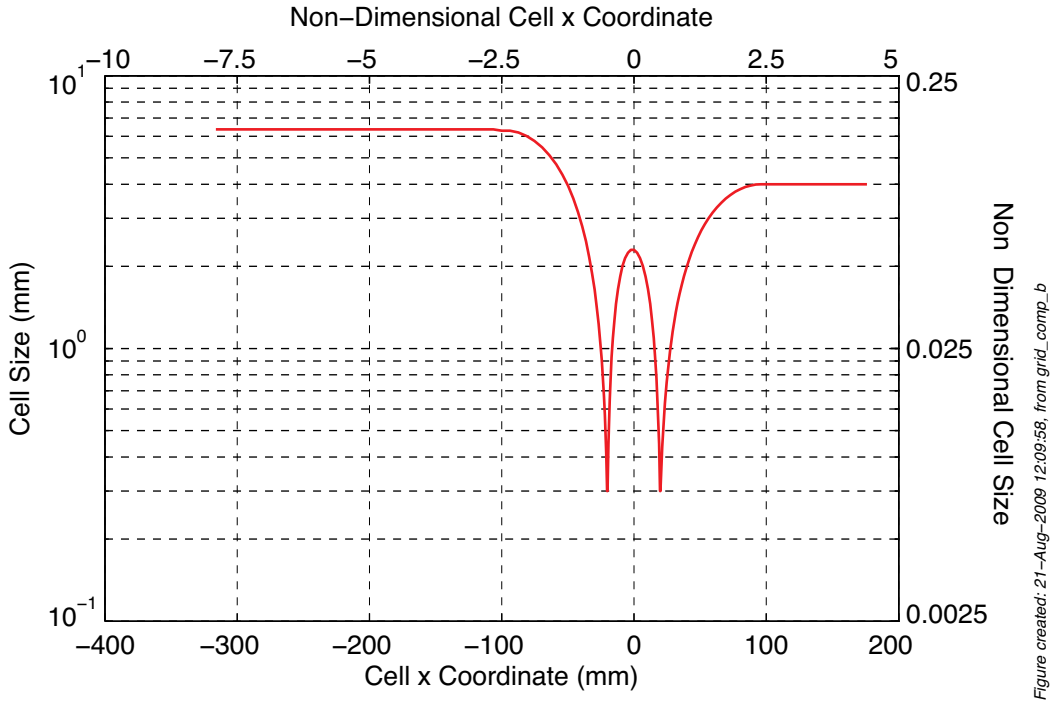


**Figure C-6 – Plot of the cell size in the *x*-direction as a function of the *x*-coordinate with the cells at *x*≥180mm not shown but kept at a uniform 4mm length.**

### C.2.2. Initial and Boundary Conditions

At the start of the computations, the fluid within the domain was assumed to be quiescent. Despite the modification of some simulation parameters – for example, the nodal count, the number of nodes per edge and the length of some of the edges – during the studies described below, the boundary conditions were unchanged and are shown in Figure C-7. The outlet boundary was set to a constant pressure outlet, the upper and lower walls were set to zero friction walls and the cylinder boundaries were set to full friction walls. No turbulent wall functions were used for any of the non-slip walls.

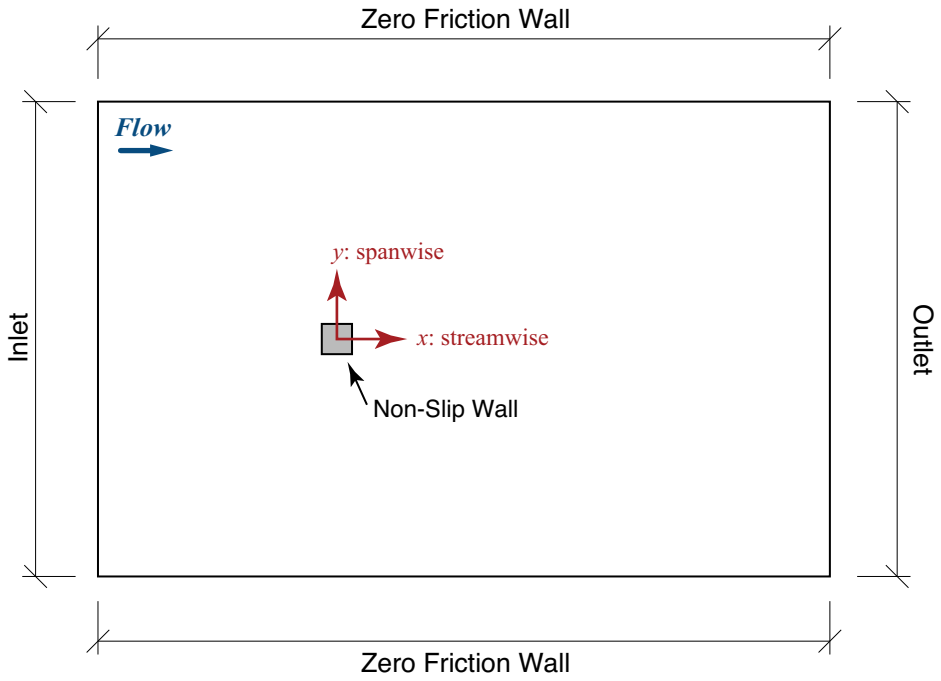


**Figure C-7 – Sketch of the boundary conditions used across all the tests.**

The inlet boundary was specified with a velocity that was uniform across the entire inlet face but to mimic the assumed two-second acceleration of a physical water tunnel it was varied as a function of time. The variation of the inlet velocity as a function of time was assumed to be a half sinusoid,

$$u_{inlet}(t) = \begin{cases} \frac{U_\infty}{2}\sin\left(\frac{\pi}{2}t - \frac{\pi}{2}\right) + \frac{U_\infty}{2} & \text{for } 0 \le t \le 2 \\ U_\infty & \text{for } t > 2 \end{cases} \qquad \text{(A.1)}$$

in which $U_\infty$ is the free stream velocity calculated from the Reynolds number,

$$\mathrm{Re}_d = \frac{U_\infty d}{\nu} \tag{A.2}$$

where $d$ is the cylinder side length and $\nu$ the kinematic viscosity, as shown in Figure C-8.

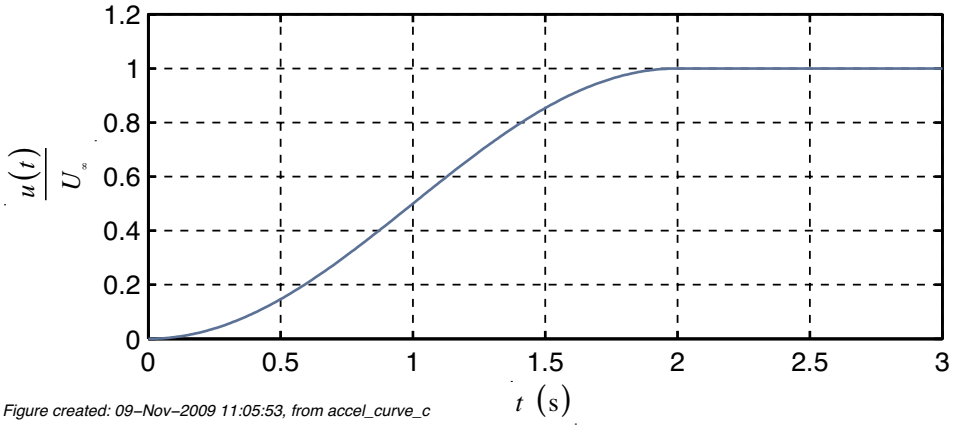


**Figure C-8 – Inlet velocity as a function of time for $t \leq 3$ s.**

## C.2.3. Solver Parameters

The solver parameters used in all the parametric studies discussed in this appendix were the same. Specifically, gravity was set to zero and the simulations were all run as unsteady with a time step, $\delta t$, of $1\times10^{-3}$ s with a simulation time of 100 s. A Crank-Nicolson time stepping scheme (Crank and Nicolson, 1947) was implemented but instead of the nominal blending factor of 0.5, 0.6 was used as per the code developers recommendation.

The computational solver used is a SIMPLEC based solver and the spatial differencing was undertaken using a 2nd order upwind with limiter scheme (Barth and Jespersen, 1989) with a blending factor of zero on the advection terms in the Navier-Stokes equations. The velocity equations were solved using a conjugate gradient solver with preconditioner (Saad, 1996) limited to 50 sweeps and a convergence criterion of $1\times10^{-4}$. Concurrently, the pressure correction equations were solved with an algebraic multigrid solver (Lonsdale, 1993) that was restricted to a maximum of 50 sweeps and convergence criterion of 0.1. The iterative cycle was set to converge at a combination of a maximum of 30 iterations, three orders of magnitude reduction in the residuals or a minimum residual of $1\times10^{-5}$. Because the explanation of these terms is required

several times throughout this thesis, the full explanation of these parameters is described in Appendix A.

## *C.3. The Effect of Varying the Length to the Outlet Boundary, $\mathfrak{L}$*

### C.3.1. Alterations to the Common Configuration for the $\mathfrak{L}$ Tests

The length to the outlet boundary, $\mathfrak{L}$, was defined as the distance parallel to the *x*-axis from the downstream face of the cylinder to the outlet boundary, as shown in Figure C-1. For these tests, the only geometric changes made were to the length of the edge hi, shown in Figure C-4. Because of the change in length of the edges, the number of nodes distributed across these edges was also amended to retain the uniform, 4mm nodal spacing. The key distances, test identifiers and node counts for the ten tests run within this parametric study are detailed in Table C-2.

**Table C-2 – List of the key geometric and mesh parameters used in the tests with the number of nodes column for the edge hi.**

| Test | Downstream Length (m) | $\mathfrak{L}/d$ | Length of Edge hi (m) | Number of Nodes | Number of Cells |
|---|---|---|---|---|---|
| 1 | 0.16 | 4 | 0.12 | 21 | 23 156 |
| 2 | 0.32 | 8 | 0.28 | 61 | 29 369 |
| 3 | 0.48 | 12 | 0.44 | 101 | 35 636 |
| 4 | 0.64 | 16 | 0.60 | 141 | 41 876 |
| 5 | 0.80 | 20 | 0.76 | 181 | 48 116 |
| 6 | 0.96 | 24 | 0.92 | 221 | 54 356 |
| 7 | 1.12 | 28 | 1.18 | 261 | 60 596 |
| 8 | 1.28 | 32 | 1.24 | 301 | 66 836 |
| 9 | 1.44 | 36 | 1.40 | 341 | 73 076 |
| 10 | 1.60 | 40 | 1.56 | 381 | 79 316 |

### C.3.2. Convergence of the Solver During the Simulations

Prior to any scrutiny of the flow results the researcher, and the reader, must be satisfied that the iterative procedure has reached the specified level of convergence at each, or at least the majority, of the time steps. For the discussion presented within this section suppose that $n_{iter}$ represents the number of iterations per time step for the solver to reach convergence. For all the time steps in all ten simulations of $\mathfrak{L}$ the solver converged within $n_{iter} \leq 15$, as shown in Figure C-9. Within Figure C-9 the data points at $n_{iter} = 0$, an otherwise nonsensical result, represent the time steps where the solver did not converge within the allocated 30 iterations.

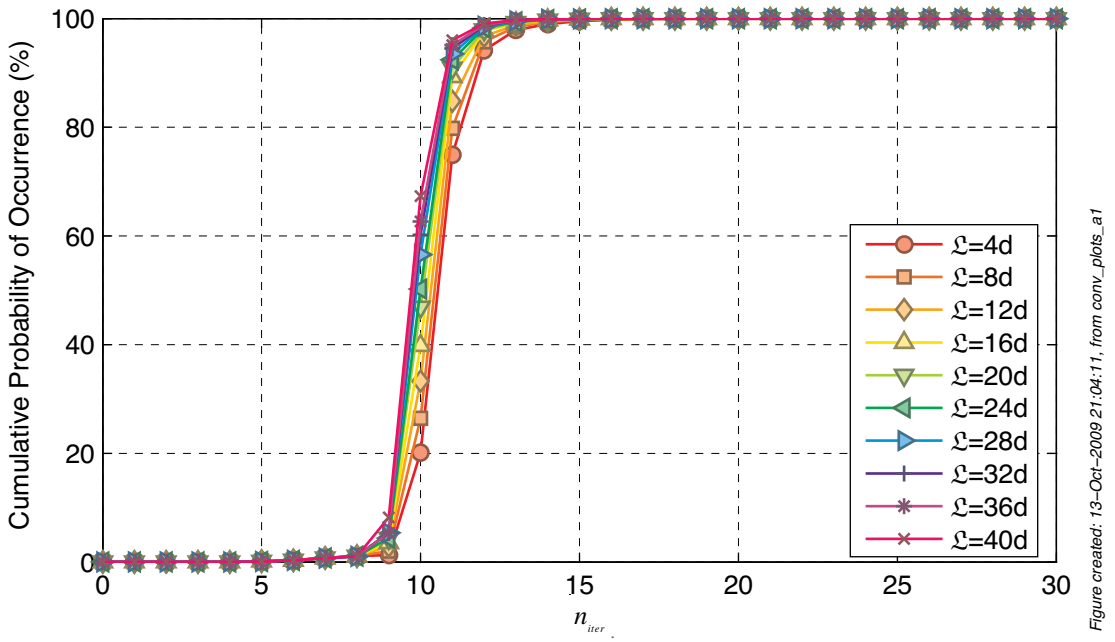


**Figure C-9 – Cumulative probability distribution of $n_{iter}$ for the ten $\mathfrak{L}$ simulations.**

Therefore, as the solver converged at each time step the results of the simulations are within the specified numerical precision. However, the resultant data must still be critically examined to ensure that, despite the numerical convergence, the computed flows are realistic.

### C.3.3. Examination of the Instantaneous Flow Field

In all the ten simulations of the parametric study into $\mathfrak{L}$, a von Kámán vortex street was formed in the downstream region behind the cylinder, shown in Figure C-10 for the $\mathfrak{L} = 20d$ test at 24s of simulation time from the start of the run. Because the vortex streets that formed in the other simulations are remarkably similar to that in Figure C-10

they will not be specifically presented in this thesis. A number of animations that detail all the simulations are included on the DVD attached to this document.

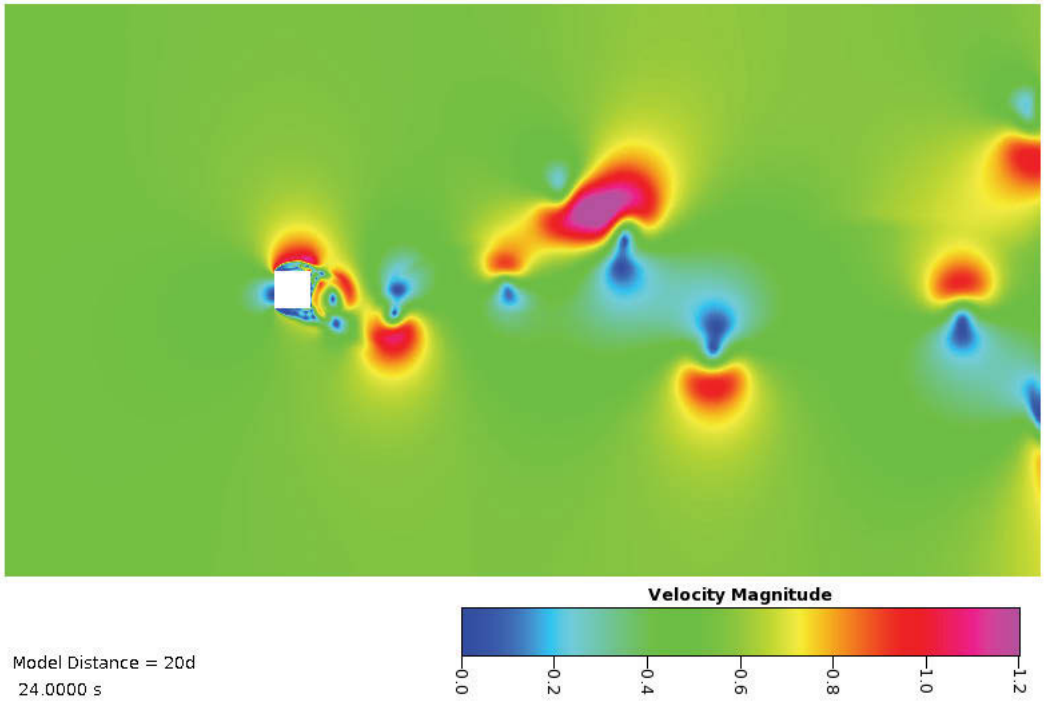


**Figure C-10 – Snapshot of the flow field from the $\mathfrak{L}$ = 20d simulation at a simulation time of *t*=24.0s visualised by velocity magnitude showing the von Kámán vortex street downstream of the square cylinder.**

Despite the formation of a von Kámán vortex street within the results of the simulations, occasionally, and for all the different $\mathfrak{L}$ values tested, an asymmetric flow pattern would emerge where the flow diverged from the centre plane, as shown in Figure C-11. The mechanism for the formation of this alternate, "ejection", flow regime is unclear but the favoured hypothesis is that they are generated because of the restriction to two dimensions. That is, the energy that would normally be transferred into the third dimension is constricted to the present two-dimensional plane. Hence, this additional energy is then available to provide the potential required for both the *u*- and *v*-velocity components to eject the fluid from the nominal wake region.

There is some evidence to support this restriction to two-dimensions hypothesis in that the present author has been unable to find any reference to similar ejections in the numerous papers published that were based on results obtained from three-dimensional simulations. However, Johansen, Wu and Shyy (2004) who were developing and investigating improved k-ε models have reported similar asymmetric flow, as shown in

Figure C-12, from their two-dimensional simulations. Johansen, Wu and Shyy (2004)

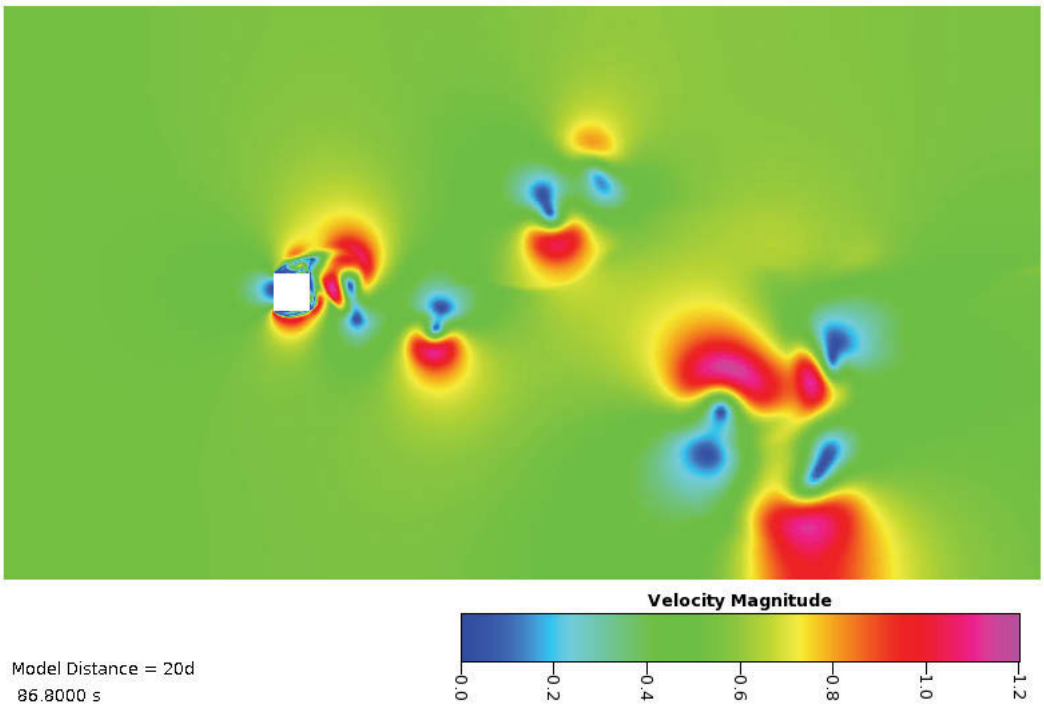


**Figure C-11 – Snapshot of the flow field from the $\mathfrak{L}$ = 20d simulation at $t$ = 86.8 s visualised by velocity magnitude showing the asymmetric flow.**

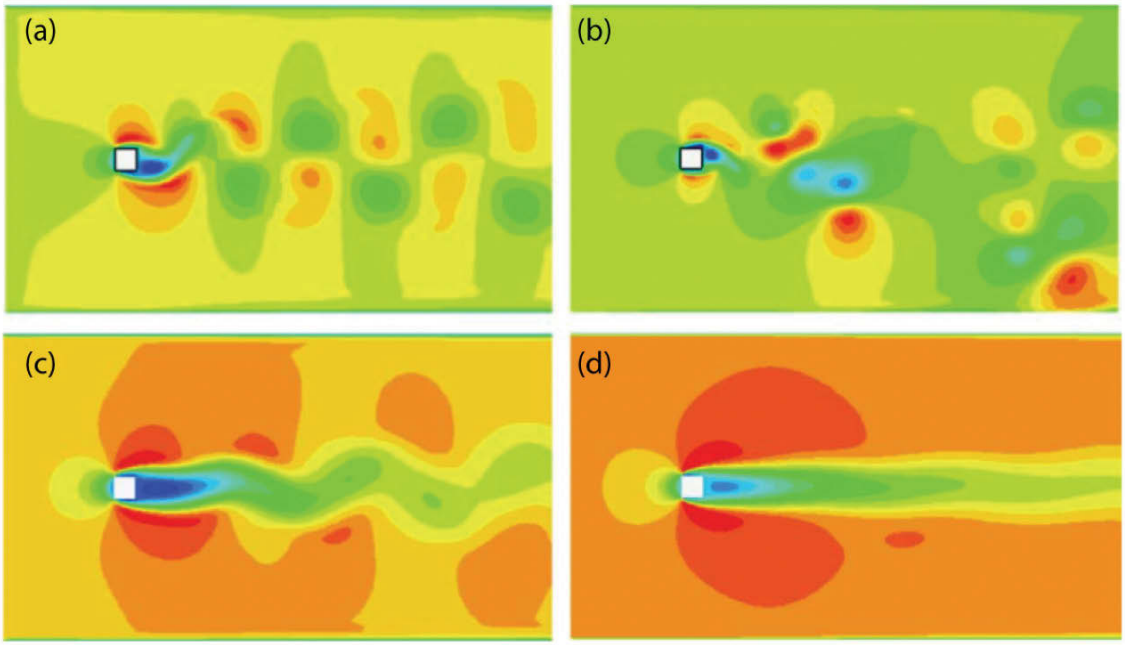


**Figure C-12 – von Kámán vortex street downstream of the square cylinder reproduced from Johansen, Wu and Shyy (2004) visualised with "axial" velocities**

**for their low (a) and high (b) resolution filter based k-ε model and their low (c) and high (d) resolution standard k-ε model.**

were developing k-ε models to overcome the known limitations of the standard k-ε model, specifically that it is overly dissipative and produces "average" results (Rodi, 1997) for example as shown in Figure C-12(c) and (d). To test their models they utilised a computational geometry based on a two-dimensional approximation of the water tunnel used by Lyn and Rodi (1994) and tested two models: a standard k-ε model and their improved model on both a low- and high-resolution meshes. The flow fields that resulted from their standard k-ε models was closer to an averaged flow, as visible in Figure C-12(c) and (d), rather than a fully developed vortex street. Therefore, the standard k-ε model is overly dissipative, such that the Reynolds number was artificially reduced to such an extent that the flow was no longer in the shedding regime. While the results from their improved k-ε model computed on a low-resolution grid do show a developed vortex street in the wake region, the vortex street appears "perfect" being both symmetrical and regular, as shown in Figure C-12(a). Finally, the results from their improved k-ε model, when run on a high-resolution grid, indicated that the flow had developed into an asymmetrical flow pattern similar to that observed in the present work, as shown in Figure C-12(d) compared with Figure C-11. Interestingly, Johansen, Wu and Shyy (2004) do not discuss the significance on these results, presumably leaving the task of interpretation to the reader.

These results support the energy dissipation hypothesis because the four results from Johansen, Wu and Shyy (2004), in decreasing order of dissipation are:

1. low-resolution, standard k-ε model, most dissipative;
2. high-resolution, standard k-ε model;
3. low-resolution, improved k-ε model;
4. high-resolution, improved k-ε model, least dissipative.

As the asymmetric flow pattern was only observed in the simulation with the least numerical dissipation, the availability of flow energy must be a driver of the flow asymmetries. Therefore, as the numerical dissipation is the least, then there is additional energy that would normally be transferred into the third dimension. However, as this additional energy cannot be transferred into the third dimension, it

must then be transported with the flow and generate the ejections shown in Figure C-11 and Figure C-12(b). Hence, these flow ejections are unphysical manifestations of the assumption of two-dimensionality of the flow. It can then be projected that for a computational model that is not overly dissipative, the inherent assumptions of flow two-dimensionality are wrong: energy must be transferred into, and possibly out of, the third dimension. It is well known that turbulence is a three-dimensional phenomenon but two-dimensional simulations can still be used to examine some aspects of turbulent flows and the numerical models used to simulate these flows.

As the assumption of two-dimensionality of the flow has been shown to be invalid, or at least questionable, the results discussed in the remainder of this Appendix will be used as guides for the trends of the model response to changes in different parameters rather than in absolute terms. That is, although it has been shown that there are limitations in the accuracy of the two-dimensional results, the trends observed from the parameter studies should still be informative for the development of the three-dimensional meshes. One of the most important parameters, in terms of number of citations at least, is the statistical properties of the lift and drag coefficients, in particular how they vary as a function of turbulence model and geometric configuration.

### C.3.4. Examination of the Lift and Drag Coefficients as a Function of Time

Both the lift and drag coefficients as a function of time appear to be largely unaffected by the size of $\mathfrak{L}$ as shown in Figure C-13 and Figure C-14 for the first 20s of the 100s of simulation time. Despite the apparent similarities of the force coefficients as a function of time, the development phase, defined as $t \leq 8$ s does appear to be affected by the location of the outlet boundary. The two simulations with the shortest $\mathfrak{L}$ of $\mathfrak{L} = 4$d and $\mathfrak{L} = 8$d, transition from the development regime into the developed earlier than the simulations with a longer $\mathfrak{L}$. Quantitatively, the onset of fully developed shedding occurs at approximately 6.5s and 7s of simulation time for the $\mathfrak{L} = 4$d and the $\mathfrak{L} = 8$d simulations, respectively, compared with the remainder of the simulations at approximately 8.5s of simulation time.

Hypothetically, the mechanism for the early shedding is the proximity of the outlet pressure boundary, specifically the reflection of waves that then propagate upstream

from the outlet boundary. Because the pressure at the outlet boundary was arbitrarily fixed at zero in contrast to the non-zero pressure field within the bulk of the domain there is a pressure discontinuity. This discontinuity may cause reflections that can be

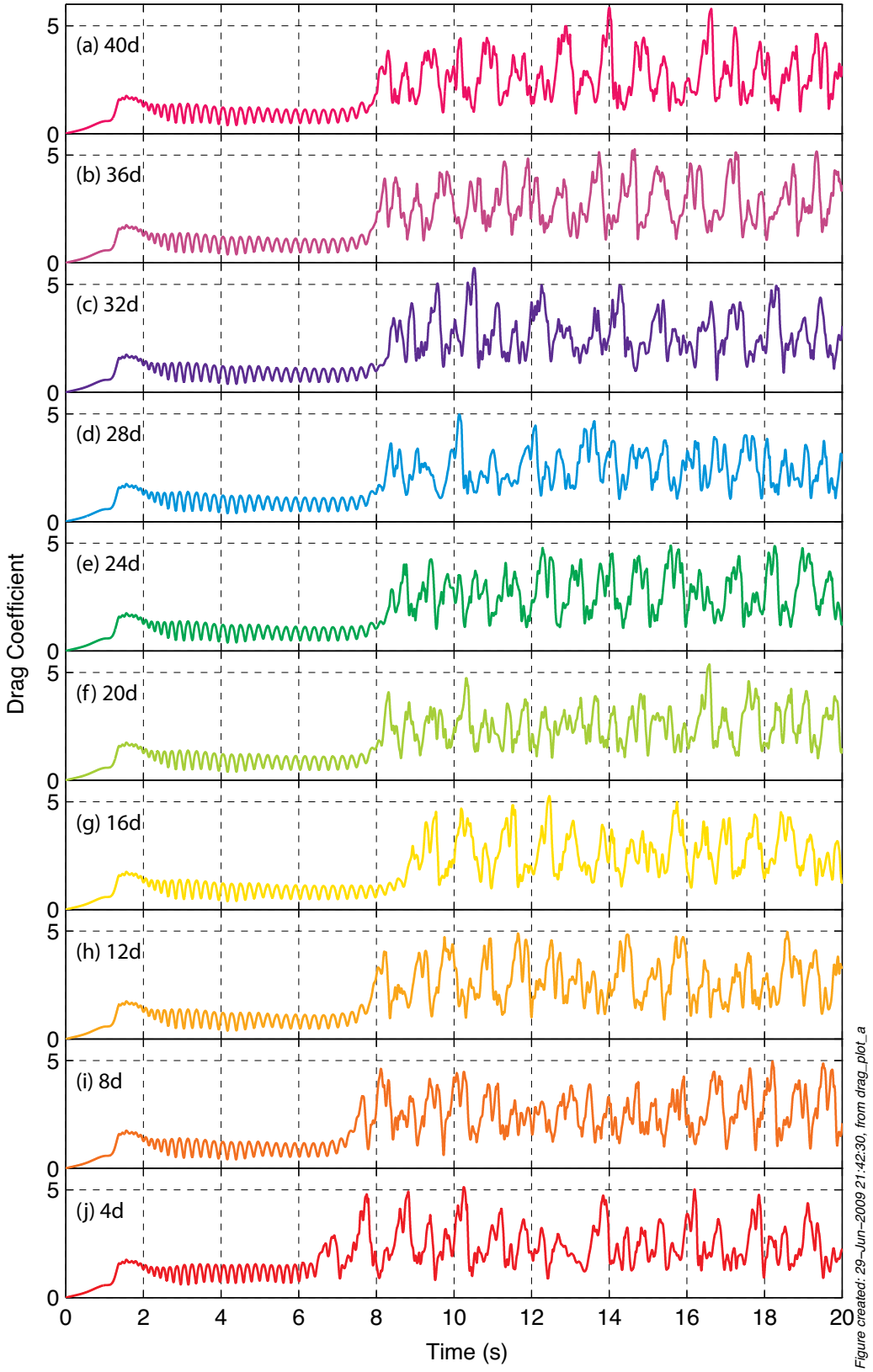


**Figure C-13 – Plot of the drag coefficients as a function of time for the ten cylinder to outlet boundary distances, $\mathfrak{L}$, investigated.**

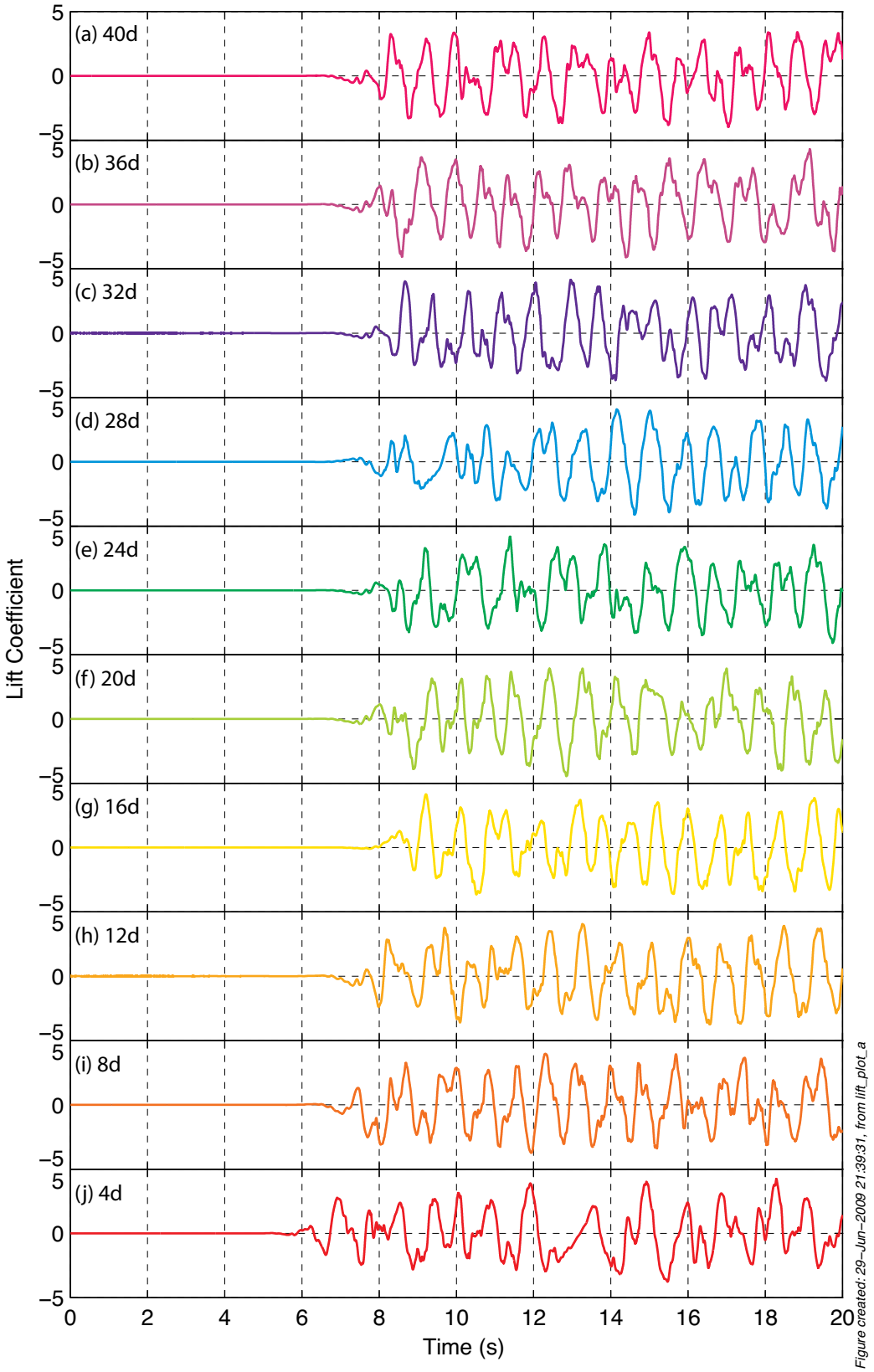


**Figure C-14 – Plot of the lift coefficients as a function of time for the ten cylinder to outlet boundary distances $\mathfrak{L}$, investigated.**

transported upstream and provide additional impetus to start the shedding. Hence, for the shorter $\mathfrak{L}$ simulations the reflections would be able to interact with the flow around the cylinder before being transported back downstream. For the longer $\mathfrak{L}$ simulations, the opposite would be true: that the reflections from the outlet boundary would not have had sufficient time to reach the cylinder before the momentum of the flow increased beyond a critical value that overwhelmed any possible reflections and transported them back downstream.

This hypothesis is supported by the progression of the time of transition from the earliest with the $\mathfrak{L}$ = 4d simulation to the latest, and from then consistent, with the $\mathfrak{L}$ = 12d simulations. That is, the simulations closest to the outlet are more likely to feel the effect of any reflections generated at the outlet boundary.

Despite the simplicity of the mechanism proposed above, the results for $C_D$ and $C_L$ obtained from the $\mathfrak{L}$=16d simulation, shown in Figure C-13(g) and Figure C-14(g) respectively, do not fit this trend, with transition occurring at approximately nine seconds or almost one second after the other long $\mathfrak{L}$ simulations. The reason for this slightly later transition is unclear but is consistent with the reflection hypothesis. That is, with the $\mathfrak{L}$=16d simulation the outlet boundary is sufficiently far away as to not cause early shedding. The discussion so far has focused on a visual inspection of the lift and drag coefficients as a function of time, yet a more rigorous examination of the distribution of these coefficients can also aid the interpretation of the simulations

As all the simulations ran for 100s of simulation time and there is a noticeable difference in lift and drag traces during the development phase, conservatively defined as for $t \leq 10$ s, the distribution functions for the lift and drag coefficients were computed over the interval

$$10 \leq t \leq 100\text{s}. \tag{A.3}$$

With the exception of the drag coefficients from the $\mathfrak{L}$=4d simulation there is no significant difference between the computed distributions from the remaining simulations, as shown in the probability and cumulative distribution plots in Figure C-15 and Figure C-16. That is, although there are small differences in the probability distribution function, shown in Figure C-15, when re-plotted as a cumulative

distribution function, shown in Figure C-16, the differences are no longer visible.

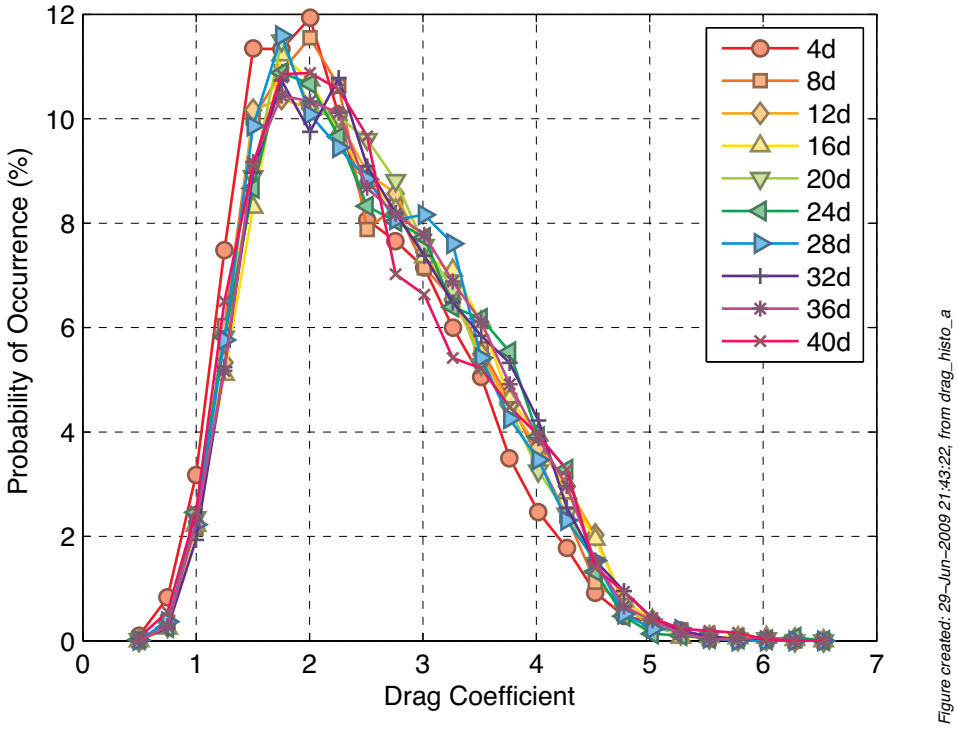


**Figure C-15 – Probability distribution function of the drag coefficients computed across the simulation time interval of $10 \leq t \leq 100$ s from the ten $\mathfrak{L}$ simulations.**

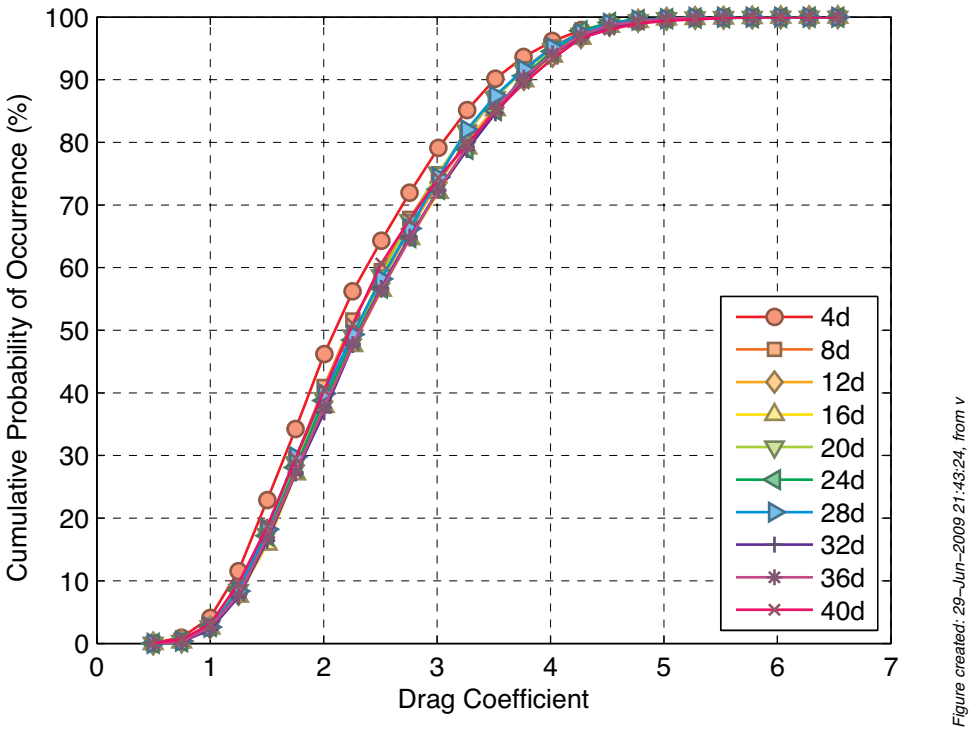


**Figure C-16 – Cumulative distribution function of the drag coefficients computed across the simulation time interval of $10 \le t \le 100$ s from the ten $\mathfrak{L}$ simulations.**

Interestingly, this result includes the $\mathfrak{L}$=16d simulation, which as noted above took longer to develop than the $\mathfrak{L}$>16d simulations, hence the delay in development has had no influence on the developed flow, at least as far as $C_D$ is concerned. This confirms the proposal that the late development of flow in the $\mathfrak{L}$=16d simulation was an artifact rather than a real flow feature: a result of the non-linearity of Navier-Stokes equations.

The distribution of the drag coefficient from the $\mathfrak{L} = 4$d simulation deviates by approximately ten percent at the 50% probability compared with the longer $\mathfrak{L}$ simulations, as shown in Figure C-16. This steeper increase in the drag coefficient is balanced at larger drag coefficients by a correspondingly steeper tail than the alternate simulations, as shown in Figure C-15.

In contrast to the differences observed in the distribution functions of the drag coefficients, there is a smaller difference in the histograms of the lift coefficients, shown in Figure C-17 and Figure C-18. This difference was observed for the $\mathfrak{L} = 4$d simulation and only at minimum and maximum lift values and is most visible in the cumulative distribution function, shown in Figure C-18. The immediate conclusion is that for the $\mathfrak{L} = 4$d simulation values of $C_L$ at the extremity of the distribution are less

likely, therefore the flow is more "moderate" and characterised by mid-range values of $C_L$. However, while the probability distribution function, shown in Figure C-17, is noisy in the plateau region centred on zero the percentage frequencies for the $\mathfrak{L}$=4d simulation appear to be generally higher than the alternate simulations. As a similar effect was not observed at longer $\mathfrak{L}$ then this must be due to the proximity of the outlet boundary, which in order to force the simulation to lower absolute values of lift must be damping the flow.

As the both the flow field and the distributions of the force coefficients have been discussed and support the conclusion that a shorter $\mathfrak{L}$ adversely affects the flow field, the final parameters to discuss are the first two statistical moments, namely the mean and standard deviation. These two parameters are the commonly quoted statistical moments in the literature, for example Voke (1996), Rodi et al (1997), Sohankar, Davidson and Norberg (1999) and Srinivas et al (2006), but as it has already been shown that the current two-dimensional flows are unphysical, these quantities will be used more for comparison between the present simulations rather than for direct comparison with experimental data and alternate numerical simulations.

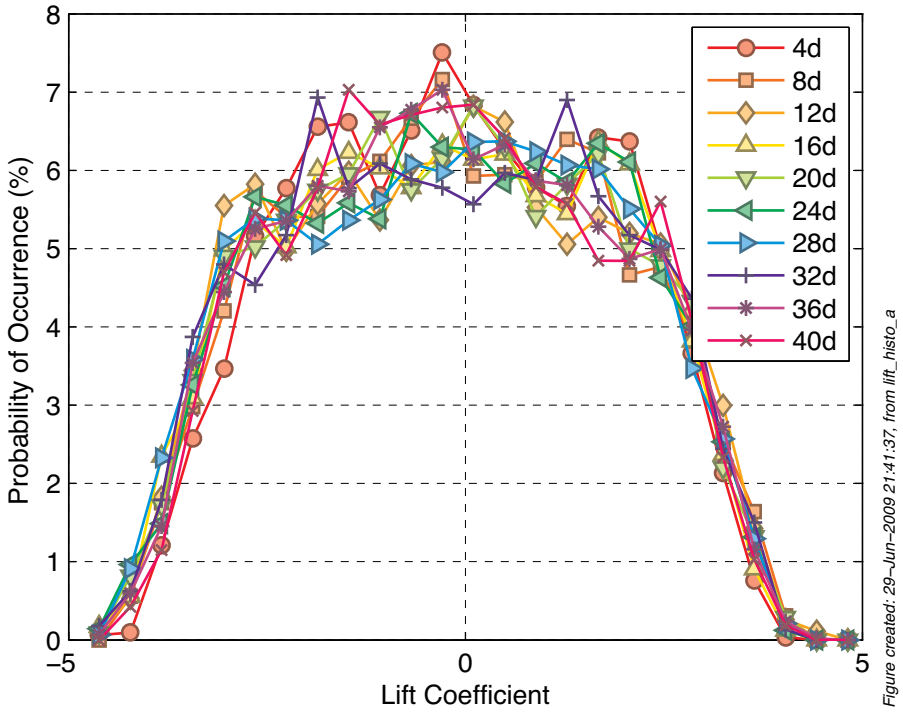


**Figure C-17 – Probability distribution function of the lift coefficients computed across the simulation time interval of $10 \leq t \leq 100$ s from the ten $\mathfrak{L}$ simulations.**

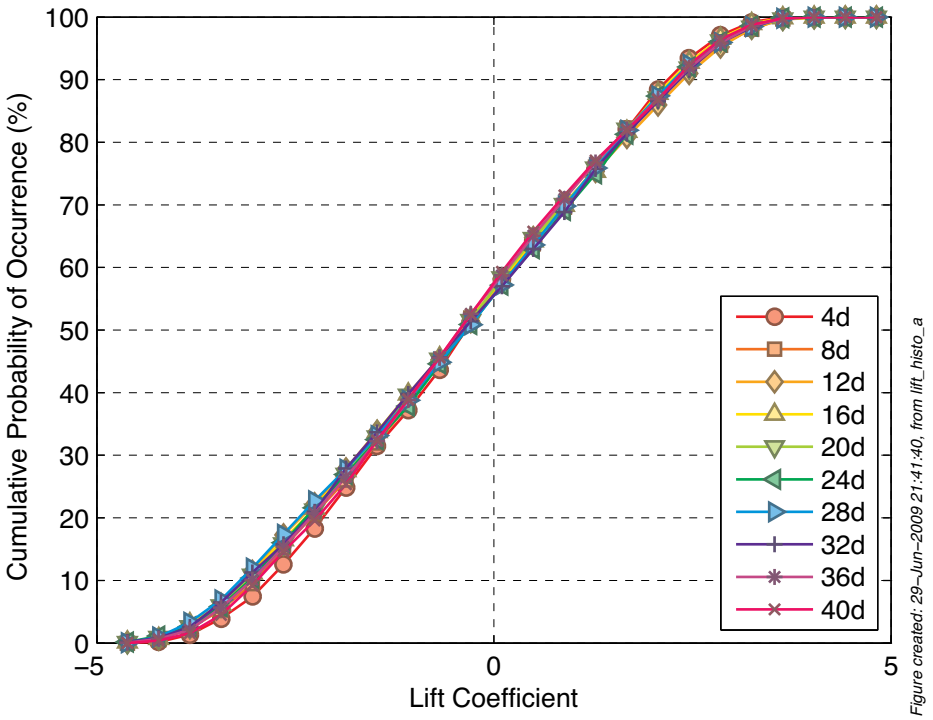


**Figure C-18 – Cumulative distribution function of the lift coefficients computed across the simulation time interval of $10 \le t \le 100$ s from the ten $\mathfrak{L}$ simulations.**

## C.3.5. Statistical Characteristics of the Force Coefficients

As with the distributions computed in §C.3.4 the statistical moments were computed over the interval as used to compute the probability distributions discussed above. The mean drag coefficient for the $\mathfrak{L}\geq$8d simulations is 2.67±0.03, as shown in Figure C-19, whereas the mean drag for the $\mathfrak{L}$=4d simulation was 2.49 or 6.5% lower than the average of the other nine simulations. This lower resultant in the mean drag for $\mathfrak{L}$=4d simulation was conjectured from the noticeably different distribution functions of the drag coefficients, shown in Figure C-15 and Figure C-16, and discussed above.

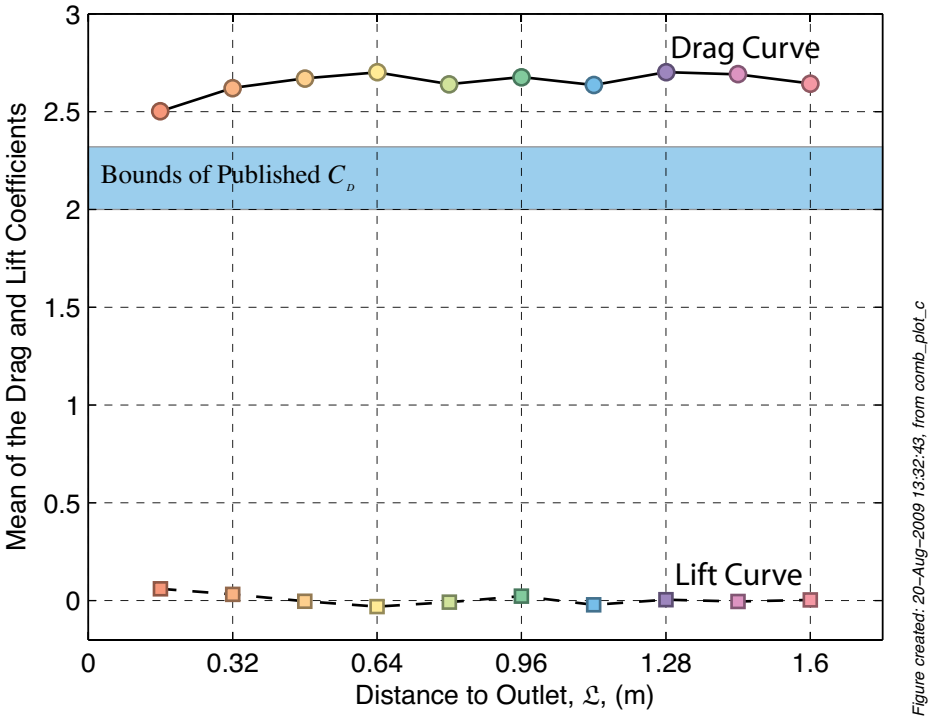


**Figure C-19 – Plot of the mean drag and lift coefficients from the ten outlet distance, ℒ, simulations together with a region representing mean drag results compiled by Sohankar, Davidson and Norberg (1999).**

All the mean lift coefficients from the present work fall within the bounds of ±0.03, which is acceptably close to zero. That is, as the lift fluctuates over the range of ±4.8 and the theoretical mean lift is zero, so the error is less than 0.7% relative to the bounds of the fluctuations. This is an important validation parameter because for this configuration the time averaged lift must be zero.

The average of the standard deviations of $C_D$ was 0.9 with a spread of ±.05 over the ten simulations. In contrast to the consistency of the drag, the standard deviations of the lift coefficients have distinct outliers specifically the $\mathcal{L} = 4d$ and $\mathcal{L} = 40d$ simulations. These outliers differ from the average by -8% and -5%, respectively, with the remaining simulations within ±2% of the average.

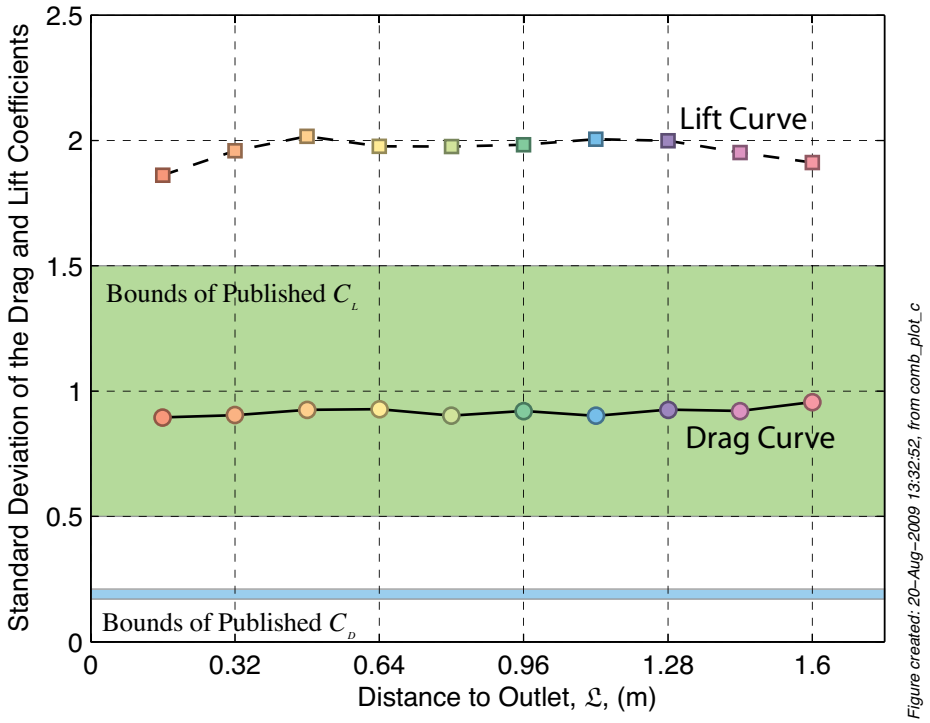


**Figure C-20 – Plot of the standard deviation of the drag and lift coefficients from the ten outlet distance, ℒ, simulations together with two regions representing published results compiled by Sohankar, Davidson and Norberg (1999).**

The combined results from the first two statistical moments support two conclusions: firstly that the two-dimensional simulations presented in the current work are generally consistent, and secondly that for the first two moments there is an observed effect from the location of the outlet boundary. The first conclusion does not warrant much discussion but the second is important for the three-dimensional simulations.

The affect of the proximity of the outlet boundary condition is subtle and is most easily visible in the results from the first two moments: the mean and the standard deviation. This claim is based on two results: the lower mean drag and the lower RMS lift coefficients for the ℒ=4d simulation when compared to the alternate simulations. Conversely, there is no observable trend as a function of ℒ, for either the mean lift or the RMS drag. However, the changes in mean drag and RMS lift coefficients are small, and must be taken in conjunction with the results presented above – by themselves they are not conclusive evidence of an affect from the proximity of the outlet boundary to the square cylinder.

With the discussion of the investigation into the length to the outlet boundary now complete the focus can turn to the remaining preliminary investigation: the study of the size of the cell immediately adjacent to the cylinder.

## *C.4. Investigation of the Effect of Varying the Wall Normal Length of the First Cell Adjacent to the Cylinder, $\mathfrak{F}$*

### C.4.1. Alterations to the Common Configuration for the $\mathfrak{F}$ Tests

For these tests the parameter $\mathfrak{F}$, was defined as the length of the side of the first adjacent cell to the cylinder normal to the cylinder, as shown in Figure C-2 (pp 329). Therefore, the only changes made to the generic grid described in §C.2 were to the edges that emanated from the square cylinder and those required for block regularity away from the cylinder.

The values of $\mathfrak{F}$ tested in this parametric study range from $\mathfrak{F}$ = 50 μm to $\mathfrak{F}$ = 5 mm in non-uniform steps, as listed in Table C-3. A hyperbolic tangent function as outlined in Equations (5.4) to (5.9) was used to distribute the nodes along the edges bc, fe and gh, shown in Figure C-4, with the node spacing furthest from the cylinder fixed as per the specifications of §C.2 and detailed in Table C-1. For six of the eight simulations, the same hyperbolic tangent function was used to distribute the nodes along the faces of the cylinder, i.e. edges ab and fg in Figure C-4. However, as the number of nodes distributed across the face of the cylinder when $\mathfrak{F}$ = 3 mm and $\mathfrak{F}$ = 5 mm was too low to achieve a satisfactorily small expansion ratio between nodes, instead of the hyperbolic tangent, a uniform distribution was used.

The structure of the discussion of the results of the parametric study into $\mathfrak{F}$ will be similar to that of the $\mathfrak{L}$ simulations presented in §C.3. That is, in order there will be a brief outline of the convergence of the solver, a discussion of the instantaneous flow field from velocity magnitude visualizations and finally an examination of the behaviour of the force coefficients.

**Table C-3 – $\mathfrak{F}$, number of nodes across the cylinder face (edges ab and fg), total cell count and the distribution function used across the cell faces.**

| Test | $\mathfrak{F}$ | Node Count for edge ab and fg | Total Cell Count | Distribution |
|---|---|---|---|---|
| 1 | 50 µm | 55 | 66 174 | Hyperbolic Tangent |
| 2 | 100 µm | 45 | 51 464 | Hyperbolic Tangent |
| 3 | 300 µm | 33 | 14 408 | Hyperbolic Tangent |
| 4 | 500 µm | 28 | 38 160 | Hyperbolic Tangent |
| 5 | 1 mm | 25 | 34 704 | Hyperbolic Tangent |
| 6 | 3 mm | 14 | 26 725 | Uniform |
| 7 | 5 mm | 9 | 21 880 | Uniform |

**Table C-4 – List of the number of nodes used in the expansion edges.**

| Test | Edges: bc and ef | Edges: gh |
|---|---|---|
| 1 | 45 | 60 |
| 2 | 34 | 52 |
| 3 | 29 | 41 |
| 4 | 28 | 36 |
| 5 | 25 | 33 |
| 6 | 20 | 23 |
| 7 | 15 | 18 |

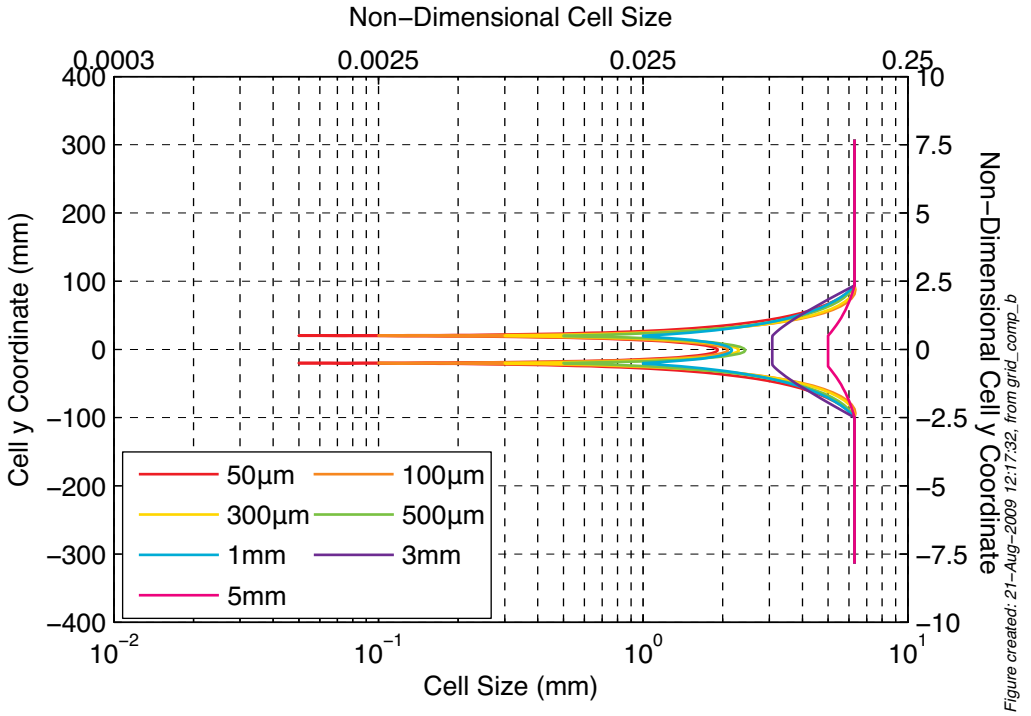


**Figure C-21 – Plot of the nodal spacing as a function of the *y*-coordinate for the seven $\mathfrak{F}$ simulations.**

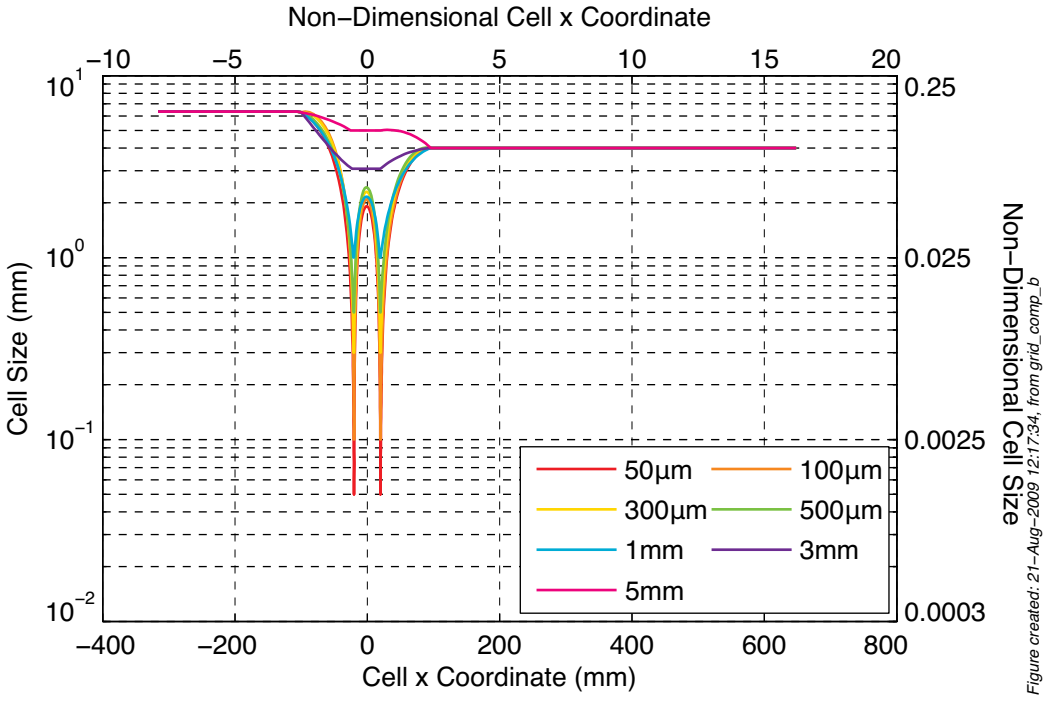


**Figure C-22 – Plot of the nodal spacing as a function of the *x*-coordinate for the seven $\mathfrak{F}$ simulations.**

## C.4.2. Convergence of the Solver during the Simulations

As with the $\mathfrak{L}$ test presented above in §C.3.2 the convergence of the numerical engine must be examined prior to a critical examination of the resultant flow data. For every time step in all seven simulations of $\mathfrak{F}$, the solver converged to the specifications within the maximum 30 iterations, as shown in Figure C-23.

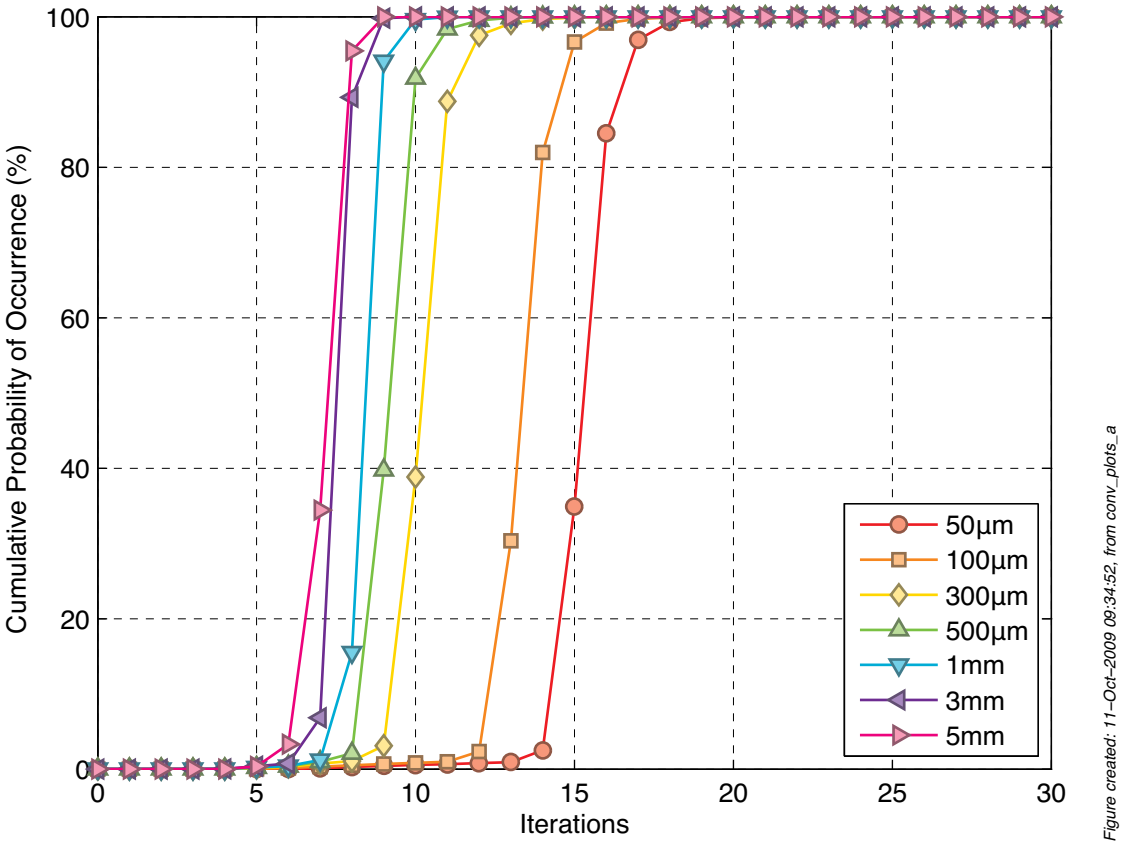


**Figure C-23 – Cumulative probability distribution of $n_{iter}$ for the seven $\mathfrak{F}$ simulations.**

Intriguingly, as $\mathfrak{F}$ was decreased, that is as the wall normal size cell length was shortened and, presumably, the level of computed detail increased, the values of $n_{iter}$ concurrently increased. However, as all seven simulations converged to the specified numerical precision, the increased iterative count is of general interest that would predict a consequent increase in computational wall time. Therefore, the physicality of the flow can be critically examined.

### C.4.3. Examination of the Instantaneous Flow Field

As the flows observed in the simulations with different $\mathfrak{F}$ were remarkably similar to those already discussed in §C.3.3, only the differences and highlights will be presented in this section. As reported above for the $\mathfrak{L}$ tests, the flow fields of the $\mathfrak{F}$ simulations were characterised by the presence of a von Kámán vortex street in the wake, as shown in Figure C-24 compared with Figure C-10, with broadly similar vortical structures visible in the wake. In a further similarity to the variable $\mathfrak{L}$ tests described above, the size and shape of the vortex street varied slightly between the tests as $\mathfrak{F}$ was modified. However, for the smaller $\mathfrak{F}$, the variations in the vortex street were sufficiently small that they have not been shown for comparison.

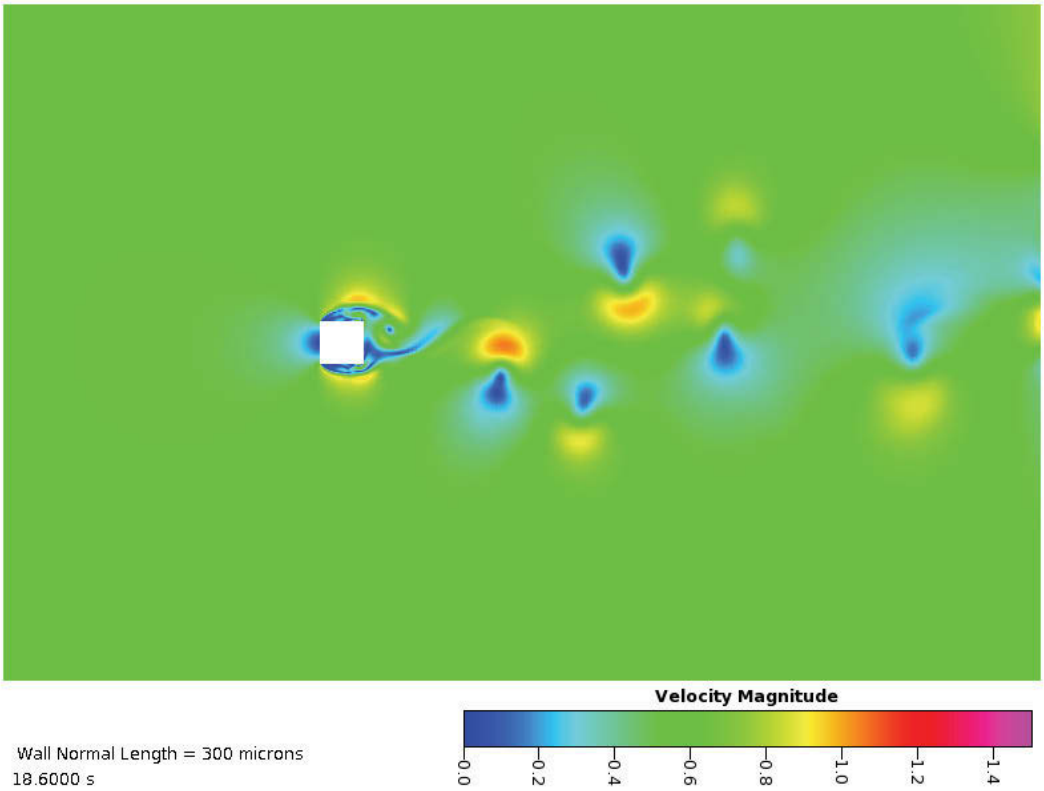


**Figure C-24 – Velocity magnitude snapshot from $\mathfrak{F}$=300µm simulation showing a nominal von Kámán vortex street being shed from the square cylinder.**

In common with the results from the $\mathfrak{L}$ simulations, the present simulations with a variable $\mathfrak{F}$ also developed flow asymmetries, as shown in Figure C-25 and Figure C-26. For the shorter $\mathfrak{F}$ lengths tested, the maximum speed of the ejected blobs and size of the asymmetrical blobs observed were broadly similar to those observed in the $\mathfrak{L}$ tests, as shown in Figure C-25 compared with Figure C-11 but please note the change in the

colour scale between the images. However, in contrast to the similarities at shorter $\mathfrak{F}$, the asymmetries observed in the in the results from the simulations with longer $\mathfrak{F}$ were up to 25% faster that the corresponding results from the $\mathfrak{L}$ tests. That is, for longer $\mathfrak{F}$

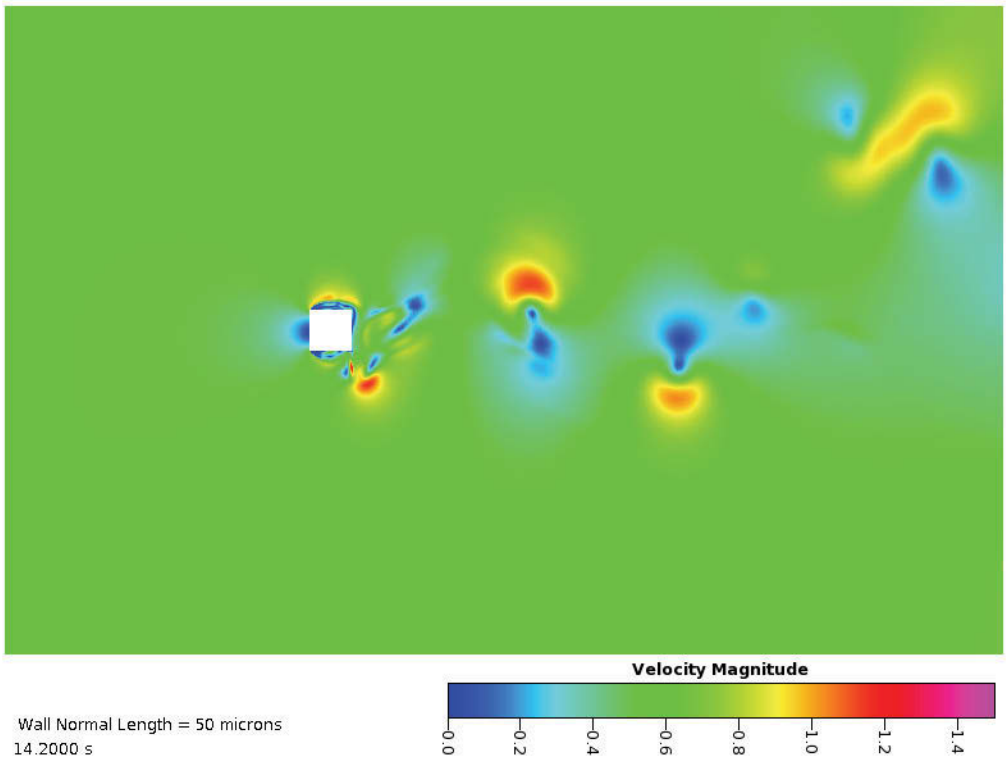


**Figure C-25 – Snapshot from the $\mathfrak{F}$=50µm simulation visualised by the velocity magnitude and showing a high-speed asymmetry in the flow being ejected.**

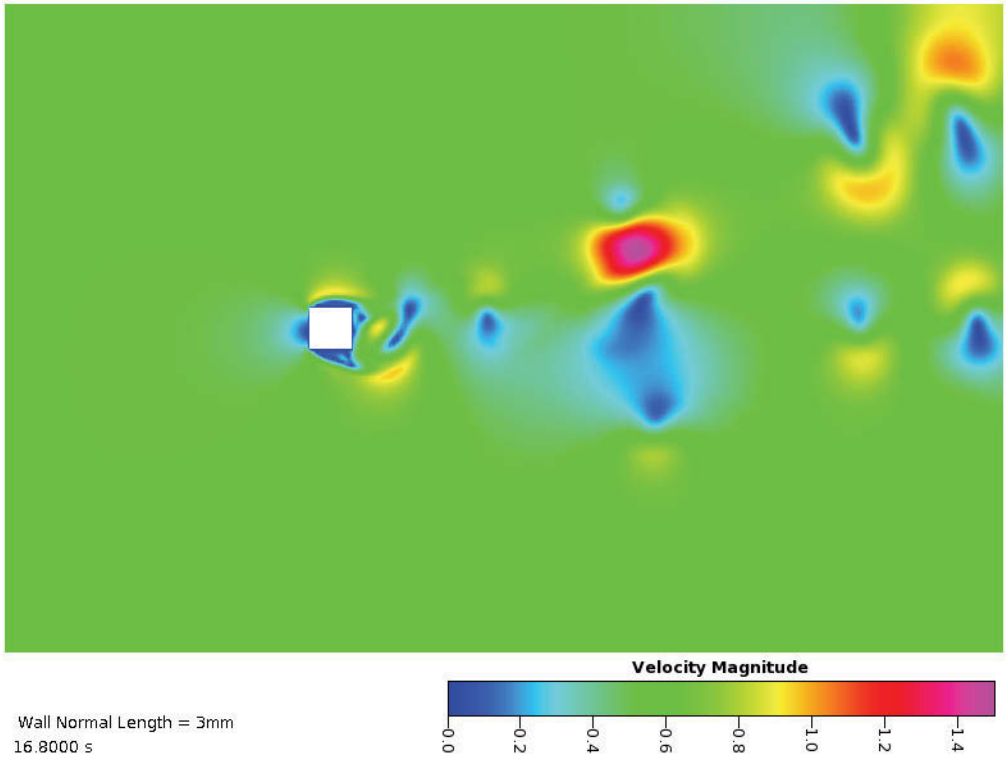


**Figure C-26 – Snapshot from the $\mathfrak{F}$=3mm simulation visualised by the velocity magnitude and showing a very high-speed asymmetry in the flow being ejected.**

the maximum observed speed of the asymmetrical blobs was in the order of 1.5m/s compared with the 1.2m/s observed in the $\mathfrak{L}$ tests and for shorter $\mathfrak{F}$. Given that the inlet velocity was set at 0.535m/s, a jump of 0.3m/s is a large fraction of the undisturbed free stream velocity.

The mechanism for the observed increase in the speed of the ejected blobs is due to the lack of resolution of the boundary layer around the cylinder. Because the cells are so large in the region of the cylinder, neither the recirculation zones nor the associated dissipative processes can be captured by the computational solver, as shown in Figure C-27. Hence, as little or no dissipation is captured in the region of the cylinder, the excess energy is still entrained with the free stream and is transformed into the faster asymmetric flow blobs.

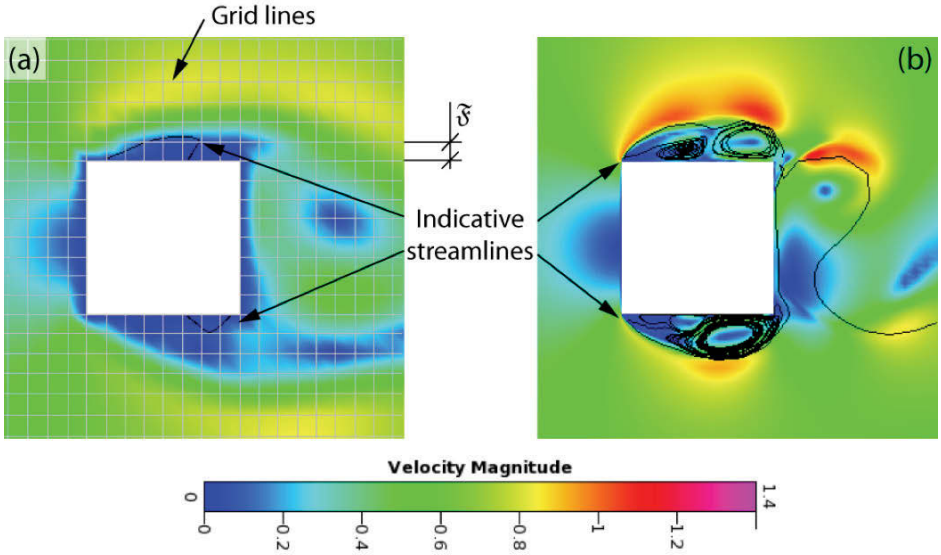


**Figure C-27 – Comparison of the resolved flow features in the F=5mm (a) and the ℱ=50μm (b) simulations with the flow visualised by the velocity magnitude and instantaneous streamlines to indicate the recirculation zones.**

Having noted that the flow field is dramatically affected by the grid resolution adjacent to the cylinder and that similar asymmetric patterns as were observed in the ℒ tests also occurred in the ℱ test simulations, similar conclusions to §C.3.3 can be drawn. That is, that the use of a two-dimensional simulation to simulate a three-dimensional flow field only has a very limited use and significant care must be take to ensure the applicability of the results. Hence, while the flow field images qualitatively show a difference in the flow field, examination of the force coefficients on the cylinder can provide quantification of the flow field changes, which can, despite the caveat discussed above, be used to guide the development of the three-dimensional meshes.

### C.4.4. Examination of the Lift and Drag Coefficients as a Function of Time

Despite minor differences, there is no clear change in the patterns of $C_D(t)$ and $C_L(t)$ for the simulations with ℱ shorter than 1 mm, as shown in Figure C-28 and Figure C-29, respectively. For this discussion the pattern of $C_D(t)$ and $C_L(t)$ will be taken a s a general descriptor of the shape of the curve, i.e. the amplitude, development region and peak-to-peak times and intermittency. However, for the simulations with ℱ = 5 mm and

$\mathfrak{F}$ = 3 mm there are a number of marked differences compared to the results from the shorter $\mathfrak{F}$ simulations.

There is one difference between the results from the simulations with $\mathfrak{F}$ = 5 mm and $\mathfrak{F}$ = 3 mm and the shorter F simulations which is that the amplitude of the shedding is significantly damped, which is manifested in two observations. Over the development phase of the simulations, roughly for the simulation times $t \leq 9$ s, where the small scale shedding has been damped to such an extent that the $C_D(t)$ plots over this time are effectively smooth. After the flow has developed, the $C_D(t)$ and $C_L(t)$ functions are simultaneously smoother and more periodic than the corresponding results from the shorter $\mathfrak{F}$ simulations. The present author expected a higher degree of "irregularity" as a visual manifestation of the chaotic nature of real flows at this, and higher, Reynolds numbers.

With this qualitative discussion of the force coefficients as a function of time a more rigorous, quantitative investigation based on the distribution of the coefficients can be undertaken. For this study the distribution statistics were computed over the interval

$$10 \leq t \leq 100\text{s}. \tag{A.4}$$

The strong modulation of the force coefficient signal amplitude is also visible as a strong peak in the probability distribution functions of both the drag, Figure C-30, and the lift, Figure C-31. A similarly high peak in the probability distribution of the lift coefficient signal from the $\mathfrak{F}$ = 5 mm simulation was also observed but centred at zero.

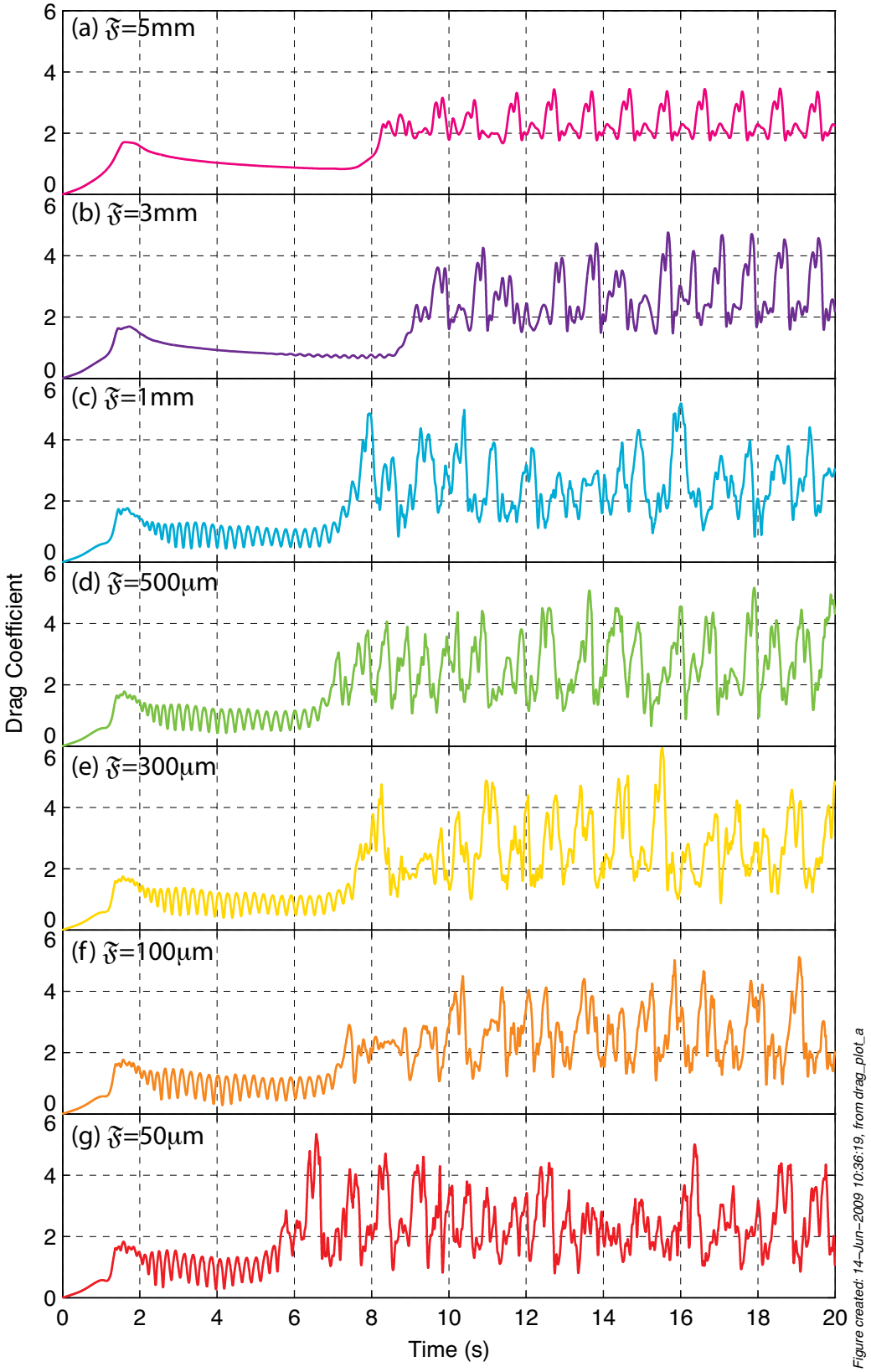


**Figure C-28 – Plot of the drag coefficient as a function of time for the seven wall normal cell distances, 𝔉, tested.**

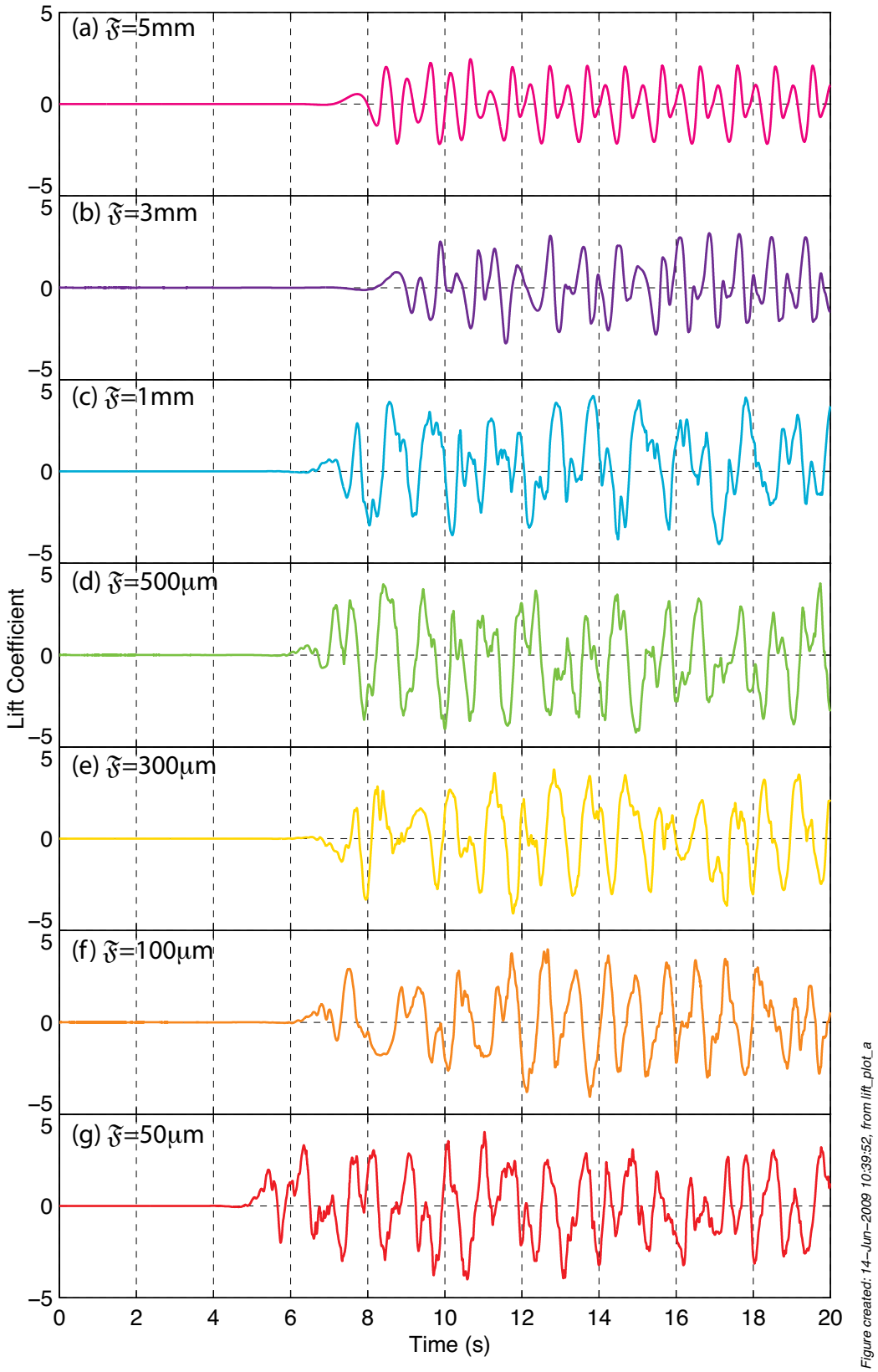


**Figure C-29 – Plot of the lift coefficients as a function of time for the seven wall normal cell distances, ℱ, tested.**

Conversely, for the shorter $\mathfrak{F}$ simulations, for example the $\mathfrak{F}$ = 50 μm, the probability distribution functions for both the drag and lift is broader with less tendency to a central peak, Figure C-30 and Figure C-31 respectively.

A similar, albeit with a reduced peak, probability distribution to the $\mathfrak{F}$=5mm simulation was observed in the $\mathfrak{F}$=3mm simulation. However, when $\mathfrak{F}$ was reduced to 1mm the probability distribution of the force coefficients changed from a peaky distribution to the broad function as described above for the $\mathfrak{F}$=50μm simulation. Therefore, with a transition from the peaky to the broad distribution between 3mm and 1mm, a conservative choice, for two-dimensional flows, would be to enforce $\mathfrak{F}$<1mm.

The shape of the distribution functions of $C_D$ for the shorter F simulations is characterised by a steep rise over the range of

$$0.6 \le C_D \le 1.8 \tag{A.5}$$

to a peak at $C_D \cong 1.8$. In contrast to the sharp rise, the tail for the range

$$C_D \ge 2 \tag{A.6}$$

is much shallower with the zero probability obtained at a maximum of $C_D \cong 5$ as shown in Figure C-30. Because of this long tail, the events at, or close to, the maximum $C_D$ were both approached and withdrawn quickly. Hence, an object in flows such as this could expect to feel large forces that arrive and depart in fast waves somewhat akin, albeit on a smaller scale, to the phenomenon of rogue oceanic waves (Mori et al., 2002, Gemmrich and Garrett, 2009). That is, the body is subject to a succession of high force, transient events.

By similar reasoning, there is no strong bias in the probability distribution of the lift coefficients. That is, for lift values between ±2 the probability distribution is almost uniform so there is statistical preference in this region. Further for the lift coefficients greater than, and less than, ±2 the probability distribution drops off steadily before terminating sharply with no visible tail. These data contrast to the drag in that with the lift the extreme events are approached both more slowly and recede more slowly.

The median, the 50% frequency in a cumulative frequency plot, for the drag coefficient varies by about 0.5 while the median for the lift coefficients varies by about

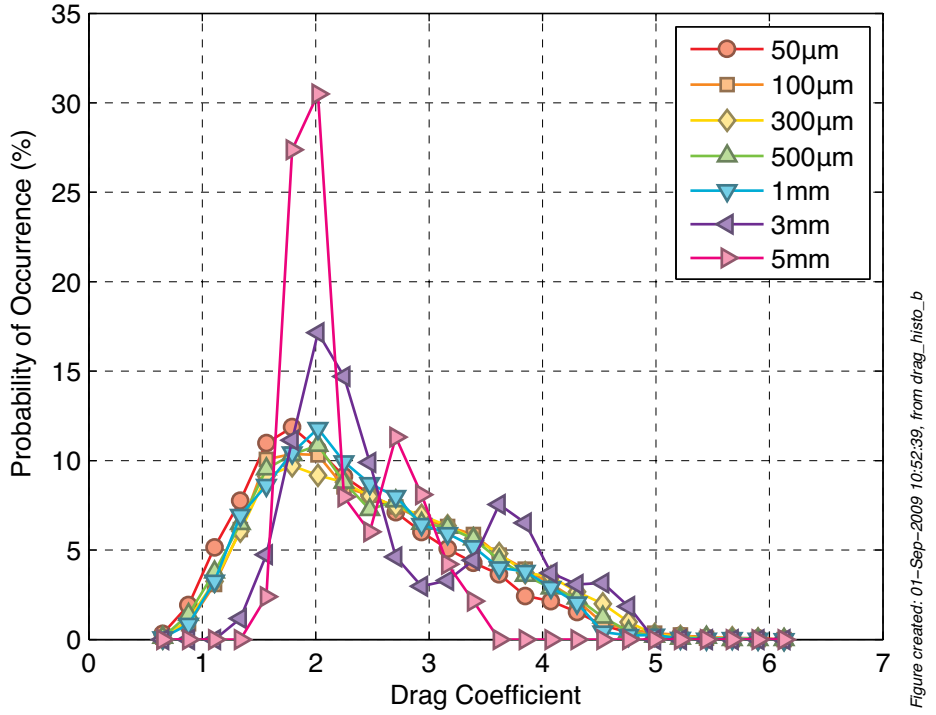


**Figure C-30 – Probability distribution functions of the drag coefficients computed across the simulation time interval $10 \leq t \leq 100$ s from the seven $\mathfrak{F}$ simulations.**

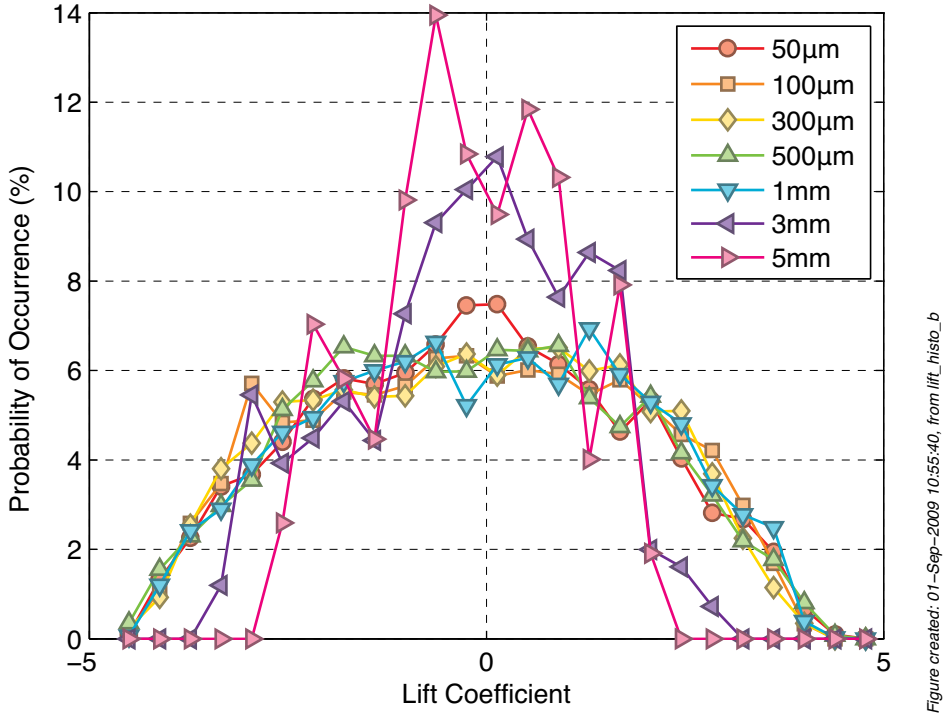


**Figure C-31 – Probability distribution functions of the lift coefficients computed across the simulation time interval $10 \leq t \leq 100$ s from the seven $\mathfrak{F}$ simulations.**

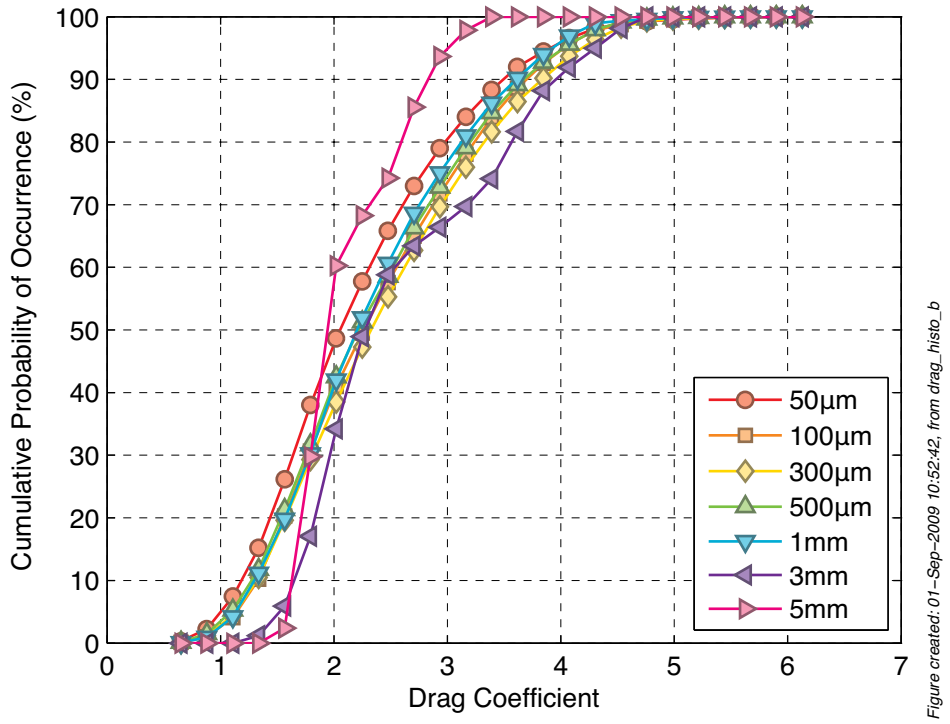


**Figure C-32 – Cumulative distribution functions of the drag coefficients computed across the simulation time interval $10 \le t \le 100$ s from the seven $\mathfrak{F}$ simulations.**

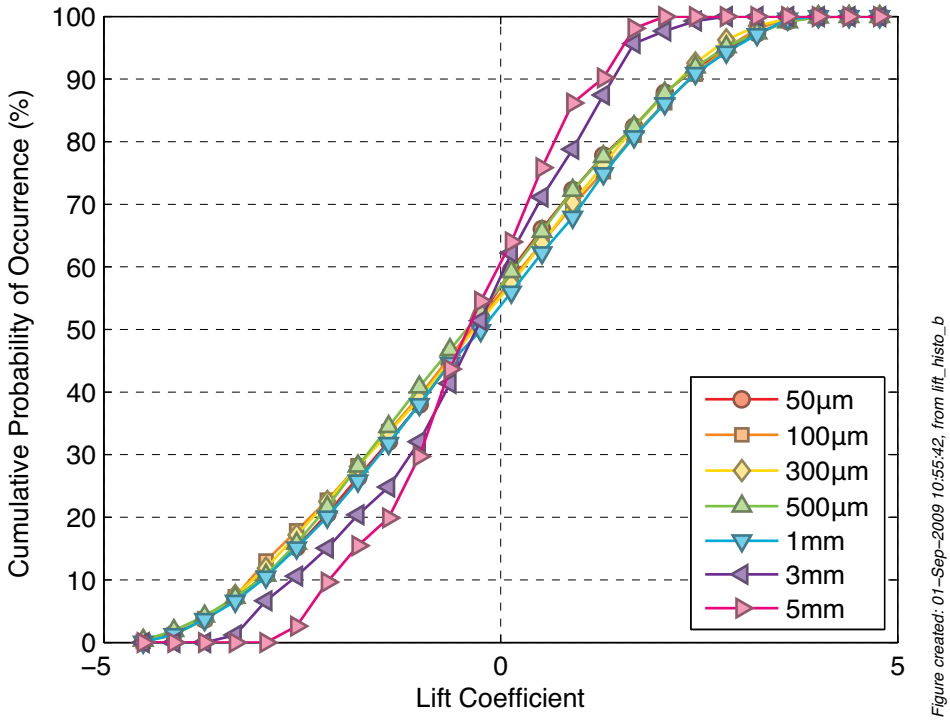


**Figure C-33 – Cumulative distribution functions of the lift coefficients computed across the simulation time interval $10 \le t \le 100$ s from the seven $\mathfrak{F}$ simulations.**

one, shown in Figure C-32 and Figure C-33 respectively. Interestingly as the median for the lift coefficients are all less than zero, and despite the discussion above, this result could indicate a possible bias in the flow computation. However, a more rigorous examination of the first four statistical moments, computed over the same time interval as described in Equation (A.4) would quantify any potential bias.

### C.4.5. Statistical Characteristics of the Force Coefficients

When computed over the time interval described in Equation (A.4) the resultant mean lift coefficients fluctuate around zero with no obvious pattern, as shown in Figure C-34. However, by the same argument as was presented in §C.3.5, that the maximum change of the mean lift from zero is significantly less than the amplitude of the lift signal, the differences of the mean lift from zero are sufficiently small as to be statistically insignificant.

In contrast to the mean lift coefficients, the mean drag coefficients over the range $\mathfrak{F} \le 500\mu m$ converge towards, but remain above, the comparison drag region shown in Figure C-34.

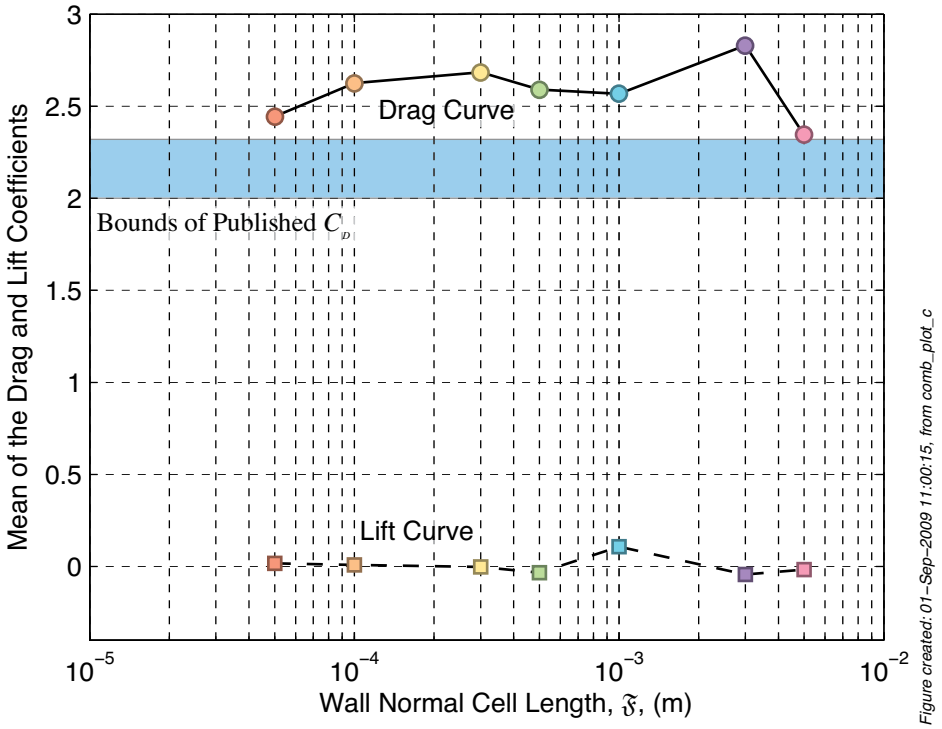


**Figure C-34 – Plot of the mean drag and lift coefficients from the seven $\mathfrak{F}$ simulations of the present work together with a region representing mean drag data compiled by Sohankar, Davidson and Norberg (1999).**

Although no simulations with a shorter $\mathfrak{F}$ were computed, the mean drag is unlikely to converge further because smaller cells in the wall region should not resolve more of the boundary layer. However, given that the flow field has already been shown to be unphysical, rather than the absolute value of the mean drag, the trend of the drag value converging below a certain wall normal value is the important conclusion.

As with the mean drag from the $\mathfrak{F}$ = 50 μm simulation, the mean drag for the $\mathfrak{F}$ = 5 mm simulation is also close to 2.35, or just above the upper bound of 2.32 from the published mean drag data. However, from an examination of the flow field around the cylinder, shown in Figure C-27, and the plot of the drag coefficient as a function of time, shown in Figure C-28, this result is coincidental. That is, the length of $\mathfrak{F}$ is sufficiently large that the computed flow field is unphysical; hence, the apparently correct mean drag and lift coefficients should be treated as a coincidence.

For the simulations with $\mathfrak{F} \leq 1$ mm the standard deviations of both the drag and lift coefficients have constant values of approximately 0.8 and 1.8, respectively, as shown in Figure C-35. Therefore, it follows that unlike the mean drag coefficient that was still converging over this range, the standard deviation is not as sensitive to the length of $\mathfrak{F}$.

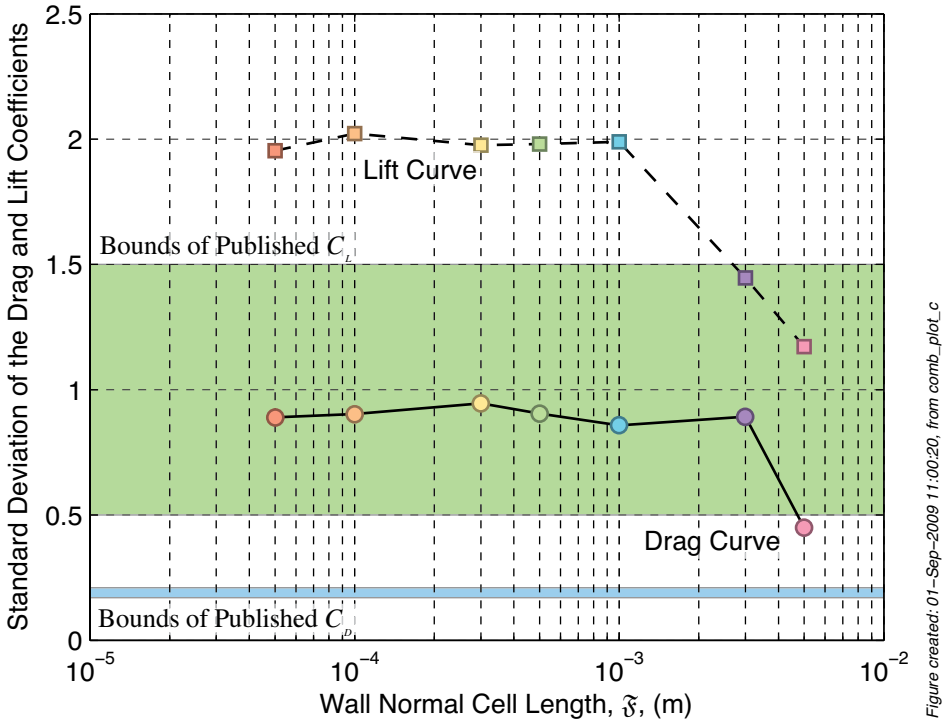


**Figure C-35 – Plot of the standard deviations of the drag and lift coefficients from the seven $\mathfrak{F}$ simulations of the present work together with two regions representing published results compiled by Sohankar, Davidson and Norberg (1999).**

However, at the longer wall lengths of

$$\mathfrak{F} > 1mm \tag{A.7}$$

there is a steep decline in the standard deviations of, in particular, the lift but also the drag. This result lends further support to the unphysical nature of the flow field and that the excellent agreement of the mean drag at larger $\mathfrak{F}$ is coincidental rather than accurate.

## *C.5. Summary and Recommendations for the Three-Dimensional Meshes*

Two preliminary studies with 17 individual tests were undertaken in an effort to develop guidelines for the construction of the three-dimensional simulations. The two studies were designed to (1) investigate the effect of the location of the outlet boundary relative to the square cylinder and (2) to explore the influence of the size of the cells adjacent to the square cylinder. As such, conservative assumptions were made about the first parameter for the second study and vice verse. These assumptions were subsequently proved to be valid.

From the results of the two studies, three recommendations were drawn:

1. That the assumptions that underpin the two-dimensional simulation are wrong and lead to the computation of unphysical flows, hence the flow must be simulated in three dimensions.
2. That the distance from the cylinder to the outlet, particularly at shorter lengths, does adversely affect the flow around the cylidner, therefore the length from the downstream face of the cylinder to the outlet should be longer than 400mm.
3. That the size of the cell, measured as a wall normal length, adjacent to the cylinder adversely affects the computed flow at longer lengths, so the wall normal cell length should be less than 500μm.

# Appendix D: Source Code

## *D.1. makefile*

```
#makefile to compile the source required for the dynamic_average.o file
#NOTE linking must be carried out by the other fortran file being compiled
#peter brady 6th may 2005

#this will be compiled as a shared library so set:
SHARED = shared
export SHARED
export $(MAKECMDGOALS)

#NAG Libraries and src
nag_dir=/usr/local/lib/NAGWare

#my general utilities
my_src=../utilities

#my libUserAce plugins
objects=
modules=

#DTF/ESI Libraries (if required, leave the directories when commenting out)
usersub_src=../cfdrc_src

INCDIR=-I$(my_src) -I$(usersub_src) -I$(nag_dir)
LIBDIR=-L$(my_src) -L$(usersub_src) -L$(nag_dir)

#compiler directives - linking done elsewhere, compile only
#linker is included for the test file ONLY
f95 = f95
CFLAGS =-u -colour -free -O4 -gc -Wc,-fPIC -C=all -c
LD = f95
LDFLAGS = -unsharedf95 -Wl,-fPIC,-shared -o

#main section to be compiled (ie default target)
.PHONY: all
all: flag_paramters.o dynamic_average.o
dynamic_average.o: subdirs dynamic_average.f90 flag_parameters.o
     $(f95) $(INCDIR) $(CFLAGS) dynamic_average.f90
flag_paramters.o : subdirs flag_parameters.f90
     $(f95) $(INCDIR) $(CFLAGS) flag_parameters.f90

#compile basic shared object for testing
.PHONY: test
test: test_average.so
test_average.so : all test_average.o
     $(LD) $(LIBDIR) $(INCDIR) $(LDFLAGS) test_average.so test_average.o \
     ../cfdrc_src/cfdrc_access_calls.o dynamic_average.o flag_parameters.o \
     ../cfdrc_src/cfdrc_user.o ../utilities/file_utils.o
test_average.o : test_average.f90
     $(f95) $(INCDIR) $(CFLAGS) test_average.f90

#test to compile other directories
SUBDIRS = ../cfdrc_src ../utilities
.PHONY: subdirs $(SUBDIRS)
subdirs: $(SUBDIRS)
$(SUBDIRS):
     $(MAKE) -C $@

#clean files for a new install
.PHONY: clean clean_test clean_all
clean:
     for d in $(SUBDIRS); do (cd $$d; $(MAKE) clean ); done
     rm dynamic_average.o dynamic_average.mod \
```

```
        flag_parameters.o flag_parameters.mod

clean_test:
     rm test_average.so test_average.o

clean_all: clean clean_test
```

## D.2. flag_parameters.f90

```
module flag_parameters
!module to contain common variable declarations for the dynamic average
!routines

use cfdrc_user, only: int_p

implicit none

!flag parameters
integer(int_p),parameter::flag_initialise=1 !initialise arrays only
integer(int_p),parameter::flag_calc_base=2 !calc base variables only
integer(int_p),parameter::flag_calc_dep=3 !calc base and dependant variables
integer(int_p),parameter::flag_write=4 !write to DTF
integer(int_p),parameter::flag_restart=5 !attempt to reload data

end module flag_parameters
```

## D.3. dynamic_average.f90

```
module dynamic_average
use cfdrc_user, only: string_length,int_p,real_p
implicit none
!dynamic_average.f90
!provides functions to do dynamic time averaging over timesteps during the
!simulation, rather than after as a post processing step
!Peter Brady, 6th May 2005
!comment added for svn

!************************
!Module Level Variables
!var_name - contains the variables to be averaged
!averages - the average array
!indices - the variable indices related to var_name
!num_cells - number of cells in the current domain
!domain_cells - number of cells per processor
!
!************************


contains

function average(flag)
!Performs all averaging functions, flag detirmines what average
use cfdrc_user_access !cfd access routines to hook into the solver
use nag_parameters !stderr numbers etc
use f90_iostat !nag error numbers
use cfdrc_user,only:string_length,int_p, real_p,geom_threed,geom_twod
use file_utils, only: get_file_handle
use flag_parameters

implicit none
!Variable list
!Function specification variables
!average - function return value 0=ok, 0<>error
!domain_cells - number of non-ghost cells on each processor
!var_name - variable name list
!indices - variable indices
!averages - average array to be allocated
```

```
!
!Working variables and initial values:
!i=0 - counting variable
!num_procs=1 - total number of processors in use, ie parallel runs
!proc=1 - the rank of the current processor
!logical_error=.false. - logical variable for cfdrc calls
!integer_error=ioerr_ok - integer system error holder

integer(int_p)::average
integer(int_p),intent(in)::flag

character(string_length),dimension(36),parameter::var_name=(/"U
",&
            "V                   ","W                   ", &
            "P                   ","VOF_VOLUME_FRACTION", &
            "T                   ","RHO                 ", &
            "Vis                 ","VOLUME              ", &
            "U_rms               ","V_rms               ", &
            "W_rms               ","P_rms               ", &
            "VOF_rms             ","T_rms               ", &
            "RHO_rms             ","Vis_rms             ", &
            "upup                ","vpvp                ", &
            "wpwp                ","PpPp                ", &
            "vof_function_sq     ","upvp                ", &
            "upwp                ","vpwp                ", &
            "Ppup                ","Ppvp                ", &
            "Ppwp                ","u_skew              ", &
            "v_skew              ","w_skew              ", &
            "p_skew              ","u_kurtosis          ", &
            "v_kurtosis          ","w_kurtosis          ", &
            "p_kurtosis          "/)
real(real_p),dimension(:,:),allocatable,save::averages
integer(int_p),dimension(36),save:: indices !variable indices
integer(int_p),save::domain_cells=-1
integer(int_p)::n_total_cells=-1
real(real_p),dimension(:,:),allocatable,save::current
real(real_p),dimension(:),allocatable,save::total_real_cells

integer(int_p)::i=0
integer(int_p)::num_procs=1
integer(int_p)::proc=1
integer(int_p)::vof_solve_module=0
integer(int_p)::var=0
integer(int_p)::geom_index=GEOM_TWOD
integer(int_p)::model_index=-1
integer(int_p)::vof_module_index=0
character(string_length),save::model_name
character(string_length)::vof_module_name="VOF"
integer(int_p)::average_count=-1
integer(int_p)::fluct_ts=-1
integer(int_p)::cell_file_handle
logical::file_exists
logical::logical_error=.false.
integer(int_p)::integer_error=ioerr_ok

logical::write_file_exists=.false.
logical::write_dtf=.false.
logical::write_flat_file=.false.
character(5)::par_ext=""
character(60)::output_filename
logical::output_file_exists
integer(int_p)::output_unit
character(3)::output_file_status

!set initial ok return value
average=ioerr_ok

!**********************************************************************
! Section to initialise variables
if (flag .eq. flag_initialise) then
```

```
   ! Add some explanation text to the log files to remind me how it works :-)
   write(unit=stderr,fmt=*) "We are doing a run with Peter Brady's average
module engaged"
   write(unit=stderr,fmt=*) "Usage:"
   write(unit=stderr,fmt=*) " Start averaging: touch do_average"
   write(unit=stderr,fmt=*) " Start RMS: touch do_rms"
   write(unit=stderr,fmt=*)
   write(unit=stderr,fmt=*) "Output location:"
   write(unit=stderr,fmt=*) " DTF file: touch dtf_file"
   write(unit=stderr,fmt=*) " Single flat file: touch flat_file"
   write(unit=stderr,fmt=*) " NOTE:"
   write(unit=stderr,fmt=*) "  1) it is possible to write to BOTH files"
   write(unit=stderr,fmt=*) "  2) if no file is present the default is dtf
only"
   write(unit=stderr,fmt=*) "  3) flat file, over writes at each step"

   !get number of processes for error logging
   call get_num_processes(num_procs,logical_error)
   if(logical_error) then
      write(unit=stderr,fmt=*) "Unable to determine if this is a parallel
run."
      average=-1
      return
   end if
   if(num_procs .gt. 1) then !we are in a parallel run, get the other data
      call get_process_id(proc,logical_error)
      if(logical_error) then
         write(unit=stderr,fmt=*) "Unable to get the current process rank."
         average=-2
         return
      end if
   end if

   !check if the vof module is used and if 3D or 2D
   call
get_module_index(vof_module_name,vof_module_index,vof_solve_module,logical_err
or)
   if(logical_error) then
      write(unit=stderr,fmt=*) "Unable to check the vof model usage, assuming
not, processor", proc
      vof_solve_module=-1
      logical_error=.false.
   end if
   call get_model_details(model_name,geom_index,model_index, logical_error)
   if(logical_error) then
      write(unit=stderr,fmt=*) "Unable to get the basic model details,
processor ", proc
      average=-3
      return
   end if

   !get the primary variable indices
   do i=1,9,1 !ie only for true variables, not the calculated
      call get_var_index(trim(var_name(i)),indices(i),logical_error)
      if (logical_error) then
         write(unit=stderr,fmt=*) "Error getting the variable index for:
",var_name(i)
         average=-4
         return
      end if
   end do

   !if we are in a parallel run open the inquire file and get the number of
real
   !cells that are in this domain
   if (num_procs .ge. 2) then
      write(unit=stdout,fmt=*) "attempting to open:", trim(model_name) //
".cells"
      inquire(file=trim(model_name) // ".cells",exist=file_exists)
```

```
      if(file_exists) then
         cell_file_handle=get_file_handle()
         if(cell_file_handle .ne. -1) then
            open(unit=cell_file_handle,file=trim(model_name) // ".cells", &
               action="read",status="old",iostat=integer_error)
            if(integer_error .eq. ioerr_ok) then
               do i = 1, proc, 1
                  read(unit=cell_file_handle,fmt=*) domain_cells
                  if(i .eq. proc) then
                     write(unit=stdout,fmt=*) "Counted Cells:", domain_cells
                     exit
                  end if
               end do
            else
               average = -5
               write(unit=stderr,fmt=*) "Unable to open .cell file",
integer_error
               return
            end if
         else
            average = -6
            write(unit=stderr,fmt=*) "Unable to get file handle for .cell
file"
            return
         end if
      else
         write(unit=stderr,fmt=*) "Cell file does not exist"
         average=-7
         return
      end if
   else
      !we are not in a parallel run so domain cells are the simple:
      call get_cells(domain_cells,logical_error)
      if(logical_error) then
         write(unit=stderr,fmt=*) "Unable to get the number of cells in the
domain"
         averages = -8
         return
      end if
   end if

   !check the domain cells -  this only checks for huge errors in the input
file
   if (domain_cells .eq. -1) then
      write(unit=stderr,fmt=*) "Domain cell check failed"
      average = -9
      return
   end if

   if(num_procs .ge. 2) then
      !allocate a temp array that includes the ghost cells and the real cells
      call get_cells(n_total_cells,logical_error)
      if(logical_error) then
         write(unit=stderr,fmt=*) "Error getting the total (including ghost
cells) number of cells"
         averages = -1
         return
      end if
   else
      !for the non-parallel case n_total_cells = domain cells
      n_total_cells = domain_cells
   end if
   allocate(total_real_cells(n_total_cells),stat=integer_error)
   if(integer_error .ne. ioerr_ok) then
      write(unit=stderr,fmt=*) "Error allocating total cell array memory,
processor ", proc
      averages = -1
      return
   end if
```

```
   !attempt to allocate memory for the general arrays, ie those without ghost
   !cells

allocate(averages(size(var_name,1),domain_cells),current(9,domain_cells),stat=
integer_error)
   if(integer_error .ne. ioerr_ok) then
      write(unit=stderr,fmt=*) "Error allocating memory for average arrays,
processor ", proc
      average=-10
      return
   else
   !initialise the first values
   averages=0.0
   current=0.0
   write(unit=stdout,fmt=*) "Averages array allocated, processor ", proc
   end if
end if

!**********************************************************************
! section to perform the average
if((flag .eq. flag_calc_base) .or. (flag .eq. flag_calc_dep)) then
   !check allocation of averages
   if(.not. allocated(averages)) then
      write(unit=stderr,fmt=*) "Averages array is not allocated."
      write(unit=stderr,fmt=*) "We can not perform an average then."
      average=-11
      return
   end if
   !increment the average counter
   if(average_count .eq. -1) then
      average_count=1
   else
      average_count=average_count + 1
   end if

   do var=1,9,1 !loop through the primary variables
      select case (var)
      case (3) !ie w velocity
         if((geom_index .ne. geom_threed) .and. (average_count .eq. 1)) then
            !ie two d or axi, but only do once
            !insert dummy value
            current(var,:)=0.0
            cycle
         elseif ((geom_index .ne. geom_threed) .and. (average_count .ge. 1))
then
            !do not get for the rest of the simulation
            cycle
         end if
      case (5) !ie vof
         if ((vof_solve_module .le. 0) .and. (average_count .eq. 1)) then
            !ie not solving for vof but only do once
            current(var,:)=0.0
            cycle
         elseif ((vof_solve_module .le. 0) .and. (average_count .ge. 1)) then
            !do not get for the rest of the simulation
            cycle
         end if
      end select
      call
get_cell_value_array(indices(var),n_total_cells,total_real_cells,logical_error
)
      if(.not. logical_error) then
         current(var,:)=total_real_cells(1:domain_cells:1)
      else
         write(unit=stderr,fmt=*) "Unable to get value for " ,var_name(var), "
processor ",proc
         average=-12
         return
      end if
```

```
   end do

   !average dependant variables
   !Average: U, V, W, P, VOF, T, Rho, Vis
   averages(1:8:1,:)=((averages(1:8:1,:) * real(average_count-1)) +
current(1:8:1,:)) / real(average_count)
   !write (unit=stderr,fmt=*) "Average 1"

   !Cell volume - constant therefore only do once
   if(average_count .eq. 1) averages(9,:)=current(9,:)

   !RMS: U, V, W, P, VOF, T, Rho, Vis
   averages(10:17:1,:)=((averages(10:17:1,:) * real(average_count-1)) +
current(1:8:1,:) ** 2.0) / real(average_count)
   !write (unit=stderr,fmt=*) "Average 2"

   if(flag .eq. flag_calc_dep) then
      !to account for differences in the start time of dependent variable
      !averaging fluct_ts records the first timestep averaged from
      if(fluct_ts .eq. -1) then
         fluct_ts=1
      else
         fluct_ts=fluct_ts + 1
      end if

      !calculate dependant variables
      !up, vp, wp, pp, VOF - redefine current to fluct rather than raw
      current(1:5:1,:)=current(1:5:1,:)-averages(1:5:1,:) !current fluctuating
      !write (unit=stderr,fmt=*) "Average 3"

      !RMS up, vp, wp, pp, VOFp
      averages(18:22:1,:)=((((averages(18:22:1,:)*real(fluct_ts-
1)))+current(1:5:1,:)**2.0)/real(fluct_ts))
      !write (unit=stderr,fmt=*) "Average 4"

      !Average up*vp, up*wp, vp*wp, pp*up, pp*vp, pp*wp
      averages(23,:)=((averages(23,:)*real(fluct_ts-
1))+current(1,:)*current(2,:))/real(fluct_ts)
      !write (unit=stderr,fmt=*) "Average 5"
      averages(24,:)=((averages(24,:)*real(fluct_ts-
1))+current(1,:)*current(3,:))/real(fluct_ts)
      !write (unit=stderr,fmt=*) "Average 6"
      averages(25,:)=((averages(25,:)*real(fluct_ts-
1))+current(2,:)*current(3,:))/real(fluct_ts)
      !write (unit=stderr,fmt=*) "Average 7"
      averages(26,:)=((averages(26,:)*real(fluct_ts-
1))+current(4,:)*current(1,:))/real(fluct_ts)
      !write (unit=stderr,fmt=*) "Average 8"
      averages(27,:)=((averages(27,:)*real(fluct_ts-
1))+current(4,:)*current(2,:))/real(fluct_ts)
      !write (unit=stderr,fmt=*) "Average 9"
      averages(28,:)=((averages(28,:)*real(fluct_ts-
1))+current(4,:)*current(3,:))/real(fluct_ts)
      !write (unit=stderr,fmt=*) "Average 10"

      !skew u, v, w, p
      averages(29:32:1,:)=((averages(29:32:1,:)*real(fluct_ts-
1))+(current(1:4:1,:)**3.0))/real(fluct_ts)
      !write (unit=stderr,fmt=*) "Average 11"

      !kurtosis u, v, w, p
      averages(33:36:1,:)=((averages(33:36:1,:)*real(fluct_ts-
1))+(current(1:4:1,:)**4.0))/real(fluct_ts)
   end if

   !print debug message
   write(unit=stderr,fmt=*) "U Avg=", averages(1,1), "Processor: ",proc, &
      "Time step: ",average_count
   if (flag .eq. flag_calc_dep) then
      write(unit=stderr,fmt=*) "U rms=", averages(10,1), "Processor: ",proc, &
```

```
         "Fluct time step: ",fluct_ts
   end if
end if

!**********************************************************************
!section to write the data out

if (flag .eq. flag_write) then
   !check allocation of averages and allocate if necessary
   if(.not. allocated(averages)) then
      write(unit=stderr,fmt=*) "Averages array is not allocated."
      write(unit=stderr,fmt=*) "We can not write to dtf."
      average=-13
      return
   end if

   write(unit=stderr,fmt=*) "About to start writing data on processor ",proc
   !allocate memory for the temporary array

   !there are alternate methods to write data
   ! so we test and if we can't find a file we use the previous method
specified

   ! Do the tests
   write(unit=stderr,fmt=*) "1 DTF, Flat", write_dtf, write_flat_file
   inquire(file="flat_file",exist=write_file_exists)
   if (write_file_exists) then
      write_flat_file = .true.
   else
      write_flat_file = .false.
   end if
   inquire(file="dtf_file",exist=write_file_exists)
   if (write_file_exists) then
      write_dtf = .true.
   else
      write_dtf = .false.
   end if
   write(unit=stderr,fmt=*) "2 DTF, Flat", write_dtf, write_flat_file

   !reset for default dtf
   if ((.not.write_dtf) .and. (.not.write_flat_file)) then
      write_dtf = .true.
   end if
   write(unit=stderr,fmt=*) "3 DTF, Flat", write_dtf, write_flat_file

   !Test for flat file write
   if(write_flat_file) then
      !write to a flat fortran binary, one per processor
      write(unit=stderr,fmt=*) "We are writing to a flat file"

      !generate the filename
      write(unit=par_ext,fmt='(i4.4)') proc
      par_ext= "_" // adjustl(par_ext)
      output_filename = trim(model_name) // par_ext // ".averages"
      write(unit=stderr,fmt=*) "Output name:", output_filename

      !test if the filename exits and open it
      inquire(file=output_filename,exist=output_file_exists)
      if(output_file_exists) then
         output_file_status="old"
      else
         output_file_status="new"
      end if
      output_unit=get_file_handle()
      if(output_unit .ne. -1) then
         open(unit=output_unit,file=output_filename,status=output_file_status,
&
            form="formatted",action="write",iostat=integer_error)
         if(integer_error .eq. ioerr_ok) then
```

```
            !now loop through and write the variables
            write(unit=output_unit,fmt='(i0)') domain_cells
            write(unit=output_unit,fmt='(i0)') size(var_name)
            do i=1,domain_cells,1
               write(unit=output_unit,fmt='(i0,",",35(f0.22,","), f0.22)')
i,averages(:,i)
            end do
            close(unit=output_unit)
         else
            write(unit=stderr,fmt=*) "Unable to open output file"
         end if
      else
         write(unit=stderr,fmt=*) "Unable to get a file unit for the output
file"
      end if
   end if

   ! Test for the DTF write option
   if(write_dtf) then
      !write directly into the dtf file
      write(unit=stderr,fmt=*) "We are writing to the DTF"

      do i=1,size(var_name,1),1
         call write_nodal_data_to_dtf(var_name(i),
size(averages,2),averages(i,:), "", logical_error)
         call write_cell_data_to_dtf(var_name(i),
size(averages,2),averages(i,:), "", logical_error)
         if (logical_error) then
            print *,"There was an error writing the nodal or cell data on
procesor ", proc
            average=-14
            return
         end if
      end do
   end if

   write(unit=stderr,fmt=*) "Finished writing data on processor ",proc
end if

end function average

end module dynamic_average
```

## D.4. libUserAce.f

```
MODULE cfdrc_user
!***********************************************************************
  IMPLICIT NONE
  SAVE

  INTEGER, PARAMETER :: int_p  = SELECTED_INT_KIND(8)

  INTEGER, PARAMETER :: string_length = 80

  INTEGER, PARAMETER :: real_p = SELECTED_REAL_KIND(8)

  ! DO NOT CHANGE THE PARAMETER VALUES. THESE ARE FOR USE ONLY.
  ! Direction parameters.
  INTEGER(int_p), PARAMETER :: XDIR = 1, YDIR = 2, ZDIR = 3

  ! geometry related parameters.
  INTEGER(int_p), PARAMETER :: GEOM_THREED = 1, GEOM_TWOD = 2, &
                               GEOM_TWOD_AXI = 3

  ! material related flags.
  INTEGER(int_p), PARAMETER :: MAT_GAS = 1, MAT_FLUID = 2, &
                               MAT_SOLID = 3, MAT_BLOCK = 4

  ! Grid Connectivity related parameters.
```

```
  INTEGER(int_p), PARAMETER :: TRI_CELL = 1, QUAD_CELL = 2, &
                               TET_CELL = 3, PYRAMID_CELL = 4, &
                               PRISM_CELL = 5, HEX_CELL = 6, &
                               POLY_CELL = 7

  INTEGER(int_p), PARAMETER :: LINE_FACE = 1, TRI_FACE = 2, &
                               QUAD_FACE = 3, POLY_FACE = 4

  ! Time option parameters.
  INTEGER(int_p), PARAMETER :: TIME_ORIGINAL = 0, TIME_PREVIOUS = 1, &
                               TIME_CURRENT = 2
  ! model parameters.
  INTEGER(int_p), PARAMETER :: MODEL_STEADY = 1, MODEL_STEADY_RESTART = 2, &
                               MODEL_TRANSIENT = 3, MODEL_TRANSIENT_RESTART =
4

  ! electric sub model options.
  INTEGER(int_p), PARAMETER :: ELECTRIC = 1, &
                               ELECTRIC_ELECTROSTATICS_FVM = 2, &
                               ELECTRIC_ELECTROSTATICS_BEM = 3, &
                               ELECTRIC_DC_CONDUCTION = 4, &
                               ELECTRIC_AC_CONDUCTION = 5, &
                               ELECTRIC_TIME_DOMAIN = 6

  ! global bc types.
  INTEGER(int_p), PARAMETER :: BC_TYPE_INLET = 1, &
                               BC_TYPE_WALL = 2, &
                               BC_TYPE_EXIT = 3, &
                               BC_TYPE_INTERFACE = 4, &
                               BC_TYPE_F_F_INTERFACE = 5, &
                               BC_TYPE_S_S_INTERFACE = 6, &
                               BC_TYPE_S_F_INTERFACE = 7, &
                               BC_TYPE_F_B_INTERFACE = 8, &
                               BC_TYPE_B_B_INTERFACE = 9, &
                               BC_TYPE_S_B_INTERFACE = 10, &
                               BC_TYPE_SYMM = 11, &
                               BC_TYPE_CYCLIC = 12, &
                               BC_TYPE_THINWALL = 13

  ! heat transfer bc subtypes
  INTEGER(int_p), PARAMETER :: BC_HEAT_INOUT = 1, &
                               BC_HEAT_SYMM = 2, &
                               BC_HEAT_ISOTHERMAL = 3, &
                               BC_HEAT_ADIABATIC = 4, &
                               BC_HEAT_FIX_Q = 5, &
                               BC_HEAT_NEWTON = 6, &
                               BC_HEAT_EXT_RADIATION = 7, &
                               BC_HEAT_CONJUGATE_INTERFACE = 8, &
                               BC_HEAT_THINWALL = 9, &
                               BC_HEAT_CYCLIC = 10, &
                               BC_HEAT_INTERFACE = 11, &
                               BC_HEAT_MIXING_PLANE = 12, &
                               BC_HEAT_COUPLE = 13, &
                               BC_HEAT_CHIMERA = 14

  ! flow bc subtypes
  INTEGER(int_p), PARAMETER :: BC_FLOW_FIXM_INLET = 1, &
                               BC_FLOW_FIXP_OUTLET = 2, &
                               BC_FLOW_WALL = 3, &
                               BC_FLOW_SYMM = 4, &
                               BC_FLOW_FIXP_EXTRAPOLAT_OUTLET = 5, &
                               BC_FLOW_FIXPT_INLET = 6, &
                               BC_FLOW_FIXP_INLET = 7, &
                               BC_FLOW_CYCLIC = 8, &
                               BC_FLOW_INTERFACE = 9, &
                               BC_FLOW_MIXING_PLANE = 10, &
                               BC_FLOW_COUPLE = 11, &
                               BC_FLOW_CHIMERA = 12
```

```
  ! electric bc subtypes.
  INTEGER(int_p), PARAMETER :: BC_ELECTRIC_FIX_POTENTIAL = 1, &
                               BC_ELECTRIC_FIX_FLUX = 2, &
                               BC_ELECTRIC_SYMM = 3, &
                               BC_ELECTRIC_CYCLIC = 4, &
                               BC_ELECTRIC_DIEL_DIEL = 5, &
                               BC_ELECTRIC_FIX_CHARGE = 6, &
                               BC_ELECTRIC_IGNORE = 7, &
                               BC_ELECTRIC_ZERO_CURRENT = 8, &
                               BC_ELECTRIC_THIN_WALL = 9, &
                               BC_ELECTRIC_INTERFACE = 10

  ! semi bc subtypes.
  INTEGER(int_p), PARAMETER :: BC_SEMI_FIX_POTENTIAL = 1, &
                               BC_SEMI_FIX_CHARGE = 2, &
                               BC_SEMI_CONJUGATE_WALL = 3, &
                               BC_SEMI_CYCLIC = 4, &
                               BC_SEMI_INTERFACE = 5

  ! DTF I/O parameters.
  INTEGER(int_p), PARAMETER :: DTF_IO_VAR_LEN = 36, DTF_IO_UNIT_LEN = 36

  ! use the following parameter to get the cell/node data from DTF file you
  ! want.
  INTEGER(int_p), PARAMETER :: USER_CURRENT_DTF_FILE = 1,
USER_RESTART_DTF_FILE = 2

  ! DIRECTION parameters for istropic/anisotropic models.
  INTEGER(int_p), PARAMETER :: DIR_ISOTROPIC = 0, DIR_NORMAL = 1, &
                               DIR_TANGENTIAL_1 = 2, DIR_TANGENTIAL_2 = 3

  ! Utility parameters.
  REAL(real_p) , PARAMETER :: zero = 0.0d0, one = 1.0d0, two = 2.0d0, &
                              three = 3.d0, four = 4.0d0, &
                              pi = 3.1415926535898d0

! Declare global variables
! USER GLOBAL VARIABLE DECLARATION BEGIN

character(string_length),dimension(28),parameter::global_var_name=(/"U
",&
              "V                   ","W                   ", &
              "P                   ","Vis                 ", &
              "T                   ","RHO                 ", &
              "VOF_VOLUME_FRACTION","upup                 ", &
              "upvp                ","upwp                ", &
              "vpvp                ","vpwp                ", &
              "wpwp                ","vof_function        ", &
              "PpPp                ","Ppup                ", &
              "Ppvp                ","Ppwp                ", &
              "u_skew              ","v_skew              ", &
              "w_skew              ","p_skew              ", &
              "u_kurtosis          ","v_kurtosis          ", &
              "w_kurtosis          ","p_kutsosis          ", &
              "VOLUME              "/)
real(real_p),dimension(:,:),allocatable::global_averages


! USER GLOBAL VARIABLE DECLARATION END

 END MODULE cfdrc_user
!**********************************************************************
!**********************************************************************
 SUBROUTINE uout(iflag)
 !DEC$ ATTRIBUTES DLLEXPORT :: uout
 !******* DO NOT REMOVE ABOVE LINE FOR MS WINDOWS OS ************
!**********************************************************************
! copyright (c) 1998  cfd research corp.  all rights reserved.
!
```

```
! purpose : for customized user output.
!
! iflag:  flag indicating calling location.
!
! This routine is called 5 times at different instances of iterative
! cycle indicated by iflag.
!
! iflag  :
!          1 - At the beginning of RUN. (At this point most of the boundary
!                                        conditions, properties are set. users
!                                        should be able to get cell or
boundary
!                                        values for different variables.)
!          2 - At the beginning of time step (only for transient problems).
!          3 - At the end of each iteration.
!          4 - At the end of each time step.(only for transient problems).
!          5 - At the end of RUN.
!
! One may use get_value_one_cell to get the values. To get the cell
! indexes, user has to supply the x,y,z locations and use the
! get_cell_index(vc_index,x,y,z,global_cell_index,error).
!-----------------------------------------------------------------------

! Include required global variables declared in cfdrc_user module.
  USE cfdrc_user, ONLY : int_p, real_p, string_length
  USE cfdrc_user, ONLY : global_averages,global_var_name
  use cfdrc_user, only : GEOM_THREED

  USE cfdrc_user_access

  IMPLICIT NONE

  INTEGER(int_p), INTENT(IN) :: iflag

! Declare required local variables here.
! USER VARIABLE DECLARATION BEGIN

!persistant arrays
!the next variable is the array to store the averages, the first dimension is
!num_var_to_avg long and represents the variables to average, the second
!dimension is ncells long and stores the value for that timestep
real(real_p),dimension(:,:),allocatable,save::local_averages
integer(int_p),dimension(:),allocatable,save:: var_indexes !variable indices
integer(int_p),save::ncells=0 !number of cells in the domain

!averaging variables
integer(int_p)::current_vc,current_cell !counting loop variables
integer(int_p)::num_vcs,vc_cells !number of vcs and cells in them respectively
real(real_p)::up,vp,wp,pp !fluct quantities
real(real_p)::inst_vof !temporary holder for vof value

!working variables
integer(int_p)::i,vc_loop !counting
integer(int_p)::n_vc_rec !vc counting variables
integer(int_p)::temp_int
character(string_length)::temp_char
logical::general_logical !logical working variable
integer(int_p)::var !counting variable for the get value loop
integer(int_p)::var_int !temporary variable to pass the variable index
integer(int_p)::global_cell !global cell index holder in get value
real(real_p)::value !return value for get_value call

!error variables
logical::logical_error=.false.
integer(int_p)::integer_error=0

!file check variables
integer(int_p)::time_step_no !time step returned from the solver
real(real_p)::model_time !model real time returned from CFD-ACE-SOLVER
```

```
character(string_length)::avg_file_name !name of the average file .avg
integer(int_p)::avg_file_unit=50 !file unit for *.avg
integer(int_p)::start_time_step,end_time_step !time steps read from .avg
logical::do_average=.false. !actually to the averaging at this time step
character(string_length)::model_name !name of the model
integer(int_p)::geom_index !geometry index -> 2D, 2D Axi, 3D
integer(int_p)::model_index !Steady/Transient etc
character(string_length)::vof_module_name="VOF"
integer(int_p)::vof_module_index !module index of the VOF module
integer(int_p)::vof_solve_module=-1 !is the VOF module active 1=yes,0=no
integer(int_p)::num_time_steps !number of time steps average from 1 to n

integer(int_p)::proc,cell_index
character(string_length)::vc_name

! USER VARIABLE DECLARATION END

!---------------------------------------------------------------------
! Start writing code here.
! USER CODE BEGIN

!set initial conditions
if(iflag.eq.1) then
   !is the first time step, get indices
   allocate(var_indexes(size(global_var_name,1)))
   do i=1,8,1 !ie only the solvefr variables, not the calculated
      temp_char=trim(global_var_name(i))
      call get_var_index(temp_char,temp_int,logical_error)
      if (logical_error) then
         print *,"Error getting the variable index for: ",temp_char
         exit
      else
         var_indexes(i)=temp_int
      end if
   end do

   !addition for cell volume
   i=28
   temp_char=trim(global_var_name(i))
   call get_var_index(temp_char,temp_int,logical_error)
   if (logical_error) then
      print *,"Error getting the variable index for: ",temp_char
   else
      var_indexes(i)=temp_int
   end if

   !get the number of cells
   if(.not. logical_error) then
      !need to loop through the vc's
call get_process_id(proc,logical_error)
      call get_number_vcs(n_vc_rec,logical_error)
      do vc_loop=1,n_vc_rec,1
         !get and sum the number of cells
         call get_cells_vc(vc_loop,vc_cells,logical_error)
call get_vc_name(vc_loop,vc_name,logical_error)
print *,"vc_cells",vc_cells
if (vc_cells .gt. 0) then
call get_cell_index_from_vc(1,vc_loop,cell_index,logical_error)
print *, "Cell index",cell_index
end if
         if(cell_index .le. 7500) then
         ncells=ncells+vc_cells
         end if
print *,proc,ncells,vc_name
      end do
      !call get_cells(ncells, logical_error) !removed for parallel runs
      if(logical_error) then
         print *,"Unable to get number of cells"
      else
print *, "Ncells:",ncells, "on processor",proc
```

```
         allocate(local_averages(size(global_var_name,1),ncells),&

global_averages(size(global_var_name,1),ncells),stat=integer_error)
         if(integer_error .ne. 0) then
            print *,"Error allocating memory for average arrays"
            logical_error=.true.
         end if
         local_averages=0.0
         print *,"Averages array allocated"
      end if
   end if
end if

if (iflag==4) then!end of time step-attempt to average
   !print *,"Average array (1,1)", local_averages(1,1)
   call get_model_details(model_name,geom_index,model_index, logical_error)
   call
get_module_index(vof_module_name,vof_module_index,vof_solve_module,logical_err
or)
   if (.not. logical_error) then
      avg_file_name=trim(adjustl(model_name))//".avg"
      inquire (file=avg_file_name,exist=general_logical)
      if (general_logical) then
         !file exists, open and read
         open (unit=avg_file_unit,file=avg_file_name, status="old",
action="read", iostat=integer_error)
         if(integer_error .eq. 0) then
            !read all variables
            read (unit=avg_file_unit,iostat=integer_error,fmt=*)
start_time_step,end_time_step
            if (integer_error .eq. 0) then
               close (unit=avg_file_unit) !sucessfully read, close the file
               !all variables read ok
               call get_time(model_time,time_step_no, logical_error)
               if (.not.logical_error) then
                  !got the time step from the solver
                  if((time_step_no .ge. start_time_step) .and. (time_step_no&
                     .le. end_time_step)) then
                     do_average=.true.
                     num_time_steps=time_step_no-start_time_step+1
                     print *, "Doing average for time step: ",time_step_no
                     print *, "Number of average time seps: ",num_time_steps
                  else
                     print *,"Not doing an average at this time step"
                  end if
               else
                  print *,"Error getting the time step"
               end if
            else
               print *, "Error reading variables from the .avg file"
            end if
         else
            print *,"Open file error number: ",integer_error
         end if
      else
         print *,"File does not exist"
      end if
   else
      print *,"unable to get model name"
   end if

   if(do_average .and. .not. logical_error) then
      !get number of vcs
      call get_number_vcs(num_vcs, logical_error)
      if(.not. logical_error) then
         do current_vc=1,num_vcs,1
            !get the number of cells
            call get_cells_vc(current_vc,vc_cells, logical_error)
            if(.not.logical_error) then
```

```
                do current_cell=1,vc_cells,1
                   !get the current global cell index
                   call get_cell_index_from_vc(current_cell, current_vc, &
                      global_cell,logical_error)
                   if(.not.logical_error) then
                      !calculate variables here
                      !u and up
                      var=1
                      var_int=var_indexes(var)
                      call
get_value_one_cell(var_int,global_cell,value,logical_error)
                      if(.not. logical_error) then

local_averages(var,global_cell)=(local_averages(var,global_cell)&
                            *real(num_time_steps-1)+value)/real(num_time_steps)
                         !u_prime
                         up=value-local_averages(var,global_cell)
                      else
                         print *,"Unable to get u value"
                         exit
                      end if
                      !v and vp
                      var=2
                      var_int=var_indexes(var)
                      call
get_value_one_cell(var_int,global_cell,value,logical_error)
                      if(.not. logical_error) then

local_averages(var,global_cell)=(local_averages(var,global_cell)&
                            *real(num_time_steps-1)+value)/real(num_time_steps)
                         !v_prime
                         vp=value-local_averages(var,global_cell)
                      else
                         print *,"Unable to get v value"
                         exit
                      end if
                      !w and wp
                      var=3
                      if (geom_index .eq. geom_threed) then
                         var_int=var_indexes(var)
                         call
get_value_one_cell(var_int,global_cell,value,logical_error)
                         if(.not. logical_error) then

local_averages(var,global_cell)=(local_averages(var,global_cell)&
                               *real(num_time_steps-
1)+value)/real(num_time_steps)
                         else
                            print *,"Unable to get w value"
                            exit
                         end if
                      else
                         !is 2D
                         value=0.0
                         local_averages(var,global_cell)=0.0
                      end if
                      !w_prime
                      wp=value-local_averages(var,global_cell)

                      !P and Pp
                      var=4
                      var_int=var_indexes(var)
                      call
get_value_one_cell(var_int,global_cell,value,logical_error)
                      if(.not. logical_error) then

local_averages(var,global_cell)=(local_averages(var,global_cell)&
                            *real(num_time_steps-1)+value)/real(num_time_steps)
                         !v_prime
                         Pp=value-local_averages(var,global_cell)
```

```
                        else
                           print *,"Unable to get P value"
                           exit
                        end if
                        !do other solver variables for this cell
                        do var=5,8,1
                           if ((vof_solve_module .eq. 1 .and. var .eq. 8) .or.
(var .lt. 8)) then
                              !vof is here, solve
                              var_int=var_indexes(var)
                              call
get_value_one_cell(var_int,global_cell,value,logical_error)
                              if(.not. logical_error) then

local_averages(var,global_cell)=(local_averages(var,global_cell)&
                                    *real(num_time_steps-
1)+value)/real(num_time_steps)
                                 if(var.eq.8) then
                                    !is VOF, store temporarily
                                    inst_vof=value
                                 end if
                              else
                                 print *,"Unable to get value
for",global_var_name(var)
                                 exit
                              end if
                           else
                              !no vof module insert dummy values
                              value=0.0
                              local_averages(var,global_cell)=value
                              inst_vof=value
                           end if
                        end do

                        !cell volume
                        var=28
                        var_int=var_indexes(var)
                        call
get_value_one_cell(var_int,global_cell,value,logical_error)
                        if(.not. logical_error) then
                           local_averages(var,global_cell)=value
                        else
                           value=-1.0
                           local_averages(var,global_cell)=value
                        end if

                        !do calculated variables
                        !up*up

local_averages(9,global_cell)=(local_averages(9,global_cell)&
                           *real(num_time_steps-1)+(up*up))/real(num_time_steps)
                        !up*vp

local_averages(10,global_cell)=(local_averages(10,global_cell)&
                           *real(num_time_steps-1)+(up*vp))/real(num_time_steps)
                        !up*wp

local_averages(11,global_cell)=(local_averages(11,global_cell)&
                           *real(num_time_steps-1)+(up*wp))/real(num_time_steps)
                        !vp*vp

local_averages(12,global_cell)=(local_averages(12,global_cell)&
                           *real(num_time_steps-1)+(vp*vp))/real(num_time_steps)
                        !vp*wp

local_averages(13,global_cell)=(local_averages(13,global_cell)&
                           *real(num_time_steps-1)+(vp*wp))/real(num_time_steps)
                        !wp*wp
```

```
local_averages(14,global_cell)=(local_averages(14,global_cell)&
                        *real(num_time_steps-1)+(wp*wp))/real(num_time_steps)
                     !vof

local_averages(15,global_cell)=(local_averages(15,global_cell)&
                        *real(num_time_steps-
1)+(inst_vof))/real(num_time_steps)
                     !Pp*Pp

local_averages(16,global_cell)=(local_averages(16,global_cell)&
                        *real(num_time_steps-1)+(Pp*Pp))/real(num_time_steps)
                     !Pp*up

local_averages(17,global_cell)=(local_averages(17,global_cell)&
                        *real(num_time_steps-1)+(Pp*up))/real(num_time_steps)
                     !Pp*Pp

local_averages(18,global_cell)=(local_averages(18,global_cell)&
                        *real(num_time_steps-1)+(Pp*vp))/real(num_time_steps)
                     !Pp*Pp

local_averages(19,global_cell)=(local_averages(19,global_cell)&
                        *real(num_time_steps-1)+(Pp*wp))/real(num_time_steps)
                     !u skew

local_averages(20,global_cell)=(local_averages(20,global_cell)&
                        *real(num_time_steps-
1)+(up*up*up))/real(num_time_steps)
                     !v skew

local_averages(21,global_cell)=(local_averages(21,global_cell)&
                        *real(num_time_steps-
1)+(vp*vp*vp))/real(num_time_steps)
                     !w skew

local_averages(22,global_cell)=(local_averages(22,global_cell)&
                        *real(num_time_steps-
1)+(wp*wp*wp))/real(num_time_steps)
                     !p skew

local_averages(23,global_cell)=(local_averages(23,global_cell)&
                        *real(num_time_steps-
1)+(pp*pp*pp))/real(num_time_steps)
                     !u Kurtosis

local_averages(24,global_cell)=(local_averages(24,global_cell)&
                        *real(num_time_steps-
1)+(up*up*up*up))/real(num_time_steps)
                     !v Kurtosis

local_averages(25,global_cell)=(local_averages(25,global_cell)&
                        *real(num_time_steps-
1)+(vp*vp*vp*vp))/real(num_time_steps)
                     !w Kurtosis

local_averages(26,global_cell)=(local_averages(26,global_cell)&
                        *real(num_time_steps-
1)+(wp*wp*wp*wp))/real(num_time_steps)
                     !p Kurtosis

local_averages(27,global_cell)=(local_averages(27,global_cell)&
                        *real(num_time_steps-
1)+(pp*pp*pp*pp))/real(num_time_steps)
                  else
                     print *,"unable to get global cell index"
                     exit
                  end if
               end do
            else
               print *,"Unable to get number of cells for vc"
```

```
               exit
            end if
         end do
      else
         print *,"unable to get number of vcs"
      end if
   end if


   !pass back to main solver
   global_averages=local_averages
end if

! USER CODE END
  RETURN
 END SUBROUTINE uout
!**********************************************************************
 SUBROUTINE uwrite_dtf
 !DEC$ ATTRIBUTES DLLEXPORT :: uwrite_dtf
!******* DO NOT REMOVE ABOVE LINE FOR MS WINDOWS OS ************
!**********************************************************************
! copyright (c) 1998  cfd research corp.  all rights reserved.
!
! purpose : for reading cell data from DTF file.
!
! This routine is called at the end of RUN when solver writes cell and
! nodal the
! DTF file for cell data. One may use write_cell_data_to_dtf, and
! write_nodal_data_to_dtf() to write the cell/nodal data to the DTF.
! or write_nodal_solution_to_dtf() to write nodal data. For this
! access routine you need to send in nodal values, not cell values.
!
! NOTE : Solver addes a prefix "User_Cell_" for cell data and
!        "User_Nodal_" for nodal data to the variable name.
!        In CFD-VIEW list you will see the variable as "User_Nodal_<name>".
!        When you want to read the variable using uread_dtf, use these
!        prefixes accordingly. The reason solver adds these prefixes to
!        avoid conflicts in names being used by solver.
!----------------------------------------------------------------------

! Include required global variables declared in cfdrc_user module.
  USE cfdrc_user, ONLY : int_p, real_p, string_length
  USE cfdrc_user, ONLY : global_averages,global_var_name

IMPLICIT NONE

! Declare required local variables here.
! USER VARIABLE DECLARATION BEGIN

integer(int_p)::i !counting variable/s
character(string_length):: varname !name placeholder for call
real(real_p),dimension(:),allocatable::values
logical::logical_error=.false.

! USER VARIABLE DECLARATION END

!----------------------------------------------------------------------
! Start writing code here.
! USER CODE BEGIN

allocate(values(size(global_averages,2)))
print *,"Attempting to write user data"
!print *,"UWRITE averages",global_averages(1,1)

do i=1,size(global_var_name,1),1
   varname=global_var_name(i)
   values=global_averages(i,:)
   call write_nodal_data_to_dtf(varname, size(global_averages,2), values, "",
logical_error)
```

```
   call write_cell_data_to_dtf(varname, size(global_averages,2), values, "",
logical_error)
   if (logical_error) then
      print *,"There was an error writing the nodal or cell data"
      exit
   end if
end do


! USER CODE END
RETURN
END SUBROUTINE uwrite_dtf
```

# Appendix E Additional Measurements from the Experimental Data of Hay (1947)

## *E.1. Introduction and Experimental Methodology*

Hay published the results of a study that towed a circular cylinder along a tow tank as a component of a larger study undertaken at Princeton University to investigate the "resistance of simple geometrically-shaped forms towed through the water surface" (Hay, 1947). The bulk of the data from these experiments was presented as a set of images of the shape of the free surface that illustrated the flow conditions at different Reynolds and Froude Numbers. Two cameras were used to capture these images with one above the free surface and the second below the surface and perpendicular to the cylinder as shown in Figure E-1.

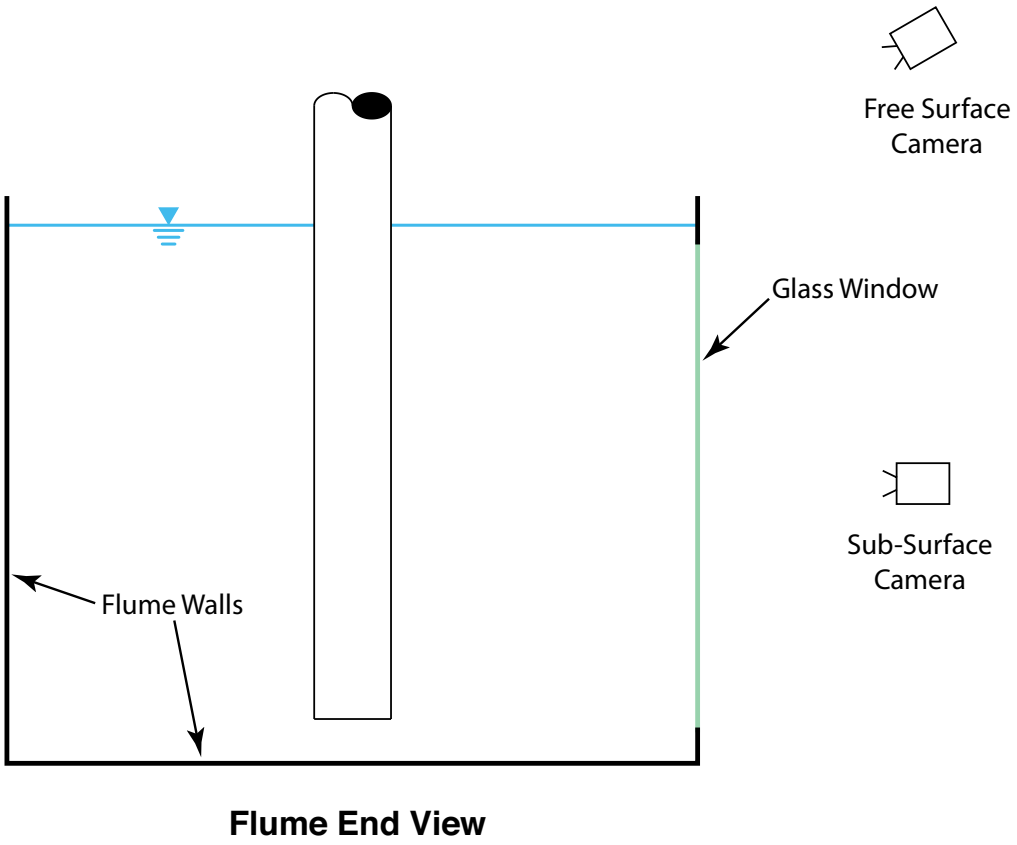


**Figure E-1 – Sketch of the two camera locations used in the experimental investigation of Hay with the direction of travel of the cylinder into the page.**

In addition to the qualitative free surface descriptions the images were projected onto a screen and scaled measurements of wave height and lengths were made.

Six wave shape parameters in total were measured, as illustrated in Figure E-2, but only four of these six, $D_1$, $L_3$, $D_3$ and $L_0$, will be used in this research. The $L_2$ and $D_2$ parameters were not used, as there was a very high degree of uncertainty in their description and, hence, their measurement. $L_3$ and $D_3$ describes the length downstream from the cylinder and height above the at rest free surface, respectively, of the rooster tail, while $D_1$ represents the height of the bow wave above the at rest free surface and $L_{ac}$ is the depth of the air column below the at rest free surface.

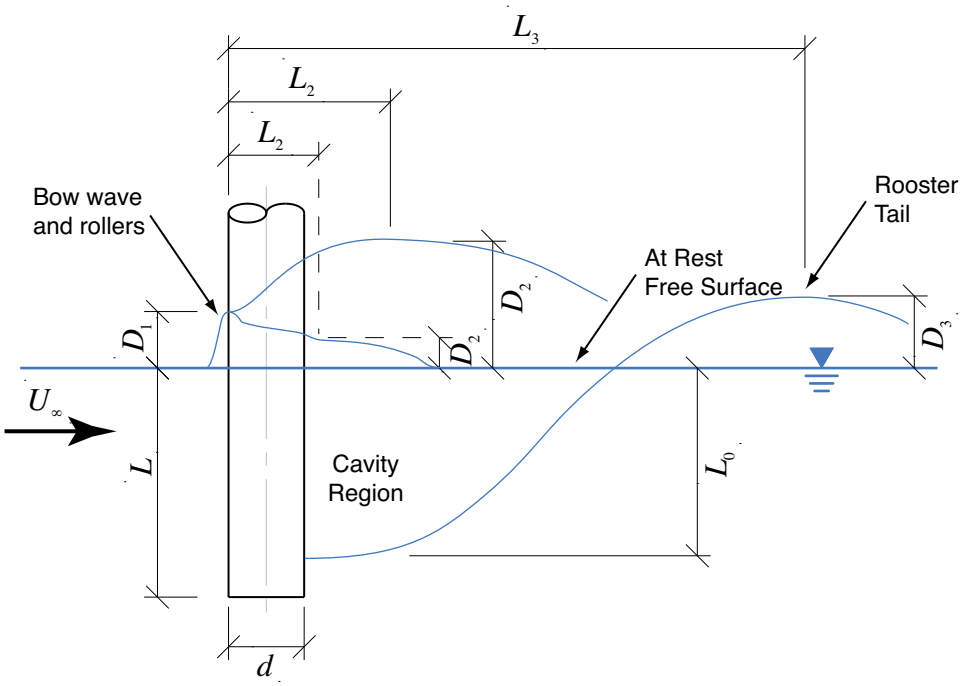


**Figure E-2 – Sketch of the Measurement Locations for the Wave Shape Parameters**

As these measurements were scaled from projections of still images of the flow there are a number of additional sources of error that could have been introduced including parallax and projection distortion. In the original paper Hay acknowledged that there were going to be errors in the data but made no effort to quantify them.

Further, as with all experimental data there were some of the parameters, shown in Figure E-2, which could either not be measured at each image or were not published by Hay. However, during the examination of the photographic data for the present research a number of the plates were identified as suitable for measurement but were

not included in the tables published by Hay (1947). Hence, measurements were taken from these plates for inclusion with the present work.

## *E.2. Additional Wave Height Measurements*

In a similar method to that used by Hay, the wave shape parameters, shown in Figure E-2, were scaled from photographic plates[1]. Whereas Hay projected the images onto a screen and scaled the data directly from the screen, Adobe Photoshop (Adobe Systems Incorporated, 2007) was used in the present work to measure the distances.

Of the 64 plates taken through the side window with the camera perpendicular to the two-inch cylinder, three were suitable for additional measurement. The remaining images either had been measured by Hay or were un-measurable due to shadowing or other optical effects. Due to the size of the waves relative to the scale of the image, only the length to the crest of the rooster tail, $L_3$, could be measured with certainty and is shown in Figure E-3, Figure E-4 and Figure E-5 for the 2", 4" and 8" depths, respectively, at a velocity of 3ft/s.

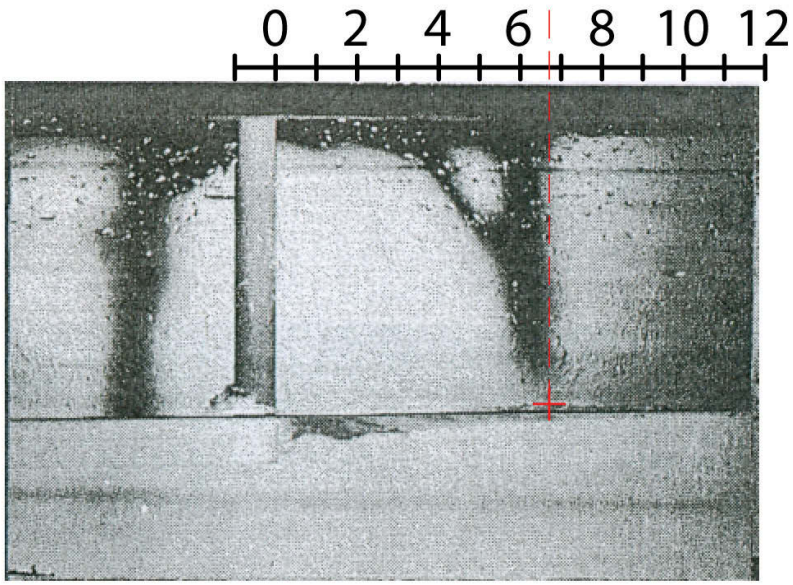


**Figure E-3 – Two inch depth, two inch diameter cylinder at 3ft/s reproduced from Hay (1947) Plate 74.**

[1] The photographic plates in the original publication (Hay, 1947) were all presented with the cylinder moving from left to right, so the flow appears to be moving from right to left. However, to maintain the convention of left to right flows used in this thesis, the photographic images of Hay were mirrored.

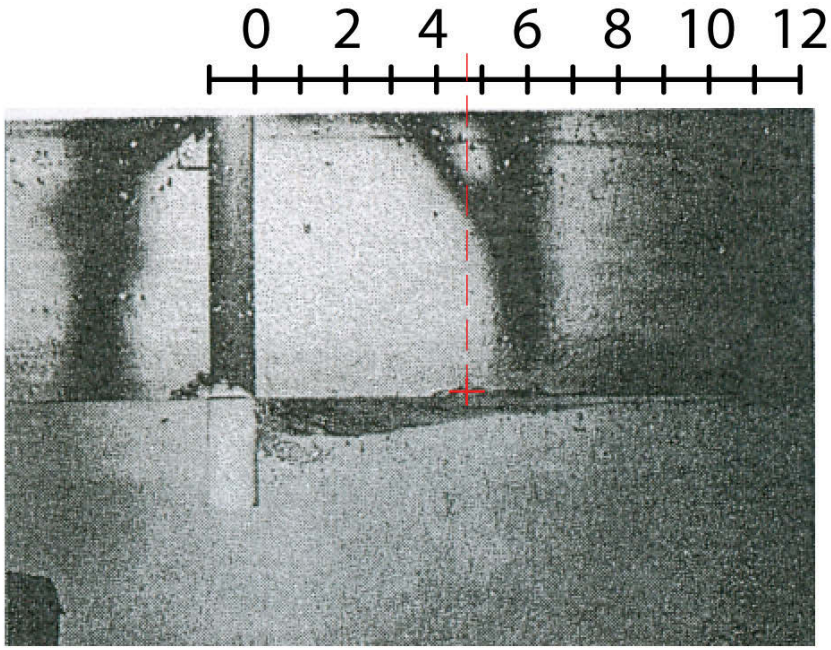


**Figure E-4 – Four inch depth, two inch diameter cylinder at 3ft/s reproduced from Hay (1947) Plate 75.**

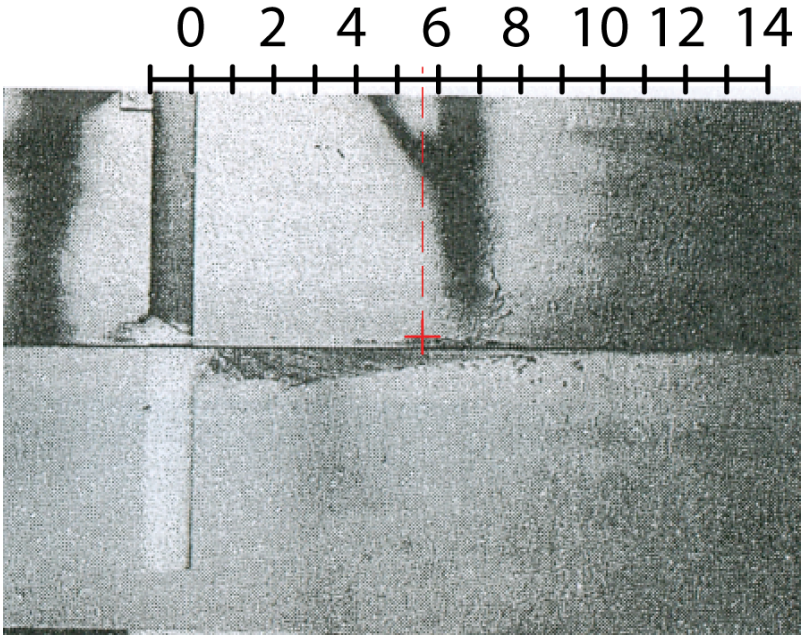


**Figure E-5 – Eight inch depth, two inch diameter cylinder at 3ft/s reproduced from Hay (1947) Plate 76.**

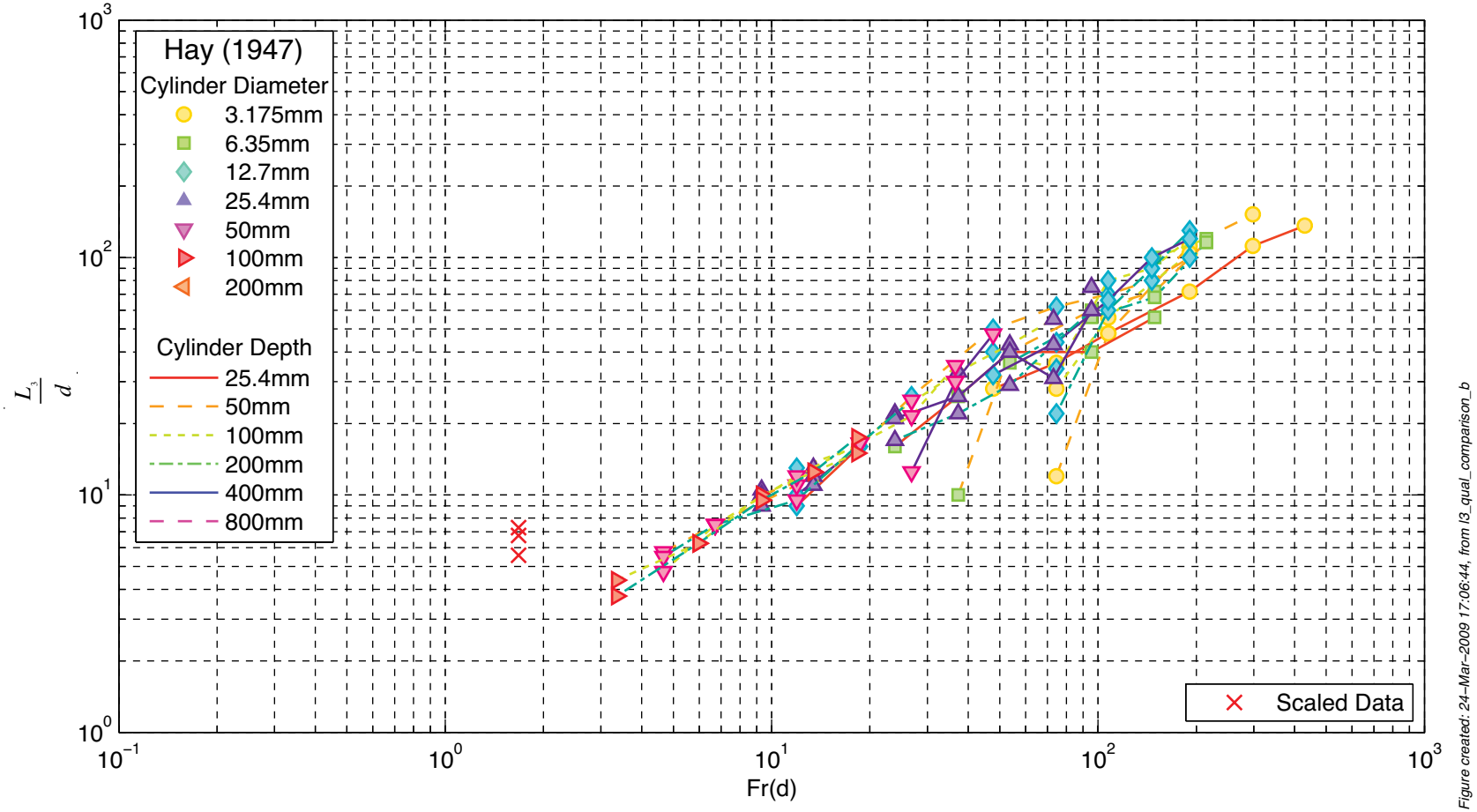


**Figure E-6 – Normalised rooster tail lengths as a function for $Fr_d$ from Hay (1947).**

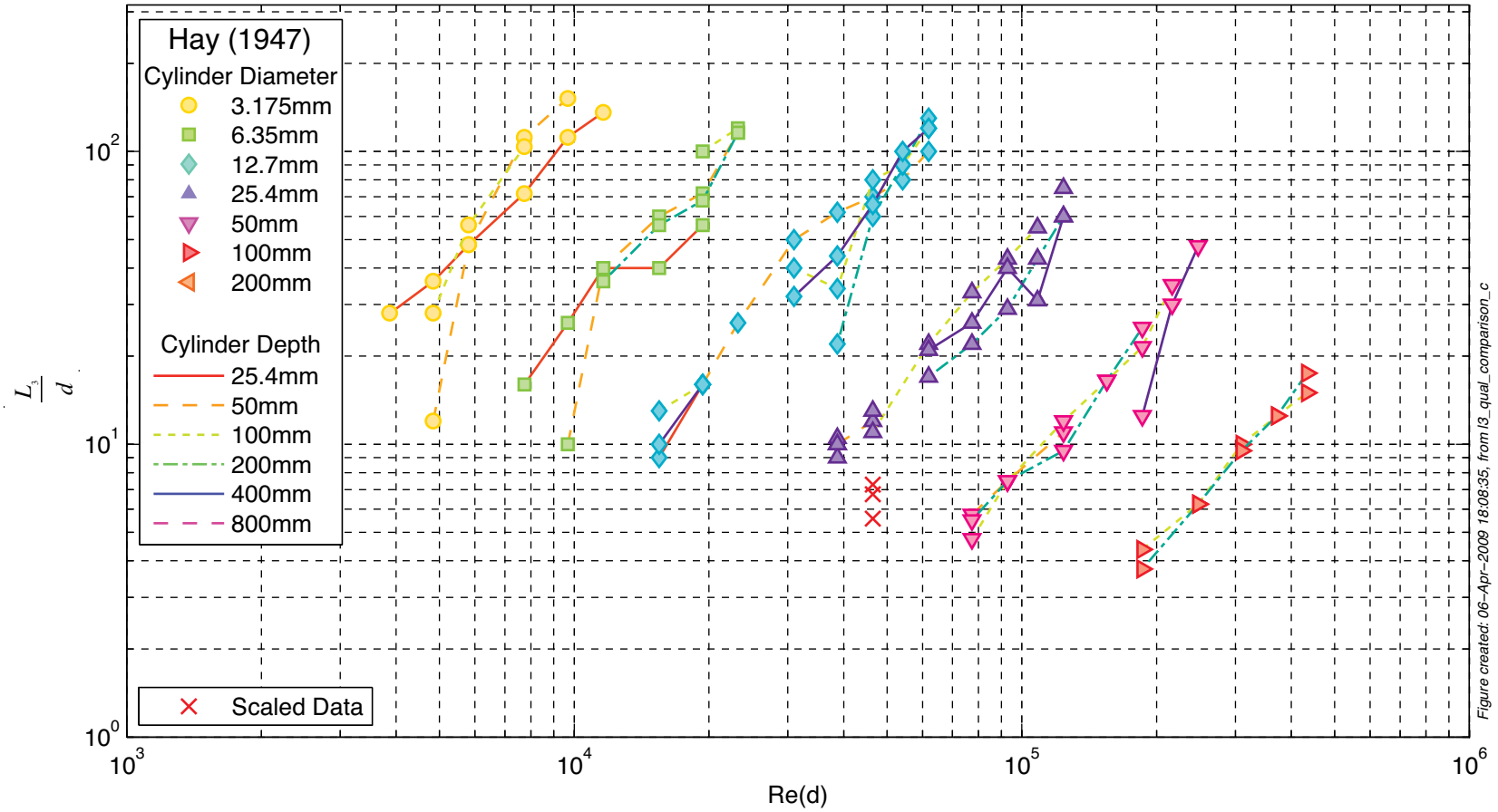


**Figure E-7 – Normalised rooster tail length as a function of $Re_d$ from Hay (1947).**